gels

Gels
Synthesis, Characterization and Applications in High Performance Chemistry

Edited by
Viorel-Puiu Paun
Printed Edition of the Special Issue Published in *Gels*

MDPI

Gels: Synthesis, Characterization and Applications in High Performance Chemistry

Gels: Synthesis, Characterization and Applications in High Performance Chemistry

Editor

Viorel-Puiu Paun

MDPI

Editor
Viorel-Puiu Paun
Department of Physics
University Politehnica of
Bucharest
Bucharest
Romania

This is a reprint of articles from the Special Issue published online in the open access journal *Gels* (ISSN 2310-2861) (available at: www.mdpi.com/journal/gels/special_issues/gels_chemistry).

For citation purposes, cite each article independently as indicated on the article page online and as indicated below:

LastName, A.A.; LastName, B.B.; LastName, C.C. Article Title. *Journal Name* **Year**, *Volume Number*, Page Range.

Contents

About the Editor

Viorel-Puiu Paun

Viorel-Puiu Paun is full university professor of Physics at Politehnica University of Bucharest, Faculty of Applied Sciences, Physics Department, and corresponding member of Academy of Romanian Scientists. The main areas of his scientific interest are the nonlinear dynamics and chaos theory, with their applications in different physico-chemical systems (nanostructures, composites), biological systems, and in human organs, such as the brain, lungs, and stomach. More precisely, he is expert in fractal interpretation of common diagnostic medical imaging tests (X-rays, CT Scan, MRI, etc.). He is further preoccupied about the knowledge and use of new composite materials, successfully used in oral rehabilitation. He is interested in material physico-chemical properties, compatibility with human tissue and their validity over time, in operation. He has extensive research competences in all the above-mentioned fields, including the time series method, fractals analysis, and diffusion process. Viorel-Puiu Paun has published more than 150 papers in national and international journals, 115 ISI journal papers, 50 communications in national and international meetings (more than 30 on invitation), 577 citations without self-citations, respectively, and 20 books, chapters in books, and monographs. His Hirsch factor value is currently 22. He was a guest/visiting professor at nine prestigious universities in Europe, including among other University of Cambridge, UK (2015), École Polytechnique Fédérale de Lausanne (EPFL), Switzerland (1996–1997, 2014), University of Florence, Italy (2011), ENSICA Toulouse, France (2007), School of Physical Sciences, Kent University, Canterbury, UK (2004, 2006).

Preface to "Gels: Synthesis, Characterization and Applications in High Performance Chemistry"

Organogels, hydrogels, and ionic gels have been investigated both in a theoretical and experimental manner. The research performed was focused on their synthesis and applications in high-performance chemistry and its important branches. All the above-mentioned gels were characterized from structural and supramolecular points of view by FTIR, NMR, X-ray diffraction, and POM. The keywords proposed in this reprint were as follows: organogels, hydrogels, ionic gels, chitosan, and fractal analysis. These terms were extremely pertinent to this research piece, hereby presented. As a result, all reference themes, as well as those associated with them, were touched upon in this reprint. We mention that the articles in this selection focused on one or more of the topics listed above.

The hydrogel investigation for wound-healing applications has been also well depicted. The hydrogel biodegradation has been monitored in media mimicking the wound exudate by gravimetrical measurements, SEM imaging, and SEM fractal analysis of representative images. The pictures of interest could be evaluated by fractal analysis, calculating the fractal parameters, respectively, fractal dimension and lacunarity values, as a quantitative measure of the homogeneity of the material and its texture through their topological analysis in some of the reference works. As a consecration of these studies developed on this occasion, materials biocompatibility, antimicrobial properties, and biodegradation have been considered in vitro in relevant scientific works that were referenced and included in this volume.

Viorel-Puiu Paun
Editor

Gels: Synthesis, Characterization and Applications in High Performance Chemistry

Viorel-Puiu Paun [1,2]

1   Department of Physics, Faculty of Applied Sciences, University Politehnica of Bucharest, 060042 Bucharest, Romania; viorel.paun@physics.pub.ro
2   Academy of Romanian Scientists, 050094 Bucharest, Romania

Organogels, hydrogels, and ionic gels are investigated both theoretically and experimentally. Detailed research is focused on both their synthesis and applications in high-performance chemistry and its important branches. All of the abovementioned gels are characterized from structural and supramolecular points of view by FTIR, NMR, X-ray diffraction, and POM. The keywords proposed on this occasion are as follows: organogels, hydrogels, ionic gels, chitosan, fractal analysis; these terms are extremely pertinent to this research piece. As a result, all these reference themes, as well as those associated with them, are touched upon in this Editorial.

The articles in this selection are assumed to focus on one or more of the topics listed above. Now that we have in front of us all of the works published in the journal under the auspices of the Special Issue proposed by the Guest Editor, who later became the editor of this volume, we can consider the central topic the refined analysis of hydrogels, including, for example, the minting of coins on chitosan. The investigation of a hydrogel for wound-healing applications has been also well received. The biodegradation of the hydrogel has been monitored in media mimicking the wound exudate by gravimetrical measurements, SEM imaging, and fractal analysis of SEM and pictures. The images of interest could be evaluated by fractal analysis, calculating the fractal dimension and the lacunarity values as a quantitative measure of the homogeneity of the material and its texture through their topological analysis in some of the reference works. In addition, its biocompatibility, antimicrobial properties, and biodegradation have been considered in vitro in scientific papers that were referenced on this occasion and included in this volume.

The works edited in this book are the ones that appeared in the journal *Gels* in a Special Issue with the same name, more precisely the 16 distinct published papers plus an Editorial, signed by the editor of this volume.

An evaluation by multifractal analysis was applied to the images related to xerogel morphology details obtained by multifractal analysis and scanning electron microscopy. This work is the first introduced in this Editorial. The title of the work is "Xerogels Morphology Details by Multifractal Analysis and Scanning Electron Microscopy Images Evaluations of 5-Fluorouracil Release from Chitosan-Based Matrix", the authors of which are Maria-Alexandra Paun, Mihai-Virgil Nichita, Vladimir-Alexandru Paun and Viorel-Puiu Paun. Four medicament delivery formulations based on 5-fluorouracil in a chitosan substantial matrix were realized in situ via 3,7-dimethyl-2,6-octadienal element hydrogelation. Representative samples of the final realized compounds were investigated from an analytic, constitutional, and morphological viewpoint via Fourier transform infrared (FTIR) spectroscopy and scanning electron microscopy (SEM). The SEM images of the formulations were investigated in concordance with fractal analysis, and the fractal dimensions and lacunarity were computed. The developed mathematical multifractal model is necessarily confirmed by the experimental measurements corresponding to the 5-fluorouracil release outside the chitosan-formed matrix [1].

The second work presented is named "A Modified Sol–Gel Synthesis of Anatase {001}-TiO$_2$/Au Hybrid Nanocomposites for Enhanced Photodegradation of Organic Contaminants", the authors of which are Abubakar Katsina Usman, Diana-Luciana Cursaru, Gheorghe Brănoiu, Raluca Şomoghi, Ana-Maria Manta, Dănuţa Matei and Sonia Mihai. A sol–gel synthesis technique was employed for the preparation of anatase phase {001}-TiO$_2$/Au hybrid nanocomposites (NCs). A scalable, schematic, and cost-efficient method was successfully modified using HF and NH4OH capping agents. The photocatalytic activity of the as-synthesized {001}-TiO$_2$/Au NCs was tested over two-cycle degradation of methylene blue (MB) dye and pharmaceutical active compounds (PhACs) of ibuprofen and naproxen under direct sunlight illumination at 35 °C and 44,000 lx. Transmission electron microscopy (TEM), high-resolution transmission electron microscopy (HR-TEM), fast Fourier transform (FFT), X-ray diffraction (XRD), X-ray photoelectron spectroscopy (XPS), energy dispersive X-ray spectroscopy (EDS), and ultraviolet–visible diffuse reflectance spectroscopy (UV–Vis DRS) were employed for the characterization of the as-prepared sample. The characterization results from the TEM, XPS, and XRD studies established both the distribution of Au colloids on the surface of TiO$_2$ material and the presence of the highly crystalline structure of anatase {001}-TiO$_2$/Au NCs. Photodegradation results from the visible light irradiation of MB indicate the enhanced photocatalytic performance of Au/TiO$_2$ NCs over TiO$_2$. The results from the photocatalytic activity test performed under direct sunlight exposure exhibited promising photodegradation efficiencies. In the first cycle, the sol–gel synthesized material exhibited relatively better efficiencies (91%) with the MB dye and ibuprofen, while the highest degradation efficiency for the second cycle was 79% for the MB dye. Pseudo first-order photodegradation rates from the first cycle were determined to be comparatively slower than those from the second degradation cycle [2].

The third work is entitled "Structural, Optical, and Sensing Properties of Nb-Doped ITO Thin Films Deposited by the Sol–Gel Method", the authors of which are Madalina Nicolescu, Daiana Mitrea, Cristian Hornoiu, Silviu Preda, Hermine Stroescu, Mihai Anastasescu, Jose Maria Calderon-Moreno, Luminita Predoana, Valentin Serban Teodorescu, Valentin-Adrian Maraloiu, Maria Zaharescu and Mariuca Gartner. The aim of the present study was the development of Nb-doped ITO thin films for carbon monoxide (CO) sensing applications. The detection of CO is imperious because of its high toxicity, with long-term exposure having a negative impact on human health. Using a feasible sol–gel method, the doped ITO thin films were prepared at room temperature and deposited onto various substrates (Si, SiO$_2$/glass, and glass). The structural, morphological, and optical characterization was performed by the following techniques: X-ray diffractometry (XRD), atomic force microscopy (AFM), scanning electron microscopy (SEM), transmission electron microscopy (TEM), and UV/Vis/NIR spectroscopic ellipsometry (SE). The analysis revealed a crystalline structure and a low surface roughness of the doped ITO-based thin films. XTEM analysis (cross-sectional transmission electron microscopy) showed that the film has crystallites of the order of 5–10 nm and relatively large pores (around 3–5 nm in diameter). A transmittance value of 80% in the visible region and an optical band-gap energy of around 3.7 eV were found for dip-coated ITO/Nb films on SiO$_2$/glass and glass supports. The EDX measurements proved the presence of Nb in the ITO film in a molar ratio of 3.7%, close to the intended one (4%). Gas testing measurements were carried out on the ITO undoped and doped thin films deposited on glass substrate. The presence of Nb in the ITO matrix increases the electrical signal and the sensitivity to CO detection, leading to the highest response for a 2000 ppm CO concentration at a working temperature of 300 °C [3].

The fourth paper in this presentation is a study entitled "Low Release Study of Cefotaxime by Functionalized Mesoporous Silica Nanomaterials", whose authors are Dan Eduard Mihaiescu, Daniela Istrati, Alina Moroșan, Maria Stanca, Bogdan Purcăreanu, Rodica Cristescu, Bogdan Ștefan Vasile and Roxana Doina Trușca. Here, a well-known antibiotic is discussed. As a third-generation β-lactam antibiotic, cefotaxime displays a broad spectrum with Gram-positive and Gram-negative bacteria activity and is included in the WHO's essential drug list. In order to obtain new materials with sustained re-

lease properties, the present research focuses on the study of cefotaxime absorption and desorption from different functionalized mesoporous silica supports. The MCM-41-type nanostructured mesoporous silica support was synthesized by the sol–gel technique using a tetraethyl orthosilicate (TEOS) route and cetyltrimethylammonium bromide (CTAB) as a surfactant, at room temperature and normal pressure. The obtained mesoporous material (MCM-41 class) was characterized through nuclear magnetic resonance (NMR), scanning electron microscopy (SEM), high-resolution transmission electron microscopy (HR-TEM), N2 absorption–desorption (BET) and Fourier transform infrared spectroscopy (FT-IR), demonstrating a good micro-structured homogeneity (SEM images), a high surface area (BET, 1029 m^2/g) correlated with high silanolic activity (Q3/Q4 peak ratio from 29Si MAS-NMR), and an expected uniform hexagonal structure (2–3 nm, HRTEM). In order to non-destructively link the antibiotic compound on the solid phase, MCM-41 was further functionalized in two steps: with aminopropyl trimethoxysilane (APTMS) and glutaraldehyde (GA). Three cefotaxime-loaded materials were comparatively studied for low release capacity: the reference material with adsorbed cefotaxime on MCM-41, MCM-41/APS (aminopropyl silyl surface functionalization) adsorbed cefotaxime material, and APTMS–GA bounded MCM-41—cefotaxime material. The slow-release profiles were obtained by using an on-flow modified HPLC system. A significant improved release capacity was identified in the case of MCM-41/APS/GA—cefotaxime due to the covalent surface grafting of the biological active compound, recommending this class of materials as an effective carrier of bioactive compounds in wound dressing, anti-biofilm coatings, advanced drugs, and other related applications [4].

The fifth work is called "TEGylated Phenothiazine-Imine-Chitosan Materials as a Promising Framework for Mercury Recovery", and has the following authors: Sandu Cibotaru, Daniela Ailincai, Bianca-Iustina Andreica, Xinjian Cheng, and Luminita Marin. This paper reports new solid materials based on TEGylated phenothiazine and chitosan, with a high capacity to recover mercury ions from aqueous solutions. They were prepared by hydrogelation of chitosan with a formyl derivative of TEGylated phenothiazine, followed by lyophilization. Their structural and supramolecular characterization was carried out by 1H-NMR and FTIR spectroscopy, as well as X-ray diffraction and polarized light microscopy. Their morphology was investigated by scanning electron microscopy, and their photophysical behaviour was examined by UV/Vis and emission spectroscopy. Swelling evaluation in different aqueous media indicated the key role played by the supramolecular organization for their hydrolytic stability. Mercury recovery experiments and the analysis of the resulting materials by X-ray diffraction and FTIR spectroscopy showed a high ability of the studied materials to bind mercury ions by coordination with the sulfur atom of phenothiazine, imine linkage, and amine units of chitosan [5].

The sixth work in this suite is "Magnetic Application of Gadolinium Orthoferrite Nanoparticles Synthesized by Sol–Gel Auto-Combustion Method", authored by Loganathan Guganathan, Chinnaiyan Rajeevgandhi, Kaliyamurthy Sathiyamurthy, Kokila Thirupathi, Madhappan Santhamoorthy, Ellappan Chinnasamy, Chaitany Jayprakash Raorane, Vinit Raj, Seong-Cheol Kim and Pichapillai Anand. In this manuscript, the synthesis of gadolinium orthoferrite nanoparticles using the sol–gel auto-combustion technique is presented. The obtained gadolinium orthoferrite nanoparticles were annealed at various temperatures, including 800 °C, 900 °C, 1000 °C, and 1100 °C. The synthesized materials were analyzed by various instrumental characterizations. The vibrational characteristics of the synthesized samples were verified by FTIR. The surface morphology of the gadolinium orthoferrite nanoparticles was analyzed by FE-SEM and HR-TEM, revealing their spherical structural morphology and uniform particle structure. The presence of the elemental features was analyzed in the gadolinium orthoferrite nanoparticles by EDAX. The surface analysis of the core ranges of the XPS-recorded spectra were obtained for the elemental states of the Gd, Fe, and O factors in the samples, and it additionally characterized the different levels of oxidative states by fitting the levels of the high-resolution parameters of Gd 4d, Fe 2p, and O 1s. The magnetic properties of the samples were investigated by VSM. The measurement

of the magnetic parameters revealed that gadolinium orthoferrite nanoparticles exhibit a ferromagnetic nature [6].

The seventh paper is called "Photocatalytic and Antibacterial Properties of Doped TiO$_2$ Nanopowders Synthesized by Sol−Gel Method", authored by Silviu Preda, Jeanina Pandele-Cușu, Simona Viorica Petrescu, Elena Mădălina Ciobanu, Gabriela Petcu, Daniela C Culita, Nicoleta G. Apostol, Ruxandra M. Costescu, Iuliana Raut, Mariana Constantin and Luminița Predoană. For environmental applications, nanosized TiO$_2$-based materials are known as the most important photocatalysts and are intensively studied for advantages including their higher activity, lower price, and chemical and photoresist properties. Zn- or Cu-doped TiO$_2$ nanoparticles with anatase crystalline structures were synthesized by the sol−gel process. Titanium (IV) butoxide was used as a TiO$_2$ precursor, with parental alcohol as a solvent, and a hydrolysing agent (ammonia-containing water) was added to obtain a solution with pH 10. The gels were characterized by TG/DTA analysis, SEM, and XPS. Based on TG/DTA results, a temperature of 500 °C was chosen for processing the powders in air. The structure of the samples thermally treated at 500 °C was analysed by XRD, and the patterns show crystallization in a single phase of TiO$_2$ (anatase). The surface of the samples and the oxidation states were investigated by XPS, confirming the presence of Ti, O, Zn, and Cu. The antibacterial activity of the nanoparticle powder samples was verified using the Gram-positive bacterium Staphylococcus aureus. The photocatalytic efficiency of the doped TiO$_2$ nanopowders for the degradation of methyl orange (MO) was examined here to evaluate the potential applications of these materials for environmental remediation [7].

The next work, eighth in order on the list, is "A Multifractal Vision of 5-Fluorouracil Release from Chitosan-Based Matrix", authored by Maria-Alexandra Paun, Vladimir-Alexandru Paun, and Viorel-Puiu Paun. A suite of four drug-deliverance formulations grounded on 5-fluorouracil enclosed in a chitosan-founded intercellular substance was produced by 3,7-dimethyl-2,6-octadienal with in situ hydrogelation. The formulations were examined from a morphological and structural point of view by Fourier transform infrared (FTIR) spectroscopy and microscopy with polarized light. The polarized optical microscopy (POM) pictures of the three obtained representative formulations were investigated by fractal analysis. The fractal dimension and lacunarity of each of them were thus calculated. In this paper, a novel theoretical method for mathematically describing medicament deliverance dynamics in the context of the polymeric medicament constitution limit has been advanced. Assuming that the polymeric drug motion unfolds only on the so-called non-differentiable curves (considered mathematically multifractal curves), it appears that in a one-dimensional hydrodynamic movement within a multifractal formalism, the drug-release physics models are provided by isochronous kinetics, but at a scale of resolution necessarily non-differentiable [8].

The ninth paper presented here is "A Molecular Description of Hydrogel Forming Polymers for Cement-Based Printing Paste Applications", with the following authors: Hajar Taheri-Afarani, Eugene Mamontov, William R. Carroll and Joseph J. Biernacki. This research endeavors to link the physical and chemical characteristics of select polymer hydrogels to differences in printability when used as printing aids in cement-based printing pastes. A variety of experimental probes including differential scanning calorimetry (DSC), NMR-diffusion ordered spectroscopy (DOSY), quasi-elastic neutron scattering (QENS) using neutron backscattering spectroscopy, and X-ray powder diffraction (XRD), along with molecular dynamic simulations, were used. Conjectures based on objective measures of printability and physical and chemical–molecular characteristics of the polymer gels are emerging that should help target printing aid selection and design and mix formulation. Molecular simulations were shown to link a higher hydrogen bond probability and larger radius of gyration to higher-viscosity gels. Furthermore, the higher-viscosity gels also produced higher elastic properties, as measured by neutron backscattering spectroscopy [9].

The tenth paper, entitled "Study on the Hydration Reaction of Typical Clay Minerals under Alkali and Sulfate Compound Activation" is authored by Siqi Zhang, Zeping Wu,

Jiaming Chen, Runsheng Xu, Meina Wang, and Wen Ni. Sand, stone, tailings, and other aggregates often contain a small amount of clay mineral, and their hydration activity is low, thereby lowering the concrete performance indexes while negatively affecting their resource utilisation. In this study, clay minerals, calcium hydroxide, and desulfurised gypsum were used to prepare cementitious materials to examine kaolinite, montmorillonite, illite, and chlorite clay mineral contents under compound activation. The effects of the curing temperature and water reducer on clay samples were analysed. The results showed that the compressive strength of kaolinite samples cured at 25 °C and 55 °C reached 1.09 and 4.93 MPa in 28 days and increased by 43% and 12%, respectively, after adding a 0.3% water reducer. Montmorillonite was activated, and its compressive strength reached 5.33 MPa after curing at 55 °C in 28 days. Illite exhibited some activity and its compressive strength reached 1.43 MPa after curing at 55 °C in 28 days, and the strength increased slightly after adding a water reducer. The chlorite sample had no strength after activation under the same conditions. Furthermore, X-ray diffraction and scanning electron microscopy and energy-dispersive spectroscopy microstructure analyses showed that after alkali and sulfate activation, the hydration products of activated clay minerals mainly included ettringite, hydrated calcium aluminate, and hydrated calcium silicate. The increase in curing temperature accelerated the reaction speed and improved the early strength. However, the effect on chlorite minerals was not obvious [10].

The eleventh study, entitled "Synthesis and Characterization of Fly Ash-Based Geopolymers Activated with Spent Caustic", was authored by Ruobing Zhang, Qian Wan, Yimin Zhang and Xuemian Zhang. The spent caustic with strong alkali first replaced the alkali activator to prepare the geopolymer. The influence of spent caustic to the geopolymer was characterized through compressive strength measurement, XRD, MIP analysis and NMR, and the immobilization efficiency of organics in geopolymer was evaluated through the measurement of the total organic carbon (TOC). The results show that the spent caustic can partially replace the alkali activator to prepare the geopolymer, and it shows a better performance than that activated with pure NaOH solution when the alkalinity was between 4 mol and 14 mol. The organic matter in the spent alkali can be effectively fixed in the geopolymer, which will hinder the geopolymerization in the initial stage of the polymerization reaction but has little effect on the chemical structure and mechanical properties of the final product. With the degree of alkalinity increasing, the immobilization efficiency is improved, and the maximum can reach 84.5%. The organics in the spent caustic will hinder geopolymerization at the initial stage but have little effect on the chemical structure and mechanical property of the final product. This study proposes a new method for the recycling of spent caustic, which also reduces the preparation cost of geopolymers [11].

The twelfth paper is entitled "Hydrogel Beads of Amidoximated Starch and Chitosan as Efficient Sorbents for Inorganic and Organic Compounds", with the authors listed as follows: Diana Felicia Loghin, Melinda Maria Bazarghideanu, Silvia Vasiliu, Stefania Racovita, Marius-Mihai Zaharia, Tudor Vasiliu, and Marcela Mihai. The synthesis of hydrogel beads involving natural polymers is, nowadays, a leading research area. Among natural polymers, starch and chitosan represent two biomolecules with proof of efficiency and a low economic impact in various utilization fields. Therefore, herein, the features of hydrogel beads obtained from chitosan and three sorts of starch (potato, wheat, and rice starches), grafted with acrylonitrile and then amidoximated, were extensively investigated for their use as sorbents for heavy-metal ions and dyes. The hydrogel beads were prepared by ionotropic gelation/covalent cross-linking of chitosan and functionalized starches. The chemical structure of the hydrogel beads was analyzed by FT-IR spectroscopy; their morphology was revealed by optical and scanning electron microscopies, while the influence of the starch functionalization strategies on the crystallinity changes was evaluated by X-ray diffraction. Molecular dynamics simulations were used to reveal the influence of the grafting reactions and grafted structure on the starch conformation in solution and their interactions with chitosan. The sorption capacity of the hydrogel beads was tested in batch experiments, as a function of the beads' features (synthesis protocol, starch sort) and

simulated polluted water, which included heavy metal ions (Cu^{2+}, Co^{2+}, Ni^{2+} and Zn^{2+}) and small organic molecules (Direct Blue 15 and Congo red) [12].

We now present paper number thirteen, "Photopolymerizable Ionogel with Healable Properties Based on Dioxaborolane Vitrimer Chemistry", whose authors are Fengdi Li, Giao T. M. Nguyen, Cédric Vancaeyzeele, Frédéric Vidal and Cédric Plesse. Ionogels are solid polymer gel networks loaded with ionic liquid (IL) percolating throughout each other, giving rise to ionically conducting solid electrolytes. They combine the mechanical properties of polymer networks with the ionic conductivity, non-volatility, and non-flammability of ILs. In the frame of their applications in electrochemical-based flexible electronics, ionogels are usually subjected to repeated deformation, making them susceptible to damage. It appears critical to devise a simple and effective strategy to improve their durability and lifespan by imparting them with healing ability through vitrimer chemistry. In this work, we report the original in situ synthesis of polythioether (PTE)-based vitrimer ionogels using fast photopolymerization through thiol-acrylate Michael addition. PTE-based vitrimer was prepared with a constant amount of the trithiol crosslinker and varied proportions of static dithiol spacers and dynamic chain extender BDB containing dynamic exchangeable boronic ester groups. The dynamic ionogels were prepared using 50 wt% of either 1-Ethyl-3-methylimidazolium bis(trifluoromethylsulfonyl) imide or 1-Ethyl-3-methylimidazolium trifluoromethanesulfonate, both of which were selected for their high ionic conductivity. They are completely amorphous (T_g below $-30\ ^\circ$C), suggesting they can be used at low temperatures. They are stretchable with an elongation at break around 60%, soft with a Young's modulus between 0.4 and 0.6 MPa, and they have high ionic conductivities for solid-state electrolytes in the order of 10^{-4} S·cm^{-1} at room temperature. They display dynamic properties typical of the vitrimer network, such as stress relaxation and healing, retained despite the large quantity of IL. The design concept illustrated in this work further enlarges the library of vitrimer ionogels and could potentially open a new path for the development of more sustainable, flexible electrochemical-based electronics with extended service life through repair or reprocessing [13].

The fourteenth paper is called "Hybrid Epoxy-Alkyl Sol–Gel Coatings Reinforced with SiO_2 Nanoparticles for Corrosion Protection of Anodized AZ31B Mg Alloy"; its authors are Emilia Merino, Alicia Durán, Silvia Ceré, and Yolanda Castro. AZ31B Mg alloys were anodized at different potentials using an alkaline electrolyte. Then, an epoxy-alkyl silane sol reinforced with SiO_2 nanoparticles was prepared by sol–gel and deposited on top of the optimized anodic layers. 1-Methyl imidazole was added to the sol to promote a partial epoxy ring aperture and improve the condensation degree of the inorganic network. The results showed that the curing temperature affects the inorganic polycondensation of the organic–inorganic network; this effect was analyzed by ^{29}Si and ^{13}C solid-state NMR spectroscopy. Electrochemical impedance spectroscopy in 3.5 wt% NaCl solution revealed that the corrosion resistance is enhanced by the anodized process obtained for Mg alloy anodized at 100 V/2 min. However, quick deterioration of the oxide film with immersion time was evident, showing a reduction in the protection efficiency (ηE%) of 76.5% after 16 h/immersion. The deposition of an epoxy-alkyl coating improved the ηE% by up to 98.6% after 72 h/immersion. The proposed hybrid coating used for post-sealing the porous anodized Mg alloy looks to be a good alternative protective barrier to control the corrosion process of Mg alloys. A suitable compromise between the cross-linking network and curing temperature is necessary to obtain a good barrier coating [14].

The penultimate paper presented, the fifteenth, is entitled "Biocompatible Chitosan-Based Hydrogels for Bioabsorbable Wound Dressings", and has the following authors: Ramona Lungu, Maria-Alexandra Paun, Dragos Peptanariu, Daniela Ailincai, Luminita Marin, Mihai-Virgil Nichita, Vladimir-Alexandru Paun, and Viorel-Puiu Paun. Supramolecular hydrogels based on chitosan and monoaldehydes are biomaterials with high potential for a multitude of bioapplications. This is due to the proper choice of the monoaldehyde that can tune the hydrogel properties for specific practices. In this conceptual framework, the present paper deals with the investigation of a hydrogel used as a bioabsorbable wound

dressing. To this aim, chitosan was cross-linked with 2-formylphenylboronic acid to yield a hydrogel with antimicrobial activity. FTIR, NMR, and POM procedures have characterized the hydrogel from a structural and supramolecular point of view. At the same time, its biocompatibility and antimicrobial properties were also determined in vitro. Furthermore, in order to assess the bioabsorbable character, its biodegradation was investigated in vitro in the presence of lysosome in media of different pH values, mimicking the wound exudate at different stages of healing. The biodegradation was monitored by gravimetrical measurements, SEM microscopy, and fractal analyses of the images. The fractal dimension values and the lacunarity of SEM pictures were accurately calculated. All these successful investigations led to the conclusion that the tested materials are at the expected high standards [15].

The sixteenth paper and final paper, entitled "Analysis of Three-Dimensional Cell Migration in Dopamine-Modified Poly(aspartic acid)-Based Hydrogels", is authored by David Juriga, Eszter Eva Kalman, Krisztina Toth, Dora Barczikai, David Szöllősi, et al. Several types of promising cell-based therapies for tissue regeneration have been in development worldwide. However, for the successful therapeutical application of cells in this field, appropriate scaffolds are also required. Recently, the research for suitable scaffolds has focused on polymer hydrogels due to their similarity to the extracellular matrix. The main limitation regarding amino-acid-based hydrogels is their difficult and expensive preparation, which can be avoided by using poly(aspartamide) (PASP)-based hydrogels. PASP-based materials can be chemically modified with various bioactive molecules for the final application purpose. In this study, dopamine containing PASP-based scaffolds is investigated, since dopamine influences several cell biological processes, such as adhesion, migration, proliferation, and differentiation, according to the literature. Periodontal ligament cells (PDLCs) of neuroectodermal origin and the SH-SY5Y neuroblastoma cell line were used for in vitro experiments. The chemical structure of the polymers and hydrogels was proved by ^{1}H-NMR and FTIR spectroscopy. Scanning electron microscopy (SEM) images confirmed the suitable pore size range of the hydrogels for cell migration. Cell viability assay was carried out according to a standardized protocol using the WST-1 reagent. To visualize the three-dimensional cell distribution in the hydrogel matrix, two-photon microscopy was used. According to our results, dopamine containing PASP gels can facilitate vertical cell penetration from the top of the hydrogel at a depth of around four cell layers (~150 µm). To quantify these observations, a detailed image analysis process was developed and first introduced in this paper [16].

To conclude this article, we would like to express our appreciation for the papers contained in this book, sixteen in number, focused on extraordinary applications of gels for pharmaceutical uses, drug release, oncologic cure, new food production, and careful monitoring of radiation, having, as stated, the intent to ameliorate the quality of life in people of modern society.

Conflicts of Interest: The author declares no conflict of interest.

References

1. Paun, M.A.; Nichita, M.V.; Paun, V.A.; Paun, V.P. Xerogels Morphology Details by Multifractal Analysis and Scanning Electron Microscopy Images Evaluations of 5-Fluorouracil Release from Chitosan-Based Matrix. *Gels* **2022**, *8*, 820. [CrossRef] [PubMed]
2. Usman, A.K.; Cursaru, D.L.; Brănoiu, G.; Şomoghi, R.; Manta, A.M.; Matei, D.; Mihai, S. A Modified Sol–Gel Synthesis of Anatase {001}-TiO$_2$/Au Hybrid Nanocomposites for Enhanced Photodegradation of Organic Contaminants. *Gels* **2022**, *8*, 728. [CrossRef] [PubMed]
3. Nicolescu, M.; Mitrea, D.; Hornoiu, C.; Preda, S.; Stroescu, H.; Anastasescu, M.; Calderon-Moreno, J.M.; Predoana, L.; Teodorescu, V.S.; Maraloiu, V.A.; et al. Structural, Optical, and Sensing Properties of Nb-Doped ITO Thin Films Deposited by the Sol–Gel Method. *Gels* **2022**, *8*, 717. [CrossRef] [PubMed]
4. Mihaiescu, D.E.; Istrati, D.; Moroșan, A.; Stanca, M.; Purcăreanu, B.; Cristescu, R.; Vasile, B.Ș.; Trușca, R.D. Low Release Study of Cefotaxime by Functionalized Mesoporous Silica Nanomaterials. *Gels* **2022**, *8*, 711. [CrossRef] [PubMed]
5. Cibotaru, S.; Ailincai, D.; Andreica, B.I.; Cheng, X.; Marin, L. TEGylated Phenothiazine-Imine-Chitosan Materials as a Promising Framework for Mercury Recovery. *Gels* **2022**, *8*, 692. [CrossRef] [PubMed]

6. Guganathan, L.; Rajeevgandhi, C.; Sathiyamurthy, K.; Thirupathi, K.; Santhamoorthy, M.; Chinnasamy, E.; Raorane, C.J.; Raj, V.; Kim, S.C.; Anand, P. Magnetic Application of Gadolinium Orthoferrite Nanoparticles Synthesized by Sol–Gel Auto-Combustion Method. *Gels* **2022**, *8*, 688. [CrossRef] [PubMed]

7. Preda, S.; Pandele-Cușu, J.; Petrescu, S.V.; Ciobanu, E.M.; Petcu, G.; Culiță, D.C.; Apostol, N.G.; Costescu, R.M.; Raut, I.; Constantin, M.; et al. Photocatalytic and Antibacterial Properties of Doped TiO$_2$ Nanopowders Synthesized by Sol−Gel Method. *Gels* **2022**, *8*, 673. [CrossRef] [PubMed]

8. Paun, M.A.; Paun, V.A.; Paun, V.P. A Multifractal Vision of 5-Fluorouracil Release from Chitosan-Based Matrix. *Gels* **2022**, *8*, 661. [CrossRef] [PubMed]

9. Taheri-Afarani, H.; Mamontov, E.; Carroll, W.R.; Biernacki, J.J. A Molecular Description of Hydrogel Forming Polymers for Cement-Based Printing Paste Applications. *Gels* **2022**, *8*, 592. [CrossRef] [PubMed]

10. Zhang, S.; Wu, Z.; Chen, J.; Xu, R.; Wang, M.; Ni, W. Study on the Hydration Reaction of Typical Clay Minerals under Alkali and Sulfate Compound Activation. *Gels* **2022**, *8*, 564. [CrossRef] [PubMed]

11. Zhang, R.; Wan, Q.; Zhang, Y.; Zhang, X. Synthesis and Characterization of Fly Ash-Based Geopolymers Activated with Spent Caustic. *Gels* **2022**, *8*, 562. [CrossRef] [PubMed]

12. Loghin, D.F.; Bazarghideanu, M.M.; Vasiliu, S.; Racovita, S.; Zaharia, M.M.; Vasiliu, T.; Mihai, M. Hydrogel Beads of Amidoximated Starch and Chitosan as Efficient Sorbents for Inorganic and Organic Compounds. *Gels* **2022**, *8*, 549. [CrossRef] [PubMed]

13. Li, F.; Nguyen, G.T.M.; Vancaeyzeele, C.; Vidal, F.; Plesse, C. Photopolymerizable Ionogel with Healable Properties Based on Dioxaborolane Vitrimer Chemistry. *Gels* **2022**, *8*, 381. [CrossRef] [PubMed]

14. Merino, E.; Durán, A.; Ceré, S.; Castro, Y. Hybrid Epoxy-Alkyl Sol–Gel Coatings Reinforced with SiO$_2$ Nanoparticles for Corrosion Protection of Anodized AZ31B Mg Alloy. *Gels* **2022**, *8*, 242. [CrossRef] [PubMed]

15. Lungu, R.; Paun, M.A.; Peptanariu, D.; Ailincai, D.; Marin, L.; Nichita, M.V.; Paun, V.A.; Paun, V.P. Biocompatible Chitosan-Based Hydrogels for Bioabsorbable Wound Dressings. *Gels* **2022**, *8*, 107. [CrossRef] [PubMed]

16. Juriga, D.; Kalman, E.E.; Toth, K.; Barczikai, D.; Szöllősi, D.; Földes, A.; Varga, G.; Zrinyi, M.; Jedlovszky-Hajdu, A.; Nagy, K.S. Analysis of Three-Dimensional Cell Migration in Dopamine-Modified Poly (aspartic acid)-Based Hydrogels. *Gels* **2022**, *8*, 65. [CrossRef] [PubMed]

Xerogels Morphology Details by Multifractal Analysis and Scanning Electron Microscopy Images Evaluations of 5-Fluorouracil Release from Chitosan-Based Matrix

Maria-Alexandra Paun [1,2,*] ![ORCID], Mihai-Virgil Nichita [3] ![ORCID], Vladimir-Alexandru Paun [4] and Viorel-Puiu Paun [5,6]

1   School of Engineering, Swiss Federal Institute of Technology (EPFL), 1015 Lausanne, Vaud, Switzerland
2   Division Radio Monitoring and Equipment, Section Market Access and Conformity, Federal Office of Communications (OFCOM), 2501 Bienne, Canton of Bern, Switzerland
3   Doctoral School, Faculty of Applied Sciences, University Politehnica of Bucharest, 060042 Bucharest, Romania
4   Five Rescue Research Laboratory, 75004 Paris, France
5   Physics Department, Faculty of Applied Sciences, University Politehnica of Bucharest, 060042 Bucharest, Romania
6   Academy of Romanian Scientists, 50085 Bucharest, Romania
*   Correspondence: maria_paun2003@yahoo.com or maria-alexandra.paun@epfl.ch

Abstract: Four medicament delivery formulations based on 5-fluorouracil in a chitosan substantial matrix were realized in situ via 3,7-dimethyl-2,6-octadienal element hydrogelation. Representative samples of the final realized compounds were investigated from an analytic, constitutional, and morphological viewpoint via Fourier transform infrared (FTIR) spectroscopy and scanning electron microscopy (SEM). The SEM images of the formulations were investigated in concordance with fractal analysis, and the fractal dimensions and lacunarity were computed. The developed mathematical multifractal model is necessarily confirmed by the experimental measurements corresponding to the 5-fluorouracil release outside the chitosan-formed matrix.

1. Introduction

Polymer networks with hydrophilic characteristics are called hydrogels. These hydrogels are a type of soft, wet material with a three-dimensional network of crosslinked polymers that hold water in intermolecular spaces. Polymers are commonly applied in the design and manufacturing of hydrogels. The materials used for the development of hydrogels are roughly classified into two types based on their origin: natural and synthetic polymers. Dried gel beads in the form of xerogels, cryogels, or aerogels are prepared using different gelation conditions (aqueous and ethanolic $CaCl_2$ solutions) and drying methods (supercritical drying, freeze drying, and oven drying) to obtain particles with a broad range of physicochemical and textural properties. Xerogels and cryogels are obtained after the atmospheric drying and freeze drying of gels, respectively.

Xerogel is a solid gel obtained by drying with unhindered shrinkage. The drying process of xerogels involves solvent evaporation under standard conditions using conventional methods. Xerogels are mesoporous materials with high thermal stability. Significantly, xerogels are non-toxic, cost-effective, and biocompatible; they also have a large surface area and high porosity, and can easily be modified.

Cryogels, which are materials with a macroporous three-dimensional structure, are produced as a result of controlled freezing during polymerization with a highly interconnected polymer network. Cryogels are used for materials that extract liquid at a much lower temperature using a vacuum (sublimation phase of the solvent).

Aerogel can be defined as a solid that forms from a gel by drying at a supercritical state. The drying process in aerogels can be described as freeze drying, supercritical drying,

or ambient pressure drying. Aerogel is a lightweight material and exhibits a large surface area that ranges between 200 and 1000 m^2/g. It has many important properties such as a large amount of controlled pore size distribution, high conductivity, transparency, low density, flexibility, low dielectric constant, and high mechanical strength.

Aerogel and xerogel are important types of solid gel materials. The key difference between aerogel and xerogel is that aerogel forms when the liquid from the gel is extracted at a supercritical state, whereas xerogel forms when the liquid from the gel is evaporated at room temperature. Moreover, aerogel has a comparatively larger surface area than xerogel. Cryogel is a commercialized name for a product developed by Aspen Aerogels. It is a flexible aerogel composite blanket, designed for insulating cold temperature environments ranging from cryogenic to ambient.

Xerogels have a solid consistency, and usually possess properties such as a greater porosity and larger surface area in conjunction with reduced pore dimensions [1]. Regarding the substances presented above, in this article, we will prioritize chitosan. Chitosan is a significant biopolymer; it is plentiful in nature, cationic (positively charged), and non-immunocompetent, and has reduced toxicity and unlimited organic sustainability [2]. The comparative apparition of the two monomeric construction elements (D-glucosamine and N-acetyl-glucosamine) is decisive to whether chitosan is mostly an ampholyte or a poly-electrolyte dominated by acidic pH values. The chemical structure is not only critical for the activity conditions localized at the surface, but is essential for sol–gel transition, which occurs frequently. In addition, chitosan, based on its stable character, is frequently utilized in industry, as well as in agriculture, food, and cosmetics [3,4]. This chemical compound has excellent moisture capture, moisture restraint, opsonization, and bacterial inhibition. It is applicable to different cosmetic products, such as moisturizing cream, shower gel, cleaning cream, mousse, and advanced ointment frost. In addition, it is applicable as an emollient and antistaling constitutive element for alimentation, vegetables, and fruits, and as a flocculant for wastewater treatment due to its medicament continuous release factor and innocuous toxicity. It is also frequently used as a dyeing–printing assistant in paper fabrication [5–9].

The second chemical element used in this study is called 5-fluorouracil. Chemically speaking, 5-fluorouracil is an element analog with uracil, and has a fluorine atom in the C-5 location [8]. As a stand-alone medicine, it can be administered both intravenously and orally. In the case of intravenous route administration, the 5-FU drug may be quickly inserted in the target cell, utilizing an identical transport mechanism to that of uracil. Administered orally, in the form of pro-medicaments (oral FPs), 5-fluorouracil is defective and disturbs bioavailability due to DPYD function variability. Accordingly, this behavior is appropriate for unpredictable levels of 5-fluorouracil in the blood plasma of patients [9].

5-fluorouracil-encapsulated chitosan nanoparticles were realized for the investigation of spatially delimited medicament release as a result of pH chitosan nanoparticles' sensibility. The chitosan-covered magnetic nanoparticles were utilized to expand the delivery of 5-fluorouracil. Chitosan is a cationic polymer. Chitosan nanoparticle size was found to be below 100 nm by Zetasizer, transmission electron microscopy (TEM), and field scanning electron microscopy (FSEM) results.

An accumulation of recent evidence has proven that the 5-fluorouracil transportation process could be passively triggered by paracellular and transcellular monolayer tumoral cells. As a demonstrated alternative, 5-fluorouracil could probably cross/exceed the so-called blood–brain obstacle via passive diffusion. Furthermore, 5-fluorouracil can convert moving metabolites into target items.

Hydrogels are important medicament release systems that increase bioavailability and can be used as implantable medicament storage systems, permitting large medicament concentrations to be provided bluntly to suffering tissue, defeating the weak bioavailability problem and diminishing the proposed goal effects. In the current situation, hydrogels afford countless benefits over solid medicament storage implants because they possess

physicochemical characteristics alike to natural tissues of living matter, mitigating rash reactions in circumambient tissue after implantation [10,11].

In accordance with tissue engineering expectations and recommendations, a multi-compatibility chitosan is an interesting option for matrix polymers [12,13]. Thus, chitosan hydrogels are sought after for the controlled restricted release of medicaments, which makes them extremely useful for our study [14].

At the moment, it is assumed that chitosan nanoparticles could avert the therapeutic side effects induced by 5-fluorouracil at administration and later in the process. Thereby, 5-FU-uploaded chitosan nanoparticles may be utilized as efficient medicament release systems, and chitosan–medicament pairs are proposed to defeat the complicated side effects caused by 5-FU presence. However, the pH sensibility of chitosan nanoparticles regarding 5-fluorouracil delivery and the subsequent mathematical modeling of deliverance kinetics has not yet been fully experimentally confirmed [15,16].

In this study, considering compartmental logical circumstances, a new procedure is advanced, taking into consideration medicament delivery dynamics in complicated real systems—recognized as effective in pharmacokinetics studies—considering that drug release dynamics can be depicted by multifractal curves [17,18]. Presuming that the implicated configurational unit dynamics of polymer–medicament pairs occur on the multifractal curves (which are continuous and nondifferentiable), this shows that in 1D hydrodynamic conventional multifractal variables, the medicament delivery process (known as Fickian diffusion or non-Fickian diffusion) [17] is produced via isochronous dynamics, depending on the change from differentiable curves to non-differentiable curves [19].

Through the experimental measurements carried out, the model has been certified. In addition, we must highlight the application of fractal analysis to the interpretation of the morphology of the samples investigated by SEM imaging. Thus, the fractal dimensions and the lacunarity of the SEM images were calculated and introduced as a voxel configuration, expressing the values of a normal network in a 3D space. These results are presented to confirm the fractal behavior of the studied drug release process.

2. Results and Discussion

2.1. Theoretical Part: Delivery Kinetics Mathematical Modeling

The polymer–medicament theoretical model of compound deliverance dynamics can be depicted by continuous curves with non-differentiable functions (named multifractal curvatures) [19,20]. Thus, the multifractal motion theory presented here in hydrodynamic configuration reaches functionality via the following equations [21,22]:

$$\frac{\partial}{\partial t} V_D^i + V^l \frac{\partial}{\partial X^l} V_D^i = -\frac{\partial}{\partial X^i} Q \tag{1}$$

$$\frac{\partial}{\partial t}\rho + \frac{\partial}{\partial X^l}\left(\rho V_D^l\right) = 0 \tag{2}$$

where $i, l = 1, 2, 3$.

In Equation (1)

$$Q = \lambda^2 (dt)^{\left[\frac{2}{f(\alpha)}\right]-1} \frac{1}{\sqrt{\rho}} \frac{\partial}{\partial X^l}\left(\frac{\partial}{\partial X^l}\right)\sqrt{\rho} \tag{3}$$

In Equations (1)–(3), the nonfractal (classic) time t has an affine parameter role of the append deliverance function, X^l is one of the multifractal 3D coordinates, and V_D^l is the "multifractal fluid" speed of differentiable scale resolution (the polymer–medicament binary system is assumed to be a "multifractal flowing substance") [23,24]. In continuation, ρ is the "multifractal fluid" state density, λ is the configurational constant associated with the deliverance procedure related to the fractal–multifractal specific passage, dt is the scale resolution factor and $f(\alpha)$ is the α order singular spectrum contingent based on the calculated fractal dimension.

The differential Equations (1) and (2) permit, in the mathematical 1D situation—together with a set of distinctly defined boundary conditions and initial conditions [25,26]—the solutions

$$V_D = \frac{V_0 \varepsilon^2 + \mu^2 xt}{\varepsilon^2 + \mu^2 t^2} \tag{4}$$

$$\rho = \frac{1}{\sqrt{\pi}(\varepsilon^2 + \mu^2 t^2)^{\frac{1}{2}}} exp\left[-\frac{(x - V_0 t)^2}{\varepsilon^2 + \mu^2 t^2}\right] \tag{5}$$

with

$$\mu = \frac{2\lambda (dt)^{\left[\frac{2}{f(\alpha)}\right] - 1}}{\varepsilon} \tag{6}$$

In Equations (4)–(6), ε is a constant value in the definition of a parameter for the initial state densities at $t = 0$ (see below), and V_0 is the initial velocity of the polymer–medicament binary structure:

$$\rho(x, t = 0) = \rho_0 exp\left[-\left(\frac{x}{\varepsilon}\right)^2\right], \quad \rho_0 = const. \tag{7}$$

in the normalized coordinates system

$$\xi = \frac{x}{\varepsilon}, \quad \eta = \frac{V_0 t}{\varepsilon}, \quad V = \frac{V_D}{V_0}, \quad \phi = \frac{\rho}{\rho_0}, \quad \rho_0 = \frac{1}{\pi^{\frac{1}{2}}\varepsilon} \tag{8}$$

For the normalized parameter

$$\sigma = \frac{2\lambda (dt)^{\left[\frac{2}{f(\alpha)}\right] - 1}}{\varepsilon V_0}, \tag{9}$$

and the normalized solutions of the multifractal differential equations system [26,27] are the following:

$$V(\xi, \eta, \sigma) = \frac{1 + \sigma^2 \xi \eta}{1 + \sigma^2 \eta^2} \tag{10}$$

$$\phi(\xi, \eta, \sigma) = \frac{1}{(1 + \sigma^2 \eta^2)^{\frac{1}{2}}} exp\left[-\frac{(\xi - \eta)^2}{1 + \sigma^2 \eta^2}\right] \tag{11}$$

In Figure 1, the three-dimensional graphical representation of the $V(\xi, \eta)$ velocity multifractal theoretical function in normalized coordinates for the $\sigma^2 = 1$ fixed value (where the calibration is indicated) is shown.

In Figure 2, the three-dimensional graphical representation of the $\phi = \phi(\xi, \eta)$ state density theoretical function in normalized coordinates for the $\sigma^2 = 1$ fixed value (where the calibration is indicated) is shown.

If the initial normalized mass of the polymer–medicament binary system's constitutional unit is μ_0, this permits the normalized delivered medicament mass definition as having the expression

$$P(\eta, \sigma, \mu) = \frac{M(\eta)}{M(\infty)} = -\mu_0 \frac{\partial \phi}{\partial \eta} \tag{12}$$

where $M(\eta)$ coincides with the medicament mass delivered at the normalized time η and $M(\infty)$ is the medicament mass delivered when the time tends towards infinity, or a finite, constant quantity.

In the frequent situation in which the polymer–medicament binary system moves at a constant speed $V \equiv 1$ (for $V_D = V_0$) and $\xi = \eta$, we have the case in which Equation (12) (because of the fact that $\mu_0 \equiv 1$ has a fixed value) becomes

$$\frac{M(\eta, \sigma)}{M(\infty)} = \frac{\sigma^2 \eta}{(1 + \sigma^2 \eta^2)^{\frac{3}{2}}} \tag{13}$$
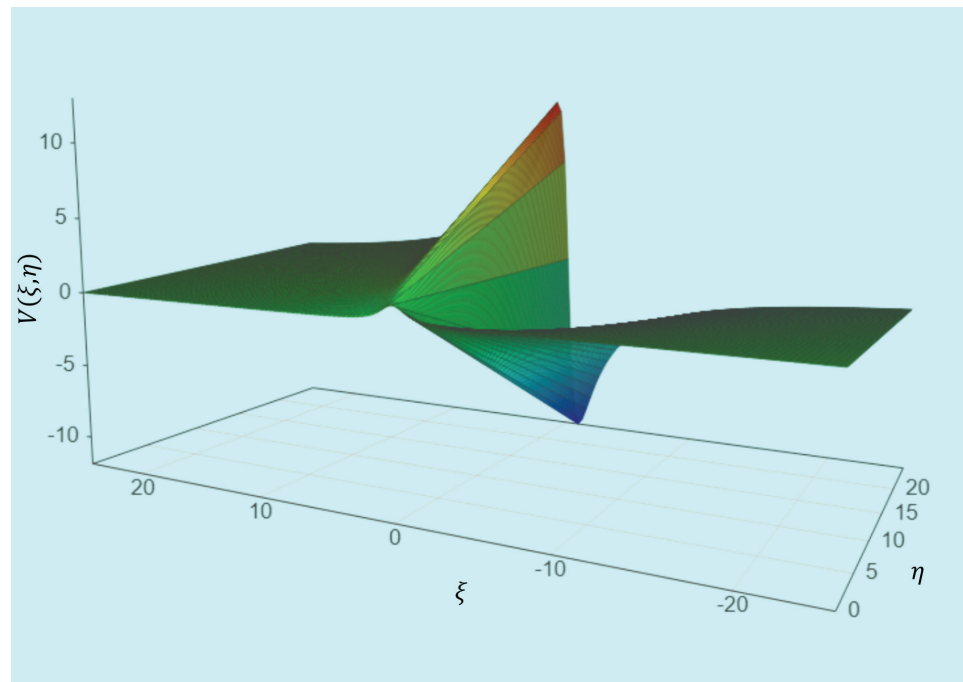
Figure 1. Three-dimensional graphical representations of $V(\xi, \eta)$ velocity multifractal theoretical function.
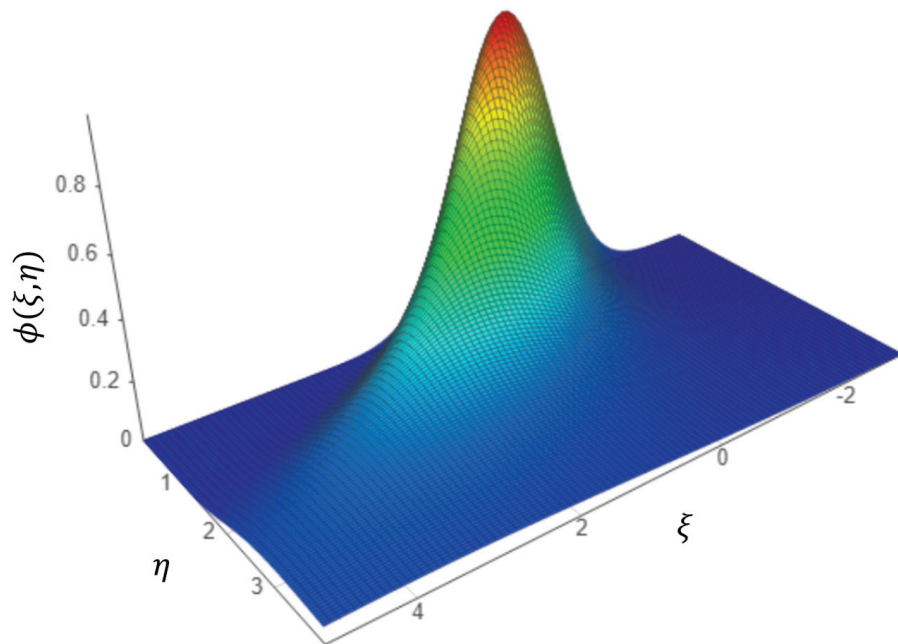
Figure 2. Three-dimensional graphical representation of the $\phi = \phi(\xi, \eta)$ mass state density theoretical function.

In Figure 3, a 3D graphical representation of drug release with a theoretical quantity/measure $M = M(\eta, \sigma)$ into the polymer–medicament binary system, associated with normalized time η for fractalization at different degrees σ, is presented. The unit (a.u.) is the abbreviation for the arbitrary unit.

However, the idea that emerges from the study of multifractal differential equations leads to the reality derived from the "good modeling practice" of delivery kinetics, namely, that everything involves identifying the most natural boundary and initial conditions involved in the physicochemical phenomena.
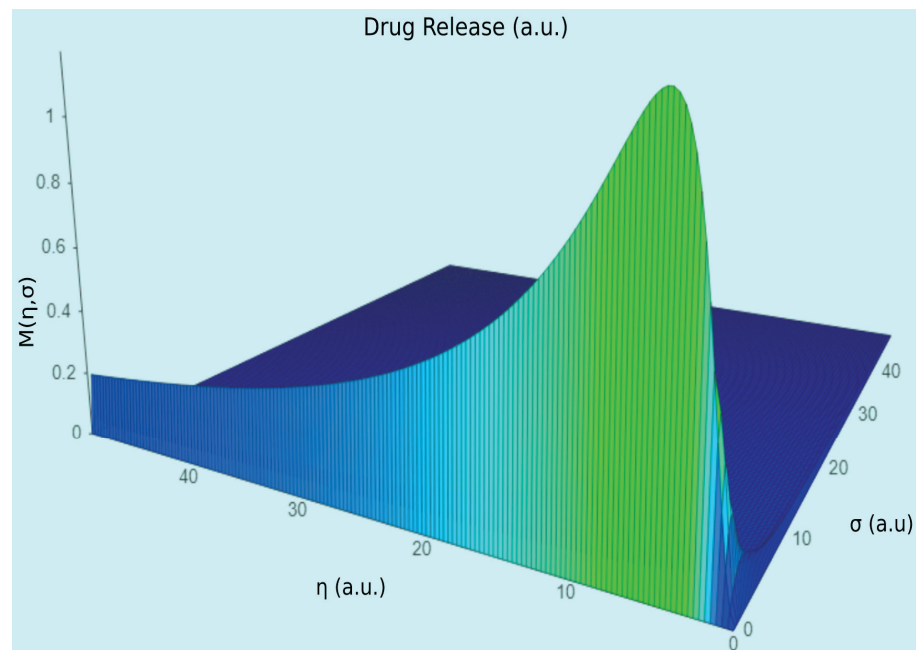
Figure 3. Three-dimensional plot of mass delivery theoretical function $M(\eta, \sigma)$.

In Figure 4, the silhouettes of cumulative medicament delivery (%) in vitro are presented for four distinct formulations.
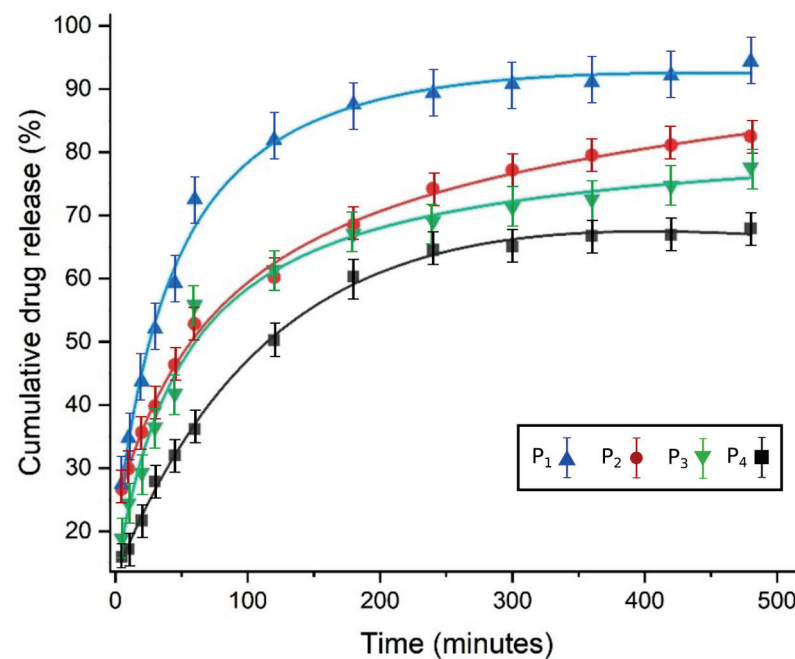
Figure 4. Cumulative % of drug release versus time.

The data shown in the graphic representation of Figure 4 were obtained in controlled 5-FU-chitosan binary system release experiments. As an obvious observation, it can be appreciated that the curves for cumulative drug release have different allures: one is a saturation curve (P_1), the other two (P_2 and P_3) tend towards infinity for large time values, while curve P_4 seems to decrease for long periods of time. The solid curves are the theoretical ones, according to the model used, and the experimental points are close to them, denoting a good agreement between them.

2.2. Box-Counting Method

The box-counting process is a reunion/assembly data procedure for analyzing repetitive complicated models and involves dividing a dataset, geometrical object, and picture into small and then smaller fragments, commonly known as "box"-form, and then analyzing the results on a scale that becomes smaller and smaller. The question now arises as to how we calculate the fractal dimension with this method [28].

Utilizing the box-counting procedure, the fractal dimension is shown by the linear regression slope where we graphically represent the *log*(N) value per *Y*-axis versus the log(1/*r*) value per *X*-axis, or more precisely

$$d = \lim_{r \to 0} \frac{\log N(r)}{\log\left(\frac{1}{r}\right)} = -\lim_{r \to 0} \frac{\log N(r)}{\log r} \tag{14}$$

An identical formula is utilized to determine the fractal dimension for computational applications of the fractal dimension to any strictly self-similar fractals. Stricto sensu, the size in question is the extent of the total fractals enclosed/inserted in a standard Euclidean space.

2.3. Lacunarity

Lacunarity makes a natural couple with the fractal dimension and is best used to depict the surface quality of a fractal object, including cracks (holes) and everything else. More specifically, it refers to the homogeneities and inhomogeneities of the texture in a global vision, with the hole statistics and their size as the distribution function. In fractal analysis, the lacunarity interprets the measure of present gaps (porous texture) or "real texture" measure [29].

It is thus ascertained as the inhomogeneity degree and translational (2D) and rotational (3D) invariance of the surface picture, wherein reduced/small lacunarity assumes homogenous existence and the rotating image changes the insignificant context. Thus, lacunarity is a concept different and separate from the fractal dimension. It has no connection with fractal topology, and more numerical variables are needed for complete decisions. This fractal measure is loudly connected with the gap size distribution of the fractal object and with its deviation from standard translational invariance. Generally, a fractal is most lacunar if its gaps are disposed to be great, as they comprise wide surface zones.

$$\Lambda(\varepsilon) = \frac{Z^{(2)}}{\left(Z^{(1)}\right)^2} \tag{15}$$

$$Z^{(1)} = \sum_{\varepsilon} P Q(P, \varepsilon) \tag{16}$$

$$Z^{(2)} = \sum_{\varepsilon} P^2 Q(P, \varepsilon) \tag{17}$$

$$Q(P, \epsilon) = \frac{n(P, \varepsilon)}{N(M, \epsilon)} \tag{18}$$

In the formulas above: size of the map = *M*; size of the box = *ε*; the box mass = *P*; *n* (*P*, *ε*) is the number of boxes containing P object pixels; N (M, *ε*) = (M-*ε*+1)^2 is the number of possible box positions; and *Q*(*P*, *ε*) is the probability calculated by Equation (1). At the same time, *P*•*Q*(*P*, *ε*) and *P*^{2}•*Q*(*P*, *ε*) are the first and second moments, while Z$^{(1)}$ and Z$^{(2)}$ are the sum of the first and second moments, calculated by Equations (3) and (4), respectively. Equation (2) is the lacunarity $\Lambda(\varepsilon)$ of the dataset for box size *ε*.

2.4. Assessment of Scanning Electron Microscope Images Using Fractal Analysis

The obtained formulations were noted with P_1, P_2, P_3, and P_4. The number associated with each letter/compound is appropriate to the molar proportion of the amino/aldehyde class, i.e., 1:1, 2:1, 3:1, and 4:1, respectively.

The 5-fluorouracil in our formulations was determined by polarized light microscopy (Figure 1), which disclosed the medicament's evident segregation in the hydrogels with large, reticulated density (P_1, P_2), while for the hydrogel compounds with lower reticulated density (P_4), a birefringent, granular structure was observed, characteristic of crystal submicrometric dimensions distributed below the apparatus detection tolerance [30].

In Figure 5, representative POM typical images are shown. More precisely, there are three POM images of the three samples obtained, each with a different concentration: P_1, P_2, and P_4. The scale bar for the POM photographic images is 20 microns. Figure 5a shows POM-P_1, Figure 5b shows POM-P_2, and Figure 5c shows POM-P_4.

(**a**)　　　　　　　　　(**b**)　　　　　　　　　(**c**)
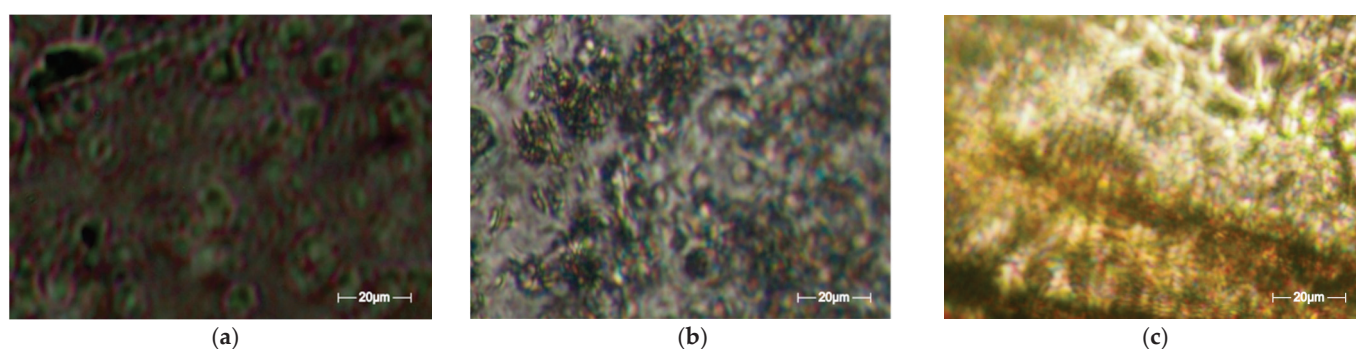
Figure 5. Typical POM pictures of the compounds/formulations: (**a**) POM-P_1; (**b**) POM-P_2; (**c**) POM-P_4.

In Figure 6, representative SEM images are shown. More precisely, there are three SEM images of the three obtained samples, each with a different concentration (P_1, P_2, and P_3). The scale bar for the SEM photographic images is 400 microns. Figure 6a shows SEM-P_1, Figure 6b shows SEM-P_2, and Figure 6c shows SEM-P_3.

(**a**)　　　　　　　　　(**b**)　　　　　　　　　(**c**)
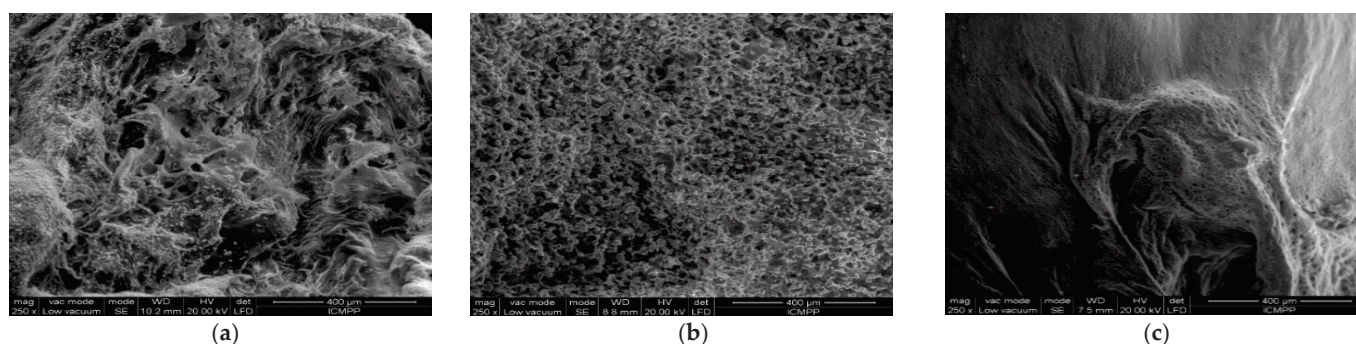
Figure 6. Typical SEM pictures of the compounds/formulations: (**a**) SEM-P_1; (**b**) SEM-P_2; (**c**) SEM-P_3.

The morphology of these three obtained formulations—P_1, P_2, and P_3—was investigated by scanning electron microscopy, and was then evaluated. Strictly speaking, in this paper, a new way of interpreting the SEM images of the samples is presented (fractal analysis), which is the main novelty of this paper compared to [8].

The fractal dimensions and gap orientations/distributions on the studied surfaces (lacunarity) of the studied SEM pictures were computed via the well-known method of fractal analysis [31]. In an attempt to determine a fine punctual context, i.e., a correct inventory at the pixel level, recent computational software for the investigation of complex neural diseases using CT and MRI pictures were utilized [32–34].

As can be observed in the SEM images, the formulations have a distinct porous structure, as can be seen by the presence of evident medicament crystals enclosed in the

orifices/pores of the walls (Figure 6). The medicament crystal caliber decreased as the crosslinking level decreased, conforming with SEM image monitoring, as mentioned in relation to chitosan-founded formulations in the literature [32]. For the quality valuation of the surface captured on the SEM images, fractal geometry indicators were applied, which led to the calculation of the fractal dimension (a ratio providing a statistical index of complexity) of the respective image, as well as it's lacunarity [33]. The voxel graphical representations for each SEM picture are also referenced individually in this paper.

Figure 7a is the original image P_1 of the entire portion, Figure 7b is the grayscale version of the original image, Figure 7c is the grayscale version of the image without luminance, and Figure 7d is the binarized version image without luminance.

Figure 7. Processing stages of P_1 image. (**a**) Original image (the entire portion); (**b**) grayscale version; (**c**) grayscale version without luminance; (**d**) binarized version.

Figure 7 shows the three phases of processing the original P_1 image in order to apply the fractal analysis procedure and calculate the fractal dimension and lacunarity. For image binarization, a threshold of 30 units was utilized.

Via the numerical assessment of the chosen picture (P_1) with fractal analysis software [35], it was found that the fractal dimension value D = 1.8621 had a standard deviation of $s = \pm\sqrt{\sigma^2} = \pm0.0733$ and a lacunarity value of $\Lambda = 0.0385$, as shown in Table 1.

Table 1. Fractal characteristic calculation of picture P_1.

Name	Fractal Dimension	Standard Deviation	Lacunarity
Image P_1	1.8621	0.0733	0.0385

Figure 8 shows a 2D graphic of the fractal dimension using the box-counting method. It can be seen that the fractal dimension is between 1.73 and 2. Figure 9 presents an

inspection of the elected P_1 picture zone (fractal dimension computation) with the Harmonic and Fractal Image Analyzer Demo computer program (Prague, Czech Republic), version 5.5.30 [36]. The fractal dimensions of the different ruler scales are equal to *r*.

Figure 8. Two-dimensional box-count algorithm: fractal dimension.
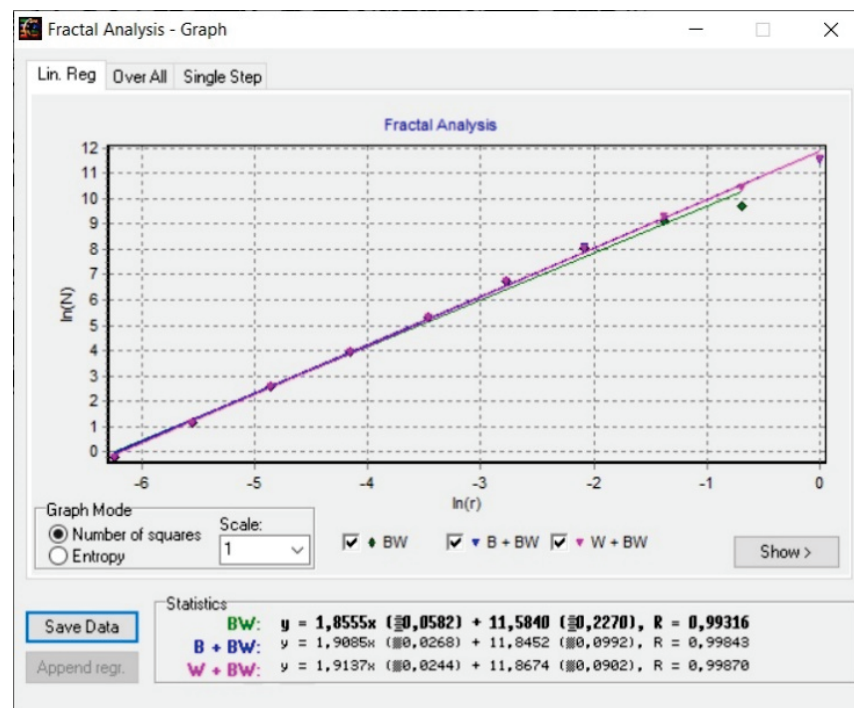
Figure 9. Graphic of fractal dimension for elected P_1 picture zone.

Figure 10 shows the voxels of the analyzed P_1 image and a 3D graphic representation. The gray level is shown on the *oZ* axis, while the corresponding numbers of pixels are on the other two axes (*oX* and *oY*) [37].
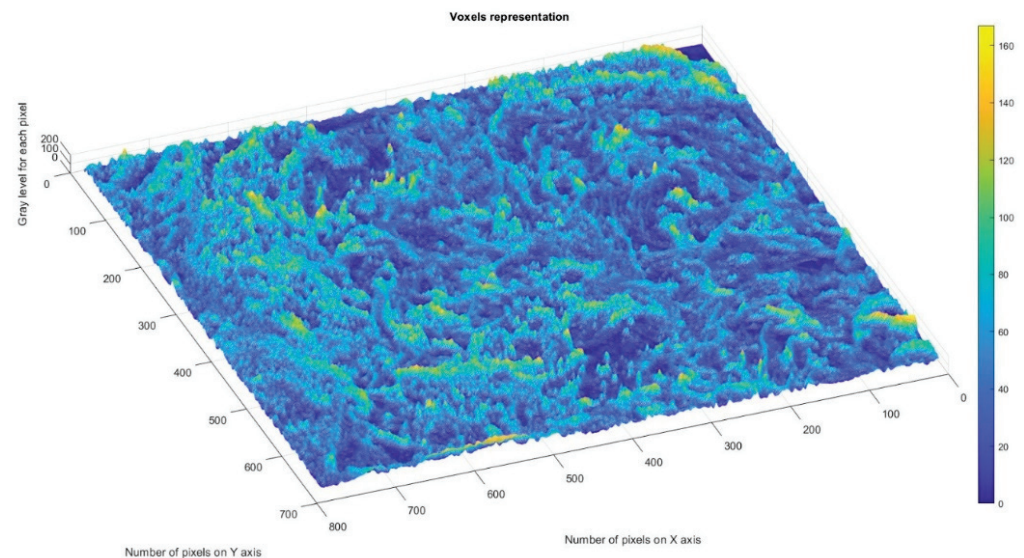
Figure 10. Three-dimensional voxel representation of P_1 image.

In a given three-dimensional (3D) graphical representation, a voxel expresses a value in a normal network in a 3D space. In the case of pixels in a two-dimensional bitmap, locations (coordinates) are not usually coded/fixed by the values represented as belonging to each of them. Conversely, associated interpretation systems deduct the voxel's real position in relation to its relative position, compared to the other voxels. Geometrical position in terms of data organization thus results in a unique volumetric image.

In Figure 11, the operation stages of the P_2 SEM image are presented. In Figure 11a, the original image of the entire portion is depicted, the grayscale version of the original image is shown in Figure 11b, the grayscale version of the image without luminance is shown in Figure 11c, and Figure 11d is the binarized version of the image without luminance.

Figure 11 shows the three phases of processing the original P_2 image in order to apply the fractal analysis procedure and calculate the fractal dimension and lacunarity. For image binarization, a threshold of 25 units was utilized.

Via the numerical assessment of the chosen picture (P_2) with fractal analysis software [35], it was found that the fractal dimension value $D = 1.8837$ had a standard deviation of $s = \pm\sqrt{\sigma^2} = \pm 0.0894$ and a lacunarity value of $\Lambda = 0.0498$, as shown in Table 2.

Table 2. Calculation of fractal characteristics of P_2 picture.

Name	Fractal Dimension	Standard Deviation	Lacunarity
Image P_2	1.8837	0.0894	0.0498

Figure 12 shows a 2D graphic of the fractal dimension using the box-counting method. It can be seen that the fractal dimension is between 1.8 and 2. Figure 13 presents an inspection of the elected P_2 picture zone (fractal dimension computation) with the Harmonic and Fractal Image Analyzer Demo program, version 5.5.30 [36]. The fractal dimensions of the different ruler scales are equal to r.

Figure 14 shows the voxels of the analyzed P_2 image and a 3D graphical representation. The gray level is shown on the oZ axis, while the corresponding numbers of pixels are on the other two axes (oX and oY) [37].

In Figure 15, the operation stages of the P_3 SEM image are presented. In Figure 15a, the original image of the entire portion is shown, the grayscale version of the original image is shown in Figure 15b, the grayscale version of the image without luminance is shown in Figure 15c, and Figure 15d is the binarized version of the image without luminance.
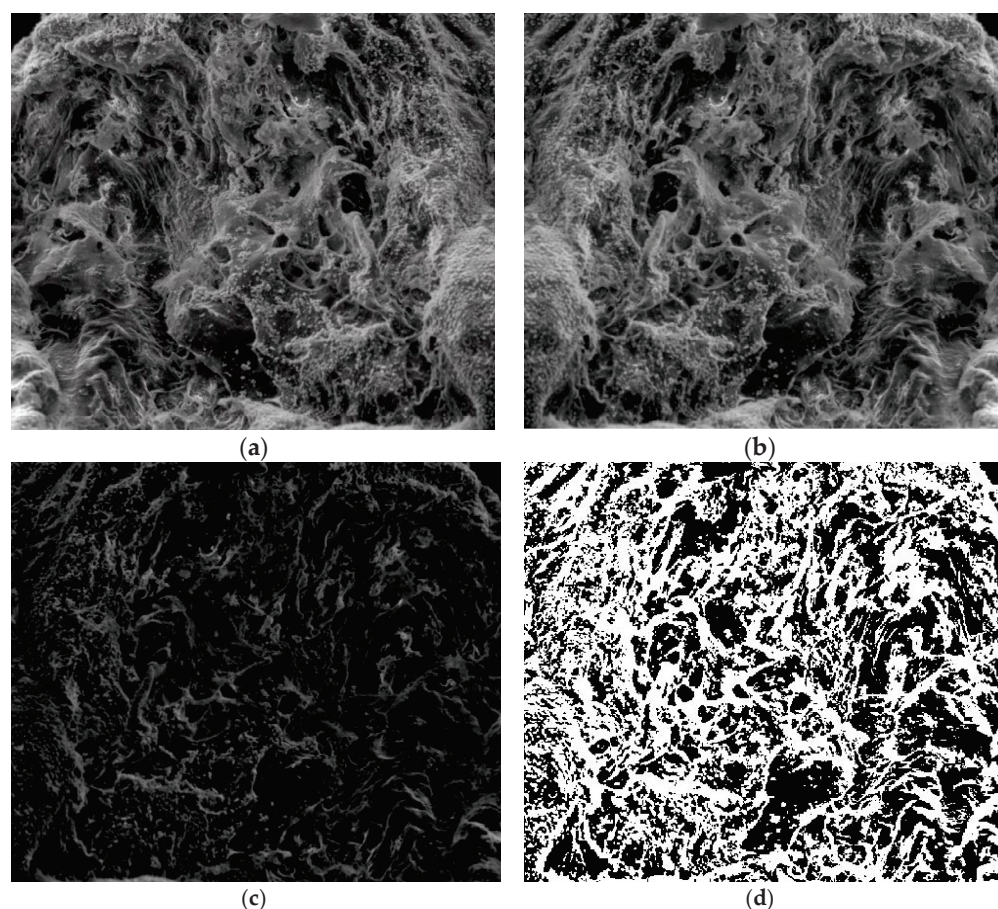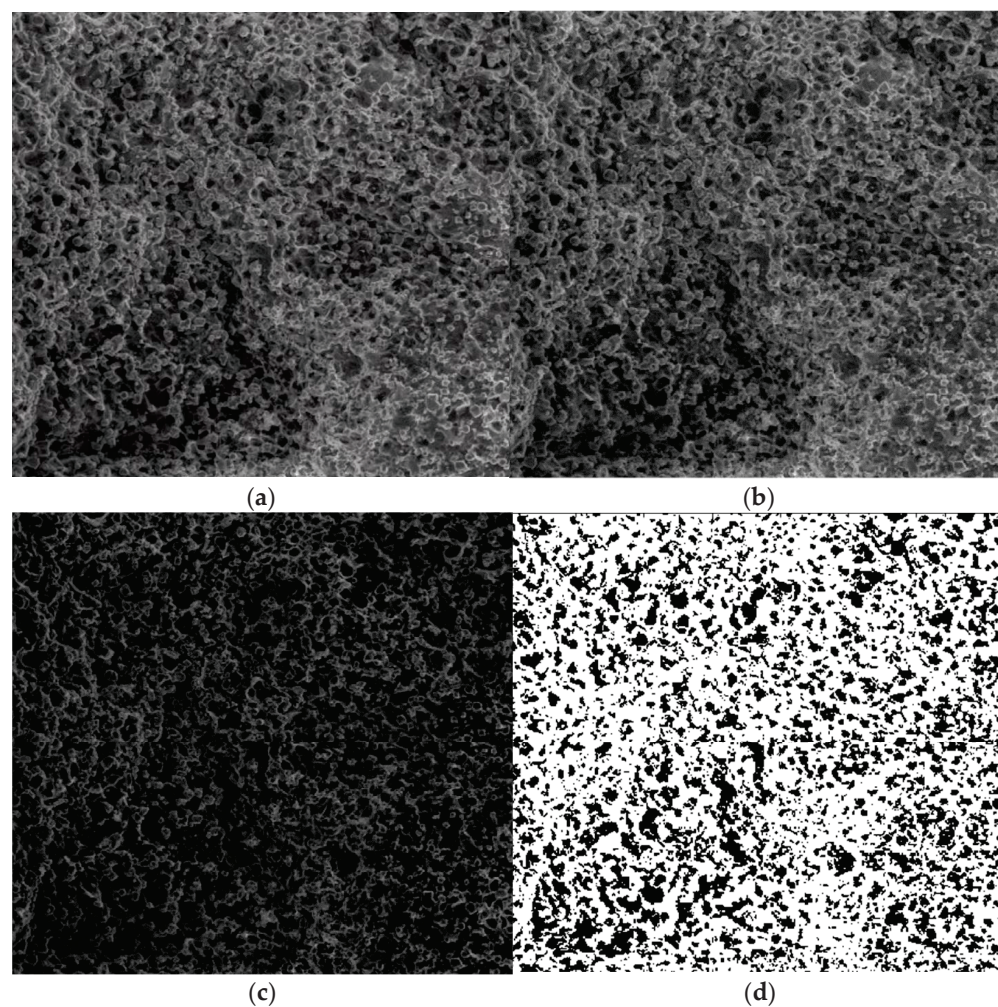
Figure 11. Processing stages of the P_2 image. (**a**) Original image (the entire portion); (**b**) grayscale version; (**c**) grayscale version without luminance; (**d**) binarized version.
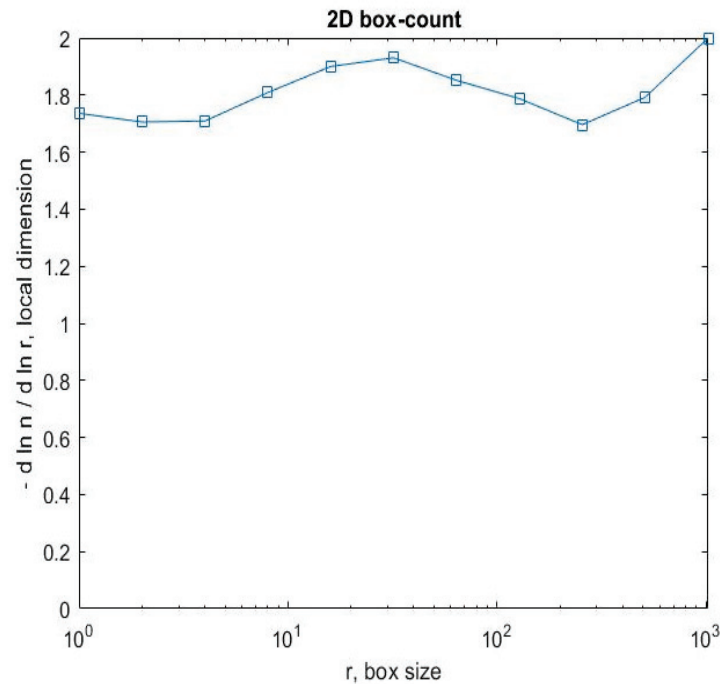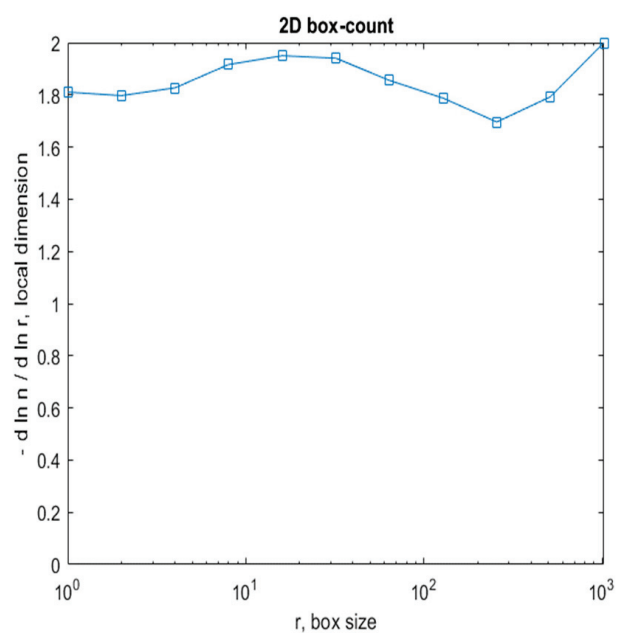

Figure 12. Two-dimensional box-count algorithm: fractal dimension.
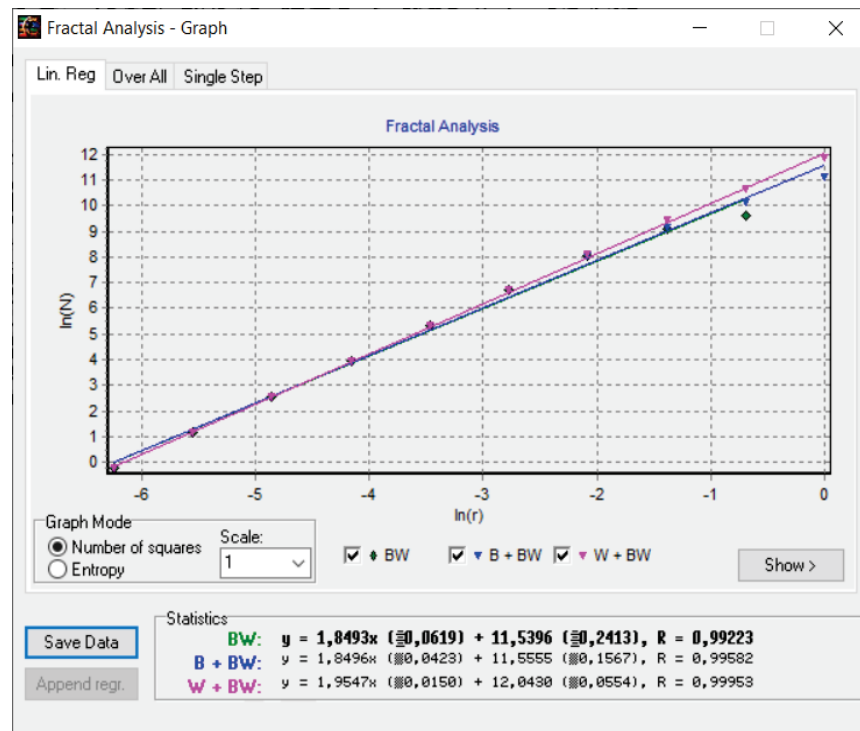
Figure 13. Graphic of fractal dimension for elected P_2 picture zone.
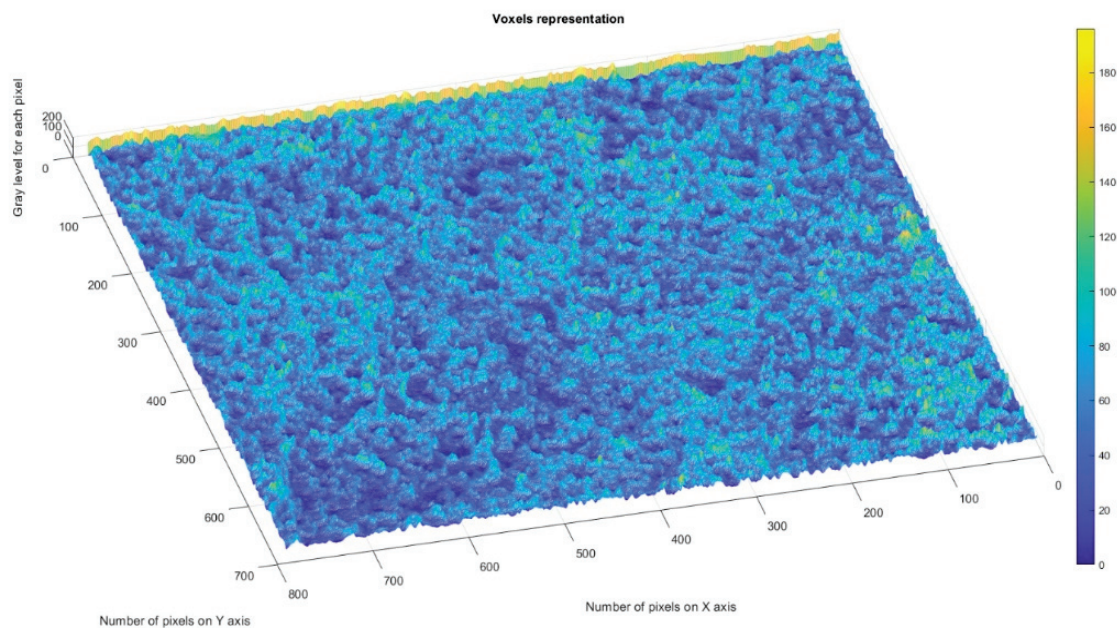
Figure 14. Three-dimensional voxel representation of P_2 image.

In Figure 15, the three phases of processing the original P_3 image are shown in order to apply the fractal analysis procedure and calculate the fractal dimension and lacunarity. For image binarization, a threshold of 10 units was utilized.

Via the numerical assessment of the chosen picture (P_3) with fractal analysis software [35], it was found that the fractal dimension value $D = 1.8561$ had a standard deviation of $s = \pm\sqrt{\sigma^2} = \pm 0.0702$ and a lacunarity value of $\Lambda = 0.0324$, as shown in Table 3.
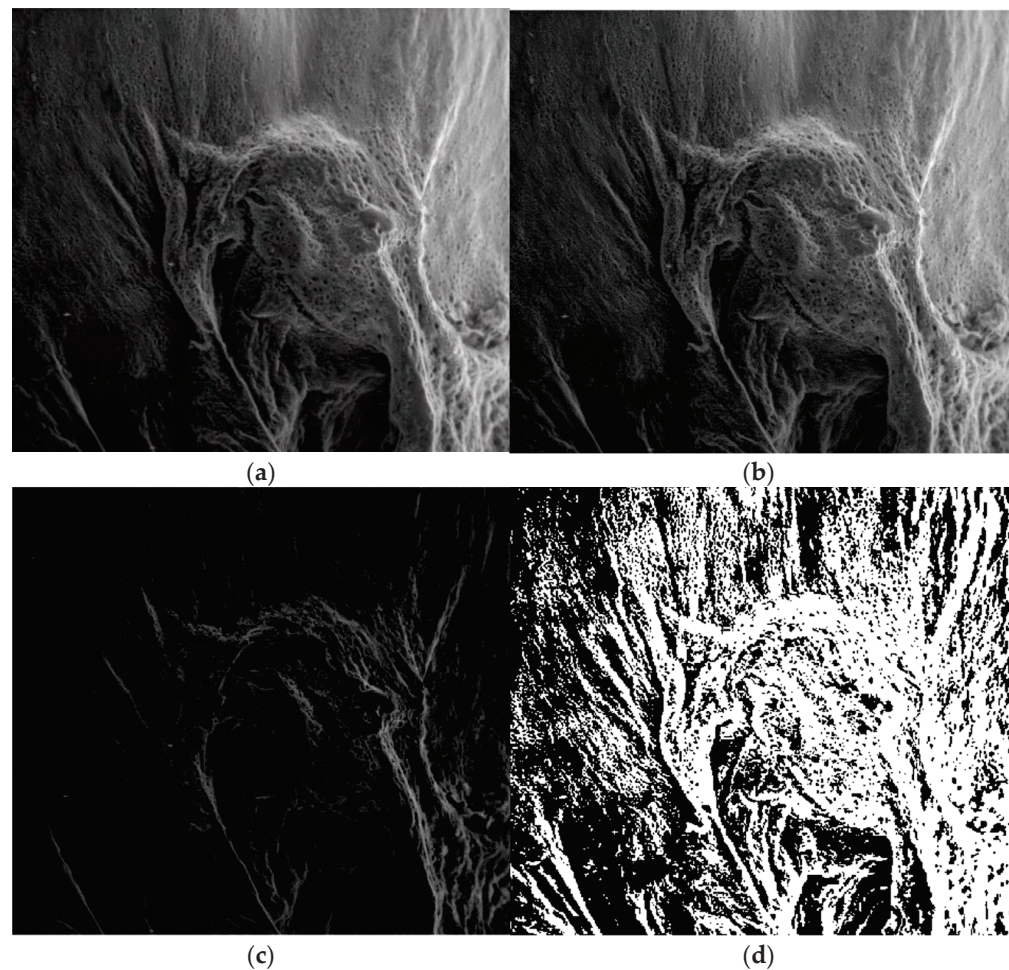
Figure 15. Processing stages of the image P_3. (**a**) Original image (the entire portion); (**b**) grayscale version; (**c**) grayscale version without luminance; (**d**) binarized version.

Table 3. Calculation of fractal characteristics of picture P_3.

Name	Fractal Dimension	Standard Deviation	Lacunarity
Image P_3	1.8561	0.0702	0.0324

Figure 16 shows a 2D graphic of the fractal dimension using the box-counting algorithm method. It can be seen that the fractal dimension is between 1.75 and 2. Figure 17 presents the inspection of the elected P_3 picture zone (fractal dimension computation) with the Harmonic and Fractal Image Analyzer Demo program, version 5.5.30 [36]. The fractal dimensions of the different ruler scales are equal to r.

Figure 18 shows the voxels of the analyzed P_3 image and a 3D graphical representation. The gray level is shown on the oZ axis, while the corresponding numbers of pixels are on the other two axes (oX and oY) [37].

In Figures 8, 12 and 16, graphical representations for determining the fractal dimensions depending on the box size r (via the box-counting method) are introduced.

Figures 9, 13 and 17 show the 2D graphical depictions of the linear regression slope findings for fractal dimension computation. Figures 10, 14 and 18 show the voxel 3D representation graphs for the pictures P_1, P_2, and P_3 from the amended zone. The three coordinate axes are assigned as follows: the pixel number is on the ox axis, the pixel number is on the oy axis, and the gray intensity level for the respective pixel is on the oz axis. In line with the generated computer graphics, the so-called voxel shows the numerical amount/value directly connected to the regular grid in a 3D spatial configuration.
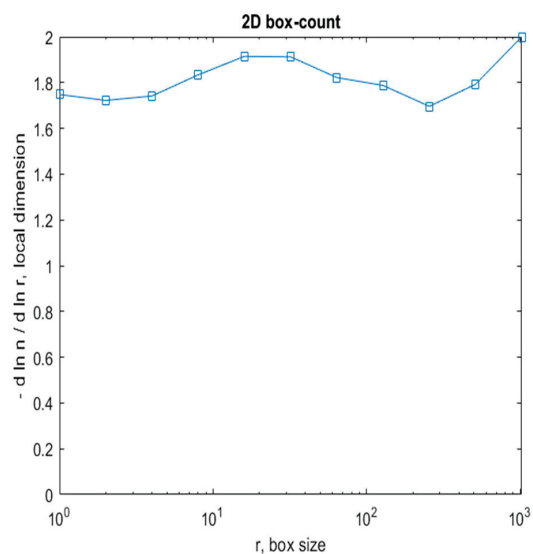
Figure 16. Two-dimensional box-count algorithm: fractal dimension.
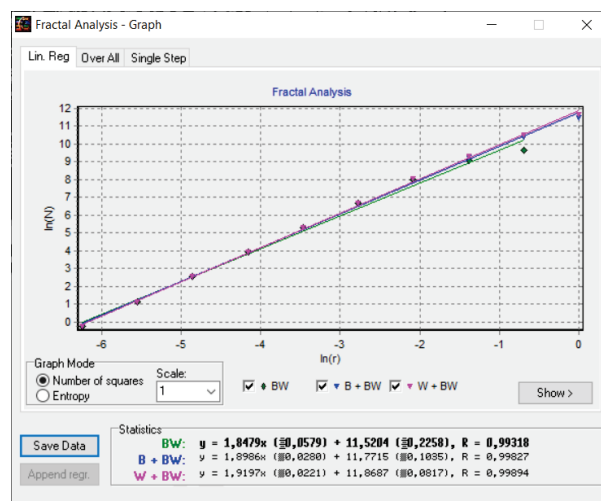
Figure 17. Graphic of fractal dimension for elected P$_3$ picture zone.
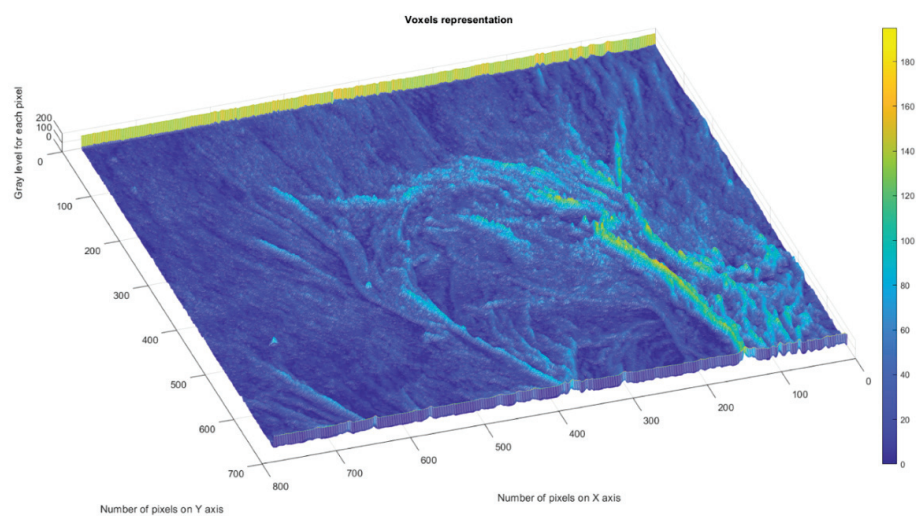
Figure 18. Three-dimensional voxel representation of P$_3$ image.

3. Conclusions

In this paper, 5-fluorouracil-encapsulated chitosan nanoparticles were realized for the investigation of the release of spatially delimited medicaments, considering the pH of chitosan nanoparticles' sensibility.

To correctly analyze the dynamic behavior of 5-fluorouracil delivery with chitosan nanoparticles, in vitro delivery information was investigated utilizing a multifractal kinetic equation. The developed mathematical multifractal model has been confirmed by the experimental measurements corresponding to 5-fluorouracil release outside the chitosan-formed matrix.

The increase in the efficiency of chitosan and 5-fluorouracil-encapsulated elements resulted in nanometer values of particle dimensions and measurement distributions. This was certified through scanning electron microscopy (SEM) observations. The P_1, P_2, and P_3 SEM images of the three formulations were found to conform with the fractal analysis procedures, and the fractal dimension and lacunarity values were calculated. Thereby, the P_1 image had the fractal dimension value of D = 1.8621 ± 0.0733 and the lacunarity value of Λ = 0.0385. The P_2 image had the fractal dimension value of D = 1.8837 ± 0.0894 and the lacunarity value of Λ = 0.0498. Finally, image P_3 had the fractal dimension value of D = 1.8561 ± 0.0702 and the lacunarity value of Λ = 0.0324.

4. Materials and Methods

4.1. Materials

Chitosan-covered magnetic nanoparticles were utilized to expand the deliverance of 5-fluorouracil [4]. Chitosan (243 kDa, DA: 87%), 3,7-dimethyl-2,6-octadienal (95%), 5-fluorouracil (purity: 99%), and phosphate tampon solution with a pH of 7.4 were purchased from Aldrich Chemical Co Inc. and brought to the required standard quality. All other reagents were of analytical grade.

4.2. Formulation Preparation

All the formulations (i.e., experimental products) obtained were adapted and realized through chitosan hydrogelation (in situ), starting with 3,7-dimethyl-2,6-octadienal and 5-fluorouracil as a direct consequence of a known protocol [21]. In a short time, 3,7-dimethyl-2,6-octadienal (2% solution) was blended into 5-fluorouracil and was dripped into the chitosan (3% solution) in an aqueous solution (1%) of dissolved acetic acid. The 5-fluorouracil element, enclosed in the chitosan nanoparticle capsules, was used to examine the localized medicament release potential of the pH sensibility of the utilized chitosan nanoparticles. The maximum reported levels of chitosan and 5-fluorouracil in the encapsulated particles were 150 nm and 250 nm in terms of particle dimension (so nanoparticles). The measurement distributions centered on the particles' small size, as confirmed via the scanning electron microscopy investigations. The provocation launched on this occasion will be examined by the medicament release of 5-fluorouracil-encapsulated chitosan particles with various pH modifications. According to the observations made, the deliverance of 5-fluorouracil from various hydrogel compounds resulted in zero-order kinetics. These obvious consequences suggest that chitosan hydrogel performs a significant function in controlling medicament deliverance to circumambient tissues.

As an immediate observation, the hydrogelation period augmented as the aldehyde quantity reduced. This happened immediately for the 1/1 molar proportion of the amine/aldehyde functional class and slowly continued for a 24-h period in the case of the 4/1 molar proportion.

The principal purpose was to realize chitosan polymeric products via a solvent evaporation emulsification procedure by utilizing various polymer proportions. Ultimately, the achieved hydrogels were lyophilized and then analyzed from a physico-chemical point of view.

4.3. Methods

The total gelation period was established when it was visually observed that the formed chemical blend was converted from a viscous consistency to a rubbery consistency. The xerogels were realized by lyophilization from the equivalent hydrogels, utilizing a Labconco FreeZone Freeze Dry device (FreeZoner2.5 Liter Freeze Dry laboratory apparatus) for one day (24 h) in temperature conditions of −50 °C and a pressure of 0.04 mbar.

Optimized polymer proportions were determined by appropriate experimental methods, including differential scanning calorimetry (DSC), X-ray diffraction (XRD), entrapment capability and particle dimension, and likeliness to succeed in enteric covering. Polarized optical microscopy pictures were achieved with a Zeiss Axio Imager M2 microscope, and hydrogels and xerogels were the compounds used in this experiment. The hydrogel morphology modifications were observed with an SEM EDAX -Quanta 200 field emission scanning electron microscope, and manipulated at an electric tension of 20 keV.

References

1. Czarnobaj, K. Sol–gel-processed silica/polydimethylsiloxane/calcium xerogels as polymeric matrices for Metronidazole delivery system. *Polym. Bull.* **2011**, *66*, 223–237. [CrossRef]
2. Wang, X.; Ben Ahmed, N.; Alvarez, G.; Tuttolomondo, M.; Hélary, C.; Desimone, M.; Coradin, T. Curr Sol-gel encapsulation of biomolecules and cells for medicinal applications. *Top. Med. Chem.* **2015**, *15*, 223–244. [CrossRef] [PubMed]
3. Prausnitz, M.R.; Langer, R. Transdermal drug delivery. *Nat. Biotechnol.* **2008**, *26*, 1261–1268. [CrossRef] [PubMed]
4. Patel, A.; Cholkar, K.; Agrahari, V.; Mitra, A.K. Ocular drug delivery systems: An overview. *World J. Pharmacol.* **2013**, *2*, 47–64. [CrossRef] [PubMed]
5. Zhang, L.; He, G.; Yu, Y.; Zhang, Y.; Li, X.; Wang, S. Design of Biocompatible Chitosan/Polyaniline/Laponite Hydrogel with Photothermal Conversion Capability. *Biomolecules* **2022**, *12*, 1089. [CrossRef]
6. Xiong, S.; Marin, L.; Duan, L.; Cheng, X. Fluorescent chitosan hydrogel for highly and selectively sensing of p-nitrophenol and 2, 4, 6-trinitrophenol. *Carbohydr. Polym.* **2019**, *225*, 115253. [CrossRef]
7. Jacob, J.; Haponiuk, J.T.; Thomas, S.; Gopi, S. Biopolymer based nanomaterials in drug delivery systems: A review. *Mater. Today Chem.* **2018**, *9*, 43–55. [CrossRef]
8. Iancu, R.; Irimiciuc, S.A.; Agop, M.; Frasila, M.; Paun, M.A.; Paun, V.A.; Paun, V.P.; Stratulat, S. 5-fluorouracil release from chitosan-based matrix. Experimental and theoretical aspects. *Mater. Plast.* **2020**, *57*, 180–188. [CrossRef]
9. Tigli Aydın, R.S.; Pulat, M. 5-Fluorouracil Encapsulated Chitosan Nanoparticles for pH-Stimulated Drug Delivery: Evaluation of Controlled Release Kinetics. *J. Nanomater.* **2012**, *2012*, 313961. [CrossRef]
10. Alvarez, G.S.; Hélary, C.; Mebert, A.M.; Wang, X.; Coradin, T.; Desimone, M.F. Antibiotic-loaded silica nanoparticle-collagen composite hydrogels with prolonged antimicrobial activity for wound infection prevention. *J. Mater. Chem. B* **2014**, *2*, 4660–4670. [CrossRef]
11. Jiang, W.; Zhao, P.; Song, W.; Wang, M.; Yu, D.-G. Electrospun Zein/Polyoxyethylene Core-Sheath Ultrathin Fibers and Their Antibacterial Food Packaging Applications. *Biomolecules* **2022**, *12*, 1110. [CrossRef]
12. Paun, V.P. Creep model for polymeric materials. *Mater. Plast.* **2003**, *40*, 25–26.
13. Paun, V.P. Relaxation model for polymeric materials in the hereditary theory of elasticity. *Mater. Plast.* **2003**, *40*, 81–82.

14. Liu, H.; Wang, H.; Lu, X.; Murugadoss, V.; Huang, M.; Yang, H.; Wan, F.; Yu, D.G.; Guo, Z. Electrospun structural nanohybrids combining three composites for fast helicide delivery. *Adv. Compos. Hybrid Mater.* **2022**, *5*, 1017–1029. [CrossRef]

15. Paun, V.P.; Paun, M.A.; Toma, A.; Ciucu, C.; Popentiu, F. Transport phenomenon simulation for linear polymers through nanometer pores. *Mater. Plast.* **2008**, *45*, 57–60.

16. Paun, M.-A.; Paun, V.-A.; Paun, V.-P. A Multifractal Vision of 5-Fluorouracil Release from Chitosan-Based Matrix. *Gels* **2022**, *8*, 661. [CrossRef]

17. Pereira, L.M. Fractal Pharmacokinetics. *Comput. Math. Methods Med.* **2010**, *11*, 161–184. [CrossRef]

18. Kosmidis, K.; Argyrakis, P.; Macheras, P. Fractal kinetics in drug release from finite fractal matrices. *J. Chem. Phys.* **2003**, *119*, 6373–6377. [CrossRef]

19. Le Mehaute, A.; Crepy, G. Introduction to transfer and motion in fractal media: The geometry of kinetics. *Solid State Ion.* **1983**, *9–10*, 17–30. [CrossRef]

20. Barkai, E.; Metzler, R.; Klafter, J. From continuous time random walk to the fractional Fokker-Planck equation. *Phys. Rev. E* **2000**, *61*, 132–138. [CrossRef]

21. Higaki, K.; Yamashita, S.; Amidon, G.L. Time-dependent oral absorption models. *J. Pharmacokinet. Pharmacodyn.* **2001**, *28*, 109–128. [CrossRef] [PubMed]

22. Karalis, V.; Tsantili-Kakoulidou, A.; Macheras, P. Quantitative structure–pharmacokinetic relationships for disposition parameters of cephalosporins. *Eur. J. Pharm. Sci.* **2003**, *20*, 115–123. [CrossRef] [PubMed]

23. Chechetkin, V.R.; Lutovinov, V.S.; Turygin, A.Y. Multifractal structure of fully developed hydrodynamic turbulence. I. Kolmogorov's third hypothesis revisited. *J. Stat. Phys.* **1990**, *61*, 573–588. [CrossRef]

24. Basu, A.; Chakrabarti, B.K. Hydrodynamic descriptions for surface roughness in fracture front propagation. *Philos. Trans. A Math. Phys. Eng. Sci.* **2019**, *377*, 20170387.

25. Kwak, K.; Yang, S. *Developing a Multi-Dimensional Hydrodynamics Code with Astrochemical Reactions*; NASA Astrophysics Data System (ADS): Cambridge, MA, USA, 2015.

26. O'Shaughnessy, B.; Procaccia, I. Analytical solutions for diffusion on fractal objects. *Phys. Rev. Lett.* **1985**, *54*, 455–458. [CrossRef]

27. Richard, R. 1D Diffusion PDE. Introduction to Partial Differential Equations. 2019. Available online: http://personal.ph.surrey.ac.uk/~{}phs1rs/teaching/l3_pdes.pdf (accessed on 7 October 2022).

28. Karperien, A.L.; Jelinek, H.F. Box-Counting Fractal Analysis: A Primer for the Clinician. In *The Fractal Geometry of the Brain*; Di Ieva, A., Ed.; Springer Series in Computational Neuroscience; Springer Science + Business Media: New York, NY, USA, 2016; Chapter 2.

29. Karperien, A.; Jelinek, H.F.; Milošević, N.T. Reviewing Lacunarity Analysis and Classification of Microglia in Neuroscience. In Proceedings of the 8th European Conference on Mathematical and Theoretical Biology, Krakow, Poland, 28 June–2 July 2011.

30. Polowsky, P.J.; Tansman, G.; Kindstedt, P.S.; Hughes, J.M. Characterization and identification of surface crystals on smear-ripened cheese by polarized light microscopy. *J. Dairy Sci.* **2018**, *101*, 7714–7723. [CrossRef]

31. Lungu, R.; Paun, M.-A.; Peptanariu, D.; Ailincai, D.; Marin, L.; Nichita, M.-V.; Paun, V.-A.; Paun, V.-P. Biocompatible Chitosan-Based Hydrogels for Bioabsorbable Wound Dressings. *Gels* **2022**, *8*, 107. [CrossRef]

32. Nichita, M.V.; Paun, M.A.; Paun, V.A.; Paun, V.P. Fractal analysis of brain glial cells. Fractals dimension and lacunarity. *Univ. Politeh. Buchar. Sci. Bull. Ser. A Appl. Math. Phys.* **2019**, *81*, 273–284.

33. Bordescu, D.; Paun, M.A.; Paun, V.A.; Paun, V.P. Fractal analysis of Neuroimagistic. Lacunarity degree, a precious indicator in the detection of Alzheimer's disease. *Univ. Politeh. Buchar. Sci. Bull. Ser. A Appl. Math. Phys.* **2018**, *80*, 309–320.

34. Postolache, P.; Borsos, Z.; Paun, V.A.; Paun, V.P. New Way in Fractal Analysis of Pulmonary Medical Images. *Univ. Politeh. Buchar. Sci. Bull. Ser. A-Appl. Math. Phys.* **2018**, *80*, 313–322.

35. Scott, D.W. *Statistics: A Concise Mathematical Introduction for Students, Scientists, and Engineers*; John Wiley & Sons, Inc.: Hoboken, NJ, USA, 2020.

36. Available online: http://imagesci.fch.vut.cz/includes/harfa_download.inc.php (accessed on 5 October 2022).

37. Li, Y.; Qi, X.; Chen, Y.; Wang, L.; Li, Z.; Sun, J.; Jia, J. Voxel field fusion for 3d object detection. In Proceedings of the IEEE Conference on Computer Vision and Pattern Recognition 2022, New Orleans, LA, USA, 21–24 June 2022.

Article

A Modified Sol–Gel Synthesis of Anatase {001}-TiO$_2$/Au Hybrid Nanocomposites for Enhanced Photodegradation of Organic Contaminants

Abubakar Katsina Usman [1,2], Diana-Luciana Cursaru [1], Gheorghe Brănoiu [3], Raluca Şomoghi [1,4], Ana-Maria Manta [1], Dănuţa Matei [1] and Sonia Mihai [1,*]

[1] Faculty of Petroleum Technology and Petrochemistry, Petroleum-Gas University of Ploiesti, 100680 Ploieşti, Romania
[2] Department of Pure and Industrial Chemistry, Bayero University Kano, PMB 3011, Kano 70006, Nigeria
[3] Faculty of Petroleum and Gas Engineering, Petroleum-Gas University of Ploiesti, 100680 Ploieşti, Romania
[4] National Institute for Research and Development in Chemistry and Petrochemistry—ICECHIM, 060021 Bucharest, Romania
[*] Correspondence: smihai@upg-ploiesti.ro

Abstract: A sol–gel synthesis technique was employed for the preparation of anatase phase {001}-TiO$_2$/Au hybrid nanocomposites (NCs). The scalable, schematic, and cost-efficient method was successfully modified using HF and NH$_4$OH capping agents. The photocatalytic activity of the as-synthesized {001}-TiO$_2$/Au NCs were tested over 2-cycle degradation of methylene blue (MB) dye and pharmaceutical active compounds (PhACs) of ibuprofen and naproxen under direct sunlight illumination at 35 °C and 44,000 lx. Transmission electron microscopy (TEM), high resolution transmission electron microscopy (HR-TEM), fast Fourier transform (FFT), X-ray diffraction (XRD), X-ray photoelectron spectroscopy (XPS), energy dispersive X-ray spectroscopy (EDS), and ultraviolet–visible diffuse reflectance spectroscopy (UV–Vis DRS) were employed for the characterization of the as-prepared sample. The characterization results from the TEM, XPS, and XRD studies established both the distribution of Au colloids on the surface of TiO$_2$ material, and the presence of the highly crystalline structure of anatase {001}-TiO$_2$/Au NCs. Photodegradation results from the visible light irradiation of MB indicate an enhanced photocatalytic performance of Au/TiO$_2$ NCs over TiO$_2$. The results from the photocatalytic activity test performed under direct sunlight exposure exhibited promising photodegradation efficiencies. In the first cycle, the sol–gel synthesized material exhibited relatively better efficiencies (91%) with the MB dye and ibuprofen, while the highest degradation efficiency for the second cycle was 79% for the MB dye. Pseudo first-order photodegradation rates from the first cycle were determined to be comparatively slower than those from the second degradation cycle.

Keywords: modified sol–gel synthesis; PhACs; nanocomposites; capping agents; anatase TiO$_2$

1. Introduction

The global replenishment of organic dyes and pharmaceutical active compounds (PhACs) into the environment exacerbates the ecological threats posed by the process and the resultant effluent pollutants to the aquatic system. These organic contaminants get into water through diverse activities of the pharmaceutical, textile, and food industries. Many studies have forewarned of the serious risks associated with these pollutants to human health, even in small traceable quantities. Data show that between 60 and 80% of PhACs are not being absorbed by humans or animals [1]; this signifies that thousands of tons of PhACs are being discharged into the environment on a daily basis. For optimum pollution control of PhACs, their sources must be targeted.

Several approaches have been employed to tackle the water pollution caused by organic dyes and pollutants of emerging concern such as PhACs. These include electrochemical methods that employ different electrode materials [2], and biological remediation such as phytoremediation or the bioreactor approach [3]. Others are ozonation and advanced oxidation [4,5] as well as photo-assisted catalysis [6]. However, conventional wastewater treatment technologies such as adsorption and biological processes are challenged by the formation of harmful bi-products, and have been extensively reported to be deficient in the complete removal of these contaminants [7,8]. This necessitates the substantial efforts being made by many researchers to design an optimal purification technique for the successful elimination of these obstinate contaminants from the surface water and groundwater.

Photo-induced heterogeneous nanocatalysis—a proficient advanced oxidation process (AOP)—has been greatly used for the removal of these recalcitrant organic pollutants from wastewater [9]. Titanium dioxide (TiO_2) serves as the researchers' paradigm of ideal photocatalytic materials, with anatase and rutile crystal structures the two most common forms of its polymorphs [10]. The anatase TiO_2 has been widely reported as the more reactive phase than the rutile. Luttrell et al. [11] reported that the bulk transfer of excitons to the anatase surface contributes to its greater surface reaction than in rutile. Another parameter that strongly determines the reactivity and photocatalytic performance of the TiO_2 is its orientation, with {001} facets proven to be more reactive than the other facets due to their greater degree of reduction and low density surface under well-layered Ti atoms [12]. However, the two main unresolved drawbacks that retard the performance of TiO_2 remain its limited light application to UV range, and the fast recombination of charge carriers.

The deposition of plasmonic metal nanoparticles (NPs) such as Pt-NPs, Ag-NPs, and Au-NPs on metal oxide photocatalysts increases the photo-current density of the nanosheets and acts as a plasmon source in the visible light region [13]. This technique is among the most promising to extend its light absorption. Recently, precious metals of Au, Ag, Pd, and Pt were used by Conte et al. [14] to modify the TiO_2 surface for renewable energy applications. The plasmon effect and optoelectronic properties of the metals as well as their function as an electron sink were principally determined to enhance the performance of TiO_2 through band gap reduction. In 2021, a platinized surface of {001}-TiO_2 NSs was successfully fabricated via the uniform dispersion of Pt colloids on TiO_2 nanosheets by Zhao et al. [15]. Pt colloids facilitated hydrogen reduction of the reactive {001} orientations on TiO_2 at 673 K.

Furthermore, various studies have demonstrated that the synthesis techniques employed in the fabrication of semiconductor-based photocatalysts largely determines their physicochemical properties and photocatalytic activity. Solution-phase methods such as sol–gel, hydrothermal/solvothermal, and co-precipitation are the most promising synthesis routes for photocatalysts because they are simple, cost-effective, and do not require complex equipment [16]. They also allow for the incorporation of capping agents that control the material growth and agglomeration. Among them, the sol–gel method is favorable because it allows for easy regulation of important variables such as size, shape, surface area, and the pore volume of the material at relatively lower process temperature and pressure [17]. Chebil et al. (2015) successfully deposited high quality ZnO on a porous, etched silicon with a preferential (100) orientation via the sol–gel spin coating method [18]. The technique aided in the attainment of porous Si, which showed better ZnO deposition than that deposited on the Si substrates.

The sol–gel synthesis method is one of the most potent wet-chemical methods for the preparation of nano-sized-metal-oxide semiconductor photocatalysts. The technique involves the formation of colloidal suspension (sol) and a semi-rigid colloidal network (gel) in two principal processing steps viz. the hydrolysis of metal oxide precursors to form the sol; and poly-condensation of the hydrolyzed sol solution into a gel-like material. Aging, drying, and calcination (thermal treatment) of the gel are other steps before the purified form of the desired material is obtained. Some of the important benefits of using

the sol–gel synthesis method includes the formation of high purity composite materials, narrow particle size distribution, and a lower processing temperature requirement. The use of capping agents such as hydrogen fluoride (HF) and ammonium hydroxide (NH$_4$OH) play a significant role in the control and stabilization of material growth. Previous studies using other wet chemical methods have revealed how the presence of fluoride (F$^-$) ions on the TiO$_2$ surface during preparation can influence the formation of the anatase phase TiO$_2$ with a {001} orientation. For example, selective growth of {001} facets of anatase TiO$_2$ was obtained by Yasir et al. in the presence of the HF capping agent using the solvothermal method [19].

In this work, degradation of PhACs of ibuprofen (Figure 1a) and naproxen (Figure 1b) as well as cationic MB (Figure 1c) under sunlight was achieved using {001}-faceted anatase-phase-TiO$_2$/Au hybrid nanocomposites (NCs) prepared by the modified sol–gel method (MSGM) with HF and NH$_4$OH as stabilizing agents. Evidence of improved photocatalytic performance of the nanocomposites was investigated using degradation of aqueous MB under controlled visible light irradiation.

(a)

(b)

(c)
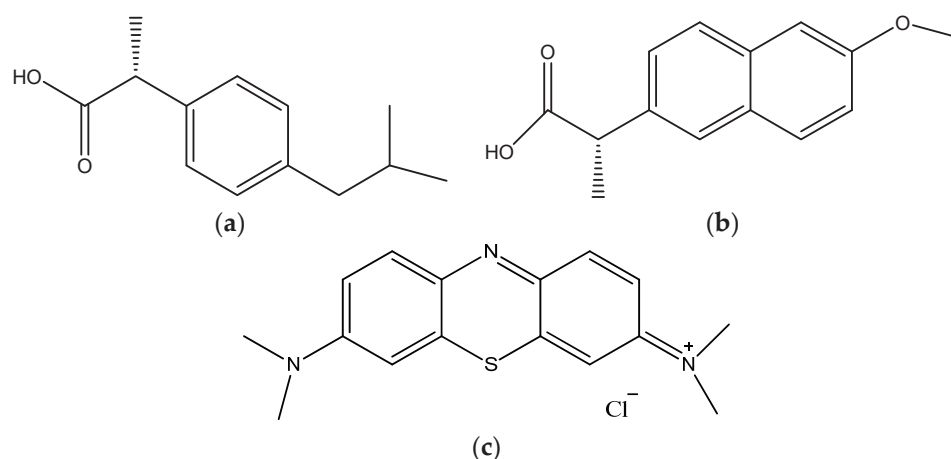
Figure 1. (**a**) Ibuprofen; (**b**) Naproxen; (**c**) Methylene blue dye.

2. Results and Discussion

2.1. X-ray Diffraction (XRD)

In Figure 2, the presence of sharp diffraction peaks at 2θ values of 25.4, 37.9, 48.1, 53.2, 55.1, 62.8, and 75° could be observed. These peaks corresponded to the respective plane values (101), (004), (200), (105), (211), (204), and (301), which firmly indicates the formation of a crystalline structure that can be identified with anatase, a polymorph phase of TiO$_2$ [20]. Exposure of the pure anatase phase surface of TiO$_2$ can be established by the non-appearance of diffraction peaks at 2θ values of 27° and 31° for the rutile and brookite phases, respectively [21]. Preferred crystal growth along the (001) facet is indicated by the appearance of a broad (004) diffraction peak at 2θ = 37.9° [22]. Diffraction peaks associated with the gold colloids could not be observed. This may either be due to the possibility of overlapping between the diffractograms of TiO$_2$ and gold colloids, or that the equipment was unable to detect the signals corresponding to gold colloids, which can be attributed to low Au-NP loading [23]. The refinement of the crystal structure by the Rietveld method of anatase TiO$_2$ with body-centered tetragonal symmetry belonging to the space group I41/amd (no. 141), the following parameters of the crystal structure were obtained: a = b = 3.760 Å and c = 9.494 Å. The refinement of the anatase crystal structure also allowed for the determination of the interplanar distances for the main planes of its crystal structure: (101) d = 3.512 Å; (004) d = 2.373 Å; (200) d = 1.890 Å; (105) d = 1.697 Å; (211) d = 1.664 Å; (204) d = 1.478 Å; (220) d = 3.336 Å; (215) d = 1.262 Å. In the anatase crystal structure, the bond length of the Ti–O connections is in the range of 1909–1946 Å;

Ti–Ti is 3034 Å; other interatomic distances being those between oxygen atoms O–O with a length between 2378–3034 Å.
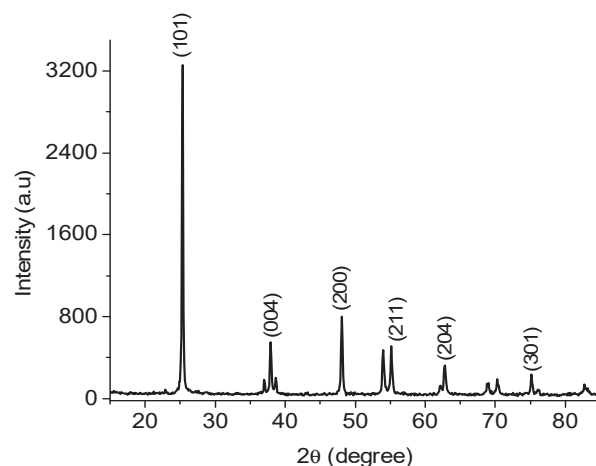
Figure 2. X-ray diffraction (XRD) patterns of the hybrid Au/TiO$_2$ nanosheets.

2.2. X-ray Photoemission Spectroscopy (XPS)

To further ascertain the electronic structure and chemical state of the as-synthesized material, XPS analysis was carried out, and it revealed clear, convoluted spectra (Figure 3a) of the Ti, Au, and O elements. Upon deconvolution of the Ti (2p) peak (Figure 3b) from the XPS spectrum, peaks corresponding to the binding energies (BE) of Ti were observed at the 458.42 and 464.08 eV states, which perfectly fit the Ti ($2p_{3/2}$) and Ti ($2p_{1/2}$) binding energy characteristics [24]. The splitting energy of 5.66 eV confirms the presence of the Ti^{4+} oxidation state between the two peaks [25]. The BE of 529.70 eV corresponding to O (1S) from the deconvoluted O (1s) XPS spectrum (Figure 3d) confirms the Ti–O–Ti chemical bonding in the synthesized material [26]. The decomposed XPS spectrum of Au (4f) (Figure 3c) was also studied to establish the presence of Au colloids in the synthesized nanosheets. The chemical state of Au in Au/{001}TiO$_2$ NSs gave rise to two peaks at 83.17 eV and 86.75 eV corresponding to the Au ($4f_{7/2}$) and Au ($4f_{5/2}$) core-level excitations. The small deviation in the Au ($4f_{7/2}$) BE peak position (83.17 eV) relative to the Au-bulk standard theoretical value of 84 eV indicates the successful preparation of Au-NPs [27]. The spin-orbit coupling of 3.58 eV between the Au ($4f_{7/2}$) and Au ($4f_{5/2}$) peaks validates the retention of the Au^0 metallic character [28].
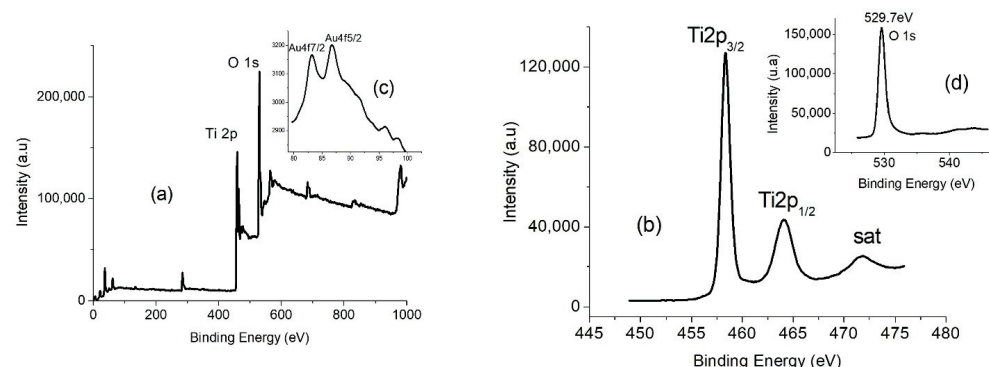
Figure 3. X-ray photoemission spectroscopy (XPS) peaks of (**a**) convoluted spectra of Ti 2p, O 1s, and Au 4f; (**b**) deconvoluted Ti 2p spectra; (**c**) deconvoluted Au 4f spectra; and (**d**) deconvoluted O1s spectra.

2.3. Transmission Electron Microscopy-Energy Dispersive X-ray (TEM-EDS)

The TEM and EDS images further indicate the prospect of Au-NPs hybridization in the accessible TiO$_2$ sites with a size range between 20 and 25 nm. The TEM image (Figure 4a)

clearly displays near ellipsoid shape particles, with darker particles randomly distributed on the TiO$_2$ surface assumed to be the Au-NPs. The polycrystalline nature and d-spacing of the as-synthesized photocatalyst were further revealed by the complementary information from HR-TEM (Figure 4b,c) and its corresponding FFT (Figure 4d) analysis using Image J software. FFT analysis of the noise-refined TEM lattice fringe images (Figure 5a–c) revealed lattice spacing of 2.39 Å and 3.51 Å with an interfacial angle of 68.3° between them, which is consistent with the theoretical characteristics of the (004) and (101) lattice planes [29]. The supplementary data from EDS (Figure 6) examination confirms the presence of Ti, Au, and O, which corroborates the XPS data, and confirms the assumption from the TEM analysis that Au-NPs are randomly distributed on the surface of TiO$_2$ NCs.

(a)

(b)

(c)
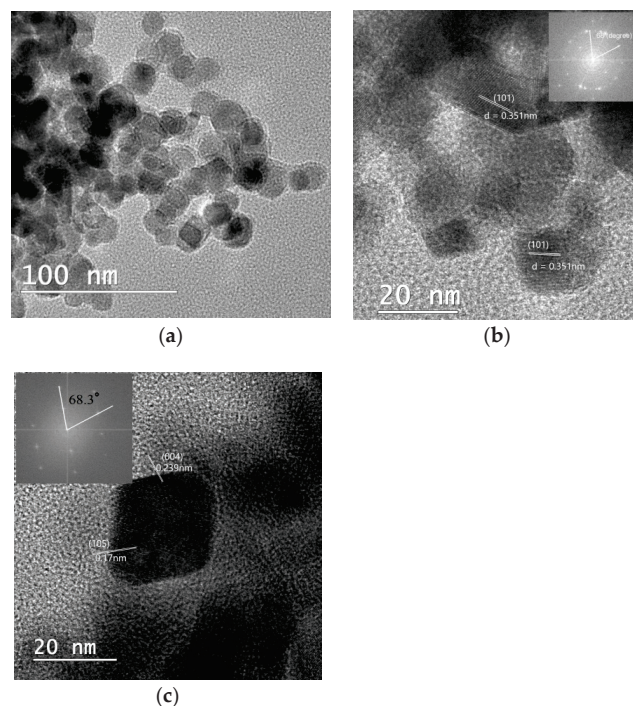
Figure 4. (**a**) TEM image of TiO$_2$ NSs; (**b**,**c**) HR-TEM images obtained from a small portion of (**a**); insert HR-TEM corresponding FFT image.

(a)

(b)

(c)
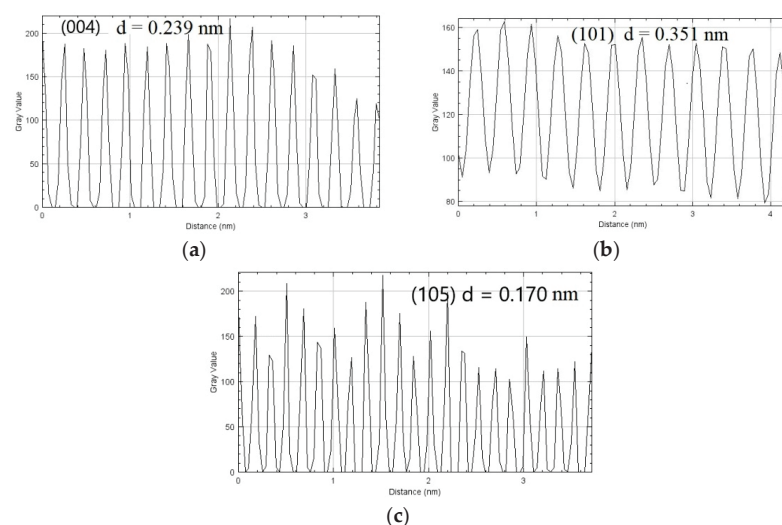
Figure 5. Magnified lattice fringes for d-spacing calculation in (**a**) (004), (**b**) (101), and (**c**) (105) peaks.
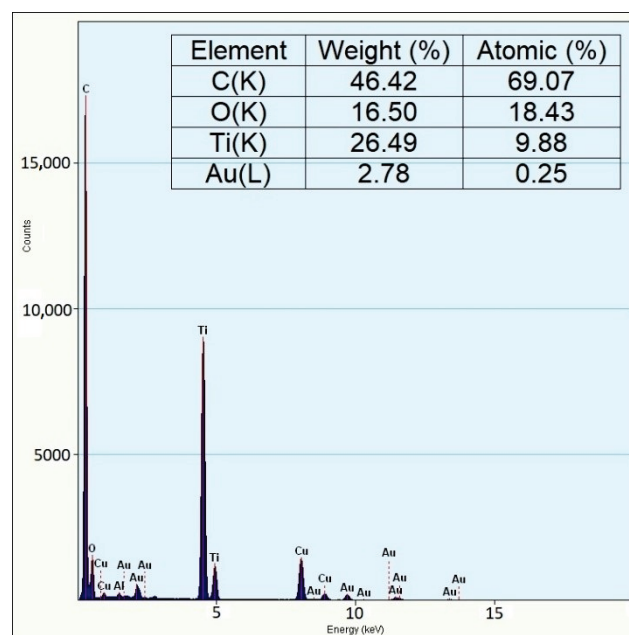
Figure 6. Energy dispersive X-ray (EDX) image for the as-synthesized TiO$_2$/Au NSs.

2.4. Ultraviolet–Visible Diffuse Reflectance Spectroscopy (UV–Vis DRS)

The band gap of the as-prepared NCs was determined by the Tauc plot from the Kubelka–Munk absorbance obtained from the UV–Vis diffuse absorption spectra. The UV–Vis diffuse absorption spectra (Figure 7a) of TiO$_2$/Au NSs displayed a strong absorption peak shoulder in the UV region at ~384 nm, and another peak shoulder in the visible region at ~592 nm, which corresponded to band gap energies of 3.23 eV for TiO$_2$ and 2.09 eV for Au-NPs. The Tauc plot (Figure 7b) shows a decrease in the band gap energy from 3.23 eV to 3.08 eV, thanks to the deposited Au-NPs in the TiO$_2$ lattice, which results in the light red shift from the UV to visible region that is believed to enhance photocatalytic activity.
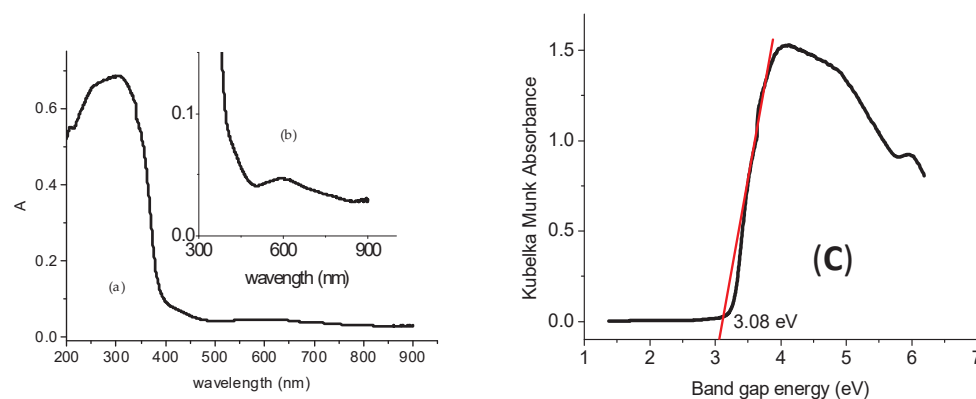
Figure 7. (**a**) UV–Vis diffuse absorption spectra of TiO$_2$/Au; and (**b**) Additional peak shoulder in the visible region; and (**c**) Tauc plot for band gap determination of TiO$_2$/Au NSs.

2.5. Photocatalytic Activity

In order to examine the photocatalytic performance of TiO$_2$ and Au/TiO$_2$ NCs, visible light degradation of MB and solar-assisted degradation of MB, ibuprofen, and naproxen were performed.

Figure 8d,e show the UV–visible absorption spectra of MB degradation by pristine TiO$_2$ and Au/TiO$_2$ NCs, respectively, using a controlled visible light illumination. It can be seen that the maximum absorption peak was around 665 nm, which corresponds to

the characteristic peak of MB. The reduction in the absorption peaks with an extension in the irradiation time signifies the progressive degradation of MB. Under visible light irradiation, both pristine TiO_2 and Au/TiO_2 NCs were able to remarkably degrade MB, with Au/TiO_2 NCs having superior photocatalytic performance over pristine TiO_2. For instance, after 60 min of controlled visible light irradiation, $Au/\{001\}\text{-}TiO_2$ NCs exhibited 93.71% photodegradation efficiency compared to the 87.14% efficiency of the pristine TiO_2.
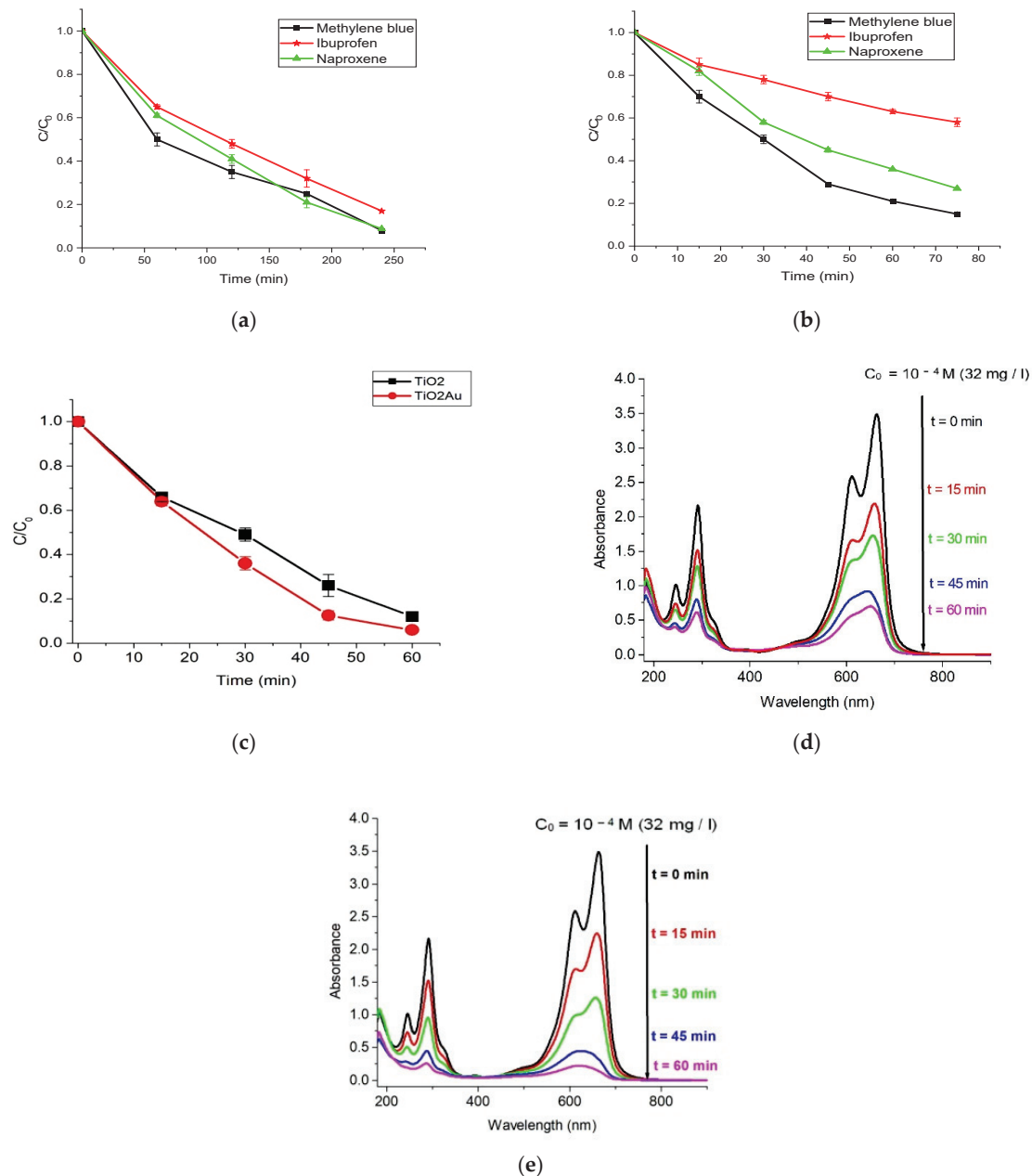
Figure 8. Photocatalytic degradation of methylene blue (MB) dye, ibuprofen, and naproxen for (**a**) cycle 1 and (**b**) cycle 2 under direct solar irradiation; (**c**) degradation of MB under controlled visible light irradiation; and UV–visible spectra of (**d**) TiO_2 and (**e**) Au/TiO_2 NCs for MB degradation.

The photocatalytic activity test of TiO_2/Au NCs was also carried out for mineralization of MB dye, ibuprofen, and naproxen in two photodegradation cycles under direct sunlight exposure. No significant mineralization was recorded for all three contaminants when the reaction was conducted in the absence of the catalyst after 2 h.

The photodegradation efficiencies for the two photodegradation cycles are presented in Table 1, with their corresponding fitting results in Figure 8a for cycle 1 and Figure 8b for cycle 2. The results from the first cycle show that naproxen had a lower degradation efficiency of about 83% than both MB and ibuprofen, with about 92% each after 4 h. However, results from cycle 2 suggest a higher degradation rate within the first 60 min than cycle 1, which can be seen from the pseudo first-order plots (Figure 9a,b). This may be connected to an improved adsorption capacity of the sample photocatalyst after cycle 1.

Table 1. Solar-assisted photodegradation efficiencies of {001}-TiO$_2$/Au NCs for cycles 1 and 2.

Cycle 1 Photodegradation Efficiency (%)				
Time	60 min	120 min	180 min	240 min
MB (4.10 × 10^{-4} M)	50.00	65.00	77.75	91.75
Ibuprofen (200 mg/L)	39.00	59.00	79.00	91.20
Naproxen (4.4 mg/L)	34.10	51.10	67.00	82.95
Cycle 2 Photodegradation Efficiency (%)				
Time	15 min	30 min	45 min	60 min
MB (4.10 × 10^{-4} M)	30.00	50.00	75.00	79.00
Ibuprofen (200 mg/L)	15.00	22.00	30.00	37.00
Naproxen (4.4 mg/L)	18.18	42.05	55.00	64.09

(a)

(b)

(c)
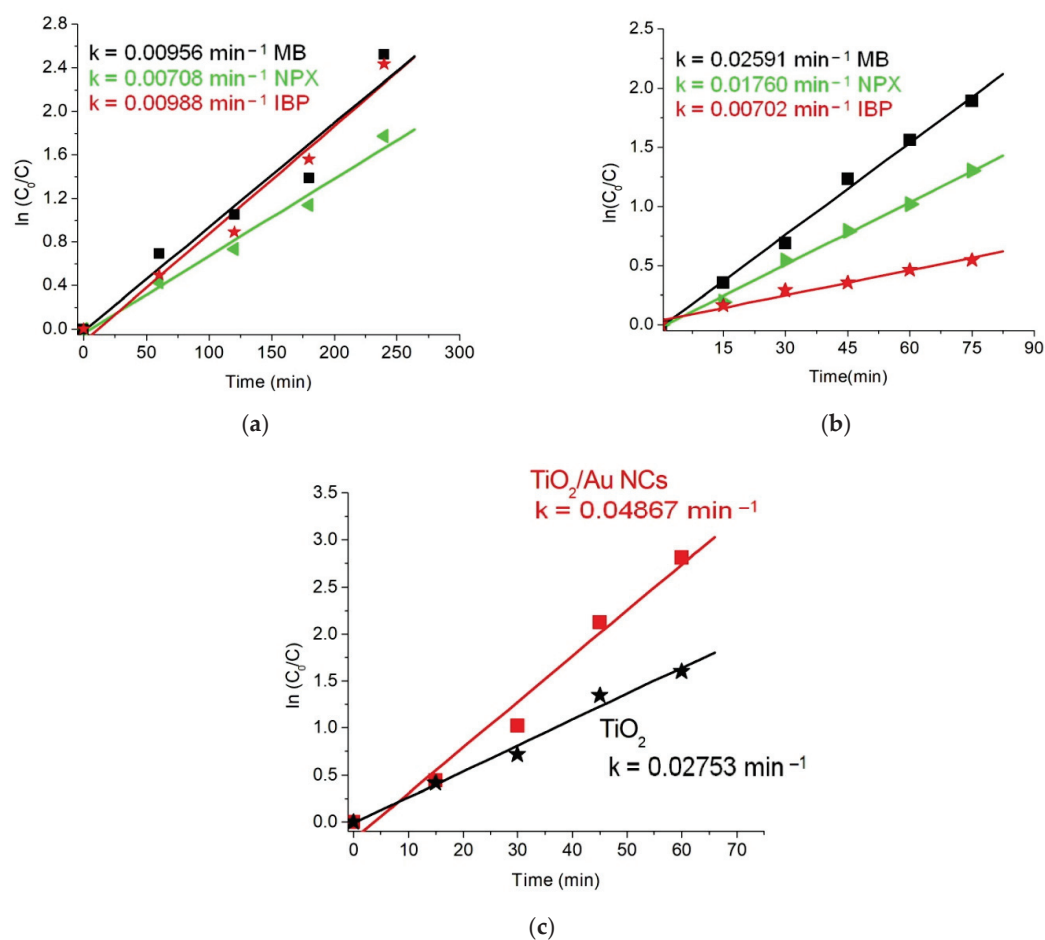
Figure 9. Pseudo-first order kinetics of (MB) dye, ibuprofen, and naproxen for (**a**) cycle 1 and (**b**) cycle 2 under direct sunlight exposure; and (**c**) MB under controlled visible light irradiation.

2.6. Proposed Mechanism

The proposed reaction mechanism based on the photocatalytic reactions data are explained in the following equations [30,31]. In summary, photo-excited charge carriers are formed upon strong absorption of the ultraviolet A (UVA) region of the solar irradiation by {001}-TiO$_2$/AuNSs.

$$\text{Au/TiO}_2\{001\} \xrightarrow{\text{hv (solar)}} \text{Au/TiO}_2\{001\}\left(e_{CB}^- + h_{VB}^+\right) \tag{1}$$

The strong absorption within the visible region was aided by the presence of the distributed Au colloids on the TiO$_2$ surface. The photo-induced holes in the VB of TiO$_2$ then migrate to the catalyst surface to react with the adsorbed hydroxyl (OH$_{adsorbed}^-$) ions on the catalyst surface, generating strong oxidizing •OH$_{adsorbed}$ radicals.

$$\text{OH}_{adsorbed}^- + h_{VB}^+ \rightarrow \bullet\text{OH}_{adsorbed} \tag{2}$$

The photo-generated electrons in the conduction band of the catalyst combine with O$_2$ to form •O$_2^-$ radicals, as follows:

$$\text{O}_2 + e_{CB}^- \rightarrow \bullet\text{O}_2^- \tag{3}$$

The highly oxidized radicals (•OH$_{adsorbed}$ and •O$_2^-$) produced in Equations (2) and (3) above can both oxidize the organic contaminants (MB dye, IBP, and NPX) coming into contact with the catalyst surface. Equations (4)–(6) below represent the degradation reactions of MB dye, naproxen, and ibuprofen with •OH$_{adsorbed}$ radicals. The corresponding reactions using •O$_2^-$ radicals are displayed in Equations (7)–(9). The photo-oxidation reactions pass through reaction intermediates that form CO$_2$ and H$_2$O on further oxidation reactions.

$$\text{Au/TiO}_2\{001\}(\bullet\text{OH}_{adsorbed}) + \text{MB} \rightarrow \text{intermediates} + \text{CO}_2 + \text{H}_2\text{O} \tag{4}$$

$$\text{Au/TiO}_2\{001\}(\bullet\text{OH}_{adsorbed}) + \text{NPX} \rightarrow \text{intermediates} + \text{CO}_2 + \text{H}_2\text{O} \tag{5}$$

$$\text{Au/TiO}_2\{001\}(\bullet\text{OH}_{adsorbed}) + \text{IBP} \rightarrow \text{intermediates} + \text{CO}_2 + \text{H}_2\text{O} \tag{6}$$

$$\text{Au/TiO}_2\{001\} (\bullet\text{O}_2^-) + \text{MB} \rightarrow \text{intermediates} + \text{CO}_2 + \text{H}_2\text{O} \tag{7}$$

$$\text{Au/TiO}_2\{001\} (\bullet\text{O}_2^-) + \text{NPX} \rightarrow \text{intermediates} + \text{CO}_2 + \text{H}_2\text{O} \tag{8}$$

$$\text{Au/TiO}_2\{001\} (\bullet\text{O}_2^-) + \text{IBP} \rightarrow \text{intermediates} + \text{CO}_2 + \text{H}_2\text{O} \tag{9}$$
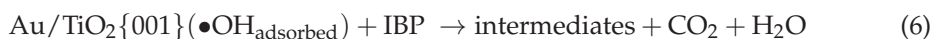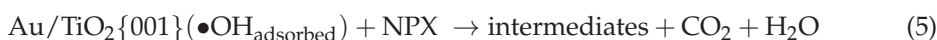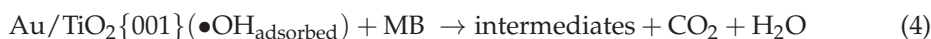
3. Conclusions

In conclusion, we have reported on the successful modification of a facile, scalable, and cost-efficient sol–gel solution-phase route, incorporating HF and NH$_4$OH as capping agents for the preparation of {001}-faceted anatase TiO$_2$/Au nanosheets. The hybrid photocatalyst was examined to be photocatalytically active for the degradation of methylene blue dye, ibuprofen, and naproxen as organic contaminants in an aqueous water solution. Performance improvement of the as-synthesized NCs was observed from the visible light degradation data of an aqueous MB solution.

4. Materials and Methods

4.1. Materials and Reagents

Titanium(IV) hydroxide [Ti(OH)$_4$], hydrogen fluoride (HF), methylene blue (C$_{16}$H$_{13}$N$_3$SCl), and ammonium hydroxide (NH$_4$OH) were purchased from Fluka Chemicals, Buchs, Switzerland, Tris(triphenylphosphinegold)oxonium tetrafluoroborate from Sigma Aldrich (Burlington, MA, USA) ibuprofen, and naproxen drugs from Antibiotic a+ and KRKA d.d., respectively. Class A glassware was used throughout the experiment, and cleaned and baked for 2 h before use.

4.2. Synthesis of Au/TiO$_2$ Photocatalyst

The gold colloid solution was first prepared according to the procedure previously reported by Mihai et al. [32]. Briefly, 0.1452 g of Schiff base [2,3-dimethyl-1- phenyl-4-(N-2-hydroxy-3-methoxybenzaldehyde)-3-pyrazolin-5-one] and 0.0740 g of Tris (triphenylphosphinegold) oxoniumtetraflororoborate {[O(Au PPh$_3$)$_3$][BF$_4$]} were dissolved in CH$_3$CN solvent at room temperature. TiO$_2$-Au NSs were synthesized via a modified sol–gel synthesis technique reported by Zhang et al. [33]. Briefly, 5 g of Ti(OH)$_4$ was mixed with 15 mL HF for 150 min at 100 °C. The solution was then mixed with 15 mL of the as-synthesized gold colloid. The resulting mixture was stirred for 30 min at room temperature. The precipitation was performed using 30 mL of 1 M aqueous NH$_4$OH solution and distilled water. The sample was then dried and calcined in air at 450 °C for 3 h at a 5 °C/min heating rate. The fabricated Au/TiO$_2$ NSs were investigated using XRD, XPS, TEM, HR-TEM, EDS, and UV–Vis DRS.

4.3. X-ray Diffraction (XRD) Analysis

The crystal structure of the as-synthesized Au-TiO$_2$ NCs was analyzed using a Bruker D8 Advance diffractometer (Karlsruhe, Germany) (θ-θ type) with characteristic CuKα radiation (λ = 1.5418 nm) and graphite monochromator operated at a voltage and current of 40 kV and 40 mA, respectively. The XRD pattern was recorded in the 2θ measurement range between 15° and 90° at a scan speed of 0.1°/5 s. NIST profile standards SRM 660a and SRM 1976 were used to calibrate the device and emission source profile. The qualitative analysis was carried out with the Diffracplus Basic software with the Search/Match option and the PDF-ICDD 2-2008 database. Quantitative analysis was performed with the Diffracplus TOPAS 4.1 software by the Rietveld refinement method and pseudo-Voigt function for peak matching.

4.4. X-ray Photolectron Spectroscopy (XPS)

The XPS spectra for the analysis of surface elements and their oxidation states were obtained using an ESCALAB XI+ Termo Scientific Photoelectron Spectrometer, Waltham, MA, U.S. Al K-α (1486.6 eV) radiation was used in the constant analyzed mode with 200 eV pass energy to plot the spectra.

4.5. Transmission Electron Microscopy (TEM)

To further study the structural and chemical nature of the as-synthesized sample, high resolution transmission electron microscopy (HR-TEM) was performed using an FEI Tecnai G2 F-20 TWINCryo-TEM (FEI American Company, Brno, Czech Republic) operated at an acceleration voltage of 200 kV with the magnification of 80,000 and 20,000.

4.6. UV–Vis Diffuse Reflectance Spectroscopy (DRS) Analysis

The spectra studies of the as-prepared materials were conducted using a UV–Vis spectrophotometer (Jasco UV–Vis V-550) (Jasco Corporation, Tokyo, Japan) in the wavelength range of 200 to 900 nm with an integrating sphere assembly. The sample was diluted with MgO (ratio 1:6) and then mechanically mixed as a reflectance standard.

4.7. Photocatalytic Experiment

To evaluate the photocatalytic activity of the prepared NSs, direct sunlight exposure and controlled visible light sources were employed. A Toption photochemical reactor, (TOPTION INSTRUMENT CO.,LTD., Xi'an China), equipped with a 300 W Xe lamp was used for the visible light degradation of an aqueous methylene blue solution by both pristine {001}-TiO$_2$ and Au/{001}-TiO$_2$ NCs. In a typical experiment, 0.025 g of the as-synthesized NCs was dispersed in 32 mg/L of the aqueous MB solution with stirring and subsequently irradiated with the photoreactor. An appropriate solution was collected at 15 min intervals to monitor the absorption spectrum using a Shimadzu 2600 UV–Vis spec-

trophotometer. Photocatalytic degradation efficiency of the materials was then calculated using Equation (10) below.

$$\text{Photodegradation efficiency } (\%) = \frac{C_0 - C_t}{C_0} \times 100\% \tag{10}$$

where C_0 is the initial concentration of aqueous MB solution, and C_t is the concentration of MB at any specific time of visible light irradiation, respectively.

Furthermore, two cycles of photocatalytic experimental studies of the as-synthesized nanosheets for the degradation of methylene blue dye and the NSAIDs of ibuprofen and naproxen were conducted under sunlight, with a light intensity of I = 44,000 lx and a temperature of 35 °C. A UV–Vis spectrophotometer was used to monitor the reaction at 60 min intervals for 4 h in the first cycle, and at 15 min intervals for 1 h in the second cycle.

The photodegradation process in all two degradation cycles for all of the organic contaminants was examined by keeping track of the changes in the concentration in the organic content (MB, ibuprofen, and naproxen) as a function of light irradiation. Throughout the photocatalytic experiments, 0.05 g of the as-synthesized photocatalyst and 15 mL each of 4×10^{-4} M methylene blue, 200 mg/L ibuprofen, and 4.4 mg/L were used.

Author Contributions: A.K.U., D.-L.C. and S.M. wrote the main manuscript; D.-L.C., A.K.U. and A.-M.M. were responsible for the synthesis of {001}-TiO$_2$/Au; D.M. was responsible for the photocatalytic experiments; A.-M.M. and A.K.U. performed the UV–Vis; D.-L.C. and S.M. were responsible for the XPS investigations; R.Ş. was responsible for the TEM investigations; G.B. prepared the XRD investigations. All authors have read and agreed to the published version of the manuscript.

Informed Consent Statement: Not applicable.

Data Availability Statement: Not applicable.

Conflicts of Interest: The authors declare no conflict of interest.

References

1. Göbel, A.; Thomsen, A.; McArdell, C.S.; Joss, A.; Giger, W. Occurrence and sorption behavior of sulfonamides, macrolides, and trimethoprim in activated sludge treatment. *Environ. Sci. Technol.* **2005**, *39*, 3981–3989. [CrossRef]
2. Radjenovic, J.; Sedlak, D.L. Challenges and Opportunities for Electrochemical Processes as Next-Generation Technologies for the Treatment of Contaminated Water. *Environ. Sci. Technol.* **2015**, *49*, 11292–11302. [CrossRef]
3. Shah, A.; Shah, M. Characterisation and bioremediation of wastewater: A review exploring bioremediation as a sustainable technique for pharmaceutical wastewater. *Groundw. Sustain. Dev.* **2020**, *11*, 100383. [CrossRef]
4. Lee, Y.; von Gunten, U. Advances in predicting organic contaminant abatement during ozonation of municipal wastewater effluent: Reaction kinetics, transformation products, and changes of biological effects. *Environ. Sci. Water Res. Technol.* **2016**, *2*, 421–442. [CrossRef]
5. Ikehata, K.; Gamal El-Din, M.; Snyder, S.A. Ozonation and Advanced Oxidation Treatment of Emerging Organic Pollutants in Water and Wastewater. *Ozone Sci. Eng.* **2008**, *30*, 21–26. [CrossRef]
6. Jin, X.; Ma, J. Synthesis and comparison of photocatalytic activity under UV-visible or visible light irradiation for Bi$_3$TaO$_7$ and Bi$_2$YTaO$_7$ photocatalysts. *J. Mater. Sci. Mater. Electron.* **2018**, *29*, 18751–18759. [CrossRef]
7. Trellu, C.; Oturan, N.; Pechaud, Y.; Hullebush, E.D.V.; Esposito, G.; Outran, M.A. Anodic oxidation of surfactants and organic compounds entrapped in micelles-selective degradation mechanisms and soil washing solution reuse. *Water Res.* **2017**, *118*, 1–11. [CrossRef]
8. Wang, T.; Costan, J.; Centeno, A.; Pang, J.S.; Darvill, D.; Ryan, M.P.; Xie, F. Broad and enhanced fluorescence using zinc-oxide nanoflower arrays. *J. Mater. Chem.* **2015**, *3*, 2656–2663.
9. Kiran, S.V.; Rajesh, J.T.; Kinjal, J.S.; Pradyuman, A.J.; Atindra, D.S.; Vimal, G.G. Photocatalytic degradation of pharmaceutical and pesticide compounds (PPCs) using doped TiO$_2$ nanomaterials: A review. *Water-Energy Nexus* **2020**, *3*, 46–61.
10. Maolin, Z.; Tiedan, C.B.; Yunjian, W. Insights into TiO$_2$ polymorphs: Highly selective synthesis, phase transition, and their polymorph-dependent properties. *R. Soc. Chem.* **2017**, *7*, 52755–52761.

11. Luttrell, T.; Halpegamage, S.; Tao, J.; Kramer, A.; Sutter, E.; Batzill, M. Why is anatase a better photocatalyst than rutile?—Model studies on epitaxial TiO_2 films. *Sci. Rep.* **2014**, *4*, 4043. [CrossRef] [PubMed]

12. Piler, K.; Bahrim, C.; Twagirayezu, S.; Benson, J.T. Chapter Two—Lattice disorders of TiO_2 and their significance in the photocatalytic conversion of CO_2. *Adv. Catal.* **2020**, *66*, 109–233.

13. Panayotov, A.D.; Frenkel, A.; Morris, J.R. Catalysis and Photocatalysis by Nanoscale Au/TiO_2: Perspectives for Renewable Energy. *ACS Energy Lett.* **2017**, *2*, 1223–1231. [CrossRef]

14. Conte, F.; Rossetti, I.; Ramis, G.; Vaulot, C.; Hajjar-Garreau, S.; Bennici, S. Low Metal Loading (Au, Ag, Pt, Pd) Photo-Catalysts Supported on TiO_2 for Renewable Processes. *Materials* **2022**, *15*, 2915. [CrossRef] [PubMed]

15. Zhao, W.; Zhou, D.; Han, S.; Li, Y.; Liu, J.; Zhou, Y.; Shen, W. Metal–Support Interaction in Pt/TiO_2: Formation of Surface Pt–Ti Alloy. *J. Phys. Chem. C* **2021**, *125*, 10386–10396. [CrossRef]

16. Bellardita, M.; Yurdakal, S.; Palmisano, L. *4—Synthesis and Characterization of Titanium Dioxide and Titanium Dioxide–Based Materials, Metal Oxides, Titanium Dioxide (TiO_2) and Its Applications*; Elsevier: Amsterdam, The Netherlands, 2021; pp. 87–165, ISBN 9780128199602. [CrossRef]

17. Zikalala, S.A.; Kuvarega, A.T.; Mamba, B.B.; Mhlanga, S.D.; Nxumalo, E.N. The effect of synthetic routes on the physicochemical properties and optical response of N-doped titania–oxidized carbon nanotube nanohybrids. *Mater. Today Chem.* **2018**, *10*, 1–18. [CrossRef]

18. Chebil, W.; Fouzri, A.; Fargi, A.; Azeza, B.; Zaaboub, Z.; Sallet, V. Characterization of ZnO thin films grown on different p-Si substrate elaborated by solgel spin-coating method. *Mater. Res. Bull.* **2015**, *70*, 719–727. [CrossRef]

19. Yasir, M.; Azizan, M.T.; Ramli, A.; Ameen, M. Solvothermal Synthesis of Anatase TiO_2 Nanosheets with Exposed {001} Facets. *SainsMalaysiana* **2017**, *46*, 2515–2521. [CrossRef]

20. Zhang, N.; Liu, S.Q.; Fu, X.Z.; Xu, Y.J. Synthesis of $M@TiO_2$ (M = Au, Pd, Pt) core–shell with tunable photoreactivity. *J. Phys. Chem. C* **2011**, *115*, 9136–9145. [CrossRef]

21. Gu, L.; Wang, J.; Cheng, H.; Du, Y.; Han, X. Synthesis of nano-sized anatase TiO_2 with reactive {001} facets using lamellar protonated titanate as precursor. *Chem. Commun.* **2012**, *48*, 6978–6980. [CrossRef]

22. Pang, Y.; Xu, G.; Feng, Q.; Lv, J.; Qin, Y.; Zhang, Y.; Zheng, Z.; Wu, Y. Crystalline orientation preference for TiO_2 nanotube arrays with efficient photoelectrochemical properties. *Phys. Lett. A* **2018**, *382*, 2759–2762. [CrossRef]

23. Machín, A.; Cotto, M.; Ducongé, J.; Arango, J.C.; Morant, C.; Márquez, F. Synthesis and Characterization of $Au@TiO_2$ NWs and their Catalytic Activity by Water Splitting: A Comparative Study with Degussa P25. *Am. J. Eng. Appl. Sci.* **2017**, *10*, 298–311. [CrossRef]

24. Yu, Y.; Wen, W.; Qian, X.Y.; Liu, J.B.; Wu, J.M. UV and visible light photocatalytic activity of Au/TiO_2 nanoforests with Anatase/Rutile phase junctions and controlled Au locations. *Sci. Rep.* **2017**, *7*, 41253. [CrossRef] [PubMed]

25. Banerjee, B.; Amoli, V.; Maurya, A. Green Synthesis of Pt-Doped TiO_2 Nanocrystals with Exposed (001) Facets and Mesoscopic Void Space for Photo-Splitting of Water under Solar Irradiation. *Nanoscale* **2015**, *7*, 10504–10512. [CrossRef] [PubMed]

26. Ida, S.; Justin, S.J.; Wilson, P.; Neppolian, B. Facile synthesis of black $N-TiO_2/N-RGO$ nanocomposite for hydrogen generation and electrochemical applications: New insights into the structure-performance relationship. *Appl. Surf. Sci. Adv.* **2022**, *9*, 100249. [CrossRef]

27. Nyholm, R.; Berndtsson, A.; Martensson, N. Core level binding energies for the elements Hf to Bi (Z = 72−83). *J. Phys. C Solid State Phys.* **1980**, *13*, L1091. [CrossRef]

28. Sahoo, S.R.; Ke, S.C. Spin-Orbit Coupling Effects in Au 4f Core-Level Electronic Structures in Supported Low-Dimensional Gold Nanoparticles. *Nanomaterials* **2021**, *11*, 554. [CrossRef]

29. Zhang, Y.; Li, L.D.; Liu, H.Y. Photocatalytic reduction activity of {001} TiO_2 co-doped with F and Fe under visible light for bromate removal. *J. Nanomater.* **2016**, *2016*, 5646175. [CrossRef]

30. Balsamo, S.A.; Sciré, S.; Condorelli, M.; Fiorenza, R. Photocatalytic H_2 Production on Au/TiO_2: Effect of Au Photo deposition on Different TiO_2 Crystalline Phases. *J* **2022**, *5*, 92–104. [CrossRef]

31. Wang, B.-Y.; Hsiao, Y.-S.; Wei, P.-C.; Liu, Y.-T.; Chu, C.-C.; Hsiao, V.K.S. Visible Light-Induced Photocatalyst with Au/TiO_2 Nanocomposites Fabricated through Pulsed Laser-Induced Photolysis. *Catalysts* **2022**, *12*, 564. [CrossRef]

32. Mihai, S. Synthesis of Gold Nanoparticles Using Schiff Base. *Acta Phys. Pol. A* **2013**, *123*, 254–255. [CrossRef]

33. Zhang, L.Y.; You, J.; Li, Q.W.; Dong, Z.H.; Zhong, Y.J.; Han, Y.L.; You, Y.H. Preparation and Photocatalytic Property of Ag Modified Titanium Dioxide Exposed High Energy Crystal Plane (001). *Coatings* **2020**, *10*, 27. [CrossRef]

Structural, Optical, and Sensing Properties of Nb-Doped ITO Thin Films Deposited by the Sol–Gel Method

Madalina Nicolescu [1], Daiana Mitrea [1],*, Cristian Hornoiu [1], Silviu Preda [1], Hermine Stroescu [1],*, Mihai Anastasescu [1], Jose Maria Calderon-Moreno [1], Luminita Predoana [1], Valentin Serban Teodorescu [2,3], Valentin-Adrian Maraloiu [2], Maria Zaharescu [1] and Mariuca Gartner [1],*

[1] "Ilie Murgulescu" Institute of Physical Chemistry, Romanian Academy, 202 Splaiul Independentei, 060021 Bucharest, Romania
[2] National Institute of Materials Physics, 405 bis Atomistilor Street, 077125 Magurele-Ilfov, Romania
[3] Academy of Romanian Scientists, 3 Ilfov Street, 050045 Bucharest, Romania
* Correspondence: dmitrea@icf.ro (D.M.); hstroescu@icf.ro (H.S.); mgartner@icf.ro (M.G.); Tel.: +40-21-316-79-12 (ext. 588) (M.G.)

Abstract: The aim of the present study was the development of Nb-doped ITO thin films for carbon monoxide (CO) sensing applications. The detection of CO is imperious because of its high toxicity, with long-term exposure having a negative impact on human health. Using a feasible sol–gel method, the doped ITO thin films were prepared at room temperature and deposited onto various substrates (Si, SiO_2/glass, and glass). The structural, morphological, and optical characterization was performed by the following techniques: X-ray diffractometry (XRD), atomic force microscopy (AFM), scanning electron microscopy (SEM), transmission electron microscopy (TEM), and UV/Vis/NIR spectroscopic ellipsometry (SE). The analysis revealed a crystalline structure and a low surface roughness of the doped ITO-based thin films. XTEM analysis (cross-sectional transmission electron microscopy) showed that the film has crystallites of the order of 5–10 nm and relatively large pores (around 3–5 nm in diameter). A transmittance value of 80% in the visible region and an optical band-gap energy of around 3.7 eV were found for dip-coated ITO/Nb films on SiO_2/glass and glass supports. The EDX measurements proved the presence of Nb in the ITO film in a molar ratio of 3.7%, close to the intended one (4%). Gas testing measurements were carried out on the ITO undoped and doped thin films deposited on glass substrate. The presence of Nb in the ITO matrix increases the electrical signal and the sensitivity to CO detection, leading to the highest response for 2000 ppm CO concentration at working temperature of 300 °C.

Keywords: Nb-doped ITO thin films; Sol–gel; Optical properties; CO detection

1. Introduction

Indium tin oxide (ITO) is an n-type semiconductor with a wide energy band gap (3.7 eV), low electrical resistance, and high optical transparency in the visible domain. The development of ITO thin films is of a great interest in the scientific community as a result of their interesting properties, which make them possible candidates for different applications, such as optoelectronic devices [1–3], transparent conductive oxides [4], solar cells [5–7], gas sensors [8,9], biosensors [10–12], thermoelectric applications [13,14], and so on. ITO thin films can be prepared by various physical (magnetron sputtering [15–19], pulsed lased deposition [20], ion beam sputtering [21], and electron beam evaporation [22]) and chemical methods (sol–gel method [23,24], spray pyrolysis [25], and low-temperature combustion synthesis method [26]).

In terms of the gas sensing properties, these materials based on doped or undoped ITO thin films have been proven to detect formaldehyde [27], CO_2 [28–30], CO [31–33], NO_2 [34,35], chlorine [35], benzene [36], toluene [37], and ammonia gases [38–40]. Additionally, ITO thin films can sense ethanol [41,42] and water vapors [43]. Furthermore,

ITO-coated glass substrates were used in liquid crystals display (LCD) [44–47] and polymer dispersed liquid crystals device fabrication [48–50]. The suitable material for a certain application can be achieved by changing several parameters involved in the preparation process as follows: the deposition technique [16], the metal doping level [51], the pre- and final annealing temperatures [19], and the film thickness [22].

Carbon monoxide (CO) is among the most harmful gases, being associated with several health problems, even death depending on exposure time. CO is released into the environment because of the partial combustion of fuels from cars and domestic or industrial activities. Consequently, CO detection is necessary because of its odorless and colorless properties [52,53]. Over time, researchers have studied metal-oxides based systems, such as SnO_2, In_2O_3, ZnO [8,54], and indium-tin oxide (ITO) [55,56], with the aim to develop CO sensors. According to scientific reports, the properties of ITO thin films can be tailored by doping with various metals: Ag [57], Ga [58], Cr [59], Zn [30,60], Ti [61], Nb [62], and so on. In contrast with metal-doped ITO films, there are few reports concerning Nb-doped ITO thin films [51,62–64]. Therefore, these films were successfully obtained by radio frequency (RF) sputtering, pulsed laser deposition (PLD), and sol–gel methods to investigate the transparent conductive oxide, optoelectronic, and electrochromic properties [51,62–64]. The sol–gel method is a versatile and efficient procedure for the preparation of pure and doped metal oxide films or powders [65,66], showing some advantages such as purity, homogeneity, possibility to introduce dopants in large quantities, low processing temperature, ease of manufacturing, control over the stoichiometry, composition, and viscosity [67].

In this work, we explored the structural, morphological, and optical properties of multilayer Nb-doped ITO thin films prepared by the sol–gel method, deposited onto different substrates (glass, SiO_2/glass, and Si). The effects of the dopant (4% Nb) and of the type of substrate were examined by X-ray diffraction (XRD), atomic force microscopy (AFM), scanning electron microscopy (SEM), transmission electron microscopy (TEM), and spectroscopic ellipsometry (SE). The Nb doping level was chosen based on our previous work regarding the Zn-doped ITO as a CO_2 sensor.

As aforementioned, our aim was also to examine the influence of Nb doping on the detection properties of ITO thin films. Although this type of material was previously studied for certain applications, as far as the authors are aware, there are no literature data regarding its sensing properties. Therefore, the novelty of this work was the improvement in the electrical properties of ITO film through Nb doping, making it a more sensitive material for CO detection. Accordingly, the sample with the most suitable properties (thickness and porosity) was used for gas measurements of CO.

2. Results and Discussion

2.1. Structural Characterization

XRD Analysis

Figure 1a–c shows the XRD profiles of multilayer ITO/Nb thin films. Different substrates (Si, SiO_2/glass, and glass) were coated by five successive layers using the ITO/Nb sol–gel solution. To highlight the influence of the dopant on the ITO film structure, previously reported data [30] on the undoped ITO thin films are presented in Figure 1. The diffraction lines, corresponding to crystal planes (2 2 2), (4 0 0), (4 4 0), and (6 2 2), were observed for both ITO/Nb and ITO thin films. ITO, which is Sn-doped In_2O_3, crystalizes in the bixbyite-type cubic structure of In_2O_3, with Ia-3 space group (ICDD file no. 06-0416). Except for the diffraction line of Si (marked with an asterisk on the Figure 1a) belonging to the substrate, no other phases were detected in the XRD patterns, indicating that the Nb and Sn dopants were incorporated into the In_2O_3 structure. The doped samples present an improved crystallinity, based on the shape of the diffraction line (higher intensity and narrower width). The lattice constants are slightly larger for the doped samples, most likely owing to the incorporation of the dopants into the cubic bixbyite structure. The crystallite

size was estimated using Scherrer's equation [68] only for the crystal plane (222) and was found to be around 10 nm (Table 1).

$$D = \frac{0.94 \times \lambda}{\beta \times cos\theta},$$ (1)

where D is the average size of the crystallites, λ is the X-ray wavelength, β is the full width at half the maximum intensity (FWHM), and θ is the location of the diffraction line (Bragg angle).
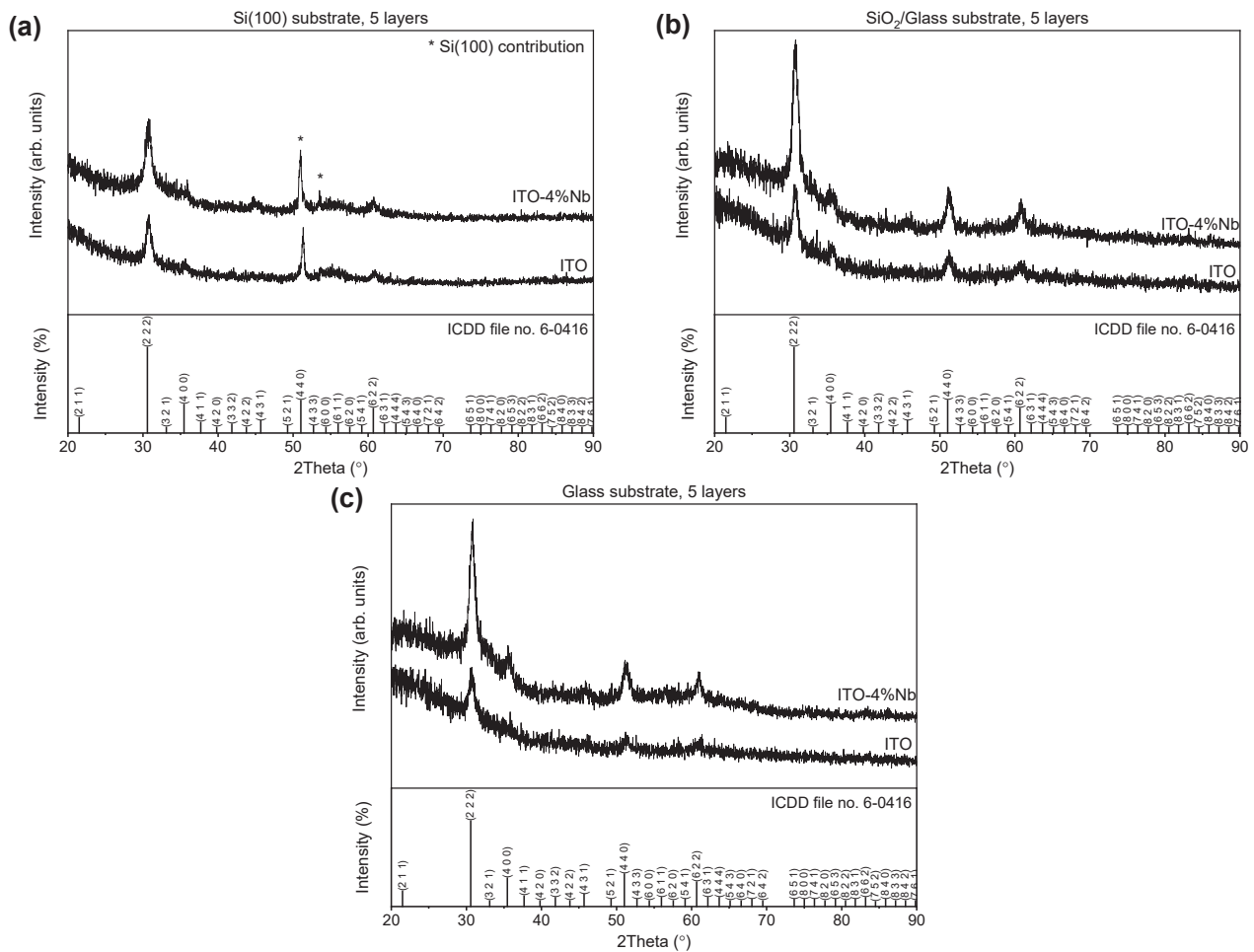
Figure 1. XRD patterns of ITO films undoped and doped with 4% Nb deposited on (**a**) Si, (**b**) SiO$_2$/glass, and (**c**) glass.

Table 1. Structural parameters and crystallite size of undoped and Nb-doped ITO films deposited by the sol–gel method on three different substrates.

Sample Name	d-Value (Å)	FWHM (°)	Lattice Constants a = b = c (Å)	α = β = γ (°)	Size D (nm)
ITO on SiO$_2$/glass	2.912(4)	0.77(5)	10.101(10)	90	11
ITO on Si	2.910(4)	0.82(5)	10.106(6)	90	10.5
ITO on Glass	2.907(6)	0.90(7)	10.137(14)	90	9.5
ITO/Nb on SiO$_2$/glass	2.910(2)	0.89(2)	10.1219(3)	90	10
ITO/Nb on Si	2.912(4)	1.00(5)	10.1356(6)	90	9
ITO/Nb on Glass	2.907(3)	0.86(3)	10.103(6)	90	10

The ITO/Nb films, as well as undoped ITO films, deposited on the SiO$_2$/glass type of support show a better crystallinity in relation to those deposited on glass or Si substrate.

2.2. Morphological Studies

2.2.1. AFM Measurements

The surface morphology and the roughness of the ITO/Nb thin films were assessed by AFM. Figure 2 shows the 2D topographic AFM micrographs at the scale of (1×1) μm^2 for the ITO/Nb films deposited on three different substrates: glass (Figure 2a), SiO$_2$/glass (Figure 2b), and Si (Figure 2c). As could be seen, the films are compact and exhibit a uniform structure of nanometric-sized particles (Figure 2) with the root-mean-square (RMS) roughness values in the range of 0.85–1.29 nm and average roughness in the range of 0.67–1.02 nm (Figure 3). It is suggested that the sol–gel deposition of a SiO$_2$ layer between the glass substrate and the ITO/Nb film slightly increases the roughness of the ITO film, in comparison with the ITO film deposited directly on glass, related to a better crystallinity as observed in XRD. On the other hand, the deposition of the ITO film on Si leads to the lowest roughness in this series, indicating a denser layer (in agreement with the refractive index curves).
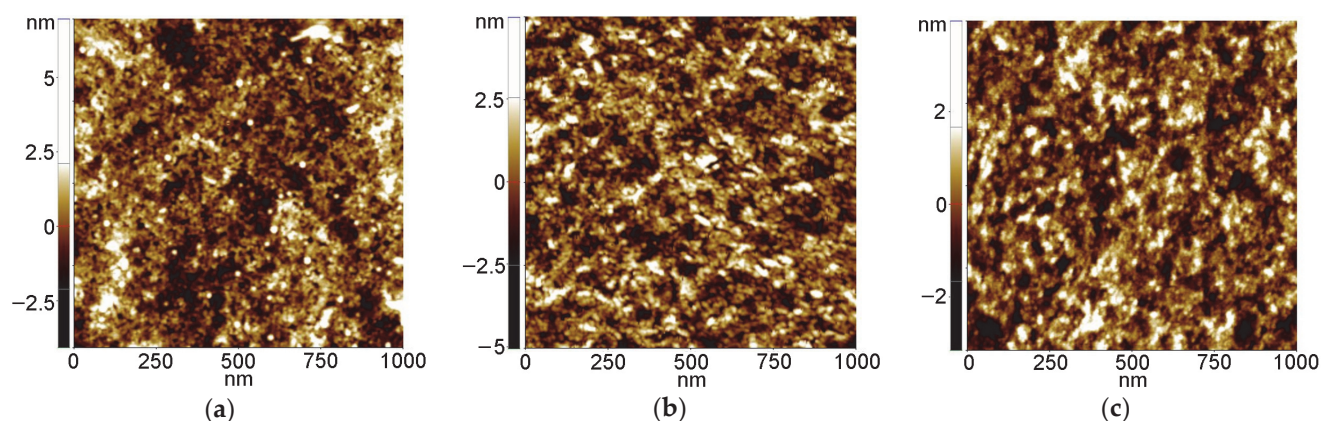
Figure 2. Topographic 2D AFM images scanned over an area of $(1 \, μm \times 1 \, μm)$, showing the morphology of the ITO/Nb films deposited on (**a**) glass, (**b**) SiO$_2$/glass, and (**c**) Si.
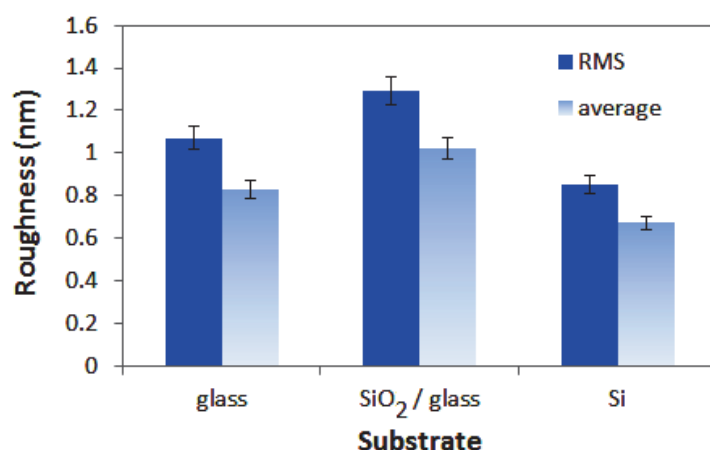
Figure 3. RMS (solid fill) and average (gradient fill) roughness for the ITO/Nb films deposited on different substrates.

2.2.2. SEM Investigation

SEM was also used for the characterization of ITO/Nb films. As can be seen in the tilted film micrographs of different magnifications (Figure 4), the surface of the film is very smooth. Figure 4a is a low-magnification (20,000×) micrograph showing a scratch on the

film surface, where the Si substrate (the darker zone marked with an arrow) is exposed. Figure 4b is a higher-magnification image (100,000×) showing the step at the edge of the film on top of the Si substrate, indicating that the film thickness is above 20 nm. The inset is the magnification of the area marked with a square in Figure 4b.
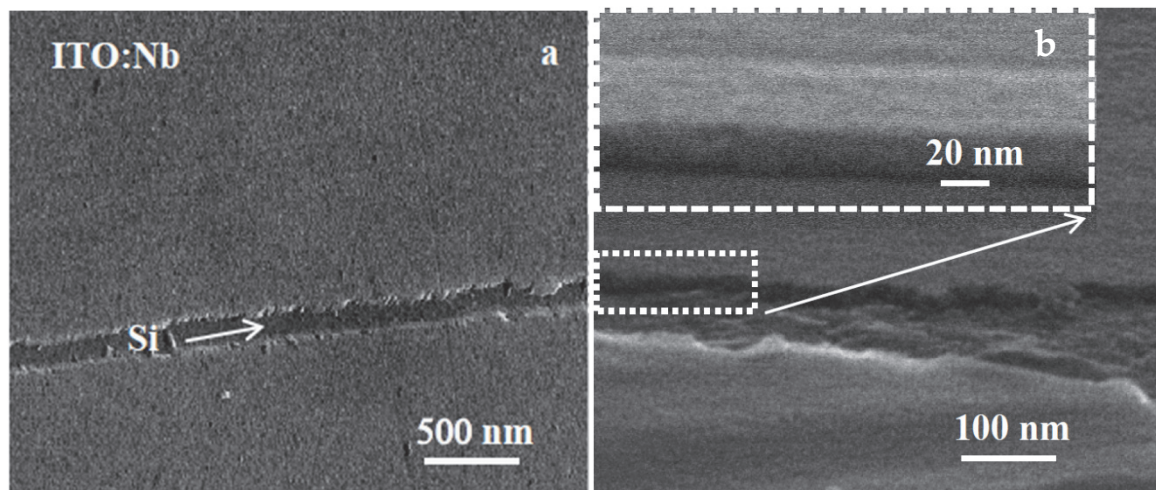
Figure 4. SEM micrographs at different magnification: (**a**) 20,000× and (**b**) 100,000× of the tilted ITO/Nb film deposited on Si, showing the smooth film surface and the film thickness.

The elemental compositional analysis by energy dispersive spectroscopy (EDX) (Table 2) revealed that niobium is incorporated into the film. A cationic ratio Nb/(In+Sn) of 0.037 was determined from the EDX measurements for the Nb-doped film.

Table 2. Cation composition measured by EDX elemental analysis of the ITO/Nb film deposited on Si substrate.

	In (%)	Sn (%)	Nb (%)
ITO	83.1	16.9	0
ITO/Nb	79.9	16.4	3.7

2.2.3. TEM Analysis

As revealed by TEM images, the thickness of the ITO/Nb film deposited on Si is generally between 26 and 29 nm for the main layer, which is in accordance with SEM and SE results.

The low-magnification XTEM images (Figure 5a) show that the film has crystallites of the order of 5–10 nm, as well as relatively large pores, around 3 to 5 nm in diameter. The deposited layers are not clearly distinguishable; instead, there is an apparent morphology in three layers separated by rows of pores (Figure 5a).

The high-resolution transmission electron microscopy (HRTEM) images of the ITO/Nb film on Si (Figure 6a) exhibit that the first layer is denser (1), followed by a pore area layer (2) and then another denser layer (3) of half thickness. In the upper area (4), no layers can be distinguished, but there is a mixture of crystallites and pores. The surface layer (5) looks like a "crust" and is less compact. No pores are present in this upper layer, leading to low roughness values as observed in AFM. The polycrystalline ITO film structure has no texture, as revealed by the SAED pattern exposed in Figure 5b. The Si substrate is oriented along the [1 1 0] zone axis and the Si reflections are connected by the white line in the SAED pattern. The HRTEM obtained in the thinner area of the XTEM specimen (Figure 6b) shows a dense morphology of the layer at the bottom of the film. This layer is from 4 to 5 nm thick and can be probably identified with the real first deposited layer. In the rest of the film, the pores appear in the film volume. These pores are aligned in the bottom part of the film

but are randomly arranged in the rest of the film. The pores are not clearly delimited and can also consist of less dense zones containing some amorphous material. The coherent lattice fringes in the HRTEM images (Figure 6b) revealed that the ITO crystallites are in the range of 5 and 10 nm. The morphology of the layer-by-layer deposited ITO film is strongly affected by the crystal growth process, because the final size of the ITO crystallites is bigger than the initial thickness of each deposited layer (about 5 nm). If we compare these results with the case of Zn-doped ITO films [30], it can be observed that the crystallization process and the total film thickness are influenced by the dopant nature [30].
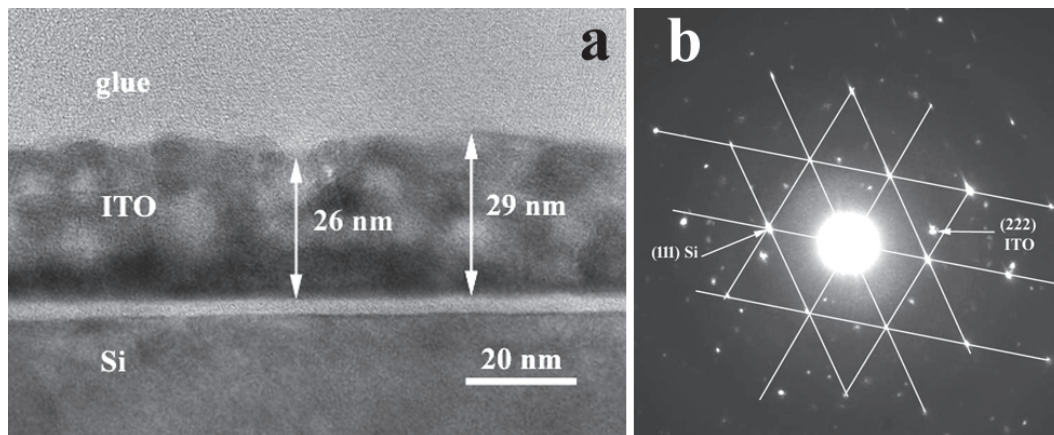
Figure 5. (**a**) Low-magnification XTEM image of the ITO/Nb film on Si and (**b**) its SAED pattern.
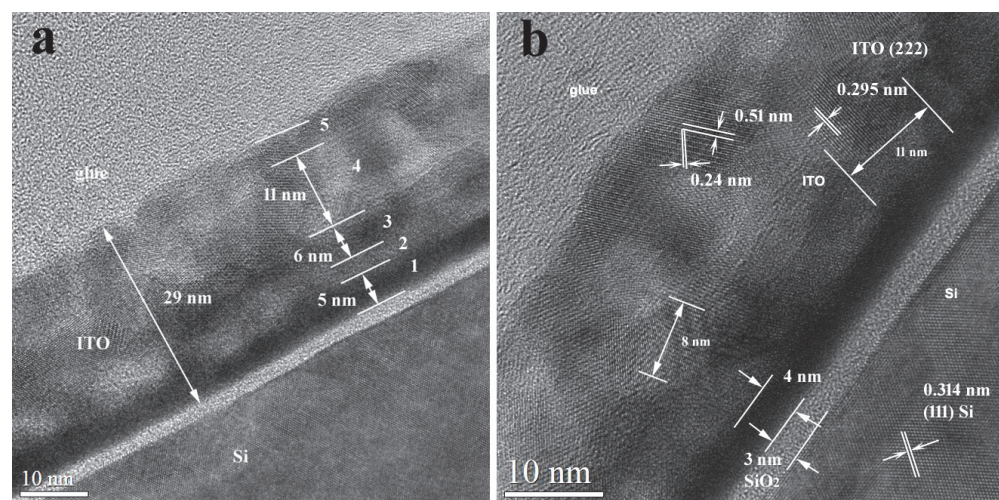
Figure 6. HRTEM images of the ITO:Nb film on Si: (**a**) morphology of the layers and (**b**) crystallite size and coherent lattice fringes.

The morphology of the apparent layers is shown in Figure 6a. The ITO crystallites size is revealed in the image by the coherent lattice fringes areas (Figure 6b). At the interface of the ITO film with the Si substrate, a SiO_2 layer with a thickness of about 3 nm is formed.

2.3. Optical Characterization
SE in UV/Vis/NIR Domain

In the UV/Vis/NIR ellipsometric data analysis, the "General Oscillator" model [69] was applied to the ITO/Nb structure considering Tauc–Lorentz and Drude oscillators. The surface roughness was considered a mixture of 50% material (film) and 50% voids (air) and was fitted with the Bruggeman's effective medium approximation (B-EMA) [70]. The layer thicknesses (d_{film}), the optical constants (refractive index—n and extinction coefficient—k),

and the band gap energy (Eg) computed by Tauc formula [71] of the ITO/Nb films evaluated from the best fit are presented in Figure 7 and Table 3. A regression analysis of optical data, based on MSE, was used to evaluate the fit quality [69].
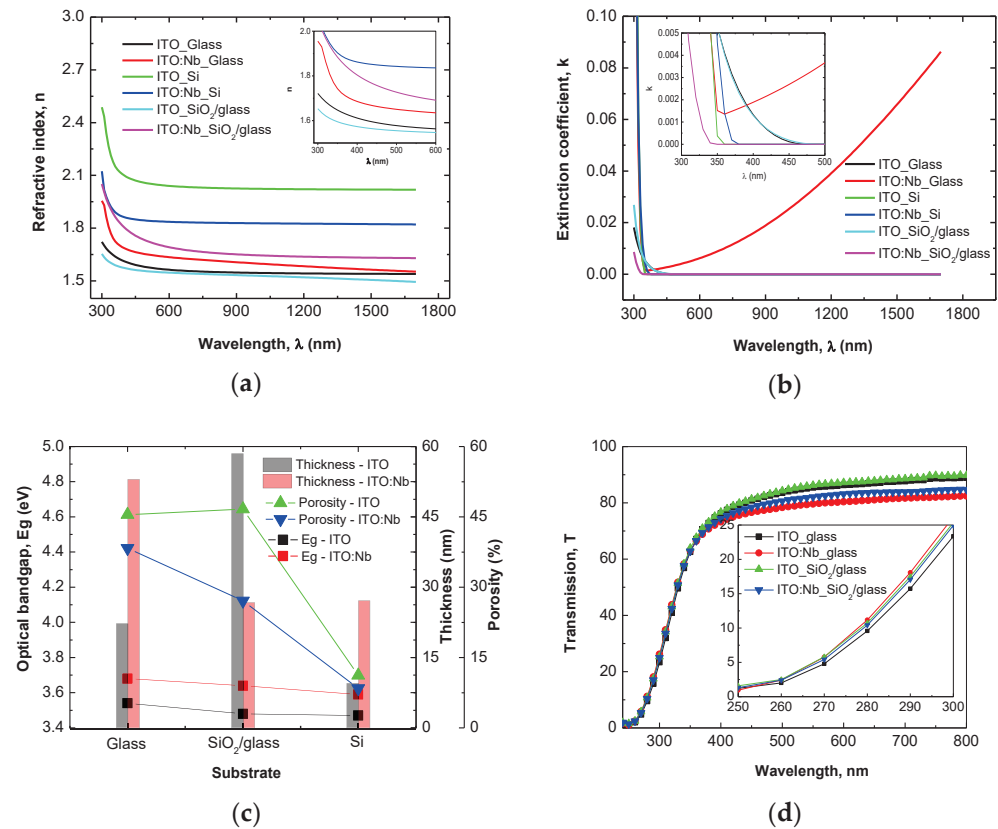
Figure 7. Optical constants (**a**) n, (**b**) k, (**c**) optical band gap—Eg, thickness, porosity—P, and (**d**) transmission—T of undoped and doped ITO thin films.

Table 3. Parameters determined by SE analysis of ITO/Nb thin films for different substrates.

Parameters	Glass	SiO$_2$/Glass	Si
d$_{SiO2}$ * (nm)	-	40.3	2.4
d$_{film}$ (nm)	53.9	26.7	27.1
d$_{rough}$ * (nm)	1.9	0.1	1.4
MSE	4.07	1.38	1.68
n **	1.63	1.72	1.85
Eg(eV)	3.68	3.64	3.59
T ** (%)	78.45	80.64	-
P ** (%)	38.32	27.09	8.44

* Note: d$_{SiO2}$ is SiO$_2$ thickness and d$_{rough}$ is the thickness of the roughness; ** note: n, T, and P are calculated for λ = 500 nm.

The porosity (P) of the films was calculated with the following formula [72]:

$$P = \left[1 - \frac{n^2 - 1}{n_d^2 - 1}\right] \times 100 \ (\%),\tag{2}$$

where n_d = 1.92 is the refractive index of the pore-free ITO (at λ = 500 nm) from WASE program and n is the refractive index of the ITO/Nb film at the same wavelength (Figure 7c).

The ITO/Nb films deposited on Si (8.44%) have the lowest porosity compared with those deposited on SiO$_2$/glass (27.09%) and glass (38.32%) (see Table 3). The transmission spectra (T) of the ITO/Nb films measured in the 250–900 nm spectral range are shown in

Figure 7 and their values at λ = 500 nm are indicated in Table 3. The ITO/Nb films deposited on glass and SiO_2/glass exhibit a good transmittance (~80%) from visible and increase to 85% at 800 nm. It was observed that the Nb-doping of ITO reduces the band gap of thin films and can be attributed to the Burstein–Moss shift [73] in the visible domain (Figure 7c).

2.4. Gas Sensing Measurements

CO Sensing Measurements

Both the comprehension of the gas/solid interaction mechanism and identification of active regions in the films (surface, grain, and grain boundaries), which are implied in analyzed gas sensing, were assessed through complex impedance analysis. Using Nyquist plots (Z″ vs. Z′), the impedance measurement results (Z = Z′ + j Z″, where Z′ and Z″ were the real and imaginary components, respectively) were represented.

Upon the exposure to a reducing gas, the resistance of the undoped and ITO/Nb films deposited on glass decreased, while the exposure to air led to an increase in this parameter. From our gas measurement results, it was concluded that the investigated films exhibited an n-type conductivity, as a consequence of the changes in terms of resistance of the films, function of the reducing gas, or air exposure.

From the intersection of the semicircle in Nyquist plots (Z″ vs. Z′), we can determine DC-resistance for our films. In Figure 8, Nyquist plots are presented for ITO/Nb glass at 300 °C for different CO concentrations. In Figure 9, the electrical response of ITO/Nb glass and ITO glass film is plotted for various concentrations of CO function of the working temperature. The difference in sensitivity between the two samples can be associated with the presence of Nb in the ITO film.
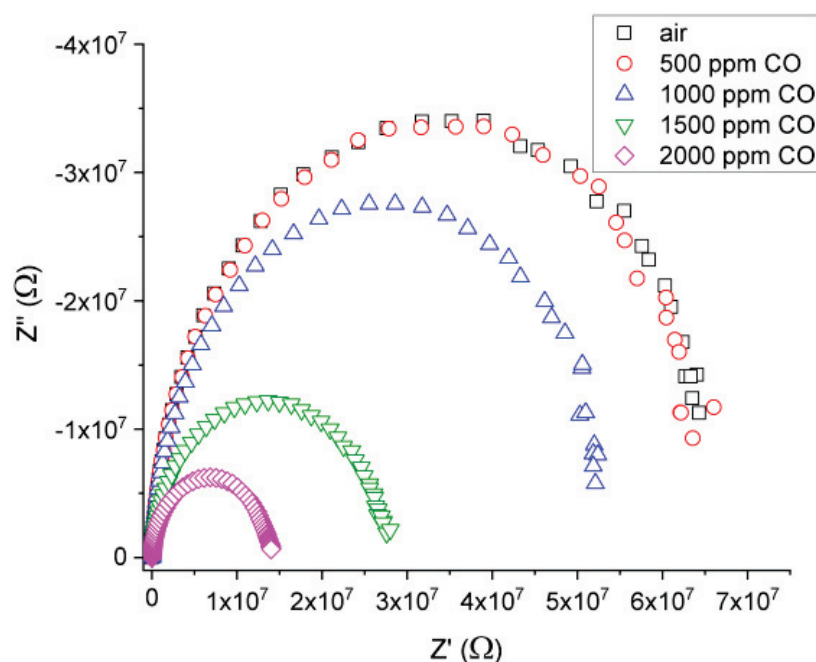
Figure 8. Nyquist plots for the ITO/Nb glass film at 300 °C for different CO concentrations.

As observed, the response of the Nb-doped ITO/glass sample exhibits a maximum at 300 °C (R_{air}/R_{CO} = 5), which will be considered the optimum working temperature of the material. It can also be stated that the films are most sensitive to the 2000 ppm CO concentration. The maximum sensitivity of ITO/Nb glass is approximately four times higher than the data achieved for Nb-doped TiO_2 samples deposited in similar conditions through a sol–gel approach [74].
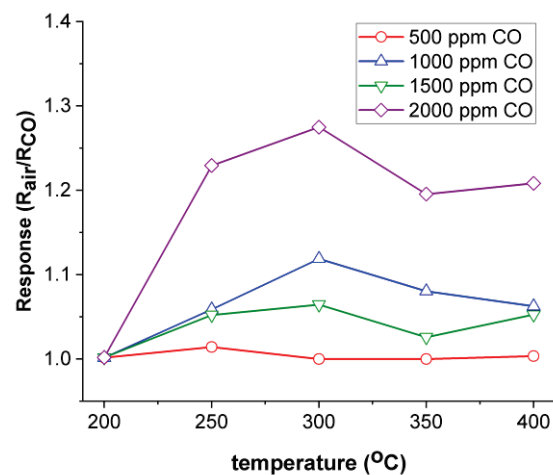
(**a**)
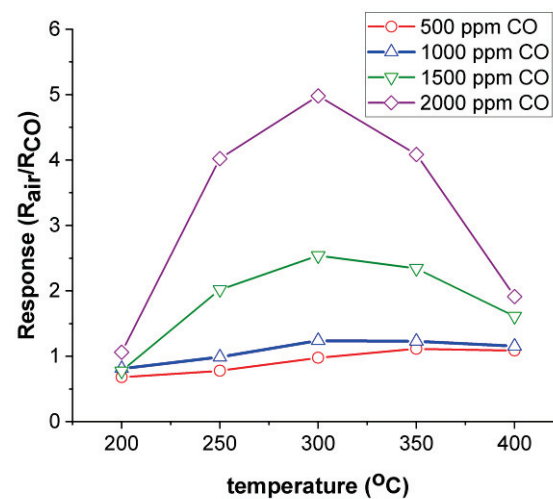
(**b**)

Figure 9. Electrical response of (**a**) ITO/Nb glass and (**b**) ITO/glass film for various concentrations of CO versus the working temperature.

3. Conclusions

ITO/Nb thin films were successfully deposited onto three different substrates through the sol–gel method. XRD analysis proved the polycrystalline nature of the films. AFM measurements indicated that all ITO/Nb films exhibit low surface roughness values, below 1 nm. SEM investigation revealed that the films are continuous, homogeneous, and adherent to the substrate. TEM analysis showed that the ITO/Nb films are very thin (26–29 nm), in agreement with SEM and SE, but with a complex morphology (a detailed study will follow in a next paper). The low-magnification XTEM images show that the film has crystallites of the order of 5–10 nm, as well as relatively large pores, around 3 to 5 nm in diameter, as also seen in the coherent lattice fringes of the HRTEM. The polycrystalline ITO film structure has no texture, as observed in SAED patterns. The morphology of the layer-by-layer deposited ITO film is significantly affected by the crystal growth process, because the final size of the ITO crystallites is bigger than the initial thickness (~5 nm) of each deposited layer. The Nb doping of ITO reduced the band gap of the films and can be attributed to the Burstein–Moss shift in the visible domain. The optical transmittance of the films deposited on transparent substrates (glass and SiO_2/glass) was found to exceed 80%. The detection properties were characterized in terms of resistance and gas-sensing response. It was found

that the response of the ITO/Nb glass sample exhibits a maximum at 300 °C (R_{air}/R_{CO} = 5) and that the ITO films are most sensitive to the 2000 ppm CO concentration. The sensitivity data are promising, but still preliminary, and will be expanded in future studies.

4. Materials and Methods

4.1. Thin Film Deposition

The Nb-doped ITO (ITO/Nb) films were prepared by the sol–gel method on the investigated substrates (glass, SiO_2/glass, and Si) using the following as precursors: indium nitrate and 2-tin-ethyl hexanoate as In_2O_3 and SnO_2 sources, 2,4-pentanedione as chelating agent, and niobium (V) ethoxide as dopant. Figure 10 describes the procedure for ITO thin films preparation: $In(NO_3)_3 \cdot H_2O$ and 2-tin-ethyl hexanoate solutions of 0.1 M concentration were homogenized by magnetic stirring at room temperature, obtaining a clear transparent solution. The dopant precursor (niobium (V) ethoxide) was added in the solution after 30 min of homogenization. Acetyl-acetone was added after 30 min and the homogenization continued for 3 h at room temperature. A light-yellow sol was obtained and it was kept at room temperature for 24 h. The as-obtained sol was used for the thin film deposition. The obtaining of ITO/Nb films with five layers was carried out by repetitive depositions (at a 5 cm/min withdrawal rate). The final films were achieved after 2 h of annealing treatment at 400 °C, with the heating rate of 5 °C/min. For the SiO_2-coated glass substrate (SiO_2/glass), the SiO_2 layer was prepared according to the sol–gel method as presented in our previous work [75], preventing the diffusion of some elements from glass to ITO.
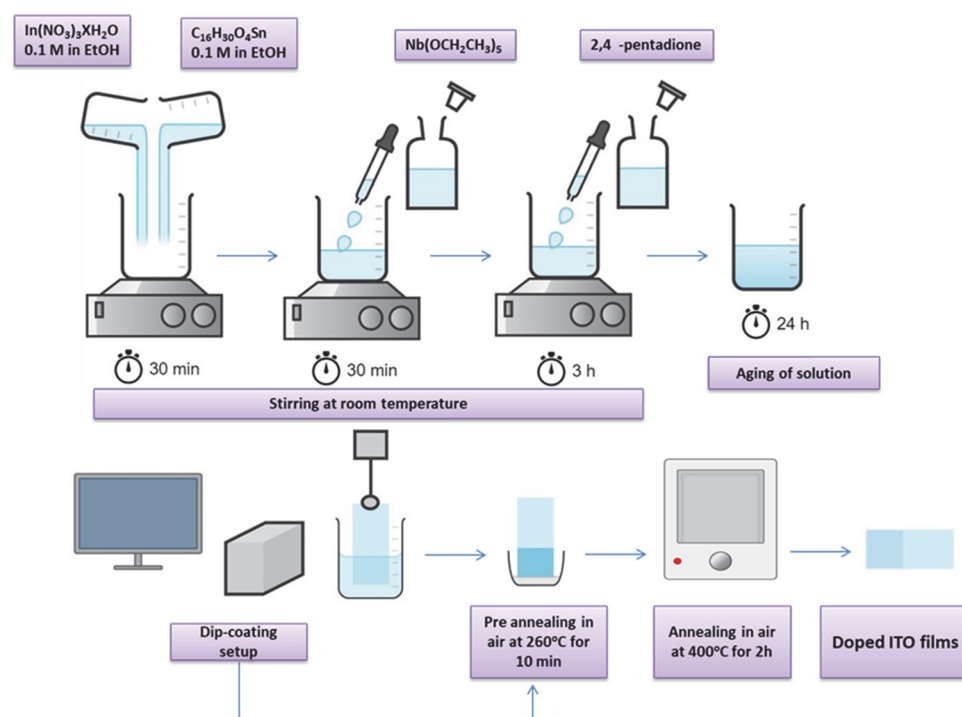
Figure 10. The flow chart of the ITO/Nb thin films preparation.

4.2. Thin Film Characterization

The structure of the ITO/Nb films was evaluated by the X-ray diffraction (XRD) method. XRD patterns were recorded using a Rigaku Ultima IV multifunctional diffraction system (Rigaku Corp., Tokyo, Japan), with Cu Kα (λ = 1.5406 Å) radiation, generated at a voltage of 30 kV and a current of 30 mA. The diffractometer was set in thin film geometry with a fixed incidence angle at α = 0.5°. The measurements were performed at a scan rate of 5° (2θ)/min over a range of 5–90°. Crystallite size was obtained from the Scherrer's formula only for the crystal plane (222).

AFM measurements were performed with an XE-100 apparatus (Park Systems) selecting the so-called non-contact working mode, in order to decrease the tip–sample interaction. All AFM images were registered using NCLR tips (Nanosensors™), with less than 8 nm radius of curvature. The AFM micrographs were processed with XEI (v.1.8.0) Image Processing Program developed by Park Systems for tilt correction and roughness evaluation.

Microstructural evaluation of the samples was achieved by SEM investigations using a FEI Quanta 3D microscope operating in the range of 5 and 30 kV.

TEM analysis working in low and high resolution as well as selected area electron diffraction (SAED) using a JEOL ARM200F analytical electron microscope operated at 200 kV was performed for systematic morphological investigations of the prepared thin films. The sample was prepared through the classical method of cross section by cutting 2×1 mm^2 pieces, gluing them face to face, followed by mechanical polishing and final ionic thinning with the help of a Gatan PIPS System.

SE measurements were carried out at room temperature on J.A. Woollam Co. Inc. (Lincoln, NE, USA) equipment composed of a variable angle spectroscopic ellipsometer. The SE spectra were recorded in the 300–1700 nm (UV/Vis/NIR) wavelength range with a 10 nm step, at an incident angle of 70°. For multi-parameter fitting, WASE program provided by Woollam was used. To minimize the difference (mean square error—MSE) between the experimental and the theoretical data, an iterative least-squares method was used. From the ellipsometric data analysis, the film thickness and the refractive index (n) were obtained with an accuracy of ± 0.2 nm and ± 0.005, respectively. The optical transmission was measured with the same equipment at a 0° incidence angle.

The ITO/Nb films deposited on glass were evaluated for gas sensing performances by impedance measurements. The four-point probe method inside a Probostat standard cell was used for gas sensing measurements. The samples were placed in a controlled atmosphere under a continuous gas flow of 177 mL/min, using a calibrated system of mass-flow controllers. Air and CO were mixed inside a vessel placed before the inlet of the impedance measurement cell. The electrical measurements were performed with a four-probe method AC impedance spectrometer equipped with a Solartron 1260 electrochemical interface, with an applied AC bias amplitude of 500 mV. Electrochemical impedance spectra (EIS) were recorded in the frequency domain from 3 MHz to 100 Hz at temperatures of 200 to 400 °C with a ProboStat cell (NorECs, Oslo, Norway).

References

1. Galle, L.; Ehrling, S.; Lochmann, S.; Kaskel, S.; Bischoff, L.; Grothe, J. Conductive ITO Interfaces for Optoelectronic Applications Based on Highly Ordered Inverse Opal Thin Films. *ChemNanoMat* **2020**, *6*, 560–566. [CrossRef]
2. Rasheed, M.; Barillé, R. Optical Constants of DC Sputtering Derived ITO, TiO_2 and TiO_2:Nb Thin Films Characterized by Spectrophotometry and Spectroscopic Ellipsometry for Optoelectronic Devices. *J. Non. Cryst. Solids* **2017**, *476*, 1–14. [CrossRef]
3. Park, D.; Park, W.; Song, J.; Kim, S.S. High-Performance ITO Thin Films for on-Cell Touch Sensor of Foldable OLED Displays. *J. Inf. Disp.* **2022**, *23*, 77–85. [CrossRef]
4. Alizadeh, A.; Rajabi, Y.; Bagheri–Mohagheghi, M.M. Effect of Crystallinity on the Nonlinear Optical Properties of Indium–Tin Oxide Thin Films. *Opt. Mater.* **2022**, *131*, 112589. [CrossRef]
5. Lunt, R.R.; Bulovic, V. Transparent, near-Infrared Organic Photovoltaic Solar Cells for Window and Energy-Scavenging Applications. *Appl. Phys. Lett.* **2011**, *98*, 113305. [CrossRef]
6. Taha, H.; Ibrahim, K.; Rahman, M.M.; Henry, D.J.; Yin, C.Y.; Veder, J.P.; Amri, A.; Zhao, X.; Jiang, Z.T. Sol-Gel Derived ITO-Based Bi-Layer and Tri-Layer Thin Film Coatings for Organic Solar Cells Applications. *Appl. Surf. Sci.* **2020**, *530*, 147164. [CrossRef]
7. Tien, W.C.; Chu, A.K. ITO Distributed Bragg Reflectors Fabricated at Low Temperature for Light-Trapping in Thin-Film Solar Cells. *Sol. Energy Mater. Sol. Cells* **2014**, *120*, 18–22. [CrossRef]
8. Filipovic, L.; Selberherr, S. Performance and Stress Analysis of Metal Oxide Films for CMOS-Integrated Gas Sensors. *Sensors* **2015**, *15*, 7206–7227. [CrossRef]
9. Shin, H.; Ahn, J.; Kim, D.H.; Ko, J.; Choi, S.J.; Penner, R.M.; Kim, I.D. Rational Design Approaches of Two-Dimensional Metal Oxides for Chemiresistive Gas Sensors: A Comprehensive Review. *MRS Bull.* **2021**, *46*, 1080–1094. [CrossRef]
10. Aydın, E.B.; Sezgintürk, M.K. Indium Tin Oxide (ITO): A Promising Material in Biosensing Technology. *TrAC—Trends Anal. Chem.* **2017**, *97*, 309–315. [CrossRef]
11. Wan, C.; Qu, A.; Deng, L.; Liu, X.; Wu, C. Preparation of an Electrochemical Biosensor Based on Indium Tin Oxide and Its Performance in Detecting Antibiotic Resistance Genes. *Microchem. J.* **2022**, *182*, 107953. [CrossRef]
12. Burnat, D.; Sezemsky, P.; Lechowicz, K.; Koba, M.; Janczuk-Richter, M.; Janik, M.; Stranak, V.; Niedziółka-Jönsson, J.; Bogdanowicz, R.; Śmietana, M. Functional Fluorine-Doped Tin Oxide Coating for Opto-Electrochemical Label-Free Biosensors. *Sens. Actuators B Chem.* **2022**, *367*, 132145. [CrossRef]
13. Luo, B.; Cao, L.; Luo, F.; Zhou, H.; Ma, K.; Liu, D.; Wang, L.; Hu, S.; Sun, K.; Zhang, S. Highly Ordered Columnar ITO Thin Film with Enhanced Thermoelectric and Mechanical Performance over Wide Temperature Range. *Ceram. Int.* **2022**, *48*, 26188–26195. [CrossRef]
14. Tchenka, A.; Agdad, A.; Mellalou, A.; Chaik, M.; el Haj, D.A.; Narjis, A.; Nkhaili, L.; Ibnouelghazi, E.L.; Ech-Chamikh, E. Spectroscopic Investigations and Thermoelectric Properties of RF-Sputtered ITO Thin Films. *J. Electron. Mater.* **2022**, *51*, 1401–1408. [CrossRef]
15. Tchenka, A.; Agdad, A.; Samba Vall, M.C.; Hnawi, S.K.; Narjis, A.; Nkhaili, L.; Ibnouelghazi, E.; Ech-Chamikh, E. Effect of RF Sputtering Power and Deposition Time on Optical and Electrical Properties of Indium Tin Oxide Thin Film. *Adv. Mater. Sci. Eng.* **2021**, *2021*, 5556305. [CrossRef]
16. Isiyaku, A.K.; Ali, A.H.; Abdu, S.G.; Tahan, M.; Raship, N.A.; Bakri, A.S.; Nayan, N. Improvement of Transparent Conductive Indium Tin Oxide Based Multilayer Films on P-Silicon through the Inclusion of Thin Copper-Aluminium Metals Interlayer. *Thin Solid Films* **2021**, *738*, 138959. [CrossRef]
17. Kim, H.T.; Jung, S.K.; Lee, S.Y. Properties of ITO Films Deposited on Paper Sheets Using a Low-Frequency (60 Hz) DC-Pulsed Magnetron Sputtering Method. *Vacuum* **2021**, *187*, 110056. [CrossRef]
18. Zhang, H.; Zhu, H.; Zhang, T.; Yu, S.; Guo, P.; Wang, Y.; Yang, Z. Effect of Sputtering Pressure on the Optical and Electrical Properties of ITO Film on Fluorphlogopite Substrate. *Appl. Surf. Sci.* **2021**, *559*, 149968. [CrossRef]
19. Sun, K.; Yang, C.; Zhang, D.; Jin, D.; Wei, Y.; Yuan, H. Effects of Ambient High-Temperature Annealing on Microstructure, Elemental Composition, Optical and Electrical Properties of Indium Tin Oxide Films. *Mater. Sci. Eng. B Solid-State Mater. Adv. Technol.* **2022**, *276*, 115534. [CrossRef]
20. Fu, X.; Yao, R.; Liang, Z.; Luo, D.; Xu, Z.; Li, Y.; Chen, N.; Hu, C.; Ning, H.; Peng, J. Effect of Laser Energy on the Properties of Neodymium-Doped Indium Zinc Oxide Thin Films Deposited by Pulsed Laser Deposition. *Superlattices Microstruct.* **2021**, *160*, 107059. [CrossRef]
21. Hurand, S.; Corvisier, A.; Lacroix, B.; Santos, A.J.; Maudet, F.; Dupeyrat, C.; Roja, R.G.; Morales, F.M.; Girardeau, T.; Paumier, F. Anisotropic Optical Properties of Indium Tin Oxide Thin Films Prepared by Ion Beam Sputtering under Oblique Angle Deposition. *Appl. Surf. Sci.* **2022**, *595*, 152945. [CrossRef]
22. Ghamari, F.; Raoufi, D.; Arjomandi, J. Influence of Thickness on Crystallographic, Stereometric, Optoelectronic, and Electrochemical Characteristics of Electron-Beam Deposited Indium Tin Oxide Thin Films. *Mater. Chem. Phys.* **2021**, *260*, 124051. [CrossRef]
23. Ren, Y.; Liu, P.; Liu, R.; Wang, Y.; Wei, Y.; Jin, L.; Zhao, G. The Key of ITO Films with High Transparency and Conductivity: Grain Size and Surface Chemical Composition. *J. Alloys Compd.* **2022**, *893*, 162304. [CrossRef]
24. Ramanathan, G.; Murali, K.R. Optical Performance of Tin Doped Indium Oxide (ITO) Thin Films Prepared by Sol Gel Dip Coating Techniques Using Acrylamide Route. *Opt. Quantum Electron.* **2022**, *54*, 652. [CrossRef]

25. Koç, M.; Kaleli, M.; Öztürk, M. Effect of Nitrogen Flow Rate During Annealing on Structural and Electro-Optical Properties of ITO Thin Films Deposited by Ultrasonic Spray Pyrolysis. *Arab. J. Sci. Eng.* **2022**, *47*, 7707–7716. [CrossRef]

26. Kim, M.G.; Kanatzidis, M.G.; Facchetti, A.; Marks, T.J. Low-Temperature Fabrication of High-Performance Metal Oxide Thin-Film Electronics via Combustion Processing. *Nat. Mater.* **2011**, *10*, 382–388. [CrossRef]

27. Vaishnav, V.S.; Patel, S.G.; Panchal, J.N. Development of ITO Thin Film Sensor for the Detection of Formaldehyde at Room Temperature. *Sens. Actuators B Chem.* **2014**, *202*, 1002–1009. [CrossRef]

28. Isik, S.; Coban, O.; Shafai, C.; Tuzemen, S.; Gur, E. Growth Conditions Effects on the H2 and CO_2 Gas Sensing Properties of Indium Tin Oxide. *J. Phys. Conf. Ser.* **2016**, *707*, 012021. [CrossRef]

29. Eslamian, M.; Salehi, A.; Miripour, Z.S. Comparing Different ITO-Metal Thin Film Structures for Ethanol and Carbon Dioxide Sensing Application. *Sens. Rev.* **2018**, *38*, 34–43. [CrossRef]

30. Gartner, M.; Anastasescu, M.; Calderon-Moreno, J.M.; Nicolescu, M.; Stroescu, H.; Hornoiu, C.; Preda, S.; Predoana, L.; Mitrea, D.; Covei, M.; et al. Multifunctional Zn-Doped ITO Sol–Gel Films Deposited on Different Substrates: Application as CO_2-Sensing Material. *Nanomaterials* **2022**, *12*, 3244. [CrossRef]

31. Donato, A.; Della Corte, F.; Gioffrè, M.; Donato, N.; Bonavita, A.; Micali, G.; Neri, G. RF Sputtered ZnO-ITO Films for High Temperature CO Sensors. *Thin Solid Films* **2009**, *517*, 6184–6187. [CrossRef]

32. Li, X.; Kale, G.M. Influence of Thickness of ITO Sensing Electrode Film on Sensing Performance of Planar Mixed Potential CO Sensor. *Sens. Actuators B Chem.* **2006**, *120*, 150–155. [CrossRef]

33. Mokrushin, A.S.; Fisenko, N.A.; Gorobtsov, P.Y.; Simonenko, T.L.; Glumov, O.V.; Melnikova, N.A.; Simonenko, N.P.; Bukunov, K.A.; Simonenko, E.P.; Sevastyanov, V.G.; et al. Pen Plotter Printing of ITO Thin Film as a Highly CO Sensitive Component of a Resistive Gas Sensor. *Talanta* **2021**, *221*, 121455. [CrossRef] [PubMed]

34. Lim, C.; Wang, W.; Yang, S.; Lee, K. Development of SAW-Based Multi-Gas Sensor for Simultaneous Detection of CO_2 and NO_2. *Sens. Actuators B Chem.* **2011**, *154*, 9–16. [CrossRef]

35. Madhi, I.; Bouzid, B.; Saadoun, M.; Bessaïs, B. Synthesis and Characterization of ITO-ZnO Nanocomposite and Its Application as NO_2 Gas Sensor. *Ceram. Int.* **2015**, *41*, 6552–6559. [CrossRef]

36. Vaishnav, V.S.; Patel, S.G.; Panchal, J.N. Development of ITO Thin Film Sensor for Detection of Benzene. *Sens. Actuators B Chem.* **2015**, *206*, 381–388. [CrossRef]

37. Vaishnav, V.S.; Patel, S.G.; Panchal, J.N. Development of Indium Tin Oxide Thin Film Toluene Sensor. *Sens. Actuators B Chem.* **2015**, *210*, 165–172. [CrossRef]

38. Lin, C.W.; Chen, H.I.; Chen, T.Y.; Huang, C.C.; Hsu, C.S.; Liu, W.C. Ammonia Sensing Characteristics of Sputtered Indium Tin Oxide (ITO) Thin Films on Quartz and Sapphire Substrates. *IEEE Trans. Electron. Devices* **2011**, *58*, 4407–4413. [CrossRef]

39. Mishra, S.K.; Kumari, D.; Gupta, B.D. Surface Plasmon Resonance Based Fiber Optic Ammonia Gas Sensor Using ITO and Polyaniline. *Sens. Actuators B Chem.* **2012**, *171–172*, 976–983. [CrossRef]

40. Kundu, S.; Kumar, A. Low Concentration Ammonia Sensing Performance of Pd Incorporated Indium Tin Oxide. *J. Alloys Compd.* **2019**, *780*, 245–255. [CrossRef]

41. Pandya, H.J.; Chandra, S.; Vyas, A.L. Fabrication and Characterization of Ethanol Sensor Based on RF Sputtered ITO Films. *Sens. Transducers* **2011**, *10*, 141–150.

42. Vasanthi Pillay, V.; Goyal, S. Influence of Sputtering Power, Annealing on the Structural Properties of ITO Films, for Application in Ethanol Gas Sensor. *Mater. Today Proc.* **2015**, *2*, 4609–4619. [CrossRef]

43. Yadav, B.C.; Agrahari, K.; Singh, S.; Yadav, T.P. Fabrication and Characterization of Nanostructured Indium Tin Oxide Film and Its Application as Humidity and Gas Sensors. *J. Mater. Sci. Mater. Electron.* **2016**, *27*, 4172–4179. [CrossRef]

44. Chinky; Kumar, P.; Sharma, V.; Malik, P.; Raina, K.K. Nano Particles Induced Vertical Alignment of Liquid Crystal for Display Devices with Augmented Morphological and Electro-Optical Characteristics. *J. Mol. Struct.* **2019**, *1196*, 866–873. [CrossRef]

45. Wu, G.M.; Liu, C.Y.; Sahoo, A.K. RF Sputtering Deposited A-IGZO Films for LCD Alignment Layer Application. *Appl. Surf. Sci.* **2015**, *354*, 48–54. [CrossRef]

46. Guo, J.; Huard, C.M.; Yang, Y.; Shin, Y.J.; Lee, K.T.; Guo, L.J. ITO-Free, Compact, Color Liquid Crystal Devices Using Integrated Structural Color Filters and Graphene Electrodes. *Adv. Opt. Mater.* **2014**, *2*, 435–441. [CrossRef]

47. Inoue, M. Review of Various Measurement Methodologies of Migration Ion Influence on LCD Image Quality and New Measurement Proposal beyond LCD Materials. *J. Soc. Inf. Disp.* **2020**, *28*, 92–110. [CrossRef]

48. Han, C.; Zhou, L.E.; Ma, H.; Li, C.; Zhang, S.; Cao, H.; Zhang, L.; Yang, H. Fabrication of a Controllable Anti-Peeping Device with a Laminated Structure of Microlouver and Polymer Dispersed Liquid Crystals Film. *Liq. Cryst.* **2019**, *46*, 2235–2244. [CrossRef]

49. Guo, S.M.; Liang, X.; Zhang, C.H.; Chen, M.; Shen, C.; Zhang, L.Y.; Yuan, X.; He, B.F.; Yang, H. Preparation of a Thermally Light-Transmittance-Controllable Film from a Coexistent System of Polymer-Dispersed and Polymer-Stabilized Liquid Crystals. *ACS Appl. Mater. Interfaces* **2017**, *9*, 2942–2947. [CrossRef]

50. Kamal, W.; Li, M.; Lin, J.; Parry, E.; Jin, Y.; Elston, S.J.; Castrejón-Pita, A.A.; Morris, S.M. Spatially Patterned Polymer Dispersed Liquid Crystals for Image-Integrated Smart Windows. *Adv. Opt. Mater.* **2022**, *10*, 2101748. [CrossRef]

51. Mohammadi, S.; Abdizadeh, H.; Golobostanfard, M.R. Effect of Niobium Doping on Opto-Electronic Properties of Sol-Gel Based Nanostructured Indium Tin Oxide Thin Films. *Ceram. Int.* **2013**, *39*, 4391–4398. [CrossRef]

52. Lee, F.Y.; Chen, W.K.; Lin, C.L.; Kao, C.H. Carbon Monoxide Poisoning and Subsequent Cardiovascular Disease Risk a Nationwide Population-Based Cohort Study. *Medicine* **2015**, *94*, e624. [CrossRef] [PubMed]

53. Nandy, T.; Coutu, R.A.; Ababei, C. Carbon Monoxide Sensing Technologies for Next-Generation Cyber-Physical Systems. *Sensors* **2018**, *18*, 3443. [CrossRef] [PubMed]

54. Chesler, P.; Hornoiu, C.; Mihaiu, S.; Vladut, C.; Moreno, J.M.C.; Anastasescu, M.; Moldovan, C.; Brasoveanu, C.; Firtat, B.; Muscalu, G.; et al. Nanostructured SnO₂ -ZnO Composite Gas Sensors for Selective Detection of Carbon Monoxide. *Beilstein J. Nanotechnol.* **2016**, *7*, 2045–2056. [CrossRef]

55. Dietrich, S.; Kusnezoff, M.; Petasch, U.; Michaelis, A. Evaluation of Indium Tin Oxide for Gas Sensing Applications: Adsorption/Desorption and Electrical Conductivity Studies on Powders and Thick Films. *Sensors* **2021**, *21*, 497. [CrossRef] [PubMed]

56. Salehi, A.; Nikfarjam, A. Room Temperature Carbon Monoxide Sensor Using ITO/n-GaAs Schottky Contact. *Sens. Actuators B Chem.* **2004**, *101*, 394–400. [CrossRef]

57. Taha, H.; Jiang, Z.T.; Henry, D.J.; Amri, A.; Yin, C.Y.; Alias, A.B.; Zhao, X. Improved Mechanical Properties of Sol-Gel Derived ITO Thin Films via Ag Doping. *Mater. Today Commun.* **2018**, *14*, 210–224. [CrossRef]

58. Wang, Y.; Wang, Z.; Huang, K.; Liang, X.; Liu, C.; Chen, C.; Liu, C. Solution-Processed ITO Thin-Film Transistors with Doping of Gallium Oxide Show High on-off Ratios and Work at 1 MV Drain Voltage. *Appl. Phys. Lett.* **2020**, *116*, 141604. [CrossRef]

59. Ali, R.; Hanif, M.; Shah, S.A.B.; Abbas, S.Z.; Karim, M.R.A.; Arshad, M.; Ahmad, S.H.A. Effect of Chromium-Doping on Structure and Opto-Electronics Properties of Nanostructured Indium Tin Oxide Thin Films. *Appl. Phys. A Mater. Sci. Process.* **2022**, *128*, 508. [CrossRef]

60. Gueddaoui, M.G.H.; Trari, R.B.M. Simple and Effective Synthesis via Sol—Gel of Zn—Doped ITO Films and Their Microstructural, Optical, and Photoelectrochemical Properties. *Appl. Phys. A* **2022**, *128*, 816. [CrossRef]

61. Pu, N.W.; Liu, W.S.; Cheng, H.M.; Hu, H.C.; Hsieh, W.T.; Yu, H.W.; Liang, S.C. Investigation of the Optoelectronic Properties of Ti-Doped Indium Tin Oxide Thin Film. *Materials* **2015**, *8*, 6471–6481. [CrossRef] [PubMed]

62. Li, S.; Ma, R.; Ma, C.; Li, D.; Xiao, Y.; He, L.; Zhu, H. Effect of Thickness on Optoelectrical Properties of Nb-Doped Indium Tin Oxide Thin Films Deposited by RF Magnetron Sputtering. *Optoelectron. Lett.* **2013**, *9*, 198–200. [CrossRef]

63. Lozano, O.; Chen, Q.Y.; Wadekar, P.V.; Seo, H.W.; Chinta, P.V.; Chu, L.H.; Tu, L.W.; Lo, I.; Yeh, S.W.; Ho, N.J.; et al. Factors Limiting the Doping Efficiency of Transparent Conductors: A Case Study of Nb-Doped In₂O₃ Epitaxial Thin-Films. *Sol. Energy Mater. Sol. Cells* **2013**, *113*, 171–178. [CrossRef]

64. Su, X.; Pan, Y.; Gao, D.; Li, S.; Wang, J.; Wang, L. Electrochromic Coloration of Single-Layer ITO:Nb Oxides Thin Film. *Mater. Res. Express* **2019**, *6*, 116404. [CrossRef]

65. Brinker, C.J.; Scherer, G.W. *Sol-Gel Science: The Physics and Chemistry of Sol-Gel Processing*; Academic Press: San Diego, CA, USA, 1990.

66. Predoana, L.; Atkinson, I.; Karaj, D.A.; Odhiambo, V.O.; Bakos, L.P.; Kovacs, T.N.; Pandele-Cusu, J.; Petrescu, S.; Rusu, A.; Szilagyi, I.M.; et al. Comparative study of the thermal behavior of Sr-Cu-O gels obtained by sol-gel and microwave-assisted sol-gel method. *J. Therm. Anal. Calorim.* **2021**, *143*, 2893–2900. [CrossRef]

67. Livage, J.; Henry, M.; Sanchez, C. Sol-gel chemistry of transition metal oxides. *Prog. Solid State Chem.* **1988**, *18*, 259–341. [CrossRef]

68. Klug, H.P.; Alexander, L.E. *X-Ray Diffraction Procedure for Polycrystalline and Amorphous Materials*, 2nd ed.; Wiley: New York, NY, USA, 1974; p. 992.

69. Tompkins, H.G. *WVASE32®Software Manual*; J.A.Woollam Co. Inc.: Lincoln, NE, USA, 2006.

70. Bruggeman, D.A.G. Berechnung verschiedener physikalischer Konstanten von heterogenen Substanzen. III. Die elastischen Konstanten der quasiisotropen Mischkörper aus isotropen Substanzen. *Ann. Phys.* **1937**, *421*, 160–178. [CrossRef]

71. Tauc, J.; Grigorovici, R.; Vancu, A. Optical Properties and Electronic Structure of Amorphous germanium. *Phys. Status Solidi B* **1966**, *15*, 627–637. [CrossRef]

72. Kajihara, K.; Nakanishi, K.; Tanaka, K.; Hirao, K.; Soga, N. Preparation of Macroporous Titania Films by a Sol-Gel Dip-Coating Method from the System Containing Poly(ethylene glycol). *J. Am. Ceram. Soc.* **2005**, *81*, 2670–2676. [CrossRef]

73. Li, S.; Ma, R.; He, L.; Xiao, Y.; Hou, J.; Jiao, S. Preparation and Characteristics of Nb-Doped Indium Tin Oxide Thin Films by RF Magnetron Sputtering. *Optoelectron. Lett.* **2012**, *8*, 460–463. [CrossRef]

74. Duta, M.; Predoana, L.; Calderon-Moreno, J.M.; Preda, S.; Anastasescu, M.; Marin, A.; Dascalu, I.; Chesler, P.; Hornoiu, C.; Zaharescu, M.; et al. Nb-Doped TiO₂ Sol-Gel Films for CO Sensing Applications. *Mater. Sci. Semicond. Process.* **2016**, *42*, 397–404. [CrossRef]

75. Nicolescu, M.; Anastasescu, M.; Calderon-Moreno, J.M.; Maraloiu, A.V.; Teodorescu, V.S.; Preda, S.; Predoana, L.; Zaharescu, M.; Gartner, M. Optical, Microstructural and Vibrational Properties of Sol–Gel ITO Films. *Opt. Mater.* **2021**, *114*, 110999. [CrossRef]

Low Release Study of Cefotaxime by Functionalized Mesoporous Silica Nanomaterials

Dan Eduard Mihaiescu [1], **Daniela Istrati** [1], **Alina Moroșan** [1,*], **Maria Stanca** [2], **Bogdan Purcăreanu** [3,4,*], **Rodica Cristescu** [5], **Bogdan Ștefan Vasile** [3] **and Roxana Doina Trușca** [3]

1   Department of Organic Chemistry "Costin Nenitescu", Faculty of Chemical Engineering and Biotechnologies, University Politehnica of Bucharest, 011061 Bucharest, Romania
2   Leather and Footwear Research Institute, 031215 Bucharest, Romania
3   Faculty of Chemical Engineering and Biotechnologies, Department of Science and Engineering of Oxide Materials and Nanomaterials, University Politehnica of Bucharest, 011061 Bucharest, Romania
4   BIOTEHNOS S.A., Gorunului Rue, No. 3-5, 075100 Otopeni, Romania
5   Lasers Department, National Institute for Lasers, Plasma and Radiation Physics, 077125 Magurele, Romania
*   Correspondence: alina.morosan@upb.ro (A.M.); bogdanpb89@gmail.com (B.P.)

Abstract: As a third-generation β-lactam antibiotic, cefotaxime shows a broad-spectrum with Gram-positive and Gram-negative bacteria activity and is included in WHO's essential drug list. In order to obtain new materials with sustained release properties, the present research focuses on the study of cefotaxime absorption and desorption from different functionalized mesoporous silica supports. The MCM-41-type nanostructured mesoporous silica support was synthesized by sol–gel technique using a tetraethyl orthosilicate (TEOS) route and cetyltrimethylammonium bromide (CTAB) as a surfactant, at room temperature and normal pressure. The obtained mesoporous material (MCM-41 class) was characterized through nuclear magnetic resonance (NMR), scanning electron microscopy (SEM), high-resolution transmission electron microscopy (HR-TEM), N_2 absorption–desorption (BET) and Fourier transform infrared spectroscopy (FT-IR), proving a good micro-structured homogeneity (SEM images), a high surface area (BET, 1029 m^2/g) correlated with high silanolic activity (Q^3/Q^4 peak ratio from ^{29}Si MAS-NMR), and an expected uniform hexagonal structure (2–3 nm, HRTEM). In order to non-destructively link the antibiotic compound on the solid phase, MCM-41 was further functionalized in two steps: with aminopropyl trimethoxysilane (APTMS) and glutaraldehyde (GA). Three cefotaxime-loaded materials were comparatively studied for low release capacity: the reference material with adsorbed cefotaxime on MCM-41, MCM-41/APS (aminopropyl silyl surface functionalization) adsorbed cefotaxime material, and APTMS–GA bounded MCM-41—cefotaxime material. The slow-release profiles were obtained by using an on-flow modified HPLC system. A significant improved release capacity was identified in the case of MCM-41/APS/GA—cefotaxime due to the covalent surface grafting of the biological active compound, recommending this class of materials as an effective carrier of bioactive compounds in wound dressing, anti-biofilm coatings, advanced drugs, and other related applications.

Keywords: MCM-41; sol–gel; low release; cefotaxime; mesoporous material

1. Introduction

The discovery of MCM-41-type mesoporous silica could be consider a milestone in the field of silica-based materials due to the uniform hexagonal pore structure, the high surface area [1], chemical, thermal stability, biocompatibility, and high loading capacity [2,3]. The abundance of silanol groups on the surface of mesoporous silica nanoparticles (MSNs) allows for enhanced flexibility for surface modification through functionalization; thus, widening their range of application. MSNs are used in various applications such as therapeutic/health, drug delivery, agricultural fields, food industries, optoelectronic sensing [4,5], catalysis [6–9], gas separation [10,11], and lanthanides recovery

from waste water [12,13]. In addition, organic/inorganic micro/nanocomposites using oxidic-based microporous structures and different strategies of surfaces functionalization are used as innovative solutions for advanced waste water treatments and pathogen inactivation approaches [14,15]. An important application of mesoporous silica consists of its usage as a carrier for biologically active compounds, such as gemcitabine [16] and quercetin [17], both used in cancer treatment. The main advantages of using mesoporous silica nanocomposites in biomedical research and application fields include their good biocompatibility, increased bio-availability of the target compounds for the tissue of interest (as example tumor tissue), sustained or controlled release of the bioactive compounds, and reduced toxicity of these compounds in healthy tissues [18,19].

V. Pardhi and collaborators improved the dissolution rate of niclosamide in the human body by using mesoporous silica as a delivery system and studied the influence of mesoporous silica morphology on the dissolution rate [20]. The study demonstrated that niclosamide loaded on mesoporous silica has a higher dissolution rate than the drug as such and silica morphology also influences the dissolution rate, this being lower for non-porous silica and higher for non-ordered mesoporous silica.

V. Nairi et al. studied the adsorption and release of ampicillin from mesoporous silica matrices, which differ from each other either by pore size or chemical properties due to the surface functionalization. The compared materials differ in pore size equivalent to electric charge (SBA-15 and MCM-41) and different surface electric charge (SBA-15 and SBA-15-NH_2). Both the adsorption and release of ampicillin are influenced by the surface electric charge more than the pore size. The surface negative charge of the two non-functionalized matrices favors rapid release at pH 7.4, being slightly higher for MCM-41. As the MCM-41 particles have smaller dimensions than the SBA-15 ones, a higher amount of drug was adsorbed. In the case of the SBA-15-NH_2 matrix, the electrostatic interactions favor an antibiotic sustained release that is slower than that of the nonfunctionalized material [21]. The biological responses could be enhanced by modifying the surface of mesoporous silica, such as the surface functionalization by attaching specific functional groups or molecules. The most common methods of functionalization are co-condensation and post-grafting. The selected approach influences both the physicochemical interaction and surface chemistry modification. The co-condensation or direct synthesis functionalization method can be performed in a single reaction vessel; and thus, has a reduced number of steps and synthesis time, leading to a more homogeneous distribution of functional groups on the surface. On the other hand, the post-grafting method uses simple and mild conditions, and involves the subsequent surface modification by direct grafting or secondary grafting. Since only molecules that are small enough can diffuse into the mesoporous matrix, this functionalization method is limited by both the pore size and architecture [22,23].

The special structure of mesoporous silica offers an efficient protection of biomolecules susceptible to metabolic transformations in the gastrointestinal tract after oral administration [24]. Silicon is a structural component of connective tissues, being essential for bones [25] and skin [26]. Acute and chronic toxicity studies have shown that the mesoporous silica does not have adverse effects for oral administration due to its low water solubility; however, the long-term pulmonary exposure to amorphous or crystalline silica (solid dispersions in the gas phase) has been associated to serious respiratory disorders [27,28].

Cefotaxime is a third-generation cephalosporin antibiotic that when it is intravenously or intramuscularly administered, becomes active against Gram-positive and Gram-negative bacteria, except pseudomonas. It is used to treat meningitis, lower respiratory tract infections, urinary tract, inflammatory pelvic diseases, skin infections, and gonorrhea [29,30]. Cefotaxime has the ability to inhibit bacterial cell wall synthesis compared to penicillin by blocking the transpeptidation step in peptidoglycan biosynthesis [31]. The cell envelope of Gram-positive and Gram-negative bacteria consist of a plasma membrane and cell wall. The difference between those two is that the Gram-negative bacteria poses an additional outer impermeable membrane to large molecules. The cell walls are similar (a single layer of peptidoglycan); however, they differ in thickness: 20–80 nm for Gram-positive bacteria

and less than 10 nm for Gram-negative bacteria [32,33]. A desorption study of cefotaxime from MCM-41 and MCM-41/APS materials proves significant advantages of the amino groups' (-NH$_2$) surface functionalization [34].

The present research focuses on the study of the absorption/desorption of cefotaxime from functionalized mesoporous silica support, specifically focusing on the significant release difference between the non-destructively linked cefotaxime and physically adsorbed compound on the solid phase. Furthermore, a different low-release experimental system was proposed, using a modified HPLC system (avoiding sampling and HPLC injection) that is able to provide on-flow analysis (more than 4000 sampling points for a single experiment).

2. Results and Discussion

The synthesis of cefotaxime-bonded MCM-41/APS/GA composites involved several reaction steps, followed by advanced investigations of the intermediate and final materials: MCM-41 synthesis by room temperature/pressure sol–gel method, APTMS surface functionalization in order to provide a -NH$_2$ linking center for the glutaraldehyde surface grafting step, followed by the final cefotaxime (non-destructive) linking to the free thiazolyl amino group. Further desorption studies were performed in order to provide the release profiles of three materials: MCM-41—cefotaxime (3:10 (*w/w*)), MCM-41/APS—cefotaxime (3:10 (*w/w*)) loaded materials (physical adsorption), and covalent-linked cefotaxime MCM-41/APS/GA (3:10 (*w/w*)). In order to obtain an effective concentration of the drug in the desorption environment, the 3:10 (*w/w*) loading level of cefotaxime was established by the previous bioactive compound loading studies [35], which provided a significant out-of-pore compound concentration (the quick release of out-of-pore cefotaxime provides a fast response in the first stage of treatment), followed by a sustained release (in-pore desorption, in order to sustain the already established cefotaxime concentration). The cefotaxime GA cross-linked composite provides a significantly lower drug release due to the involvement of the secondary aldiminic bound cleavage from the solid support. This behavior would be a significant advantage in wound dressing, advanced drugs design, and antibiofilm coatings applications because the pH drop from bacterial activity will be followed by the desorption enhancement due to an accelerated aldiminic-bound cleavage.

SEM images (Figure 1) of MCM-41 (a), MCM-41 with particle size details (b), MCM-41/APS (c), MCM-41/APS/GA (d), and cefotaxime-linked MCM-41/APS/GA (e) materials exhibit a relative uniform microgranular structure both in shape and particle size. APTMS surface functionalization, the glutaraldehyde surface-grafting step, and the final cefotaxime-loading process do not affect the morphology of the composites; in terms of both shape and particle size, a slight particle aggregation can be observed (e) for the loaded material, as expected from the out-of-pore cefotaxime loading. The microstructured spherical particle distribution was the subject of several MCM-41 synthesis optimization steps, avoiding as possible the low-diameter nanoparticles (almost pharmaceutical release applications avoiding nanometer scale-range particles due to the significant tissue penetration).

Functionalization of MCM-41 with APTMS is demonstrated by the appearance of the peak corresponding to nitrogen; in addition, the peaks corresponding to silicon and oxygen are only revealed by energy dispersive spectroscopy (EDS) (Figure 2).

Figure 3 exhibits HR-TEM images of non-functionalized MCM-41 material (because of the high electron energy, surface grafted materials are less suitable for this analysis). The HR-TEM images confirm the MCM-41 granular mesoporous silica morphology (200–1500 nm particle size) and its mesoporous hexagonal structure. For the MCM-41 synthesis operated at normal pressure and temperature, the obtained structure shows a good hexagonal ordering degree and an average pore size of about 2–3 nm, proved also by the high surface area.
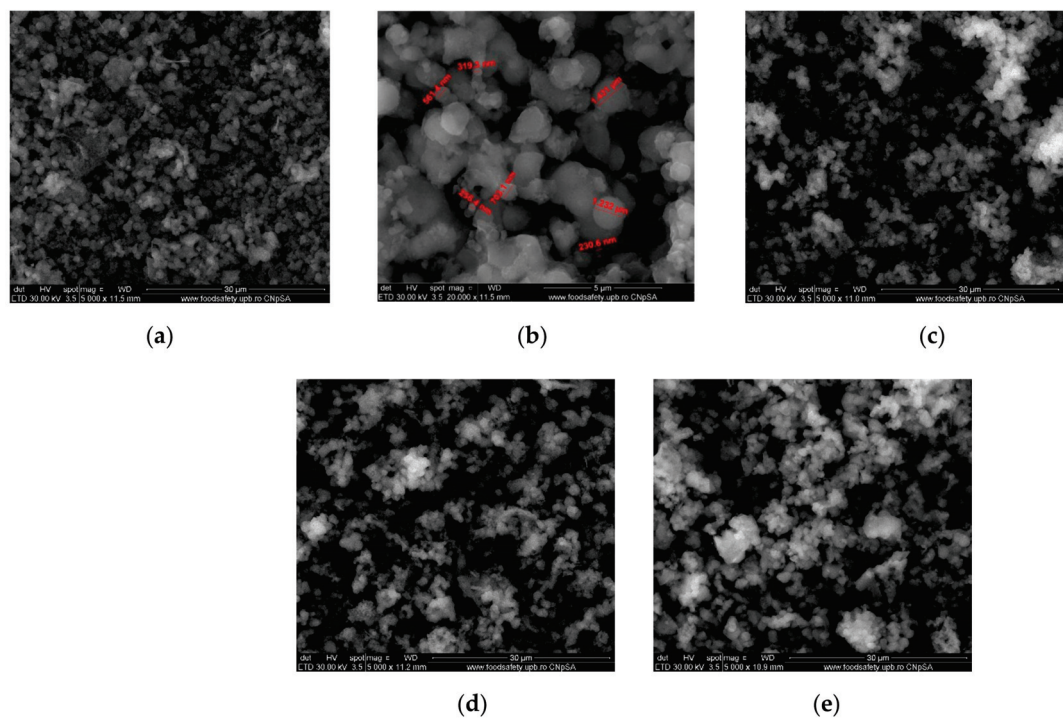
Figure 1. SEM images for initial MCM-41 material (**a**), MCM-41 with particle size details (**b**), MCM-41/APS (**c**), MCM-41/APS/GA (**d**) and MCM-41/APS/GA-cefotaxime (**e**).
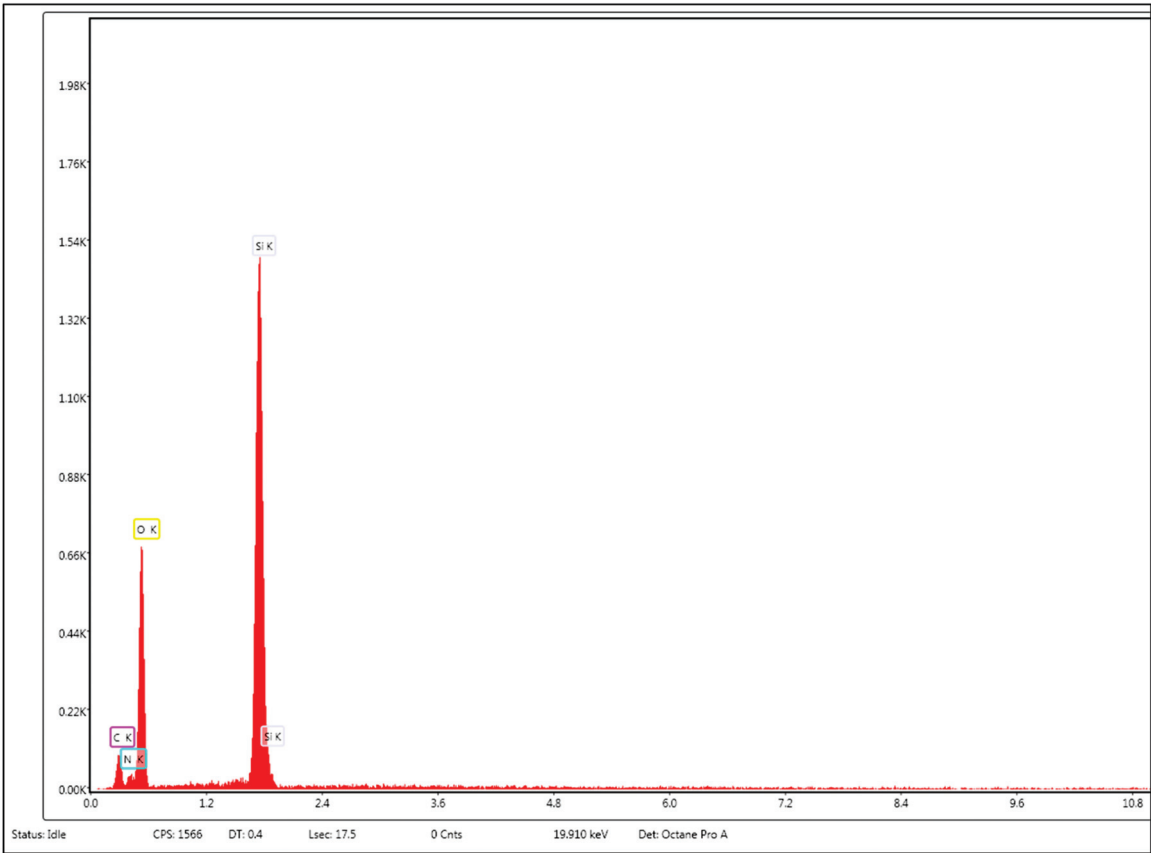
Figure 2. The EDS spectrum for MCM-41/APS.

(a)   **(b)**
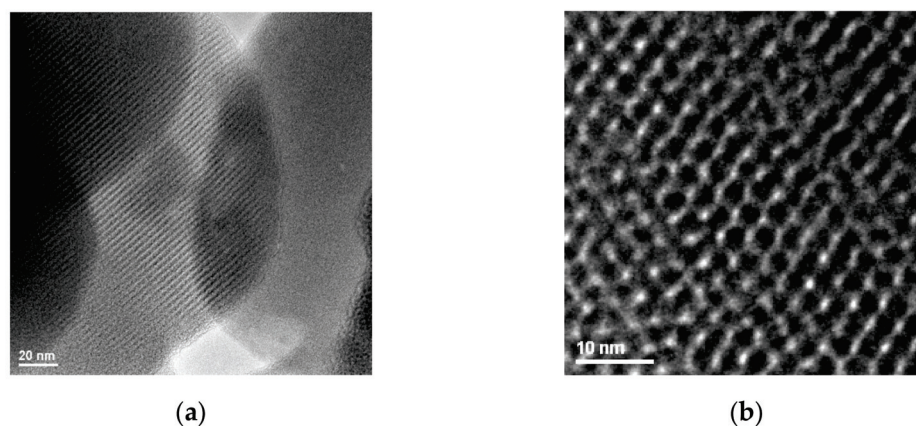
Figure 3. Representative HR-TEM images of non-functionalized MCM-41 material for 20 nm (**a**) and MCM-41/APS for 10 nm (**b**) scale bars.

According to IUPAC, the N_2 adsorption/desorption isotherm is type IV, specific to MCM-41 type materials (Figure 4). This feature highlights the characteristics of the MCM-41 material: the specific surface area of 1029.06 m^2 g^{-1} pore sizes of 2.41 nm and pore volume of 0.62 cm^3 g^{-1}, being characteristic of mesoporous materials, which also confirms our HR-TEM data. The pore size distribution (Figure 4) confirms the uniformity of the pore diameter.
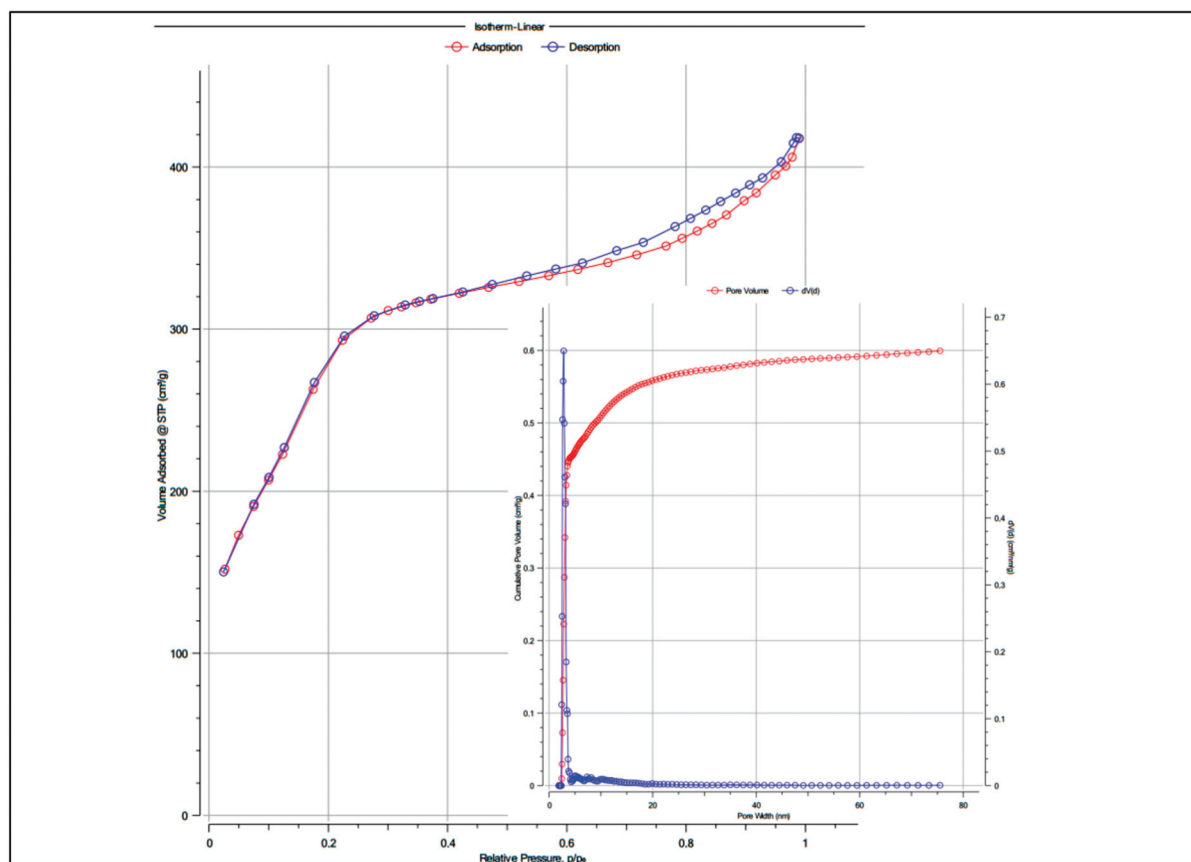
Figure 4. N_2 adsorption/desorption isotherm and pore size distribution for MCM-41.

^{29}Si –NMR MAS analysis of the MCM-41 and MCM-41/APS materials highlight some unique structural aspects of the mesoporous silica silanolic surface, such as the presence of silicon atoms Q^4, Q^3, and Q^2 (single and geminal silanolic groups). Figure 5a

shows a small Q^2 geminal and high Q^3 bands, evidencing the presence of almost single silanolic groups on the silica surface. The APTMS functionalization provides effective binding of MCM-41 single silanolic groups (Figure 5b), Q^3 band significant mitigation correlated with the presence of a T^3 band, attesting to the existence of a new covalent silicon—carbon bound [36].
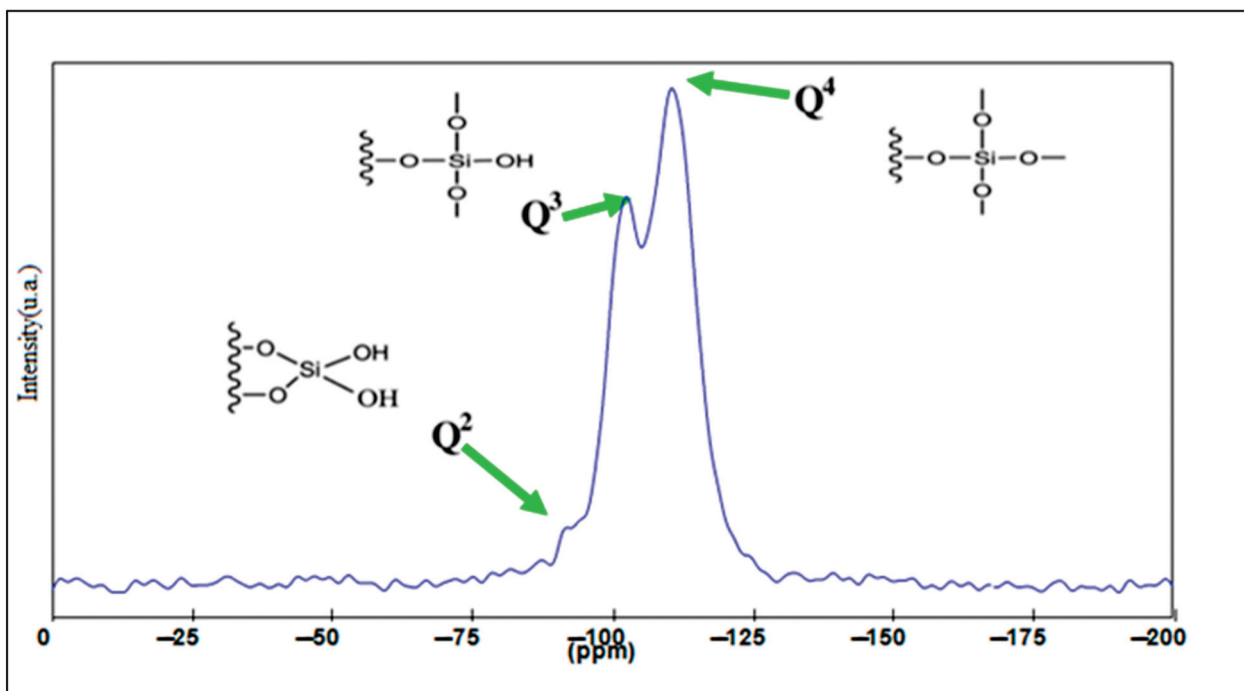
(**a**)
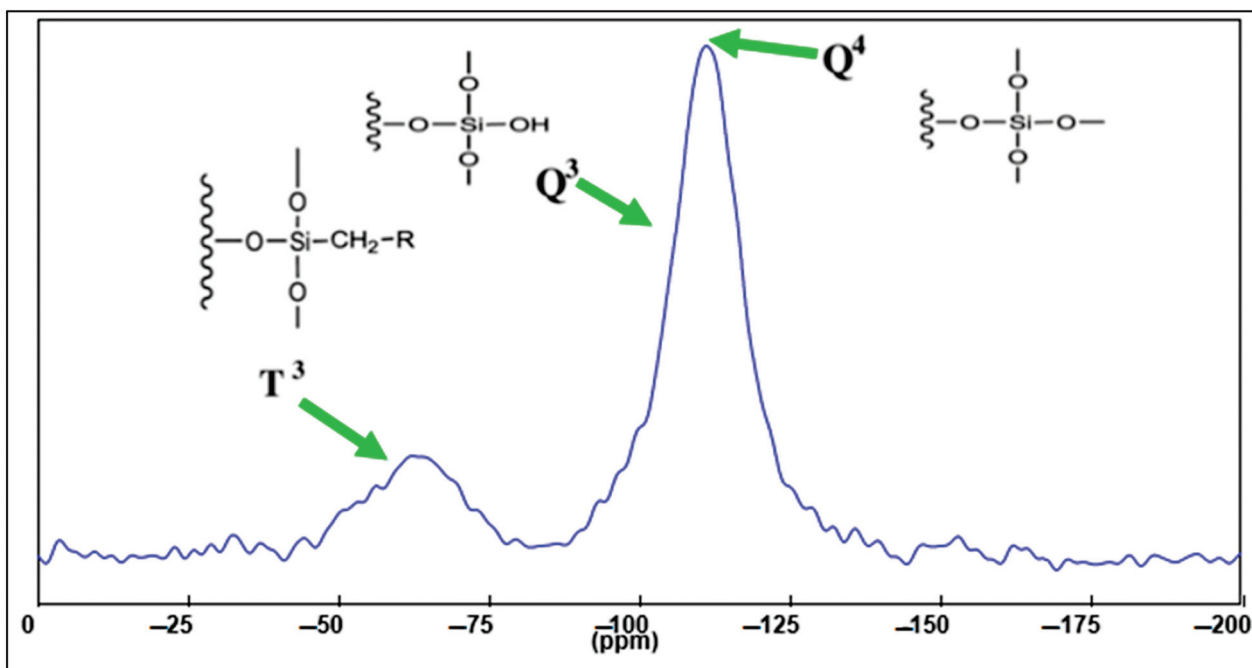
(**b**)

Figure 5. ^{29}Si MAS NMR spectrum (8 kHz rotation frequency) of non-functional mesoporous silica (**a**) and APS-grafted (**b**) materials.

In order to correlate the specific vibrational information with the MAS-NMR results, further FT-IR and Raman investigations of the intermediate and final materials were performed.

The presence of the saturated chain of glutaraldehyde is confirmed by the absorption band at 2933 cm^{-1}, with a significantly higher intensity compared to the MCM-41/APS band (2941 cm^{-1}) correlated with the presence of the propyl chain (Figure 6).
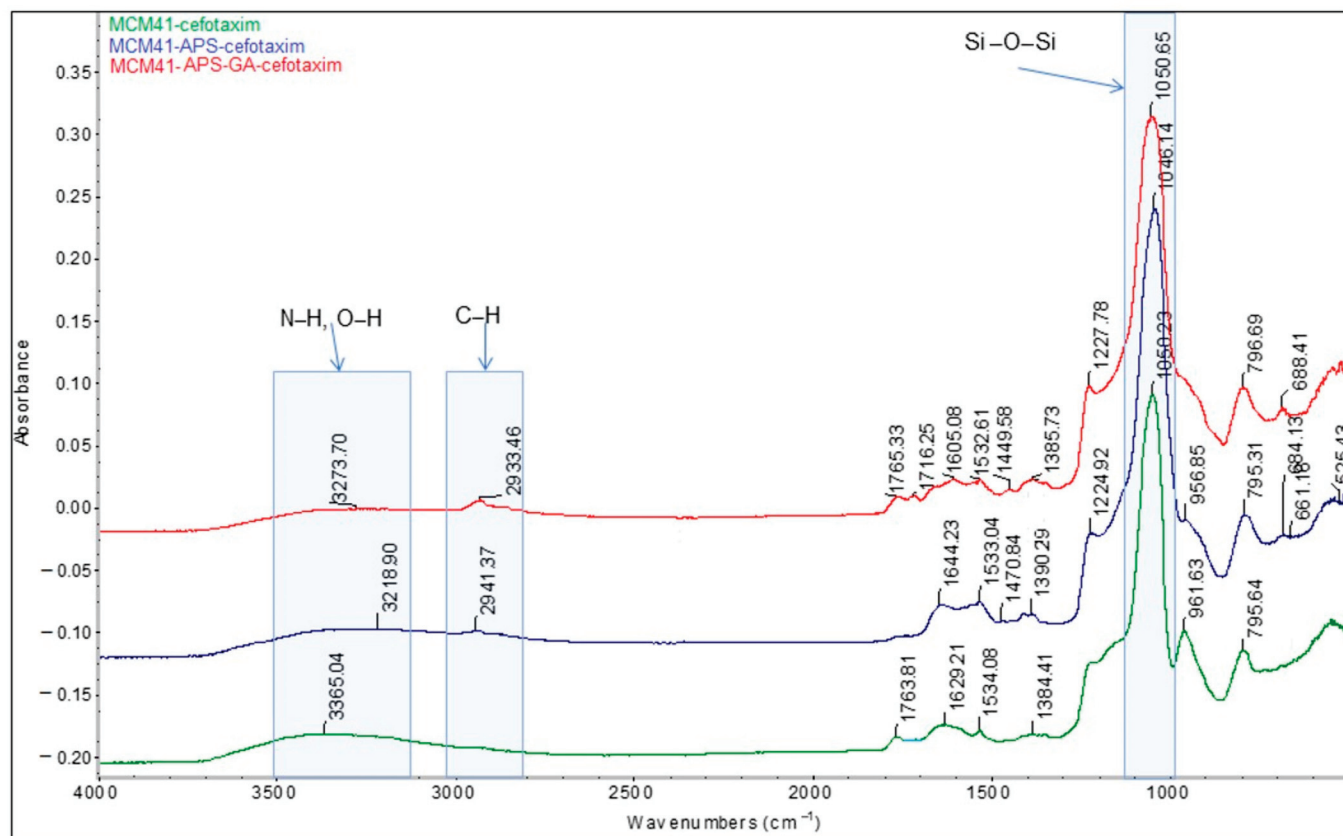
Figure 6. Comparative horizontal attenuated total reflectance (HATR)-FT-IR spectra of MCM-41/cefotaxime, MCM-41/APS—cefotaxime, and MCM-41/APS/GA—cefotaxime (the final 3 cefotaxime-loaded materials used for the desorption experiments).

The comparative FT-IR and Raman spectra of MCM-41, MCM-41/APS, and MCM-41/APS/GA confirm the presence of the saturated chain of GA due to the presence of absorption bands centered at 2929 and 2871 cm^{-1}, respectively, in Figure 7; and 2925 and 2913 cm^{-1}, respectively, in Figure 8. The absorption bands centered at 2935 and 2878 cm^{-1}, respectively, in Figure 7; and 2918 and 2892 cm^{-1}, respectively, in Figure 8, confirm the presence of APS-saturated chains; while the -NH$_2$ groups can be observed at 3361 and 3290 cm^{-1}, respectively, in Figure 7; and 3369 and 3310 cm^{-1}, respectively, in Figure 8 (correlated to the presence of the peak corresponding to nitrogen in the EDS spectrum Figure 2 and T^3 peak from MAS-NMR Figure 5). Moreover, the intensity of the characteristic bands of -NH$_2$ groups from the MCM-41/APS/GA significantly decreased in comparison to the mesoporous silica–amino groups.
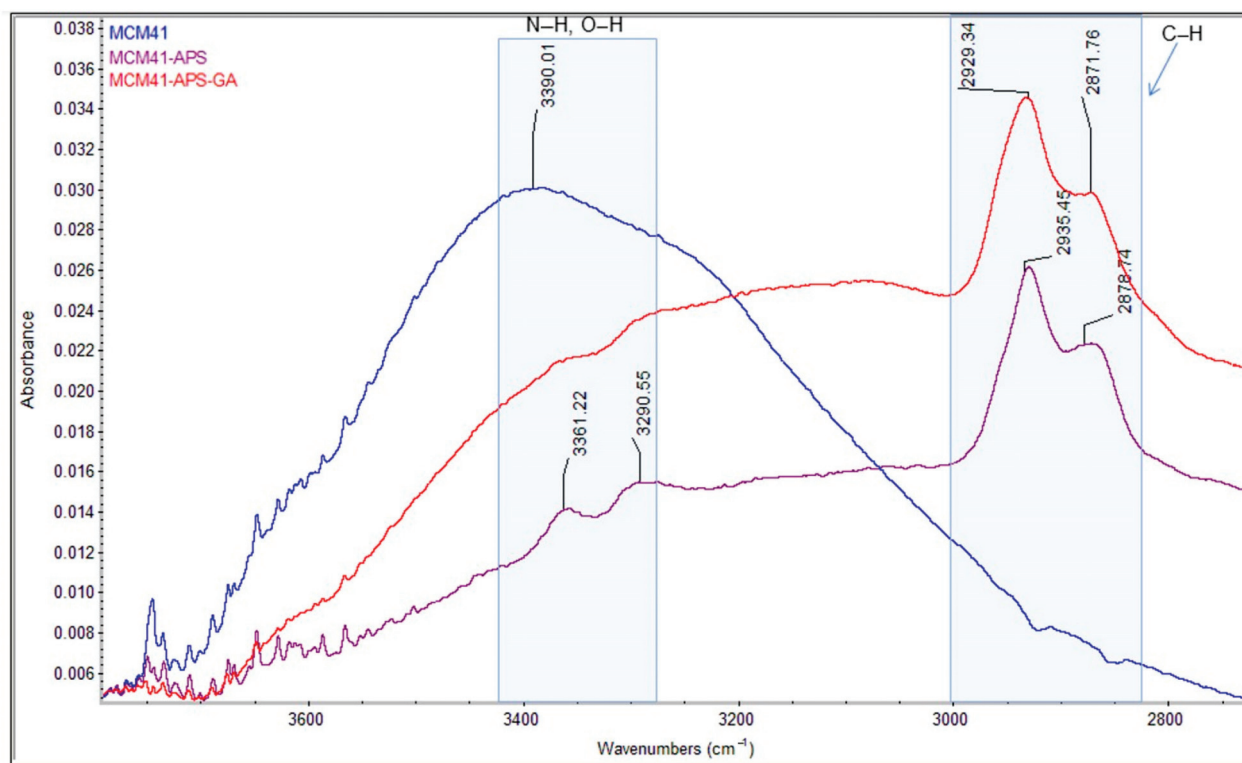
Figure 7. Comparative HATR-FT-IR spectra of MCM-41, MCM-41/APS, and MCM-41/APS/GA materials.
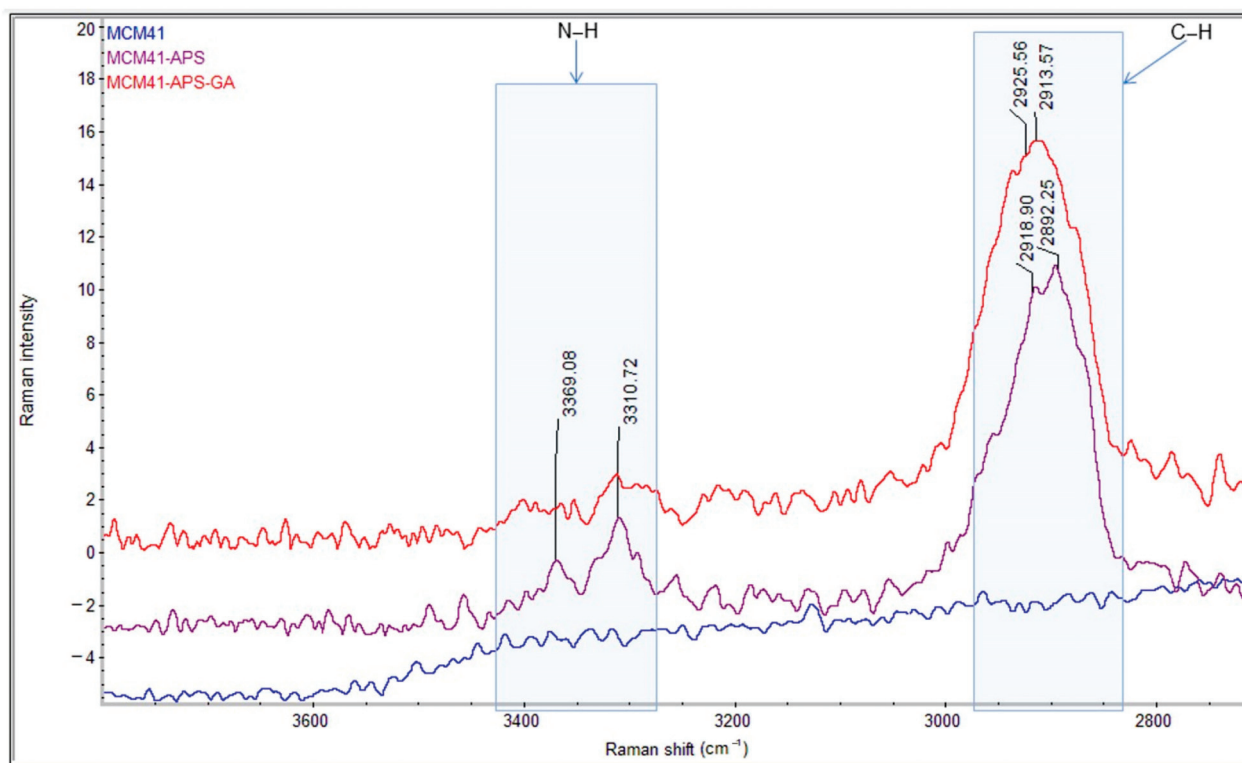
Figure 8. Comparative Raman spectra of MCM-41, MCM-41/APS, and MCM-41/APS/GA materials.

In order to estimate the release particularities linked to the different interactions between the biologically active compound and the solid mesoporous support, the final

step of this study was related to the comparative low-release capacity evaluation of the three loaded materials: MCM-41—cefotaxime, MCM-41/APS—cefotaxime, and MCM-41/APS/GA—cefotaxime. The experimental system (Figure 9) uses an Agilent 1200 series HPLC system with a manual injector, with several significant modifications: the solvent feed line of the upper mobile phase bottle was inserted in the release vessel, directly passing the liquid phase to the HPLC pump and further through the injection loop; the column was bypassed (the liquid flow from the pump was directly connected with the UV–Vis detector); and the detector exhaust line was redirected to the release vessel for the purpose of closing the whole on-flow loop. Together with the insertion of the desorption bag in the release solution, a formal blank manual injection was performed to start the data acquisition, the acquired "chromatogram" actually containing the desired desorption profile. For a proper decontamination of the whole system and cross-contamination mitigation, several washing steps were performed after each experiment, with different liquid phase pH values and baseline monitoring. For quantitative measurements, the calibration profiles were obtained and a mean value of 50 data points from each calibration profile was used for the linear regression calculations (the data points were extracted from the flat final region of the calibration profiles; the calibration samples were fully dissolved, yielding a final flat profile of the desorption curve after 10 min of release).
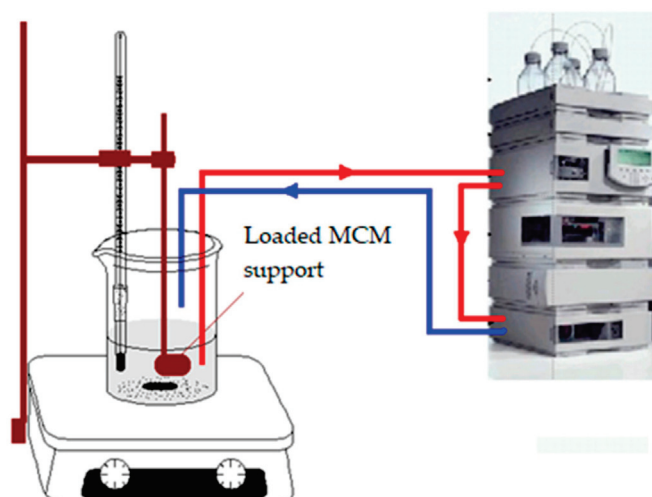
Figure 9. The experimental system (modified HPLC) used for the desorption profile acquisition.

In comparison to other on-flow or discontinuous sampling systems, our proposed desorption system provides significant advantages: high sampling rates (5–20 Hz range, feasible values for the proposed experiments are lower than 5 Hz due to the low absorbance changes compared to a normal HPLC analysis) and smooth shape of the desorption profile; low detection limits—correlated with the high HPLC detector performance; a low dead volume due to the HPLC lines; low volume of the UV–Vis detection flow cell; and long-term desorption capability (more than 48 h with a proper experiment setup).

All the desorption experiments were performed in ultrapure water (at 6.5 pH), using a similar experiment setup and acquisition conditions.

A significant release difference between the non-destructively linked cefotaxime and physically adsorbed compound on the APS functionalized MCM-41 solid phase can be established from Figure 10. Significant release differences are observed in the two important regions of the desorption profiles: the first region involves a fast release of cefotaxime in the first 20–30 min, while the final region, with a significant slope difference, involves a low, sustained release of the compound. The GA covalent-linked cefotaxime composite shows an intermediate release concentration (between the other two materials) after 120 min; however, it shows a significant lower release trend. The higher cefotaxime release concentration, compared to the MCM-41/APS adsorbed compound one, could be explained

by a lower in-pore surface access of cefotaxime after the glutaraldehyde link (in the final loading stage of composite synthesis), by a higher amount of the out-of-pore cefotaxime available for a fast release in the first 20–30 min. Following the final slope trend of the two profiles, there is expected to be a higher release concentration of the MCM-41/APS adsorbed cefotaxime at several hours of desorption time (overpassing the GA-bonded cefotaxime profile) due to the differences in the release mechanism (desorption and aldiminic bond cleavage, respectively).
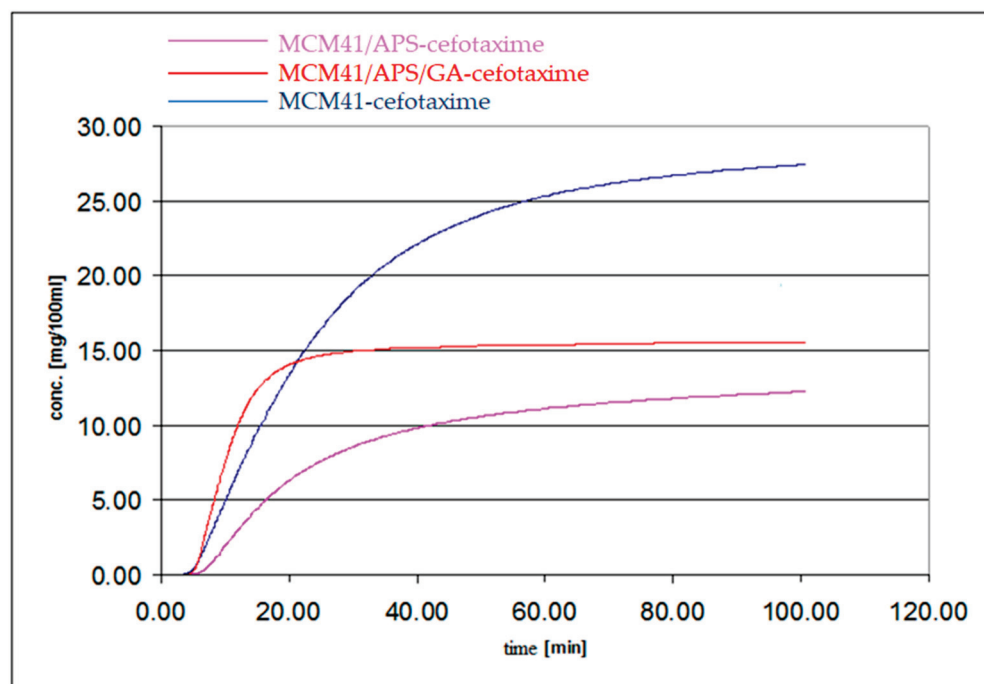
Figure 10. Desorption profiles of cefotaxime on the three support types.

The significant slope difference of the two profiles in the first 20 min of desorption can be explained by a lower interaction of the out-of-pore cefotaxime with the GA-grafted surface due to the hydrophobic saturated carbon chain of glutaraldehyde, yielding an increased release of the out-of-pore cefotaxime.

Because of the significant differences of the silanolic access of loaded cefotaxime, the non-functionalized MCM-41 material shows a significant release difference when compared to functionalized materials. In addition, due to the higher access of water at the polar silanolic surface, an enhanced release of cefotaxime is expected (because of the hydrogen bond interaction of cefotaxime with the silanolic groups, expected at -NH-, -NH$_2$, and -OH sites; the water dissolution rate will be controlled by the water molecules access at the silanolic surface. For the APS-grafted surface, the water access at the silanolic groups is significantly reduced, providing a lower release compared to MCM-41. The APS/GA material exposes a significantly lower polarity surface to the water environment; and thus, a faster release of the out-of-pore absorbed cefotaxime is expected). Despite the significant differences, a similarity between the final slopes of the MCM-41 and MCM-41/APS materials must be noticed, proving a similar in-pore diffusion mechanism. Certainly, this result correlated with the significant slope difference of the GA linked-material, which should sustain the desorption mechanism differences.

3. Conclusions

The present work describes the synthesis, characterization, and comparative low release study of a new mesoporous composite material, with covalent cefotaxime grafting on a MCM-41/propylamino/glutaraldehyde (MCM-41/APS/GA) solid phase.

The obtained materials were characterized by BET, FT-IR, RAMAN, SEM, HR-TEM, and NMR investigation methods. MCM-41 synthesis was conducted to micrometer range particles (avoiding low-diameter silica nanoparticles), with a 1029 m^2g^{-1} specific surface area (BET), pore size of 2.41 nm, and pore volume of 0.62 $cm^3\ g^{-1}$; and a high silanolic surface trough Q^3 silanolic group peak from the ^{29}Si MAS NMR spectrum. The further APS surface functionalization (performed by MCM-41—APTMS reaction) was proved by the presence of free -NH_2 groups (EDS, IR, Raman), and GA surface grafting was obtained by the glutaraldehyde aldiminic link. The last stage involved MCM-41, MCM-41/APS, and MCM-41/APS/GA materials loading with cefotaxime (3:10 (*w/w*).

We proposed a low release experimental system, using a modified HPLC system (avoiding sampling and HPLC injection) that is able to provide on-flow analysis (more than 4000 sampling points for a single experiment). The three mesoporous materials: MCM-41—cefotaxime, MCM-41/APS—cefotaxime, and MCM41/APS/GA-cefotaxime were tested in desorption experiments in water. A significant release difference between the non-destructively linked cefotaxime, physically adsorbed compound on the APS functionalized, MCM-41 solid phase was established. Moreover, significant release differences were observed in the two important regions of the desorption profiles: the first region involving a fast release of cefotaxime in the first 20–30 min and the final region, with a significant slope difference involving a low, sustained release of the compound. The GA covalent-linked cefotaxime composite shows an intermediate release concentration (between the other two materials) after 120 min; however, it shows a significant lower release trend. The low release capacity of the mesoporous glutaraldehyde-linked cefotaxime composite would be a significant advantage in wound dressing applications, advanced drugs design, antibiofilm coatings, and other related applications.

4. Materials and Methods

4.1. Reagents and Equipment

Cefotaxime hydrochloride, tetraethylorthosilicate (TEOS), glutaraldehyde (GA), amino-propyl trimethoxysilane (APTMS), methanol, ethanol, acetonitrile (ACN), and ammonium hydroxide solution 25% were purchased from Sigma-Aldrich and were used without further purification. Cetyltrimethylammonium bromide (CTAB) was purchased from Fluka and used as such. All the chemicals were of analytical purity and used as received.

Scanning electron microscope (SEM) QUANTA INSPECT F (Thermo Fisher—formerly FEI, Eindhoven, The Netherlands) field emission gun of resolution 1.2 nm was used to investigate the sample surface morphology, using energy dispersive X-ray (EDX) with the resolution to MnKα 133 eV.

High-resolution electron transmission microscope (HR-TEM) were performed on a Tecnai G2 F30 S-TWIN equipped with energy dispersive spectroscopy (EDS) as well as a selected area electron diffraction detector (SAED) purchased from Thermo Fisher—formerly FEI (Hillsboro, OR, USA). The microscope was operated in transmission mode at 300 kV; the HR-TEM point resolution was 2 Å and line resolution was 1 Å.

Fourier transform infrared (FT-IR) spectra were recorded using a Nicolet iS50FT-IR (Thermo Nicolet, Massachusetts, USA) spectrometer equipped with a DTGS detector and Raman accessory. The measurements were carried out in the range of 4000–400 cm^{-1}, using the resolution 4 cm^{-1} and 100 scans per spectrum. All the spectra were recorded using horizontal attenuated total reflectance (HATR) with diamond crystal. FT-Raman spectra were collected using the same device, using an InGaAs detector, a CaF_2 beamsplitter, 100 scans per spectrum, and the excitation laser power at 0.50 W.

The release profiles were recorded using a modified HPLC system, as previously presented [35].

Brunauer–Emmett–Teller (BET) analysis. The nitrogen adsorption/desorption isotherms were registered at 77 K in the relative pressure range p/po = 0.005–1.0, by a NOVA 800 Gas Sorption Analyzer (Anton Paar QuantaTec, Inc., Boyton Beach, FL, USA). Data processing was performed using Kaomi software. Prior to adsorption measurements, the samples were

degassed up to 180 °C under vacuum for 4 h. The standard Brunauer–Emmett–Teller (BET) equation was used to determine the specific surface area. The gas volume absorbed at a relative pressure p/po~1 allowed the estimation of the total pore volume. The Barrett–Joyner–Halenda (BJH) model was used to obtain the pore size distribution and mesopore volume from the desorption branch of the isotherm.

NMR was performed using a Bruker Avance III spectrometer (Bruker, MA, USA), with a 14.1 Tesla magnet (600 MHz proton resonance frequency). The samples were analyzed in solid state (^{29}Si) using a 3.2 mm diameter rotor and a rotational frequency of 8 kHz. For ^{29}Si nuclei, the NMR MAS "one pulse" technique was used.

4.2. Synthesis

The method of mesoporous silica synthesis is similar to that of previously described work [35]. Further, the mesoporous MCM-41 material was functionalized with propyl-amino groups by reaction with APTMS in acetonitrile.

Pressure Vessel Functionalization

Mesoporous silica (100 mg) was mixed with APTMS–ACN solution (1:4). The reaction mixture was placed in a pressure-tight reaction vessel and kept for 12 h at 85 °C. After cooling, the mixture was separated by centrifugation, washed with ultrapure water (at least 5×), and dried at 105 °C for 7 h.

In addition, a second functionalization method (microwave assisted) was attempted in order to improve the APS surface grafting; however, the results obtained sustained an in-pore polycondensation of the silane with a large surface area loss. This surface functionalization method could still be a good alternative to pressured vessel synthesis, using low microwave (MW) exposure times and reaction conditions optimization.

Further grafting of glutaraldehyde on the amino functionalized silica surface was performed as follows: the amino functionalized material (100 mg) was dispersed in ultrapure water (2 mL) and mixed with 20% solution of glutaraldehyde (2 mL). The obtained mixture was kept for 5 h at 55 °C. After cooling, the solid was separated by centrifugation and washed (at least 5×) times with ultrapure water. The final material was dried for 7 h at 55 °C.

Cefotaxime loading was performed as follows: the functionalized amino–glutaraldehyde material (100 mg) was mixed with cefotaxime (30 mg) in 10 mL methanol and subsequently, dried under vacuum in a rotary evaporator at 30 °C. The solvent evaporation process provides a cefotaxime concentration gradient, respectively, a high pore loading of the final product, and an out-of-pore distribution of the cefotaxime excess. A final drying stage was performed for 12 h at 55 °C. This method assures no bioactive compound loss in the loading stage (compared to the liquid phase loading methods that involve a solid–liquid partition).

Institutional Review Board Statement: Not applicable.

Informed Consent Statement: Not applicable.

Data Availability Statement: Available on demand.

Conflicts of Interest: The authors declare no conflict of interest.

References

1. Singh, B.; Na, J.; Konarova, M.; Wakihara, T.; Yamauchi, Y.; Salomon, C.; Gawande, M.B. Functional Mesoporous Silica Nanomaterials for Catalysis and Environmental Applications. *Bull. Chem. Soc. Jpn.* **2020**, *93*, 1459–1496. [CrossRef]

2. Gustafsson, H.; Isaksson, S.; Altskär, A.; Holmberg, K. Mesoporous silica nanoparticles with controllable morphology prepared from oil-in-water emulsions. *J. Colloid Interface Sci.* **2016**, *467*, 253–260. [CrossRef] [PubMed]

3. Popova, T.; Voycheva, C.; Tzankov, B. Study on the influence of technological factors on drug loading of poorly water-soluble drug on MCM-41 mesoporous carrier. *Pharmacia* **2020**, *67*, 351–356. [CrossRef]

4. Nayl, A.A.; Abd-Elhamid, A.I.; Aly, A.A.; Bräse, S. Recent progress in the applications of silica-based nanoparticles. *RSC Adv.* **2022**, *12*, 13706–13726. [CrossRef] [PubMed]

5. Martínez-Carmona, M.; Gun'ko, Y.K.; Vallet-Regí, M. Mesoporous Silica Materials as Drug Delivery: "The Nightmare" of Bacterial Infection. *Pharmaceutics* **2018**, *10*, 279. [CrossRef] [PubMed]

6. Jeenpadiphat, S.; Björk, E.M.; Odén, M.; Tungasmita, D.N. Propylsulfonic acid functionalized mesoporous silica catalysts for esterification of fatty acids. *J. Mol. Catal. A Chem.* **2015**, *410*, 253–259. [CrossRef]

7. More, P.M.; Umbarkar, S.B.; Dongare, M.K. Template-free sol–gel synthesis of high surface area mesoporous silica based catalysts for esterification of di-carboxylic acids. *Comptes Rendus Chim.* **2016**, *9*, 1247–1253. [CrossRef]

8. Sánchez-Bastardo, N.; Alonso, E. Maximization of monomeric C5 sugars from wheat bran by using mesoporous ordered silica catalysts. *Bioresour. Technol.* **2017**, *238*, 379–388. [CrossRef]

9. Nejati-Shendi, M.; Tebyanian, H.; Zare, R.; Ayoubi-Chianeh, M.; Roshani, K.; Kassaee, M.Z.; Rashidiani, J. Hollow Mesoporous Silica Sphere (HMSS) as a RecyclableNano-catalyst in an Efficient One-Pot MulticomponentSynthesis of 2-Amino-3-Cyano-4H-Pyran Derivatives. *Biointerface Res. Appl. Chem.* **2020**, *10*, 6640–6651. [CrossRef]

10. Waheed, N.; Mushtaq, A.; Tabassum, S.; Gilani, M.A.; Ilyas, A.; Ashraf, F.; Jamal, Y.; Bilad, M.R.; Khan, A.U.; Khan, A.L. Mixed matrix membranes based on polysulfone and rice husk extracted silica for CO2 separation. *Sep. Purif. Technol.* **2016**, *170*, 122–129. [CrossRef]

11. Zornoza, B.; Téllez, C.; Coronas, J. Mixed matrix membranes comprising glassy polymers and dispersed mesoporous silica spheres for gas separation. *J. Membr. Sci.* **2011**, *368*, 100–109. [CrossRef]

12. Ramasamy, D.L.; Khan, S.; Repo, E.; Sillanpää, M. Synthesis of mesoporous and microporous amine and non-amine functionalized silica gels for the application of rare earth elements (REE) recovery from the waste water-understanding the role of pH, temperature, calcination and mechanism in Light REE and Heavy REE separation. *J. Chem. Eng.* **2017**, *322*, 56–65. [CrossRef]

13. Ramasamy, D.L.; Repo, E.; Srivastava, V.; Sillanpää, M. Chemically immobilized and physically adsorbed PAN/acetylacetone modified mesoporous silica for the recovery of rare earth elements from the waste water-comparative and optimization study. *Water Res.* **2017**, *114*, 264–276. [CrossRef] [PubMed]

14. Karki, S.; Ingole, P.G. Development of polymer-based new high performance thin-film nanocomposite nanofiltration membranes by vapor phase interfacial polymerization for the removal of heavy metal ions. *Chem. Eng. J.* **2022**, *446*, 137303. [CrossRef]

15. He, J.; Zeng, X.; Lan, S.; Lo, I.M.C. Reusable magnetic Ag/Fe, N-TiO$_2$/Fe$_3$O$_4$@SiO$_2$ composite for simultaneous photocatalytic disinfection of E. coli and degradation of bisphenol A in sewage under visible light. *Chemosphere* **2019**, *217*, 869–878. [CrossRef]

16. Dai, J.-T.; Zhang, Y.; Li, H.-C.; Deng, Y.-H.; Elzatahry, A.A.; Alghamdi, A.; Fu, D.-L.; Jiang, Y.-J.; Zhao, D.-Y. Enhancement of gemcitabine against pancreatic cancer by loading in mesoporous silica vesicles. *Chin. Chem. Lett.* **2017**, *28*, 531–536. [CrossRef]

17. Sarkar, A.; Ghosh, S.; Chowdhury, S.; Pandey, B.; Sil, P.C. Targeted delivery of quercetin loaded mesoporous silica nanoparticles to the breast cancer cells. *Biochim. Biophys. Acta-Gen. Subj.* **2016**, *1860*, 2065–2075. [CrossRef]

18. Niculescu, V.-C. Mesoporous Silica Nanoparticles for Bio-Applications. *Front. Mater.* **2020**, *7*, 36. [CrossRef]

19. Vadia, N.; Rajput, S. Importance & Applications of Nanotechnology. In *Applications of Mesoporous Material for Drug Delivery*; MedDocs Publishers LLC: Gujarat, India, 2019.

20. Pardhi, V.; Chavan, R.B.; Thipparaboina, R.; Thatikonda, S.; Naidu, V.G.M.; Shastri, N.R. Preparation, characterization, and cytotoxicity studies of niclosamide loaded mesoporous drug delivery systems. *Int. J. Pharm.* **2017**, *528*, 202–214. [CrossRef]

21. Nairi, V.; Medda, L.; Monduzzi, M.; Salis, A. Adsorption and release of ampicillin antibiotic from ordered mesoporous silica. *J. Colloid Interface Sci.* **2017**, *497*, 217–225. [CrossRef]

22. Chircov, C.; Spoială, A.; Păun, C.; Crăciun, L.; Ficai, D.; Ficai, A.; Andronescu, E.; Turculeţ, Ș.C. Mesoporous Silica Platforms with Potential Applications in Release and Adsorption of Active Agents. *Molecules* **2020**, *25*, 3814. [CrossRef] [PubMed]

23. Sartori, B.; Amenitsch, H.; Marmiroli, B. Functionalized Mesoporous Thin Films for Biotechnology. *Micromachines* **2021**, *12*, 740. [CrossRef] [PubMed]

24. Diab, R.; Canilho, N.; Pavel, I.A.; Haffner, F.B.; Girardon, M.; Pasc, A. Silica-based systems for oral delivery of drugs, macro-molecules and cells. *Adv. Colloid Interface Sci.* **2017**, *249*, 346–362. [CrossRef]

25. Jugdaohsingh, R. Silicon and bone health. *J. Nutr. Health Aging* **2007**, *11*, 99–110. [PubMed]

26. de Araújo, L.A.; Addor, F.; Campos, P.M.B.G.M. Use of silicon for skin and hair care: An approach of chemical forms available and efficacy. *An. Bras. Dermatol.* **2016**, *91*, 331–335. [CrossRef]

27. Bhattacharjee, P.; Paul, S.; Bhattacharjee, P. Risk of occupational exposure to asbestos, silicon and arsenic on pulmonary disorders: Understanding the genetic-epigenetic interplay and future prospects. *Environ. Res.* **2016**, *147*, 425–434. [CrossRef]

28. Khan, A.H.; Bienia, O.B. Identifying Potential Inhalation Risks Associated with Exposure to Different Forms of Silica at the Nanomolecular Level as it Relates to Antimicrobial Agents. *Adv. Biotechnol. Microbiol.* **2021**, *16*, 27–30. [CrossRef]

29. Beckett, W. Airways Disease. In *xPharm: The Comprehensive Pharmacology Reference*; Enna, S.J., Bylund, D.B., Eds.; Elsevier: Amsterdam, The Netherlands, 2008; p. 472.

30. Hathout, R.M.; Abdelhamid, S.G.; El-Housseiny, G.S.; Metwally, A.A. Comparing cefotaxime and ceftriaxone in combating meningitis through nose-to-brain delivery using bio/chemoinformatics tools. *Sci. Rep.* **2020**, *10*, 21250. [CrossRef]

31. LeFrock, J.L.; Prince, R.A.; Leff, R.D. Mechanism of action, antimicrobial activity, pharmacology, adverse effects, and clinical efficacy of cefotaxime. *Pharmacotherapy* **1982**, *2*, 174–184. [CrossRef]

32. Varghese, M.; Balachandran, M. Antibacterial efficiency of carbon dots against Gram-positive and Gram-negative bacteria: A review. *J. Environ. Chem. Eng.* **2021**, *9*, 106821. [CrossRef]

33. He, J.; Zheng, Z.; Lo, I.M.C. Different responses of gram-negative and gram-positive bacteria to photocatalytic disinfection using solar-light-driven magnetic TiO_2-based material, and disinfection of real sewage. *Water Res.* **2021**, *207*, 117816. [CrossRef] [PubMed]

34. Maria, G.; Stoica, A.-I.; Luta, I.; Stirbet, D.; Radu, G.L. Cephalosporin release from functionalized MCM-41 supports interpreted by various models. *Microporous Mesoporous Mater.* **2012**, *162*, 80–90. [CrossRef]

35. Istrati, D.; Mihaiescu, D.E.; Gudovan, D.; Gudovan, I.A.; Traistaru, V.; Marton, A. Controlled release profiles of Cefepime from MCM-41-NH2 materials. *Rev. Roum. Chim.* **2015**, *60*, 1125–1131.

36. Protsak, I.S.; Morozov, Y.M.; Dong, W.; Le, Z.; Zhang, D.; Henderson, M. A ^{29}Si, ^{1}H, and ^{13}C Solid-State NMR Study on the Surface Species of Various Depolymerized Organosiloxanes at Silica Surface. *Nanoscale Res. Lett.* **2019**, *14*, 160. [CrossRef] [PubMed]

Article

TEGylated Phenothiazine-Imine-Chitosan Materials as a Promising Framework for Mercury Recovery

Sandu Cibotaru [1,*], Daniela Ailincai [1], Bianca-Iustina Andreica [1], Xinjian Cheng [2] and Luminita Marin [1,*]

[1] "Petru Poni" Institute of Macromolecular Chemistry, Gr. Ghica Voda Alley, 41A, 700487 Iasi, Romania
[2] School of Chemistry and Environmental Engineering, Wuhan Institute of Technology, Wuhan 430079, China
* Correspondence: cibotaru.sandu@icmpp.ro (S.C.); lmarin@icmpp.ro (L.M.)

Abstract: This paper reports new solid materials based on TEGylated phenothiazine and chitosan, with a high capacity to recover mercury ions from aqueous solutions. They were prepared by hydrogelation of chitosan with a formyl derivative of TEGylated phenothiazine, followed by lyophilization. Their structural and supramolecular characterization was carried out by ^{1}H-NMR and FTIR spectroscopy, as well as X-ray diffraction and polarized light microscopy. Their morphology was investigated by scanning electron microscopy and their photophysical behaviour was examined by UV/Vis and emission spectroscopy. Swelling evaluation in different aqueous media indicated the key role played by the supramolecular organization for their hydrolytic stability. Mercury recovery experiments and the analysis of the resulting materials by X-ray diffraction and FTIR spectroscopy showed a high ability of the studied materials to bind mercury ions by coordination with the sulfur atom of phenothiazine, imine linkage, and amine units of chitosan.

Keywords: phenothiazine; chitosan; imine; mercury recovery

1. Introduction

Environmental pollution by heavy metals is a major global concern, severely impacting human and animal health [1]. Heavy metals are hazardous pollutants; they are not biodegradable and contaminate the air, soil, and waters, entering the food chain and ultimately reaching the human body. Even if some metals, such as copper, zinc, manganese, selenium, chromium, and molybdenum, are important in the daily diet in small amounts, their overexposure causes poisoning and long-term organ damage, especially for children [2]. Other metals, such as arsenic, cadmium, lead, and mercury, were identified as extremely dangerous for the human body even in small amounts and were included on the list of carcinogenic agents by health agencies; i.e., U.S. Food and Drug Administration, World Health Organization (WHO), Joint Food and Agricultural Organization (FAO), the U.S. Environmental Protection Agency (EPA), and Centre for Disease Control (CDC) [3,4]. Nevertheless, heavy metal pollution is strongly correlated with technological development that cannot cannot be stopped and, consequently, the world agencies included these metals on the list of substances that need to be monitored with priority, establishing desirable maximum levels in water and soils [5,6]. Among these toxic metals, mercury is especially dangerous because it easily sublimates, contaminates the air, and deposits in the waters and soil, being a constant pollution source [7]. In living organisms, mercury denatures proteins, killing cells, including the neurons [8]. This is why the desirable limits for mercury are very low, not higher than 0.002 ppm [9]. In this context, the researchers' attention is focused on the development of materials capable of detecting and recovering mercury from the environment and human body [10–22].

Global warming is another side effect of technological development, which is threatening life on Earth. To limit its effect, the development of new materials from renewable resources, which are environmentally friendly and do not affect the eco-system, is recommended [23,24]. In line with this requirement, eco-materials based on biopolymers, able to

detect and recover heavy metals, constituted the base of new materials designed to detect or recover mercury. Cellulose-, lignin-, chitosan-, or peptide-based hydrogels/xerogels proved to have a high ability to bond mercury, encouraging their deeper consideration, in order to create high-performance adsorbent materials [23,25–34]. It was established that polysaccharides are excellent sorbents for heavy metals thanks to their ability to develop physical and electrostatic forces, which can be further improved by grafting moieties capable of coordinating metals.

Considering all of these factors, this study aimed to design and prepare a chitosan-based material capable of recovering mercury ions from wastewater. To increase the ability of chitosan to bind mercury, a phenothiazine moiety was covalently linked via imine bonds, with both units having a good ability to coordinate the mercury ions [35]. Besides, a triethylene glycol unit was grafted on the phenothiazine heterocycle in order to improve the material's swellability, and thus its ability to retain metal ions from wastewater. The rational design of the studied material is schematically represented in Scheme 1.
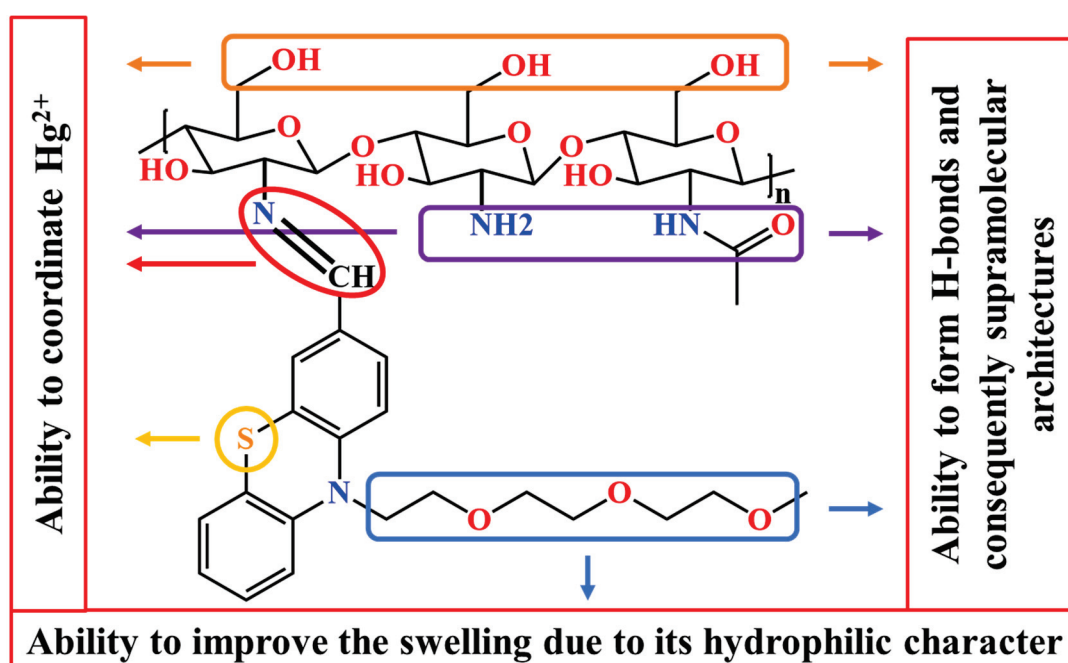
Scheme 1. Pictorial representation of the rational design of the studied materials.

2. Results and Discussion

2.1. Synthesis and Characterization of the Hydrogels/Xerogels

A series of three chitosan-based hydrogels was prepared by imination reaction with a formyl derivative of triethylene glycol-phenothiazine (PTF) (Scheme 2). The hydrogelation of chitosan in the presence of PTF aldehyde can take place because of the formation of imine units and their self-assembly in ordered clusters, with the role of cross-linking nodes [36–38]. Furthermore, it is expected that the presence of the triethylene glycol chain in the PTF structure will promote the formation of hydrogen bonds with the chitosan chain, thereby strengthening the hydrogel's structure by an additional physical cross-linking. As the PTF derivative has moderate solubility in water, to ensure the homogeneity of the chitosan/PTF system, the imination reaction was achieved in a mixture of solvents, water/acetone. By varying the molar ratio of the glucosamine units of chitosan and PTF, three hydrogels with different degrees of imination were obtained (Table 2).
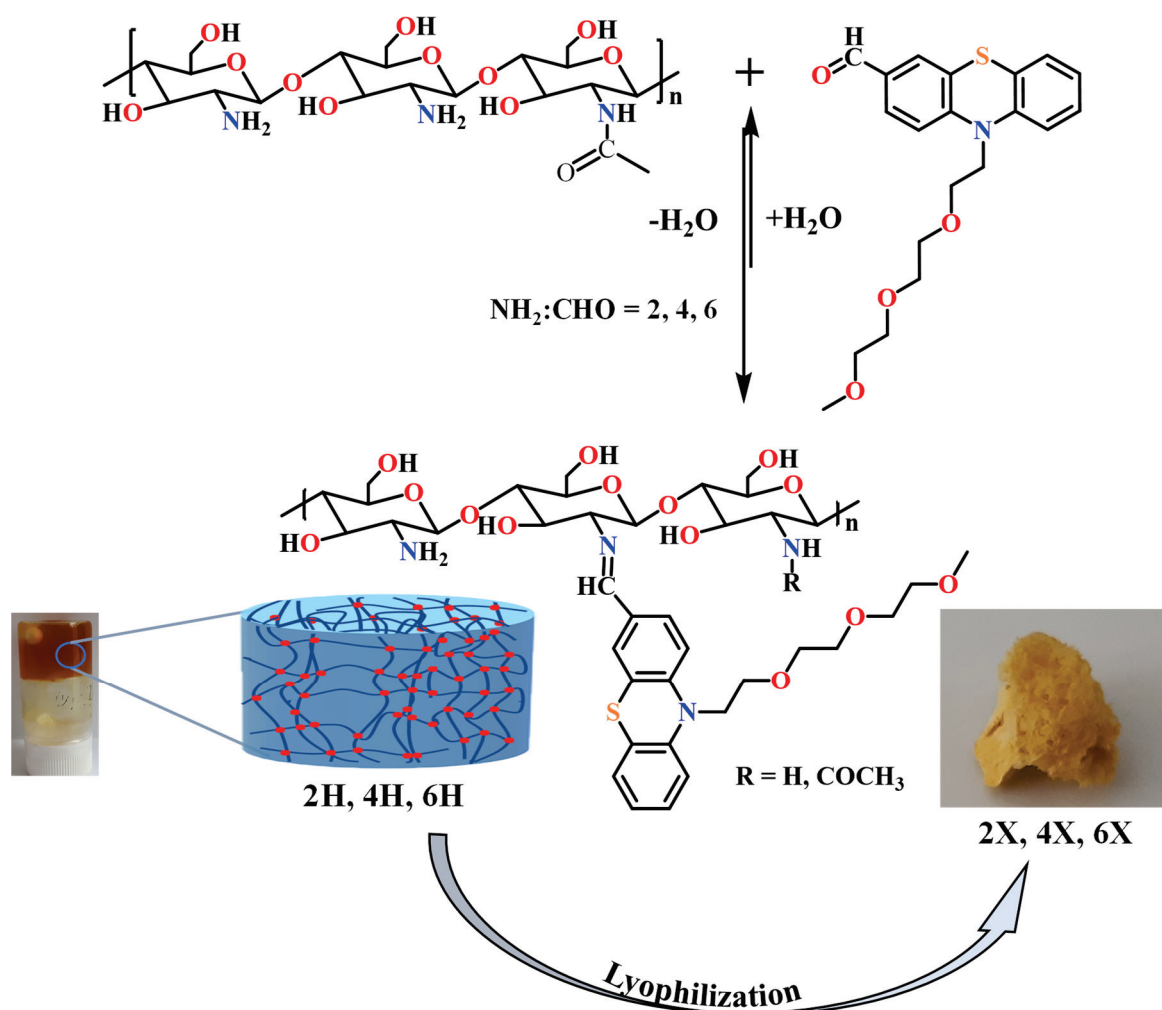
Scheme 2. The condensation reaction of chitosan with PTF and representative images of the obtained hydrogels and the corresponding xerogels.

The obtained hydrogels appeared as soft, transparent materials, which successfully passed the inverted tube test and, by lyophilization, they formed porous, solid materials. The hydrogels obtained were coded with 2H, 4H, and 6H, and the corresponding xerogels obtained by lyophilization were coded with 2X, 4X, and 6X, respectively (Table 2). For an accurate comparison, a chitosan xerogel reference was prepared in the same conditions as the hydrogels and coded CX.

The ^{1}H-NMR spectra of the obtained hydrogels revealed a partial conversion of the aldehyde in imine units (Figure 1), in agreement with the reversibility of the imine linkage in acidic water [36], and because the phenothiazine-based aldehyde has low reactivity, as proven by previous studies [35,39,40].

On the other hand, the FTIR spectra recorded on xerogels showed the presence of the absorption band characteristic to the imine bonds at 1640 cm^{-1} and the disappearance of the band characteristic to the absorption of the formyl group of PTF at 1686 cm^{-1}, indicating that lyophilization favoured the conversion of the aldehyde into imine units (Figure 2). This is due to the shifting of the imination equilibrium to products, as the water is gradually removed from the system [36]. The band characteristic of the vibration of the imine bonds was intense and partially superposed with the band characteristic of the stretching vibration of the amide bond C-N of the acetylated units of chitosan, at 1660 cm^{-1} [41]. Another sign of the progress of the imination reaction was provided by the evolution of the band characteristic to the vibration of amine bonds of chitosan, at 1546 cm^{-1}. Despite overlapping with the vibration bands of the double bonds of phenothiazine, as the PTF

content in the xerogels increased, the intensity of the band decreased. This suggested the consumption of the amine groups by conversion into imine bonds. The other bands characteristic of the vibration of the main bonds of chitosan and PTF were also present in the spectra, confirming the success of the imination reaction. Thus, in the fingerprint domain, the bands characteristic of the vibration of the C=C bonds in the phenothiazine heterocycle can be observed at 1598, 1573, and 1558 cm^{-1} and the band specific to the C-H out-of-plane bending vibration was present at 750 cm^{-1}. The band specific to the vibration of the aliphatic C-H bonds, which occurs at 1470 cm^{-1} in PTF and 1422 cm^{-1} in chitosan, appeared in xerogels at intermediate values, at ~1466 cm^{-1}, due to their overlapping. Similarly, the bands corresponding to the C-O-C bond, which occur at 1150, 1075, and 1031 cm^{-1} in chitosan and 1142, 1107, and 1037 cm^{-1} in PTF, appeared in xerogels at values slightly shifted to the left or to the right, indicating not only their overlapping, but also the formation of new hydrogen bonds between the two components, chitosan and the TEG chain of PTF.
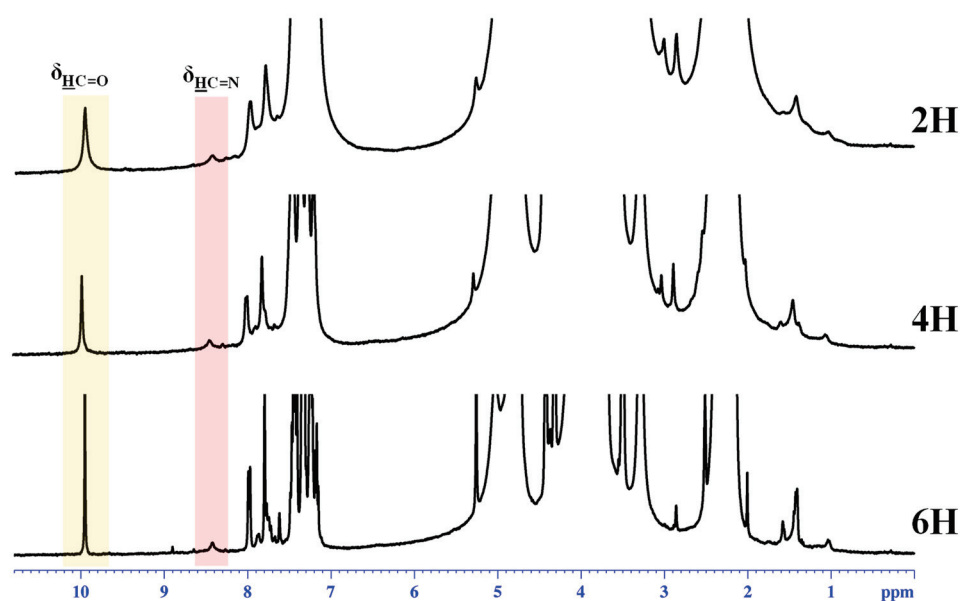
Figure 1. ^{1}H-NMR spectra of the hydrogels recorded in D$_2$O/acetone-d$_6$ (1/1.3) at 25 °C.

Previous studies have shown that chitosan's imination is accompanied by re-organization of the hydrogen bonds network, reflected in changes in the 3700–3000 cm^{-1} spectral domain, which is characteristic of both the vibrations of amino and hydroxyl groups and the intra- and inter-molecular hydrogen bonds formed between them [36,37,40]. In the case of the investigated xerogels, a decrease in the band's intensity compared with other bands was noticed along with an increase in the phenothiazine content. This can be explained by a diminution of the hydrogen bonds promoted by the two types of groups, by the simple fact that the number of amine groups diminished as they turned into imine bonds. Moreover, a slight change in the shape of the band could be remarked by the predominant decrease in its intensity in the 3300–3000 range, characteristic of the occurrence of the symmetric and asymmetric vibrations of the amine bonds. All changes in the FTIR spectra suggested that, by reacting the amine groups of chitosan with the PTF aldehyde, the hydrogen bonding network of chitosan changed, by decreasing the density of H-bonds promoted by amine units and increasing the density of H-bonds promoted by the TEG unit of PTF. In this way, an additional physical crosslinking took place, which was evidenced by the physical appearance of the xerogels; the 2X xerogel with a higher amount of PTF promoting a higher amount of H-bonds was soft and flexible, while the 6X xerogel with the lowest amount was slightly brittle.
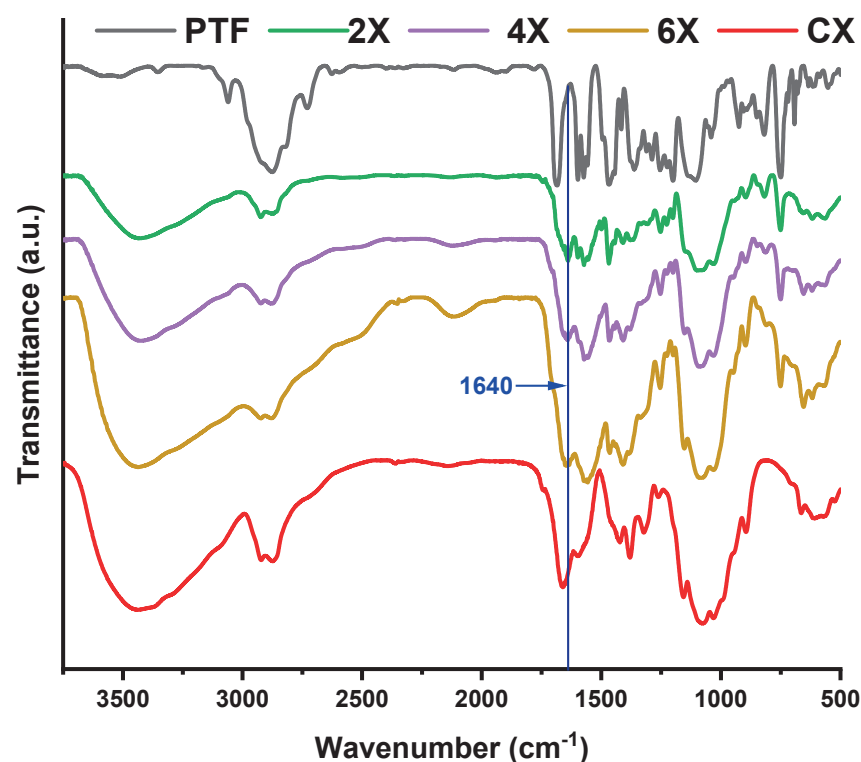
Figure 2. Comparative FTIR spectra of the xerogels, PTF, and chitosan.

2.2. Supramolecular Characterization

To highlight the morphological changes suggested by the FTIR spectra, wide-angle X-ray diffractograms were recorded on xerogel pellets. As can be seen in Figure 3a, chitosan shows two reflections at 11.6° and 22°, corresponding to the intra-molecular (7.8 Å) and inter-chain (4.2 Å) distances, respectively, that define its well-known semicrystalline structure [42,43]. The imination reaction with PTF prompted the modification of the diffractogram, a fact especially noted in the case of the 2X sample, with the highest crosslinking degree. It was observed that (i) the appearance of a new reflection in the small angle domain, at 3°, and (ii) the displacement of the reflection bands from 11.6° to 10.5° and from 22° to 20.9°. The reflection band from 3° is characteristic to a layered morphology, suggesting a hydrophilic/hydrophobic ordering of the imino-chitosan derivative, with hydrophobic layers of phenothiazine and hydrophilic layers of chitosan and TEG [36,40]. The corresponding inter-layer distance of 29.4 Å (calculated using Bragg's law) is close in value to the sum of two lengths of phenothiazine molecules, one of TEG and one of glucosamine (10.2 + 10.2 + 8.19 + 5.1) Å (Figure 3b), suggesting a supramolecular structure in which the imine units are arranged in an antiparallel manner, forming double layers (Figure 3c). This arrangement of phenothiazine-imine units between the chitosan chains has also been confirmed by molecular modelling and simulation studies (Figure 3b,c). The proposed model is also in line with the shifting of the reflection bands from wide to low angles, corresponding to larger inter- and intra-molecular distances, owing to the fact that the hydrophilic–hydrophobic ordering will lead to the emergence of new inter-molecular distances between the phenothiazine units and will impose higher distances between the chitosan chains [36,40].
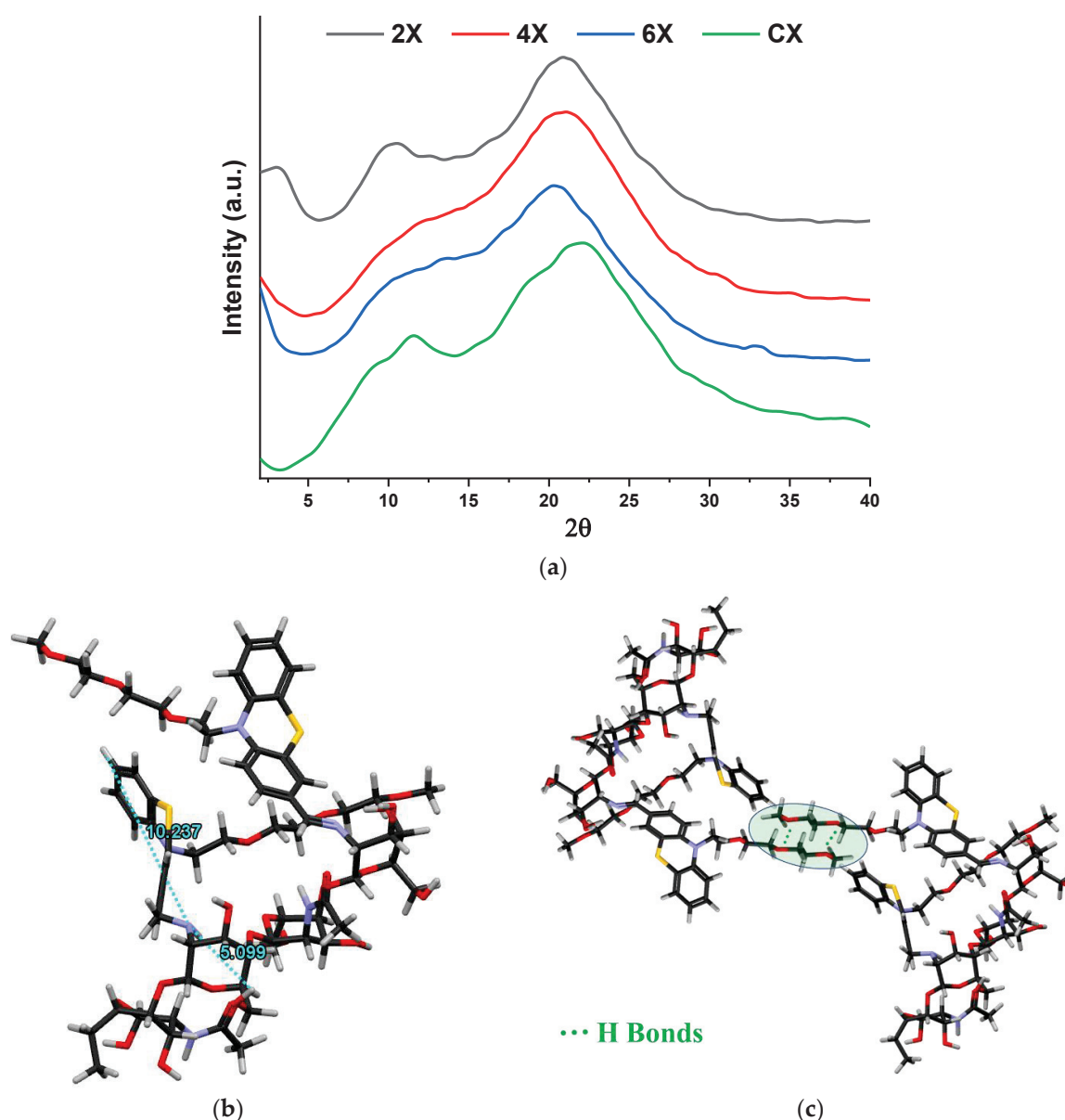
Figure 3. (**a**) X-ray diffractograms of the xerogels and (**b**,**c**) simulation of the layered architecture by HyperChem Professional 8.0 software.

The supramolecular organization of the xerogels was supported by the polarized light microscopy images acquired in reflection mode, which displayed birefringence spots on the pores' walls (Figure 4).

Merging the structural and supramolecular data, it can be assumed that the hydrogelation of chitosan with PTF took place because of the supramolecular ordering of the phenothiazine-imine units and the occurrence of the H-bonds between the ether, hydroxyl, and amine groups of TEG units of phenothiazine and chitosan, respectively. In this way, the hydrogelation process is in close correlation with the occurrence of imine units, which is why the preservation of a homogenous reaction medium played a key role.
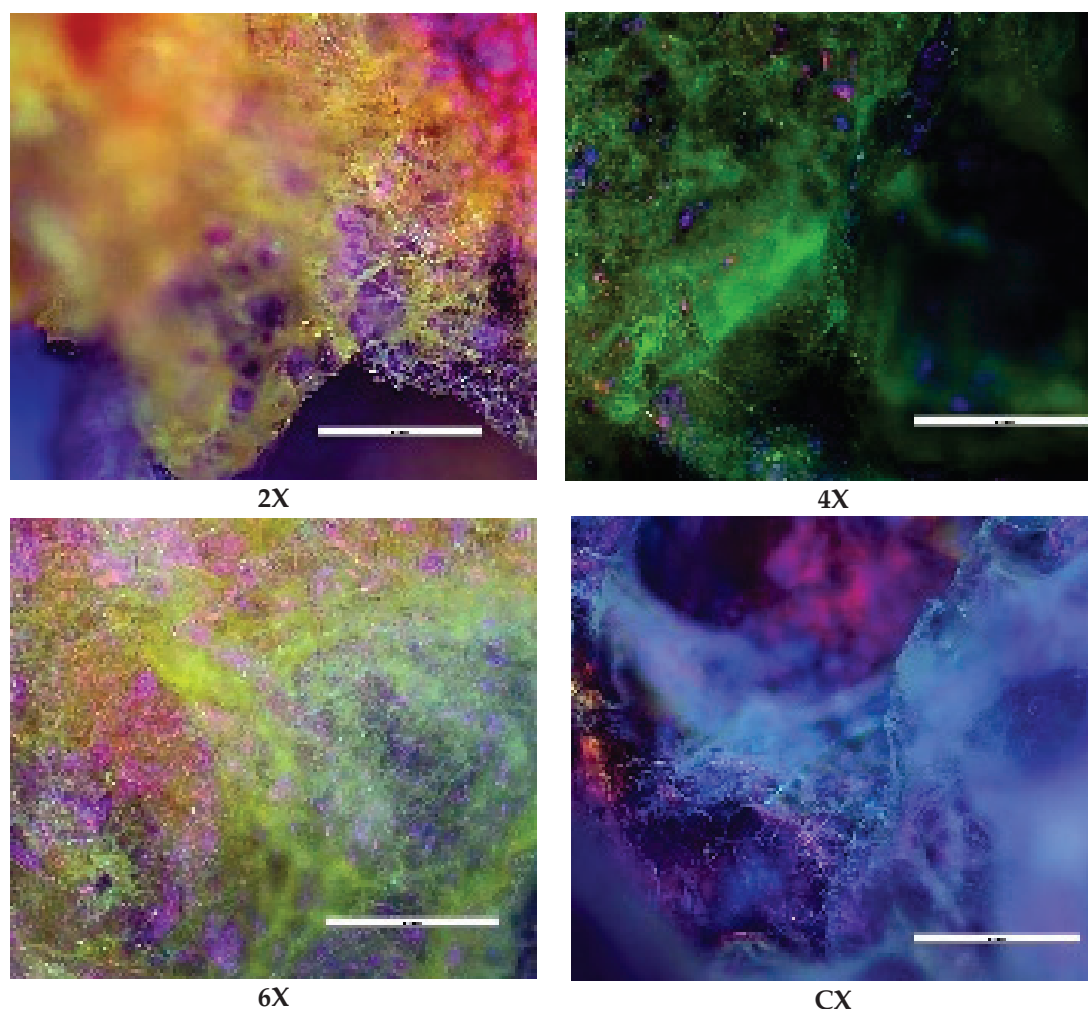
Figure 4. Representative POM images of the xerogels (scale bar: 100 μm).

2.3. Morphology

The xerogels showed a sponge-like morphology, with interconnected pores and a heterogenous distribution of their diameter between 2 and 35 μm (Figure 5). While literature data report the increase in the pores' diameter as the crosslinking degree decreased, no such trend was observed for these samples. Most probably, this is because the imination degree in the hydrogel state was not high enough to control the morphology, thus the water freezing prior to the lyophilization played the determinant role. Thus, the shifting of the imination equilibrium to products during lyophilization just reinforced the morphology patterned in the freezing step. Moreover, the morphology was influenced by the different sublimation rates of water/acetone crystals in the frozen hydrogels. The lower density and freezing point of acetone induced its faster sublimation compared with water, determining an agglomeration of the hydrophobic phenothiazine units at the xerogel surface, forming a thin film (Figure 5c).
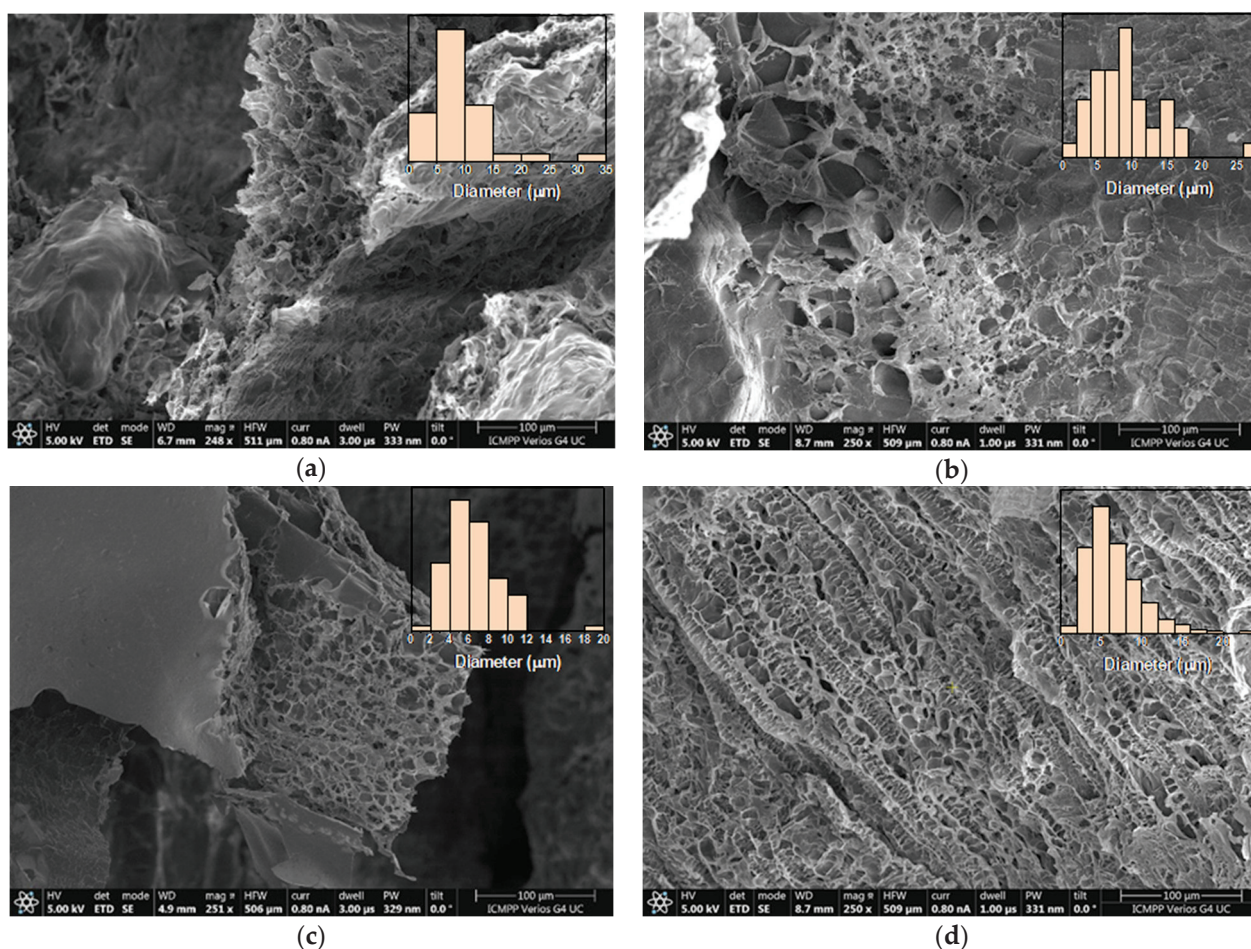
Figure 5. Representative SEM images of the xerogels: (**a**) 2X, (**b**) 4X, (**c**) 6X, (**d**) CX. In the inset, the histograms of pores' dimensions are given.

2.4. Photophysical Properties

As phenothiazine is a chromophore unit capable of conferring light-emitting ability to the materials containing it [44,45], the photophysical properties of the xerogels were investigated by absorption/emission spectroscopy. Remarkably, the absorption intensity of all xerogels was very high, an absorption spectrum that can only be recorded when the phenothiazine content was decreased to an amine/aldehyde ratio of 60/1 (Figure 6a). The PTF displayed two absorption maxima, that is, an intense, sharp one at 282 nm and a broad band of low intensity with a maximum at 378 nm, attributed to the π-π* transitions in the phenothiazine heterocycle and in the conjugated phenothiazine-formyl system, respectively. Compared with the PTF reference, the absorption maximum of lower energy was bathochromic shifted to 385 nm in the xerogel, indicating a more extended electronic conjugation. Considering that the newly formed imine units are weaker electron donors compared with the formyl groups, the increased electronic conjugation can be attributed to higher planarity of the phenothiazine heterocycle induced by the supramolecular organization in hydrophobic layers, as the X-ray diffraction suggested [39].

Exciting the xerogel samples with the light corresponding to the maximum absorption, the samples gave a broad emission band of low intensity, with the maximum in the range of 530–590 nm (Figure 6b). The low intensity of the emission was confirmed by the low quantum yield of around 1.4% and low luminescence when the samples were illuminated under UV light (Figure 6c). It can be explained by the formation of hydrophobic clusters of phenothiazine, which favoured the non-radiative decay channels due to excimer formation [46].
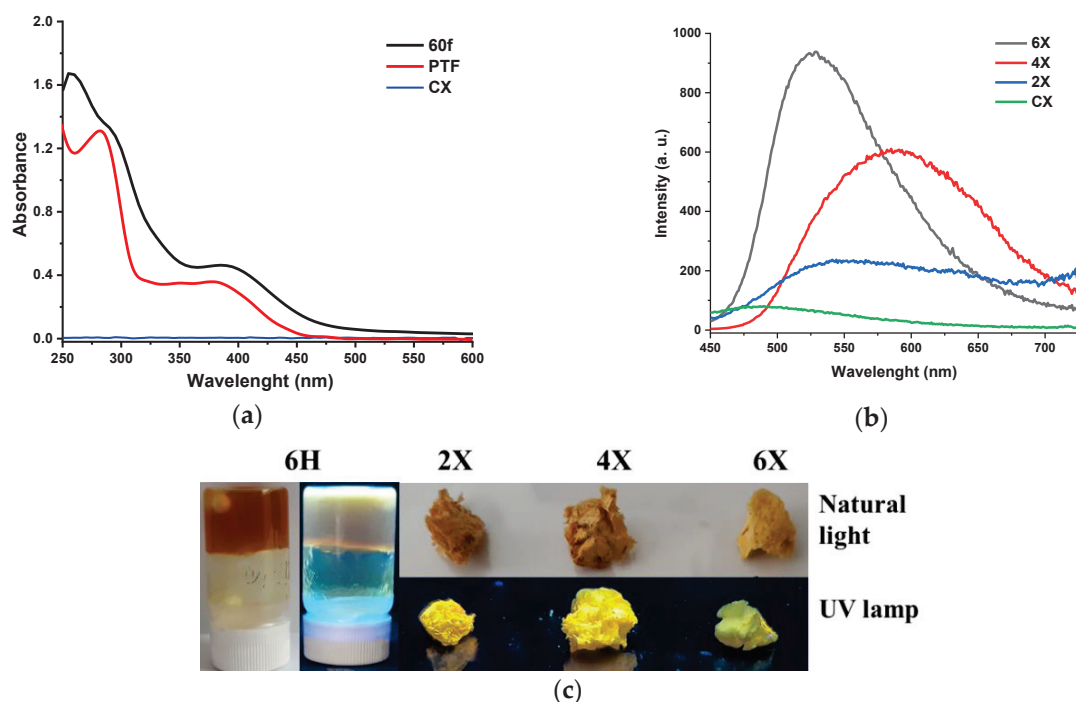
Figure 6. Photophysical behaviour of the samples: (**a**) UV/Vis absorption spectra of a film prepared from chitosan and PTF in a 60/1 molar ratio of amine/aldehyde functional groups (60f) and of chitosan and PTF references; (**b**) emission spectra of the hydrogels and chitosan; and (**c**) images of hydrogels and xerogels when illuminated with a UV lamp.

2.5. The Xerogels' Behavior in an Aqueous Medium

The xerogels' behaviour in aqueous media is important in order to establish their possible application. Immersed in water, the xerogels had a typical sponge-like behaviour, absorbing water with no evident modification of their aspect or volume.

In view of the application of the studied materials as mercury adsorbents, it is important to know their behaviour in acidic solutions generated by mercury salts. To this end, the hydrolytic stability of the studied xerogels in an aqueous solution of pH = 3.7, in the presence or absence of mercury ions, was investigated.

When immersed in an acidic aqueous solution of low pH (pH = 3.7, equal to that of 5 g/mL mercury acetate solution), the xerogel 2X rehydrated forming the corresponding hydrogel, while the xerogels 4X, 6X, and CX started to disintegrate. After 30', the sample CX was completely dissolved and the samples 4X and 6X were disintegrated in small pieces, while the xerogel 2X swelled, reaching a swelling degree of 42.6 $\pm$ 9 g/g (Figure 7a). It was obvious that the crosslinking degree influenced the stability of xerogels and a higher crosslinking degree endowed the xerogels with higher hydrolytic stability, even in acidic media. This is the most probably due to the formation of phenothiazine hydrophobic clusters, which protected the imine units [47].

Contrary to the previous situation, the immersion of the xerogels in mercury ions solution had no effect, with no disintegration or dissolution being observed (Figure 7a). The samples swelled and their swelling degree increased along with the decrease in the crosslinking degree, reaching the value of 114 $\pm$ 10 g/g for CX (Figure 7b). Moreover, by swelling, they transformed into elastic hydrogels, with a rubbery aspect, indicating that mercury ions can crosslink the phenothiazine-chitosan network (Figure 7c) [48]. The xerogels were hydrolytically stable even in acidic solutions containing small amounts of mercury ions (Figure 7a). It was also noticed that the mercury ion solutions were slightly yellow, attributed to the oxidation occurrence. Interestingly enough, the solution remained colourless in the presence of the control sample CX.
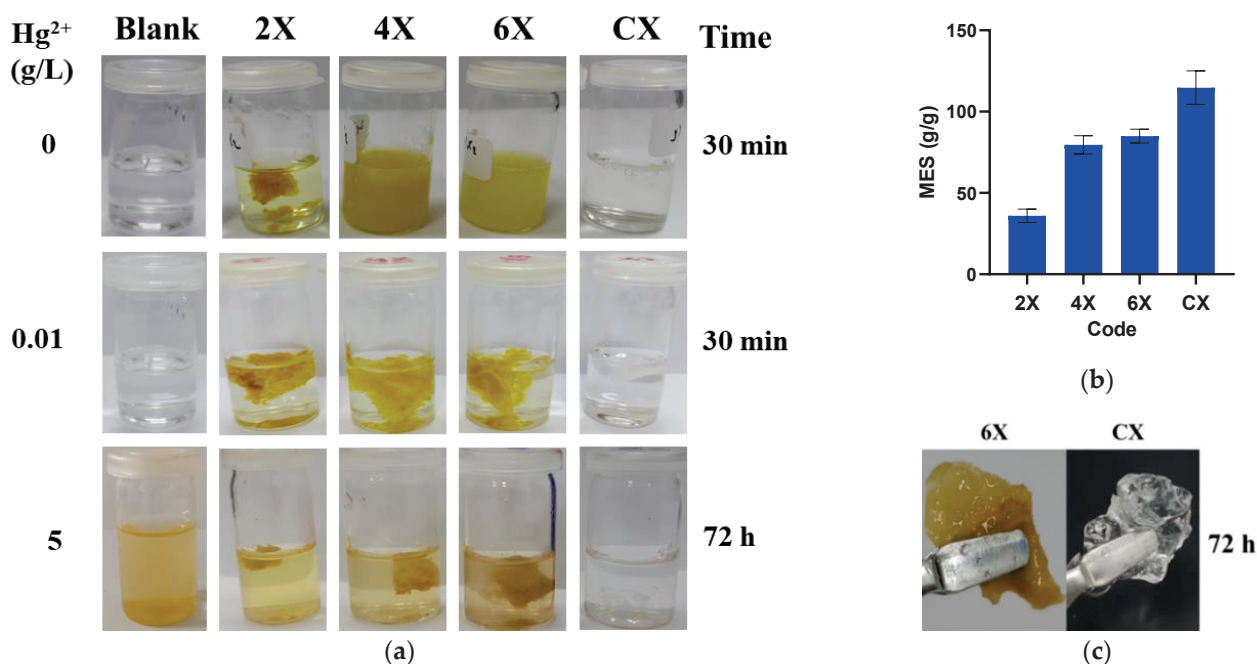
Figure 7. The xerogels' behaviour in aqueous solutions: (**a**) images of xerogels immersed in acetic acid solution (pH = 3.7), after 30 min; in mercury acetate solution (10 mg/L, pH = 6), after 30 min; and in mercury acetate solution (5 g/L, pH = 3.7), after 72 h. (**b**) The swelling degree of the samples in the solution of mercury ions. (**c**) Aspect of the xerogels after embedding mercury ions.

2.6. Mercury Recovery Ability

It is known that phenothiazine and chitosan have a good affinity for mercury, presenting good premises that their combination into a network will retain high amounts of this heavy metal [19,49–54]. Moreover, the investigation of the swelling behaviour of the xerogels suggested that the mercury ions produced the reinforcement of the chitosan-phenothiazine network, indicating their suitability for mercury recovery.

A mercury recovery experiment by immersing the xerogel samples into $Hg(CH_3COO)_2$ solutions revealed the deposition of a brown solid on the vials, attributed by X-ray diffraction to the formation of HgO by reaction of $Hg(CH_3COO)_2$ with water in acidic medium [55]. This hampered the quantitative analysis of the mercury retained in xerogels by analysis of the supernatant, and the quantitative analysis was realized by weighting. The experiment was realized using two solutions of different concentrations of 5 and 10 g/L, respectively (Figure 8a). It can be seen that the mercury recovery was dependent on the crosslinking degree of the xerogels and the solution's concentration. As expected, the samples were able to recover larger amounts of heavy metal from the solutions of a higher concentration, a fact easily explained by the higher density of mercury ions that reached to the sample. Regarding the influence of the crosslinking degree, it was remarked that the phenothiazine-chitosan samples had almost double the retention capacity than neat chitosan. Surprisingly, the retention capacity grew monotonously along with the decrease in the phenothiazine amount, with the highest amount of 0.9 g/g being recorded for the sample 6X. It can be envisaged that, along with the content of phenothiazine-imine units, the swelling ability of the xerogels strongly influenced the heavy metal absorption. Thus, the sample 6X appeared to meet an optimum balance between the phenothiazine-imine bonds and the morphology determined by the crosslinking degree. It is expected that a high density of imine bonds will lead to a high crosslinking degree and confer to the pores' walls high rigidity and, consequently, low swelling ability and low access of the mercury ions. On the contrary, a lower density of imine units led to a lower crosslinking degree and, consequently, to a loose morphology, favouring a higher swelling ability and easier access for mercury ions.
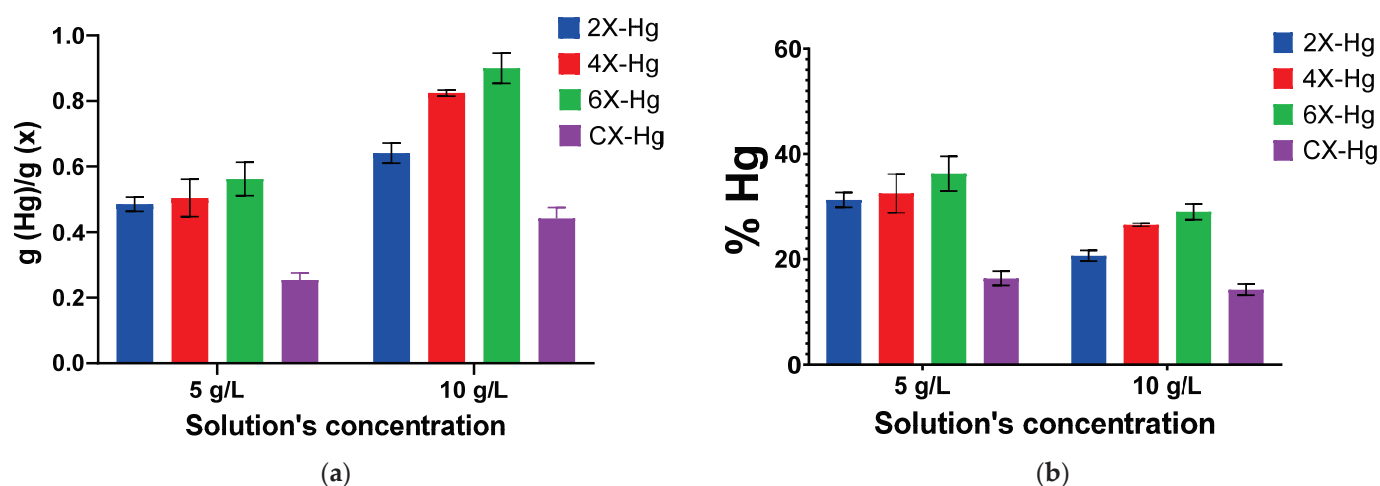
Figure 8. Graphical representation of the (**a**) amount of mercury retained into the xerogel samples and (**b**) removal percentage of mercury, as a function of the solution's concentration and crosslinking degree. The symbol Hg in samples' codes indicates the presence of mercury.

On the other hand, analysing the recovery percentage of mercury ions from solution (Figure 8b), it can be seen that the efficiency of mercury removal is growing in diluted solutions, suggesting that the xerogels are capable to recover this heavy metal even when it is in low concentrations.

To establish the performance of the studied xerogels compared with other chitosan-based materials, a comparative study was realized and the data are presented in Table 1. It can be seen that the studied xerogels have excellent performance, with their mercury retention capacity being higher than the majority of chitosan-based materials reported in the literature. It can be concluded that the TEGylated phenothiazine-imine-chitosan network is an excellent framework for the recovery of mercury ions and further morphology optimization can improve their retention capacity.

Table 1. Comparative analysis of the mercury adsorption capacity of the studied samples with other chitosan-based materials reported in the literature.

Adsorbent	Adsorption Degree (g/g)	Reference
6X	0.900	This study
Citralidene CS	0.333	[51]
Cross-linked CS-poly(aspartic acid) chelating resin	0.175	[52]
SeberCS-PAM-MCM	0.270	[54]
Magnetic polydopamine-CS nanoparticles	0.245	[56]
CS or CS-Ac nanoparticles	0.344	[53]
Poly(itaconic acid)-grafted CS nanoparticles	0.870	[57]
Phenothiazine-chitosan hydrogels	1.673	[19]
CS–PVA hydrogel	0.585	[58]
Chitosan-graft-Polyacrylamide Semi-IPN Hydrogels	2.001	[59]

SEM analysis revealed no clear mercury crystals, but did reveal small growths on the pores' walls, difficult to be attributed to a chemical state, while EDAX evidenced mercury on the samples' surface (Figure 9).
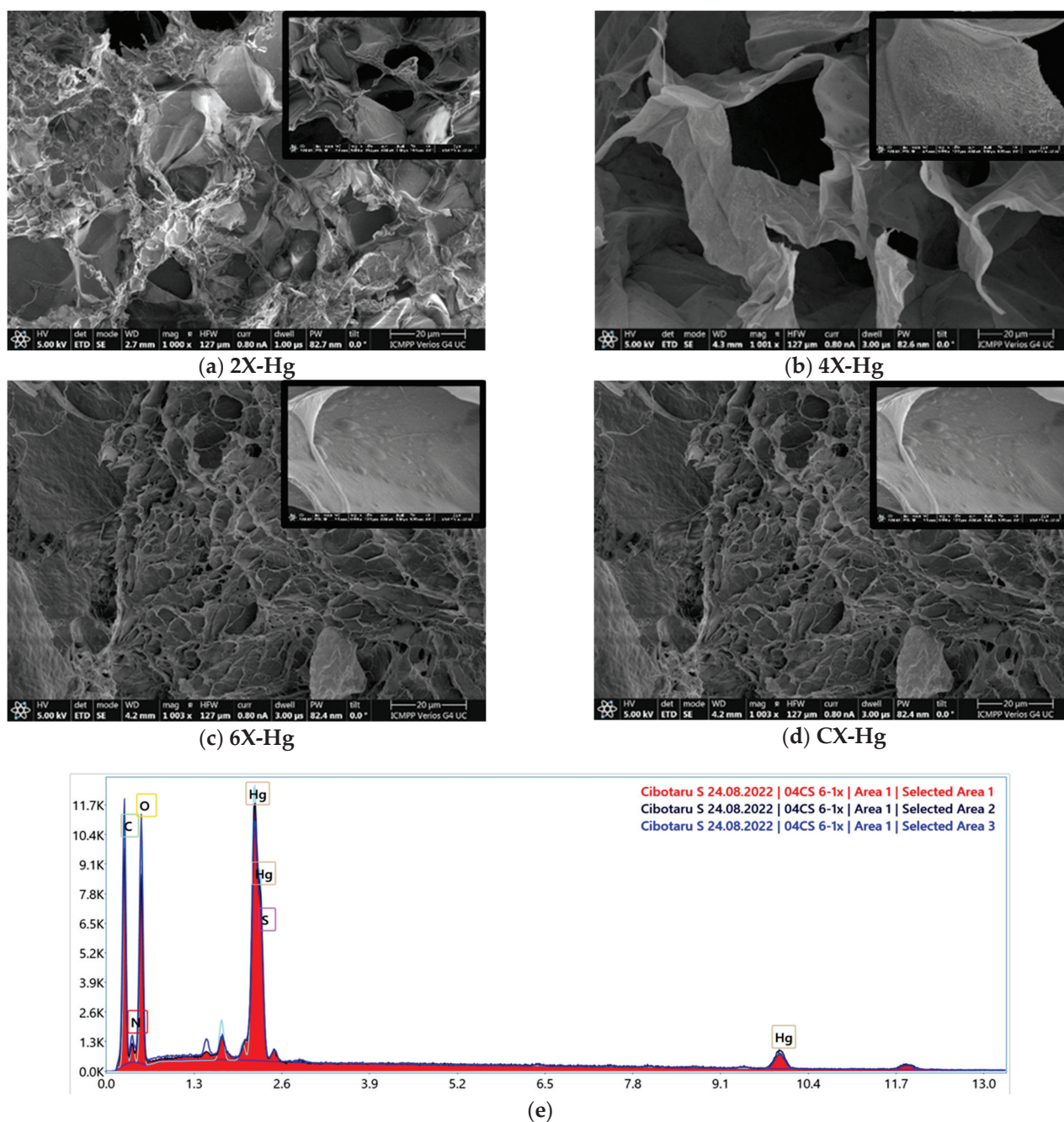
Figure 9. (**a**–**d**) SEM images of the xerogels at the end of the mercury recovery experiment and (**e**) SEM-EDAX spectrum of 6X-Hg.

The analysis of the X-ray diffractograms of the samples after mercury recovery compared with those of HgO and $Hg(CH_3COO)_2$ indicated the predominant absorption of the mercury ions through chemical bonds to the detriment of the deposition of HgO (Figure 10). The diffractograms displayed that the intense diffraction band around 9° in $Hg(CH_3COO)_2$ shifted to lower angles at 7.5° in xerogels, and the diffraction bands at a lower angle of the xerogels shifted from 3° to 6°. These indicated supramolecular rearrangements in the xerogels' architecture after interaction with mercury ions. On the other hand, the intense diffraction bands of HgO, especially those at 30° and 37°, are present as bands of low intensity and superposed with those from mercury salts. These modifications of the diffractograms suggest a chemical bonding of the mercury into xerogel, most probably realized by complexation.
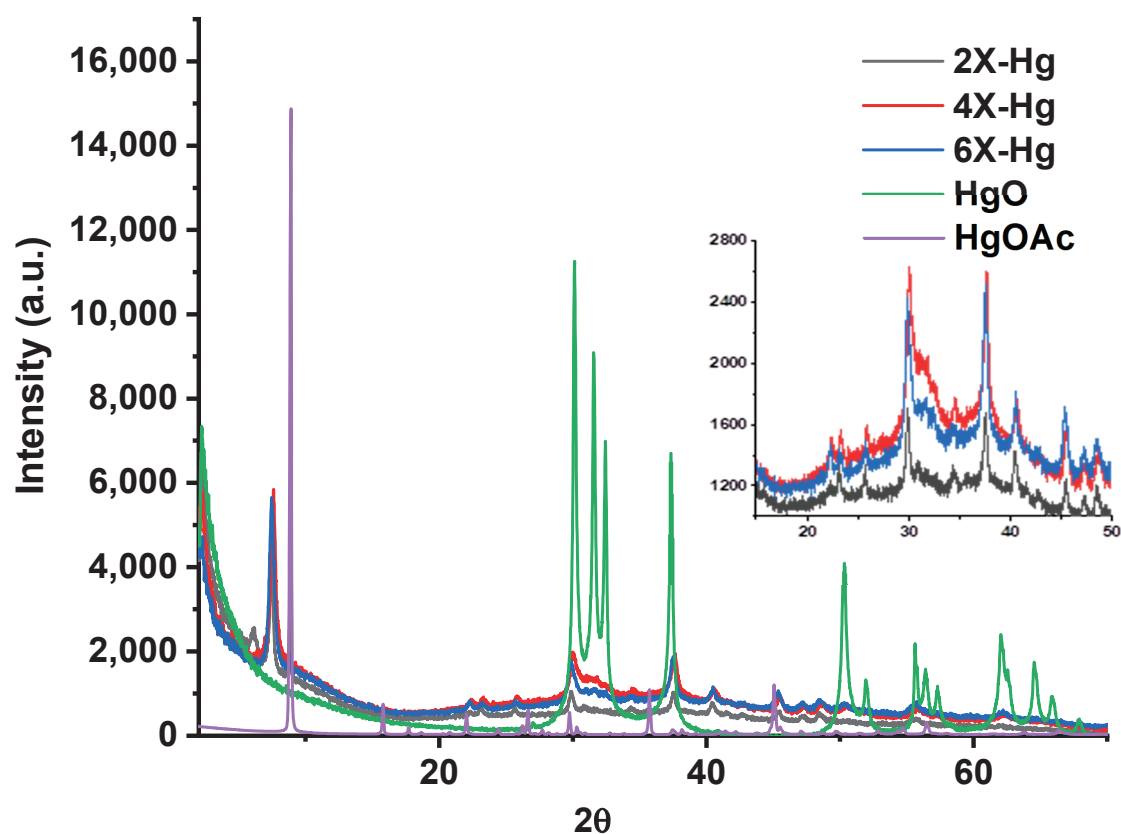
Figure 10. X-ray diffractograms of the xerogels at the end of the mercury recovery experiment compared with the diffractogram of HgO deposited on the vials (confirmed by similarity with diffraction card 2310656) and that of Hg(CH$_3$COO)$_2$.

To further attribute the nature of the mercury bonding to xerogels, FTIR spectra were recorded before and after mercury retention (Figure 11). The FTIR spectra after mercury recovery showed obvious modifications, in terms of position and intensity of the bands. The most evident was the almost total disappearance of the vibration band of the imine bond at 1640 cm^{-1} and the appearance of a new band as a shoulder at 1596 cm^{-1}, suggesting that imine units coordinated the mercury ions [19,60]. Moreover, the vibration band characteristic of the amine units was also shifted to lower wavelengths, indicating they coordinated mercury too [61,62]. Another significant modification of the spectrum was the intensification of the stretching vibration band of C-S-C from the phenothiazine heterocycle at 1324 cm^{-1} [63] and the appearance of two vibration bands at 668 cm^{-1} and 684 cm^{-1}, characteristic of the coordinative bonds of sulfur with mercury [64]. All of these factors indicate that the mercury was predominantly retained in the xerogels by coordination bonds with sulfur of phenothiazine and imine bonds, as well as with amine groups of chitosan.
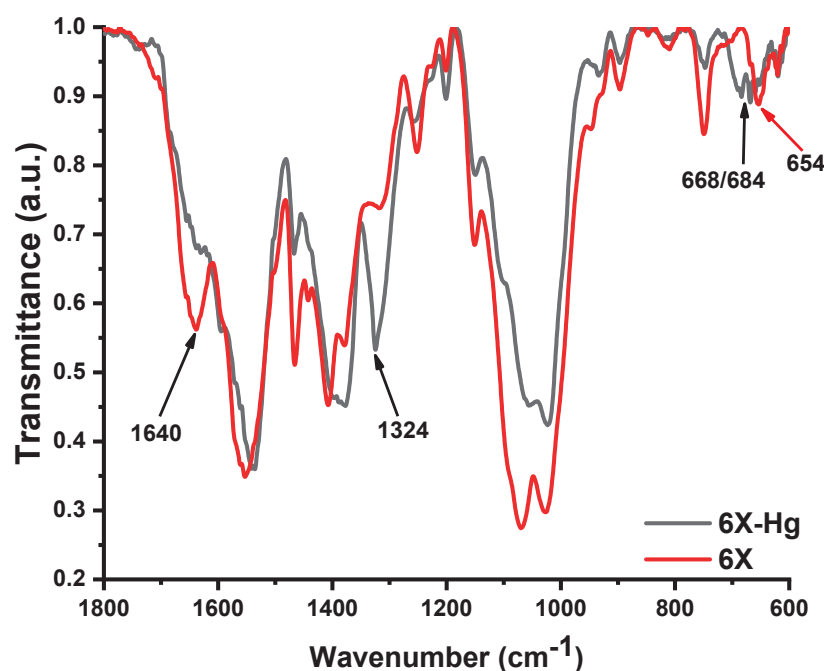
Figure 11. FTIR spectra of the xerogel 6X before (6X) and after mercury recovery (6X-Hg).

3. Conclusions

The paper reports the synthesis of new porous materials in the form of xerogels from chitosan and phenothiazine, as an excellent framework for mercury recovery. The materials were prepared by chitosan hydrogelation with a formyl derivative of TEGylated phenothiazine, in different molar ratios of the amine/aldehyde functional groups, followed by lyophilization. Structural and supramolecular characterization by ^{1}H-NMR, FTIR, X-ray diffraction, and polarized light microscopy demonstrated that the hydrogelation was the result of the formation of phenothiazine-imine units on chitosan backbones and their self-ordering into hydrophobic arrays, creating physico-chemical bridges between the chitosan chains. The lyophilized hydrogels behave as sponge-like materials in water and are rehydrated in acidic medium. They strongly absorbed UV light and slightly emitted green/yellowish light. In contact with mercury ions, they were able to absorb high amounts of this heavy metal, up to 0.9 g/g, by coordination with imine, phenothiazine, and amine units. All of these factors suggest the chitosan-imine-phenothiazine framework as an excellent platform to create materials for mercury recovery from wastewater.

4. Experimental

4.1. Materials

Phenothiazine 98%, sodium hydride 95%, triethylene glycol monomethyl ether 97%, phosphorus (V) oxychloride 99%, magnesium sulfate ($MgSO_4$) 99.5 %, and low molecular weight chitosan were purchased from Sigma-Aldrich, Darmstadt, Germany. The molecular mass of chitosan (198 kDa) was calculated by measuring the viscosity with an Ubbelohde type viscometer based on the Mark–Houwink equation, and the degree of acetylation (DA = 18%) was determined from ^{1}H-NMR. Dichloroethane (DCE) 99%, dichloromethane (DCM) 99.5 %, and acetone were purchased from ROTH, Karlsruhe, Germany. Mercury (II) acetate and acetic acid were purchased from VWR, Radnor, PA, U.S.A. All reagents and solvents were used as received.

4.2. Biomaterials' Preparation

The synthesis of the aldehyde (**PTF**) used for chitosan's crosslinking was carried out using the protocol described in our previous work [35]. Its structure was confirmed by ^{1}H-NMR and FTIR spectra, as follows.

PTF

^{1}H-NMR (400 MHz, DMSO-d$_6$, ppm): δ = 9.80 (s, 1H, H11), 7.72 (dd, 1H, 3J = 8 Hz, 4J = 2 Hz, H2), 7.60 (d, 1H, 4J = 2 Hz, H4), 7.22 (td, 1H, 3J = 8 Hz, 4J = 2 Hz, H8), 7.21 (d, 1H, J = 8 Hz, H1), 7.16 (dd, 1H, 3J = 8 Hz, 4J = 1 Hz, H6), 7.12 (d, 1H, 3J = 8 Hz, H9), 7.01 (t, 1H, 3J = 8 Hz, H7), 4.13 (t, 2H, J = 8 Hz, H12), 3.77 (t, 2H, J = 8 Hz, H13), 3.50–3.46 (m, 6H, H14, 15), 3.39–3.36 (m, 2H, H15), 3.20 (s, 3H, H16); FT-IR (KBr, cm^{-1}): 2875 (νC-H$_{aliphatic}$), 1679 (νC=O), 1593, 1570, 1460 (νC=C), 1292 (νC-N), 1105 (νC-O-C), 751 (δC-H).

The as-obtained aldehyde (PTF) was reacted with chitosan in order to obtain hydrogels, as follows. In three different vials, 60 mg of chitosan (0.29 mmol glucosamine units) was dissolved in 2 mL aqueous solution of acetic acid (0.7 %) to obtain 3% chitosan solutions. In another three different vials, 54 mg (0.145 mmol), 27 mg (0.07 mmol), and 18 mg (0.048 mmol) of PTF were dissolved in 2.6 mL acetone to obtain three different solutions. All of the prepared solutions were heated up to 57 °C and maintained at this temperature for 15 min under magnetic stirring. After that, the aldehyde solutions were slowly dropped over those of chitosan, and then the obtained mixtures were stirred with a vortex until the transparent yellow gel was formed. The formed gels were kept on a water bath at 50 °C for 3 h in order to favour the condensation reaction of aldehyde with amine groups. Following the same protocol, a chitosan-based hydrogel without aldehyde was obtained, to be used as a positive control. The quantities of reagents used for hydrogels' obtaining and the ratio between chitosan and aldehyde are given in Table 2. By lyophilization of the hydrogels at −85 °C and 1.51 mBar, the corresponding xerogels were obtained.

Table 2. The receipt for obtaining the hydrogels and corresponding xerogels, as well as their codes.

Samples' Codes	m_{CS} (mg)	V_{water} (mL)	$V_{acetic\ acid}$ (mL)	m_{PTF} (mg)	$V_{acetone}$ (mL)	Molar Ratio NH$_2$/CHO	Gellation Time (min)
2H/2X			0.014	54		2/1	<5
4H/2X			0.014	27	2.6	4/1	<5
6H/2X	60	2	0.014	18		6/1	<5
CH/CX			0.014	-		-	-

4.3. Equipment and Methods

Infrared spectra were recorded on a FTIR Bruker Vertex 70 Spectrometer (Billerica, MA, USA), in the transmission mode, using KBr pellets, at room temperature, with a resolution of 2 cm^{-1} and an accumulation of 32 scans. The spectra were processed using Origin8 software.

NMR analysis was performed on a 400 MHz Bruker Avance Neo Spectrometer (Billerica, MA, USA) equipped with a 5 mm four-nuclei direct detection z-gradient probe.

UV/Vis absorption and photoluminescence spectra were recorded on an Agilent Cary 60 UV/Vis (Santa Clara, CA, USA) and a PerkinElmer LS 55 spectrophotometer on solid samples. In order to record an absorption spectrum in the detection limit of the equipment, a solid film was prepared by casting on a quartz lamella, a small amount of hydrogel, prepared from chitosan and aldehyde (60/1 NH$_2$/CHO).

SEM images were acquired with a scanning electron microscope (SEM) EDAX—Quanta 200 (Waltham, MA, USA), at a lower accelerated electron energy of 20 Kev.

The supramolecular structure of the hydrogel was investigated with a Benchtop Miniflex 600 Rigaku diffractometer (Tokyo, Japan), from 2 to 90°, registered with a step of 0.01 and speed of 3°/min, on the xerogel pellets, and with a polarized optical microscope (Zeiss Axio Imager.A2m, camera Axiocam 208 cc (Wetzlar, Germany)) on thin xerogel slices.

The gravimetric measurements were performed using a KERN analytical balance with five decimals.

The layered architecture of the obtained hydrogels was simulated using HyperChem Professional 8.0 software.

The swelling degree and the hydrolytic stability of the obtained xerogels were investigated in aqueous media of different pH, in the presence or absence of mercury ions. Thus, samples weighing 2 mg were immersed in vials containing 1 mL of water, 5 g/L mercury acetate solution, and 0.0125% acetic acid solution. Both solutions of acetic acid and mercury acetate had the same pH = 3.7. The swelling process was monitored for 24 h by gravimetric measurements. The hydrolytic stability was visually monitored. The experiment was performed in triplicate and the results were presented as average values.

The mercury recovery ability was investigated for xerogels, in solutions of mercury acetate 5 g/L and 10 g/L. Here, 8 mg of xerogel samples was immersed in 5 mL of freshly prepared mercury acetate solution. After 24 h, the recovered xerogels were lyophilized and immediately weighed, and the mass of the recovered mercury was calculated by the difference between the final mass of xerogels and their initial mass. During the absorption process, a brown deposit was observed on the walls of the vials. The vials were dried on a heat plate and weighed again to measure the quantity of the obtained precipitate. The amount of recovered mercury was complementary calculated as the difference between the initial mass of mercury in the solution and the final mass of mercury precipitated. The removal percentage of mercury was calculated as the percent of recovered mercury for the initial mass of mercury in solution. The experiment was performed in triplicate. After gravimetric measurements, mercury-loaded xerogels were pressed using a 10-ton manual press to obtain pallets for wide-angle X-ray diffraction.

Complementary to the gravimetric method, the degree of mercury loading was also calculated from the data obtained by SEM-EDAX analysis. The analysis was performed on all loaded samples, investigating at least six areas of the xerogels, to calculate the average amount of detected mercury. The data were provided as the atomic to mass ratio of the mercury atom to the rest of the atoms in the chemical composition of the xerogel. The amount of mercury absorbed was calculated in g (Hg)/g (xerogel) based on both ratios (atomic and mass) and was shown in representative graphs.

References

1. Wu, D.; Sedgwick, A.C.; Gunnlaugsson, T.; Akkaya, E.U.; Yoon, J.; James, T.D. Fluorescent Chemosensors: The Past, Present and Future. *Chem. Soc. Rev.* **2017**, *46*, 7105–7123. [CrossRef]
2. Balali-Mood, M.; Naseri, K.; Tahergorabi, Z.; Khazdair, M.R.; Sadeghi, M. Toxic Mechanisms of Five Heavy Metals: Mercury, Lead, Chromium, Cadmium, and Arsenic. *Front. Pharmacol.* **2021**, *12*, 643972. [CrossRef]

3. Tchounwou, P.B.; Yedjou, C.G.; Patlolla, A.K.; Sutton, D.J. Heavy Metal Toxicity and the Environment. *Exp. Suppl.* **2012**, *101*, 133–164. [CrossRef]

4. Bansod, B.; Kumar, T.; Thakur, R.; Rana, S.; Singh, I. A Review on Various Electrochemical Techniques for Heavy Metal Ions Detection with Different Sensing Platforms. *Biosens. Bioelectron.* **2017**, *94*, 443–455. [CrossRef]

5. Kinuthia, G.K.; Ngure, V.; Beti, D.; Lugalia, R.; Wangila, A.; Kamau, L. Levels of Heavy Metals in Wastewater and Soil Samples from Open Drainage Channels in Nairobi, Kenya: Community Health Implication. *Sci. Rep.* **2020**, *10*, 8434. [CrossRef]

6. New Limits for Heavy Metals in Food Supplements. Available online: https://www.gmp-compliance.org/gmp-news/new-limits-for-heavy-metals-in-food-supplements (accessed on 26 September 2022).

7. Bodnar, D.; Burlibasa, L.; Varlan, C.; Marcov, N.; Georgescu, S.; Marcov, C. Mercury, Biocompatibility and Its Impact on Environment. *Metal Int.* **2009**, *14*, 95–100.

8. Dórea, J.G. Integrating Experimental (In Vitro and In Vivo) Neurotoxicity Studies of Low-Dose Thimerosal Relevant to Vaccines. *Neurochem. Res.* **2011**, *36*, 927–938. [CrossRef] [PubMed]

9. Aragay, G.; Pons, J.; Merkoçi, A. Recent Trends in Macro-, Micro-, and Nanomaterial-Based Tools and Strategies for Heavy-Metal Detection. *Chem. Rev.* **2011**, *111*, 3433–3458. [CrossRef]

10. Fouda, S.R.; El-Sayed, I.E.; Attia, N.F.; Abdeen, M.M.; Abdel Aleem, A.A.H.; Nassar, I.F.; Mira, H.I.; Gawad, E.A.; Kalam, A.; Al-Ghamdi, A.A.; et al. Mechanistic Study of Hg(II) Interaction with Three Different α-Aminophosphonate Adsorbents: Insights from Batch Experiments and Theoretical Calculations. *Chemosphere* **2022**, *304*, 135253. [CrossRef]

11. Mahmoud, M.E.; Abdelwahab, S.M.; Ibrahim, G.A.A. The Design of SnO2-Crosslinked-Chitosan Nanocomposite for Microwave-Assisted Adsorption of Aqueous Cadmium and Mercury Ions. *Sustain. Chem. Pharm.* **2022**, *28*, 100731. [CrossRef]

12. Zhang, L.; Jiao, X.; Zhang, H.; He, S.; Cheng, X. Novel Chitosan–Naphthalimide–Amino Acid Fluorescent Powder for Selective Detection and Removal of Hg2+/Hg+ and Fe2+ in Aqueous Solution. *Chem. Pap.* **2022**, *76*, 7037–7049. [CrossRef]

13. Lin, H.; Duan, Y.; Zhao, B.; Feng, Q.; Li, M.; Wei, J.; Zhu, Y.; Li, M. Efficient Hg(II) Removal to Ppb Level from Water in Wider PH Based on Poly-Cyanoguanidine/Graphene Oxide: Preparation, Behaviors, and Mechanisms. *Colloids Surf. Physicochem. Eng. Asp.* **2022**, *641*, 128467. [CrossRef]

14. Saenchoopa, A.; Klangphukhiew, S.; Somsub, R.; Talodthaisong, C.; Patramanon, R.; Daduang, J.; Daduang, S.; Kulchat, S. A Disposable Electrochemical Biosensor Based on Screen-Printed Carbon Electrodes Modified with Silver Nanowires/HPMC/Chitosan/Urease for the Detection of Mercury (II) in Water. *Biosensors* **2021**, *11*, 351. [CrossRef] [PubMed]

15. Michailidou, G.; Koumentakou, I.; Liakos, E.V.; Lazaridou, M.; Lambropoulou, D.A.; Bikiaris, D.N.; Kyzas, G.Z. Adsorption of Uranium, Mercury, and Rare Earth Elements from Aqueous Solutions onto Magnetic Chitosan Adsorbents: A Review. *Polymers* **2021**, *13*, 3137. [CrossRef] [PubMed]

16. Seidi, F.; Reza Saeb, M.; Huang, Y.; Akbari, A.; Xiao, H. Thiomers of Chitosan and Cellulose: Effective Biosorbents for Detection, Removal and Recovery of Metal Ions from Aqueous Medium. *Chem. Rec.* **2021**, *21*, 1876–1896. [CrossRef] [PubMed]

17. Yang, C.; Jiang, J.; Wu, Y.; Fu, Y.; Sun, Y.; Chen, F.; Yan, G.; Hu, J. High Removal Rate and Selectivity of Hg(II) Ions Using the Magnetic Composite Adsorbent Based on Starch/Polyethyleneimine. *J. Mol. Liq.* **2021**, *337*, 116418. [CrossRef]

18. Liakos, E.V.; Mone, M.; Lambropoulou, D.A.; Bikiaris, D.N.; Kyzas, G.Z. Adsorption Evaluation for the Removal of Nickel, Mercury, and Barium Ions from Single-Component and Mixtures of Aqueous Solutions by Using an Optimized Biobased Chitosan Derivative. *Polymers* **2021**, *13*, 232. [CrossRef] [PubMed]

19. Bejan, A.; Doroftei, F.; Cheng, X.; Marin, L. Phenothiazine-Chitosan Based Eco-Adsorbents: A Special Design for Mercury Removal and Fast Naked Eye Detection. *Int. J. Biol. Macromol.* **2020**, *162*, 1839–1848. [CrossRef] [PubMed]

20. Bessa, A.; Gonçalves, G.; Henriques, B.; Domingues, E.M.; Pereira, E.; Marques, P.A.A.P. Green Graphene–Chitosan Sorbent Materials for Mercury Water Remediation. *Nanomaterials* **2020**, *10*, 1474. [CrossRef]

21. Fauzi, N.I.M.; Fen, Y.W.; Omar, N.A.S.; Saleviter, S.; Daniyal, W.M.E.M.M.; Hashim, H.S.; Nasrullah, M. Nanostructured Chitosan/Maghemite Composites Thin Film for Potential Optical Detection of Mercury Ion by Surface Plasmon Resonance Investigation. *Polymers* **2020**, *12*, 1497. [CrossRef] [PubMed]

22. Dinu, M.V.; Humelnicu, I.; Ghiorghita, C.A.; Humelnicu, D. Aminopolycarboxylic Acids-Functionalized Chitosan-Based Composite Cryogels as Valuable Heavy Metal Ions Sorbents: Fixed-Bed Column Studies and Theoretical Analysis. *Gels* **2022**, *8*, 221. [CrossRef] [PubMed]

23. Dragan, E.S.; Dinu, M.V. Advances in Porous Chitosan-Based Composite Hydrogels: Synthesis and Applications. *React. Funct. Polym.* **2020**, *146*, 104372. [CrossRef]

24. Spiridon, I.; Anghel, N.; Dinu, M.V.; Vlad, S.; Bele, A.; Ciubotaru, B.I.; Verestiuc, L.; Pamfil, D. Development and Performance of Bioactive Compounds-Loaded Cellulose/Collagen/Polyurethane Materials. *Polymers* **2020**, *12*, 1191. [CrossRef] [PubMed]

25. Dinu, M.V.; Humelnicu, D.; Lazar, M.M. Analysis of Copper(II), Cobalt(II) and Iron(III) Sorption in Binary and Ternary Systems by Chitosan-Based Composite Sponges Obtained by Ice-Segregation Approach. *Gels* **2021**, *7*, 103. [CrossRef] [PubMed]

26. Humelnicu, D.; Dragan, E.S.; Ignat, M.; Dinu, M.V. A Comparative Study on Cu2+, Zn2+, Ni2+, Fe3+, and Cr3+ Metal Ions Removal from Industrial Wastewaters by Chitosan-Based Composite Cryogels. *Molecules* **2020**, *25*, 2664. [CrossRef] [PubMed]

27. Wang, X.; Shi, J.; Zhuang, J.; Chen, C.; Ouyang, K.; Xu, M.; Xu, Z. Characterization and Evaluation of the Adsorption Potential of Chitosan-Impregnated Cellulose Nanofiber Multi-Walled Carbon Nanotube Aerogel for Copper Ions. *New J. Chem.* **2022**, *46*, 3156–3167. [CrossRef]

28. Pinelli, F.; Nespoli, T.; Rossi, F. Graphene Oxide-Chitosan Aerogels: Synthesis, Characterization, and Use as Adsorbent Material for Water Contaminants. *Gels* **2021**, *7*, 149. [CrossRef]

29. van Hoa, N.; Minh, N.C.; Cuong, H.N.; Dat, P.A.; Nam, P.V.; Viet, P.H.T.; Phuong, P.T.D.; Trung, T.S. Highly Porous Hydroxyapatite/Graphene Oxide/Chitosan Beads as an Efficient Adsorbent for Dyes and Heavy Metal Ions Removal. *Molecules* **2021**, *26*, 6127. [CrossRef]

30. Emamy, F.H.; Bumajdad, A.; Lukaszewicz, J.P. Adsorption of Hexavalent Chromium and Divalent Lead Ions on the Nitrogen-Enriched Chitosan-Based Activated Carbon. *Nanomaterials* **2021**, *11*, 1907. [CrossRef]

31. Shan, W.; Zhang, D.; Wang, X.; Wang, D.; Xing, Z.; Xiong, Y.; Fan, Y.; Yang, Y. One-Pot Synthesis of Mesoporous Chitosan-Silica Composite from Sodium Silicate for Application in Rhenium(VII) Adsorption. *Microporous Mesoporous Mater.* **2019**, *278*, 44–53. [CrossRef]

32. Sun, W.; Sun, Q.; Zhao, Q.; Marin, L.; Cheng, X. Fluorescent Porous Silica Microspheres for Highly and Selectively Detecting Hg^{2+} and Pb^{2+} Ions and Imaging in Living Cells. *ACS Omega* **2019**, *4*, 18381–18391. [CrossRef] [PubMed]

33. Xiong, S.; Duan, L.; Cheng, X. A Novel Coumarin-Chitosan Fluorescent Hydrogel for the Selective Identification of Fe^{2+} in Aqueous Systems. *Polym. Chem.* **2020**, *11*, 6066–6072. [CrossRef]

34. Wang, D.; Marin, L.; Cheng, X. Fluorescent Chitosan-BODIPY Macromolecular Chemosensors for Detection and Removal of Hg2+ and Fe3+ Ions. *Int. J. Biol. Macromol.* **2022**, *198*, 194–203. [CrossRef] [PubMed]

35. Cibotaru, S.; Nicolescu, A.; Marin, L. Dynamic PEGylated Phenothiazine Imines; Synthesis, Photophysical Behavior and Reversible Luminescence Switching in Response to External Stimuli. *J. Photochem. Photobiol. Chem.* **2022**, *435*, 114282. [CrossRef]

36. Iftime, M.-M.; Morariu, S.; Marin, L. Salicyl-Imine-Chitosan Hydrogels: Supramolecular Architecturing as a Crosslinking Method toward Multifunctional Hydrogels. *Carbohydr. Polym.* **2017**, *165*, 39–50. [CrossRef]

37. Lungu, R.; Paun, M.-A.; Peptanariu, D.; Ailincai, D.; Marin, L.; Nichita, M.-V.; Paun, V.-A.; Paun, V.-P. Biocompatible Chitosan-Based Hydrogels for Bioabsorbable Wound Dressings. *Gels* **2022**, *8*, 107. [CrossRef]

38. Olaru, A.-M.; Marin, L.; Morariu, S.; Pricope, G.; Pinteala, M.; Tartau-Mititelu, L. Biocompatible Chitosan Based Hydrogels for Potential Application in Local Tumour Therapy. *Carbohydr. Polym.* **2018**, *179*, 59–70. [CrossRef]

39. Zabulica, A.; Balan, M.; Belei, D.; Sava, M.; Simionescu, B.C.; Marin, L. Novel Luminescent Phenothiazine-Based Schiff Bases with Tuned Morphology. Synthesis, Structure, Photophysical and Thermotropic Characterization. *Dye. Pigment.* **2013**, *96*, 686–698. [CrossRef]

40. Bejan, A.; Ailincai, D.; Simionescu, B.C.; Marin, L. Chitosan Hydrogelation with a Phenothiazine Based Aldehyde: A Synthetic Approach toward Highly Luminescent Biomaterials. *Polym. Chem.* **2018**, *9*, 2359–2369. [CrossRef]

41. Anisiei, A.; Rosca, I.; Sandu, A.-I.; Bele, A.; Cheng, X.; Marin, L. Imination of Microporous Chitosan Fibers—A Route to Biomaterials with "On Demand" Antimicrobial Activity and Biodegradation for Wound Dressings. *Pharmaceutics* **2022**, *14*, 117. [CrossRef]

42. Gartner, C.; López, B.L.; Sierra, L.; Graf, R.; Spiess, H.W.; Gaborieau, M. Interplay between Structure and Dynamics in Chitosan Films Investigated with Solid-State NMR, Dynamic Mechanical Analysis, and X-Ray Diffraction. *Biomacromolecules* **2011**, *12*, 1380–1386. [CrossRef] [PubMed]

43. Kempaiah, R.; Gurappa, G.; Tomar, R.; Poletto, M.; Jun-ior, H.L.O.; Annadurai, V.; Somashekar, R. FTIR and WAXS Studies on Six Vegetal Fibers. *Cellul. Chem. Technol.* **2020**, *54*, 187–197. [CrossRef]

44. Okazaki, M.; Takeda, Y.; Data, P.; Pander, P.; Higginbotham, H.; Monkman, A.P.; Minakata, S. Thermally Activated Delayed Fluorescent Phenothiazine–Dibenzo[a,j]Phenazine–Phenothiazine Triads Exhibiting Tricolor-Changing Mechanochromic Luminescence. *Chem. Sci.* **2017**, *8*, 2677–2686. [CrossRef] [PubMed]

45. Cibotaru, S.; Sandu, A.-I.; Belei, D.; Marin, L. Water Soluble PEGylated Phenothiazines as Valuable Building Blocks for Bio-Materials. *Mater. Sci. Eng. C* **2020**, *116*, 111216. [CrossRef] [PubMed]

46. Bejan, A.; Shova, S.; Damaceanu, M.-D.; Simionescu, B.C.; Marin, L. Structure-Directed Functional Properties of Phenothiazine Brominated Dyes: Morphology and Photophysical and Electrochemical Properties. *Cryst. Growth Des.* **2016**, *16*, 3716–3730. [CrossRef]

47. Godoy-Alcántar, C.; Yatsimirsky, A.K.; Lehn, J.-M. Structure-Stability Correlations for Imine Formation in Aqueous Solution. *J. Phys. Org. Chem.* **2005**, *18*, 979–985. [CrossRef]

48. Lone, S.; Yoon, D.H.; Lee, H.; Cheong, I.W. Gelatin–Chitosan Hydrogel Particles for Efficient Removal of Hg from Wastewater. *Environ. Sci.* **2019**, *5*, 83–90. [CrossRef]

49. Wang, H.; Qiu, N.; Kong, X.; Hu, Z.; Zhong, F.; Tan, H. Phenothiazine-Based Porous Organic Polymers with High Sensitivity and Selective Fluorescence Response to Mercury Ions. *J. Solid State Chem.* **2022**, *315*, 123522. [CrossRef]

50. Vengaian, K.M.; Britto, C.D.; Sivaraman, G.; Sekar, K.; Singaravadivel, S. Phenothiazine Based Sensor for Naked-Eye Detection and Bioimaging of Hg and F. *RSC Adv.* **2015**, *5*, 94903–94908. [CrossRef]

51. Alikutty, P.; Abdul Mujeeb, V.M.; Zubair, M.A.; Muraleedharan, K.; Mujeeb Rahman, P. Studies on the Sorption Capacity for Pb(II) and Hg(II) of Citralidene Chitosan. *Polym. Bull.* **2014**, *71*, 1919–1932. [CrossRef]

52. Chen, X.J.; Cai, J.C.; Zhang, Z.H.; Liu, L.J.; Yang, G.L. Investigation of Removal of Pb(II) and Hg(II) by a Novel Cross-Linked Chitosan-Poly(Aspartic Acid) Chelating Resin Containing Disulfide Bond. *Colloid. Polym. Sci.* **2014**, *292*, 2157–2172. [CrossRef]

53. Mahmoud, M.E.; Abou Kana, M.T.H.; Hendy, A.A. Synthesis and Implementation of Nano-Chitosan and Its Acetophenone Derivative for Enhanced Removal of Metals. *Int. J. Biol. Macromol.* **2015**, *81*, 672–680. [CrossRef] [PubMed]

54. Li, K.; Wang, Y.; Huang, M.; Yan, H.; Yang, H.; Xiao, S.; Li, A. Preparation of Chitosan- Graft -Polyacrylamide Magnetic Composite Microspheres for Enhanced Selective Removal of Mercury Ions from Water. *J. Colloid. Interface Sci.* **2015**, *455*, 261–270. [CrossRef] [PubMed]

55. King, R.B. *Encyclopedia of Inorganic Chemistry*; King, R.B., Crabtree, R.H., Lukehart, C.M., Atwood, D.A., Scott, R.A., Eds.; John Wiley & Sons, Ltd.: Chichester, UK, 2006; Volume 10, ISBN 0470860782.

56. Wang, Y.; Zhang, Y.; Hou, C.; Liu, M. Mussel-Inspired Synthesis of Magnetic Polydopamine–Chitosan Nanoparticles as Biosorbent for Dyes and Metals Removal. *J. Taiwan Inst. Chem. Eng.* **2016**, *61*, 292–298. [CrossRef]

57. Ge, H.; Hua, T.; Wang, J. Preparation and Characterization of Poly (Itaconic Acid)-Grafted Crosslinked Chitosan Nanoadsorbent for High Uptake of Hg2+ and Pb2+. *Int. J. Biol. Macromol.* **2017**, *95*, 954–961. [CrossRef] [PubMed]

58. Wang, X.; Deng, W.; Xie, Y.; Wang, C. Selective Removal of Mercury Ions Using a Chitosan–Poly(Vinyl Alcohol) Hydrogel Adsorbent with Three-Dimensional Network Structure. *Chem. Eng. J.* **2013**, *228*, 232–242. [CrossRef]

59. Saber-Samandari, S.; Gazi, M. Removal of Mercury (II) from Aqueous Solution Using Chitosan- Graft -Polyacrylamide Semi-IPN Hydrogels. *Sep. Sci. Technol.* **2013**, *48*, 1382–1390. [CrossRef]

60. Ferraz de Paiva, R.E.; Nakahata, D.H.; de Carvalho, M.A.; Rodrigues Goulart Bergamini, F.; Corbi, P.P. *N*, *N′*, *N″ versus N*, *N′*, *O* Imine-Containing Coordination Motifs: Ligand-Directed Synthesis of Mononuclear and Binuclear Cu II Compounds. *Acta Crystallogr. E Crystallogr. Commun.* **2017**, *73*, 1563–1567. [CrossRef]

61. Sultan, J.S.; Lateaf, S.M.; Rashid, D.K. Synthesis, Characterization and Antibacterial Activity of Mixed Ligand (HL) Complexes Mn(Ll), Co(Ll), Ni(Ll), Zn(Ll), Cd(Ll) and Hg(Ll) with Azide. *Open J. Inorg. Chem.* **2015**, *5*, 102–111. [CrossRef]

62. Nawar, N.; Hosny, N.M. Transition Metal Complexes of 2-Acetylpyridine o-Hydroxybenzoylhydrazone(APo-OHBH): Their Preparation, Characterisation and Antimicrobial Activity. *Chem. Pharm. Bull.* **1999**, *47*, 944–949. [CrossRef]

63. Parmar, S.; Kumar, Y.; Mittal, A. Synthesis, Spectroscopic and Pharmacological Studies of Bivalent Copper, Zinc and Mercury Complexes of Thiourea. *S. Afr. J. Chem.* **2010**, *63*, 123–129.

64. Debbeti, V.; Ahmad, T.J.; Ananda, S.; Made Gowda, N.M. Transition Metal Complexes of Ethopropazine: Synthesis and Characterization. *Am. J. Chem.* **2013**, *2*, 294–298. [CrossRef]

Magnetic Application of Gadolinium Orthoferrite Nanoparticles Synthesized by Sol–Gel Auto-Combustion Method

Loganathan Guganathan [1,2,†], Chinnaiyan Rajeevgandhi [3,*,†], Kaliyamurthy Sathiyamurthy [3], Kokila Thirupathi [4], Madhappan Santhamoorthy [5], Ellappan Chinnasamy [2], Chaitany Jayprakash Raorane [5,†], Vinit Raj [5], Seong-Cheol Kim [5,*] and Pichapillai Anand [3]

1   Department of Physics, Annmalai University, Annamalainagar, Chidambaram 608002, Tamilnadu, India
2   Freelance Researcher, Chidambaram 608001, Tamilnadu, India
3   Department of Physics, Sri Indu College of Engineering & Technology, Ibrahimpatan 501510, Telangana, India
4   Department of Physics, Sri Moogambigai College of Arts and Science for Women, Palacode 636808, Tamilnadu, India
5   School of Chemical Engineering, Yeungnam University, Gyeongsan 38544, Korea
*   Correspondence: rajeevphdphy@gmail.com (C.R.); sckim07@ynu.ac.kr (S.-C.K.); Tel.: +91-96-0091-5458 (C.R.)
†   These authors contributed equally to this work.

Abstract: In this manuscript, we present the synthesis of gadolinium orthoferrite nanoparticles using the sol–gel auto-combustion technique. The obtained gadolinium orthoferrite nanoparticles were annealed at various temperatures, such as 800 °C, 900 °C, 1000 °C, and 1100 °C. The synthesized materials were analyzed by various instrumental characterizations. The vibrational characteristics of the synthesized samples were verified by FTIR. The surface morphology of the gadolinium orthoferrite nanoparticles was analyzed by FE-SEM and HR-TEM, revealing their spherical structural morphology and uniform particle structure. The presence of the elemental features was analyzed in the gadolinium orthoferrite nanoparticles by EDAX. The surface analysis of the core ranges of the XPS-recorded spectra were obtained for the elemental states of the Gd, Fe, and O factors in the samples, and it additionally characterized the different levels of oxidative states by fitting the levels of the high-resolution parameters of Gd 4d, Fe 2p, and O 1s. The magnetic properties of the samples were investigated by VSM. The measurement of the magnetic parameters revealed that gadolinium orthoferrite nanoparticles exhibit a ferromagnetic nature.

Keywords: $GdFeO_3$; Sol–Gel auto-combustion method; synthesis; characterization

1. Introduction

Perovskite-type materials have been emerging in importance in recent years due to their extensive applications in different technologies. Perovskite materials' photochromic behavior might open up applications in consumer products and electronic devices. There is visible photoluminescence peak in lead-halide perovskite materials under a two-photon absorption process while tuning the excitation wavelength. Recently, several lead-halide perovskites have been demonstrated to be functional materials with hydrochronic, thermochromic, and photochromic properties for anticounterfeiting applications [1–3]. $GdFeO_3$ is one of the most vital types of lanthanide metal-oxide perovskites ABO_3 (A = La, Sm, Eu, Gd). The best perovskite has a cubic crystal structure, composed of a 3D shape of corner-sharing BO_6 octahedral B-sites [4]. Orthoferrite materials have more properties, including optical, electrical, and magnetic ones; therefore, they are technologically and scientifically significant [5]. RE orthoferrites' ($ReFeO_3$) crystals have an orthorhombic, distorted perovskite-type belonging to Pbnm, with the space group D162h. $ReFeO_3$ materials exhibit interesting physical and chemical properties due to their ionic and electronic defects [6]. The ionic radius of Gd^{3+} is 0.093 nm, which is superior to that of Fe^{3+}, which is 0.067 nm, and as a result, the quantity of Fe^{3+} ions replaced by Gd^{3+} ions is confined, and

solubility restriction also occur in the replacement of Fe^{3+} ions by Gd^{3+} ions. For this reason, it is expected that an excess substitution of Gd^{3+} ions will tend to aggregate around the grain boundaries in the form of $GdFeO_3$ [7]. Gadolinium orthoferrite nanoparticles have been successfully obtained by various synthesis methods, including co-precipitation [8], sol–gel [9–12], and microwave [13–15]. As compared to other materials, gadolinium orthoferrite nanoparticles are generally considered as efficient materials in various applications, including better gas-sensing performance and medical applications, and gadolinium complexes are the most widely used of all MRI contrast agents [16]. The present work focuses on the synthesis of perovskite $GdFeO_3$ nanoparticles using the sol–gel auto-combustion technique. The emergence of this material with a controlled size and shape is scientifically necessary due to the strong correlation between these parameters and their magnetic properties. Herein, we discuss how $GdFeO_3$ nanoparticles can be successfully prepared on a large scale via the sol–gel technique. The size and shape of the final product it can be readily tuned in the extensive range by tuning-process likewise simple techniques, low cost, high yield, an eco-friendly, the reaction temperature time and molar ratio. Our special observation is made based on the characterization of the thermal, structural, and magnetic behavior of the given material, with great importance in the role of its structure and enhanced magnetic properties.

2. Results and Discussion

2.1. Thermal Analysis

The TG-DTA of the prepared $GdFeO_3$ nanoparticles, which were measured in the temperature range of 35 °C to 1100 °C at the rate of 20 °C/min, is shown Figure 1. In this plot of the TGA curve, three predictable weight losses were measured between in range between 35 °C and 1100 °C. The absorption of water molecules was observed at 180 °C during the first weight loss. The absorption of organic templates was observed in the ranges 180 °C to 410 °C and measured in second weight loss. The crystallization of the final product in the range between 410 °C and 650 °C was due to the third weight loss. No evidential weight loss was identified beyond the 720 °C range, which indicates the formation of $GdFeO_3$ nanoparticles. A broad endothermic peak at 300 °C was exhibited in the DTA curve, owing to the dehydration. Three stages of the decomposition of the anhydrous precursor were observed after dehydration. In conclusion, the as-prepared perovskite gadolinium orthoferrite nanoparticle revealed the phase transition of the materials beyond 720 °C [17].
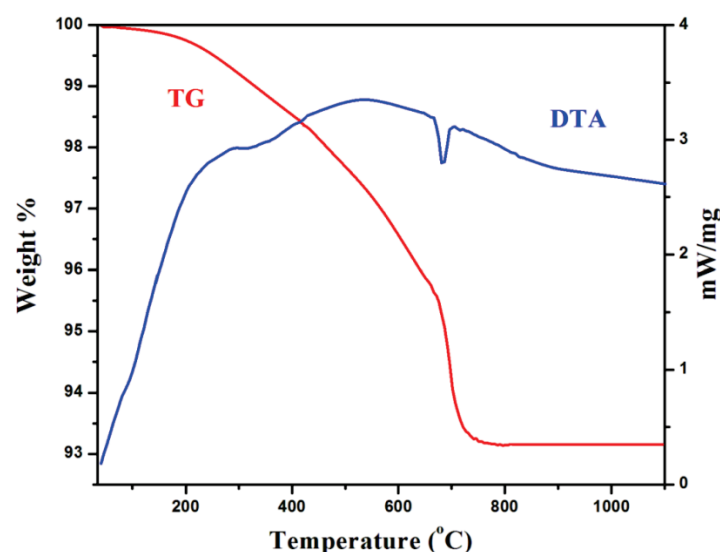
Figure 1. TG-DTA pattern of as-prepared gadolinium orthoferrite.

2.2. XRD Analysis

The XRD features of the as-synthesized material and the different levels at 800 °C, 900 °C, 1000 °C, and 1100 °C of the annealed $GdFeO_3$ nanoparticles are shown in Figure 2. As can be seen from the as-synthesized product, no crystallographic peaks appeared. This indicates that the annealing process is crucial to steadying the crystallites' sizes and to avoiding their agglomeration. The increase in the annealing temperature was mostly correlated with variations in the material microstructure during the annealing and the thermally induced ordering or reordering of the material. The XRD pattern of all of the annealed gadolinium ferrites exhibits peaks with h, k, and l values of (110), (111), (020), (112), (200), and (312), and the planes indicate the perovskite-like orthorhombic type. The crystallographic peaks are well-matched with JCPDS card # 78-0451. The clarity of the observed peaks shows the formation of gadolinium orthoferrite nanoparticles. The mean crystallite sizes were calculated using the Debye-scherrer's formula [18].
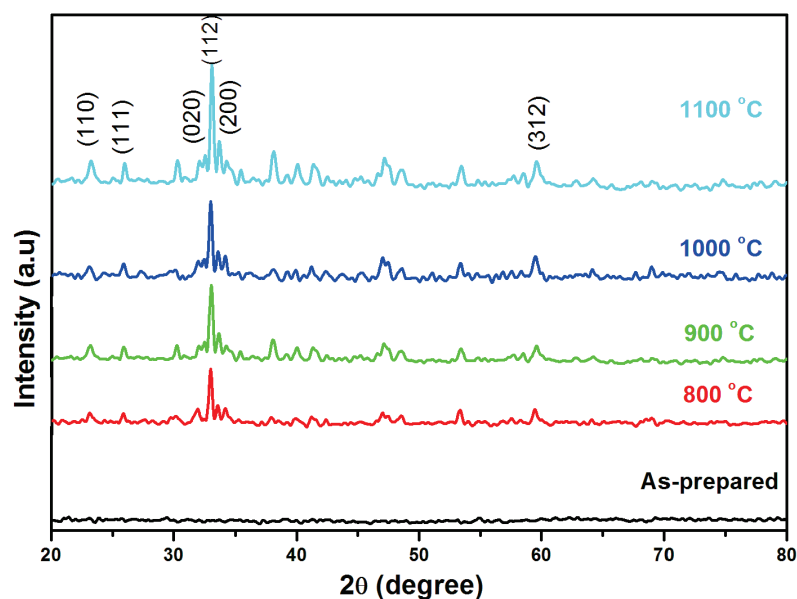
Figure 2. X-ray diffraction of gadolinium orthoferrite annealed at 800 °C, 900 °C, 1000 °C, and 1100 °C.

Table 1 shows that the increasing temperature levels of the annealing process result in the gradual increase of the crystallite size. The crystallite size increases are 20, 23, 25, and 27 nm with respect to the increasing temperatures of 800 °C, 900 °C, 1000 °C, and 1100 °C. The observed behavior revealed the development of the gadolinium orthoferrite nanoparticles. We have analyzed the prepared $GdFeO_3$ nanoparticles using XRD analysis to characterize the primary confirmation of the formed $GdFeO_3$ crystal structures. We found that the materials that were annealed at 800 °C showed better crystallinity order than did the other samples, which were annealed at 900 °C and 1000 °C. Therefore, we chose to use the sample prepared at 800 °C for all of the other characterization techniques.

Table 1. Crystallite sizes of the gadolinium orthoferrite.

GdFeO$_3$	Crystallite Size (nm)
800 °C	20.2
900 °C	23.6
1000 °C	25.1
1100 °C	27

2.3. Infrared Spectroscopy

The FTIR spectra of the $GdFeO_3$ nanoparticles performed in the range of 4000–400 cm^{-1} is shown in Figure 3. It is clear from the FTIR analysis of the different levels of the annealed $GdFeO_3$ samples that, in the lower-wave numbers of the region, strong absorption bands are around 559–561 cm^{-1}. The observed values are assigned as GdO and FeO due to the formation of stretching vibrations in Gd-O-Fe and Fe-O-Fe [19]. In the higher wave number region, two vibrations are observed at 554–556 and 593–597 cm^{-1}. As a product of evaluation with the wave numbers of vibrations of natural cubic iron and Gd-O, it can be assumed that these two vibrations are most likely related to the Gd-O and Fe-O stretching vibrations, respectively. The observed values of the absorption bands around 432–436 cm^{-1} are most likely credited to the O-Fe-O bending vibrations in the octahedral B-site, respectively [20,21]. We concluded that the recorded spectra confirm the absorption bands between 441–443, 554–556, and 593–597 cm^{-1} are characteristic of gadolinium orthoferrite. This observation reveals some shift in the vibrations in the FTIR spectra of the annealing samples in contrast with the sol–gel hydroxides; this may be due to effect of the formation of the α-$GdFeO_3$ crystal structure.
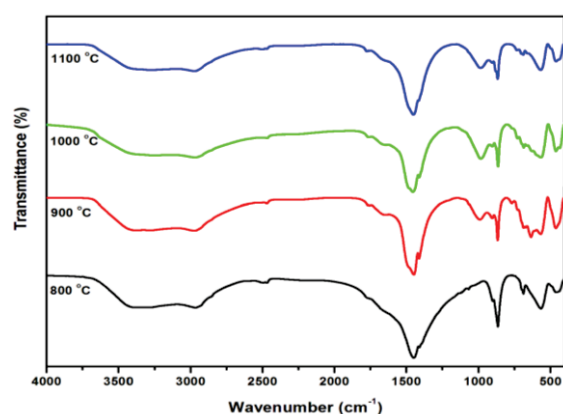
Figure 3. FTIR spectra of $GdFeO_3$ nanoparticles annealed at temperatures of 800 °C, 900 °C, 1000 °C, and 1100 °C.

2.4. FE-SEM with EDAX Analysis

The FE-SEM images of the gadolinium orthoferrite nanoparticles annealed at 800 °C are shown in Figure 4. It is clear from the micrograph that gadolinium orthoferrite exhibits aspherical type with some agglomeration. The agglomeration of the prepared gadolinium orthoferrite nanoparticles indicates the magnetic interaction between the samples. The elemental composition of $GdFeO_3$ was investigated with EDX, and it contained Fe, Gd, and O. From the Energy Dispersive X-ray Analysis data, the Gd, Fe ratio of the samples was 1:2. No additional lines were detected in the elemental mapping, confirming that they were pure gadolinium orthoferrite nanoparticles.

2.5. HRTEM Analysis with SAED

An HRTEM micrograph of the gadolinium orthoferrite nanoparticles annealed at 800 °C is shown in Figure 5. In this work, perovskite and orthorhombic-type gadolinium orthoferrite nanoparticles were present with a spherical structure [22]. The spherical structure was measured using ImageJ viewer software, demonstrating that the perovskite-like orthorhombic type of gadolinium orthoferrite nanoparticles' size was 15 nm. In addition, the SAED pattern of the perovskite-like orthorhombic structure for the gadolinium orthoferrite nanoparticles revealed that they joined to diverse diffraction planes. The clear diffraction spots disclose good dispersion and good crystallinity behavior.
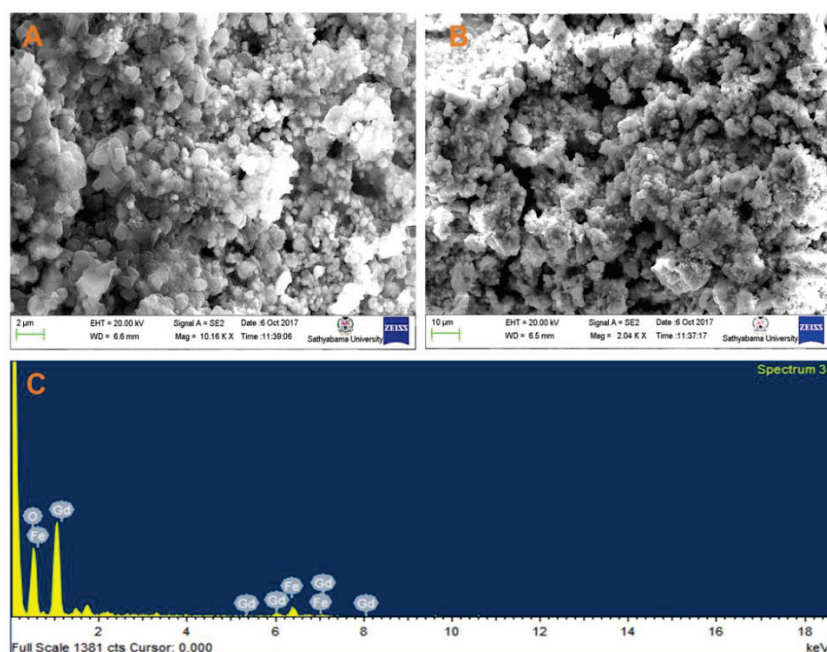
Figure 4. FE-SEM image of GdFeO$_3$ nanoparticles annealed at a temperature of 800 °C (**A**,**B**) and the corresponding EDAX mapping (**C**).
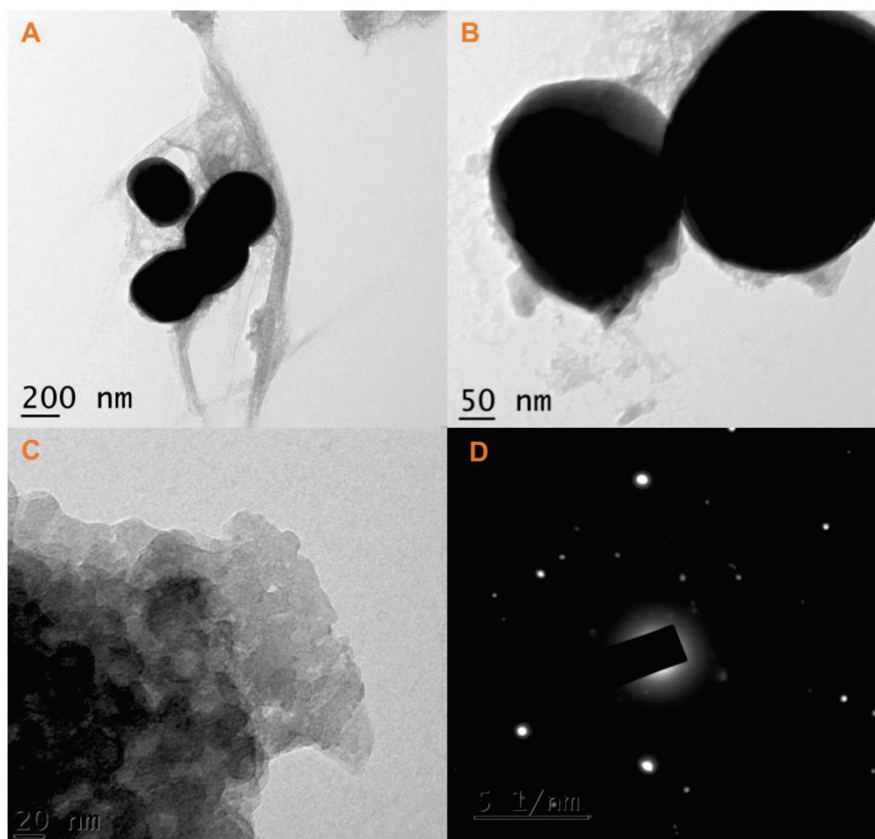
Figure 5. HRTEM images of GdFeO$_3$ nanoparticles annealed at a temperature of 800 °C (**A–C**) and the corresponding SAED pattern for Figure 5c (**D**).

2.6. X-ray Photoelectron Spectra

Figure 6A–D shows the oxidation states of the metals in the GdFeO$_3$ sample as examined by X-ray photoelectron spectroscopy. The XPS spectra of the GdFeO$_3$ powder annealed at 800 °C reveals the presence of Gd, Fe, and O. Therefore, the equivalent XPS peaks were used to find the relative contribution of the distinct oxidation state [23]. As shown in Figure 6A, the two prominent peaks at 530 eV and 535.02 eV indicate the O1s. Figure 6C the observed peaks around 709.62, 711.65, 717.75, and 723.64 are preferred to the Fe^{3+} at the octahedral and tetrahedral sites, respectively. In addition, a satellite peak was noticeable at a binding energy of around 709.62 eV. On the basis of the spin-orbit coupling rule, the Fe 2p orbital exhibits a doublet of Fe 2p3/2 and Fe 2p1/2 peaks at binding energies of 709.62 and 723.96 eV, attributed to the exchange interaction between the outer 3d electrons and the remaining 3s electron of the atom. We may conclude from Figure 6B that the XPS analysis for Gd 4p and Gd 4d regions of gadolinium show that they are incorporated in ferrite. The spectra of the prepared samples contain foremost binding energy peaks present around 152.02, 146.88, and 140.34 eV, respectively. From the graph, we can see the presence of a shoulder peak at 146.88, 140.34 eV (major) assigned to Gd^{3+}. Additionally, a satellite peak was observed at 152.02 (minor). The major O 1s peak observed at 530 for the prepared samples correspond to O^{2-} anions in the gadolinium orthoferrite crystal lattice. The second peak that appeared at 535.02 eV could be recognized as under-coordinated lattice oxygen, recommending a structural defect, which is shown in Figure 6A. The measured gadolinium orthoferrite oxidation state values are presented in Table 2. From the XPS analysis, it may be concluded that the prepared gadolinium orthoferrite nanoparticles survived in multiple oxidation states [24].
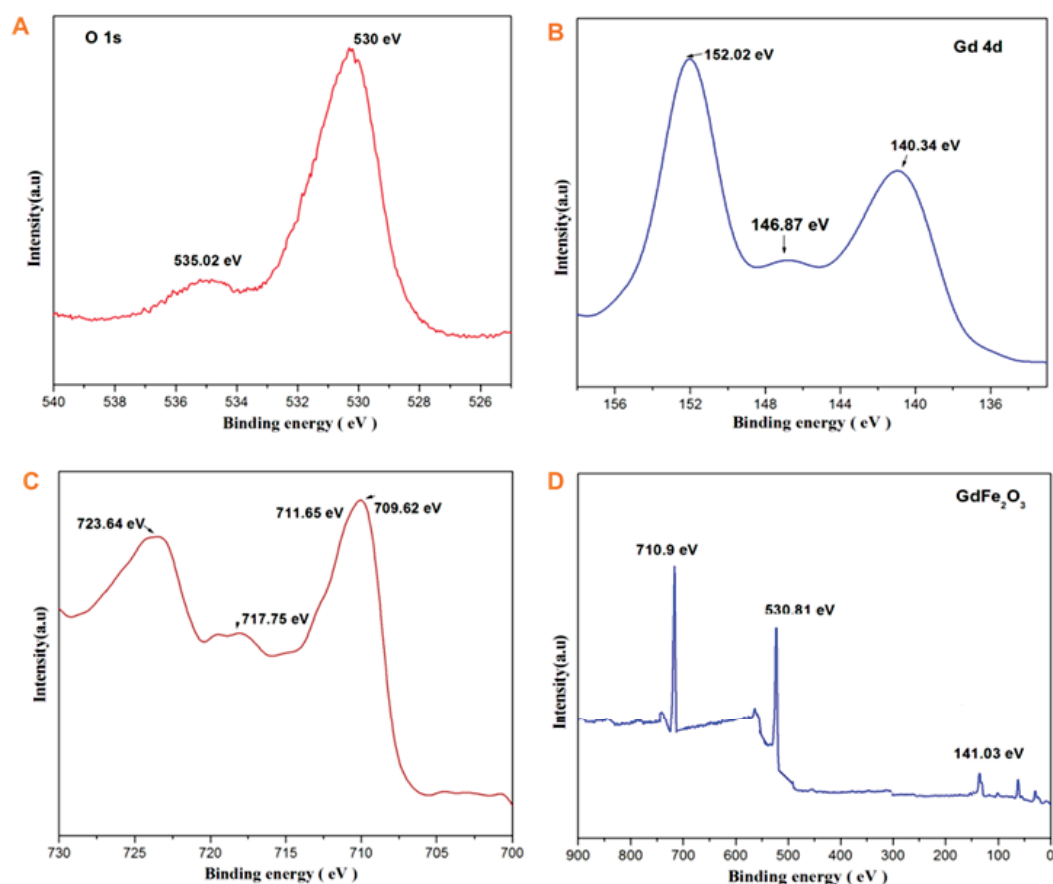
Figure 6. (**A–D**) XPS spectra of GdFeO$_3$ nanoparticles annealed at a temperature of 800 °C.

Table 2. XPS spectra of gadolinium orthoferrite annealed at 800 °C.

Element	Peak Binding Energy
Gd 4d	152.02
	146.87
	140.34
Fe 2p	709.62
	717.75
	723.64
	711.65
O 1s	530
	535.02

2.7. Magnetic Analysis

Magnetic measurements of the $GdFeO_3$ nanoparticles at various annealing temperatures were recorded as falling between $-5G$ and $+15G$ as performed by VSM. Figure 7 depicts the room-temperature magnetic hysteresis curve of the $GdFeO_3$ nanoparticles annealed at the different temperatures of 800 °C, 900 °C, 1000 °C, and 1100 °C. The measurement of the saturation magnetization (Ms), and Coercivity (HC) values are discussed. As shown in Table 3, when the annealing temperature increased, the related saturation magnetization (Ms) value increased from 33.3 emu/g to 53 emu/g, and the Coercivity (HC) value increased from 544 G to 729 G. The Coercivity (Hc) is the magnetic field necessary for overcoming the magneto-crystalline anisotropy to turn over the magnetic momentum. In the $GdFeO_3$ perovskite structure, Fe^{3+} ions are bounded by six O^{2-} ions in an octahedral symmetry; as an effect, the Fe^{3+} ions interact with O^{2-}; therefore, a maximum number of unpaired electrons are generated, which results in magnetic momentum. In $GdFeO_3$, both the Fe^{3+} and Gd^{3+} ions have magnetic properties, and the resultant magnetic momentum comes from the donation of both the ions [25]. In the present work, the different levels of annealed samples confirmed the existence of a ferromagnetic nature. As observed in Figure 7A–D, the magnetization curve for the sample prepared at 800 °C showed a different curve pattern than those of the other samples, which were prepared at 900 °C, 1000 °C, and 1100 °C, respectively. We believe that this might be caused due to the change of the order of magnetization properties of the $GdFeO_3$ nanoparticles from a weak ferromagnetic arrangement to a strong ferromagnetic order, with respect to the increase in the annealing temperature.
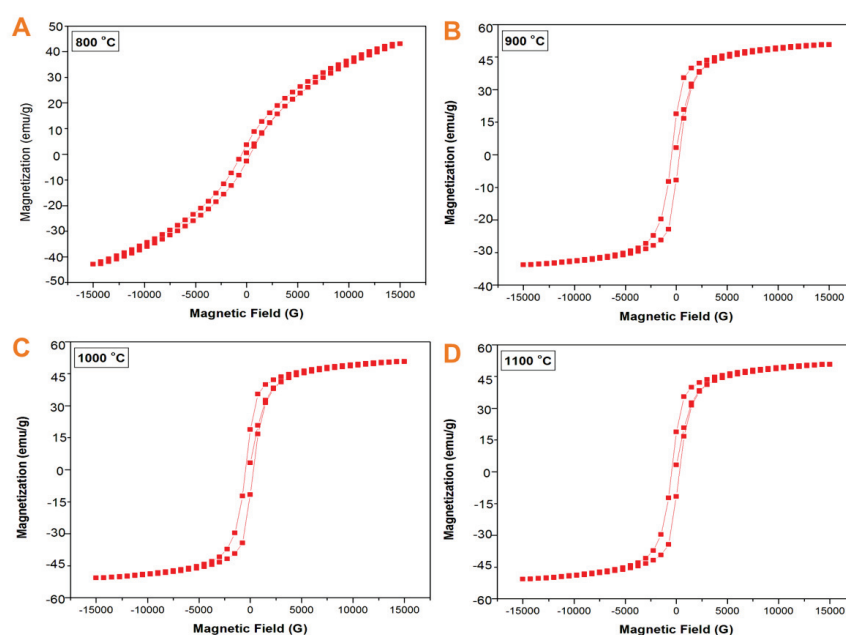
Figure 7. (**A–D**). Magnetization curves of the $GdFeO_3$ nanoparticles at different temperatures.

Table 3. Magnetization of gadolinium orthoferrite.

Temperature	Saturation Magnetization (Ms) emu/g	Coercivity G
800 °C	33.1	544
900 °C	38.7	605
1000 °C	47.2	684
1100 °C	53.1	729

3. Conclusions

In the present work, $GdFeO_3$ nanoparticles were synthesized using the sol–gel auto-combustion technique, and the structural, morphological, and magnetic properties of $GdFeO_3$ depend on several factors, such as the experimental synthesis, chemical composition, and particle size. The formation of orthorhombic ferrite was confirmed by XRD spectra, and the crystallite sizes were found to increase with the increase in the annealing temperature. FTIR analysis revealed the formation of a ferrite structure with two strong peaks at around 575–583 cm^{-1} and 432–438 cm^{-1}, respectively. The HRTEM results revealed perovskite and orthorhombic-type gadolinium orthoferrite nanoparticles present in a spherical structure, and the particle size was 15 nm. XPS analysis confirmed that the gadolinium orthoferrite nanoparticles survived multiple oxidations. VSM analysis revealed that the different levels of annealed gadolinium orthoferrite samples increased with increases in saturation magnetization (Ms) from 33.3 to 53 emu/g, and the Coercivity (HC) value was 544–729 G, which confirmed the existence of a ferromagnetic nature. The prepared material is promising for magnetic recording and applications.

4. Materials and Methods

For the synthesis of gadolinium orthoferrite using the sol–gel auto-combustion technique, 0.2 M of ferric nitrate, 0.1 M gadolinium nitrate, and 0.29 M of citric acid were dissolved in 20 mL of de-ionized water individually, and those solutions were added one by one, respectively. A suitable amount of ammonia solution was added to maintain the pH level. The prepared solution was magnetically stirred for 5 h at 70 °C. A black-colored gel appeared, and after few minutes, it burned via auto-combustion, and the residual product was obtained. Afterwards, the burned powder was dried in a hot-air oven for 2 h at 100 °C. The forms of gadolinium orthoferrite powder samples were annealed 2 h at different temperature levels, such as 800 °C, 900 °C, 1000 °C, and 1100 °C. Furthermore, the different levels of annealed powder were characterized by XRD, FTIR, FE-SEM with EDAX, HRTEM with SAED, XPS, and VSM.

In this work, we chose the sol–gel auto-combustion method to prepare $GdFeO_3$ nanoparticles due to their advantages, such as the strong correlation between these synthetic parameters, including large-scale production, reaction time, and combustion temperature, which control the magnetic properties of $GdFeO_3$ materials. The size and shape of the final products can be readily tuned in a wide range by tuning process parameters, such as a simple method, a high yield, being eco-friendly, the reaction temperature, and the molar ratio of the material.

Characterization Techniques

The synthesized gadolinium orthoferrite powders were characterized by employing different characterizations. A TG-DTA study was performed at a heating rate of 10 °C min^{-1} in an air atmosphere using a NETZSCH-STA 449 F3 JUPITER. The phase confirmations of the annealed gadolinium orthoferrite were performed using an X-ray diffraction (XRD)PANalytical XPERT-PRO with monochromatic Cu Kα radiation (λ = 1.54060 Å) at 30 mA and 40 kV with a 0.05 step in the 2θ range of 20°–80°. FTIR spectra were carried out using a Perkin Elmer Spectrum BX model infrared spectrophotometer recording in the range from 4000–400 cm^{-1}. Structural measurements were carried out using a field-emission scanning electron microscope (SUPRA 55, CARL ZEISS, GERMANY) to record

the FE-SEM with EDAX. Ahigh-resolution transmission electron microscope (HRTEM) Jeol/JEM 2100, with a source of LaB6 and with a resolution 0.23nm, a lattice of 0.14 nm, with a voltage of 200 kV was used. XPS studies were performed using a Thermo Fisher Scientific ESCALAB 250Xi X-ray spectrometer. The magnetizations of $GdFeO_3$ were measured with a vibrating sample magnetometer, instrument model 7407, Lakeshore, USA, with a maximum magnetic field of 2.5 T, with a dynamic moment range of 1×10^{-6}–1×10^3 emu M-H at room temperature. The magnetic measurement of the gadolinium orthoferrite was carried out by VSM.

References

1. Qarony, W.; Hossain, M.K.; Hossain, M.I.; Zeng, L.; Ma, S.; Yu, K.M.; Salleo, A.; Knipp, D.; Tung Yup, C.; Tsang, Y.H. Reversible photochromic and photoluminescence in iodide perovskites. *Thin Solid Film.* **2021**, *737*, 138950. [CrossRef]
2. Feng, J.; Wang, J.; Wang, D.; Han, M.; Qian, G.; Wu, F.; Lin, Q.; Hu, Z. Reversible Phase Transitions of all Inorganic Copper-Based Perovskites: Water-Triggered Fluorochromism for Advanced Anticounterfeiting Applications. *ACS Appl. Electron. Mater.* **2022**, *4*, 225–232. [CrossRef]
3. Hoefler, S.F.; Trimmel, G.; Rath, T. Progress on lead-free metal halide perovskites for photovoltaic applications: A review. *Mon. Für Chem.-Chem. Mon.* **2017**, *148*, 795–826. [CrossRef] [PubMed]
4. Ruffo, A.; Mozzati, M.C.; Albini, B.; Galinetto, P.; Bini, M. Role of non-magnetic dopants (Ca, Mg) in $GdFeO_3$ perovskite nanoparticles obtained by different synthetic methods: Structural, morphological and magnetic properties. *J. Mater. Sci. Mater. Electron.* **2020**, *31*, 18263–18277. [CrossRef]
5. Mir, S.A.; Ikram, M.; Asokan, K. September. Effect of Ni doping on optical, electrical and magnetic properties of Nd orthoferrite. *J. Phys. Conf. Ser.* **2014**, *534*, 012017. [CrossRef]
6. Somvanshi, A.; Husain, S.; Manzoor, S.; Tiwari, S.; Fatema, M.; Khan, W. Room temperature dual ferroic behavior induced by (Bi, Ni) co-doping in nanocrystalline $Nd_{0.7}Bi_{0.3}Fe_{1-x}NixO_3$ ($0 \le x \le 0.3$). *J. Mater. Sci. Mater. Electron.* **2020**, *31*, 11010–11020. [CrossRef]
7. Mathur, S.; Shen, H.; Lecerf, N.; Kjekshus, A.; Fjellvaag, H.; Goya, G.F. Nanocrystalline orthoferrite $GdFeO_3$ from a novel heterobimetallic precursor. *Adv. Mater.* **2002**, *14*, 1405–1409. [CrossRef]
8. Popkov, V.I.; Albadi, Y. The effect of co-precipitation temperature on the crystallite size and aggregation/agglomeration of $GdFeO_3$ nanoparticles. *ао фа ааа* **2021**, *12*, 224–231. [CrossRef]
9. Santhosh, B.S.; Yashas, S.R.; Kumara Swamy, N.; Shivaraju, H.P. Application of non-hierarchical gadolinium ortho-ferrite nanostructure for LED-driven photocatalytic mineralization of doxycycline hydrochloride. *J. Mater. Sci. Mater. Electron.* **2022**, *33*, 11676–11686. [CrossRef]
10. Alecu, A.-E.; Costea, C.-C.; Surdu, V.-A.; Voicu, G.; Jinga, S.-I.; Busuioc, C. Processing of Calcium Magnesium Silicates by the Sol–Gel Route. *Gels* **2022**, *8*, 574. [CrossRef]
11. Nawaz, A.; Ullah, S.; Alnuwaiser, M.A.; Rehman, F.U.; Selim, S.; Al Jaouni, S.K.; Farid, A. Formulation and Evaluation of Chitosan-Gelatin Thermosensitive Hydrogels Containing 5FU-Alginate Nanoparticles for Skin Delivery. *Gels* **2022**, *8*, 537. [CrossRef]
12. Mocioiu, O.-C.; Vlăduţ, C.M.; Atkinson, I.; Brătan, V.; Mocioiu, A.-M. The Influence of Gel Preparation and Thermal Treatment on the Optical Properties of SiO_2-ZnO Powders Obtained by Sol–Gel Method. *Gels* **2022**, *8*, 498. [CrossRef]
13. Mariyappan, V.; Keerthi, M.; Chen, S.M.; Jeyapragasam, T. Nanostructured perovskite type gadolinium orthoferrite decorated RGO nanocomposite for the detection of nitrofurantoin in human urine and river water samples. *J. Colloid Interface Sci.* **2021**, *600*, 537–549. [CrossRef]
14. Guo, Y.; Li, H.; Li, S.; Chen, L.; Li, Z. Study on the Structure, Magnetic Properties and Mechanism of Zn-Doped Yttrium Iron Garnet Nanomaterial Prepared by the Sol-gel Method. *Gels* **2022**, *8*, 325. [CrossRef]

15. Jovanovic, J.D.; Adnadjevic, B.K. Kinetics of the Release of Nicotinamide Absorbed on Partially Neutralized Poly(acrylic-co-methacrylic acid) Xerogel under the Conditions of Simultaneous Microwave Heating and Cooling. *Gels* **2021**, *7*, 193. [CrossRef]

16. Wei, K.; Liang, B.; Sun, C.; Jiang, Y.; Yuan, M. Metal Halide Perovskites for Red-Emission Light-Emitting Diodes. *Small Struct.* **2022**, *3*, 2200063. [CrossRef]

17. Albadi, Y.; Martinson, K.D.; Shvidchenko, A.V.E.; Buryanenko, I.V.; Semenov, V.G.; Popkov, V.I. Synthesis of GdFeO$_3$ nanoparticles via low-temperature reverse co-precipitation: The effect of strong agglomeration on the magnetic behavior. *ao φa aaa* **2020**, *11*, 252–259. [CrossRef]

18. Sathiyamurthy, K.; Rajeevgandhi, C.; Bharanidharan, S.; Sugumar, P.; Subashchandrabose, S. Electrochemical and magnetic properties of zinc ferrite nanoparticles through chemical co-precipitation method. *Chem. Data Collect.* **2020**, *28*, 100477. [CrossRef]

19. Ilhan, S.; Izotova, S.G.; Komlev, A.A. Synthesis and characterization of MgFe$_2$O$_4$ nanoparticles prepared by hydrothermal decomposition of co-precipitated magnesium and iron hydroxides. *Ceram. Int.* **2015**, *41*, 577–585. [CrossRef]

20. Vandana, C.S.; Rudramadevi, B.H. Effect of Cu^{2+} substitution on the structural, magnetic and electrical properties of gadolinium orthoferrite. *Mater. Res. Express* **2018**, *5*, 046101. [CrossRef]

21. Datt, G.; Raja, M.M.; Abhyankar, A.C. Steering of Magnetic Interactions in Ni$_{0.5}$Zn$_{0.5}$Fe$_{2-x}$(Mn)$_x$O$_4$ Nanoferrites via Substitution-Induced Cationic Redistribution. *J. Phys. Chem. C* **2021**, *125*, 10693–10707. [CrossRef]

22. Jiang, L.; Yang, S.; Zheng, M.; Chen, H.; Wu, A. Synthesis and magnetic properties of nanocrystalline Gd$_3$Fe$_5$O$_{12}$ and GdFeO$_3$ powders prepared by sol–gel auto-combustion method. *Mater. Res. Bull.* **2018**, *104*, 92–96. [CrossRef]

23. Dehsari, H.S.; Asadi, K. Impact of Stoichiometry and Size on the Magnetic Properties of Cobalt Ferrite Nanoparticles. *J. Phys. Chem. C* **2018**, *122*, 29106–29121. [CrossRef]

24. Sena, N.C.; Castro, T.J.; Garg, V.K.; Oliveira, A.C.; Morais, P.C.; da Silva, S.W. Gadolinium ferrite nanoparticles: Synthesis and morphological, structural and magnetic properties. *Ceram. Int.* **2017**, *43*, 4042–4047. [CrossRef]

25. Puli, V.S.; Adireddy, S.; Ramana, C.V. Chemical bonding and magnetic properties of gadolinium (Gd) substituted cobalt ferrite. *J. Alloys Compd.* **2015**, *644*, 470–475. [CrossRef]

Photocatalytic and Antibacterial Properties of Doped TiO$_2$ Nanopowders Synthesized by Sol−Gel Method

Silviu Preda [1], Jeanina Pandele-Cușu [1], Simona Viorica Petrescu [1], Elena Mădălina Ciobanu [1], Gabriela Petcu [1], Daniela C. Culiță [1], Nicoleta G. Apostol [2], Ruxandra M. Costescu [2], Iuliana Raut [3], Mariana Constantin [3,4] and Luminița Predoană [1,*]

1   Institute of Physical Chemistry "Ilie Murgulescu" of the Romanian Academy, 202 Splaiul Independenței, 060021 Bucharest, Romania
2   National Institute of Materials Physics, Atomiștilor 405A, 077125 Măgurele, Romania
3   National Institute for Research & Development in Chemistry & Petrochemistry−ICECHIM, 202 Splaiul Independenței, 060021 Bucharest, Romania
4   Faculty of Pharmacy, "Titu Maiorescu" University, 16 Gh. Sincai, 040441 Bucharest, Romania
*   Correspondence: lpredoana@icf.ro; Tel.: +4-021-318-85-95

Abstract: For environmental applications, nanosized TiO$_2$-based materials are known as the most important photocatalyst and are intensively studied for their advantages such as their higher activity, lower price, and chemical and photoresist properties. Zn or Cu doped TiO$_2$ nanoparticles with anatase crystalline structure were synthesized by sol−gel process. Titanium (IV) butoxide was used as a TiO$_2$ precursor, with parental alcohol as a solvent, and a hydrolysing agent (ammonia-containing water) was added to obtain a solution with pH 10. The gels were characterized by TG/DTA analysis, SEM, and XPS. Based on TG/DTA results, the temperature of 500 °C was chosen for processing the powders in air. The structure of the samples thermally treated at 500 °C was analysed by XRD and the patterns show crystallization in a single phase of TiO$_2$ (anatase). The surface of the samples and the oxidation states was investigated by XPS, confirming the presence of Ti, O, Zn and Cu. The antibacterial activity of the nanoparticle powder samples was verified using the gram−positive bacterium *Staphylococcus aureus*. The photocatalytic efficiency of the doped TiO$_2$ nanopowders for degradation of methyl orange (MO) is here examined in order to evaluate the potential applications of these materials for environmental remediation.

Keywords: copper/zinc doped TiO$_2$ powders; sol−gel method; thermal behaviour; photocatalytic activity; antibacterial properties

1. Introduction

The intensive use of oxide nanoparticles in various applications is based on a number of exceptional properties of these oxides, among which we can mention good thermal and chemical stability, electrical and optical properties and high photocatalytic activity, low cost, etc. Based on potential technological applications, metal oxide nanoparticles are attracting considerable interest from researchers in the fields of materials chemistry, biomedical, optical, electronics, medicine, agriculture, information technology, catalysis, environment, energy, and sensing.

Among these metal oxides, TiO$_2$ is one of the most studied materials for many potential applications, particularly for its photocatalytic activity.

The improvement of the photocatalytic activity (by increasing the photon absorption, increasing the recombination time of the electron–hole pairs and improving the separation efficiency of photocarriers) of titanium dioxide was done by self-doping, non-metal doping, transitional metal doping and rare-earth metal doping [1–7].

Some of these dopants, such as transitional metals (e.g., Fe, Cr, Ru, Cu, V etc.) or non-metals (C, N, S etc.) [8–15] lead to an increase in photocatalytic activity due to the formation of a new electron energy levels inside the bandgap (Figure 1).
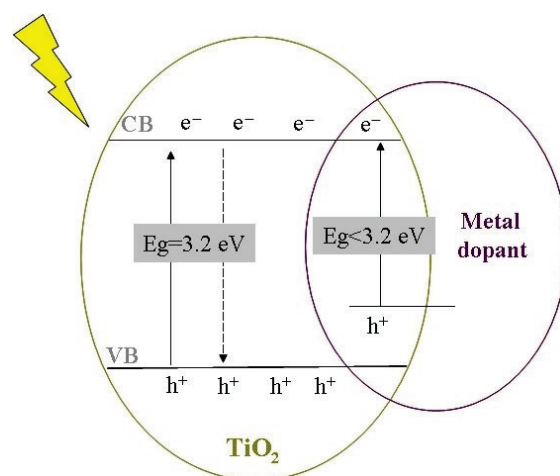
Figure 1. Schematic representation of bandgap narrowing by TiO$_2$ doping.

The synthesis methods, the doping techniques, and the dopant types influence the structural properties of TiO$_2$. Many works reported that a co-catalyst bonded to a semiconductor's surface can act as an electron trap to reduce the recombination of the photogenerated electron−hole pairs and thus improve the photocatalytic activity [16–18]. Furthermore, the loading of metal dopants on TiO$_2$ was shown to lead to a red shift, moving the absorption maxima to the visible region, as the wide band of bare TiO$_2$ is not suitable for absorbing visible light for practical applications [19–21]. However, by increasing thermal treatment the dopants diffuse on the particle's surface, where they precipitate and create *q*-sites with plasmonic effects, improving the photocatalytic activity of the material [22].

To improve the TiO$_2$ antibacterial properties, Cu and Zn doping are an attractive approach because both are antibacterial elements [23,24]. The effect of dopants on the antibacterial properties of titanium dioxide materials was investigated by different groups [10,20,23] and showed that the doped TiO$_2$ extend the light absorption spectrum toward the visible light domain and improves the bacteria inactivation efficiency of the nanoparticles. A schematic diagram of the various nanoparticles' effects on bacteria cells is shown in Figure 2. NPs can attack and kill bacterial cells through multiple mechanisms. Thus, the formation of ROS causes membrane and DNA damage, protein denaturation, inhibiting the electron transport chain, enzyme disruption, and photocatalysis.
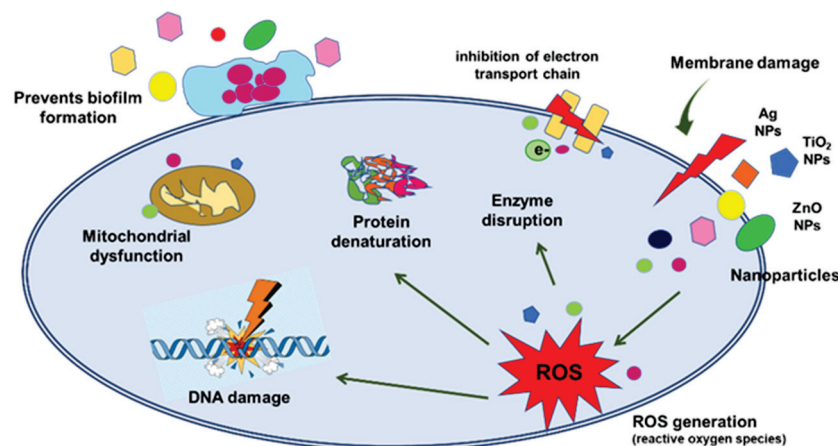
Figure 2. Antimicrobial mechanisms of various nanoparticles (adapted from ref. [25]).

For the preparation of TiO$_2$ or doped TiO$_2$ materials, different methods are available [26–30]. Among them, the sol−gel method is often used to synthesize doped TiO$_2$ because it has advantages such as high purity, relatively low processing temperature and the fact that it offers the possibility of controlling stoichiometry [31–36].

In accordance with one of the most exhaustive definitions [37], the sol−gel process takes place in two steps: the first step is the formation of an inorganic polymeric network by reaction in solution at low temperatures. During the second step, a conversion of the inorganic amorphous polymers to glass or into crystalline materials takes place. The process temperatures are significantly lower than the melting point of the corresponding oxides.

The advantages of the sol−gel method against other preparation methods are a good mixture of the reagents at the molecular level, leading to a homogeneous end−product; the ability to obtain pre−established structures and shapes (gels, films, fibres, powders, etc.) by varying the experimental conditions [38].

In the present paper, Cu− and Zn− doped TiO$_2$ nanometre-sized powders were prepared by the sol−gel method in a basic medium. The aim of this work was the doping of TiO$_2$ in order to improve the absorption capacity in a visible light domain to decrease the bandgap and to increase the recombination time by introducing additional energy levels. The influence of the dopant on the structure and the properties of these materials were evaluated. The photocatalytic activity of the doped TiO$_2$ nanopowders for degradation of methyl orange (MO) is here examined in order to evaluate the potential of these materials for environmental applications. The antibacterial activity of the nanoparticle powder samples was tested using the gram−positive bacterium *Staphylococcus aureus*.

2. Results and Discussion

The samples were investigated following the thermal behaviour, morphology, structure and their properties (antimicrobial or photocatalytic). In the case of the TiO$_2$−Cu 2.0% sample a white−green amorphous powder was obtained, while for the TiO$_2$−Zn 2.0% sample the obtained powder was amorphous and had a white colour powder.

2.1. As Prepared Samples
2.1.1. SEM Results

SEM analysis was performed to investigate the morphology of the as-prepared samples, and the micrographs are shown in Figure 3.
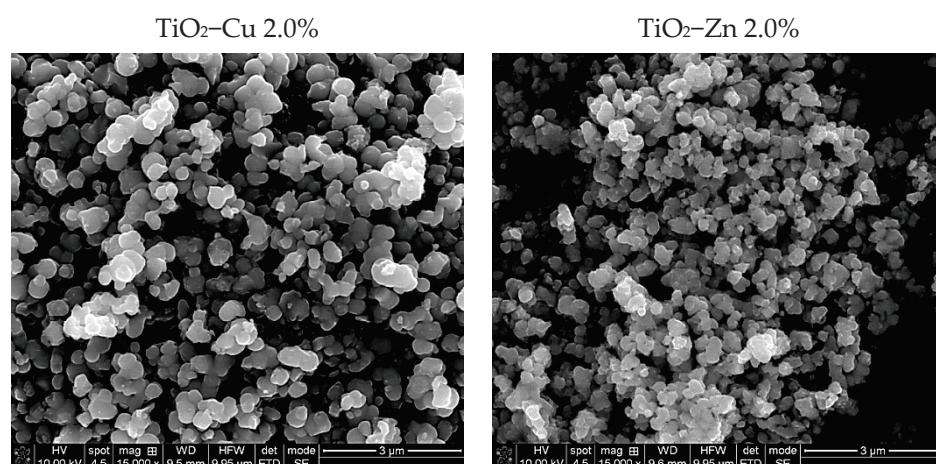
Figure 3. SEM micrographs of the as−prepared samples.

According to SEM observations, for the as-prepared samples, the nanoparticles' surfaces appear to be well-defined with quasi-spherical profiles. The mean diameter, found by Image J software, is 86 nm in TiO$_2$−Cu 2.0% sample slightly larger than 75 nm for TiO$_2$−Zn 2.0%, which also seems to be more agglomerated.

2.1.2. Thermal Behaviour

The thermogravimetric and differential thermal analysis (TG/DTA) were used to examine the thermal behaviour of the as-prepared samples and to set the subsequent thermal treatment. The mass loss and the thermal effects are shown in Figure 4. From Figure 4a the TG curves of the TiO_2-Cu 2.0% sample show a total mass loss of 21%. Three important heat effects are observed on the DTA curve. The endothermic effect at 71 °C is assigned to the elimination of adsorbed water; the two exothermic effects are the one at 288 °C assigned to the decomposition of the samples, by the elimination of the organic residues and the structural hydroxyls (dehydroxylation), and the one at 451 °C, which can be attributed to the crystallization of anatase phase. In Figure 4b, the TG curves of the TiO_2-Zn 2.0% sample show a total mass loss of 22.3%.
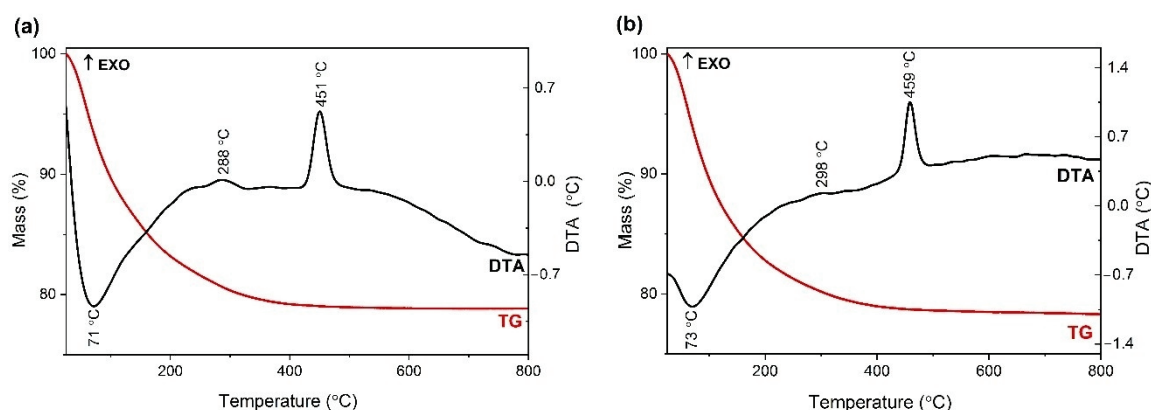
Figure 4. The TG (red)/DTA (black) curves of (**a**) TiO_2-Cu 2.0% sample and (**b**) TiO_2-Zn 2.0% sample; heating rate was 10 °C/min and using air as carrier gas.

Three important heat effects are observed on the DTA curve. The endothermic effect at 73 °C is attributed to the elimination of adsorbed water; the two exothermic effects are the one at 298 °C assigned to the decomposition of the samples, by the elimination of the organic residues and the structural hydroxyls (dehydroxylation) and the one at 459 °C, which can be assigned to the crystallization of anatase phase. In both cases, no further weight loss could be observed at temperatures above 500 °C.

2.1.3. XPS on the As-Prepared Samples

The oxidation states of the elements and the surface of the samples were analysed by X−ray Photoelectron Spectroscopy (XPS). The analysis showed the presence of the Ti 2p, O 1s, Zn 2p and Cu 2p core levels and indicates the presence of different species as follows: Ti(IV), Zn(II) and Cu(I). The binding energy (BE) for Ti 2p3/2 is around 458.53 eV with a spin-orbit splitting of 5.7 eV, consistent with the database [39]. The Zn 2p3/2 peak is centred at 1021.26 eV attributed to Zn(II) [40] and for Cu 2p3/2 we found the BE at 931.44 eV, which could be attributed to Cu(I), with a very weak specific satellite at about 945 eV [41]. Table 1 lists the essential parameters (binding energy and at. %) obtained as a result of the deconvolutions of the spectra for the core levels of interest, of Ti 2p, O 1s, Zn 2p, and Cu 2p for the as-prepared samples (see the Figures 5–7). The values of the amplitude were normalized by the atomic sensitivity factors given by ref. [42].

Table 1. Binding energies (BE) at. % and interpretation of the components of the core levels of interest for the samples prepared by sol-gel method.

Sample	Core Levels		BE (eV)	at. %	Interpretation
TiO_2-Zn 2.0%	Ti 2p	C1	458.53	42.40	Ti(IV) vol.
		C2	459.00	1.60	Ti(IV) surf.
	O 1s	C1	530.02	35.61	Ti(IV) (vol + surf)
		C2	531.02	19.89	Ti(IV) + Zn(II) + cont
	Zn 2p	C1	1021.26	0.50	Zn(II)
TiO_2-Cu 2.0%	Ti 2p	C1	458.23	42.35	Ti(IV) vol.
		C2	459.10	2.71	Ti(IV) surf.
	O 1s	C1	529.74	29.93	Ti(IV)
		C2	530.54	24.52	Ti(IV) + Zn(II) + cont
	Cu 2p	C1	931.44	0.48	Cu(I)

(**a**) (**b**) (**c**)
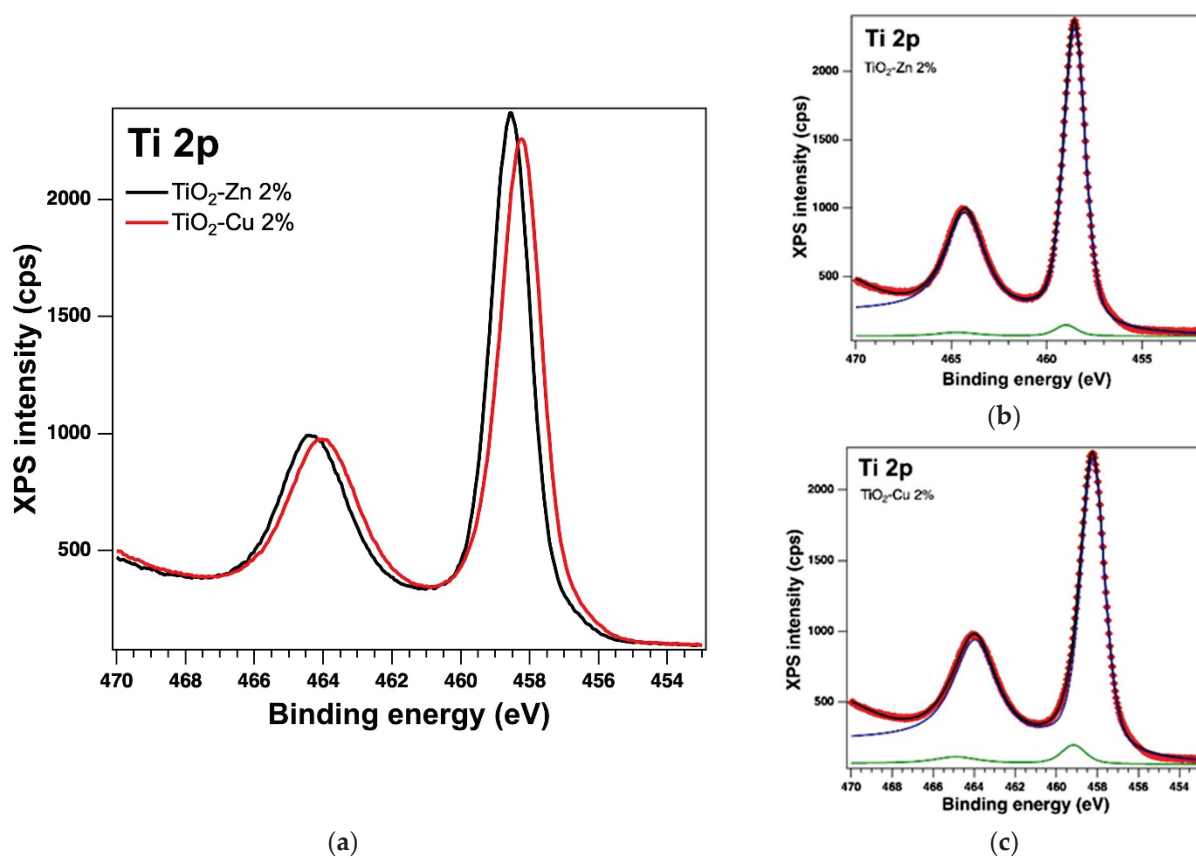
Figure 5. XPS spectra of the core level Ti 2p (**a**) overlayed XPS spectra of the samples prepared by the sol−gel method and the experimental data (red symbols) with the fit and deconvolutions given separately for (**b**) the sample with Zn and (**c**) the sample with Cu; deconvolutions: components C1–blue line and C2–green line.
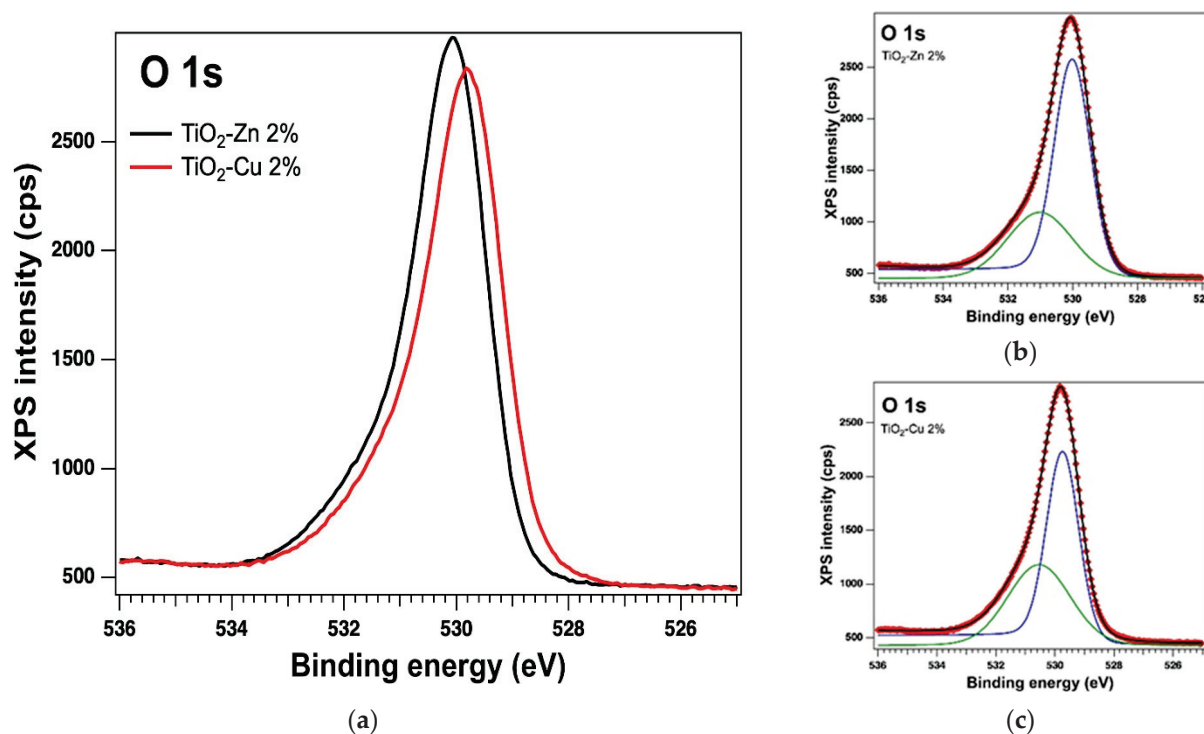
Figure 6. XPS spectra of the core level O 1s (**a**) overlayed XPS spectra of the samples prepared by the sol−gel method and the experimental data (red symbols) with the fit and deconvolutions given separately for (**b**) the sample with Zn and (**c**) the sample with Cu; deconvolutions: components C1–blue line and C2–green line.

The as-prepared powders were thermally treated at 500 °C for 1 h. No mass loss was measured above this temperature and anatase phase crystallization is already completed.

2.2. Thermally Treated Samples (Powders)

2.2.1. SEM Results

The surface morphology of the thermally treated powders, performed by SEM, is presented in Figure 8, showing nanoparticles clusters with similar sizes compared with as−prepared samples. Following the thermal treatment, the samples' surfaces are slightly aggregate, with more irregular shapes, related to untreated ones, as confirmed by BET measurements.

2.2.2. X−ray Diffraction (XRD)

The crystallinity and structure of the thermally treated samples were assessed by X−ray diffraction (XRD). Figure 9 shows the patterns of thermally treated Cu− and Zn−doped TiO_2 samples at 500 °C for 1 h. Moreover, the undoped TiO_2 sample (Ti−Bu−SG) was measured as a reference. Single-phase anatase TiO_2 was identified in all the samples, according to ICDD file no. 21-1272. No diffraction lines related to TiO_2 polymorph phases or additional diffraction lines related to Zn or Cu compounds were detected in the XRD patterns, which may suggest that Cu and Zn were in a dispersed state or the ions were properly entered into the anatase lattice. The lattice parameters, as well as the mean crystalline domain sizes, calculated by the Williamson−Hall method, are shown in Table 2. No major differences in terms of unit cell parameters are noticed against the standard reference file (ICDD 21-1272), pointing out that Cu and Zn dopants probably substitute for Ti in the TiO_2 host lattice. The mean crystalline domain sizes of the Ti−Bu−SG and TiO_2−Cu 2.0% TT samples are similar (~14 nm), while the value for the TiO_2−Zn 2.0% TT sample is 1 nm smaller (~13 nm).

Figure 7. XPS spectra of the core levels Zn 2p (**a**) and Cu 2p (**c**) overlayed XPS spectra of both kinds of samples and the experimental data (red symbols) with the fit and deconvolutions for (**b**) the sol−gel sample with Zn (deconvolutions: components C1–blue line and C2–green line) and (**d**) the sol−gel sample with Cu (only one component–black line).

TiO_2−Cu 2.0% TiO_2−Zn 2.0%
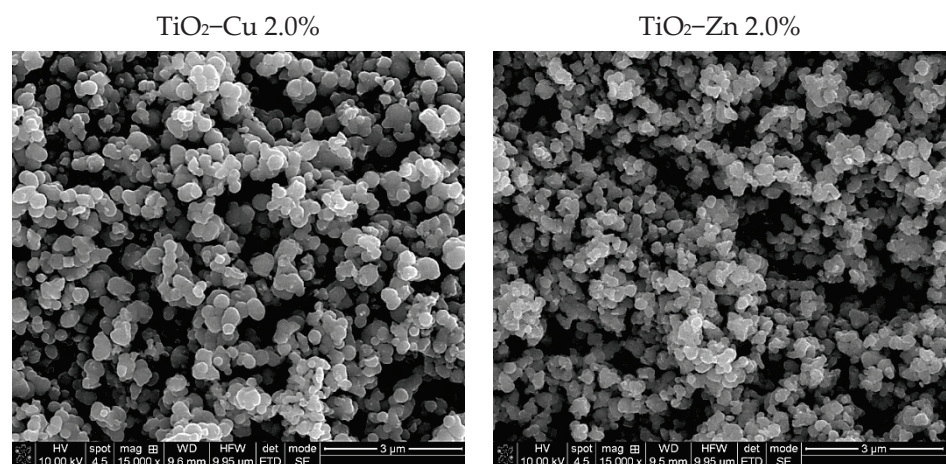
Figure 8. SEM images of the thermally treated samples at 500 °C 1h.
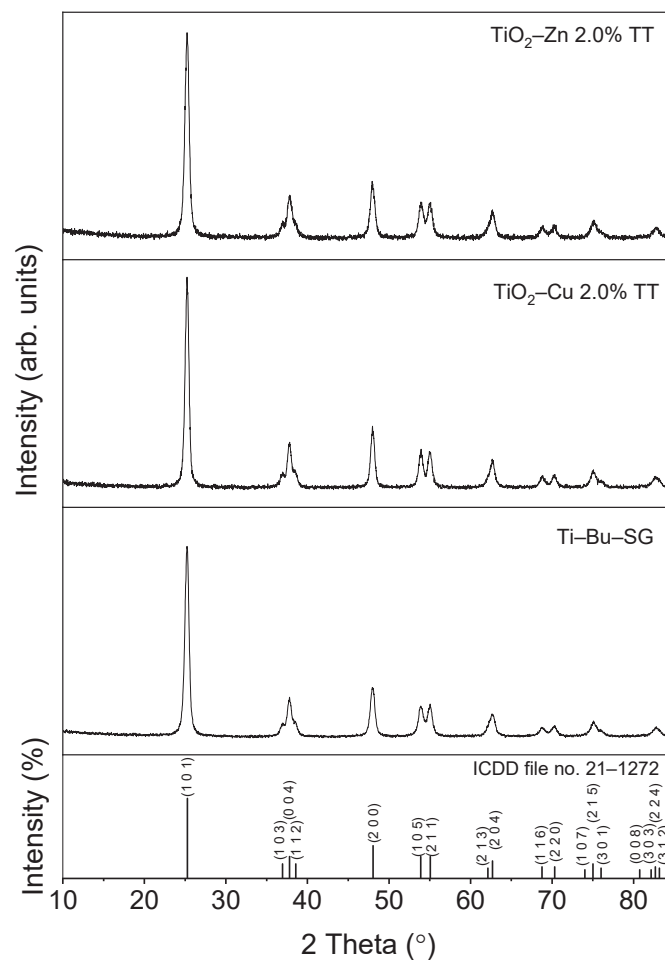
Figure 9. X−ray patterns for powders thermally treated at 500 °C 1 h.

Table 2. The lattice parameters and the mean crystalline domain sizes (Dm) of the samples.

Sample	$a = b$ (Å)	c (Å)	D_m (nm)
Ti−Bu−SG [43]	3.7837 (6)	9.4969 (15)	14
TiO$_2$−Cu 2.0% TT	3.7892 (2)	9.5145 (6)	14
TiO$_2$−Zn 2.0% TT	3.7854 (10)	9.496 (3)	13
Anatase, syn ICDD 21−1272	3.7850	9.5140	-

2.2.3. X−ray Fluorescence (XRF)

Concerning the presence of the dopant in the samples, X−ray fluorescence analysis was performed, which demonstrated the presence of dopant (copper or zinc) in both studied samples. The elemental composition of the samples is listed in Table 3. Other elements (C, S, Si) were detected as traces. Oxide composition by mass percentage was also calculated. More Cu was detected in the final mixture compared to Zn. A possible explanation can be that, during synthesis, a small amount of compound was lost by washing.

Table 3. XRF results of the analysed samples.

Sample	Composition	Values	U.M.	Line
TiO₂−Zn 2.0%	Ti	58.0482	mass%	Ti−KA
	Zn	1.6157	mass%	Zn−KA
	O	39.2373	mass%	O−KA
	C, S, Si (traces)	1.0989	mass%	
	TiO₂	94.1104	mass%	Ti−KA
	ZnO	1.9373	mass%	Zn−KA
	C, S, Si oxides (traces)	3.9524	mass%	
TiO₂−Cu 2.0%	Ti	58.7187	mass%	Ti−KA
	Cu	1.9474	mass%	Cu−KA
	O	38.3098	mass%	O−KA
	C, Si, S (traces)	1.0241	mass%	
	TiO₂	94.0071	mass%	Ti−KA
	CuO	2.3092	mass%	Cu−KA
	C, S, Si oxides (traces)	3.6837	mass%	

2.2.4. XPS on the Thermally Treated Samples

The surface of the thermally treated samples was also examined by X−Ray Photo-electron Spectroscopy (XPS). The core levels of interest were deconvoluted using the same method [44] as for the as-prepared samples. In the case of thermally treated samples, the XPS measurements also confirmed the presence of the Ti 2p, O 1s, Zn 2p and Cu 2p core levels and from the deconvolutions, we obtained: Ti(IV), which is the major component, Zn(II) and Cu(I); but in the case of the TiO₂−Cu 2.0% TT sample we observed the presence of a small amount of Ti(II) and Cu(0), which can be assumed to be related to the thermal treatment. The integral area was used to determine the atomic composition. The integral area was computed using the Voigt profiles deconvolution procedure and scaled the atomic sensitivity factors provided by ref. [42]. The XPS spectra of the Ti 2p, O 1s, Zn 2p and Cu 2p core levels of the thermally treated samples are displayed in Figures 10–12. Table 4 lists the binding energy and at. %, obtained as a result of the deconvolutions of the spectra for the core levels of interest.

2.2.5. Antibacterial Activity

The antibacterial activity of the nanoparticle powder samples was investigated using the gram-positive bacterium *Staphylococcus aureus*. In previous experiments using the diffusion method on doped samples, the best results were obtained for *S. aureus* [45], therefore we continued with this bacterium for the experiments in a broth culture medium. For this experiment, the method of testing in a liquid culture medium was used. The evaluation of the antibacterial activity was performed by measuring the absorbance (see Table 5) after 24 h of incubation. The negative control was represented by the nanoparticle powders immersed separately in the culture medium without inoculating the *S. aureus* strain. The real OD (optical density) of the samples is obtained through the subtraction of the OD of the samples with *S. aureus* and the OD of the negative controls (samples containing the nanopowders but without bacteria) and, in the end, the results are compared with the biological positive control of *S. aureus*.
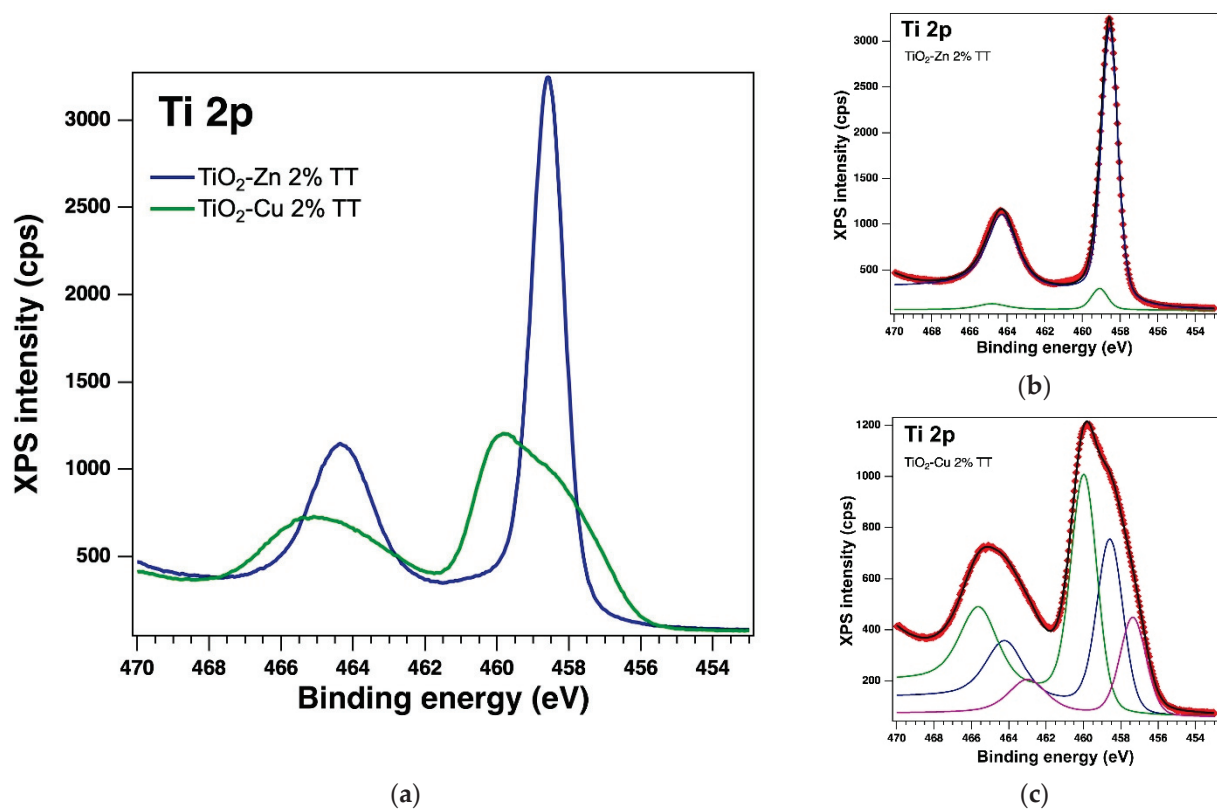
Figure 10. XPS spectra of the core level Ti 2p (**a**) overlayed XPS spectra of the thermally treated samples and the experimental data (red symbols) with the fit and deconvolutions for (**b**) the sample with Zn (deconvolutions: components C1 – blue line and C2–green line) and (**c**) the sample with Cu (deconvolutions: components C1–blue line, C2–green line and C3–magenta line).
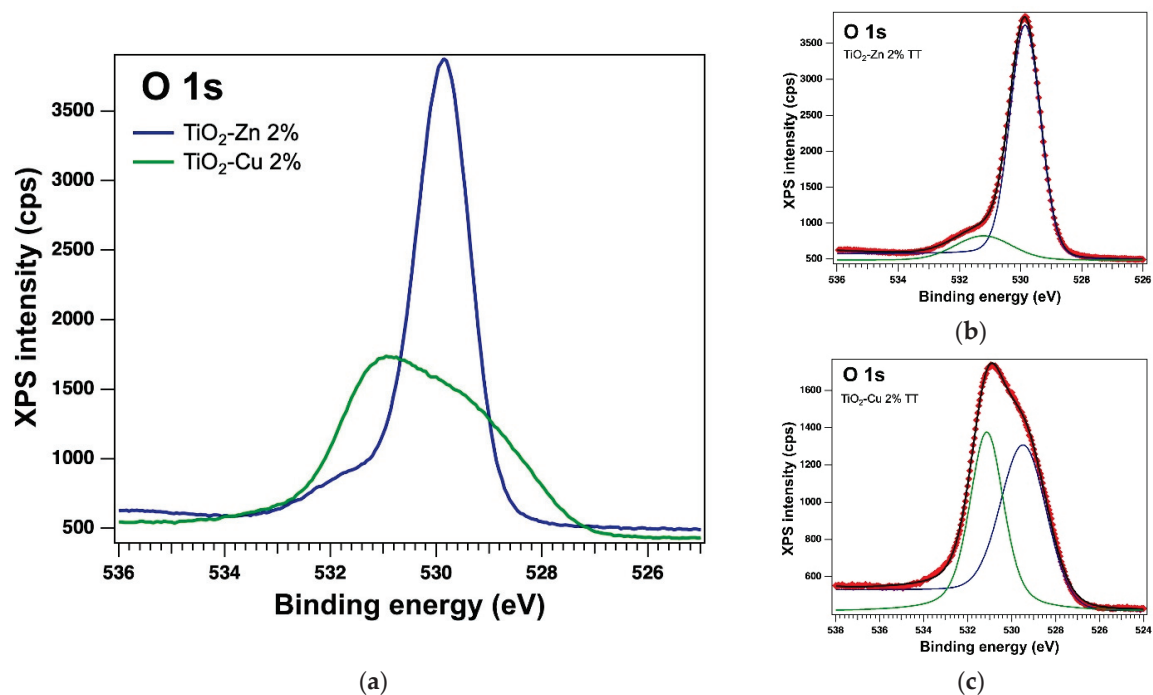
Figure 11. XPS spectra of the core level O 1s (**a**) overlayed XPS spectra of the thermally treated samples and the experimental data (red symbols) with the fit and deconvolutions for (**b**) the sample with Zn and (**c**) the sample with Cu; deconvolutions: components C1–blue line and C2–green line.

(**a**)

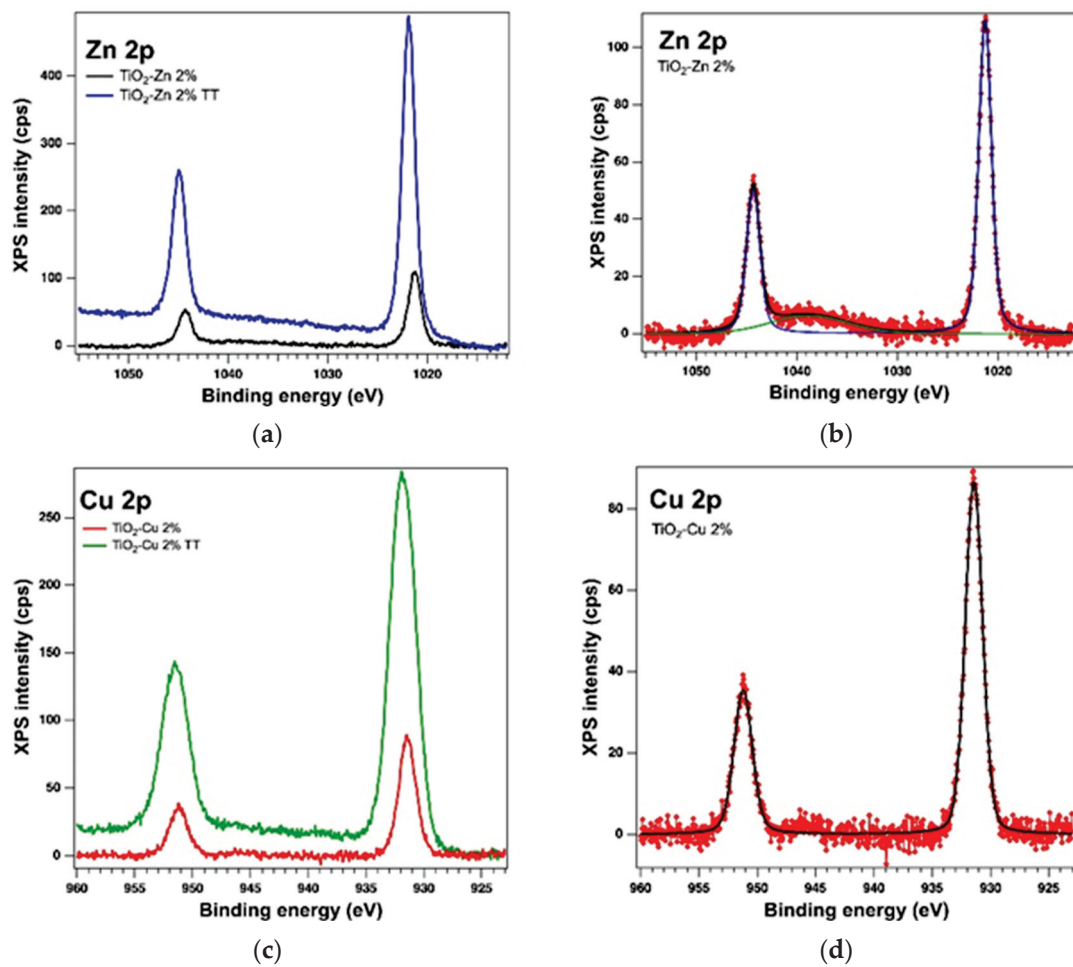(**b**)

(**c**)

(**d**)
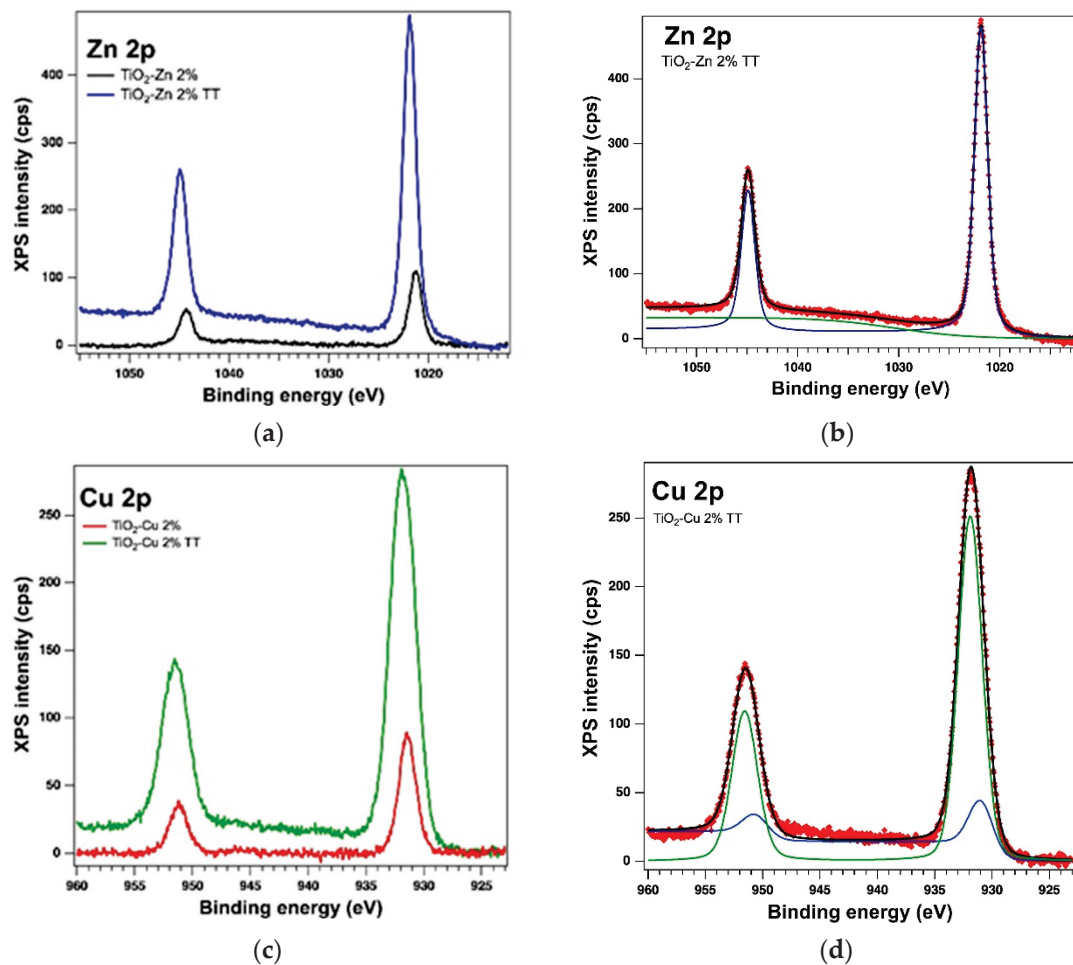
Figure 12. XPS spectra of the core levels Zn 2p (**a**) and Cu 2p (**c**) overlayed XPS spectra of both kinds of samples and the experimental data (red symbols) with the fit and deconvolutions for (**b**) the thermally treated sample with Zn (deconvolution with component C1–blue line; the green line represents an Auger line, which is not taken into account in the chemical analysis) and (**d**) the thermally treated sample with Cu (deconvolutions: components C1–blue line and C2–green line).

Table 4. Binding energies, at. % and interpretation of the components of the core levels of interest for the thermally treated samples.

Sample	Core Levels		BE (eV)	at. (%)	Interpretation
TiO$_2$−Zn 2.0% TT	Ti 2p	C1	458.58	0.78	Ti(IV) vol.
		C2	459.78	39.04	Ti(IV) surf.
	O 1s	C1	529.85	48.77	Ti(IV) (vol + surf)
		C2	531.22	9.21	Ti(IV) + Zn(II) + cont
	Zn 2p	C1	1021.85	2.2	Zn(II)
TiO$_2$−Cu 2.0% TT	Ti 2p	C1	457.29	6.8	Ti(II)
		C2	458.56	12.42	Ti(IV) vol.
		C3	459.97	18.12	Ti(IV) surf.
	O 1s	C1	529.43	29.96	Ti(IV) (vol + surf)
		C2	531.13	30.19	Cu(I) + cont
	Cu 2p	C1	930.95	0.32	Cu(0)
		C2	931.91	2.19	Cu(I)

Table 5. Absorbance values for nanopowders in broth medium.

Sample	Concentration	OD of Sample with *S. aureus*	Inhibition Rate %
Ti−Bu−SG	200 µg mL^{-1}	0.060	96.29
TiO$_2$−Zn 2.0% TT	200 µg mL^{-1}	0.235	85.47
TiO$_2$−Cu 2.0% TT	200 µg mL^{-1}	0.245	84.85
Biological positive control of *S. aureus*	3×10^5 CFU mL^{-1}	1.618	-

Additionally, the bacterial growth inhibition rate was calculated according to the formula and can be seen in Table 5.

The antibacterial activity of nanopowders against *S. aureus* in Mueller Hinton broth was the highest for the Ti−Bu−SG sample with an inhibition rate of 96.29%, followed by TiO$_2$−Cu 2.0% TT and TiO$_2$−Zn 2.0% TT, with inhibition of 85.47% and 84.85%, respectively. Many studies have shown the good antimicrobial activity of TiO$_2$ nanoparticles [46,47].

2.2.6. Textural Characterization

For the textural characterization of the thermally treated Cu and Zn doped and undoped TiO$_2$, the adsorption−desorption isotherms N$_2$ were registered and are shown in Figure 13. The specific surface area (SSA) was calculated by the Brunauer−Emmett−Teller (BET) method. The pore size distribution and average pore diameter were determined by Barrett−Joyner−Halenda (BJH) analysis. The textural parameters (BET surface area (SBET), total pore volume, and average pore size) are listed in Table 6. All three samples exhibit type IV isotherms accompanied by H3 hysteresis loops according to IUPAC classification [48], characteristic of mesoporous materials with slit−shape pores. The undoped TiO$_2$ sample (Ti−Bu−SG) presents the largest surface area of 52.3 m^2/g. Doping with Cu and Zn causes a decrease in surface area by 40% and 20%, respectively. At the same time, an increase in average pore diameter and a slight widening of pore size distribution could be observed, most probably due to the higher particle agglomeration. The total pore volume is influenced differently depending on the dopant ion. Compared to undoped TiO$_2$, it shows a contraction of 10% upon doping with Cu and an increase of 10% upon doping with Zn, respectively.

2.2.7. Photocatalysis Investigation

Figure 14 shows the absorbance spectra of TiO$_2$−type materials, undoped and doped with 2.0% Zn or Cu, respectively. The spectrum of undoped TiO$_2$ (Ti−Bu−SG sample) shows a band edge absorption located at ~370 nm, typically for the band gap of TiO$_2$ nanoparticles in the anatase phase. In the case of sample TiO$_2$−Zn 2.0% TT, no additional absorption band can be observed, ZnO exhibiting a band at ~369 nm [49]. Furthermore, a decrease in the absorption intensity after Zn addition can be observed, probably due to the displacement of titanium ions by zinc into the anatase phase, as XRD analysis suggested. By contrast, the absorption bands of TiO$_2$−Cu 2.0% at around 250–550 nm can be observed due to the O^{2-} (2p) → Ti^{4+} (3d) transitions in the tetrahedral symmetry. Additionally, a broad absorption band in the visible domain was evidenced, proving the presence of Cu species. According to Colon et al. [50], the absorption band between 400 nm and 600 nm, can be assigned to the presence of Cu^{1+} clusters, resulting after a partial reduction of Cu^{2+} species by a strong interaction between TiO$_2$ support and copper nitrate. This strong interaction is also suggested by the obtaining of Ti(II) species in the case of the TiO$_2$−Cu 2.0% sample, as XPS results revealed. The large absorption band located between 600–800 nm indicates the increase of CuO in octahedral symmetry [50]. Thus, the introduction of the dopants leads to a red shift of the absorption band, as was previously reported [51]. This behaviour can be attributed to the formation of impurity levels within the band gap states of TiO$_2$. The band gap value of the bare TiO$_2$ was 3.15 eV. When doping with a transitional metal (Cu or Zn), the band gap values decrease (see Table 6), these values being in agreement with the previously reported data [51,52]. It was suggested through theoretical calculations

that the band gap narrows after Cu doping due to new electronic levels in the valence band resulting from the covalent interaction between Cu and O [53]. For the TiO_2-Zn 2.0% TT sample, the band gap energy decreased due to the synergistic effect between the conduction band of TiO_2 and that of ZnO. Both impurities and defects were introduced to the forbidden band of TiO_2, leading to the formation of some sub-bands, thus, the value of the band gap energy was decreased [52].
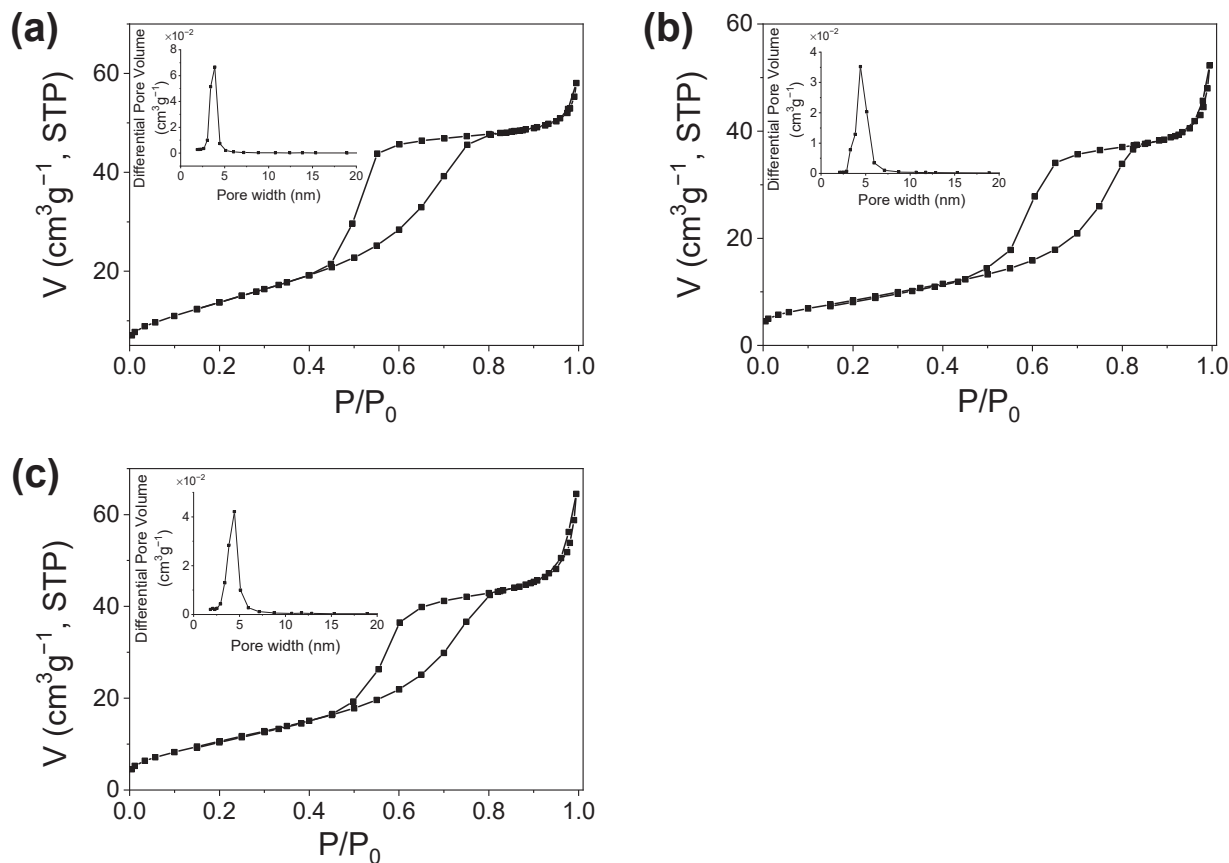
Figure 13. N_2 adsorption–desorption isotherms and pore size distributions (inset of the figures) of Ti−Bu−SG (**a**), TiO_2-Cu 2.0% TT (**b**), and TiO_2-Zn 2.0% TT (**c**) samples.

Table 6. The specific BET surface areas (S_{BET}), total pore volume (V_{total}), average pore diameter (d) and band gap values of the samples.

Sample	S_{BET} (m^2g^{-1})	V_{total} (cm^3g^{-1})	d_{BJH} (nm)	Band Gap (eV)
Ti−Bu−SG	52.3	0.089	4.4	3.15
TiO_2-Cu 2.0% TT	31.3	0.080	6.2	1.5
TiO_2-Zn 2.0% TT	41.5	0.099	6.1	2.85
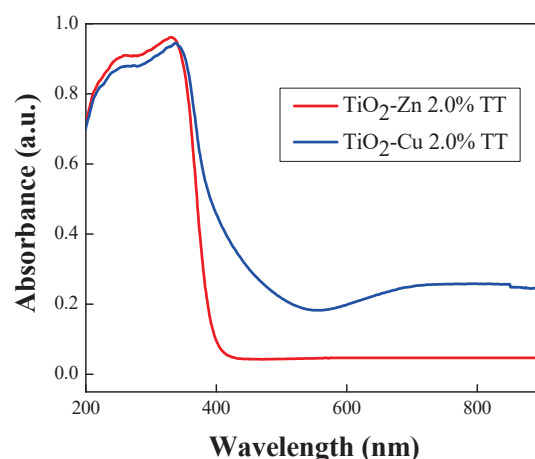
Figure 14. DR−UV−Vis absorption spectrum for TiO_2−Zn 2.0% TT and TiO_2−Cu 2.0% TT samples.

The photocatalytic degradation of methyl orange solution in the presence of undoped and doped TiO_2 was carried out under UV and visible light irradiation. The results presented in Figure 15 showed that the introduction of a doping element in titanium dioxide leads to a higher photocatalytic activity.
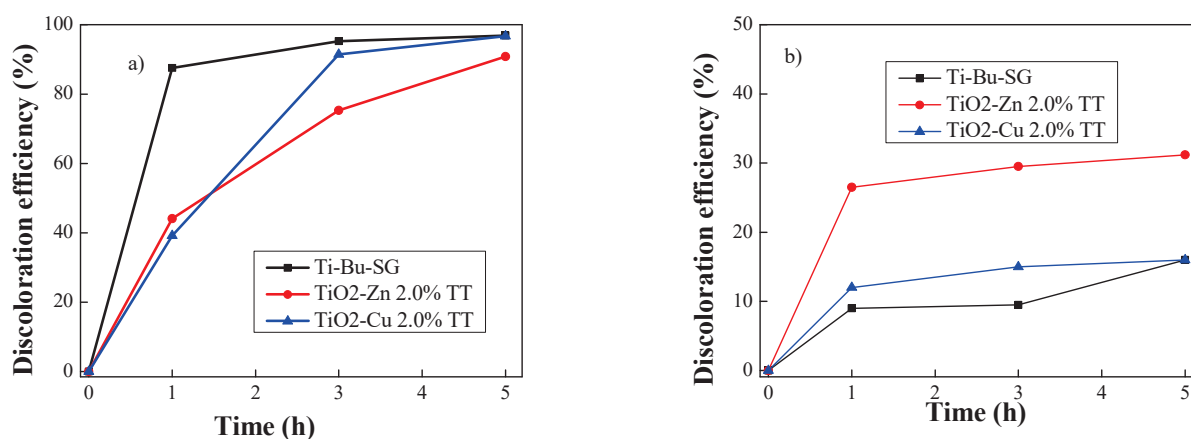
Figure 15. Discoloration of methyl orange under UV (**a**) and visible (**b**) light irradiation using synthesized materials.

It was observed that in the UV domain, the TiO_2−Cu 2.0% TT sample, with crystalline domains size of 14 nm, presented the highest activity in photocatalytic degradation of MO, removing ~97% of the dye in 300 min (Figure 15), while the sample with a smaller value of crystalline domains size (13 nm), TiO_2−Zn 2.0% TT, presented a lower degradation efficiency, about 90%. In the case of visible light irradiation, the most effective was the sample TiO_2−Zn 2.0% TT, removing a total of 30% of MO in 300 min, while the sample doped with Cu presents activity comparable with the bare TiO_2 (Ti−Bu−SG sample) (~ 16%). It can be observed that the presence of a doping metal (Cu, respectively, Zn) led to an increase of photocatalytic activity in the visible domain compared to bare TiO_2. Furthermore, the higher photocatalytic activity of the TiO_2−Zn 2.0% TT materials can be attributed to their increased absorption capacity due to a higher surface area compared to TiO_2−Cu 2.0% TT (see Table 6) a process that ensures the presence of the dye molecules close to the active centres located on the surface, thus facilitating the photodegradation process.

3. Conclusions

In the present work, copper- and zinc-doped TiO$_2$ materials prepared by the sol–gel method were investigated for their photocatalytic and antibacterial activities. The main results can be summarized as follows: by thermal analysis, the heat treatment temperature was set to 500 °C in order to obtain a crystalline phase without organic residues. By XRD, single-phase anatase with nanometre-sized crystallites was identified and, by XRF, the presence of the dopants was detected. The surface and the oxidation states of the samples prepared by the sol−gel method and thermally treatment method investigated by XPS confirmed, also, the presence of Ti 2p, O 1s, Zn 2p and Cu 2p core levels. The textural characterization of the TiO$_2$ doped with Cu or Zn causes a decrease in surface area by 40% and 20%, respectively. Compared to undoped TiO$_2$, it shows a contraction of 10% upon doping with Cu and an increase of 10% upon doping with Zn, respectively. The photocatalytic activity of doped TiO$_2$ increased under visible light irradiation compared to the undoped TiO$_2$ due to the newly formed sub-bands and to the active centres located on the surface, thus facilitating the photodegradation process. In the UV domain, a relation between the crystalline domain sizes and the photocatalytic discoloration of methyl orange was noticed. This paper examined the inhibitory effect determined by TiO$_2$ nanopowders against *S. aureus*. The results of the antimicrobial test confirmed a considerable antimicrobial activity against gram-positive bacteria of the doped nanopowders.

4. Materials and Methods

4.1. Sample Preparation

Nanopowders of Cu− or Zn−doped TiO$_2$ were prepared by the sol−gel method. The initial calculated compositions corresponding to a TiO$_2$:CuO or TiO$_2$:ZnO molar percentage of 98:2 were chosen. The reaction started from titanium (IV) butoxide [TBOT = Ti(OC$_4$H$_{10}$)$_4$] (Merck) as a precursor of TiO$_2$ and copper nitrate [Cu(NO$_3$)$_2$·3H$_2$O] (Merck) as a precursor of CuO or zinc nitrate [Zn(NO$_3$)$_2$·6H$_2$O] (Merck) as a precursor of ZnO. Butanol [C$_4$H$_9$-OH] (J.T. Baker) was used as the solvent, H$_2$O as the hydrolysis agent, and ammonium hydroxide [NH$_4$OH] (Riedel-de Haën) as the catalyst. The synthesis took place at room temperature and the solution of reagents was homogenized for 60 min. The oxide powder was separated by filtration from the solution, washed with distilled water to remove adsorbed compounds, dried and then thermally treated at 500 °C, in air, with a plateau of 1 h and a heating rate of 1 °C/min, in order to eliminate the water and organic residues and to obtain crystallized nanometre-sized powders. A flowchart of the methodology used for the sample preparation is given in Figure 16. The thermal treatment was established based on the TG/DTG/DTA results.

The samples were denoted (TiO$_2$−Cu 2.0%) and (TiO$_2$−Zn 2.0%), and the thermally treated samples (TiO$_2$−Cu 2.0% TT) and (TiO$_2$−Zn 2.0% TT), respectively.

The composition of the solutions and the experimental conditions used are shown in Table 7.

The synthesis procedure for the sample Ti−Bu−SG was described in our previous work (ref. [43]).
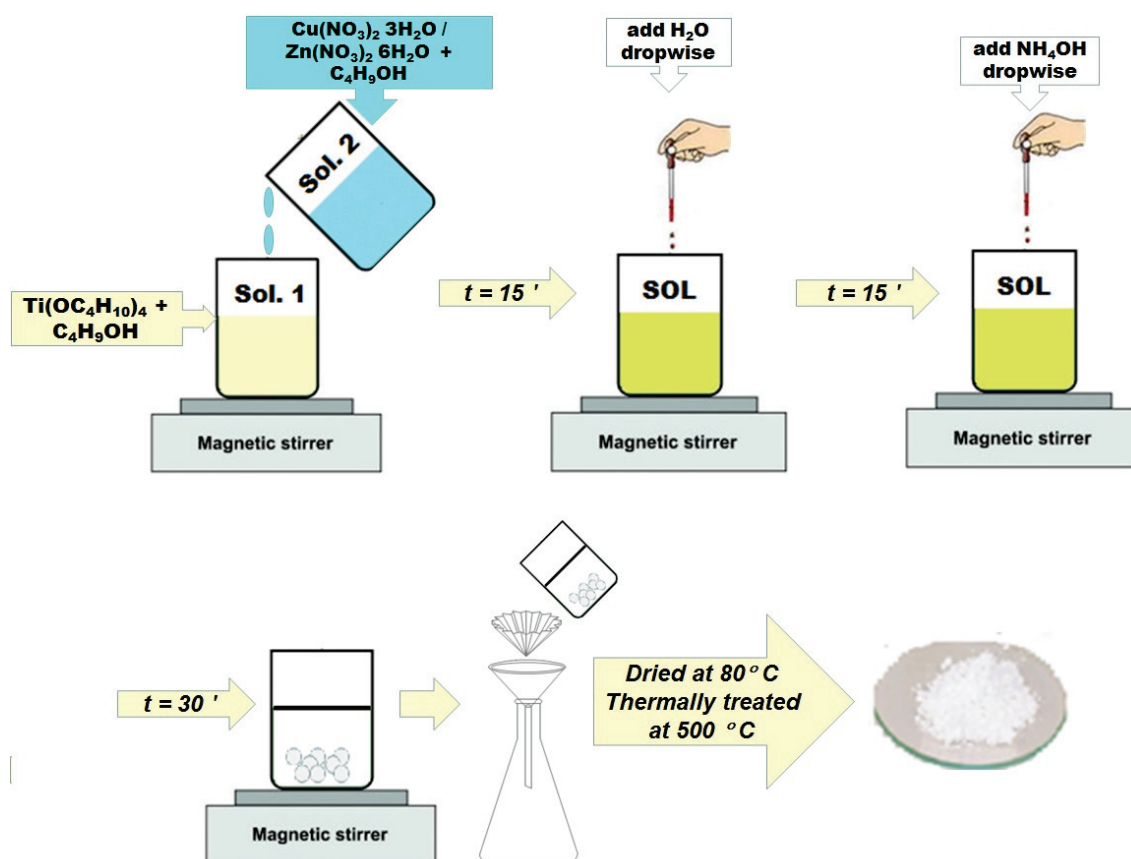
Figure 16. The flowchart of the sample preparation by sol-gel method.

Table 7. The composition of the solution and the experimental parameters of the sol preparation.

Sample	Precursors	Molar Ratio			pH Sol	Experimental Conditions	
		$\frac{ROH}{\sum precursor}$	$\frac{H_2O}{\sum precursor}$	$\frac{catalyst}{\sum precursor}$		T (°C)	t (h)
TiO_2-Cu 2.0%	$Ti(OC_4H_{10})_4$ + $Cu(NO_3)_2 \cdot 3H_2O$	36.5	3	0.003	10	25	60
TiO_2-Zn 2.0%	$Ti(OC_4H_{10})_4$ + $Zn(NO_3)_2 \cdot 6H_2O$	36.5	3	0.003	10	25	60

ROH = C_4H_9-OH.

4.2. Methods of Characterization

The thermal behaviour of the as-prepared samples was determined by thermogravimetric and differential thermal analysis (TG/DTA) using Mettler Toledo TGA/SDTA 851e (Greifensee, Switzerland) equipment in open Al_2O_3 crucibles and in flowing air atmosphere. The maximum temperature was set at 800 °C and the heating rate was 10 °C/min.

SEM micrographics were recorded using FEI Quanta 3D FEG microscope (FEI, Brno, Czech Republic), operating at an accelerating voltage of 10 kV. The specimens were placed on conductive carbon tape and scanned in high vacuum mode in an uncoated state.

X−ray Photoelectron Spectroscopy (XPS) was performed in an AXIS Ultra DLD (Kratos Surface Analysis, Manchester, UK) system, using Al $K_{\alpha 1}$ (1486.74 eV) radiation produced by a monochromatized X−ray source at operating power of 240 W (12 kV × 20 mA) and a charge neutralizer operating at 1.7 A filament current, 2.8 V charge balance, 2.00 V filament bias. High-resolution core-level spectra were recorded using hybrid lens mode, 40 eV pass energy, and slot aperture. The binding energy scale was calibrated to the C 1s standard value of 284.6 eV. The core level spectra were deconvoluted using Voigt profiles, based on the methods described in ref. [44].

X−Ray Diffraction (XRD) patterns were recorded using a Rigaku Ultima IV X−ray diffractometer. The equipment was set in parallel beam geometry, with cross beam optics (CBO), operated at 40 kV and 30 mA, using CuKα radiation. The data were collected over the 2θ range 10−80° at a scanning rate of 2°/min. Rigaku's PDXL software, connected to ICDD PDF−2 database, was used for phase identification. Lattice constants were refined using the diffraction line position. The mean crystalline domain size is calculated from the diffraction line width. The diffraction line position and width were corrected by the external standard method.

X−ray fluorescence (XRF) was used for elemental analysis. The measurements were performed using a Rigaku ZSX Primus II spectrometer (Rigaku Corp., Tokyo, Japan), equipped with 4.0 kW X−ray Rh tube. EZ−scan combined with Rigaku SQX fundamental parameters software (standard less) was used for data analysis.

Gram−positive bacteria *Staphylococcus aureus* ATCC 25,923, purchased from the German Collection of Microorganisms and Cell Cultures (DSMZ) (Braunschweig, Germany), was used in the experiment. The working method for testing antibacterial activity of nanoparticle powders was as follows. First, the bacterial strain *Staphylococcus aureus* was replicated on the TSA (Tryptic Soy Agar) medium and incubated at 35 ± 2 °C for 24 h. The working inoculum was made by suspending 2–3 bacterial colonies in sterile physiological water (0.85%), obtaining turbidity of 3×10^5 CFU/mL, which was adjusted spectrophotometrically by measuring the absorbance. The study was carried out in 100-millilitre Erlenmeyer flasks with 30 mL culture medium. Doped TiO_2 nanopowders were tested using a concentration of 200 μg mL^{-1}. The nanoparticle powders were immersed in the Mueller Hinton broth (MHB) inoculated with 1 mL suspension of *Staphylococcus aureus* and incubated at 35 ± 2 °C for 24 h and 130 rpm. The composition of the culture media was Mueller Hinton broth from Scharlau, Sentmenat, Spain (1.5 g/L starch; 2 g/L meat extract; 17.5 g/L peptone). Tryptic Soy Agar from Scharlau, Sentmenat, Spain (2.5 g/L dextrose; 5 g/L sodium chloride; 20 g/L peptone; 2.5 g/L dipotassium phosphate; 15 g/L agar). Nanoparticle powders were also immersed in the culture medium without bacterial strain for the negative control. The positive biological control does not contain nanoparticle powders. The samples were inoculated in five replicates in 96-well plates, 200 μL in each well and incubated at 35 ± 2 °C for 24. After incubation, the absorbance was measured at 600 nm with the help of the Clariostar plate reader.

The inhibition rate (%) was determined using the following formula [54]:

$$\text{Inhibition of Efficiency (\%)} = \text{Control O.D.} \times \frac{\text{Test O.D.}}{\text{Control O.D.}} \times 100 \tag{1}$$

Nitrogen adsorption−desorption isotherms at 77 K were recorded on a Micromeritics ASAP 2020 automated gas adsorption system (Norcross, GA, USA). The samples were degassed at 200 °C for 5 h under vacuum before analysis.

The UV−Vis diffuse reflectance spectra were recorded on a JASCO V570 spectrophotometer (Tokyo, Japan). Photocatalytic experiments were carried out in batches with 5 mg photocatalyst in 10 mL methyl orange (MO) dye (1×10^{-5} M). The suspension was stirred during the experiment. The reaction mixture was first stirred in dark for 30 min in order to establish the adsorption of MO dye on the photocatalyst surface. Then it was irradiated in a closed box with an UV−Vis lamp at specific wavelengths. Photocatalytic experiments were performed for 300 min. There were taken the same aliquots of MO solution at regular time intervals and filtered using a 0.45 mm Millipore film in order to evaluate the progress of the reaction. The discoloration efficiency was evaluated as reported before [55].

Conflicts of Interest: The authors declare no conflict of interest.

References

1. Cao, G. *Nanostructures and Nanomaterials: Synthesis, Properties and Applications*; Imperial College Press: London, UK, 2004. [CrossRef]
2. Alagarasi, A. Chapter 1—Introduction to nanomaterials. In *Nanomaterials*; Viswanathan, B., Ed.; Narosa Publishing House: Mumbay, India, 2009; pp. 2–25.
3. Canas-Carrell, J.E.; Li, S.; Parra, A.M.; Shrestha, B. Chapter 10—Metal oxide nanomaterials: Health and environmental effects. In *Health and Environmental Safety of Nanomaterials*; Njuguna, J., Pielichowski, K., Zhu, H., Eds.; Woodhead Publishing: Kidlington, Oxford, UK, 2014; pp. 200–221. [CrossRef]
4. Athar, T. Chapter 14—Metal oxide nanopowder. In *Micro and Nano Technologies, Emerging Nanotechnologies for Manufacturing*, 2nd ed.; Ahmed, W., Jackson, M.J., Eds.; William Andrew Publishing: San Diego, CA, USA, 2015; pp. 343–401. [CrossRef]
5. Athar, T. Chapter 17—Smart precursors for smart nanoparticles. In *Micro and Nano Technologies, Emerging Nanotechnologies for Manufacturing*, 2nd ed.; Ahmed, W., Jackson, M.J., Eds.; William Andrew Publishing: San Diego, CA, USA, 2015; pp. 444–538. [CrossRef]
6. Banerjee, A.N. The design, fabrication, and photocatalytic utility of nanostructured semiconductors: Focus on TiO_2-based nanostructures. *Nanotechnol. Sci. Appl.* **2011**, *4*, 35–65. [CrossRef] [PubMed]
7. Huang, F.; Yan, A.; Zhao, H. Chapter 2—Influences of Doping on Photocatalytic Properties of TiO2 Photocatalyst. In *Semiconductor Photocatalysis—Materials, Mechanisms and Applications*; Cao, W., Ed.; IntechOpen: London, UK, 2016; pp. 31–80.
8. Pandele-Cușu, J.; Atkinson, I.; Rusu, A.; Apostol, N.; Teodorescu, V.; Predoană, L.; Szilágyi, I.M.; Pokol, G.; Zaharescu, M. Thermal behavior of Cu-doped TiO_2 gels synthesized by the sol-gel method. *Rev. Roum. Chim.* **2021**, *66*, 221–229. [CrossRef]
9. Stanciu, I.; Predoană, L.; Pandele-Cușu, J.; Preda, S.; Anastasescu, M.; Vojisavljević, K.; Malič, B.; Zaharescu, M. Thermal behaviour of the TiO_2 based gels obtained by microwaves assisted sol-gel method. *J. Therm. Anal. Calorim.* **2017**, *130*, 639–651. [CrossRef]
10. Gomez-Polo, C.; Larumbe, S.; Gil, A.; Muñoz, D.; Fernández, L.R.; Barquín, L.F.; García-Prieto, A.; Fdez-Gubieda, M.L.; Muela, A. Improved photocatalytic and antibacterial performance of Cr doped TiO_2 nanoparticles. *Surf. Interfaces* **2021**, *22*, 100867. [CrossRef]
11. Shen, J.-H.; Chuang, H.-Y.; Jiang, Z.-W.; Liu, X.-Z.; Horng, J.-J. Novel quantification of formation trend and reaction efficiency of hydroxyl radicals for investigating photocatalytic mechanism of Fe-doped TiO_2 during UV and visible light-induced degradation of acid orange. *Chemosphere* **2020**, *251*, 126380. [CrossRef]
12. Matias, M.L.; Pimentel, A.; Reis-Machado, A.S.; Rodrigues, J.; Deuermeier, J.; Fortunato, E.; Martins, R.; Nunes, D. Enhanced Fe-TiO2 Solar Photocatalysts on Porous Platforms for Water Purification. *Nanomaterials* **2022**, *12*, 1005. [CrossRef]
13. Zhou, Y.; Zhang, Q.; Shi, X.; Song, Q.; Zhou, C.; Jiang, D. Photocatalytic reduction of CO_2 into CH_4 over Ru-doped TiO_2: Synergy of Ru and oxygen vacancies. *J. Colloid Interf. Sci.* **2022**, *608*, 2809–2819. [CrossRef]
14. Mancuso, A.; Morante, N.; De Carluccio, M.; Sacco, O.; Rizzo, L.; Fontana, M.; Esposito, S.; Vaiano, V.; Sannino, D. Solar driven photocatalysis using iron and chromium doped TiO_2 coupled to moving bed biofilm process for olive mill wastewater treatment. *Chem. Eng. J.* **2022**, *45015*, 138107. [CrossRef]
15. Piątkowska, A.; Janus, M.; Szymański, K.; Mozia, S. C-,N- and S-Doped TiO_2 Photocatalysts: A Review. *Catalysts* **2021**, *11*, 144. [CrossRef]
16. Li, X.; Wen, J.; Low, J.; Fang, Y.; Yu, J. Design and fabrication of semiconductor photocatalyst for photocatalytic reduction of CO_2 to solar fuel. *Sci. China Mater.* **2014**, *57*, 70–100. [CrossRef]
17. Ran, J.; Jaroniec, M.; Qiao, S.-Z. Cocatalysts in Semiconductor-based Photocatalytic CO_2 Reduction: Achievements, Challenges, and Opportunities. *Adv. Mater.* **2018**, *30*, 1704649. [CrossRef] [PubMed]
18. Qin, Q.; Wang, J.; Xia, Y.; Yang, D.; Zhou, Q.; Zhu, X.; Feng, W. Synthesis and Characterization of Sn/Ni Single Doped and Co–Doped Anatase/Rutile Mixed–Crystal Nanomaterials and Their Photocatalytic Performance under UV–Visible Light. *Catalysts* **2021**, *11*, 1341. [CrossRef]
19. Bachvarova-Nedelcheva, A.; Yordanov, S.; Iordanova, R.; Stambolova, I.; Stoyanova, A.; Georgieva, N.; Nemska, V. The Influence of Nd and Sm on the Structure and Properties of Sol-Gel-Derived TiO_2 Powders. *Molecules* **2021**, *26*, 3824. [CrossRef] [PubMed]
20. Tahmasebizad, N.; Hamedani, M.T.; Shaban Ghazani, M.; Pazhuhanfar, Y. Photocatalytic activity and antibacterial behavior of TiO_2 coatings co-doped with copper and nitrogen via sol–gel method. *J. Sol-Gel. Sci. Technol.* **2020**, *93*, 570–578. [CrossRef]

21. Nakamura, M.; Ono, A.; Bae, E.; Murakami, N.; Ohno, N. Improvement of visible light responsivity of rutile TiO$_2$ nanorods by site-selective modification of iron (III) ion on newly exposed faces formed by chemical etching treatment. *Appl. Catal. B* **2013**, *130*, 264–269. [CrossRef]
22. Savio, A.K.P.D.; Fletcher, J.; Hernandez, F.R. Sonosynthesis of nanostructured TiO$_2$ doped with transition metals having variable bandgap. *Ceram. Int.* **2013**, *39*, 2753–2765. [CrossRef]
23. Suzuki, K.; Yokoi, T.; Iwatsu, M.; Furuya, M.; Yokota, K.; Mokudai, T.; Kanetaka, H.; Kawashita, M. Antibacterial properties of Cu-doped TiO$_2$ prepared by chemical and heat treatment of Ti metal. *J. Asian Ceram. Soc.* **2021**, *9*, 1448–1456. [CrossRef]
24. Wang, Y.; Yang, H.; Xue, X. Synergistic antibacterial activity of TiO$_2$ co-doped with zinc and yttrium. *Vacuum* **2014**, *107*, 28–32. [CrossRef]
25. Shaikh, S.; Nazam, N.; Mohd, S.; Rizvi, D.; Ahmad, K.; Baig, M.H.; Lee, E.J.; Choi, I. Mechanistic Insights into the Antimicrobial Actions of Metallic Nanoparticles and Their Implications for Multidrug Resistance. *Int. J. Mol. Sci.* **2019**, *20*, 2468. [CrossRef]
26. Kumar, S.G.; Rao, K.S.R.K. Polymorphic phase transition among the titania crystal structures in solution based approach: From precursor chemistry to nucleation process. *Nanoscale* **2014**, *6*, 11574–11632. [CrossRef]
27. Lu, C.W.; Cao, Y.; Li, H.; Webb, C.; Pan, W.P. Synthesis of TiO$_2$ based on hydrothermal methods using elevated pressures and microwave conditions. *J. Therm. Anal. Calorim.* **2014**, *116*, 1241–1248. [CrossRef]
28. Bregadiolli, B.A.; Fernandes, S.L.; Graef, C.F.O. Easy and Fast Preparation of TiO$_2$—Based Nanostructures Using Microwave Assisted Hydrothermal Synthesis. *Mater. Res.* **2017**, *20*, 912–919. [CrossRef]
29. Falk, G.S.; Borlaf, M.; López-Muñoz, M.J.; Farinas, J.C.; Rodrigues Neto, J.B.; Moreno, R. Microwave-assisted synthesis of TiO$_2$ nanoparticles: Photocatalytic activity of powders and thin films. *J. Nanopart. Res.* **2018**, *20*, 23. [CrossRef]
30. Kéri, O.; Kocsis, E.; Karajz, D.A.; Nagy, Z.K.; Parditka, B.; Erdélyi, Z.; Szabó, A.; Hernádi, K.; Szilágyi, I.M. Photocatalytic Crystalline and Amorphous TiO$_2$ Nanotubes Prepared by Electrospinning and Atomic Layer Deposition. *Molecules* **2021**, *26*, 5917. [CrossRef] [PubMed]
31. Vinogradov, A.V.; Vinogradov, V.V. Low-temperature sol–gel synthesis of crystalline materials. *RSC Adv.* **2014**, *4*, 45903–45919. [CrossRef]
32. Nachit, W.; Ait Ahsaine, H.; Ramzi, Z.; Touhtouh, S.; Goncharova, I.; Benkhouja, K. Photocatalytic activity of anatase-brookite TiO$_2$ nanoparticles synthesized by sol gel method at low temperature. *Opt. Mater.* **2022**, *129*, 112256. [CrossRef]
33. Sadek, O.; Touhtouh, S.; Rkhis, M.; Anoua, R.; El Jouad, M.; Belhora, F.; Hajjaji, A. Synthesis by sol-gel method and characterization of nano-TiO$_2$ powders. *Mater. Today Proc.* **2022**, *66*, 456–458.
34. Szołdra, P.; Frąc, M.; Pichór, W. Effect of sol composition on the properties of TiO$_2$ powders obtained by the sol–gel method. *Powder Technol.* **2021**, *387*, 261–269. [CrossRef]
35. Keshari, A.K.; Choudhary, P.; Shukla, V.K. Precursor induced evolution in single anatase phase synthesis of TiO$_2$ nanoparticles for water treatment and dye-sensitized solar cell. *Phys. B Condens. Matter* **2022**, *631*, 413716. [CrossRef]
36. Rathore, N.; Kulshreshtha, A.; Shukla, R.K.; Sharma, D. Study on morphological, structural and dielectric properties of sol–gel derived TiO$_2$ nanocrystals annealed at different temperatures. *Phys. B Condens. Matter* **2020**, *582*, 411969. [CrossRef]
37. Schmidt, H. Chemistry of material preparation by the sol–gel process. *J. Non-Cryst. Solids* **1998**, *100*, 51–64. [CrossRef]
38. Sakka, S.; Kamya, K. The Sol–Gel Transition in the Hydrolysis of Metal Alkoxides in Relation to Formation of Glass Fibers and Films. *J. Non-Cryst. Solids* **1982**, *48*, 31–46. [CrossRef]
39. ThermoFisher Scientific XPS Database. Available online: https://www.thermofisher.com/ro/en/home/materials-science/learning-center/periodic-table/transition-metal/titanium.html (accessed on 26 September 2022).
40. *NIST X-ray Photoelectron Spectroscopy Database, NIST Standard Reference Database Number 20*; Version 4.1, Last Update to Data Content: 2012, (retrieved 26 September 2022), 20899; National Institute of Standards and Technology: Gaithersburg, MD, USA, 2000. [CrossRef]
41. ThermoFisher Scientific XPS Database. Available online: https://www.thermofisher.com/ro/en/home/materials-science/learning-center/periodic-table/transition-metal/copper.html (accessed on 26 September 2022).
42. Wagner, C.D.; Davis, L.E.; Zeller, M.V.; Taylor, J.A.; Raymond, R.M.; Gale, L.H. Empirical atomic sensitivity factors for quantitative analysis by electron spectroscopy for chemical analysis. *Surf. Interface Anal.* **1981**, *3*, 211–225. [CrossRef]
43. Pandele-Cuşu, J.; Petrescu, S.; Preda, S.; Petcu, G.; Ciobanu, M.; Predoană, L. Comparative study of the TiO$_2$ nanopowders prepared from diferent precursors and chemical methods for heterogeneous photocatalysis application. *J. Therm. Anal. Calorim.* **2022**. [CrossRef]
44. Teodorescu, C.M.; Esteva, J.M.; Karnatak, R.C.; El Afif, A. An approximation of the Voigt I profile for the fitting of experimental X-ray absorption data. *Nucl. Instrum. Meth. Phys. Res. A* **1994**, *345*, 141–147. [CrossRef]
45. Fruth, V.; Todan, L.; Codrea, C.I.; Poenaru, I.; Petrescu, S.; Aricov, L.; Ciobanu, M.; Jecu, L.; Ion, R.M.; Predoana, L. Multifunctional Composite Coatings Based on Photoactive Metal-Oxide Nanopowders (MgO/TiO$_2$) in Hydrophobic Polymer Matrix for Stone Heritage Conservation. *Nanomaterials* **2021**, *11*, 2586. [CrossRef] [PubMed]
46. Khashan, K.S.; Sulaiman, G.M.; Abdulameer, F.A.; Albukhaty, S.; Ibrahem, M.A.; Al-Muhimeed, T.; AlObaid, A.A. Antibacterial Activity of TiO$_2$ Nanoparticles Prepared by One-Step Laser Ablation in Liquid. *Appl. Sci.* **2021**, *11*, 4623. [CrossRef]
47. Azizi-Lalabadi, M.; Ehsani, A.; Divband, B.; Alizadeh-Sani, M. Antimicrobial activity of Titanium dioxide and Zinc oxide nanoparticles supported in 4A zeolite and evaluation the morphological characteristic. *Sci. Rep.* **2019**, *9*, 17439. [CrossRef]

48. Sing, K.S.W. Reporting Physisorption Data for Gas/Solid Systems with Special Reference to the Determination of Surface Area and Porosity (Recommendations 1984). *Pure Appl. Chem.* **1985**, *57*, 603–619. [CrossRef]

49. Fageria, P.; Gangopadhyay, S.; Pande, S. Synthesis of ZnO/Au and ZnO/Ag nanoparticles and their photocatalytic application using UV and visible light. *RSC Adv.* **2014**, *4*, 24962–24972. [CrossRef]

50. Colon, G.; Maicu, M.; Hidalgo, M.C.; Navıo, J.A. Cu-doped TiO$_2$ systems with improved photocatalytic activity. *Appl. Catal. B Environ.* **2006**, *67*, 41–51. [CrossRef]

51. Augilar, T.; Novas, J.; Alcantara, R. A route for the synthesis of Cu-doped TiO$_2$ nanoparticles with a very low band gap. *Chem. Phys. Lett.* **2013**, *571*, 49–53. [CrossRef]

52. Perkgoz, N.K.; Toru, R.S.; Unal, E.; Sefunc, M.A.; Tek, S.; Mutlugun, E.; Soganci, I.M.; Celiker, H.; Celiker, G.; Demir, H.V. Photocatalytic Hybrid Nanocomposites of Metal Oxide Nanoparticles Enhanced Towards the Visible Spectral Range. *Appl. Catal. B* **2011**, *105*, 77–85. [CrossRef]

53. Navas, J.; Sánchez-Coronilla, A.; Aguilar, T.; Hernández, N.C.; de los Santos, D.M.; Sánchez-Márquez, J.; Zorrilla, D.; Fernández-Lorenzo, C.; Alcántara, R.; Martín-Calleja, J. Experimental and theoretical study of the electronic properties of Cu-doped anatase TiO$_2$. *Phys. Chem. Chem. Phys.* **2014**, *16*, 3835–3845. [CrossRef] [PubMed]

54. Mahdy, S.A.; Raheed, Q.J.; Kalaichelvan, P. Antimicrobial activity of zero-valent iron nanoparticles. *IJMER* **2012**, *2*, 578–581.

55. Gingașu, D.; Mîndru, I.; Culiță, D.C.; Predoană, L.; Petcu, G.; Ciobanu, M.; Preda, S.; Pandele-Cușu, J.; Petrescu, S. MgO obtained by chemical and green synthesis methods and applied in photocatalytic degradation of methyl orange. *Rev. Roum. Chim.* **2021**, *66*, 463–473. [CrossRef]

A Multifractal Vision of 5-Fluorouracil Release from Chitosan-Based Matrix

Maria-Alexandra Paun [1,2] , Vladimir-Alexandru Paun [3] and Viorel-Puiu Paun [4,5,*]

1 School of Engineering, Swiss Federal Institute of Technology (EPFL), 1015 Lausanne, Switzerland
2 Division Radio Monitoring and Equipment, Section Market Access and Conformity, Federal Office of Communications (OFCOM), 2501 Bienne, Switzerland
3 Five Rescue Research Laboratory, 75004 Paris, France
4 Physics Department, Faculty of Applied Sciences, University Politehnica of Bucharest, 060042 Bucharest, Romania
5 Academy of Romanian Scientists, 050085 Bucharest, Romania
* Correspondence: viorel.paun@physics.pub.ro or viorel_paun2006@yahoo.com

Abstract: A suite of four drug deliverance formulations grounded on 5-fluorouracil enclosed in a chitosan-founded intercellular substance was produced by 3,7-dimethyl-2,6-octadienal with in situ hydrogelation. The formulations have been examined from a morphological and structural point of view by Fourier transform infrared (FTIR) spectroscopy and microscopy with polarized light, respectively. The polarized optical microscopy (POM) pictures of the three representative formulations obtained were investigated by fractal analysis. The fractal dimension and lacunarity of each of them were thus calculated. In this paper, a novel theoretical method for mathematically describing medicament deliverance dynamics in the context of the polymeric medicament constitution limit has been advanced. Assuming that the polymeric drug motion unfolds only on the so-called non-differentiable curves (considered mathematically multifractal curves), it looks like in a one-dimensional hydrodynamic movement within a multifractal formalism, the drug-release physics models are provided by isochronous kinetics, but at a scale of resolution necessarily non-differentiable.

1. Introduction

A topical field of pharmaceutical research is the development of new semi-solid pharmaceutical systems as potential vehicles for the topical release of medicinal substances using excipients of natural origin. The benefits presented by these types of formulations are determined both by the diversity of excipients and by their particularly advantageous specific properties, namely, relative abundance, biocompatibility, biodegradability, non-irritability, innocuousness, and low-cost price. Hydrogels represent an important category of ointment bases, and are frequently used in the formulation of dermatological and cosmetic preparations due to the many advantages they offer. This group also includes biocompatible hydrogels based on natural polymers (e.g., chitosan, pectins, gums) which have been intensively studied in the last decade due to the benefits provided by the specific characteristics of the gel-forming agents.

An initial direction of research was aimed at the development and pharmaco-technical characterization of some hydrogel bases containing a natural hydrophilic polymer, chitosan, as a gelling agent, and different co-solvents able to incorporate and dissolve a large number of medicinal substances insoluble in water. At this stage of the study, the influence of the type and concentration of the co-solvent on the physico-chemical and rheological characteristics of the hydrogel bases with chitosan in different concentrations was evaluated. At the second stage of the experimental research, the possibility of formulating and preparing

new biocompatible topical hydrogels based on chitosan together with different natural absorption promoters was investigated.

Chitosan-based pharmaceutical compounds are of great interest in the medicament delivery domain, and are suitable due to their inherent properties of biocompatibility, degradation comportment, and biodegradability, which are advised for current practices in vivo [1–3]. In order to further ameliorate chitosan's capacity to anchor great medicaments' quantity and to liberate them in a supervised fashion, a lot of tests consisting particularly of chitosan composition crosslinking by different agents have been designed. In this line of conduct, an ecological method was detailed by crosslinking chitosan with eco-friendly products of the monoaldehyde type [4]. The mentioned procedure was found to be a remarkable one, delivering hydrogels whose properties of an aldehyde nature were easily commanded. Therefore, by utilizing the native aldehyde 3,7-dimethyl-2,6-octadienal, well known typically as a right commercial denomination by citral, hydrogels with superior biocompatibility, biodegradability, non-toxic, and non-irritating qualities and with their own antifungal activity were achieved for matrix components for medicament release systems.

Principally, the approach that will be made in the present work, otherwise known as the fractal manner of pharmaco-kinetics (PK) attitude, assumes the utilization of fractal analysis and fractional calculus. Additionally, by increasing the accuracy of performance on the fractal dimension and lacunarity notion, maximum confidence will be achieved when interpreting the images obtained through microscopy. Similarly, it is possible in the context of the analysis of several compartments [5] to successfully describe the polymeric networks' dynamics and diffusion in porous fractal media. It can be said that, recently, the analysis of several compartments by PK has allowed the modeling of processes such as medication dissolution [6], drug absorption [7], as well as real distribution, together with arranging the constituent parts to achieve the whole [8].

Other things worth mentioning in the introduction are studies that refer to the design of biocompatible chitosan with a high photothermal conversion capability [9], ultrathin fibers and their antibacterial food packaging applications [10] and, last but not least, electrospun structural nanohybrids combining three composites for fast helicopter delivery [11].

In the presented context, special attention was paid to the open problem related to the time development of the kinetics dependent on the major bio-molecular reactions [6]. In continuation, we can say that the compartmental ideal analysis, the newest method for reporting drug delivery dynamics in elaborate systems (operating at a level of fractional derivatives or alternative ordinary procedures utilized in PK), can be depicted, including non-differentiable curves (named multifractal curves).

Afterwards, as a work alternative with a single mathematical variable represented by a non-differentiable rigid function, it is feasible that we trust only in the approximations of these mathematically defined functions, procured by averaging functions at various scales of determination–resolution. In the aftermath, all proposed variables to depict drug delivery processes will continue to work as the mathematical functions are limited, thus dictating a life with non-differentiable character in the case of scale-zero/nil value resolutions differentiable in different circumstances. Ultimately, the theoretical multifractal model is consequently certified by the empirical experimental data associated with the 5-fluorouracil deliverance out of the chitosan-founded matrix.

2. Results and Discussion

Theoretical Model

Typical investigations on drug-release kinetics deliver significant information on chemical systems' function. To better explain the subtle transport mechanism and the structure versus function connection of a chemical system, it is decisive to diminish the difference between the experimental macroscopic data and the transport comportment at the atomic and molecular structural level. Obviously, the transport mechanisms at the microscopic level will prevail; these are mechanisms that we also have in mind for the model proposed in the article.

In these circumstances of pharmaco-kinetic behavioral consideration, a novel theoretical method for mathematically describing medicament deliverance kinetics, in the context of the polymeric medicament constitution limit, is advanced [12,13]. Presuming that the polymeric medicament dynamics unfolds only on the so-called non-differentiable curves (considered mathematically multifractal curves), it looks like in a one-dimensional hydrodynamic conventionalism of multifractal arguments, the drug-release physics models are provided by kinetics of synchronous type, but at a scale of resolution necessarily non-differentiable.

The one-dimensional multifractal hydrodynamic equation [11–15] is

$$\frac{\partial}{\partial t}V_D + V_D \frac{\partial}{\partial x}V_D = -\frac{\partial}{\partial x}\left[-2\lambda(dt)^{\left[\frac{4}{f(\alpha)}\right]-2} \frac{\frac{\partial}{\partial x}\left(\frac{\partial}{\partial x}\sqrt{\rho}\right)}{\sqrt{\rho}} \right] \tag{1}$$

$$\frac{\partial}{\partial t}\rho + \frac{\partial}{\partial x}(V_D\rho) = 0 \tag{2}$$

In the communicated expressions above, x is the fractal spatial coordinate (one-dimensional), t is the classical (non-fractal) time which plays the role of an affine parameter within the movement curves [14,15]. The speed V_D is the differential velocity (scale resolution dt, independent of time), the function $f(\alpha)$ is the singularity spectrum, α is dependent, and $\sqrt{\rho}$ is a function of the state's amplitude.

The initial conditions (3) and boundary conditions (4) of the above equations are

$$V_D(x, t = 0) = V_0, \quad \rho(x, t = 0) = \frac{1}{\sqrt{\pi\alpha}}exp\left[-\left(\frac{x}{\alpha}\right)^2\right] \tag{3}$$

$$V_D(x = V_0 t) = V_0, \quad \rho(x = -\infty, t) = \rho(x = +\infty, t) = 0 \tag{4}$$

where V_0 is the initial speed, while α is the Gaussian distribution parameter of the position variable x.

According to the mathematical procedures recommended in bibliographical references [16], differential Equations (1) and (2) accept the following solutions

$$V_D(x, t, \sigma, \alpha) = \frac{V_0\alpha^2 + \left(\frac{\sigma}{\alpha}\right)^2 xt}{\alpha^2 + \left(\frac{\sigma}{\alpha}\right)^2 t^2} \tag{5}$$

$$\rho(x, t, \sigma, \alpha) = \frac{\pi^{-1/2}}{\left(\alpha^2 + \left(\frac{\sigma}{\alpha}\right)^2 t^2\right)^{1/2}} \exp\left[-\frac{(x - V_0 t)^2}{\alpha^2 + \left(\frac{\sigma}{\alpha}\right)^2 t^2}\right] \tag{6}$$

where

$$\sigma = \lambda(dt)^{\left[\frac{2}{f(\alpha)}\right]-1} \tag{7}$$

is the multifractal degree.

According to the stated fractal theory, the non-differentiable velocity V_F will have the formula

$$V_F(x, t, \sigma, \alpha) = \sigma \frac{(x - V_0 t)}{\alpha^2 + \left(\frac{\sigma}{\alpha}\right)^2 t^2} \tag{8}$$

By inserting the dimensionless variables in the above expressions

$$\xi = \frac{x}{V_0\tau_0}, \quad \eta = \frac{t}{\tau_0} \tag{9}$$

as well as the dimensionless parameters

$$\mu = \frac{\sigma\tau_0}{\alpha^2}, \quad \phi = \frac{\alpha}{V_0\tau_0} \tag{10}$$

where τ_0 is named specific time. Formulas (5), (6) and (8) are written as

$$V \equiv V_D(\xi, \eta, \mu) = \frac{V_D(x, t, \sigma, \alpha)}{V_0} = \frac{1 + \mu^2 \xi \eta}{1 + \mu^2 \eta^2} \tag{11}$$

$$\rho(\xi, \eta, \mu, \phi) = \pi^{\frac{1}{2}} \alpha \rho(x, t, \sigma, \alpha) = \left(1 + \mu^2 \eta^2\right)^{-\frac{1}{2}} exp\left[-\frac{(\xi - \eta)^2}{\phi^2(1 + \mu^2 \eta^2)}\right] \tag{12}$$

$$U \equiv V_F(\xi, \eta, \mu) = \frac{V_F(x, t, \sigma, \alpha)}{V_0} = \mu\frac{(\xi - \eta)}{1 + \mu^2 \eta^2} \tag{13}$$

In Figure 1a,b, 3D plot representations of the $U(\xi, \eta)$ multifractal function are presented for two distinct sets of variable values ξ and η, utilized for drug-release analysis.

(**a**) (**b**)
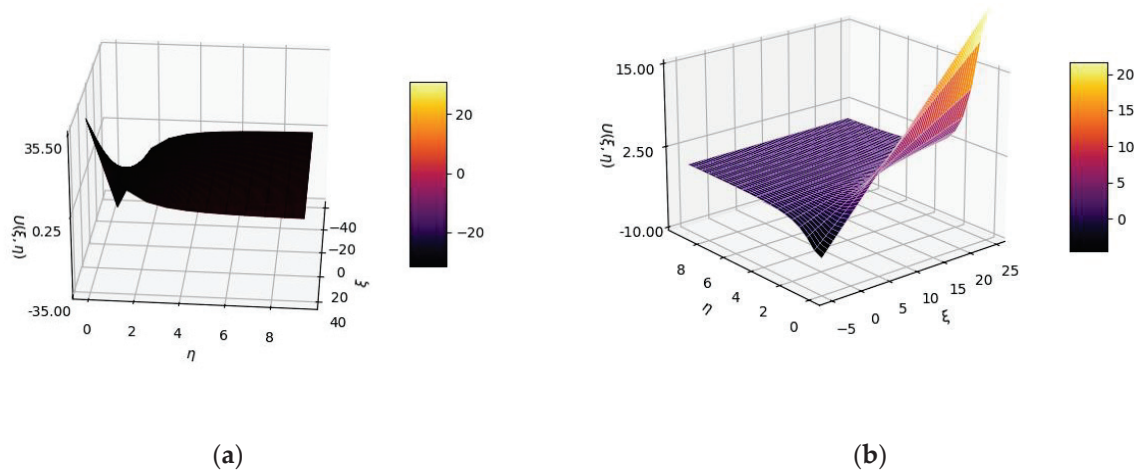
Figure 1. Three-dimensional plot representations of $U(\xi, \eta)$ multifractal function for two distinct sets of variable values ξ and η: (**a**) ξ from -40 to 40; η from 0 to 10; (**b**) ξ from -5 to 25; η from 0 to 10.

In Figure 2, 3D plot representations of the $V(\xi, \eta)$ multifractal function are presented for two distinct sets of variable values ξ and η, utilized for drug-release analysis.

(**a**) (**b**)
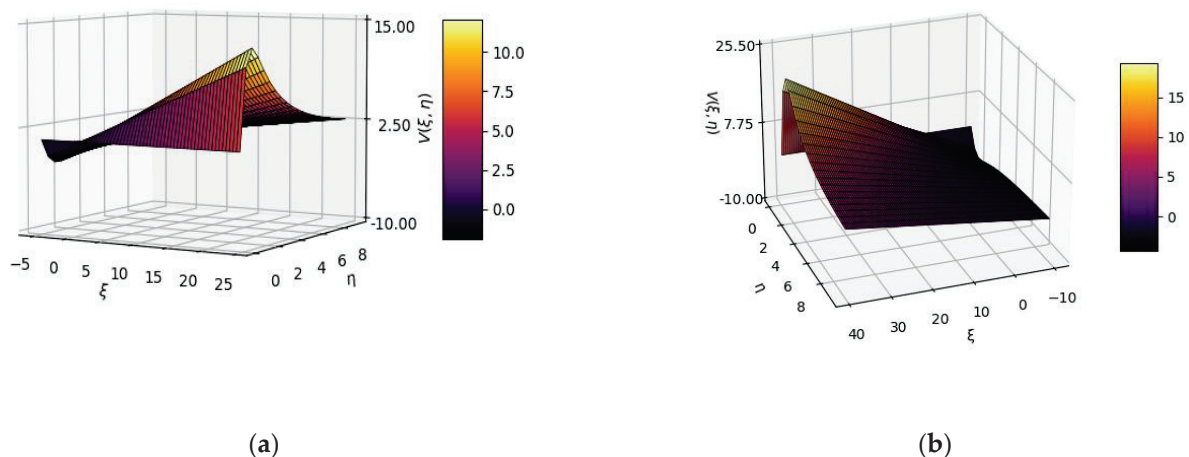
Figure 2. Three-dimensional plot representations of $V(\xi, \eta)$ multifractal function for two distinct sets of variable values ξ and η: (**a**) ξ from -5 to 25; η from 0 to 10; (**b**) ξ from -40 to 40; η from 0 to 10.

If we now make the ratio between U and V, respectively, U/V, we obtain a homographic expression dependent of ξ and η, as presented below:

$$\frac{U}{V} = \frac{\mu(\xi - \eta)}{1 + \mu^2 \xi \eta} \tag{14}$$

In Figure 3, 3D plot representations of the U/V multifractal function, with expressions dependent of the ξ and η variables, are presented.
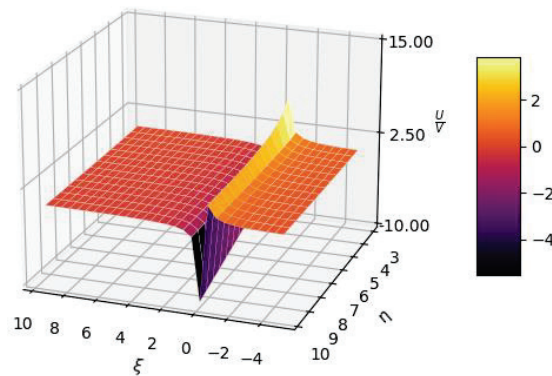
Figure 3. Three-dimensional plot representations of U/V multifractal function.

In the case of the condition validity in which the differential of the ratio U/V is zero (so-called dynamic simultaneity)

$$d\left(\frac{U}{V}\right) = \frac{dU - dV}{V^2} = 0 \Leftrightarrow V = constU \tag{15}$$

we have between U and V the relationship $V = constU$.

This coincides with the prolongation of the Newton first principle to any scale resolution, or similarly, with to the "synchronizations" of drug-release dynamics at a non-differentiable scale. Additionally, it can be mentioned that the varied "mechanisms" implicated in drug-release activity may be mimicked by doubling the period, or a manifested quasi-periodicity and the process' intermittent solicitations [15].

Following the activation of Restriction (15), in the formulation V=-U and Equations (1) and (2), the multifractal-type conservation laws become a unique multifractal equation, a law of "diffusion" type

$$\partial_t \rho = \lambda (dt)^{\left[\frac{2}{f(\alpha)}\right] - 1} \partial_l \partial^l \rho = \sigma \partial_l \partial^l \rho \tag{16}$$

As an immediate result, these evidentiated mechanisms manifests themselves as diffusion processes in a multifractal space but at diverse scale resolutions, which can be at large classified in the category of Fickian diffusion (when polymer relaxation time t_r is much greater than the value t_d, characteristic solvent diffusion time) or, as non-Fickian-type diffusion (when $t_r \approx t_d$), with the same ease. If the medicament release is of the multifractal type and takes place in a perfect immersed state, the initial conditions and conditions at the boundary are accepted

$$t = 0, \ -\frac{\alpha}{2} < x < \frac{\alpha}{2}, \ \rho = \rho_0 t > 0, \ x = \pm\frac{\alpha}{2}, \ \rho = \rho_1 \tag{17}$$

wherein ρ_0 is the primary drug density of the multifractal-type states, as part of the fractal-type "mechanism" used, and ρ_1 is the current medicament density according to

polymer–fluid fractal interdependence. The equation solution in the given conditions may now be presented in the complex form as below [16]:

$$f = \frac{\rho_t}{\rho_\infty} = 2\left(\frac{\sigma t}{\delta^2}\right)^{\frac{1}{2}} = \left\{\pi^{-1/2} + \sum_{n=1}^{\infty} (-1)^n erfc\left[\frac{n\delta}{2(\sigma t)^{\frac{1}{2}}}\right]\right\} \tag{18}$$

A precise expression was achieved for little values of time t

$$f = \frac{\rho_t}{\rho_\infty} = 2\left(\frac{\sigma t}{\delta^2}\right)^{\frac{1}{2}} = const(t)^{\frac{1}{2}} \tag{19}$$

In these circumstances, the ratio $\frac{\rho_t}{\rho_\infty}$ can be approved as an equivalent dissolved drug fraction, i.e., $\frac{M_t}{M_\infty} \equiv \frac{\rho_t}{\rho_\infty}$, where M_t is the drug quantity dissolved in time t and M_∞ is the drug quantity dissolved in the total time, considering that the pharmaceutical graduation shape has been already exhausted.

The function f depends on t, and σ plays the role of the parameter. In Figure 4, a 2D curve is obtained for a fixed value of the parameter. Thus, the black color represents the value $\sigma = 1$, the blue color represents $\sigma = 2$, the red color represents $\sigma = 3$, the green color represents $\sigma = 4$, and the olive color represents $\sigma = 5$. In Figure 4, a 3D function $f = f(t, \sigma)$ is considered by three variables; one allows the variation of σ continuously with a parameter value between 0 and 10.

(**a**)　　　　　　　　　　　　　　　(**b**)
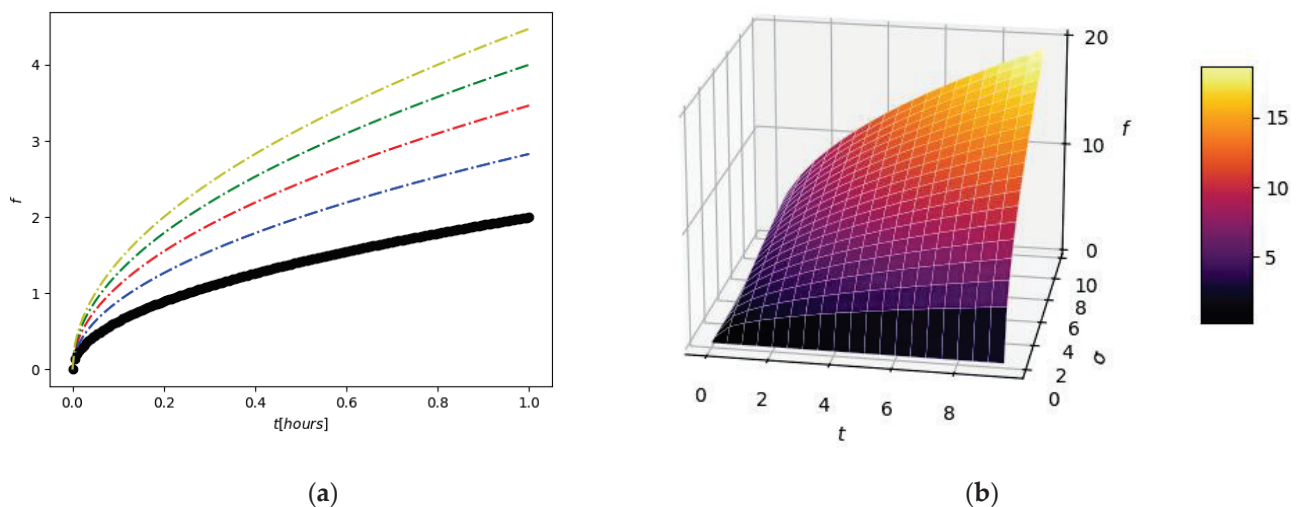
Figure 4. Two-dimensional contour (**a**) and three-dimensional plot (**b**) representations of f multifractal function.

In Figure 5, a model confirmation of the 5-fluorouracil release out of the chitosan-founded matrix is depicted. The experimental results are fit tightly with the mathematical theoretical functions of multifractal conception replica. The obtained graphical figure demonstrated that the realized model is ready to successfully prophesy the drug-deliverance kinetics [15,16].

The legend of Figure 5, with the symbols for defining the experimental points and the colors for each type of fractal curve used in the case of the four tested substances, is presented above. As can be seen in Figure 5, from the graphic representation of cumulative drug release as a function of time, curves U_1 and U_4 are classic saturation curves, while curves U_2 and U_3 are increasing with time (tend to infinite values).
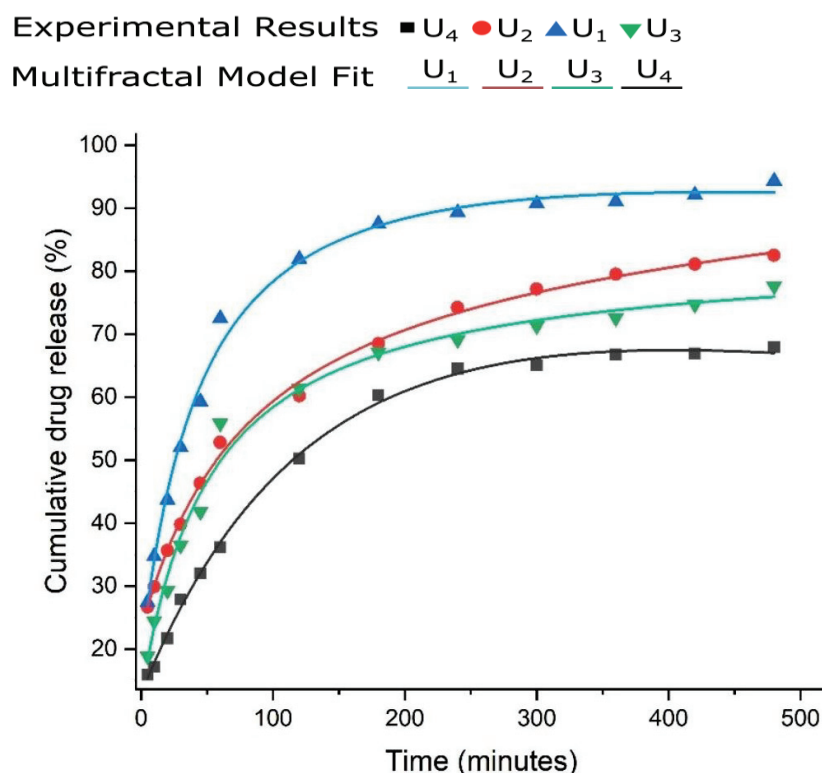
Figure 5. 5-fluorouracil release of experimental presentation [17]; the formulations are accommodated in multifractal theoretical replica (solid-colored lines).

3. Evaluation of Polarized Optical Microscopy Pictures by Fractal Analysis

5-fluorouracil's existence in chemical formulations was confirmed by means of polarized light microscopy (Figure 6). In the provided images, the obvious drug segregation into the hydrogels is clearly visible, with great density of crosslinking in compounds U_1 and U_2, in contrast with the hydrogel formulations of reduced crosslinking density (U_4), about which several things are discussed. Thus, a birefringent comportment and a granular texture were declared; a specific feature of the crystal is its sub-micrometric dimensions, but it still falls below the detection limit of the analysis devices used [17].

(**a**) (**b**) (**c**)
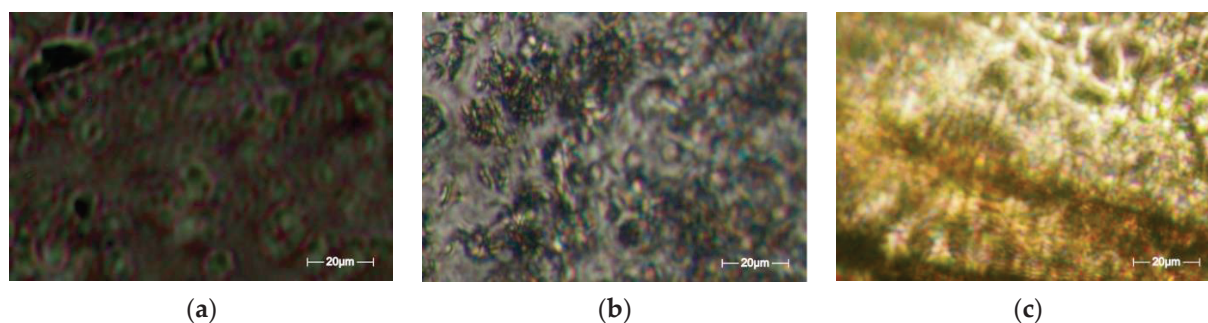
Figure 6. Representative POM images [17] of the formulations (**a**) U_1; (**b**) U_2; (**c**) U_4.

The scale bar for the POM photographic images (from Figure 6: (a) U_1; (b) U_2; (c) U_3) is 20 microns. The POM image in Figure 7 of experimentally produced formulations were processed according to fractal analysis standards, calculating the fractal dimension and lacunarity of each one. The processing method and the values obtained for fractal dimension and lacunarity, together with the voxel representation for each image separately are presented below, in paper continuation.

(a) (b)

(c) (d)

Figure 7. Primary processing of the selected image U_1. (**a**)—original image (the entire portion); (**b**)—the grayscale version; (**c**)—the gray scale version without luminance; (**d**)—binarized version. A threshold of 14 was used for binarization.

The fractal dimension and the lacunarity of the investigated POM images were calculated according to known fractal analysis procedures [18,19]. The same advanced mathematical utilities were successfully used in a previous work, but for images obtained by scanning electron microscopy (SEM), which will prove to be a complementary reading [20]. In order to obtain a high resolution, the calculation programs/software developed for the evaluation of some medical diseases with CT and MRI images were used. It is known that significant differences are noticed at the pixel level in order to give an early quantitative diagnosis (see [21–23]).

Following the numerical evaluations with the appropriate software of the selected image U_1, the values of fractal dimension $D = 1.7602$, standard deviation $s = \pm\sqrt{\sigma^2} = \pm 0.2026$ (see [24]) and lacunarity $\Lambda = 0.0215$ were obtained [24–26], as in Table 1.

Table 1. Calculation of fractal parameters for picture U_1.

Name	Fractal Dimension	Standard Deviation	Lacunarity
Image U_1	1.7602	± 0.2026	0.0215

The graph in Figure 8 shows the results of the 2D box-count algorithm and the local fractal dimension of the investigated image U_1 [25,27].

Figure 9 shows the verification of the selected U_1 image area with the software Harmonic and Fractal Image Analyser Demo version 5.5.30 [28] of the fractal dimension for various ruler scales *r*.

Figure 10 represents a three-dimensional graph of the voxel representation for the image U_1 from the modified area.

The POM image in Figure 11 of experimentally produced formulations were processed according to fractal analysis standards, calculating the fractal dimension and lacunarity of each one.
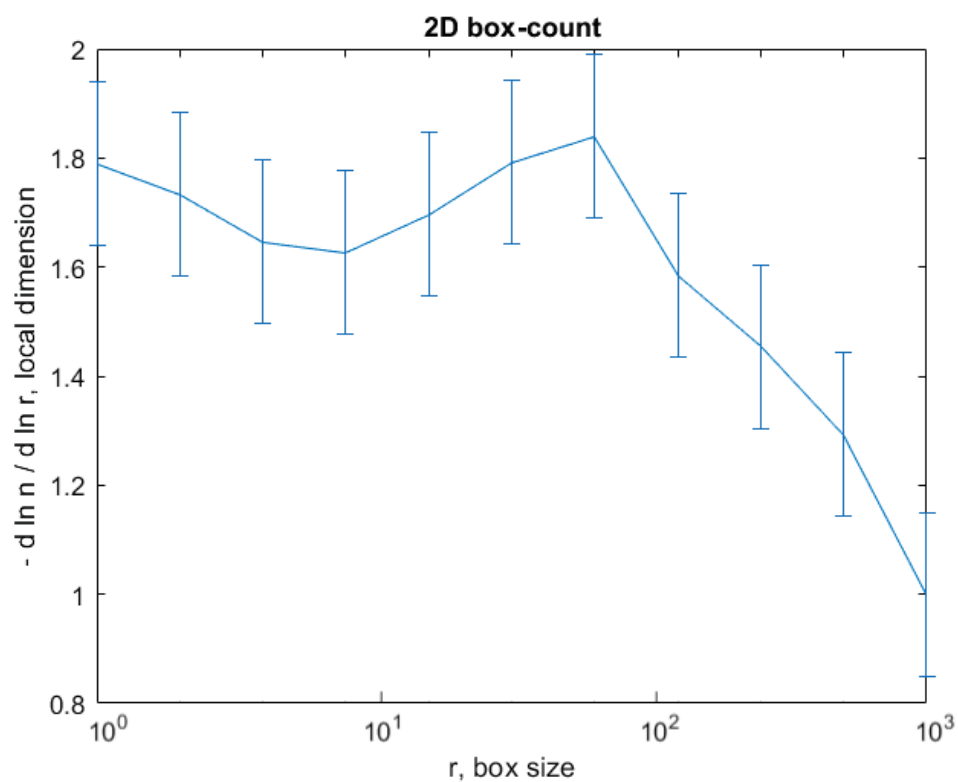
Figure 8. Box-count algorithm results: fractal dimension.
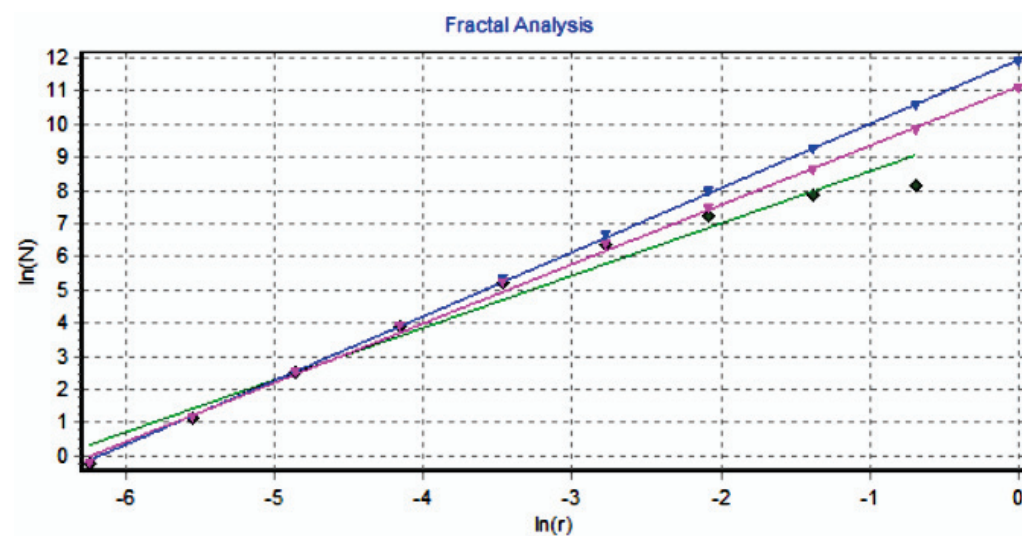
Figure 9. Graphic of fractal dimension for selected U_1 image area.
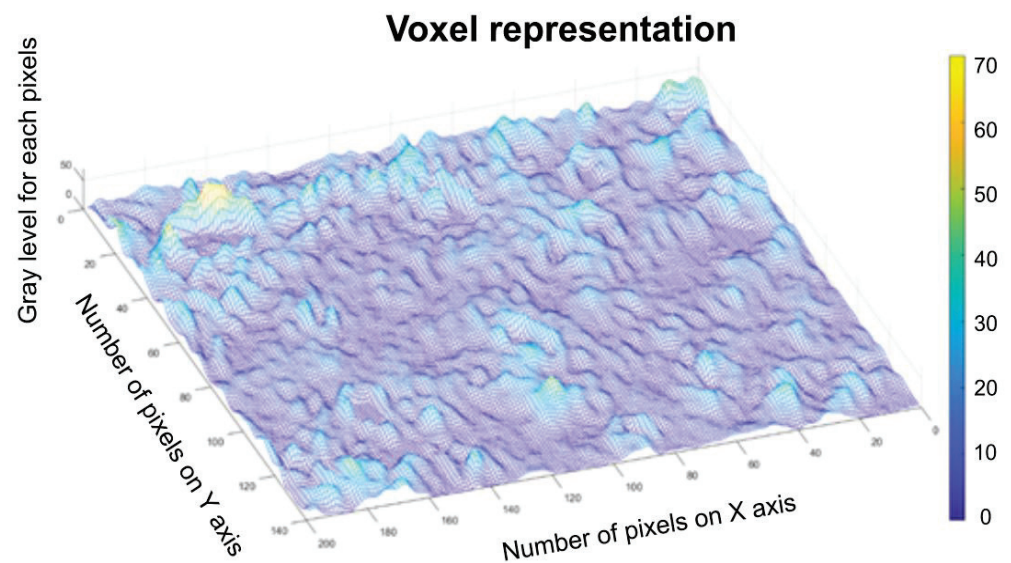
Figure 10. Voxel representation for the image U_1.

| (a) | (b) |
| (c) | (d) |
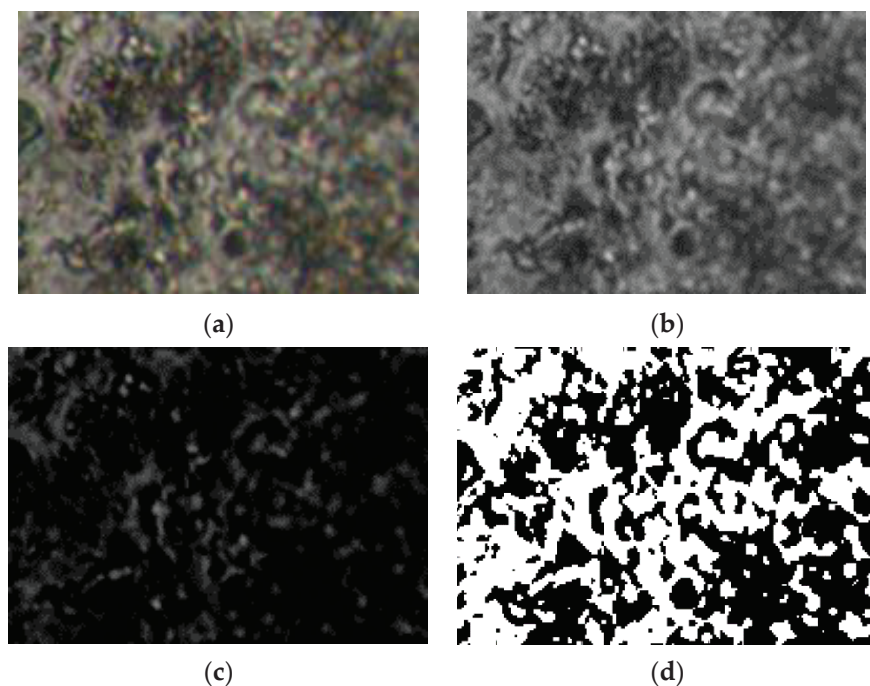
Figure 11. Primary processing of the selected image U_2. (**a**)—original image (the entire portion); (**b**)—the grayscale version; (**c**)—the gray scale version without luminance; (**d**)—binarized version. A threshold of 25 was used for binarization.

Following the numerical evaluations with the appropriate software of the selected image U_2, the values of fractal dimension $D = 1.7523$, standard deviation $s = \pm\sqrt{\sigma^2} = \pm0.1949$ (see [24]) and lacunarity $\Lambda = 0.0363$ were obtained [24–26], as in Table 2.

Table 2. Calculation of fractal parameters for picture U_2.

Name	Fractal Dimension	Standard Deviation	Lacunarity
Image U_2	1.7523	±0.1949	0.0363

The graph in Figure 12 shows the results of the 2D box-count algorithm and the local fractal dimension of the investigated image U_2 [25,27].
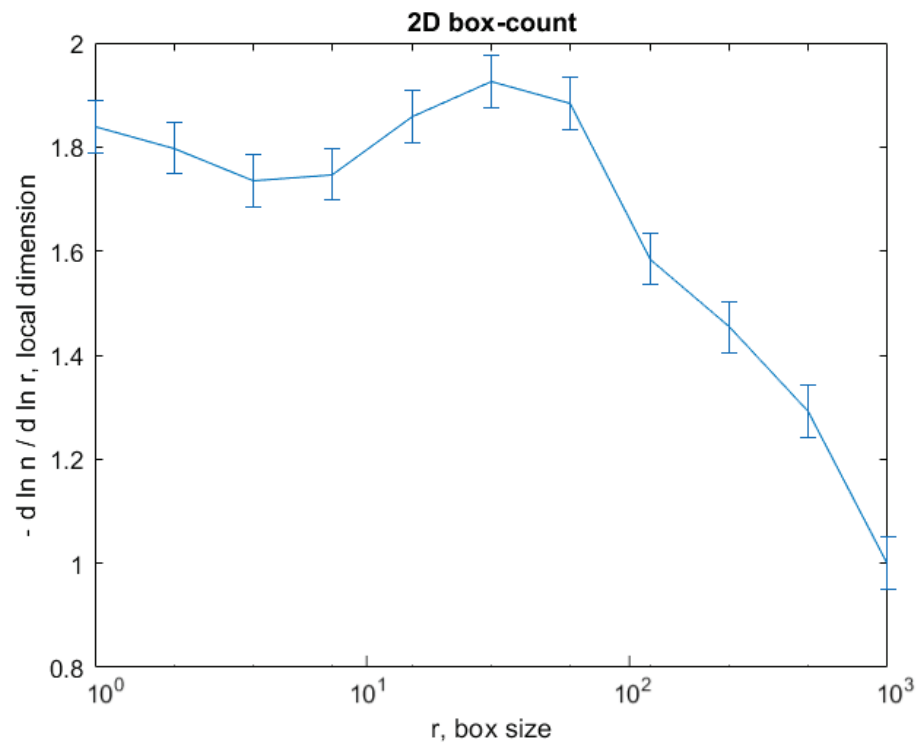
Figure 12. Box-count algorithm results: fractal dimension.

Figure 13 shows the verification of the selected U_2 image area with the software Harmonic and Fractal Image Analyser Demo version 5.5.30 [28] of the fractal dimension for various ruler scales r.
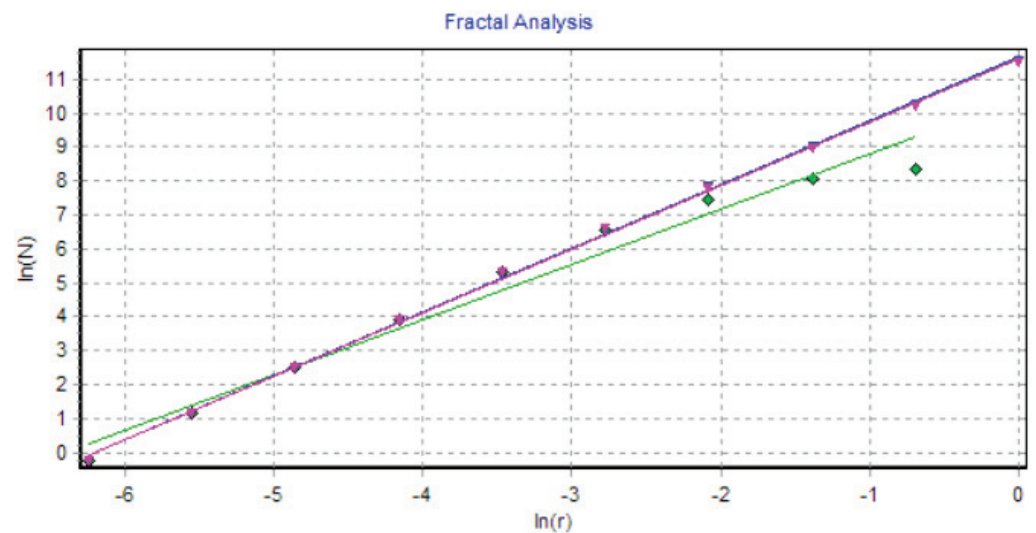
Figure 13. Graphic of fractal dimension for selected U_2 image area.

Figure 14 represents the three-dimensional graph of voxel representation for the image U_2 from the modified area.

Following the numerical evaluations with the appropriate software of the selected image U_4, the values of fractal dimension $D=1.7352$, standard deviation $s = \pm\sqrt{\sigma^2} = \pm 0.1831$ (see [24]) and lacunarity $\Lambda = 0.0385$ were obtained [24–26], as in Table 3.
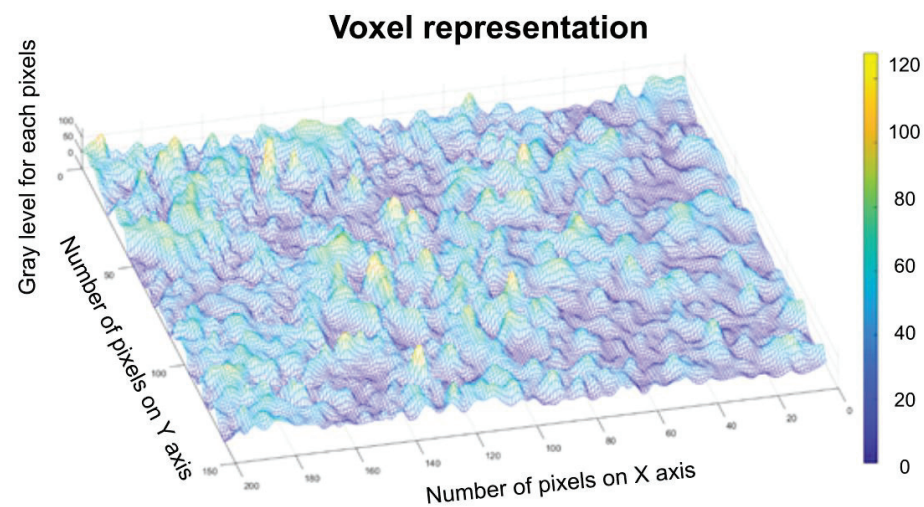
Figure 14. Voxel representation for the image U_2.

Table 3. Calculation of fractal parameters for picture U_4.

Name	Fractal Dimension	Standard Deviation	Lacunarity
Image U_4	1.7352	± 0.1831	0.0385

Figure 7a–d, Figures 11a–d and 15a–d show the three transformations (b, c and d) of the original of Figures 7a, 11a and 15a. Thus, the following changes were obtained: (b) the grayscale version; (c) the gray scale version without luminance; (d) the binarized version. The thresholds of 14, 25, and 35 were used for binarization. In [Tables 1–3], the values of fractal dimension, standard deviation and lacunarity that were obtained following the evaluation of images U_1, U_2 and U_3 from the original Figures 7a, 11a and 15a are shown.
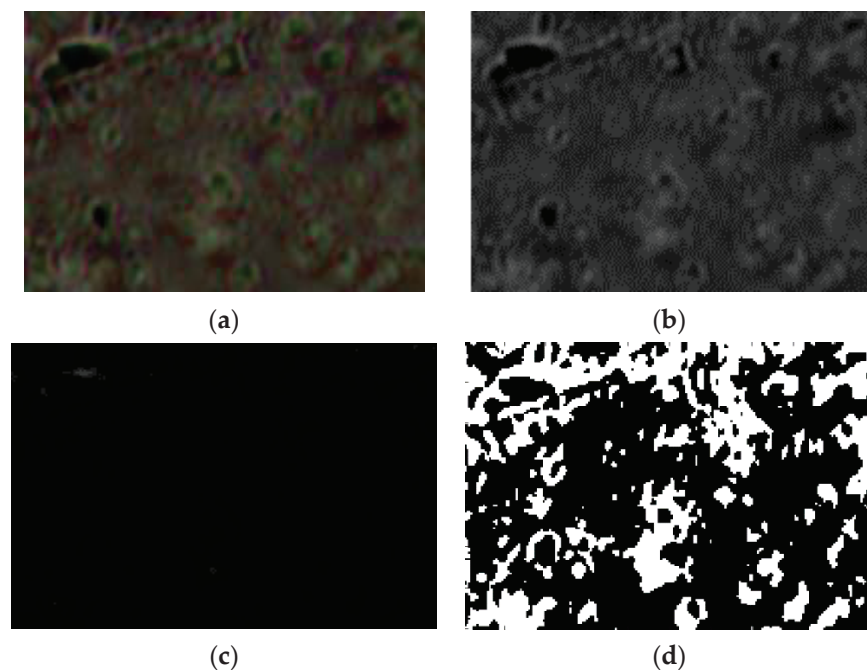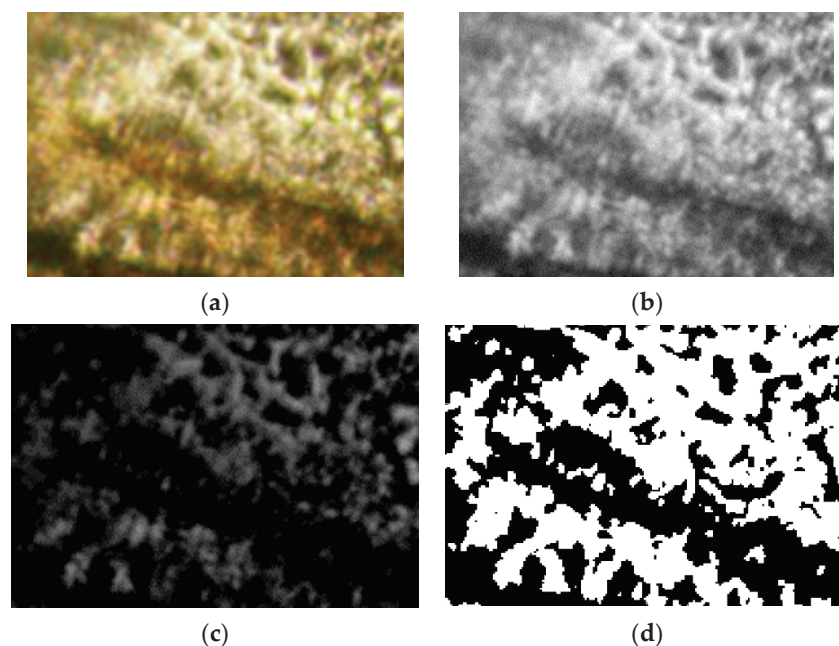

Figure 15. Primary processing of the selected image U_4. (**a**)—original image (the entire portion); (**b**)—the grayscale version; (**c**)—the gray scale version without luminance; (**d**)—binarized version. A threshold of 35 was used for binarization.

The POM image in Figure 15 of experimentally produced formulations were processed according to fractal analysis standards, calculating the fractal dimension and lacunarity of each one.

The graph in Figure 16 shows the results of the 2D box-count algorithm and the local fractal dimension of the investigated image U_4, [25,27].
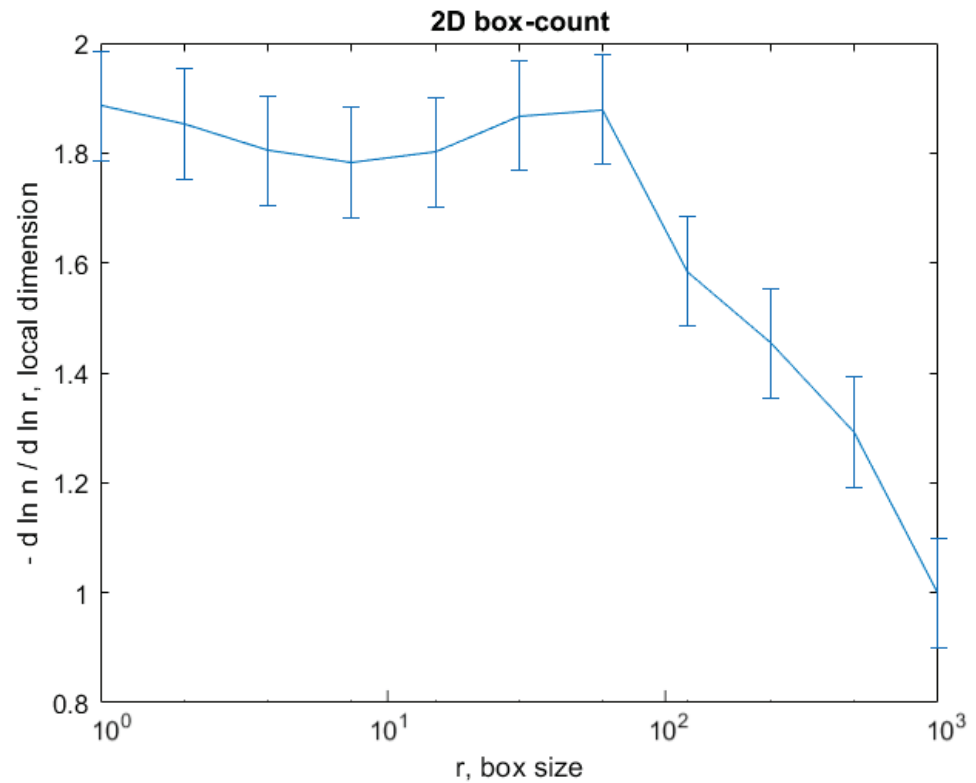
Figure 16. Box-count algorithm results: fractal dimension.

Figure 17 shows the verification of the selected U_4 image area with the software Harmonic and Fractal Image Analyser Demo version 5.5.30 [28] for the fractal dimension with various ruler scales *r*.
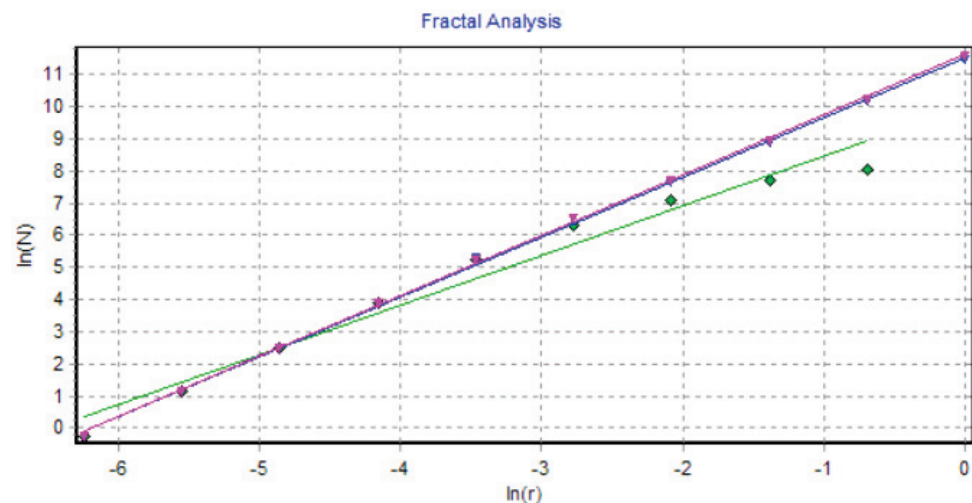
Figure 17. Graphic of fractal dimension for selected U_4 image area.

Figure 18 represents the three-dimensional graph of the voxel representation for the image U_4 from the modified area.
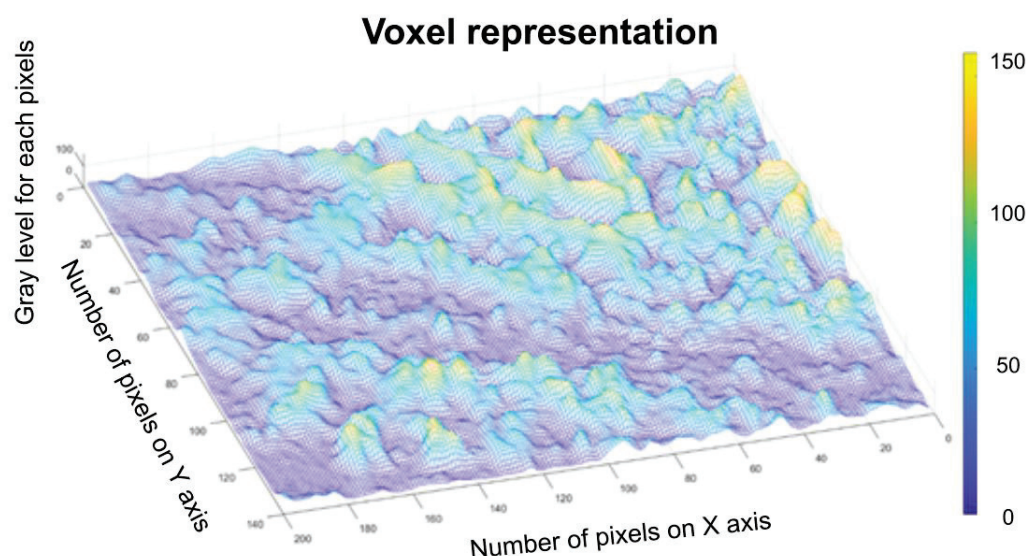
Figure 18. Voxel representation for the image U_4.

Figures 8, 9, 12, 13, 16 and 17 present the graphic representations of the 2D fractal dimension used for the linear regression slope calculation of the fractal dimension. Figures 10, 14 and 18 represent the three-dimensional graphs of voxel representation for the images U_1, U_2 and U_4 from the modified area. The three coordinate axes are distributed as follows: the number of pixels on the ox axis, the number of pixels on the oy axis, and the gray level for each pixel on the oz axis. In 3D computer graphics, the voxel represents a numerical value associated with the regular grid of a three-dimensional coordinate space.

4. Conclusions

Suites of drug delivery arrangements were realized by 5-fluorouracil encapsulation in the hydrogel matrix configured by the reticulation of chitosan-based with 3,7-dimethyl-2,6-octadienal. The hydrogel demonstrated a special capability to anchor the medicament, ensuring its prolonged deliverance close to 24 h. The release speed was adjusted by fluctuating the crosslinking consistency, arriving at 90% for a great reticulation density and at 70 % for a reduced one. In the stated multi fractal paradigm, a mathematical model was evolved for the comprehension of the drug delivery dynamics, taking into account that these special comportments are closely related to the fact that the movement takes place on non-differentiable curves.

Worth mentioning is the fact that, for the one-dimensional case of the multifractal hydrodynamic formalism, the ratio between the differentiable and non-differentiable velocities of a distinct distance is contingent on time, in a homographic fashion. The simultaneous dynamic conditions suggest the synchronization of the drug deliverance techniques at both scale resolutions, formulated by the multifractal diffusion functions, since we have the diffusion process depending on the scale resolutions. The fitted curves of the theoretical model are in good agreement with the obtained experimental results.

The three images of the U_1, U_2 and U_4 compounds, obtained by means of polarized light microscopy, were investigated according to the standards of fractal analysis. Thus, for image U_1, we found the fractal dimension D = 1.7602 ± 0.2026 and lacunarity $\Lambda = 0.0215$; for image U_2, we found the fractal dimension D = 1.7523 ± 0.1949 and lacunarity $\Lambda = 0.0363$; and for Image U_4, we found the fractal dimension D = 1.7352 ± 0.1831 and lacunarity $\Lambda = 0.0385$.

5. Materials and Methods

5.1. Materials

From the point of view of chemistry, the chitosan (CS) is a basic polysaccharide acquired by the deacetylation of chitin, one of the most plentiful native biopolymers in the world, with the exception of cellulose, evidently. In large part due to its high biocompatibility, biodegradability and reduced toxicity, chitosan has been utilized on a large scale in the pharmaceutical industry. In the last decade, chitosan utilization as a conveyor of continuous-release preparations to resolve the half-life period of chemotherapy medicaments has been announced [29]. In addition, chitosan-covered magnetic nanoparticles were utilized to extend the liberation of 5-fluorouracil (5-FU) [4]. CS (243 kDa, DA: 87%), 3,7-dimethyl-2,6-octadienal (95%), 5-FU, and phosphate tampon solution with a pH of 7.4 were acquisitioned from Aldrich chemical company and utilized as they were received.

5.2. Synthesis of the Hydrogel Formulation Preparations

The formulations used were fabricated through the hydrogelation in situ method of chitosan (CS) with 3,7-dimethyl-2,6-octadienal in the company of 5-fluorouracil (5-FU), which is a respected and classic protocol [3,4]. In a very short time, a 2% solution of 3,7-dimethyl-2,6-octadienal combined with 5-fluorouracil was gently dripped into a 3% chitosan-dissolved solution in aqueous acetic acid solution (1%). All substances were fabricated by Aldrich chemical company.

According to the observations made, it was accepted that 5-fluorouracil was fixed in the matricial structure as a crystalline component, and its size was assorted with the crosslinking density value. The in vitro drug release simulated in an environment that imitates the physiological habitat disclosed a 5-fluorouracil gradual deliverance, in close relation with the value of crosslinking density [23].

The drug and chitosan quantity were both retained steadily, while the 3,7-dimethyl-2,6-octadienal amount was diversified to touch various molar proportions of the amine/aldehyde groups, from the ratio of 1/1 to 4/1, in order to achieve hydrogels with different values of crosslinking consistency [7]. In the end, it was found that the hydrogelation period increased as the aldehyde quantity decreased. Thereby, the 1/1 molar ratio of amine/aldehyde functional classes immediately took place and continued sluggishly for 24 h for the 4/1 molar ratio of the same classes. Eventually, the acquired hydrogels were lyophilized and subjected to detailed analysis. Moreover, for the inventory, the formulations received the labels U_1, U_2, U_3, U_4, where the attached number was in agreement with the amino/aldehyde classes' molar ratio.

5.3. Methods

The gelation period was visually established in the moment when the reaction blend was transformed out of its initial viscous state to a rubbery final state. We mention that the xerogels were realized by lyophilization of the adequate hydrogels, utilizing the Labconco FreeZone Freeze Dry System, (FreeZoner2.5 Liter Freeze Dry Systems) instrument, for a duration of 24 h at a temperature of -50 °C and pressure of 0.04 mbar. The formulations produced were described by FTIR spectroscopy using the FT-IR Bruker Vertex 70 Spectrophotometer(Art photonics GmbH, 12489 Berlin, Germany).

The drug-release kinetics of the detailed medicaments' delivery systems were identified by recording the absorbance at 265 nm from the supernatant where the release was completed. The concentration of the solution was computed with the help of the Beer–Lambert law. The supernatant UV–vis spectra were recorded on a Horiba spectrophotometer, but the absorbance was accommodated on a previously drawn calibration curve. The 5-fluorouracil curve of calibration was drawn utilizing the absorption maximum spectrum at 265 nm.

References

1. Prausnitz, M.R. Langer, R. Transdermal drug delivery. *Nat. Biotechnol.* **2008**, *26*, 1261–1268. [CrossRef] [PubMed]
2. Patel, A.; Cholkar, K.; Agrahari, V.; Mitra, A.K. Ocular drug delivery systems: An overview. *World J. Pharmacol.* **2013**, *2*, 47–64. [CrossRef]
3. Jacob, J.; Haponiuk, J.T.; Thomas, S.; Gopi, S. Biopolymer based nanomaterials in drug delivery systems: A review. *Mater. Today Chem.* **2018**, *9*, 43–55. [CrossRef]
4. Xiong, S.; Marin, L.; Duan, L.; Cheng, X. Fluorescent chitosan hydrogel for highly and selectively sensing of p-nitrophenol and 2, 4, 6-trinitrophenol. *Carbohydr. Polym.* **2019**, *225*, 115253. [CrossRef] [PubMed]
5. Pereira, L.M. Fractal Pharmacokinetics. *Comput. Math. Methods Med.* **2010**, *11*, 161–184.
6. Kosmidis, K.; Argyrakis, P.; Macheras, P. Fractal kinetics in drug release from finite fractal matrices. *J. Chem. Phys.* **2003**, *119*, 6373–6377. [CrossRef]
7. Le Mehaute, A.; Crepy, G. Introduction to transfer and motion in fractal media: The geometry of kinetics. *Solid State Ionics* **1983**, *9-10*, 17–30. [CrossRef]
8. Barkai, E.; Metzler, R.; Klafter, J. From continuous time random walk to the fractional Fokker-Planck equation. *Phys. Rev. E* **2000**, *61*, 132–138. [CrossRef]
9. Zhang, L.; He, G.; Yu, Y.; Zhang, Y.; Li, X.; Wang, S. Design of Biocompatible Chitosan/Polyaniline/Laponite Hydrogel with Photothermal Conversion Capability. *Biomolecules* **2022**, *12*, 1089. [CrossRef] [PubMed]
10. Jiang, W.; Zhao, P.; Song, W.; Wang, M.; Yu, D.-G. Electrospun Zein/Polyoxyethylene Core-Sheath Ultrathin Fibers and Their Antibacterial Food Packaging Applications. *Biomolecules* **2022**, *12*, 1110. [CrossRef] [PubMed]
11. Liu, H.; Wang, H.; Lu, X.; Murugadoss, V.; Huang, M.; Yang, H.; Wan, F.; Yu, D.-G.; Guo, Z. Electrospun structural nanohybrids combining three composites for fast helicide delivery. *Adv. Compos. Hybrid Mater.* **2022**, *5*, 1017–1029. [CrossRef]
12. Higaki, K.; Yamashita, S.; Amidon, G.L. Time-dependent oral absorption models. *J. Pharmacokinet. Pharmacodyn.* **2001**, *28*, 109–128. [CrossRef] [PubMed]
13. Karalis, V.; Tsantili-Kakoulidou, A.; Macheras, P. Quantitative structure–pharmacokinetic relationships for disposition parameters of cephalosporins. *Eur. J. Pharm. Sci.* **2003**, *20*, 115–123. [CrossRef]
14. Chechetkin, V.R.; Lutovinov, V.S.; Turygin, A.Y. Multifractal structure of fully developed hydrodynamic turbulence. I. Kolmogorov's third hypothesis revisited. *J. Stat. Phys.* **1990**, *61*, 573–588. [CrossRef]
15. Basu, A.; Chakrabarti, B.K. Hydrodynamic descriptions for surface roughness in fracture front propagation. *Philos Trans A Math Phys Eng Sci.* **2019**, *377*, 20170387. [CrossRef]
16. Kwak, K.; Yang, S. Developing a Multi-Dimensional Hydrodynamics Code with Astrochemical Reactions. *IAU Gen. Assem.* **2015**, *29*, 2250754.
17. Iancu, R.; Irimiciuc, S.A.; Agop, M.; Frasila, M.; Paun, M.-A.; Paun, V.-A.; Paun, V.-P.; Stratulat, S. 5-fluorouracil release from chitosan-based matrix. Experimental and theoretical aspects. *Mater. Plast.* **2020**, *57*, 180–188. [CrossRef]
18. O'Shaughnessy, B.; Procaccia, I. Analytical solutions for diffusion on fractal objects. *Phys. Rev. Lett.* **1985**, *54*, 455–458. [CrossRef]
19. Richard, R. 1D Diffusion PDE. Introduction to Partial Differential Equations. 2019. Available online: http://personal.ph.surrey.ac.uk/~{}phs1rs/teaching/l3_pdes.pdf (accessed on 15 June 2022).
20. Polowsky, P.J.; Tansman, G.; Kindstedt, P.S.; Hughes, J.M. Characterization and identification of surface crystals on smear-ripened cheese by polarized light microscopy. *J. Dairy Sci.* **2018**, *101*, 7714–7723. [CrossRef]
21. Karperien, A.L.; Jelinek, H.F. Box-Counting Fractal Analysis: A Primer for the Clinician. In *The Fractal Geometry of the Brain*; Di Ieva, A., Ed.; Second Chapter; Springer Series in Computational Neuroscience; Springer Science + Business Media: New York, NY, USA, 2016.
22. Karperien, A.; Jelinek, H.F.; Miloševic, N.T. Reviewing Lacunarity Analysis and Classification of Microglia in Neuroscience. In Proceedings of the 8th European Conference on Mathematical and Theoretical Biology, Kraków, Poland, 28 June–2 July 2011; pp. 1–6.

23. Lungu, R.; Paun, M.-A.; Peptanariu, D.; Ailincai, D.; Marin, L.; Nichita, M.-V.; Paun, V.-A.; Paun, V.-P. Biocompatible Chitosan-Based Hydrogels for Bioabsorbable Wound Dressings. *Gels* **2022**, *8*, 107. [CrossRef]

24. Nichita, M.V.; Paun, M.A.; Paun, V.A.; Paun, V.P. Fractal analysis of brain glial cells. Fractals dimension and lacunarity. *Univ. Politeh. Buchar. Sci. Bull. Ser. A Appl. Math. Phys.* **2019**, *81*, 273–284.

25. Bordescu, D.; Paun, M.A.; Paun, V.A.; Paun, V.P. Fractal analysis of Neuroimagistic. Lacunarity degree, a precious indicator in the detection of Alzheimer's disease. *Univ. Politeh. Buchar. Sci. Bull. Ser. A Appl. Math. Phys.* **2018**, *80*, 309–320.

26. Postolache, P.; Borsos, Z.; Paun, V.A.; Paun, V.P. New Way in Fractal Analysis Of Pulmonary Medical Images. *Univ. Politeh. Buchar. Sci. Bull. Ser. A Appl. Math. Phys.* **2018**, *80*, 313–322.

27. Scott, D.W. *Statistics: A Concise Mathematical Introduction for Students, Scientists, and Engineers*; John Wiley & Sons, Inc.: Hoboken, NJ, USA, 2020.

28. Available online: http://imagesci.fch.vut.cz/includes/harfa_download.inc.php (accessed on 15 June 2022).

29. Wang, X.; Ahmed, B.N.; Alvarez, S.G.; Tuttolomondo, M.V.; Hélary, C.; Desimone, M.F.; Coradin, T. Sol-gel encapsulation of biomolecules and cells for medicinal applications. *Curr. Top. Med. Chem.* **2015**, *15*, 223–244. [CrossRef] [PubMed]

A Molecular Description of Hydrogel Forming Polymers for Cement-Based Printing Paste Applications

Hajar Taheri-Afarani [1], Eugene Mamontov [2], William R. Carroll [3] and Joseph J. Biernacki [1,*]

1   Department of Chemical Engineering, Tennessee Technological University, 1 William L. Jones Dr., Cookeville, TN 38505, USA
2   Oak Ridge National Laboratory, 1 Bethel Valley Road, Oak Ridge, TN 37830, USA
3   Department of Chemistry, Tennessee Technological University, 1 William L. Jones Dr., Cookeville, TN 38505, USA
*   Correspondence: jbiernacki@tntech.edu; Tel.: +1-931-372-3297

Abstract: This research endeavors to link the physical and chemical characteristics of select polymer hydrogels to differences in printability when used as printing aids in cement-based printing pastes. A variety of experimental probes including differential scanning calorimetry (DSC), NMR-diffusion ordered spectroscopy (DOSY), quasi-elastic neutron scattering (QENS) using neutron backscattering spectroscopy, and X-ray powder diffraction (XRD), along with molecular dynamic simulations, were used. Conjectures based on objective measures of printability and physical and chemical-molecular characteristics of the polymer gels are emerging that should help target printing aid selection and design, and mix formulation. Molecular simulations were shown to link higher hydrogen bond probability and larger radius of gyration to higher viscosity gels. Furthermore, the higher viscosity gels also produced higher elastic properties, as measured by neutron backscattering spectroscopy.

Keywords: cement; Portland; 3D printing; additive manufacturing; neutron scattering; NMR; molecular dynamics; modeling; hydrogel; gel; admixture

1. Introduction

Water-swollen polymeric networks, such as polymeric hydrogels, are complex dynamic systems [1]. Understanding how water interacts with gel-forming polymeric materials is critical to identify the underlying processes that make gels effective in specific applications [2,3]. A number of studies using molecular dynamic simulations [4,5] and experimental techniques, including nuclear magnetic resonance (NMR) spectroscopy [6–8], differential scanning calorimetry (DSC) [9–11], thermally stimulated depolarization currents (TSDC) [12], dielectric relaxation spectroscopy (DRS) [13], quasi-elastic neutron scattering (QENS) [4,14–16] and thermo-gravimetric analysis (TGA) [17], have been conducted to investigate the association and dynamics of water in polymeric hydrogels in various and unique applications. One such application is in construction materials [17–20]. The dynamics of the abovementioned techniques span a wide range of time scales. For instance, solvent and solute diffusion through network pores, segmental chain dynamics, matrix–solvent proton exchange, and local rotational state transitions differ by many orders of magnitude [1]. Despite significant progress in understanding the basic structure-property relationships of hydrogels, much remains to be learned about how the foundational macromolecular building blocks transmit properties across length-scales to the macroscopic sample. Fundamental grand challenges include understanding the relationship between network structure, dynamics, and mechanical properties [21]. One of the important factors is the state of water in such materials. Previous studies showed that water in hydrogels can generally be classified into three different categories [5,9,22,23]: freezable water (free water), non-freezable water (bound water), and freezable bound water. Free water behaves like bulk water. Free water freezes and thaws at 0 °C [5], though freezing may not be

nucleated at 0 °C. Moreover, free water flows freely in hydrogels [5]. Although free water can be physically entrapped within the polymer network, it can be easily removed at ambient temperatures [24]. Free water does not participate in hydrogen bonds with the gel polymer molecules [24,25]. Freezable bound water is weakly bonded to the polymer chains or interacts weakly with non-freezable water. Freezable bound water undergoes a thermal phase transition at a temperature lower than 0 °C. Finally, non-freezable water is directly bound to the polymer chains through hydrophilic groups or via hydrogen bonds. Non-freezable water is strongly associated with polar groups of hydrogels by hydrogen bonds, which results in low mobility of non-freezable water [5]. As a result, such types of water cannot be easily separated from the hydrogel. During hydrogel swelling, water molecules that enter the polymer first form non-freezable water [5]. Additionally, non-freezable water does not exhibit a phase transition over the temperature range from -70 to 0 °C [5,9,22–25]. Different types of polymers show their own unique characteristics when in contact with water molecules. These characteristics lead to various effects on hydrogen-bonding, due to the presence of different types and contents of water molecules based on the aforementioned categories. Therefore, determining the content of water in the abovementioned categories is crucial for understanding the properties of hydrogels and their dynamic behavior. Furthermore, the dynamics of water is highly affected by the confinement environment, e.g., mesoporous silicas (MCM-41) [26], carbon nanotubes, mesoporous organo-silicas, zeolites [27] and cementitious systems [28,29].

There has been widespread interest in the structure and dynamics of water in confined media and the influence of confinement on hydrogen bonding, interfacial transport, and mechanical toughness of the surfaces [30]. Therefore, studying the association of water confined in hydrogels might provide useful information on the molecular structure, interfacial properties, interactions, and the dynamic behavior of such materials [4,31–33]. However, there are still few studies based on polymeric hydrogels confined within hard walls, such as in the abovementioned structures. Selected hydrogel-forming polymers have recently been used to produce cement-based printing pastes with good printability outcomes [34,35]. Yet, the interaction of these hydrogel-forming polymers with cement and other types of hard walls and the dynamic behavior of water in such systems have not been investigated thoroughly. Thus, a comprehensive description of such systems requires a range of experimental approaches and interpretive models. For instance, QENS [36] was used to study the dynamics of both water and poly N-isopropylacrylamide (PNIPA) molecules in concentrated PNIPA solutions. In that system it was shown that hydration plays an important role for the stabilization of the aqueous system [36]. Results showed that when water and cement materials interacted with each other, the commencement of the hydration reaction allows free water to convert to chemically bound water which is representative of the motionless state of water. For systems including polymeric hydrogels, the formation of hydrogen bonding between polymers and hydrating water molecules reduces the free energy of the solutions [36]. QENS was also used to explore early-age hydration kinetics of Portland cement with nano-additives, such as nano-silica (NS) [37].

Small-angle neutron scattering (SANS) is another promising approach to elucidate properties of hydrogels and their network structures [21,38]. SANS studies have been used to characterize the shape, size, and dimensions of gel fibers [39–41], e.g., SANS was used to investigate the microstructure and relative homogeneity of tetra-functional poly ethylene glycol (PEG) networks [21]. Qualitative analysis and model-fitting of SANS data showed that at the concentrations of 35 kg.mol^{-1} and 12 kg.mol^{-1} tetra-functional PEG hydrogels have a remarkably homogeneous network structure with low junction functionality [21]. In another study, the rheological and structural properties of a pharmaceutical multicomponent hydrogel, consisting of a hydrogel-forming (acrylic acid) polymer (Carbopol® 974P, BF Goodrich Europe, UK), microbicide (monocaprin, Danisko Ingedients, Denmark), nonionic surfactant (Tween 20® or Tween 40®, Sigma Chemical Co., St. Louis, MI, USA), and preservatives, was characterized using rheological measurement and SANS [42]. The rheological measurements showed that the formation of large-scale structures was weakened at higher

pH values. These results agreed with the SANS results which showed that at high system pH, repulsive electrostatic forces reduce the tendency to form chain associations, whereas at low pH the electrostatic repulsive forces are suppressed in the hydrogel, and this leads to the association and the production of large-scale structural heterogeneities [42].

QENS measurements using neutron backscattering spectroscopy (such as those performed at BASIS [43]), is also a capable approach for measuring a dynamic spectrum near the elastic peak of around ± 100 μeV in the energy transfer with an elastic energy resolution of 3.7 μeV (full width at half-maximum value averaged over all scattering angles) [44]. Due to its large dynamic range and high energy resolution, BASIS is a suitable instrument for studying dynamics of confined supercooled water.

Molecular dynamics simulation (MDS) techniques have also been used to characterize the molecular structure and properties of various materials [5,45–47]. Such studies can provide detailed information about the structure and behavior of systems on the molecular level. To this end, a molecular dynamic simulation was carried out [5] to explore the content of non-freezable water, freezable water, and free water at various degrees of cross-linking for poly (vinyl) alcohol (PVA) [5]. The simulation results showed that the amounts of non-freezable water and freezable water were slightly less than those found experimentally [5]. To better understand the interaction between water and polymers and the role of hydrogen bonds in hydrogels, MDS of PVA, poly (vinyl methyl ether) (PVME), and PNIPA was used [45]. Results suggest that the largest numbers of hydrogen bonds occurred between water and polymers for PVA (the more hydrophilic polymer), while the smallest numbers were observed for PVME (the more hydrophobic polymer) [45]. Since PVA is more hydrophilic than PVME and PNIPA, the greatest numbers of water molecules were found to be non-freezable. However, for PVME, the most hydrophobic polymer, a larger amount of water was free water [45].

One of the most interesting features of hydrogels is their tribological properties. Tribology refers to applying the concepts of friction, lubrication and wearing to study interacting surfaces in relative motion [48]. Hydrogels have been used as anti-friction materials in various industries [49]. Methyl cellulose and its derivatives, for example, are hydrogels that have been used to provide lubrication properties which are important in the cement extrusion industries [50–54]. To better understand the tribological properties from an atomistic point of view, MDS was used [55] to examine the role of sliding orientation on the tribological properties of polyethylene (PE). PE surfaces were slid against each other in two different directions: (1) perpendicular to the aligned direction of the polymer chains and (2) parallel to the chains. Sliding in the parallel direction showed a lower friction coefficient than sliding in the perpendicular direction [55]. Greater levels of shear strain were also stored during sliding in the perpendicular direction. Furthermore, their results suggested that the friction coefficient was dependent on the local orientation of polymer chains with respect to the sliding direction and molecular motion.

In the authors' previous works, rheological properties, including flow properties of hydrogels made from hydroxy ethyl methyl cellulose (HEMC), hydroxy propyl methyl cellulose (HPMC) and poly ethylene oxide (PEO), and oscillatory rheology of the neat gels and gel-cement pastes, were correlated to the printability of the same paste systems using rigorous techniques for quantification of print fidelity [34,35]. A number of inferences emerged: (1) printing outcomes in order of best to worst were for gel-based pastes made with HEMC, HPMC and PEO, (2) neat gels exhibited shear time-independent shear thinning behavior, (3) There was an inverse relationship between the storage modulus of the neat gel and the storage modulus of the gel-based cement pastes, i.e., higher gel storage modulus produces lower paste modulus and (4) pastes with higher gel modulus were preferred and produced better printing outcomes at the same polymer contents. Notably, the range of polymers that produce hydrogels is broad; however, not all hydrogels are applicable as cement-paste printing aides. The three gels used in the prior work of the authors exhibited both mechanical and chemical stability when used in aqueous suspension of Portland cement. Such gels must remain stable under conditions of high shear, which are imposed

during mixing and must be stable in the high pH environment of Portland cement, i.e., pH of up to nominally 12.5. Hydroxylated celluloses and PEO are representative polymers with different chemical architectures and so were selected as case study materials. In the present study, HEMC, HPMC and PEO were again used to form gels, thus, extending the prior work of the authors [34,35]. In order to elucidate how water interacts with polymeric hydrogels, as well as with other materials, such as cement, MDS were conducted alongside experimental probes. This study intends to look at molecular scale connections between gel structure and printability. Thus, in the current work, the BASIS spectrometer at Oak Ridge National Laboratory (ORNL) was used to compare the structure of hydrogels, the phase behavior, and the dynamics of water in neat cement pastes and water in cement pastes made using hydrogels. Moreover, diffusion-ordered nuclear magnetic resonance (DOSY-NMR) spectroscopy was also used to study the mobility of polymers and water in the gel phase and differential scanning calorimetry (DSC)-based thermoporometric measurements were made to investigate the porous structures of the hydrogels. By studying water dynamics in cement paste and in hydrogels at the molecular level, basic information is provided for the formulation of new additive platforms and to engineer additives for specific applications in the cement industry.

The following discourse first looks at the characterization of the three polymer types and the gels formed therefrom, systematically discussing the findings by the following applied test methods: X-ray diffraction, differential scanning calorimetry, neutron scattering and, finally, molecular dynamic simulation. The results are followed by a description of the experimental methods and computational procedures. The present study is concerned only with the selection of gel-forming polymers for printability and does not address the issues of properties of the printed composites, e.g., strength or durability. Print quality, however, is addressed in the authors prior studies wherein the gel-cement pastes were printed and the printed objects were characterized for print fidelity [34,35], i.e., how the dimensions of the printed objects compared to that of the model or target object.

2. Results and Discussion

2.1. Microstructural Analysis

X-ray powder diffraction (XRD) patterns of the three raw polymers are shown in Figure 1. HEMC was found to have a semi-crystalline structure, HPMC was totally amorphous, and PEO was completely crystalline. The XRD pattern of PEO showed two high intensity diffraction peaks at 19.36° and 23.72°, which were assigned to the (120) and (112) planes, respectively [56]. While this information was interesting, it is provided here for information only and as a form of characterization of the raw material, since, once infused with water, all three gel types were amorphous.
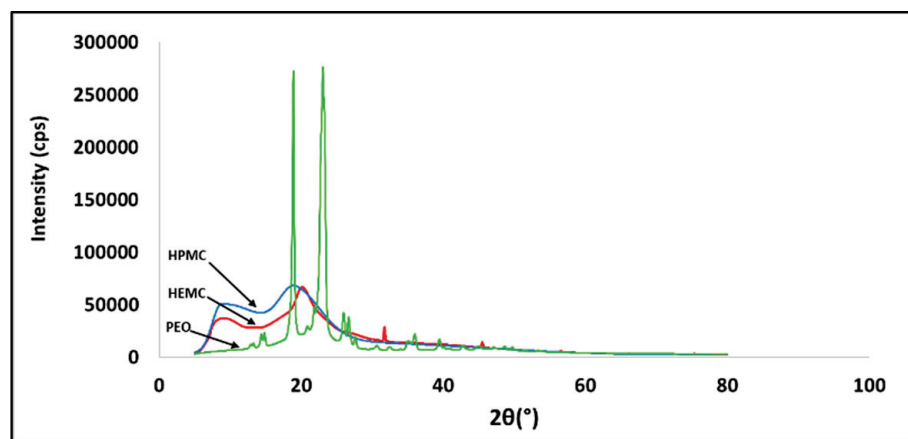
Figure 1. X-ray diffraction pattern of HEMC, HPMC, and PEO.

2.2. Differential Scanning Calorimetry (DSC)

Differential scanning calorimetry-based thermoporosimetry of the three hydrogels at 4 mass % polymer content was used to study the qualitative pore structure and association of water and polymer in the gels. The melting curves of all three hydrogels displayed a broad primary endothermic peak [8,57], shown in Figure 2. PEO hydrogels also exhibited a small peak at about −8 °C. This small peak might be assigned to the melting of a small amount of PEO trihydrate complex that crystallized during the cooling step [57–59]. Therefore, it might be considered as non-freezing water, i.e., water that was strongly bonded to the polymeric chains. Melting of pure water starts at 0 °C ± ½ °C, while for the three hydrogels melting was initiated at between −10 °C and −7 °C [60]. Moreover, since melting began below the normal temperature of fusion for water, this indicated a porous structure, i.e., water confined within small gel pores. Confined water has a depressed freezing point [61], and the finer the pore structure, i.e., the smaller the pores, the greater the freezing point depression, as indicated by the Laplace equation [62,63].
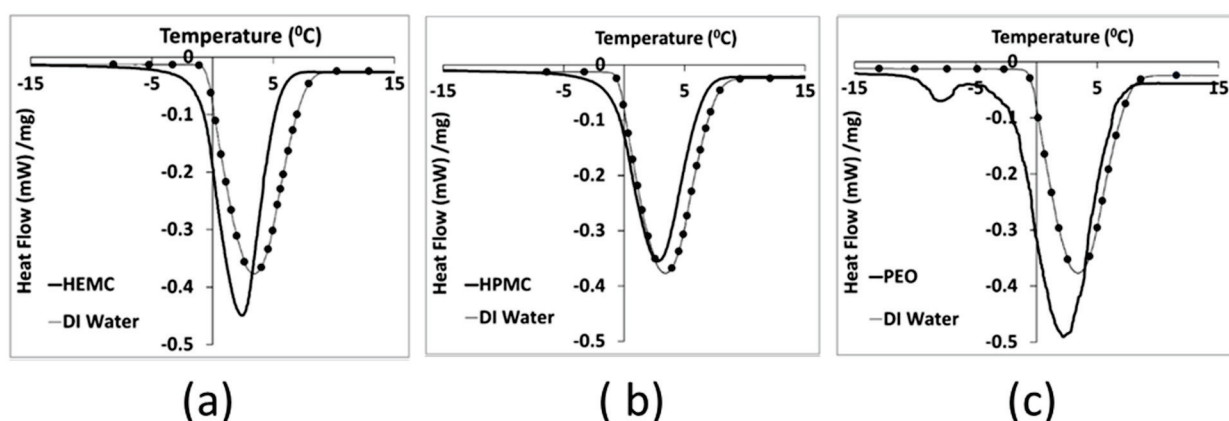
Figure 2. DSC heating curves for: (**a**) Gel 1 (HEMC), (**b**) Gel 2 (HPMC) and (**c**) Gel 3 (PEO), compared to deionized water, i.e., line with dots.

PEO appeared to have the finest pore structure, while HPMC had the coarsest structure, as seen by comparing the thawing curves for the gels to that of DI water. HEMC exhibited an intermediate pore structure, while it also exhibited better printability results in comparison to that of HPMC and PEO. Therefore, gel pore structure alone does not appear to be a direct indicator of paste printability, i.e., printability does not monotonically increase or decrease with changes in pore fineness as measured by freezing point depression. Gel pore structure, however, is one indicator of gel-to-gel differences that can be considered alongside other metrics in the search for connections between molecular structure and printability.

2.3. NMR DOSY Experiments

Diffusion ordered NMR spectroscopy was used to investigate the self-diffusivity of polymer and residual water in the gels [64,65]. DOSY experiments for 0.5 mass % HEMC, 2.0 mass % PEO, and 0.2 mass % PEO gels were carried out, since the polymer structures were different. Figure 3 presents the signal intensity decays of the deuterium oxide (HOD solvent residual in D$_2$O) and polymer molecules present in the hydrogels, in relation to the increasing field gradient strength as the scan number increased. Such signal attenuation is dependent on several parameters, including the original signal intensity (concentration), the gradient pulse area, the diffusion time, and the diffusion coefficient of the molecule [66,67]. It is clear that NMR signals, due to different diffusing species, are attenuated at different rates. As mentioned before, this is due to different diffusion coefficients, i.e., the signals at 3.5 and 4.8 ppm belong to HOD and polymer molecules which are diffusing at different rates. The decay of the signal originating from the residual solvent (HOD, δ 4.8 ppm) was fast, again refer to Figure 3, which is an indicator of mobility.
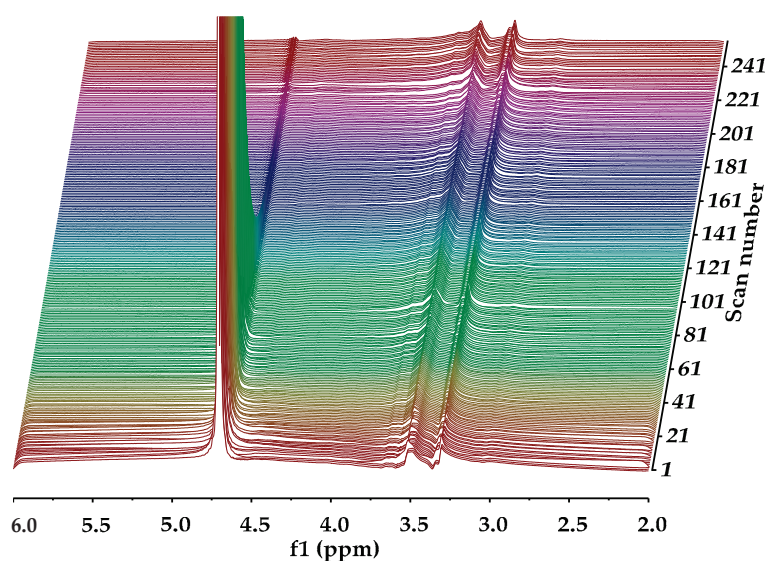
Figure 3. NMR DOSY experiment for the 0.5 mass % HEMC hydrogels: a series of NMR diffusion spectra with varying gradient strengths. Chemical shifts (in ppm) lie on the horizontal axis while magnetic gradient pulse amplitude is on the orthogonal axis, increasing with increasing scan number.

Whereas the signal from the solvated polymer (multiple peaks around δ 3.5 ppm) did not decay during the timeframe of the experiment. This indicated that the polymer molecule moved slowly relative to the free HOD. The diffusivity of the water molecules (HOD) was found to be 2.61×10^{-9} m^2/s in HEMC gels, respectively. Notably, the self-diffusivity of free water at the same temperature is 2.299×10^{-9} m^2/s [68]. The diffusivity of solvated dissolved HEMC was found to be 3.13×10^{-11} m^2/s. The solvated HEMC appearing in the solution state NMR data presented here represented molecules much larger than water. It was consistent with our expectation that it would diffuse more slowly than water. It is expected that any solid HEMC would experience line broadening, due to dipolar couplings, that prevent it from providing a clear solution state NMR signal.

Figures 4–6 show the 2D DOSY NMR spectra of 0.5 mass % HEMC, 0.2 mass % PEO, and 2.0 mass % PEO solvated with D$_2$O. ^{1}H NMR spectrum and the diffusion coefficient domain are represented on the x- and y-axes, respectively. In each plot there was an observable solvent residual peak around δ 4.8 ppm and a signal for free solvated polymer, either HEMC or PEO, at δ 3.5 ppm and δ 3.6 ppm, respectively. Both high concentration PEO samples (2.0 mass %) that formed a gel and lower concentration PEO (0.2 mass %) samples forming a vicus solution were examined. In each case, as in the HEMC case, water diffused at nominally the bulk water self-diffusivity, with 0.2 mass % PEO samples showing 2.32×10^{-9} m^2/s and 2.0 mass % PEO samples showing 2.45×10^{-9} m^2/s. Notably, the line-broadness was not the same for each. PEO samples had a broader signal for HOD and for the polymer, observed in the diffusion domain. This was consistent with DSC thermoporosimetry outcomes that clearly indicated a confined water environment in all three gel types with greater confinement in the PEO gels. Water participating in several chemical environments displays a diversity of diffusion coefficients and chemical shifts not seen in bulk water. Figure 6 shows the DOSY PEO results for 2.0 mass % solution in D$_2$O. These results were also consistent with DSC findings that suggested that PEO has a finer pore structure than HEMC. As mentioned above, however, this finer pore structure alone does not necessarily translate to good or bad printability outcomes; however, the data elucidates quantifiable differences in pore structure. Observable in this spectrum were further broadened signals beyond those observed in the lower concentration sample. Similarly to HEMC, the polymer signals in the PEO samples diffused more slowly than those of HOD.
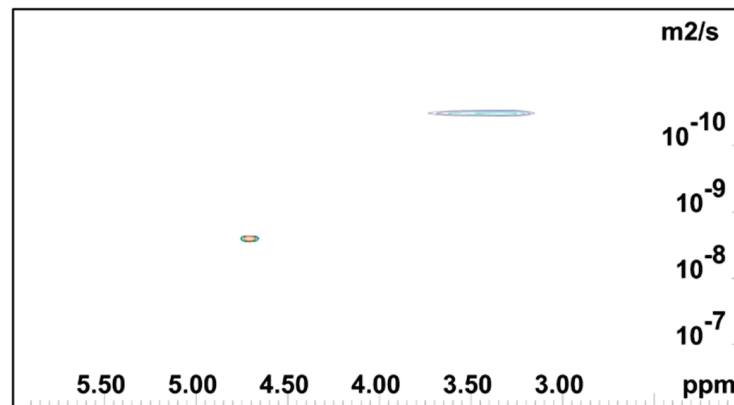
Figure 4. 2D DOSY log(D) plot for HEMC 2 mass % gel.
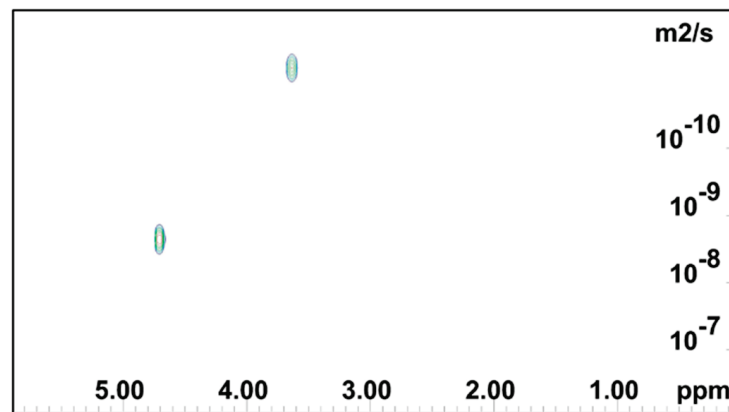
Figure 5. NMR DOSY log(D) plot for 0.2 mass % PEO gel.
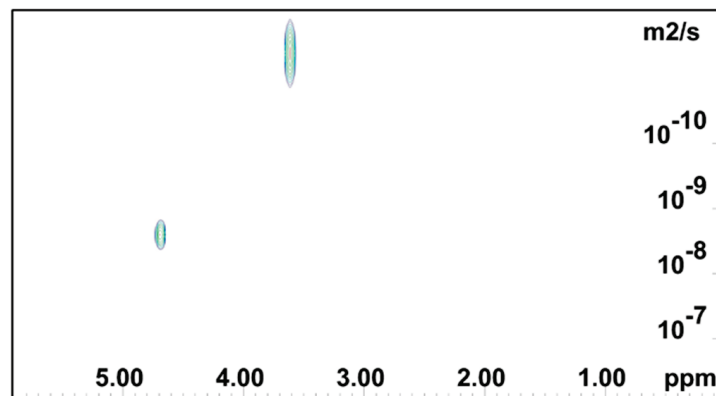
Figure 6. 2D DOSY log(D) plot for PEO 2 mass % gel.

2.4. Neutron Scattering

2.4.1. Energy-Resolved "Elastic" Scattering

The "elastic" scattering intensity (due to neutrons scattered from the sample with an energy transfer within the FWHM of the energy resolution line) was recorded on both cooling of samples and on heating. Refer to Figure 7 for gel and gel-cement paste data and to Figure 8 for neat cement paste data. The raw elastic intensity was normalized with respect to water content, i.e., mass of water. For the pure gel samples the raw intensities were divided by 0.38 g. For the gel-cement samples, a normalization factor of 0.18 g, i.e., 20% of the 4:1 cement: gel sample mass, was used.
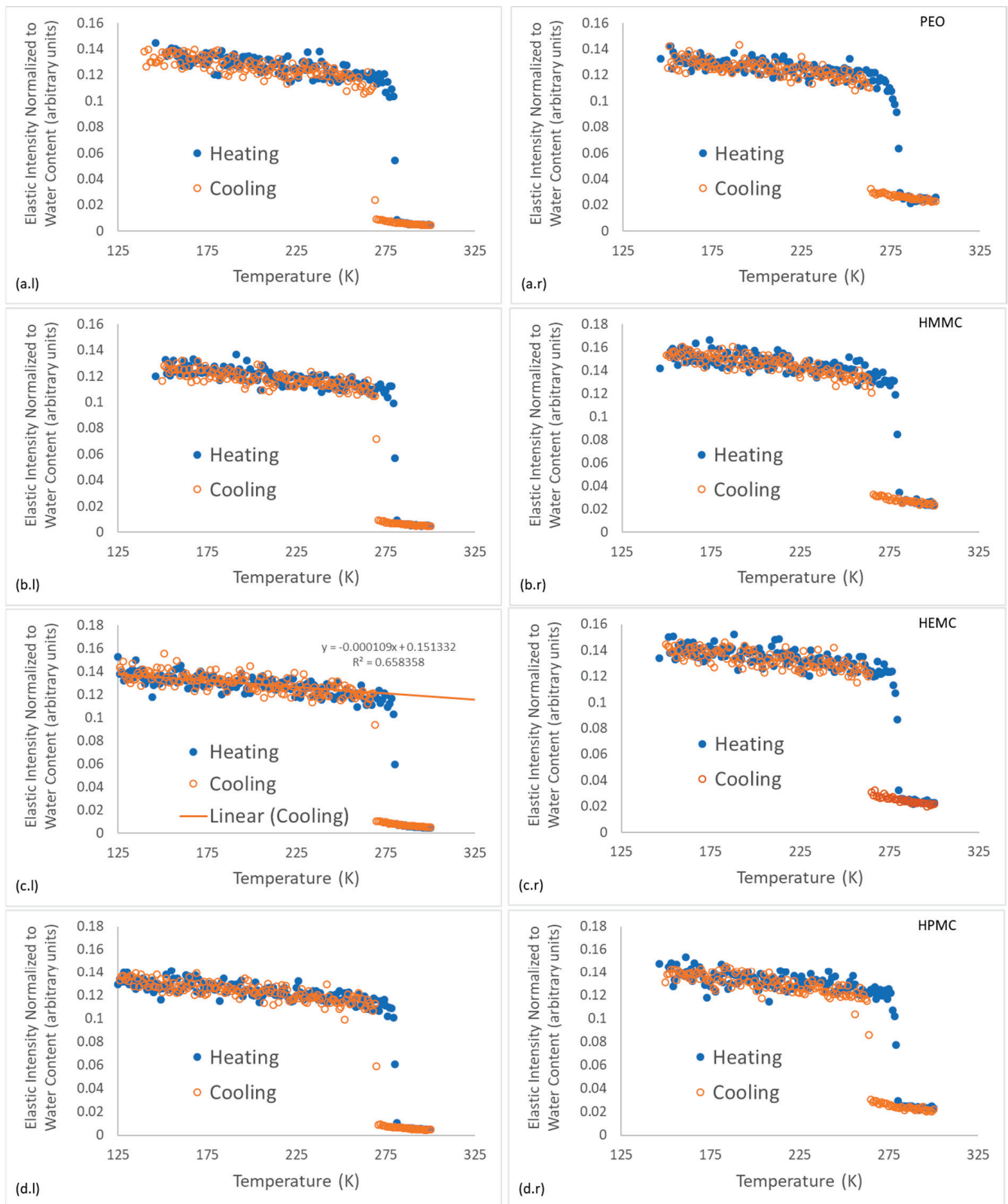
Figure 7. Energy-resolved "elastic" scattering data for hydrogels and hydrogel-cement pastes; the cooling curves are plotted with solid markers and the heating curves are plotted with open markers. Figures on the left (**l**) are the neat gels and figures on the right (**r**) are the gel-cement pastes. Subfigures are shown for each gel type: (**a**) PEO, (**b**) HMMC, (**c**) HEMC and (**d**) HPMC.
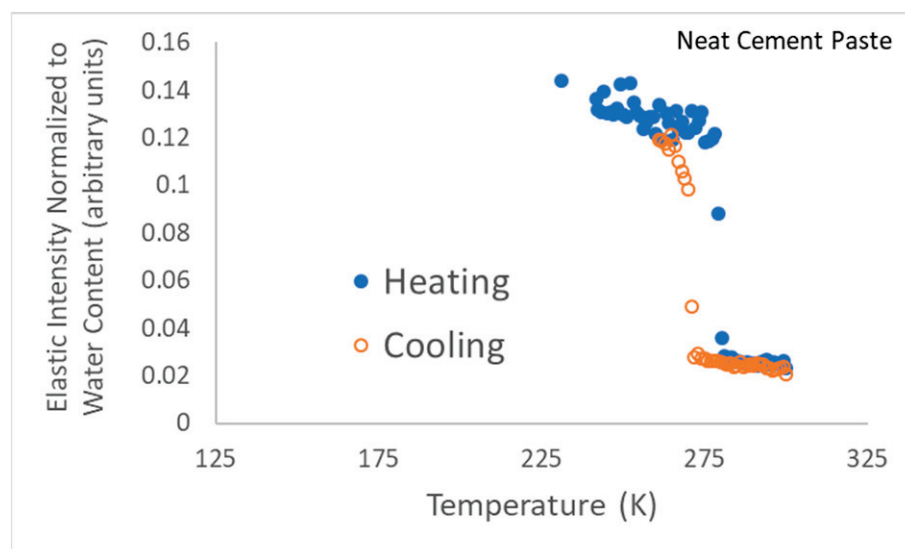
Figure 8. Energy-resolved "elastic" scattering data for neat cement paste, i.e., without gel. Note that this neutron scattering run was terminated just after the phase transition since the team's neutron beamtime was running out.

The energy-resolved "elastic" intensity scans provide insights into the gel-water structure and dynamics. As expected, a phase transition for the freezing of water was observed for all samples between 263–271 K and was characterized as an abrupt change in elastic intensity as the scattering centers became effectively immobile. Further cooling resulted in a continuous and monotonic increase in elastic intensity with decreasing temperature for all materials, as shown for HEMC in Figure 7c.l. Upon heating all samples demonstrated melting, indicated by an abrupt decrease in elastic intensity at about 275 K, i.e., near the melting point of water, 273.15 K.

Figure 7 illustrates that some supercooling before freezing was evident in all the gels, though a larger supercooling was required for the gel-cement samples, with only small variations. Gel-cement samples freeze at a temperature between 263 K and 265 K, while neat gels freeze between 268 K and 271 K. PEO froze at the notably lowest temperature of 268 K, a finding that was both consistent with the DSC results, indicating a finer pore structure, and the NMR DOSY results, which indicate the same. Very little variation was observed for melting.

For clarity, the "elastic" intensity data for each hydrogel was plotted separately; all the individual figures are shown, refer to Figure 7 which presents the plots of normalized elastic intensity as a function of temperature for the entire 4 mass % gel series, including PEO, HMMC, HEMC and HPMC. The linear region of the cooling section was fit with a straight line, as shown on Figure 7c.l as an example. The slope and intercept and respective standard errors were obtained. The resulting values are compared in the form of bar charts, refer to Figure 9. This data provides information about the structural characteristics of the gel and pastes, albeit in the frozen state. The intercept is a measure of the amount of "elastic" scattering, i.e., the intensity of "elastically" scattered neutrons. The higher the intensity, the greater the number of "elastic" scattering sites. In this case, the majority of the elastic scattering came from the frozen water. For gels, the amount of frozen water was nominally constant, gel-to-gel, since the water content of the gels was constant at 4 mass %. Furthermore, the elastic intensity had been normalized to water content. Thus, the intercept data, which for the neat gels indicated little or no variation with polymer type, said little about the effect of the polymer on the number of elastic scattering sites.
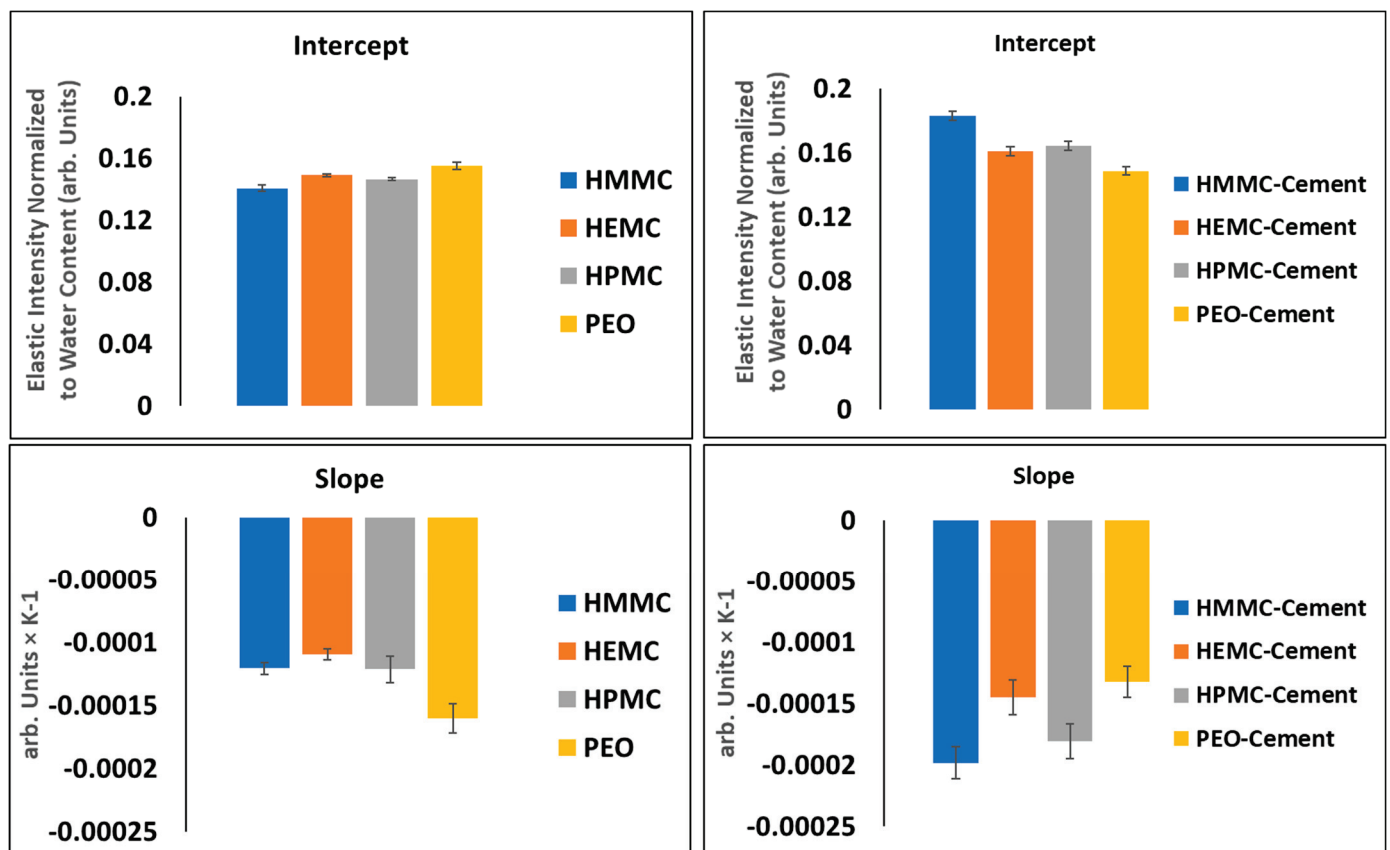
Figure 9. Regression analysis of linear region of cooling section for gel (**left-side**) and gel-cement pastes (**right-side**).

The slope, however, is the rate of change of intensity with respect to temperature and is proportional to the Debye-Waller (DW) factor which is a function of a material's elastic modulus, "*a*," i.e., the elastic constant of the vibrating "spring" that binds each atom to its equilibrium position, refer to Equations (1)–(3) [69]. For the linear portion of the *I(T)* vs. *T* curve, the quotient of the elastically scattered intensity at some *T* and some reference T_0, is defined as the Debye-Waller factor, refer to Equation (1). By transforming Equation (1) using the definition of the linear slope of the *I(T)* vs. *T* line, the Debye-Waller factor thus becomes a function of the slope, hence relating the material modulus to slope, refer to Equation (3). It is easily seen that for a perfectly rigid material, the slope must be zero. The relative stiffness of gels and gels confined within the gel-cement pastes are indicated by comparing the slopes of the *I(T)* lines; stiffer materials have lower slopes. The data indicated that the neat HEMC was stiffer than other hydrogels. This finding was consistent with rheological data which showed that HEMC had higher viscosity than either HPMC or PEO [34,35].

$$\frac{I(T)}{I(T_0)} = DW = exp\left\{-\frac{12\pi^2 k}{ad^2}(T - T_0)\right\} \tag{1}$$

$$s = slope = \frac{I(T) - I(T_0)}{T - T_0} \tag{2}$$

$$s\frac{(T - T_0)}{I(T_0)} + 1 = exp\left\{-\frac{12\pi^2 k}{ad^2}(T - T_0)\right\} \tag{3}$$

where, *k* is the Boltzmann constant, *d* is the atomic spacing, *T* is absolute temperature and the subscript "*0*" indicates some arbitrary reference state [69].

2.4.2. Dynamic Scattering

QENS dynamic scattering data measured at BASIS is in the form of the scattering function, I (Q, E), and this can be understood as the convolution of the dynamic structure factor with the instrumental resolution function, refer to Equation (4) [70]. In the incoherent approximation, this function is related to the self-correlation function of the water protons in time and space through the Fourier transform from frequency (energy) to time and from wave-vector (Q) space to real space [70], as shown here:

$$I(Q, E) = [x{\cdot}\delta(E) + (1 - x){\cdot}S(Q, E)] \otimes R(Q, E) + B{\cdot}E + C \tag{4}$$

where, *Q* (the momentum transfer) can be obtained [71] from:

$$hQ = h\left(k_i - k_f\right),\ k_i = \frac{2\pi}{\lambda_i}, k_f = \frac{2\pi}{\lambda_f} \tag{5}$$

and where *I (Q, E)* is the neutron scattering intensity as a function of momentum transfer and energy, $h = 4.135 \times 10^{-15}$ eVs is Planck's constant, λ is the neutron wavelength, x is the weighting fraction of the elastic component approximated by the function $\delta(E)$, $S(Q, E)$ is the Lorentzian dynamic structure factor corresponding to the sample (i.e., the Lorentzian function), $R(Q, E)$ is the resolution function of the spectrometer and $\otimes$ is the numerical convolution [72]. The BASIS raw dynamic scattering data were fit with a resolution-convolved Lorentz function plus a linear background term of ($B{\cdot}E + C$) for the gel samples and a superposition of a resolution-convolved Lorentz function and a delta-function (δ (E)) for elastic, or "settled water" intensity plus a linear background for the cement and gel-cement samples. The experimental $I(Q, E)$ was fit using a single Lorentzian function $S(Q, E)$ where $\Gamma(Q)$ is the half-width at half-maximum (HWHM) [72–74]:

$$S(Q, E) = \frac{1}{\pi}{\cdot}\frac{\Gamma(Q)}{E^2 + \Gamma^2(Q)} \tag{6}$$

The half-width at half-maxima (HWHM) of the Lorentzian function is proportional to Q^2 and, thus, provides a well-established method for determination of diffusion coefficients [72–74]. The dynamic range of BASIS (3.7 to 200 μeV) is suitable for studies of water diffusion [72]. The resulting half-width at half-maxima (HWHM(Q^2)) of the Lorentzian functions are presented in Figure 10. From these data, the water diffusivities, *D*, were obtained from a linear fit of HWHM(Q^2) with a (Q^2 + offset) function using Equation (7) [72–74]. The non-zero offset term was due to multiple scattering effects in the samples.

$$D_s(Q) = \frac{\Gamma(Q)}{hQ^2} \tag{7}$$

Table 1 shows the diffusivities and the "elastic", or "settled", water fractions for the cement and gel-cement samples. Hydroxy methyl methyl cellulose (HMMC) was included in the series, expanding the study to four gels, to provide a more complete description of how properties change with the cellulose derivative moiety. The half-width at half-maxima of the *S(Q, E)* spectra obtained from the model fit [72–74] shows a strong *Q*-dependence, refer to Figure 10, confirming a long-range translational diffusion process for water molecules in the samples. It was evident that there was an increase in the Γ for the gel-cement pastes compared to that of the neat gels. From Table 1, it is clear that the diffusion coefficient of water molecules in HMMC gel was greater than for the other three gels. However, the water diffusivity was almost the same for pastes, and independent of gel type. It was notable that the water diffusivity in the cement paste was lower than in gel-cement-based hydrogel pastes. This might be attributed to the hydration effect. As is shown in Figure 11, the gel-forming polymers used in this study had a complex effect on hydration. It was notable that HEMC both slowed the rate of hydration and delayed the onset of rapid hydration. For the neat cement paste, the rate of diffusivity of water was

slightly lower, which might have been due to the higher extent of hydration of the neat cement, again refer to Figure 11. From Table 1, the elastic signal fraction of neat cement was somewhat higher than cement-based hydrogel pastes, which might be evidence that neat cement was more hydrated and, thus, the observed water diffusivity was lower.
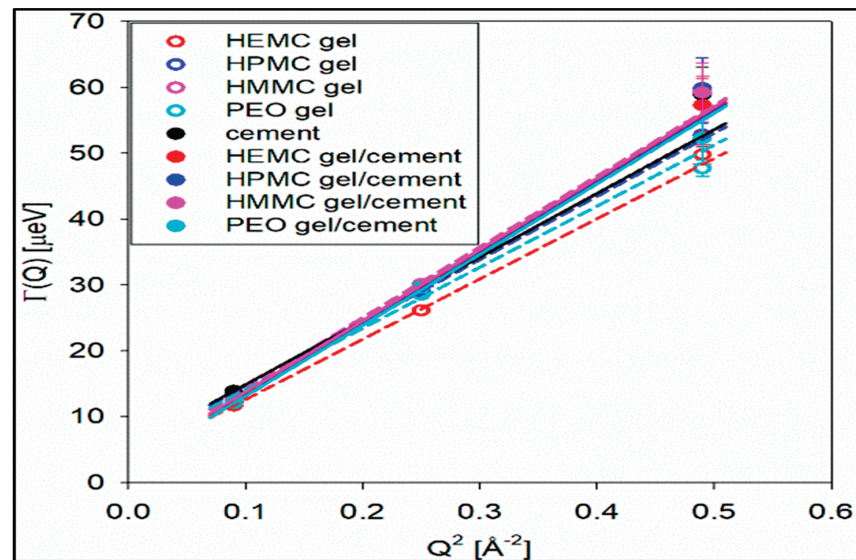
Figure 10. Plot of Lorentzian HWHM versus Q^2 for all samples.

Table 1. Diffusion coefficients obtained from fit of the HWHM for DQ^2 + offset.

Sample	Diffusivity, 10^{-10} m^2/s	Elastic Signal Fraction
HEMC gel	13.9043 ± 0.2715	NA
HMPC gel	14.5941 ± 0.3757	NA
HMMC gel	16.3169 ± 0.3816	NA
PEO gel	14.0958 ± 0.2824	NA
cement	14.6989 ± 0.5890	$1.729 \times 10^{-1} \pm 4.327 \times 10^{-3}$
HEMC gel-cement	16.3777 ± 0.6809	$1.562 \times 10^{-1} \pm 4.894 \times 10^{-3}$
HMPC gel-cement	16.3929 ± 0.6986	$1.523 \times 10^{-1} \pm 5.027 \times 10^{-3}$
HMMC gel-cement	16.4233 ± 0.6736	$1.698 \times 10^{-1} \pm 4.702 \times 10^{-3}$
PEO gel-cement	16.3169 ± 0.6755	$1.683 \times 10^{-1} \pm 5.321 \times 10^{-3}$
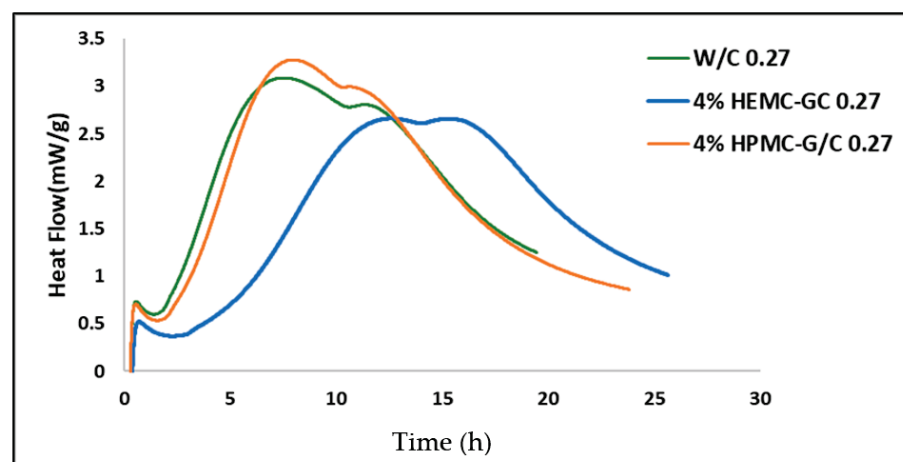
Figure 11. Hydration Calorimetry results for neat cement and gel-cement pastes containing 4 mass % HEMC and HEMC at a gel/cement ratio of 0.27.

The diffusivity in the gel-cement samples was somewhat higher, on average, than the diffusivity in the corresponding gel samples. Compared to the neat cement sample, the gel-cement diffusivities were also somewhat higher, and the elastic (settled) water fractions somewhat lower. It should be noted that the pure bulk water diffusivity value at 300 K was ca. 24×10^{-10} m^2/s [72].

2.5. Atomistic Simulations

In support of the experimental probes, molecular-scale simulations were also done. Atomistic simulations were performed on the cellulose derivative hydrogels only, i.e., HEMC and HPMC, in order to study their molecular behavior. The initial monomer structures were built using Materials Studio (Accelrys, now BIOVIA) while the data runs were made with LAMMPS (Large-scale Atomic/Molecular Massively Parallel Simulator, a free and open-source software developed by researchers at Sandia National Laboratory (SNL) and Temple University). H$_2$O molecules were added using the Grand Canonical Monte Carlo (GCMC) technique [75–77]. Each system was equilibrated using an NVT (constant number, volume and temperature) canonical ensemble at 298.15 K. The systems were relaxed using an NPT (constant number, pressure and temperature) ensemble, and, finally, the systems were again equilibrated using an NVT ensemble. These MDSs focused on polymer conformation, mobility of both water and polymer and hydrogen bonding structures. Polymer conformations were investigated at different concentrations. The equilibrated molecular structures for 4 mass % and 20 mass % HEMC and HPMC are shown in Figure 12 with water rendered as points. Inferences from images like these suggest that HEMC formed a more swollen, open, or dispersed structure than did HPMC. This more open structure might be partly responsible for HEMC's better performance as a printing aid. It is also likely responsible for the higher viscosity as well.
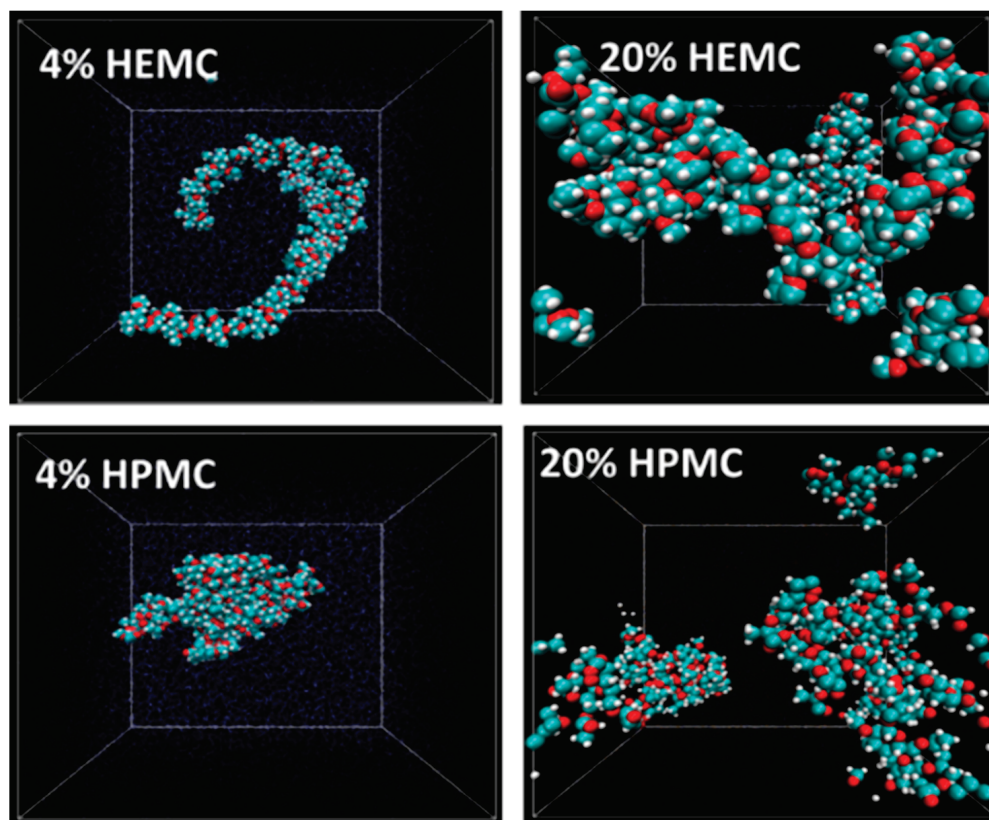
Figure 12. Conformation of HEMC and HPMC at 4 mass % and 20 mass %; O-red, C-blue and H-white. Box size is square and constant at 4.2 nm (42 Å).

Radii of gyration (Rg), a more direct indicator of the extent of swelling or openness of the molecule, were calculated for different polymer concentrations. The radius of gyration of a dissolved polymer provides an indication of the polymer's size in that environment. Figure 13 shows the Rg of the gel-forming polymers as a function of polymer concentration for HEMC and HPMC. For all concentrations, the size of the HEMC polymer was greater than the HPMC polymer. With a periodic simulation box of size approximately 42 Å, the Rg for HEMC indicated that the polymers spanned the entire box forming a percolated network.
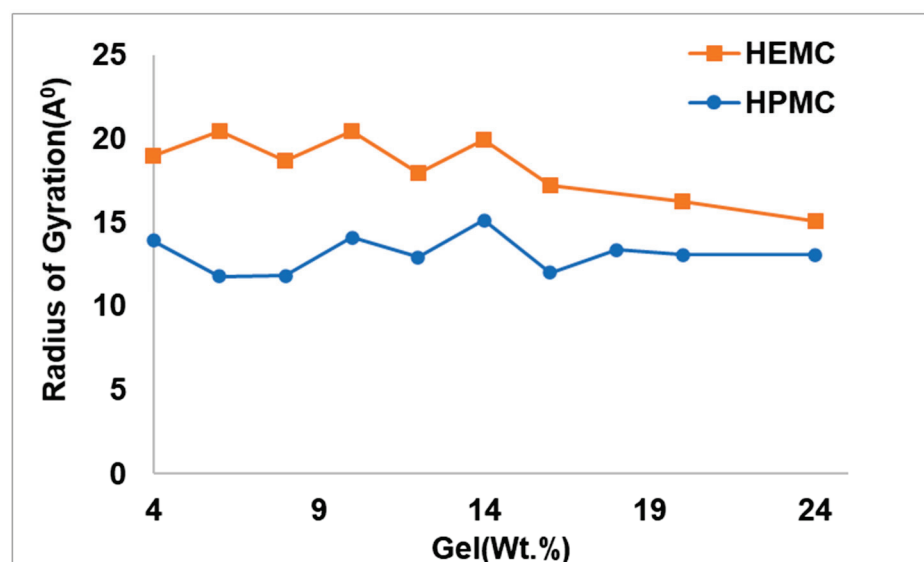
Figure 13. Radius of gyration of HEMC and HPMC at different polymer concentrations.

To obtain the self-diffusivity of water at different concentrations, the mean squared displacement of the center of mass of water molecules in HEMC and HPMC gels was plotted as a function of time and parametrically as a function of gel polymer mass percentage, refer to Figure 14. For both polymers, the mobility of water decreased with an increase in polymer concentration, as expected. However, the drop in the mobility of water in HEMC was larger than that in HPMC. This was consistent with the gel rheology experiments that showed a higher viscosity for HEMC.
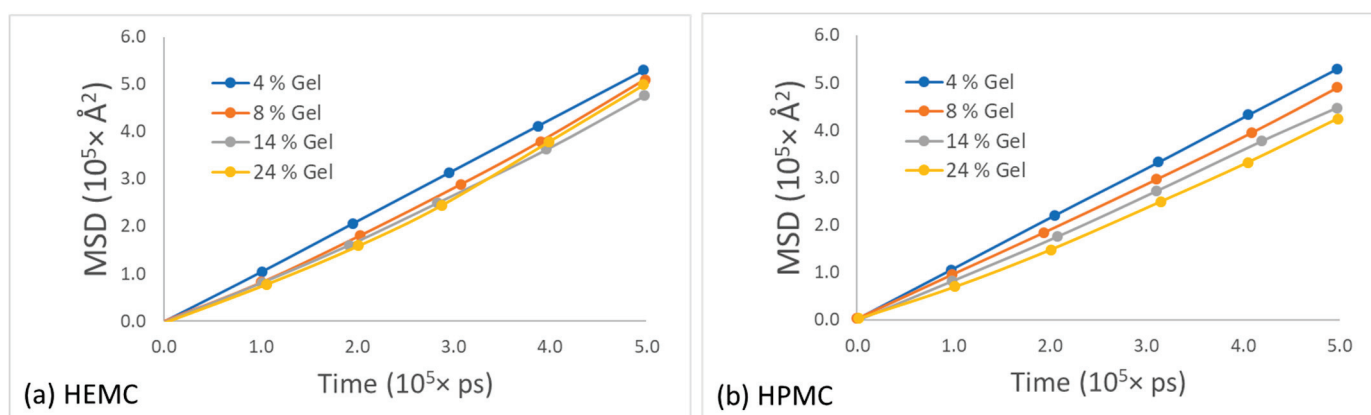
Figure 14. Mean square displacement of water for different polymer concentration gels for: (**a**) HEMC and (**b**) HPMC.

Likewise, the mean squared displacement of polymer centers of mass for the two gels at various concentrations is shown in Figure 15. The most apparent observation from this

data was that the mobility of these two polymers appeared similar at low polymer content, while the HPMC mobility appeared greater than that of HEMC at high polymer content. One explanation for this was consistent with the qualitative observation that HEMC formed a more percolated network than HPMC, and, thus, HEMC molecules had more restricted motion than HPMC, particularly at higher concentrations. This was also consistent with the experimentally measured viscosities.
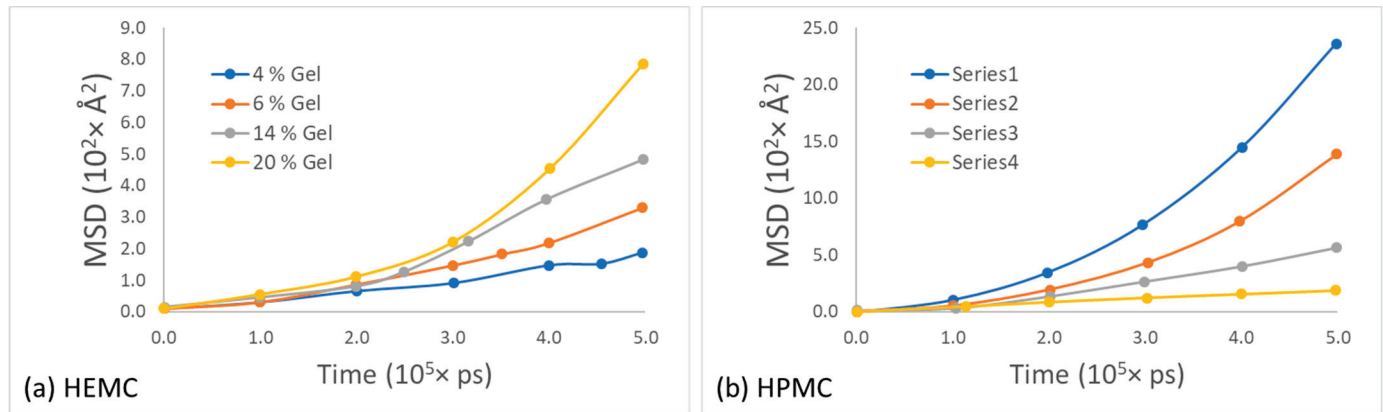
Figure 15. Mean square displacement of polymer at different concentrations of gel for: (**a**) HEMC and (**b**) HPMC.

To investigate the effect of hydrogen bonding on printability results, the probabilities of hydrogen bonding within the polymer and between polymer and water were calculated, refer to Figure 16. Here, the probability was defined as the number of hydrogen bonds actually formed divided by the total number of hydrogen bonds possible in a given system. The probability of hydrogen bond formation within the polymer was highest for HEMC, refer to Figure 16a. However, the trend was reversed for hydrogen bonds between polymer and water, with more hydrogen bonds between polymer and water observed for HPMC than HEMC, though marginally higher, refer to Figure 16b. These finding were again consistent with the observed viscosity of the gels and indicated that the greater number of hydrogen bonds within the polymer resulted in lower mobility of the chains and higher viscosity, as in this case for HEMC.
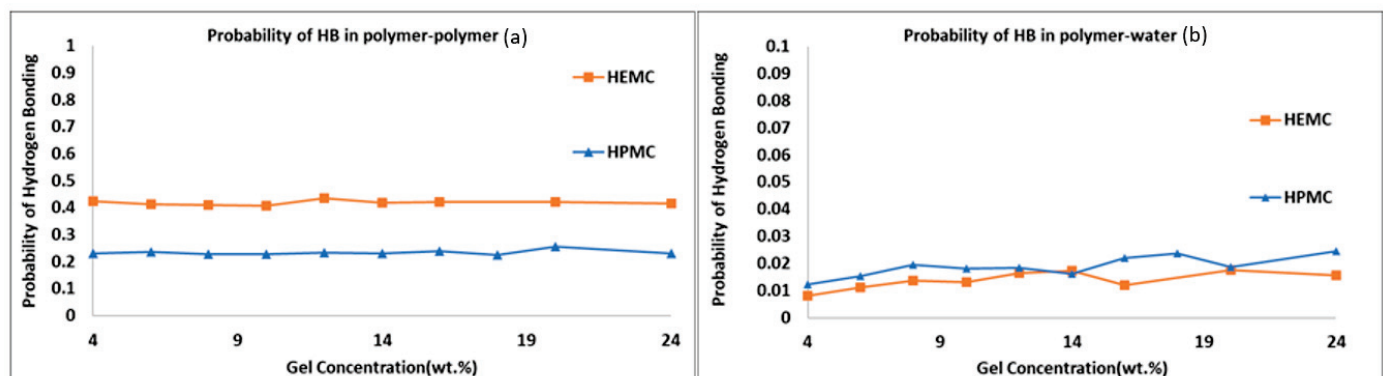
Figure 16. Probability of hydrogen bonding: (**a**) polymer-to-polymer, and (**b**) polymer-to-water.

3. Conclusions

The gels of three hydrogel-forming polymers, which were previously used as printing aids for cement-based pastes, were characterized using a range of experimental and computational techniques that bridged a wide domain of length scales. Prior experimental studies showed that polymers that form more viscous gels produce better printing outcomes.

Furthermore, those same gels produce cement-based printing pastes with lower storage moduli. The present multi-scale analysis showed that higher gel viscosity was produced by polymers that were more swollen, i.e., having expanded, polymeric networks, and which correlated to larger radii of gyration. These hydrogels seem to form more intramolecular hydrogen bonds, i.e., more entangled structures, and are more favorable as printing aids, since the high degree of polymer-to-polymer bonding produces higher gel viscosity at low polymer content. This research affirmed that rates of diffusion could be measured for residual water in polymer gels. It was shown, using DOSY, that the polymer gels themselves moved two orders of magnitude slower than the surrounding solvent (HOD). These rates were largely consistent with the bulk water rate of diffusion with slightly slower rates consistent with increased viscosity of the gel structures. Broadening on DOSY water peaks suggested that small populations of water were likely in chemical environments different from bulk water. This broadening phenomenon was larger for PEO than for either of the modified cellulose polymers and corroborated with DSC freezing studies, which implied a comparatively finer porous structure for PEO.

"Elastically" scattered neutrons from QENS measurements at BASIS indicated the mobility of hydrogen atoms of water molecules in a frozen state. The relationship between the slope of the neutron elastic intensity versus Temperature, and the Debye-Waller factor, were used to indicate relative differences in the modulus of frozen gels and frozen gels confined within cement paste. The modulus of neat HEMC gel was found to be higher than that for the other gel-forming polymers, consistent with rheological findings and the previously observed printing outcomes, which suggested that higher modulus gels produce better printing outcomes.

Dynamic data from QENS measurements at BASIS indicated that water diffuses slower within both neat gels and gel-cement than in bulk neat water, likely due to the presence of the polymer. This was somewhat inconsistent with DOSY findings that were unable to detect a significant difference between bulk water diffusion and diffusion in the presence of polymer.

4. Materials and Methods

4.1. Materials

Type I/II Portland cement was used and three different hydrogel-forming polymers were chosen: WALOCEL™ M-20678 hydroxyethyl methyl cellulose (HMEC), METHO-CEL™ 240 hydroxypropyl methyl cellulose (HPMC), and DOW Chemical POLYOX™ WSR 301 polyethylene oxide (PEO). Gels made with the various polymers were referred to as: HEMC (Gel 1), HPMC (Gel 2), and PEO (Gel 3). Deionized water was used in all the experiments where water was required [34,35]. Deuterium oxide (D_2O, 99.8 mass %) was used for all NMR DOSY and specific neutron scattering experiments. NMR diffusion experiments were done to measure both the mobility of the polymer and water.

To establish the water mobility, it was necessary to drop the concentration of water in the sample to within the detectable range of the instrument. Pure water would saturate the detector so D_2O was used as a diluent. In addition, the D_2O signal was used to adjust the magnetic field to be uniform through the sample; this common NMR practice is done by locking and shimming the instrument with D_2O.

4.2. Gel Preparation Procedures

4.2.1. Gels for Differential Scanning Calorimetry

To characterize the pore structure of hydrogels, 4.0 mass % hydrogels of the three selected polymers were prepared using procedures described in detail elsewhere [34,35]. In summary, gels were prepared by dispersing a requisite amount of the neat polymer into either cold or hot water and stirring vigorously until the solid was completely dispersed and a clear gel formed. Gels were then stored in sealed containers at 5 °C (refrigerated) until used. Gels were used within five days of preparation.

4.2.2. Gels for NMR

Hydrogels containing 0.5 mass % of HEMC, 0.2 mass % of PEO, and 2.0 mass % of PEO were prepared using the procedure summarized above and detailed elsewhere [34,35]. Clean and dried NMR tubes were used for this experiment. Stainless steel syringe tips with a length of 15 mm and outer diameter of 3.5 mm were used to fill the NMR tubes with the prepared hydrogels. To reduce macroscopically entrapped air within the NMR tube, i.e., visible bubbles, a vacuum pump was used. Filled tubes were repeatedly placed under vacuum and then brought to atmospheric pressure until the majority of the visible air had been removed, typically requiring several cycles.

4.2.3. Gels and Cement Pastes for Neutron Scattering

Gels used for neutron backscattering spectroscopy studies were prepared using deionized water, using the same procedures described previously [34,35]. Similarly, gel-cement pastes were prepared by hand mixing and shearing, using procedures also described in detail elsewhere [34,35].

4.3. Microstructural Analysis (XRD)

X-ray powder diffraction (XRD) was used for phase identification of the as-received polymers. The diffraction patterns were collected using Cu Kα radiation from a Rigaku Ultima IV diffractometer. The diffractometer was equipped with a D/tex Ultra-high-speed detector with fluorescence reduction. Diffraction patterns were collected from 20–80° 2θ in θ/2θ mode using a scan speed of 1°/min. The X-ray powder diffraction profiles for HEMC, HPMC, and PEO are shown in Figure 1. As expected, the PEO was highly ordered (crystalline), whereas the cellulose-derived materials were a combination of amorphous and crystalline matter characteristic of the parent cellulose [74,78–80].

4.4. Differential Scanning Calorimetry-Based Thermoporosimetry (DSC)

The melting behavior of water in the three hydrogels was investigated using thermoporosimetry. A DSC 2010 (Waters TA Instruments, New Castle, DE, USA) was used to investigate the pore structure and association between water and polymer in the hydrogels. Stainless steel pans with covers and O-rings (Perkin Elmer, Inc., Waltham, MA, USA) were used to prevent water evaporation. After carefully weighing the pans, covers, and O-rings, nominally 65 mg $\pm$ 5 mg of gel was placed inside a pan and the pan was hermetically sealed and again weighed. The pan was first cooled to -55 °C and then heated at a rate of 0.5 °C/min to 25 °C under a nitrogen purge gas flow of 40 cm^3/min. DSC runs were done in triplicate to establish experimental error. The DSC heating graphs (melting curves) for HEMC, HPMC, PEO gels and deionized water are shown in Figure 2.

4.5. Diffusion-Ordered Nuclear Magnetic Resonance Spectroscopy (DOSY)

DOSY data was used to determine the self-diffusivity of residual partially deuterated water, i.e., deuterated water (HOD) in deuterium oxide (D_2O) in neat hydrogels. DOSY experiments were conducted using a Advance III 500 MHz NMR (Bruker, Billerica, MA, USA) with a liquid nitrogen cooled Prodigy Cryoprobe. This work used the standard Bruker pulse programs Stimulated Echo Sequence (stepg1s) pulse sequence and a one-dimensional (1D) longitudinal eddy current delay experiment using bipolar gradients (ledbpgp2s1d), along with the Bruker automation program for DOSY experiments. Self-diffusion coefficients were measured using a pulsed field gradient spin echo (PGSE) method [81–86]. DOSY experiments were performed at 25 °C. The DOSY spectra were acquired with the ledbpgp2s pulse program from Bruker TopSpin software. The gradient strength was logarithmically incremented in 32 steps from 5% up to 95% of the maximum gradient strength. All measurements were performed with a diffusion delay Δ = 100 ms to keep the relaxation contribution to the signal attenuation constant for all samples. The gradient pulse length δ was 5 ms in order to ensure full signal attenuation. The resulting NMR spectra were

processed using Bruker Dynamics Center 2.5.6.b1, and DOSY maps were generated using Bruker Dynamics Center 2.5.6.b1 and MNova [87].

4.6. Quasi-Elastic Neutron Scattering

BASIS, a near-backscattering spectrometer at the Oak Ridge National Laboratory Spallation Neutron Source (ORNL/SNS) [88], was used in standard configuration, providing an energy resolution at the elastic line of ca. 3.7 μeV (full width at half maximum, FWHM) and accessible range of energy transfers of plus-minus 100 μeV. Besides measurements of the dynamic spectra (the neutron scattering intensity as a function of the energy and momentum transfer, I (Q, E)), BASIS was also used for measuring the temperature dependence of the energy-resolved "elastic" scattering intensity, as is customarily done for characterization of the phase state of the sample as a function of temperature [89]. Each sample was loaded into a flat-plate aluminum, indium-wire-sealed sample holder, 30 mm wide, 50 mm tall, and 0.5 mm thick. The temperature of the sample in the neutron beam was controlled with an accuracy of $\pm$ 0.25 K using a top-loading closed-cycle refrigerator. Loading of the sample holder was a somewhat tedious procedure which took roughly 30 min. An additional 15 min were used to place the loaded sample holder into the instrument. Samples were subsequently exposed to neutrons over a 2-h long dynamic measurement cycle to collect scattered intensities, I (Q, E). Thus, for each sample, the measurements of I (Q, E) at 300 K were completed in 2 h 45 min from the time that gel-cement samples were prepared or from the time that the neat gel samples were loaded. It should be noted that the procedure of preparation of neat gels and gel-cement- based pastes is described in detail elsewhere [35]. Following this measurement, the "elastic" intensity scans were collected, first on cooling to 10 K and then on warming at a rate of about 0.75 K/min. The timeline presented in Table 2 details the run cycle.

Table 2. Timeline for the sample preparation and data collection for experiments at BASIS.

Procedure	Time
Preparation of gels and storage	Gel preparation procedure is described elsewhere [34,35].
Mixing gels with cement particles to make gel-cement paste	Between 5 to 10 min from time of first contact of gel and cement; the mixing procedure is described elsewhere [34,35].
Loading either neat gel or gel-cement sample into the holder before exposure to beam	Roughly 30 min to load and seal the holder.
Placing the sample in the instrument	Additional 15 min to load sample into the beam path (required the removal of previous sample).
Exposing sample to the beam	2 h for the dynamic runs, then an additional 12 to 24 h of exposure (depending upon neutron beam stability) to gather the freezing/melting elastic scan data.

4.7. Atomistic Simulation

In support of the experimental observations, and to gain molecular-level insight into the structure and dynamics of hydrogel-forming polymers and their gels, atomistic molecular dynamic simulations (MDS) were performed for two cellulose-based polymers at various concentrations in water. A single polymer chain with 20 monomers was constructed using the Chain Builder module of Materials Studio and two such chains were packed into an orthogonal simulation box with periodic boundary conditions using the Amorphous Cell module. Water molecules were added to the initial box using the Grand Canonical Monte Carlo technique, in which water molecules are randomly inserted into the void spaces within the box. The number of water molecules was chosen to vary the concentration of polymers from 2 mass % to 20 mass %. The initial box size and the external pressure were chosen to be large enough to increase the probability of random insertion of water molecules. Once the required number of water molecules were added, the low-density system was subjected to energy minimization in a constant number, volume and temperature (NVT) ensemble, at 298.15 K, to relax the bonds, bond angles, and dihedrals of all constituents.

This was then followed by a compression run using a constant number, pressure, and temperature (NPT) ensemble at 298.15 K and 1 atm to adjust the size of the simulation box corresponding to the correct density. The CVFF and SPC/E forcefields were used to model the polymers and water, respectively. The ensemble was then equilibrated at NVT for 50 ns with a timestep of 1 fs and energies were monitored to check for equilibration. The data for analyses were collected from additional production runs of about 10 ns. Whereas systems were constructed using Materials Studio, all simulations were carried out using the LAMMPS simulation package, including energy minimization, compression equilibration and production runs. This was done as a preference of the authors and could have been done a number of other ways.

References

1. Cavalieri, F.; Chiessi, E.; Finelli, I.; Natali, F.; Paradossi, G.; Telling, M.F. Water, solute, and segmental dynamics in polysaccharide hydrogels. *Macromol. Biosci.* **2006**, *6*, 579–589. [CrossRef]
2. Ping, Z.H.; Nguyen, Q.T.; Chen, S.M.; Zhou, J.Q.; Ding, Y.D. States of water in different hydrophilic polymers—DSC and FTIR studies. *Polymer* **2001**, *42*, 8461–8467. [CrossRef]
3. O'Neill, H.; Pingali, S.V.; Petridis, L.; He, J.; Mamontov, E.; Hong, L.; Urban, V.; Evans, B.; Langan, P.; Smith, J.C.; et al. Dynamics of water bound to crystalline cellulose. *Sci. Rep.* **2017**, *7*, 11840. [CrossRef]
4. Chiessi, E.; Cavalieri, F.; Paradossi, G. Water and polymer dynamics in chemically cross-linked hydrogels of poly(vinylalcohol): A molecular dynamics simulation study. *J. Phys. Chem. B* **2007**, *111*, 2820–2827. [CrossRef]
5. Jiang, X.; Wang, C.; Han, Q. Molecular dynamic simulation on the state of water in poly(vinyl alcohol) hydrogel. *Comput. Theor. Chem.* **2017**, *1102*, 15–21. [CrossRef]
6. Baumgartner, S.; Lahajnar, G.; Sepe, A.; Kristl, J. Investigation of the state and dynamics of water in hydrogels of cellulose ethers by 1H NMR spectroscopy. *AAPS PharmSciTech* **2002**, *3*, 86. [CrossRef]
7. Capitani, D.; Crescenzi, V.; Segre, A.L. Water in hydrogels. An NMR study of water/polymer interactions in weakly cross-linked chitosan networks. *Macromolecules* **2001**, *34*, 4136–4144. [CrossRef]
8. Gun'ko, V.M.; Savina, I.N.; Mikhalovsky, S.V. Properties of water bound in hydrogels. *Gels* **2017**, *3*, 37. [CrossRef]
9. Ostrowska-Czubenko, J.; Pieróg, M.; Gierszewska-Drużyńska, M. State of water in noncrosslinked and crosslinked hydrogel chitosan membranes–DSC studies. *Prog. Chem. Appl. Chitin Deriv.* **2011**, *16*, 147–156.
10. Talik, P.; Hubicka, U. The DSC approach to study non-freezing water contents of hydrated hydroxypropylcellulose (HPC). *J. Therm. Anal. Calorim.* **2018**, *132*, 445–451. [CrossRef]
11. Yudianti, R.; Karina, M.; Sakamoto, M.; Azuma, J. DSC analysis on water state of salvia hydrogels. *Macromol. Res.* **2009**, *17*, 1015–1020. [CrossRef]
12. Hartmann, L.; Spanooudaki, A.; Kyritsis, A.; Pissis, P.; Pelster, R.; Shinyashiki, N.; Rodriguez Hernandez, J.C.; Gomez Ribbeles, J.L.; Monleon Pradas, M. Water and polymer dynamics in hydrogels. *Mod. Polym. Mater. Environ. Appl.* **2010**, *4*, 109–118.

13. Kyritsis, A.; Pissis, P.; Grammatikakis, J. Dielectric relaxation spectroscopy in poly(hydroxyethyl acrylates)/water hydrogels. *J. Polym. Sci. B Polym. Phys.* **1995**, *33*, 1737–1750. [CrossRef]

14. Paradossi, G.; Cavalieri, F.; Chiessi, E.; Telling, M.T.F. Supercooled water in PVA matrixes: I. An incoherent quasi-elastic neutron scattering (QENS) study. *J. Phys. Chem. B* **2003**, *107*, 8363–8371. [CrossRef]

15. Paradossi, G.; Finelli, I.; Natali, F.; Telling, M.T.F.; Chiessi, E. Polymer and water dynamics in poly(vinyl alcohol)/poly(methacrylate) networks. A molecular dynamics simulation and incoherent neutron scattering investigation. *Polymers* **2011**, *3*, 1805–1832. [CrossRef]

16. Zhao, Z.-J.; Wang, Q.; Zhang, L.; Wu, T. Structured water and water-polymer interactions in hydrogels of molecularly imprinted polymers. *J. Phys. Chem. B* **2008**, *112*, 7515–7521. [CrossRef]

17. Thermal Analysis to Determine Various Forms of Water Present in Hydrogels, TA Instruments. Available online: http://www.tainstruments.com/pdf/literature/TA384.pdf (accessed on 7 September 2022).

18. Krafcik, M.J.; Macke, N.D.; Erk, K.A. Improved concrete materials with hydrogel-based internal curing agents. *Gels* **2017**, *3*, 46. [CrossRef]

19. Erk, K.A.; Bose, B. Using polymer science to improve concrete: Superabsorbent polymer hydrogels in highly alkaline environments. In *Gels and Other Soft Amorphous Solids, Chapter 17, ACS Symposium Series*; ACS Publications: Washington, DC, USA, 2018; Volume 1296, pp. 333–356. [CrossRef]

20. Farzanian, K.; Wehbe, Y.; Ghahremaninezhad, A. The effect of superabsorbent polymers (SAP) on the performance of cementitious materials. In Proceedings of the 4th International Conference Sustainable Construction Materials Technologies, Las Vegas, NV, USA, 7–11 August 2016.

21. Saffer, E.M.; Lackey, M.A.; Griffin, D.M.; Kishore, S.; Tew, G.N.; Bhatia, S.R. SANS study of highly resilient poly(ethylene glycol) hydrogels. *Soft Matter* **2014**, *10*, 1905–1916. [CrossRef]

22. Hodge, R.M.; Edward, G.H.; Simon, G.P. Water absorption and states of water in semicrystalline poly(vinyl alcohol) films. *Polymer* **1996**, *37*, 1371–1376. [CrossRef]

23. Higuchi, A.; Komiyama, J.; Iijima, T. The states of water in gel cellophane membranes. *Polym. Bull.* **1984**, *11*, 203–208. [CrossRef]

24. Pasqui, D.; De Cagna, M.; Barbucci, R. Polysaccharide-based hydrogels: The key role of water in affecting mechanical properties. *Polymers* **2012**, *4*, 1517–1534. [CrossRef]

25. Omidian, H.; Park, K. Introduction to hydrogels. In *Biomedical Applications of Hydrogels Handbook*; Ottenbrite, R.M., Park, K., Okano, T., Eds.; Springer: New York, NY, USA, 2010; pp. 1–16.

26. Ito, K.; Yoshida, K.; Bellissent-Funel, M.-C.; Yamaguchi, T. Dynamic properties of water confined in sephadex G15 gel by quasi-elastic neutron scattering and neutron spin echo measurements. *Bull. Chem. Soc. Jpn.* **2014**, *87*, 603–608. [CrossRef]

27. Swenson, J.; Jansson, H.; Howells, W.S.; Longeville, S. Dynamics of water in a molecular sieve by quasielastic neutron scattering. *J. Chem. Phys.* **2005**, *122*, 084505. [CrossRef] [PubMed]

28. Bordallo, H.N.; Aldridge, L.P.; Desmedt, A. Water dynamics in hardened ordinary portland cement paste or concrete: From quasielastic neutron scattering. *J. Phys. Chem. B* **2006**, *110*, 17966–17976. [CrossRef]

29. Padureanu, I.; Aranghel, D.; Rotarescu, G.H.; Dragolici, F.; Turcanu, C.; Brzozowski, R.; Stepinski, M.; Pawel, S.; Kozlov, Z.A.; Semenov, V.A. Structure and dynamics of confined H_2O and D_2O in cement paste matrix studied by quasielastic and inelastic neutron scattering. *Romanian J. Phys.* **2005**, *50*, 551–559.

30. Youssef, M.; Pellenq, R.J.-M.; Yildiz, B. Glassy nature of water in an ultraconfining disordered material: The case of calcium-silicate-hydrate. *J. Am. Chem. Soc.* **2011**, *133*, 2499–2510. [CrossRef]

31. Chen, J.; Zhou, S.-M.; Ma, B.-G.; Zhang, L.-M.; Yi, J.-Z. Molecular dynamics simulations on dextran hydrogels. *e-Polymers* **2013**, *13*, 32–39. [CrossRef]

32. Keten, S.; Xu, Z.; Ihle, B.; Buehler, M.J. Nanoconfinement controls stiffness, strength and mechanical toughness of β-sheet crystals in silk. *Nat. Mater.* **2010**, *9*, 359–367. [CrossRef]

33. Hu, M.; Goicochea, J.V.; Michel, B.; Poulikakos, D. Water nanoconfinement induced thermal enhancement at hydrophilic quartz interfaces. *Nano Lett.* **2010**, *10*, 279–285. [CrossRef]

34. Taheri-Afarani, H.; Moser, N.H.; Garboczi, E.J.; Nasr-Esfahani, E.; Biernacki, J.J. Print fidelity metrics for additive manufacturing of cement-based materials. *Addit. Manuf.* **2022**, *55*, 102784. [CrossRef]

35. Taheri Afarani, H.; Carroll, W.; Garboczi, E.J.; Biernacki, J.J. Designing 3D printable cementitious materials with gel-forming polymers. *Constr. Build Mater.* **2021**, *268*, 121709. [CrossRef]

36. Osaka, N.; Shibayama, M.; Kikuchi, T.; Yamamuro, O. Quasi-elastic neutron scattering study on water and polymer dynamics in thermo/pressure sensitive polymer solutions. *J. Phys. Chem. B* **2009**, *113*, 12870–12876. [CrossRef] [PubMed]

37. Kupwade-Patil, K.; Bumajdad, A.; Brown, C.M.; Tyagi, M.; Butch, N.P.; Jamsheer, A.F.; Büyüköztürk, O. New insights into water dynamics of Portland cement paste with nano-additives using quasielastic neutron scattering. *J. Mater. Sci.* **2019**, *54*, 4710–4718. [CrossRef]

38. Bhattacharyya, T.; Saha, P.; Dash, J. Guanosine-derived supramolecular hydrogels: Recent developments and future opportunities. *ACS Omega* **2018**, *3*, 2230–2241. [CrossRef] [PubMed]

39. Chiang, W.-S.; Fratini, E.; Baglioni, P.; Liu, D.; Chen, S.-H. Microstructure determination of calcium-silicate-hydrate globules by small-angle neutron scattering. *J. Phys. Chem. C* **2012**, *116*, 5055–5061. [CrossRef]

40. Buerkle, L.E.; Li, Z.; Jamieson, A.M.; Rowan, S.J. Tailoring the properties of guanosine-based supramolecular hydrogels. *Langmuir* **2009**, *25*, 8833–8840. [CrossRef]

41. Peters, G.M.; Skala, L.P.; Plank, T.N.; Oh, H.; Manjunatha Reddy, G.N.; Marsh, A.; Brown, S.P.; Raghavan, S.R.; Davis, J.T. G4-quartet·M+ borate hydrogels. *J. Am. Chem. Soc.* **2015**, *137*, 5819–5827. [CrossRef]

42. Thorgeirsdóttir, T.O.; Kjøniksen, A.-L.; Knudsen, K.D.; Kristmundsdóttir, T.; Nyström, B. Viscoelastic and structural properties of pharmaceutical hydrogels containing monocaprin. *Eur. J. Pharm. Biopharm.* **2005**, *59*, 333–342. [CrossRef]

43. Backscattering Spectrometer—BASIS Laboratory, Oak Ridge National Laboratory. Available online: https://neutrons.ornl.gov/basis (accessed on 7 September 2022).

44. Le, P.; Fratini, E.; Ito, K.; Wang, Z.; Mamontov, E.; Baglioni, P.; Chen, S.-H. Dynamical behaviors of structural, constrained and free water in calcium- and magnesium-silicate-hydrate gels. *J. Colloid Interface Sci.* **2016**, *469*, 157–163. [CrossRef]

45. Tamai, Y.; Tanaka, H.; Nakanishi, K. Molecular dynamics study of polymer-water interaction in hydrogels. 1. Hydrogen-bond structure. *Macromolecules* **1996**, *29*, 6750–6760. [CrossRef]

46. Walter, J.; Sehrt, J.; Vrabec, J.; Hasse, H. Molecular dynamics and experimental study of conformation change of poly(N-isopropylacrylamide) hydrogels in mixtures of water and methanol. *J. Phys. Chem. B* **2012**, *116*, 5251–5259. [CrossRef] [PubMed]

47. Lee, S.G. *Structure-Property Relationship of Hydrogel: Molecular Dynamics Simulation Approach*; Georgia Institute of Technology: Atlanta, GA, USA, 2011.

48. Prabhakar, K.; Debnath, S.; Ganesan, R.; Palanikumar, K. A review of mechanical and tribological behaviour of polymer composite materials. In Proceedings of the IOP Conference Series: Materials Science and Engineering, The 3rd International Conference on Science, Technology, and Interdisciplinary Research (IC-STAR), University of Lampung, Lampung, Indonesia, 18–20 September 2017.

49. Chawla, R.; Sharma, S. A molecular dynamics study on Young's modulus and tribology of carbon nanotube reinforced styrene-butadiene rubber. *J. Mol. Model.* **2018**, *24*, 96. [CrossRef] [PubMed]

50. Bayer, R.; Knarr, M. Thermal precipitation or gelling behavior of dissolved methylcellulose (MC) derivatives—Behavior in water and influence on the extrusion of ceramic pastes. Part 1: Fundamentals of MC-derivatives. *J. Eur. Ceram.* **2012**, *32*, 1007–1018. [CrossRef]

51. Guan, W.; Ke, G.; Tang, C.; Liu, Y. Study on lubrication properties of carboxymethyl cellulose as a novel additive in water-based stock. In Proceedings of the WTC2005 World Tribology Congress III, Washington, DC, USA, 12–16 September 2005.

52. Lutz, H.; Bayer, R. Dry mortars. In *Ullmann's Encyclopedia of Industrial Chemistry*; Wiley-VCH Verlag GmbH & Co. KGaA: Weinheim, Germany, 2010; pp. 1–41.

53. Rowe, R.C.; Sheskey, P.J.; Weller, P.J. *Handbook of Pharmaceutical Excipients*, 4th ed.; Pharmaceutical Press: London, UK, 2003.

54. Zecher, D.; Gerrish, T. Cellulose derivatives. In *Thickening and Gelling Agents for Food*, 1st ed.; Imeson, A.P., Ed.; Springer: Boston, MA, USA, 1997; pp. 60–85. [CrossRef]

55. Heo, S.J.; Jang, I.; Barry, P.R.; Phillpot, S.R.; Perry, S.S.; Sawyer, W.G.; Sinnott, S.B. Effect of the sliding orientation on the tribological properties of polyethylene in molecular dynamics simulations. *J. Appl. Phys.* **2008**, *103*, 083502. [CrossRef]

56. Dey, A.; Karan, S.; De, S.K. Effect of nanofillers on thermal and transport properties of potassium iodide–polyethylene oxide solid polymer electrolyte. *Solid State Commun.* **2009**, *149*, 1282–1287. [CrossRef]

57. Cursaru, B.; Stanescu, P.S.; Teodorescu, M. The states of water in hydrogels synthesized from diepoxy-terminated poly(ethylene glycol)s and aliphatic polyamines. *Sci. Bull. Ser. B* **2010**, *72*, 99–114.

58. Yanul, N.A.; Kirsh, Y.E.; Verbrugghe, S.; Goethals, E.J.; Du Prez, F.E. Thermo responsive properties of poly(N-vinylcaprolactam) poly(ethylene oxide)aqueous systems: Solutions and block copolymer networks. *Macromol. Chem. Phys.* **2001**, *202*, 1700–1709. [CrossRef]

59. Graham, N.B.; Zulfiqar, Z.; Nwachuku, N.E.; Rashid, A. Interaction of poly(ethylene oxide) with solvents: 2. Water-poly(ethylene glycol). *Polymer* **1989**, *30*, 528–533. [CrossRef]

60. Shiblee, M.D.N.I.; Ahmed, K.; Khosla, A.; Kawakami, M.; Furukawa, H. 3D printing of shape memory hydrogels with tunable mechanical properties. *Soft Matter* **2018**, *14*, 7809–7817. [CrossRef]

61. Ginot, F.; Lenavetier, T.; Dedovets, D.; Deville, S. Solute effects in confined freezing. *arXiv* **2019**, arXiv:1907.10502. [CrossRef]

62. Liu, F.; Zargarzadeh, L.; Chung, H.-J.; Elliott, J.A.W. Thermodynamic investigation of the effect of interface curvature on the solid−liquid equilibrium and eutectic point of binary mixtures. *J. Phys. Chem. B* **2017**, *121*, 9452–9462. [CrossRef] [PubMed]

63. Zhang, C.; Liu, Z. Freezing of water confined in porous materials: Role of adsorption and unfreezable threshold. *Acta Geotech.* **2018**, *13*, 1203–1213. [CrossRef]

64. Agarwal, N.; Nair, M.S.; Mazumder, A.; Poluri, K.M. Characterization of nanomaterials using nuclear magnetic resonance spectroscopy. In *Characterization of Nanomaterials*; Bhagyaraj, S., Oluwafemi, O.S., Kalarikkal, N., Thomas, S., Eds.; Woodhead Publishing: Sawston, UK, 2018; pp. 61–102. [CrossRef]

65. Alcalde, A.B. New Methods in Mixture Analysis. Ph.D. Thesis, The University of Manchester, School of Chemistry, Manchester, UK, 2011.

66. Marega, R.; Aroulmoji, V.; Bergamin, M.; Feruglio, L.; Dinon, F.; Bianco, A.; Murano, E.; Prato, M. Two-dimensional diffusion-ordered NMR spectroscopy as a tool for monitoring functionalized carbon nanotube purification and composition. *J. Am. Chem. Soc.* **2010**, *4*, 2051–2058. [CrossRef] [PubMed]

67. Pagès, G.; Gilard, V.; Martino, R.; Malet-Martino, M. Pulsed-field gradient nuclear magnetic resonance measurements (PFG NMR) for diffusion ordered spectroscopy (DOSY) mapping. *Analyst* **2017**, *142*, 3771–3796. [CrossRef] [PubMed]

68. Wang, J.H. Self-diffusion coefficients of water. *J. Phys. Chem.* **1965**, *69*, 4412. [CrossRef]

69. Sasaki, N.; Saitoh, Y.; Sharma, R.K.; Furusawa, K. Determination of the elastic modulus of β-lactoglobulin amyloidfibrils by measuring the Debye-Waller factor. *Int. J. Biol. Macromol.* **2016**, *92*, 240–245. [CrossRef]

70. Chen, S.-H.; Bellissent-Funel, M.-C. Structure and dynamics of water in confined geometry. In *Hydrogen Bond Networks*; Dore, J.C., Bellissent-Funel, M.C., Eds.; Springer: Dordrecht, The Netherlands, 1994; Volume 435, pp. 307–336. [CrossRef]

71. González Sánchez, F. Water Diffusion through Compacted Clays Analyzed by Neutron Scattering and Tracer Experiments. Doctor of Philosophy, University of Bern, Faculty of Science, Bern, Switzerland, 2007.

72. Ishai, P.B.; Mamontov, E.; Nickels, J.D.; Sokolov, A.P. Influence of ions on water diffusion—A neutron scattering study. *J. Phys. Chem. B* **2013**, *117*, 7724–7728. [CrossRef]

73. Allen, G. Neutron scattering studies of self-diffusion in rubbers and polymer melts. *Pure Appl. Chem.* **1974**, *39*, 151–160. [CrossRef]

74. Abdelrazek, E.M.; Abdelghany, A.M.; Badr, S.I.; Morsi, M.A. Structural, optical, morphological and thermal properties of PEO/PVP blend containing different concentrations of biosynthesized Au nanoparticles. *J. Mater. Res. Technol.* **2018**, *7*, 419–431. [CrossRef]

75. Adams, D.J. Grand canonical ensemble Monte Carlo for a Lennard-Jones fluid. *Mol. Phys.* **1975**, *29*, 307–311. [CrossRef]

76. Mezei, M. A cavity-biased (T, V, μ) Monte Carlo method for the computer simulation of fluids. *Mol. Phys.* **1980**, *40*, 901–906. [CrossRef]

77. Mezei, M. Grand-canonical ensemble Monte Carlo study of a dense liquid: Lennard Jones, soft spheres and water. *Mol. Phys.* **1987**, *51*, 565–582. [CrossRef]

78. Zhang, Q. Investigating Polymer Conformation in Poly(Ethylene Oxide) (PEO) Based Systems for Pharmaceutical Applications. Master's Thesis, Chalmers University of Technology, Gothenburg, Sweden, 2011.

79. Körner, A.; Piculell, L.; Iselau, F.; Wittgren, B.; Larsson, A. Influence of different polymer types on the overall release mechanism in hydrophilic matrix tablets. *Molecules* **2009**, *14*, 2699–2716. [CrossRef] [PubMed]

80. Deka, C.; Kakati, D.; Bora, M. Cellulose graft copolymerization by gama and electron beam irradiation. In *Cellulose-Based Graft Copolymers: Structure and Chemistry*, 1st ed.; Thakur, V.K., Ed.; CRC Press: Boca Raton, FL, USA, 2015. [CrossRef]

81. Santoro, M.; Marchetti, P.; Rossi, F.; Perale, G.; Castiglione, F.; Mele, A.; Masi, M. Smart approach to evaluate drug diffusivity in injectable agar-carbomer hydrogels for drug delivery. *J. Phys. Chem. B* **2011**, *115*, 2503–2510. [CrossRef]

82. Groves, P. Diffusion ordered spectroscopy (DOSY) as applied to polymers. *Polym. Chem.* **2017**, *8*, 6700–6708. [CrossRef]

83. Bakkour, Y.; Darcos, V.; Li, S.; Coudane, J. Diffusion ordered spectroscopy (DOSY) as a powerful tool for amphiphilic block copolymer characterization and for critical micelle concentration (CMC) determination. *Polym. Chem.* **2012**, *3*, 2006–2010. [CrossRef]

84. Claridge, T.D.W. Diffusion NMR spectroscopy. In *High-Resolution NMR Techniques in Organic Chemistry*, 3rd ed.; Claridge, T.D.W., Ed.; Elsevier Science: Amsterdam, The Netherlands, 2009; pp. 303–334.

85. Kerssebaum, R. *DOSY and Diffusion by NMR*; NMR Application Lab, Bruker Biospin GmbH: Rheinstetten, Germany, 22 May 2022.

86. DOSY/Diffusion on Avance III Spectrometers. Available online: https://www2.chem.wisc.edu/~{}cic/nmr/Guides/Ba3vug/AV3_DOSY-diffusion.pdf (accessed on 7 September 2022).

87. MestReNova Manual, Mestrelab Research. Available online: https://mnova.pl/files/download/MestReNova-12-0-0_Manual.pdf (accessed on 7 September 2022).

88. Mamontov, E.; Herwig, K.W. A time-of-flight backscattering spectrometer at the Spallation Neutron Source, BASIS. *Rev. Sci. Instrum.* **2011**, *82*, 085109. [CrossRef]

89. Mamontov, E.; Luo, H.; Dai, S. Proton dynamics in N,N,N′,N′-tetramethylguanidinium bis(perfluoroethylsulfonyl)imide protic ionic liquid probed by quasielastic neutron scattering. *J. Phys. Chem. B* **2009**, *113*, 159–169. [CrossRef]

Article

Study on the Hydration Reaction of Typical Clay Minerals under Alkali and Sulfate Compound Activation

Siqi Zhang [1,*][iD], **Zeping Wu** [1], **Jiaming Chen** [1], **Runsheng Xu** [2], **Meina Wang** [1] and **Wen Ni** [1]

1 School of Civil and Resource Engineering, University of Science and Technology Beijing, Beijing 100083, China
2 School of Metallurgical and Ecological Engineering, University of Science and Technology Beijing, Beijing 100083, China
* Correspondence: zsq2017@ustb.edu.cn

Abstract: Sand, stone, tailings and other aggregates often contain a small amount of clay mineral and their hydration activity is low, thereby lowering concrete performance indexes while negatively affecting their resource utilisation. In this study, clay minerals, calcium hydroxide and desulfurised gypsum were used to prepare cementitious materials to examine kaolinite, montmorillonite, illite and chlorite clay mineral contents under compound activation. The effects of curing temperature and water reducer on clay samples were analysed. The results showed that the compressive strength of kaolinite samples cured at 25 °C and 55 °C reached 1.09 and 4.93 MPa in 28 days and increased by 43% and 12%, respectively, after adding a 0.3% water reducer. Montmorillonite was activated and its compressive strength reached 5.33 MPa after curing at 55 °C in 28 days. Illite exhibited some activity and its compressive strength reached 1.43 MPa after curing at 55 °C in 28 days and the strength increased slightly after adding a water reducer. The chlorite sample had no strength after activation under the same conditions. Furthermore, X-ray diffraction and scanning electron microscope and energy-dispersive spectroscopy microstructure analyses showed that after alkali and sulfate activation, the hydration products of activated clay minerals mainly included ettringite, hydrated calcium aluminate and hydrated calcium silicate. The increase in curing temperature accelerated the reaction speed and improved the early strength. However, the effect on chlorite minerals was not obvious.

Keywords: clay minerals; hydration product; compound activation; ettringite; calcium aluminate hydrate

1. Introduction

Clay minerals, which are typically layered silicate minerals with a thickness of <2 μm, are a major component of soil. Their type and content greatly influence soil properties. Clay minerals are usually attached to the sandstone aggregate surface during their formation, excavation and crushing. Due to their layered structural characteristics and large specific surface areas, they have a certain adsorptive effect on the water reducer, which negatively affects various properties of concrete.

Studies have shown that clay minerals attached to aggregates, such as gravel and sand, infiltrate into the concrete system during concrete production, which reduces the workability [1,2], strength [3], deformation performance [4,5] and durability [6] of concrete to varying degrees. D. C. Pike revealed that increasing kaolinite, illite and montmorillonite content reduces concrete strength, with montmorillonite having a significant effect followed by illite and kaolinite [7]. M. A. Fam et al. suggested that clay minerals can adsorb cement hydration products, thereby affecting the hydration reaction of cement [8].

One of the most significant current directions in clay mineral usage is to stimulate the activity of clay minerals to make them become valuable components in the concrete system. D. Read et al. explored the long-term contact interface between cement and clay and found that a very thin transition layer appeared on the contact interface between the

two. Through microstructure observation, the original structure of the two was damaged and new minerals were produced [9]. D. F. Noble et al. studied the reaction of clay cement mixture containing kaolinite, illite and montmorillonite and found only a small reduction of calcium hydroxide after long-term curing at room temperature; calcium hydroxide was also completely consumed after curing at 79 °C [10].

E. C. Gaucher et al. studied the transformation and dissolution kinetics of minerals in montmorillonite. Temperature and pH increase the dissolution rate, and the products include zeolite, hydrated calcium silicate and hydrated calcium aluminosilicate [11]. F. G. Bell et al. found that almost all clay minerals reacted with lime. When lime was added to the soil, clay minerals first reacted with Ca^{2+} at the bond breaking point under highly alkaline conditions (pH = 12.4) and the products included hydrated calcium silicate and aluminate [12]. Furthermore, E.C. Gaucher found that the reaction speed of clay minerals was slow under alkaline conditions (pH = 12, 13), but increasing the curing temperature to 150–200 °C favoured the reaction of clay minerals. The crystal structure of clay minerals has been shown to be seriously damaged under high temperatures [11].

Our previous research revealed that under the condition of compound activation by alkali and sulfate, aluminosilicate minerals with low hydration activity can be stimulated, mainly relying on the four environmental ions, Ca^{2+}, SO_4^{2-}, OH^- and $Al(OH)^-$, to form ettringite ($3CaO \cdot Al_2O_3 \cdot 3CaSO_4 \cdot 32H_2O$) first. Owing to its small solubility, the formation of ettringite will continue to absorb the ions in the environment, thereby promoting further hydration reactions [13,14]. Xu Wang et al. used mineral micro powder to partially replace metakaolin to prepare a mineral micro powder metakaolin-based geopolymer under alkali activation. They found that the presence of calcium in mineral micro powder promoted the geopolymerisation reaction and at a powder content of 30 wt%, the polymer exhibited superior mechanical properties [15]. Mengya Niu et al. prepared a green and low-carbon geopolymer concrete using MFA as a partial replacement for metakaolin. The type of hydrated gel products was still a calcium silicoaluminate-based silicoaluminate gel in their study [16]. Xiaoyun Yang et al. explored the potential of using ultrafine calcined coal gangue and ground granulated blast furnace slag to develop a new geopolymer with the activation of a single activator (sodium hydroxide) or mixed activator (sodium hydroxide, liquid sodium silicate and desulfurization gypsum). They find the coal gangue geopolymers were mainly C–A–S–H, N–A–S–H and C–N–A–S–H gels and the mixed activator tended to yield higher strengths than the single activator because the hydration reaction was violent and produced more gels [17].

In this study, four typical clay minerals (kaolinite, montmorillonite, illite and chlorite), calcium hydroxide and desulfurised gypsum are used to prepare cementitious materials. Different curing temperatures and water reducer are selected as variable. Through X-ray diffraction (XRD), scanning electron microscope (SEM) and energy dispersive spectroscopy (EDS) analyses, the mineralogical changes and hydration reaction under composite activation conditions are studied.

2. Results and Discussion

2.1. Compressive Strength

The compressive strength of each group of samples taken at 3, 7 and 28 days was tested, and the results are shown in Figure 1 and Table 1. As the curing age increased, the compressive strength of the samples increased to varying degrees. Increasing the curing temperature significantly promoted improved compressive strength. Adding a water-reducing agent to the control group samples with the same composition reduced the amount of water used in the sample preparation process to a certain extent, slightly lowered the water binder ratio and slightly increased the strength of the water-reducing agent group. As shown in Figure 1a, while the strength of G0 at 3 days, cured at 25 °C, was not measured, that of G0-2 at 3 days cured at 55 °C reached 2.42 MPa; the 3-days strength of G1 curing only reached 0.79 MPa, but that of G1-2 curing reached 3.78 MPa; after 28 days of curing, G0-2 strength was 4.93 MPa, which was ~352% higher than G0 strength (1.09 MPa). M0 and M1, cured at

25 °C for 3 days, had no strength and could only maintain the shape. However, after curing at 55 °C for 3 days, the strengths of M0-2 and M1-2 reached 2.48 and 2.26 MPa, respectively, and the strengths of 28 days curing reached 4.53 and 5.33 MPa, respectively. After curing at 55 °C for 3 days, the strength of Y1-2 added with the water reducer was 0.27 MPa. After 28 days of curing, the strength reached 1.92 MPa, which was 34% higher than that of Y0-2 after 28 days of curing. However, at curing temperatures of 25 °C and 55 °C or by adding a water-reducing agent, the chlorite samples did not generate strength in each test age.
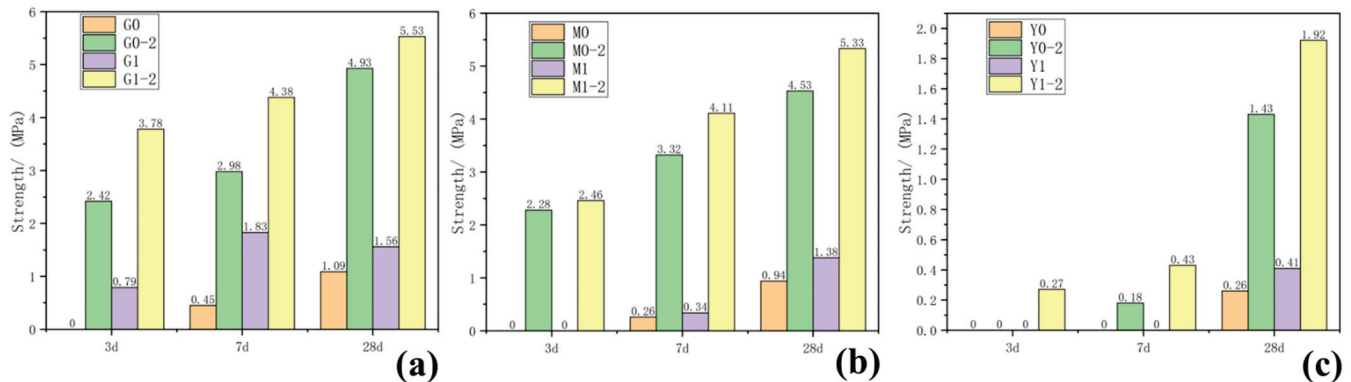
Figure 1. Results of 3-, 7- and 27-day compressive strength of samples: (**a**) group G, (**b**) group M, (**c**) group Y.

Table 1. Compressive strength of samples at different ages.

Samples	Water Reducer (g)	Curing Temperature (°C)	Three-Day Compressive Strength (MPa)	Seven-Day Compressive Strength (MPa)	Twenty-Eight-Day Compressive Strength (MPa)
G0	0	25	—	0.45	1.09
G0-2	0	55	2.42	2.98	4.93
G1	1.2	25	0.79	1.83	1.56
G1-2	1.2	55	3.78	4.38	5.53
M0	0	25	—	0.26	0.94
M0-2	0	55	2.48	3.32	4.53
M1	1.2	25	—	0.34	1.38
M1-2	1.2	55	2.26	4.11	5.33
Y0	0	25	—	—	0.26
Y0-2	0	55	—	0.18	1.43
Y1	1.2	25	—	—	0.41
Y1-2	1.2	55	0.27	0.43	1.92
L0	0	25	—	—	—
L0-2	0	55	—	—	—
L1	1.2	25	—	—	—
L1-2	1.2	55	—	—	—

2.2. XRD Phase Characteristics of Clay Samples

Figure 2a shows the XRD pattern of the kaolinite raw material. The main diffraction peak occurred at 2θ = 12.32°, 20.22° and 24.86° and the crystalline phase was mainly kaolinite, with a small amount of halloysite and mica. G0 samples are shown in Figure 2b. Under the condition of 25 °C curing, small amounts of monosulfide calcium aluminate hydrate, ettringite, clinoptilolite and calcium aluminate hydrate were generated in the G0 samples for 3 days. At 7 days, the peak of monosulfide calcium aluminate hydrate disappeared and the products were ettringite, calcium aluminate hydrate and clinoptilolite. After 28 days of curing, the peak strength of calcium hydroxide decreased. As shown in Figure 2c, under the condition of curing at 55 °C, a small amount of amorphous crystalline zeolite-like phase was found in the G0-2 sample of 3 days; the diffraction peak of calcium hydroxide disappeared after 7 days, which reappeared together with that of desulfurised

gypsum after 28 days and the peak intensity of the product exceeded that of G0. Increasing the curing temperature in the early and middle stages of the reaction effectively accelerated the reaction speed of the kaolin group samples and the diffraction peak intensity of primary minerals decreased significantly. Figure 2d shows that the G1-2 sample was at diffraction peak 2 after adding a water reducer and curing at 55 °C for 3 days, the peak of monosulfide calcium aluminate hydrate at 9.8° and calcium aluminate hydrate formed a small 'bulge'. After 7 days of curing, the diffraction peak intensity of ettringite and monosulfide calcium aluminate hydrate increased significantly and the characteristic peak of kaolinite decreased. After 28 days of curing, the diffraction peak of desulfurised gypsum did not appear in the G1-2 samples, the diffraction peak of calcium hydroxide was weak and the amount of ettringite increased slightly. The addition of a water-reducing agent did not significantly affect the reaction degree of kaolinite samples.

Figure 2. XRD patterns of kaolinite: (**a**) raw material, (**b**) 3-, 7- and 28-day curing age G0, (**c**) 3-, 7- and 28-day curing age G1, (**d**) 3-, 7- and 28-day curing age G1-2.

Figure 3a shows the XRD pattern of the montmorillonite raw material. The main diffraction peak occurred at $2\theta = 5.8°$, $19.8°$ and $61.9°$ and the crystalline phase was mainly montmorillonite, with a small amount of quartz doping. Figure 3b shows that ettringite and hydrated calcium aluminate were generated in the M0 samples cured for 3 days. After 7 days of curing, a small amount of hydrated calcium aluminate and ettringite was generated, which probably contained orthophosphate zeolite. The diffraction peak intensity decreased after 28 days of curing, the reaction speed was relatively slow at 25 °C and the main products remained unchanged. As shown in Figure 3c, under the condition of curing at 55 °C, the diffraction peak intensity of M0-2 samples at 3, 7 and 28 days was basically the same. Increasing the temperature made montmorillonite consume much gypsum at the reaction's early stage, thereby accelerating the early reaction degree. Adding a water reducer did not affect the raw material minerals and reaction products and only a small

amount of it could improve the compressive strength (Figure 3d), which had no significant effect on the reaction speed and degree of montmorillonite in the system.

Figure 3. XRD patterns of montmorillonite: (**a**) raw material, (**b**) 3-, 7- and 28-day curing age M0, (**c**) 3-, 7- and 28-day curing age M1, (**d**) 3-, 7- and 28-day curing age M1-2.

Figure 4a illustrates the XRD pattern of the illite raw material. The crystalline phase was mainly illite, with a small number of overlapping quartz phase peaks. The figure shows that a small amount of ettringite and hydrated calcium aluminate, except for unreacted desulfurised gypsum and calcium hydroxide, existed for the Y0 samples cured for 3 days. After 7 days of curing (Figure 4b), no new products were generated. After 28 days, except for the diffraction peak intensity of the existing products that slightly changed, no new products were generated and residues of desulfurised gypsum and calcium hydroxide remained. Y0 samples participated in the reaction less and the hydration reaction was slow. Under the condition of curing at 55 °C (Figure 4c), Y0-2 samples were cured for 3 and 7 days. In addition to calcium hydroxide and desulfurised gypsum peaks, a small amount of ettringite and hydrated calcium aluminate were newly produced. At 28 days, the characteristic peaks in the samples were similar and the intensity of the ettringite diffraction peak increased. Comparing the XRD patterns of Y0 at 28 days and Y0-2 at 3 days, the diffraction peak intensities of the reactants and products of both groups were equivalent, indicating that the reaction degrees of the two groups were similar. By adding a water reducer (Figure 4d), the characteristic peaks were basically the same, which only increased the compressive strength of illite samples to a certain extent; notably, increasing the curing temperature can induce improved compressive strength to a certain extent.
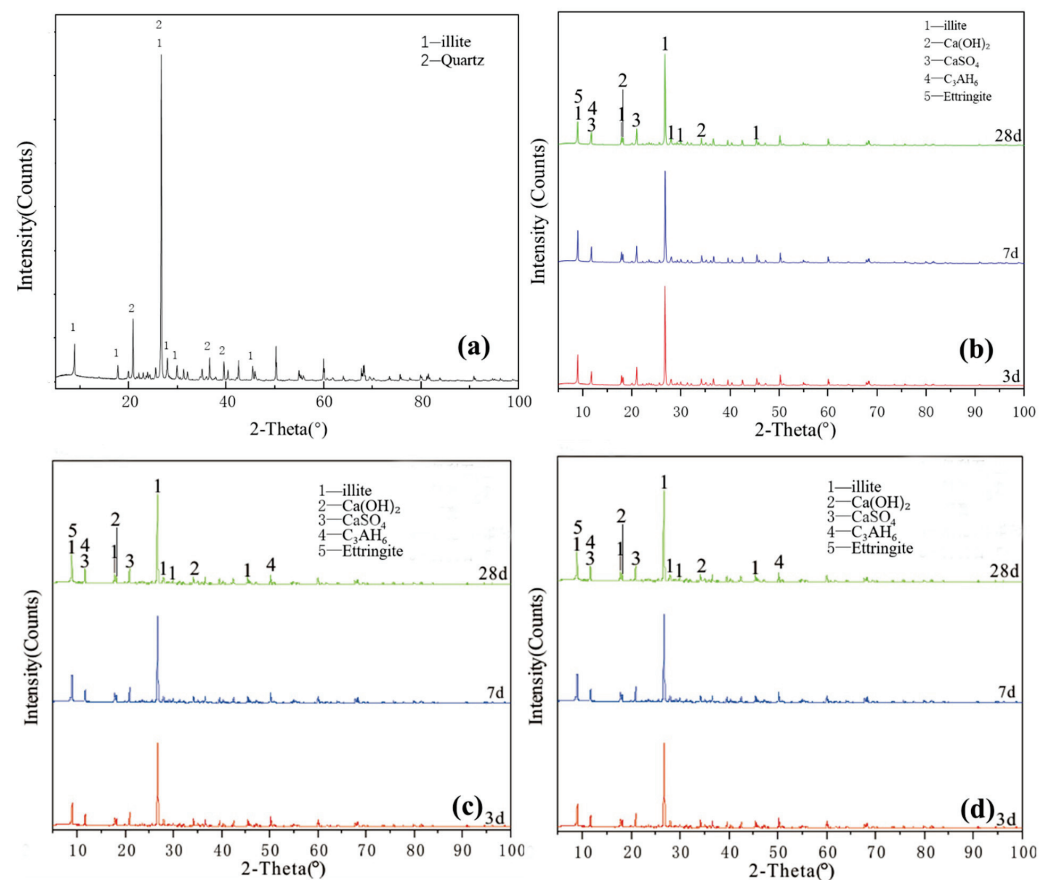
Figure 4. XRD patterns of illite: (**a**) raw material, (**b**) 3-, 7- and 28-day curing age Y0, (**c**) 3-, 7- and 28-day curing age Y1, (**d**) 3-, 7- and 28-day curing age Y1-2.

Figure 5a illustrates the XRD pattern of the chlorite raw material. The crystalline phase was mainly chlorite, with a small amount of talc crystalline phase peak. Figure 5a–c shows that the characteristic peaks of hydration products of L0, L0-2 and L1-2 at various ages slightly changed and the crystallisation degree of reaction products was poor. The new products formed probably included a small amount of ettringite, calcium aluminate hydrate, clinoptilolite and calcium silicate hydrate. The diffraction peak intensity of chlorite, talc, desulfurised gypsum and calcium hydroxide slightly decreased, indicating that chlorite did not participate in the reaction with desulfurised gypsum and calcium hydroxide; the paucity of the type and quantity of hydration products explained why the compressive strength of chlorite group samples was almost 0. After increasing the temperature and adding a water-reducing agent, the change in the degree of diffraction peak was extremely low and the sample was relatively stable; no obvious diffraction peak of reaction products was observed during the 28-day curing time. These findings showed that increasing the curing temperature does not significantly improve the reaction speed and degree of the chlorite system. The chlorite group samples were unable to harden during the curing process of 3–28 days, indicating that temperature and water reducer slightly affect the compressive strength of chlorite and desulfurised gypsum system and that chlorite cannot harden in this system for 28 days.
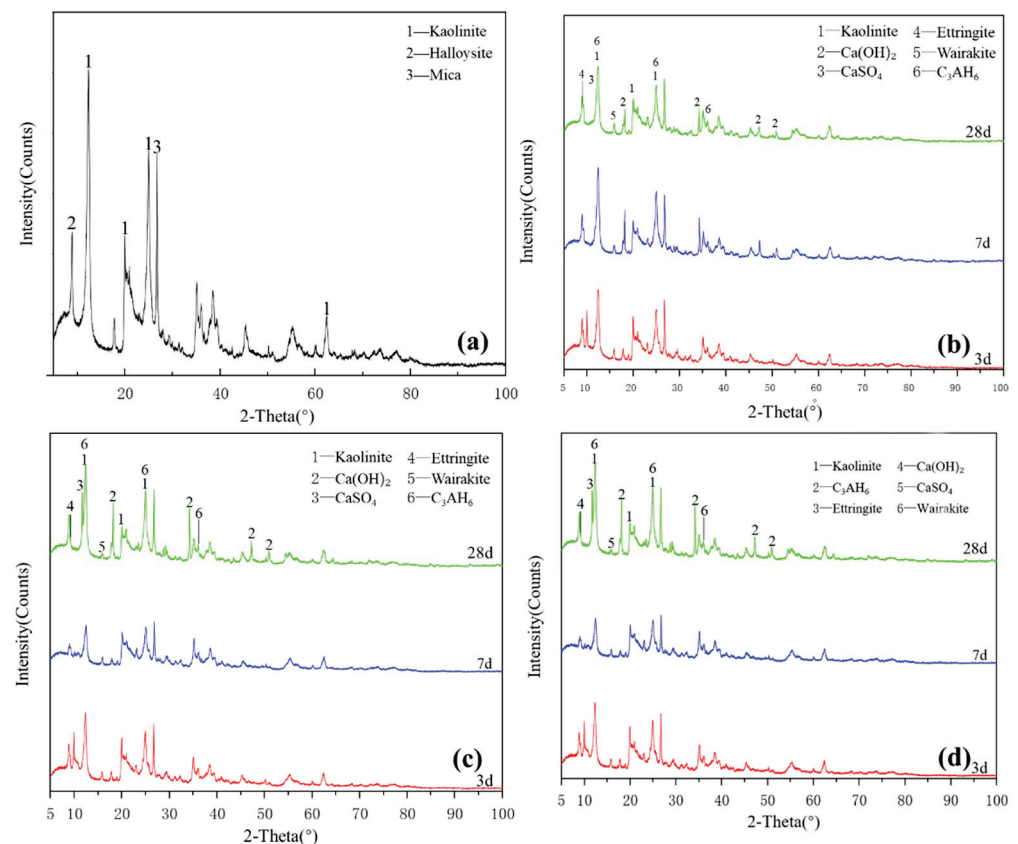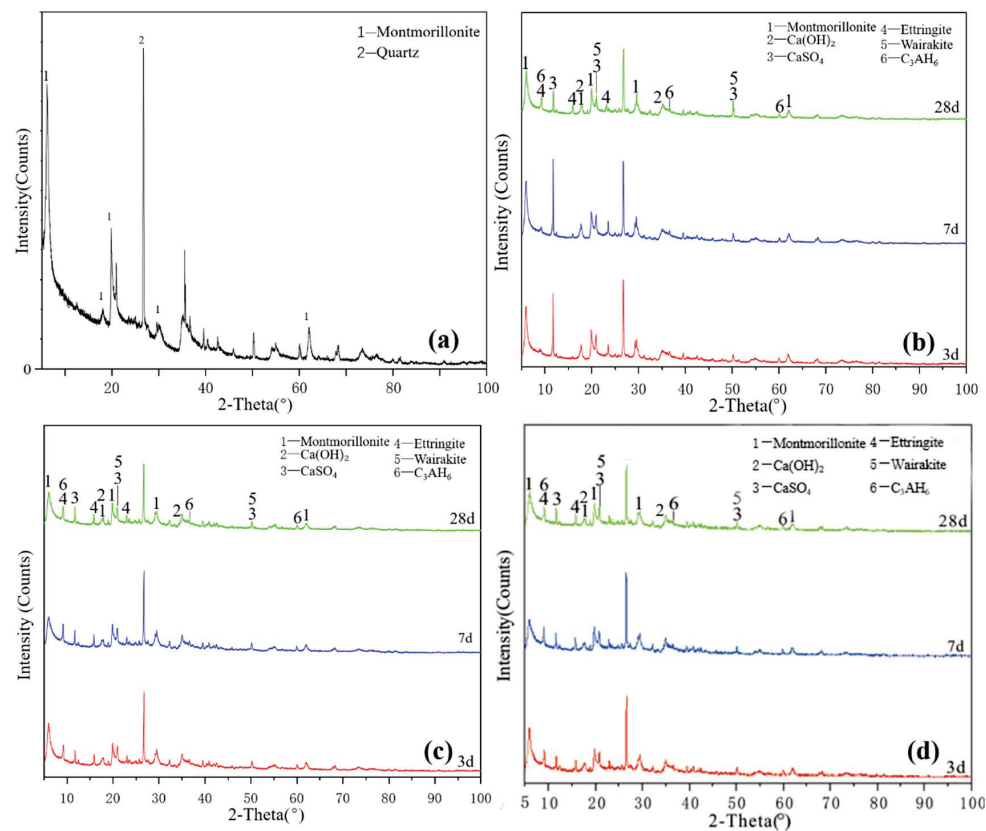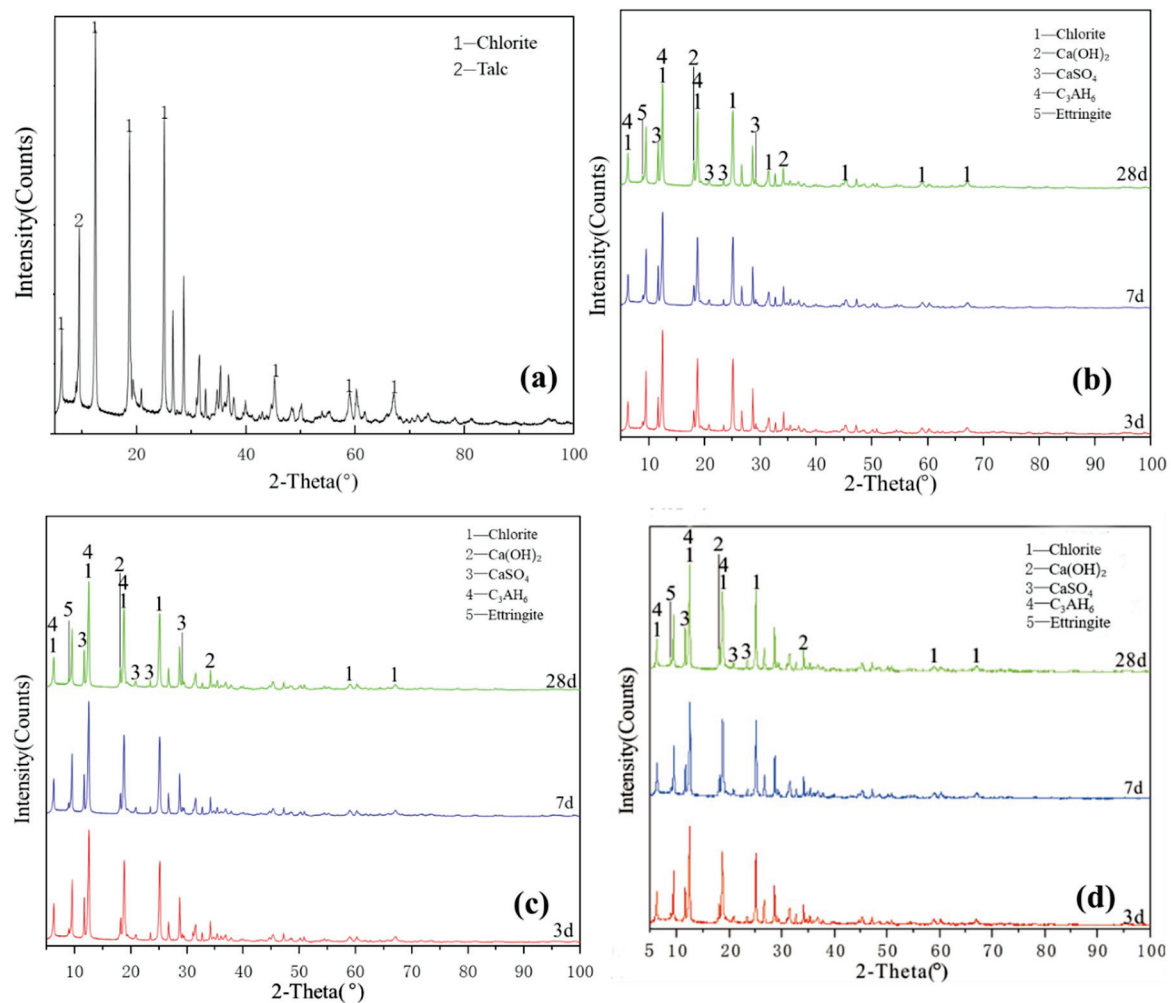
Figure 5. XRD patterns of chlorite: (**a**) raw material, (**b**) 3-, 7- and 28-day curing age Y0, (**c**) 3-, 7- and 28-day curing age Y1, (**d**) 3-, 7- and 28-day curing age Y1-2.

2.3. SEM–EDS Micromorphology Characterisation of Clay Samples

As shown in Figure 6A, kaolinite raw materials are mainly irregular flakes under SEM and a single crystal size is 2–6 μm in the form of flakes and laminated. Acicular minerals are mainly halloysite and the crystal size is 1–3 μm. For the G0 sample cured for 3 days at 25 °C (Figure 6B), the generated gel-like substances bonded the particle, and some short columnar and acicular crystals were observed on the surface. Combined with EDS surface scan analysis, the crystals were monosulfide calcium aluminate hydrate. For the samples cured for 7 days (Figure 6C), spherical hydrated calcium aluminate appeared on the surface of the original mineral and a large number of amorphous gel-like substances were observed on the surface. Furthermore, a small amount of ettringite cluster aggregates with short crystals was observed in the samples cured for 28 days (Figure 6D). Three days after curing at 55 °C, a large number of hydration products were observed in the G0-2 samples, including a large number of cluster/cluster aggregates (Figure 6E). According to the EDS analysis, Table 2 shows ettringite. The microsurfaces of the 7-day sample were relatively dense, indicating that the reaction degree exceeded that of the G0 sample and the number of newly generated products was greater (Figure 6F). As shown in Figure 6G,H and Table 1, the surface of the G0-2 sample became very dense after curing for 28 days and a large number of ettringite appeared at the cracks and fractures. Compared with the samples of 7 days, the crystal size and number of ettringite increased significantly; ettringite appeared in clusters and columnar aggregates, with gel-like substances filling the gaps between the original minerals and the overall structure of the microsurface was further compacted.

These findings showed that the kaolin samples had higher reaction degrees and reaction rates at high temperatures. As the curing time increased, the morphology of kaolinite crystals gradually disappeared, the crystal form of ettringite crystals gradually grew and thickened to form a frame structure and the hydrated calcium aluminate gel was filled in the gap to make the whole become dense. Increasing the curing temperature favoured this reaction and the number of reaction products significantly increased compared with that of G0, suggesting that increasing the reaction temperature can improve the reaction speed.
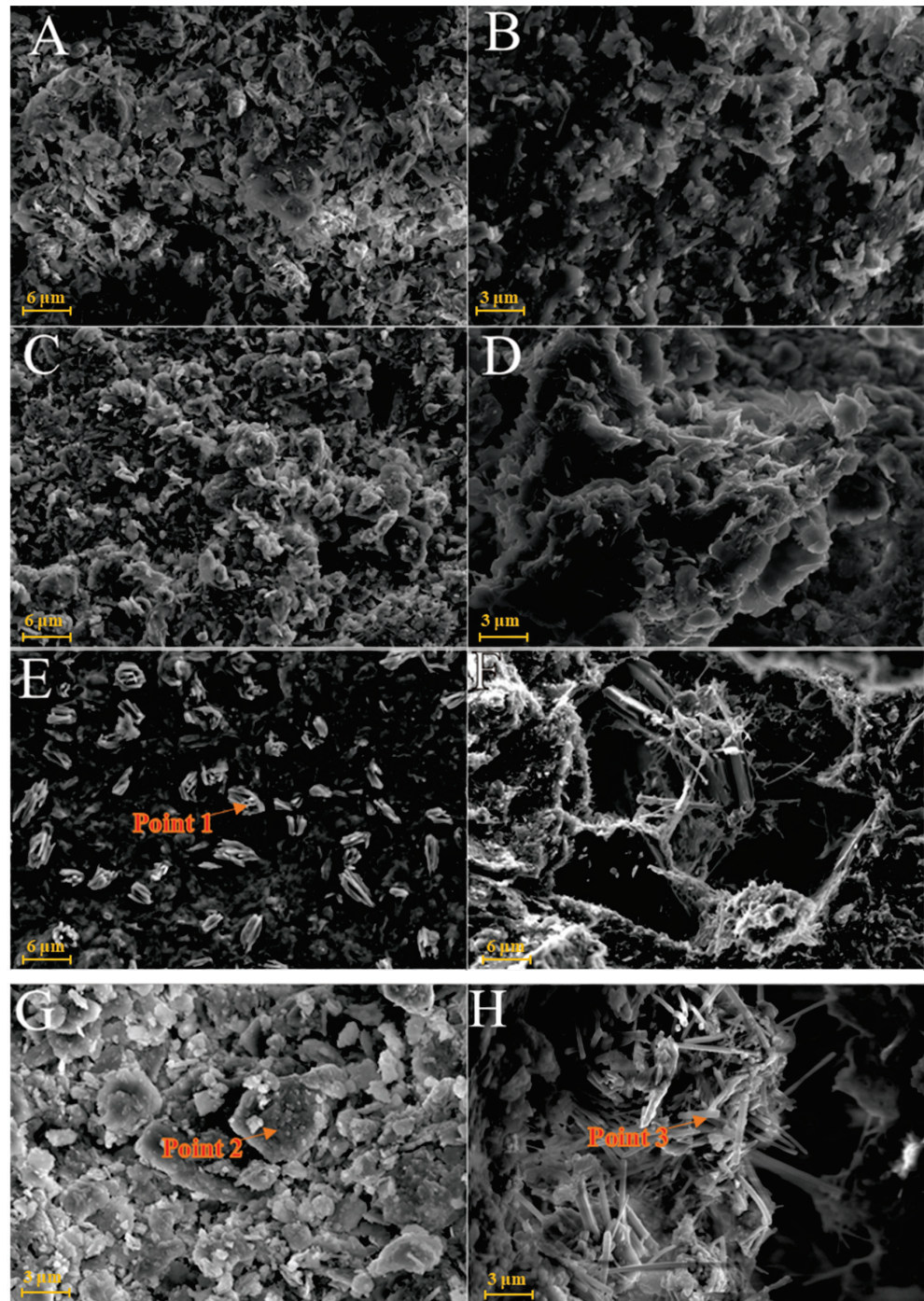
Figure 6. SEM images of kaolinite samples: (**A**)—kaolinite raw material; (**B**)—G0 samples cured for 3 days; (**C**)—G0 samples cured for 7 days; (**D**)—G0 samples cured for 28 days; (**E**)—G0-2 samples cured for 3 days; (**F**)—G0-2 samples cured for 7 days; (**G**)—G0-2 samples cured for 28 days; (**H**)—samples of G0-2 cured for 28 days.

Table 2. EDS dotting analysis of clay samples (Atomic percentage %).

Element	O	Al	Si	S	Ca
Point 1	58.62	10.64	1.22	10.29	19.24
Point 2	61.25	6.85	14.71	0.91	16.28
Point 3	30.93	13.19	0.86	15.87	39.15
Point 4	56.22	8.72	19.52	0.53	15.01
Point 5	57.87	9.58	22.04	4.08	6.43
Point 6	59.59	10.19	17.02	5.03	8.17
Point 7	64.20	5.83	19.08	4.82	6.07

Figure 7A is the SEM pattern of montmorillonite raw material, showing laminated montmorillonite aggregates, lamellar montmorillonite crystals, honeycomb-mixed layers of Yimeng and other clastic minerals. When cured at 25 °C for 3 days, a small amount of gel-like crystalline substance was produced on the microsurface of M0 to cover the mineral surface (Figure 7B). Figure 7C,D show that the original form of montmorillonite gradually disappeared after 7 and 28 days of curing and the M0 sample was gradually compacted as a whole. Ettringite was observed in clusters or bundles, with crystals of about 1–2 μm or more. The shape of the original honeycomb-mixed layer was replaced by gel-like substances and granular gel aggregates existed on the microsurface. Under the condition of curing at 55 °C, a large number of granular gel aggregates were observed on the microsurface of the M0-2 sample for 3 days and short columnar crystal aggregates appeared in the cracks (Figure 7E and Table 2). After 28 days of curing, a large amount of ettringite was generated in the M0-2 samples (Figures 7F and 8) and ettringite staggered to form a frame structure. The microsurface of the sample was very dense and the morphology of the original minerals was not found. Calcium silicate hydrate and calcium aluminate hydrate wrapped ettringite, which further improved the overall strength.

Figure 9A shows that the SEM images of illite raw material have a single crystal with a smooth surface and broken edges. In the Y0 samples cured at 25 °C for 3 days, small pieces of precipitates formed by the adhesion of illite could be seen (Figure 9B) and fine granular gel substances and needle crystals were observed on the illite surface. The morphology of illite crystals in the Y0 samples cured for 7 and 28 days could also be seen, with a rougher surface (Figure 9C,D). Furthermore, acicular ettringite and granular calcium hydrate aluminate covered the illite surface and the number of products significantly increased compared with that of the 3-day sample (Table 2). For the Y0-2 sample cured at 55 °C for 3 days (Figure 9E,F), granular hydrated calcium aluminate gel and needle-shaped ettringite could be observed on the surface of the sample attached to the illite surface and the gap between particles. Needle-shaped ettringite appeared in Y0-2 samples after 28 days of curing, growing on the surface like 'hair' and illite crystals were covered by ettringite and calcium aluminate hydrate gel. Ettringite crystals were fine and the number of ettringite crystals increased significantly as the curing temperature increased. As the amount of hydrated calcium aluminate is usually small, the overall compactness of the sample is poor.
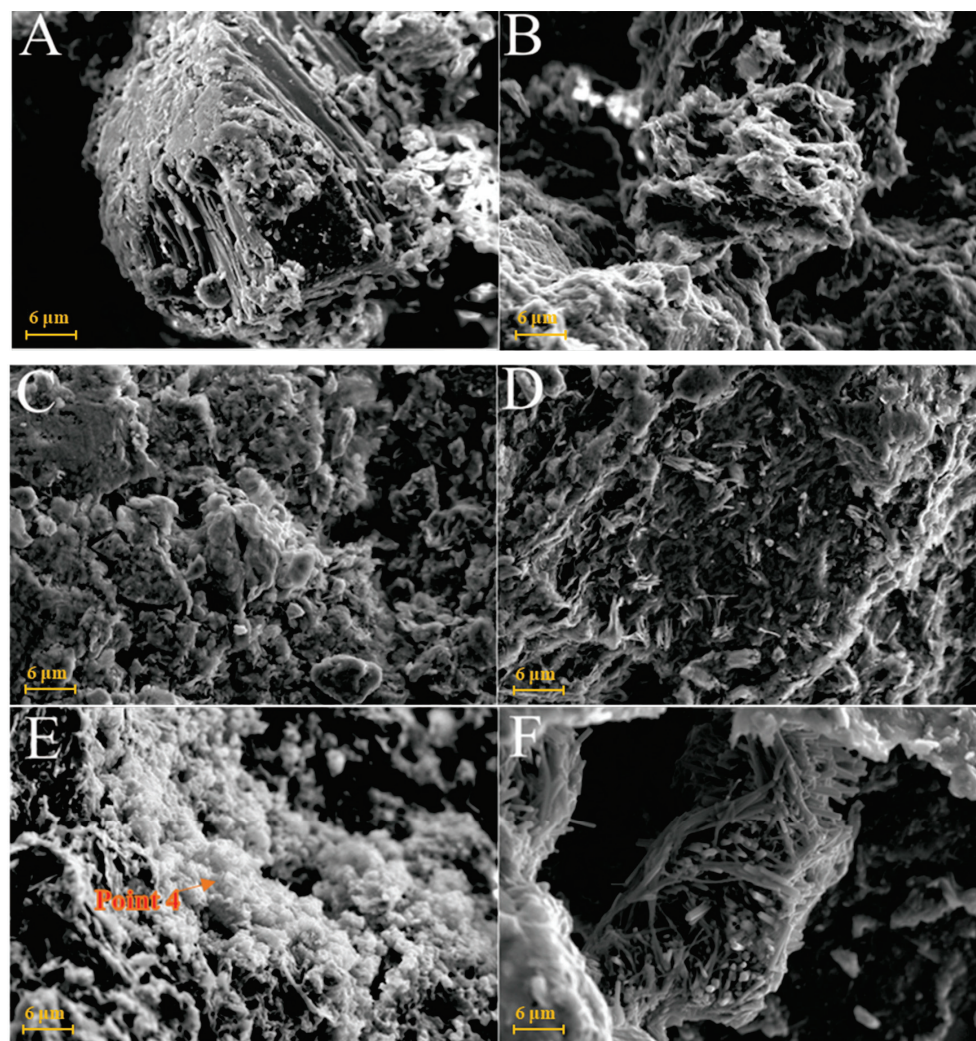
Figure 7. SEM images of montmorillonite samples: (**A**)—montmorillonite raw material; (**B**)—M0 samples cured for 3 days; (**C**)—M0 samples cured for 7 days; (**D**)—M0 samples cured for 28 days; (**E**)—M0-2 samples cured for 3 days; (**F**)—M0-2 samples cured for 7 days.
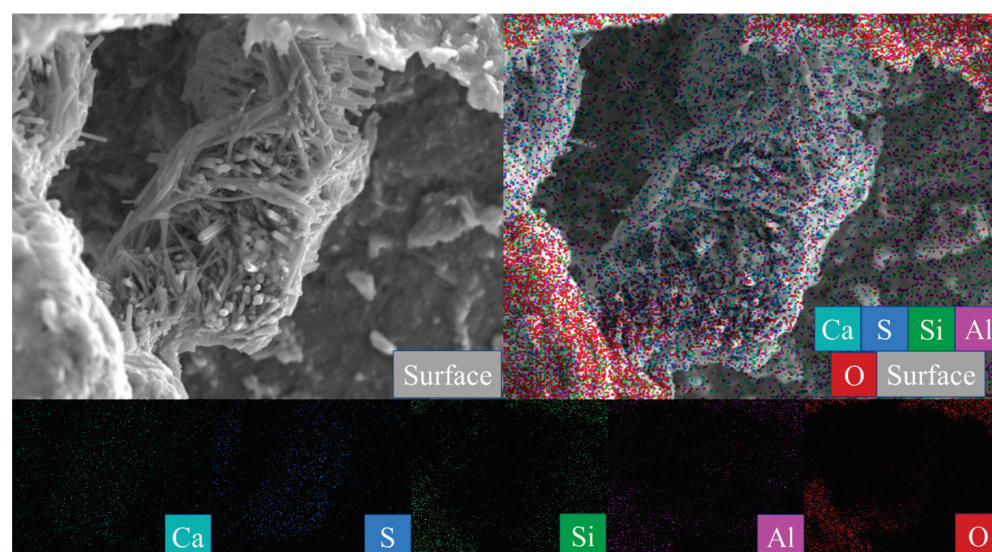
Figure 8. Scanning image of the M0-2 sample surface after 28 days of curing.
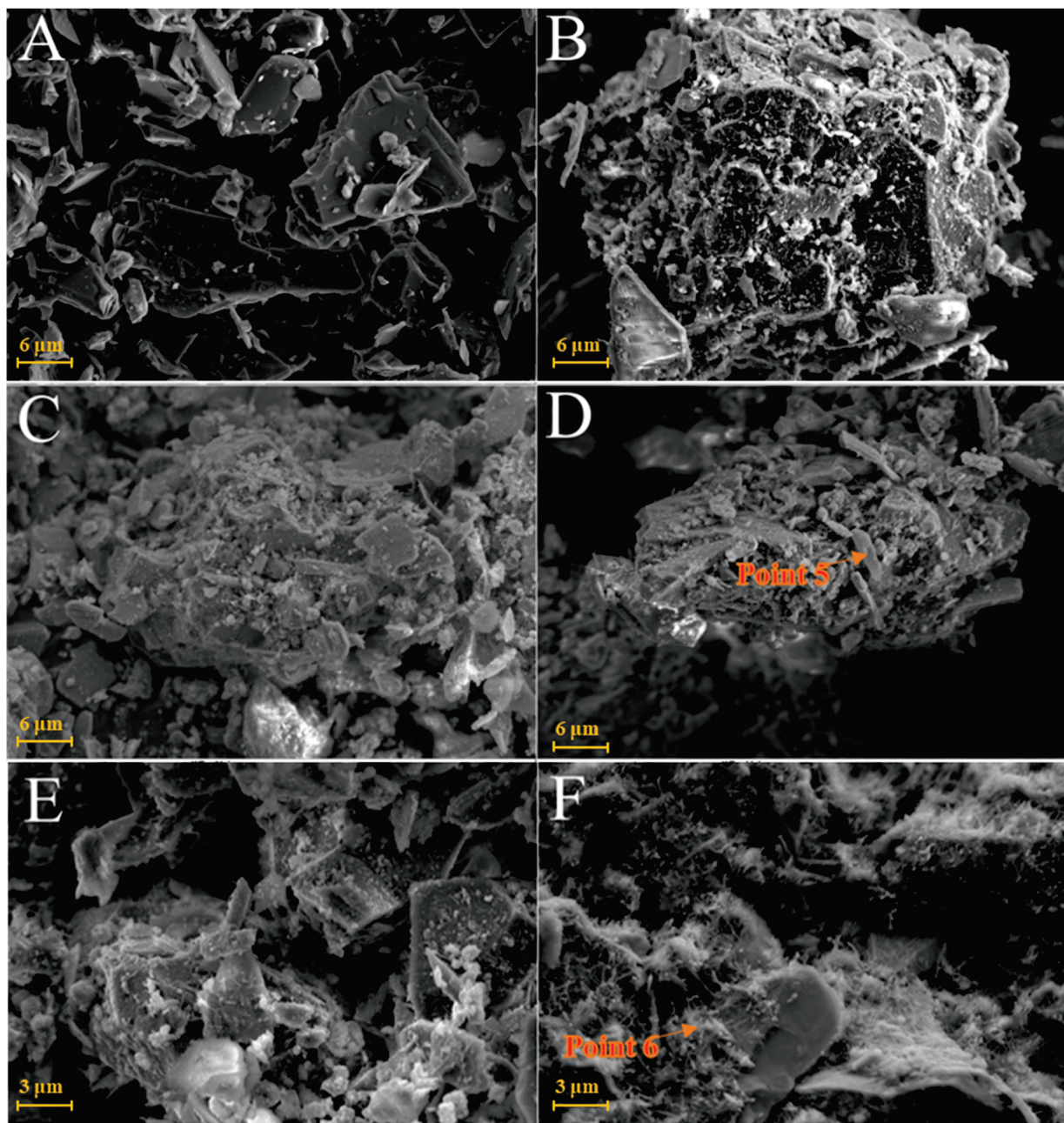
Figure 9. SEM images of illite samples: (**A**)—illite raw material; (**B**)—Y0 samples cured for 3 days; (**C**)—Y0 samples cured for 7 days; (**D**)—samples of Y0 cured for 28 days; (**E**)—Y0-2 samples cured for 3 days; (**F**)—Y0-2 samples cured for 3 days.

The chlorite raw material exhibited a broken sheet plate shape under SEM (Figure 10A). Gel and acicular ettringite were rarely observed on the surface of the L0 samples cured at 25 °C (Figure 10B–D). At 55 °C (Figure 10E,F), needle-like crystals and blocky gel with a large number of crystals on the surface were observed in the L0-2 samples after 3 days. After 28 days of curing (Table 2), the crystal form of chlorite itself remained complete and the whole was not dense. The formation of ettringite in the sample followed an increasing trend but remained in a fine needle-like shape. Chlorite was relatively stable in the system of desulfurised gypsum, calcium hydroxide and water. Although the curing temperature increased, the reaction speed did not significantly improve.
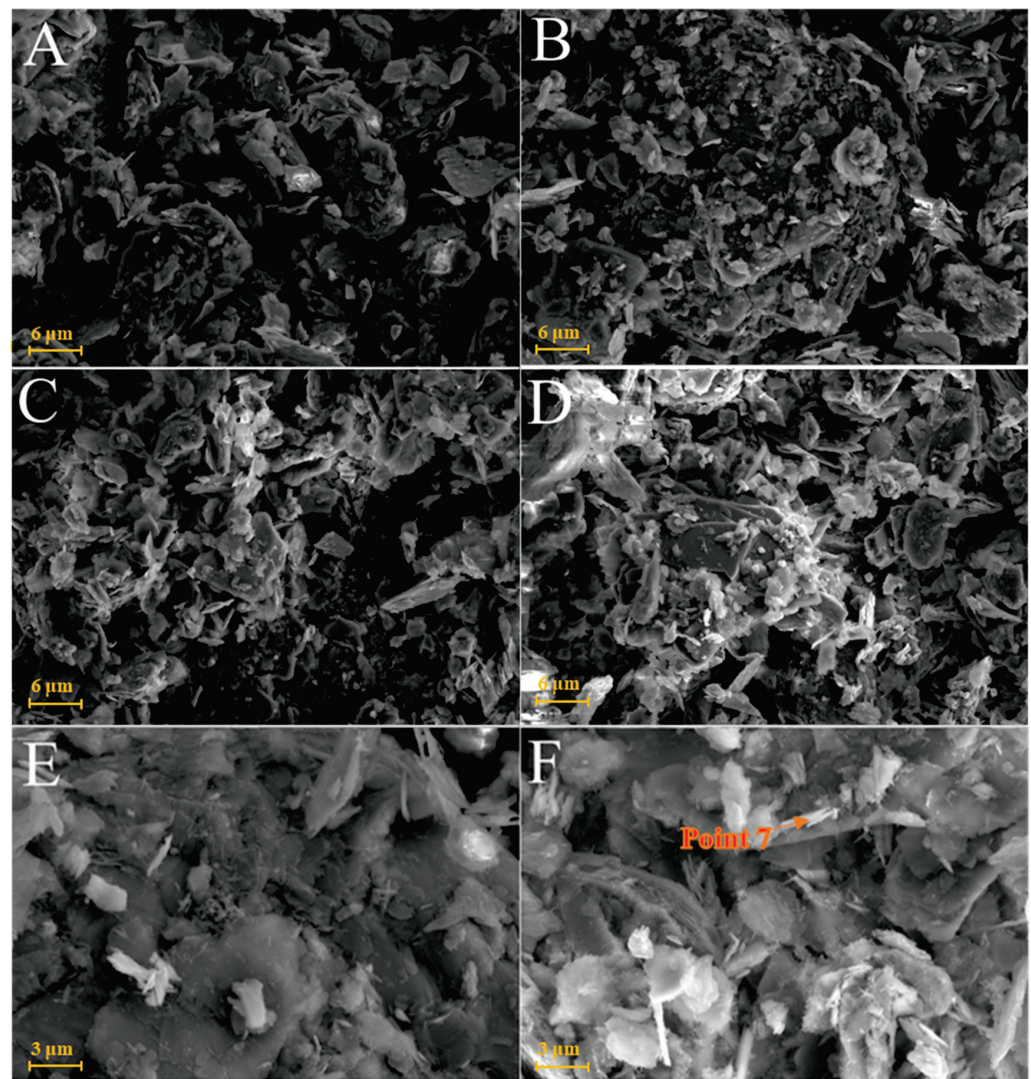
Figure 10. SEM images of chlorite samples: (**A**)—chlorite raw material; (**B**)—L0 samples cured for 3 days; (**C**)—L0 samples cured for 7 days; (**D**)—L0 samples cured for 28 days; (**E**)—L0-2 samples cured for 3 days; (**F**)—L0-2 sample cured for 28 days.

2.4. Discussion

The order of the compressive strength of the four clay mineral samples cured in the same en vironment for 28 days was kaolinite > montmorillonite > illite > chlorite, from large to small. The water-reducing agent promoted the compressive strength of kaolinite, montmorillonite and illite, without any effect on the compressive strength of the chlorite group. Raising the curing temperature significantly accelerated the reaction speed of kaolinite and montmorillonite and had a certain effect on illite without any effect on chlorite, primarily because the hydration ability of clay minerals differs due to the difference in the middle domain in the microstructure [18]. Notably, since the interlayer of montmorillonite is a van der Waals force (i.e., the interlayer force is weak) and its cation exchange capacity is high, montmorillonite has good hydration and high dispersion. The van der Waals force also exists between kaolinite layers and the hydration is good. The illite layer is K^+ and the chlorite layer is a brucite flake. These two minerals have very weak hydration and poor cation exchange capacity.

As shown in Figures 2–5, XRD was used to analyse the products generated by the reaction of four clay minerals with calcium hydroxide and desulfurised gypsum, mainly including ettringite, hydrated calcium aluminate [15–17]. A small amount of hydrated calcium

silicate was produced in the montmorillonite group, which is consistent with the theoretical product inferred by P. Puscha et al.

The XRD data can be confirmed by SEM analysis of the micromorphology of the samples, but no calcium zeolite with a good crystal form was observed. The micromorphology of kaolinite and montmorillonite groups changed significantly. The morphology of the original mineral single crystal basically disappeared, ettringite formed a framework structure and calcium aluminate hydrate gel filled in the particle gap, making the whole become dense. The illite in the illite group also maintained its original form and the particles were bonded together by calcium aluminate hydrate gel, with ettringite forming a layer of needle-like crystals similar to 'hair' on the surface. The chlorite group only produced a small amount of ettringite crystals and gel on the surface and the chlorite itself did not change. These findings revealed that the strength source of group G and M samples was the joint action of gel, such as ettringite and hydrated calcium aluminate and that of illite group samples was acicular ettringite; meanwhile, no reaction was actually observed in the chlorite group samples, except for a small amount of ettringite that was formed, so strength was absent.

After adding water to the mixed raw materials, calcium hydroxide and desulfurised gypsum provided Ca^{2+}, SO_4^{2-} and OH^- for the system. Clay minerals underwent hydration and generated Al^{3+}, Ca^{2+} and Mg^{2+} in a strong alkaline environment. In this system, Ca^{2+}, Al^{3+}, Ca^{2+}, Mg^{2+}, SO_4^{2-}, OH^- and $Al(OH)^-$ were continuously consumed and combined to form reaction products, such as ettringite, calcium aluminate hydrate, calcium silicate hydrate and zeolite-like phase, which continuously reduced the number of the above ions and ion groups in the system [19–21]. Concurrently, silica tetrahedron and alumina tetrahedron or alumina coordination polyhedron with potential reaction in clay mineral structure were destroyed in the alkaline environment (in clay mineral structure, Si–O bond is the strongest, Al–O is slightly weaker, Mg–O is the second and Ca–O is the weakest), making ettringite and hydrated calcium silicate to form continuously. At the later stage of the reaction, the Si-Add 0.3% water reducer with total mass during the preparation of the four clay mineral samples, as calculated in Table 3. Except for group Y, the water-reducing rate of group G, M and L water reducers was only 10–12%, significantly lower than the nominal water-reducing rate of 25–30%. Compared with kaolinite, montmorillonite and illite samples with water reducers, the compressive strength of water reducer samples at the same age significantly improved, without any effect on the chlorite group. Adding a water-reducing agent to the sample could promote the system reaction to a certain extent while enhancing the dispersion effect of clay mineral particles and favouring the reaction to a certain extent. However, due to the large specific surface area of clay minerals, the water-reducing effect of a water-reducing agent will be greatly reduced, the O bond will be destroyed and active aluminium will be released to form hydrated calcium silicate gel. Increasing the curing temperature favours the acceleration of the reaction speed of the system; it only affects the number of reaction products and does not produce new products.

Table 3. Water-reducing effect of water reducer on four clay mineral paste systems.

Group	G	M	Y	L
Reduce water consumption	21.80 g	15.80 g	61.30 g	20.00 g
Water reduction rate	11.37%	10.14%	36.77%	12.14%

The hydration reaction in the clay mineral composite system is slow when there is only alkali excitation, but it is significantly accelerated by the addition of sulfate because the alkaline-activated of calcium hydroxide breaks the silica-aluminate mineral structure and promotes the dissolution of active silica-oxygen tetrahedra and alumina-oxygen tetrahedra [19,20], and then generates C–S–H gel (Equation (1)) and C–A–S–H gel (Equation (2)), while the desulfurisation gypsum plays a sulfate excitation role in the composite. The FGD gypsum plays a sulfate-activated role in the complex system [21], where the dissolved

SO_4^{2-} and Ca^{2+} continuously combine and react with the activated alumina tetrahedra to form calcium alumina [20]; see Equation (3), which forms the reaction driver and drives the hydration reaction of the whole system. Related studies [22] have shown that in the reaction system of slag, gypsum and cement rich in the glass phase of silica-alumina minerals, the equilibrium concentration of Aft and Al^{3+} or $H_3A1O_4^-$ in solution is extremely low, which is much lower than the equilibrium concentration of Al^{3+} or $H_3A1O_4^{2-}$ in solution of silica-alumina minerals, so that the continuous precipitation of calcium alumina drives the aluminum oxygen tetrahedra in silica-alumina minerals continuously. As a result, the precipitation of calcium alumina promotes the dissolution of aluminum-oxygen tetrahedra from silica-aluminate minerals, and the production of calcium alumina increases.

$$Ca(OH)_2 + H_2O + SiO_2 = \text{C-S-H} \tag{1}$$

$$Ca(OH)_2 + (n - 1)H_2O + Al_3O_2 + SiO_2 = CaOSiO_2 \cdot Al_2O_3 \cdot nH_2O \text{ (C-A-S-H)} \tag{2}$$

$$3Ca(OH)_2 + Al_2O_3 + 3(CaSO_4 \cdot 2H_2O) + 23H_2O = 3CaO \cdot Al_2O_3 \cdot 3CaSO_4 \cdot 32H_2O \text{ (Ettringite)} \tag{3}$$
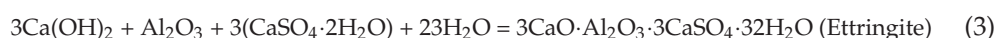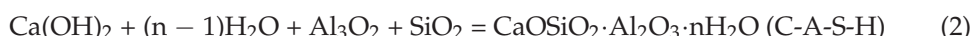
3. Conclusions

(1) The samples of group G, M and Y were cured at 25 °C for 28 days and the compressive strength values were 1.09, 0.94 and 0.26 MPa, respectively, which were 4.93, 4.53 and 1.43 MPa, respectively, after curing at 55 °C for 28 days. These values increased significantly by 12.17%, 17.66% and 34.27%, respectively, after adding a water reducer. Increasing curing temperature and adding water-reducing agent promoted the compressive strength of group G, M and Y samples, with no obvious effect on group L.

(2) XRD and SEM–EDS analyses showed that kaolinite, montmorillonite and illite reacted under the combined excitation of calcium hydroxide and desulfurised gypsum. The hydration products mainly included ettringite, hydrated calcium aluminate, hydrated calcium silicate and other gel. Increasing the curing temperature promoted the hydration reaction. Only a small amount of products were produced in the chlorite group samples after 28 days of curing and the hydration reaction was not obvious.

(3) Kaolinite, montmorillonite and chlorite had a significant impact on the water-reducing performance of high-performance polycarboxylate water reducer and the water-reducing efficiency was reduced from 25–30% to 10–13%. The water reduction rate of the polycarboxylic acid water reducer for the illite group samples reached 36.77%.

(4) The hydration activity of clay minerals is facilitated by using the compound activation method of alkali and sulfate, which can provide a basis for the utilisation of clay minerals in cementitious materials and concrete.

4. Materials and Methods

4.1. Preparation of Materials

Kaolinite, which was ground through a 200-mesh sieve, was selected from a kaolin factory in Shanxi Province. The chemical composition is shown in Table 4. The main components are SiO_2 (56.34%) and Al_2O_3 (49.44%). The raw material of montmorillonite used in the study was produced in Xinyang, Henan Province, with a fineness of 1250 mesh. The chemical composition is shown in Table 4. The main components are SiO_2 (69.15%) and Al_2O_3 (18.43%). The illite raw material was obtained from Hebei, with a fineness of 800 mesh. The chemical composition is shown in Table 4. The main components are SiO_2 (73.22%) and Al_2O_3 (17.45%). The chlorite raw material was obtained from Hebei, with a fineness of 1250 mesh. The chemical composition is shown in Table 4. The main components are SiO_2 (40.84%), MgO (38.45%) and Al_2O_3 (49.44%).

Table 4. XRF analysis results of clay minerals used in this study.

	SiO_2	Al_2O_3	K_2O	Fe_2O_3	MgO	CaO	Na_2O	TiO_2	P_2O_5	MnO
Kaolinite	56.34	39.44	2.62	0.46	0.24	0.14	0.11	0.01	0.24	0.07
Montmorillonite	69.15	18.43	1.07	2.34	4.18	4.41	0.06	0.15	0.02	0.04
Illite	73.22	17.45	6.53	1.03	0.24	0.12	1.10	0.11	0.04	0.02
Chlorite	40.84	13.61	0.42	4.70	38.45	1.10	——	0.59	0.11	0.05

The desulfurised gypsum used in the study was the industrial solid waste desulfurised gypsum discharged from the wet desulfurisation of Chengde Iron and Steel group. The main component is basically similar to that of the natural desulfurised gypsum and the main mineral component is $CaSO_4 \cdot 2H_2O$. The calcium hydroxide used was analytical pure calcium hydroxide produced by the Shanghai Sinopharm reagent group, with $Ca(OH)_2$ more than 95%. The water reducer used was a polycarboxylic acid (PC) high-efficiency water reducer produced by Beijing Muhu admixture Co., Ltd. (Beijing, China).

4.2. Methods

This study followed a previous single-mineral research [23]. The internal environment of the slurry was set according to that of the hydration process of solid waste-based cementitious materials. When clay minerals (91%), calcium hydroxide (6%) and flue-gas gypsum (3%) were used as cementitious materials and the water binder ratio was 0.2–0.3, the four samples could not be demoulded in order to test their strength. When calcium hydroxide (10%) was added, the samples were still unable to demould and had no strength. Therefore, the content of calcium hydroxide and flue-gas gypsum increased simultaneously. Finally, clay minerals (83%), calcium hydroxide (10%) and flue-gas gypsum (7%) were used as cementitious materials that could be demoulded and tested for strength. The curing temperature and the dosage of the water reducer were changed to design comparative experiments. Table 5 lists the experimental proportions.

Table 5. Content of each sample component.

Group 25 °C/55 °C	Mineral Raw Materials (g)	Calcium Hydroxide (g)	Flue-Gas Gypsum (g)	Water (g)	Water Reducer (g)	Water Binder Ratio
G0/G0-2	332	40	28	191.8	0	0.48
G1/G1-2	332	40	28	170	1.2	0.43
M0/M0-2	332	40	28	155.8	0	0.39
M1/M1-2	332	40	28	140	1.2	0.35
Y0/Y0-2	332	40	28	166.7	0	0.42
Y1/Y1-2	332	40	28	105.4	1.2	0.26
L0/L0-2	332	40	28	164.8	0	0.41
L1/L1-2	332	40	28	144.8	1.2	0.36

Note. Mineral Raw Materials: G: Kaolinite; M: Montmorillonite; Y: Illite; L: Chlorite; 0 indicates the 25 °C curing temperature group and without water reducing agent; 1 indicates the group with water reducing agent addition; -2 indicates 55 °C curing temperature group.

The slurry test blocks were made according to the standard of Portland cement and ordinary Portland cement (GB/T175-2007).

As shown in Figure 11, the raw materials of kaolinite, montmorillonite, illite and chlorite were made into $30 \times 30 \times 50$ mm test blocks with calcium hydroxide and desulfurised gypsum, respectively. The test blocks were grouped according to the curing temperature (25 °C/55 °C) and the experimental group with the same ratio was set to add an additional water reducer. The samples were placed in self-sealing bags to reduce the impact of water and carbon dioxide in the curing environment. Because a water reducer was added, the water binder ratio decreased slightly and the water reducer was 0.3% of the total mass of the experimental raw materials. After 3, 7 and 28 days of curing, the compressive

strength of the test block was tested, respectively and the central part of the test block was soaked in absolute ethanol to remove the free water in the sample to terminate the sample's hydration reaction.
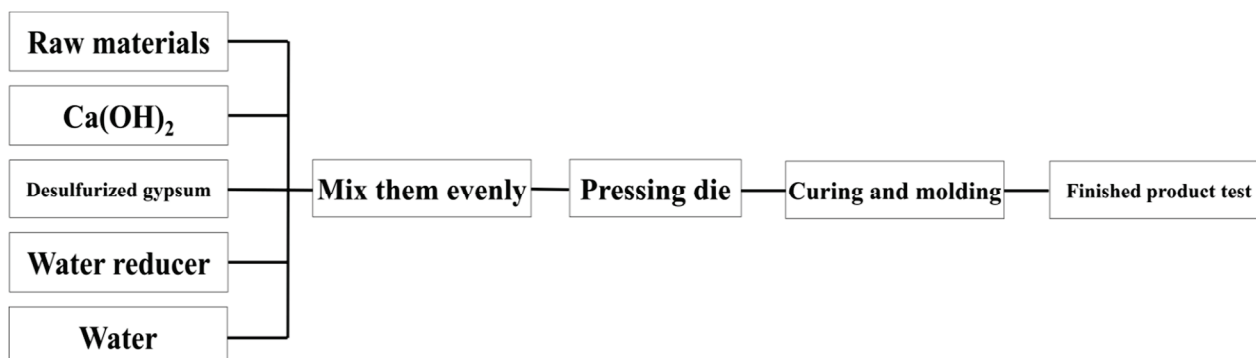
Figure 11. Flow chart of sample preparation of slurry test blocks.

4.3. Test and Analysis Method

(1) Compressive strength

The compressive strength measurements were performed according to the Test Method for Strength of Cement Mortar (ISO method) (GB/T17671—1999).

(2) Characterisation of samples

The mineral composition and crystallisation degree of raw materials and samples were characterised via XRD analysis (Japanese Neo-Confucianism Rigakuultima—Type IV powder crystal X-ray diffractometer, Cu target, wavelength 154.06 A, working current 40 mA, working voltage 40 kV, scanning range 5–90°, step size 0.02°).

A SEM was used to examine the micromorphology of raw minerals and the changes in new products and overall structure after the reaction. After carbon spraying on the sample surface, the sample was analysed using an SEM instrument (ZEISS SUPRA 55 field emission SEM). A Schottky field emission electron source was also adopted, which was equipped with an in-lens secondary electron detector, E–T secondary electron detector and 4Q BSD backscattered electron detector; resolution of X-ray energy spectrometer (EDS): 132eV@MnK α; detection element range: Be (4)~Fm (100); accelerating voltage: 0.1–30 kV.

References

1. Shi, J. Effect of concrete fine aggregate content on concrete strength and work productivity. *Inn. Mong. Water Resour.* **2014**, *4*, 19–20.
2. Wang, C.; Zhang, M. Effect of earthy side effects on mortar properties andmud content limits. *J. Chifeng Univ. (Nat. Sci. Ed.)* **2015**, *31*, 55–57.
3. Zhang, R. Effect of mud content on concrete strength. *Res. Appl. Build. Mater.* **2007**, *8*, 8–9.
4. Xiao, R.; Zhang, X.; Zhang, X.; Mao, R.; Shi, F.; Zhang, H. Effects of mix proportion of concrete on drying shrinkage. *Concrete* **2003**, *7*, 37–40.
5. Shakoor, A.; West, T.R. Influence of Petrography of Argillaceous Carbonateson Their Frost Resistance in Concrete. *Cem. Concr. Aggreg.* **1984**, *6*, 84–89.
6. Li, W. Study on the effect of sludge content in sand on concrete properties. *Coal Ash* **2015**, *27*, 33–35.
7. Pike, D.C. Methodologies for Assessing the Variability of Fines in Sands Used for Concretes and Mortars. Ph.D. Thesis, University of Reading, Reading, UK, 1992.
8. Fam, M.A.; Santamarina, J.C. Study of Clay-Cement Slurries with Mechanical and Electromagnetic Waves. *J. Geotech. Eng.* **1996**, *122*, 365–373. [CrossRef]
9. Read, D.; Glasser, F.P.; Ayora, C.; Guardiola, M.T.; Sneyers, A. Mineralogical and microstructural changes accompanying the interaction of Boom Clay with ordinary Portland cement. *Adv. Cem. Res.* **2001**, *13*, 175–183. [CrossRef]
10. Noble, D.F.; Plaster, R.W. *Reactions in Portland Cement-Clay Mixtures*; No. VHRC 70-R13; Virginia Transportation Research Council: Charlottesville, ID, USA, 1970.
11. Gaucher, E.C.; Blanc, P. Cement/clay interactions—A review: Experiments, natural analogues, and modeling. *Waste Manag.* **2006**, *26*, 776–788. [CrossRef] [PubMed]
12. Bell, F.G. Lime stabilisation of clay soils. *Bull. Eng. Geol. Environ.* **1989**, *39*, 67–74. [CrossRef]
13. Xu, C.; Ni, W.; Li, K.; Zhang, S.; Xu, D. Activation mechanisms of three types of industrial by-product gypsums on steel slag–granulated blast furnace slag-based binders. *Constr. Build. Mater.* **2021**, *288*, 123111. [CrossRef]
14. Xu, C.; Ni, W.; Li, K.; Zhang, S.; Li, Y.; Xu, D. Hydration mechanism and orthogonal optimisation of mix proportion for steel slag–slag-based clinker-free prefabricated concrete. *Constr. Build. Mater.* **2019**, *228*, 117036. [CrossRef]
15. Wang, X.; Zhang, C.; Zhu, H.; Wu, Q. Reaction kinetics and mechanical properties of a mineral-micropowder/metakaolin-based geopolymer. *Ceram. Int.* **2022**, *48*, 14173–14181. [CrossRef]
16. Niu, M.; Zhang, P.; Guo, J.; Wang, J. Effect of Municipal Solid Waste Incineration Fly Ash on the Mechanical Properties and Microstructure of Geopolymer Concrete. *Gels* **2022**, *8*, 341. [CrossRef] [PubMed]
17. Xiaoyun, Y.; Yan, Z.; Cheng, L. Microstructure Analysis and Effects of Single and Mixed Activators on Setting Time and Strength of Coal Gangue-Based Geopolymers. *Gels* **2022**, *8*, 195. [CrossRef] [PubMed]
18. Mao, H.; Guo, Y.; Wang, G.; Yang, C. Evaluation of influence of clay mineral fabric on hydration. *Rock Soil Mech.* **2010**, *9*, 40–45.
19. Zhang, S.; Shi, T.; Ni, W.; Li, K.; Gao, W.; Wang, K.; Zhang, Y. The mechanism of hydrating and solidifying green mine fill materials using circulating fluidized bed fly ash-slag-based agent. *J. Hazard. Mater.* **2021**, *415*, 125625. [CrossRef] [PubMed]
20. Zhang, Y.; Zhang, S.; Ni, W.; Yan, Q.; Gao, W.; Li, Y. Immobilisation of high-arsenic-containing tailings by using metallurgical slag-cementing materials. *Chemosphere* **2019**, *223*, 117–123. [CrossRef] [PubMed]
21. Liu, J.; Zhou, Z.; Wu, A.; Wang, Y. Preparation and hydration mechanism of low concentration Bayer red mud filling materials. *Chin. J. Eng.* **2020**, *42*, 1457–1464.
22. Ni, W.; Li, Y.; Xu, D.; Xu, C.W.; Jiang, Y.Q.; Gao, G.J. Hydration mechanism of blast furnace slag-reduction slag based solid waste cementing materials. *J. Cent. South Univ. (Sci. Technol.)* **2019**, *50*, 2342–2351.
23. Geng, B. Preparation of High-Performance Concrete Adhesives from Fujian Youxi Lead-Zinc Tailings. Ph.D. Thesis, University of Science and Technology Beijing, Beijing, China, 2016.

Article

Synthesis and Characterization of Fly Ash-Based Geopolymers Activated with Spent Caustic

Ruobing Zhang [1,2,3,4], Qian Wan [1,2,3,4,*] ![ORCID], Yimin Zhang [1,2,3,4,*] and Xuemian Zhang [1,2,3,4]

1   School of Resource and Environmental Engineering, Wuhan University of Science and Technology, Wuhan 430081, China
2   State Environment Protection Key Laboratory of Mineral Metallurgical Resources Utilization and Pollution Control, Wuhan University of Science and Technology, Wuhan 430081, China
3   Collaborative Innovation Center of Strategic Vanadium Resources Utilization, Wuhan 430081, China
4   Hubei Provincial Engineering Technology Research Center of High Efficient Cleaning Utilization for Shale Vanadium Resource, Wuhan 430081, China
*   Correspondence: wanqian@wust.edu.cn (Q.W.); zym126135@126.com (Y.Z.)

Abstract: The spent caustic with strong alkali first replaced the alkali activator to prepare the geopolymer. The influence of spent caustic to the geopolymer was characterized through compressive strength measurement, XRD, MIP analysis and NMR, and the immobilization efficiency of organic in geopolymer was evaluated through the measurement of total organic carbon (TOC). The results show that the spent caustic can partially replace the alkali activator to prepare the geopolymer, and it shows a better performance than that which was activated with pure NaOH solution when the alkalinity is between 4 mol and 14 mol. The organic matter in the spent alkali can be effectively fixed in the geopolymer, which will hinder the geopolymerization in the initial stage of the polymerization reaction but has little effect on the chemical structure and mechanical properties of the final product. With the degree of alkalinity increasing, the immobilization efficiency is improved, and the maximum can reach 84.5%. The organics in the spent caustic will hinder geopolymerization at the initial stage but has little effect on the chemical structure and mechanical property of the final product. This study proposes a new method for the recycling of spent caustic, which also reduces the preparation cost of geopolymers.

Keywords: spent caustic; alkali activator; geopolymer; immobilization; organics

1. Introduction

Spent caustic is a kind of the liquid wastes generated in various chemical industries, especially in oil and gas refineries [1]. It may account for more than 90% of the total contamination generated by refineries in terms of oil and grease. Due to being used to remove organic sulfides, hydrogen sulfide and carbon dioxide, the typical spent caustic usually contains high alkalinity (5–12 wt% NaOH), sulfide content (0.5–4 wt% sulfide-S), phenols, oils and other organic contamination [2,3]. It has a high alkali (pH > 12) and chemical oxygen demand (COD), so it is classified as a hazardous waste according to the National Hazardous Waste List [4,5]. The technology for the treatment of spent caustic includes neutralization, incineration, Fenton oxidation and wet air oxidation (WAO). At present, wet air oxidation is widely used as a common treatment method for spent caustic [6,7]. After treatment by the wet air oxidation process, the sulfide is oxidized to sulfate so as to remove the odor, and the organics are also partially decomposed into CO_2 and H_2O to reduce COD. However, treated spent caustic still needs additional treatment, such as acid neutralition, before being discharged to the sewage treatment plant, due to its high COD level and high alkalinity [4]. This treatment process not only requires additional acid, and also does not utilize the high alkalinity of spent caustic, thereby causing waste of resources.

Geopolymers are a kind of environmentally friendly aluminosilicate material with a comparable strength performance to the Ordinary Portland Cement, and are considered to be a good potential substitute for the latter [8]. The low permeability, resistance to acid attack and long-term durability of geopolymers make it an excellent potential in solidification/stabilization of the hazardous wastes [9,10]. In recent years, the immobilization of organic wastes in geopolymer materials has been extensively studied [11]. Cantarel et al. [12] studied the influence of liquid oil waste on the mechanical performance and leaching rate of organic materials. The results showed that the cumulative quantity of oil compounds released in the leachate at 30 days does not exceed 0.19% of the organic material initially encapsulated in the sample. Al-Mashaqbeh et al. [13] investigated the immobilization of organic dyes in geopolymer. It was found that all kinds of dyes can been immobilized in geopolymers, and the efficiency is higher than 94%. Therefore, it is feasible to use geopolymer technology to immobilize the high content of organic contaminants in spent caustic. In addition, geopolymers are synthesized through activating the raw materials with a highly alkaline solution [14]. In the life cycle assessment of geopolymers, the use of alkali activators contributed the highest CO_2 footprint in most life cycle categories and was also associated with high costs [15,16]. Daniel et al. also elaborated the life cycle assessment of a geopolymer concrete, and they reported that the use of alkali activators represents the most important environmental burden [17]. Fortunately, the mass fraction of NaOH and Na_2CO_3 in the treated spent caustic can reach about 20% [18], which has the potential to partially replace the alkali activator to prepare geopolymers, and can further reduce the cost and the CO_2 emission of geopolymer preparation.

In this work, we have studied the preparation of geopolymers using spent caustic to partially replace NaOH solution as an alkali activator, and pure NaOH solution with comparable alkalinity was used as a control group. The effect of spent caustic on the compressive strength and microstructure of geopolymers was studied, and the immobilization efficiency of organics in geopolymers was evaluated. This study proposes a new method for the utilization of spent caustic, which also reduces the preparation cost of geopolymers.

2. Experimental

2.1. Materials

The class F fly ash used in this paper was purchased from a plant in Hubei province, China, which was used as a raw material in the synthesis of geopolymers. Table 1 shows the chemical analysis of fly ash measured by XRF. The spent caustic was provided from Sinopec Wuhan petrochemical company. The organics in spent caustic measured by gas chromatography spectrometry (GC, LEEMAN LABS Clarus 680) are shown in Figure 1, in which a large amount of organic matter appears. The concentration of organic total organic carbon (TOC) in spent caustic is 4312 ppm, indicating large quantities of organics in it. The alkalinity of spent caustic is equivalent to 2.08 mol/L NaOH solution, which was evaluated by titrating with HCl solution until pH = 7. This can be attributed to the incomplete oxidation of organics during the WAO process [19]. The sodium hydroxide (ACS reagent grade) was used as alkali activator.

Table 1. Chemical composition of fly ash.

Component	SiO$_2$	Al$_2$O$_3$	K$_2$O	Fe$_2$O$_3$	TiO$_2$	CaO	MgO	LOI
wt%	49.18	33.80	2.28	4.89	0.73	4.84	0.81	3.47

2.2. Synthesis of Geopolymers

The activator solution was prepared by mixing NaOH with spent caustic or deionized water in different proportions. Figure 2 shows the diagram of the geopolymer preparation process. In a typical synthesis of geopolymers, the fly ash and alkali activator was stirred in the homogeneous mixture and poured into a 5 cm × 5 cm × 5 cm steel mold. After being vibrated on a vibration table to release the air bubble, the mold was sealed with polyethy-

lene film and cured at 60 °C for 6 h. Then, the samples were demolded and sealed in plastic bags in the natural environment for 7 days. The diagram of the geopolymer preparation process is shown in Table 2. In the preparation of geopolymers with spent caustic, the amount of fly ash and spent caustic was constant, at 100 g and 25 mL, respectively; the content of NaOH was the unique variable from 0 g to 12 g. A series of samples synthesized with the same alkalinity prepared with NaOH were used for comparison.

1- Phenol,2,5-dimethyl
2- Phenol,2-ethyl-Phenol,o-ethyl
3- Benzen, 1-methoxy-4-propyl
4- Phenol,3-(1-methylethyl)
5- 1,3-Cyclohexanedione,2-(2-propenyl)
6- Phenol,3-1thyl-5-methyl
7- Phenol,3,4,5-trimethyl
8- 3-Morpholinopropyl2,4-dihydroxybenzoate
9- 6-Methyl-4-indanol
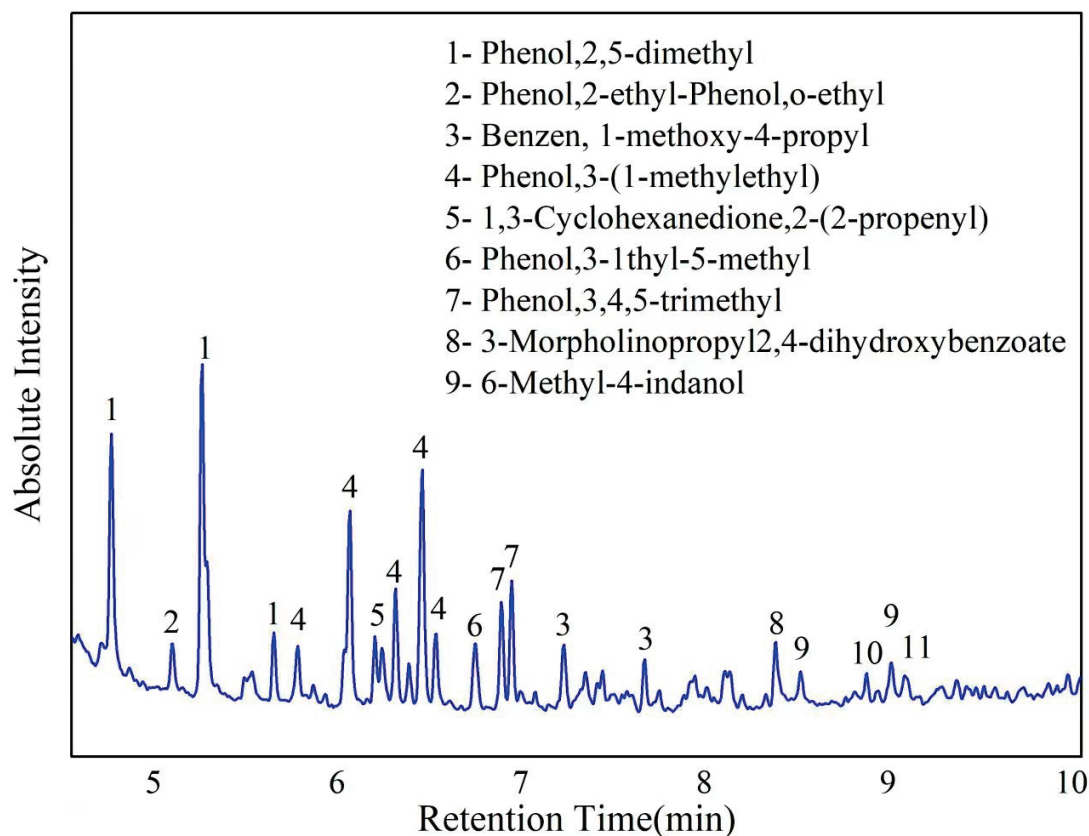
Figure 1. GC analysis of spent caustic.
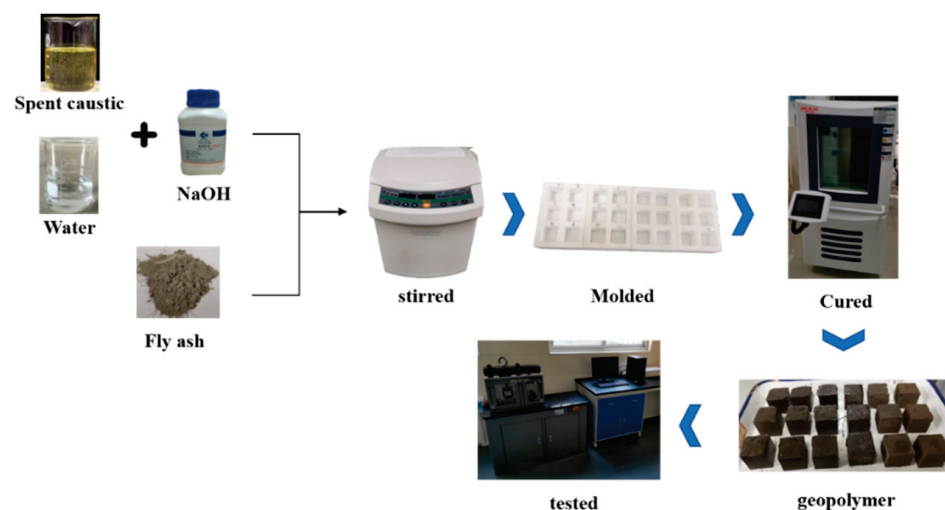
Figure 2. The diagram of the geopolymer preparation process.

177

Table 2. Preparation regime of geopolymers.

Specimen No.	Fly Ash	NaOH	Spent Caustic	Water
1		0 g		
2		2 g		
3		4 g		
4		6 g	25 mL	/
5		8 g		
6		10 g		
7	100 g	12 g		
8		2 g		
9		4 g		
10		6 g		
11		8 g	/	25 mL
12		10 g		
13		12 g		
14		14 g		

2.3. Immobilization of Organic Contamination

According to the Chinese Ministry of Environmental Protection Standard HJ/T 300–2007, the immobilization efficiency of organics in geopolymers was evaluated by the leaching toxicity of organics. In this method, the leaching process was performed with the liquid/solid ratio of 20 mL/g for 18 h, which is the same as it in the USEPA TCLP method. However, the extraction solution was prepared by dissolving 17.25 mL acetic acid into 1 L deionized water, and the amount of acid was almost three times that of the latter, so this standard is more severe. In addition, a zero-headspace extraction vessel was used to prevent the volatilization during the leaching process; the specific operation refers to Reference [20]. The leachate was filtered through a 0.45 μm filter. The amount of organic contamination in the extraction liquid, spent caustic and leachate were analyzed by measuring the total organic carbon (TOC).

2.4. Characterization of Geopolymers

The mechanical property of geopolymers was tested by a mechanical tester (Hangzhou Xingo Technology, EHC-1300) in accordance with the ASTM Test C-39. In the measurement, at least three specimens were tested, and the average value was used. The mineralogical study of geopolymers was characterized by X-ray diffraction (XRD, Brucker D8) with Cu Ka radiation. The pore distribution of geopolymers was analyzed by mercury intrusion porosimetry analysis (MIP, AutoPore IV 9520). [29]Si nuclear magnetic resonance (NMR, Bruker AVANCE III) spectra were used to analyze the microstructure of geopolymer gel. The spectra were collected at 79.5 kHz on a 7 mm probe with a spinning speed of 5 kHz, a pulse width of 6.5 μs and a relaxation delay of 10 s. The [29]Si chemical shift was referenced to an external standard of tetramethylsilane.

3. Results and Discussion

3.1. Compressive Strength

Figure 3 shows the compressive strength of geopolymers synthesized with different alkali activators. The compressive strength of geopolymers activated with only spent caustic is 2.67 MPa in 7 d, which indicates that spent caustic can be used as an alkali activator for geopolymerization. With the alkalinity of alkali solution increasing from 2 mol/L to 14 mol/L, the compressive strength of geopolymers increased to 21.86 MPa. The 7-day compressive strength of all samples with spent caustic are less than that of the samples without spent caustic at the same degree of alkalinity. This may be due to the fact that the organics in the spent caustic hinder the hydration of geopolymers and reduce the strength of the product [12]. For compressive strength at 28 days, the geopolymer with spent caustic is also lower than that without spent caustic when the alkalinity is

2 mol/L. However, with the degree of alkalinity increasing from 4 mol/L to 10 mol/L, the compressive strength significantly increased, and the geopolymer with spent caustic is higher than that without spent caustic. Considering that the main component in spent caustic is NaOH and Na_2CO_3, it can be attributed to the combined effect of Na_2CO_3 and NaOH as alkaline activator in preparation of geopolymers. Zhang et al. [21] investigated different alkali-activators on the performance of alkali-activated nickel slag, and they also reported that the $NaOH/Na_2CO_3$-activated system showed higher compressive and flexural strengths than the NaOH-activated system. When the alkalinity is further increased to higher than 12 mol/L, the proportion of alkali in the spent caustic is much less than that of sodium hydroxide, which has less of an effect on the geopolymer, resulting in a similar strength.
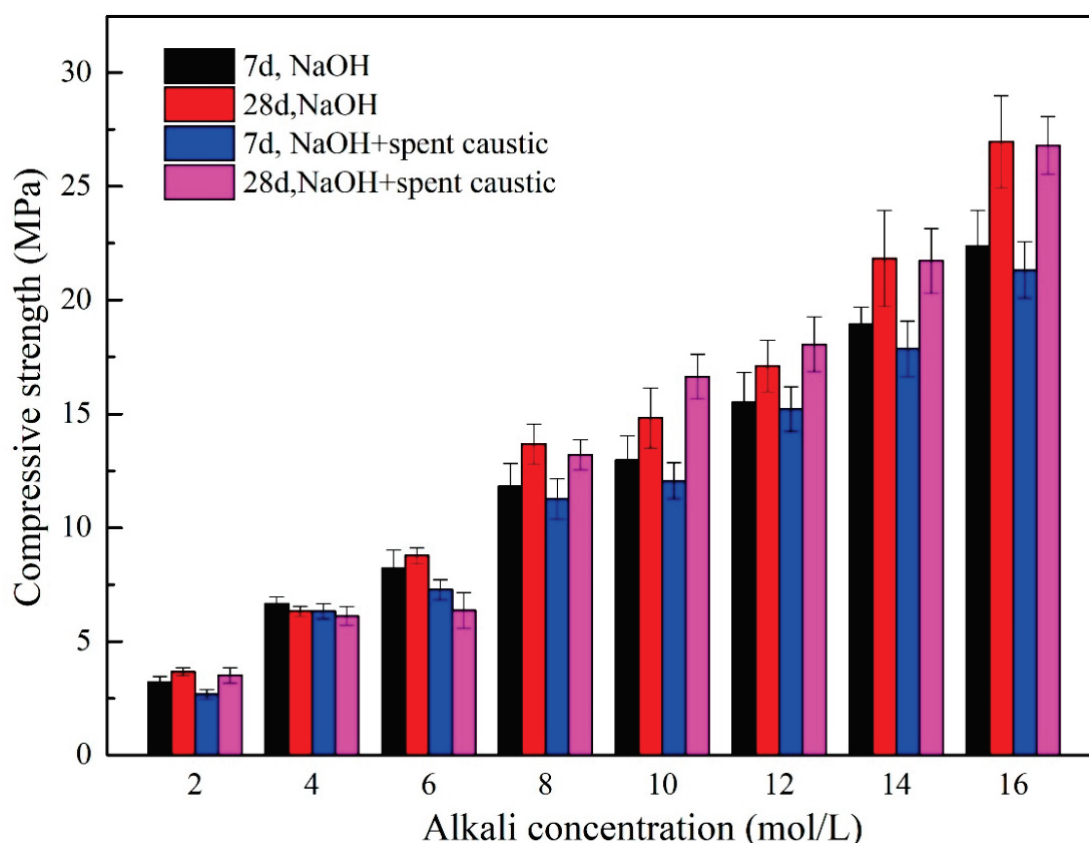
Figure 3. The compressive strength of geopolymers synthesized with different alkali activators.

3.2. X-ray Diffraction (XRD)

In order to study the activation effect of spent caustic on the structure of fly ash-based geopolymers, XRD analyses carried out on NaOH-activated geopolymers and spent caustic-activated geopolymers is shown in Figure 4. In fly ash, there is a typical dispersion peak of amorphous aluminosilicate at the position of 20–25° with crystal structures of mullite (Reference code: 01-079-1457) and quartz (Reference code: 01-070-3755). For geopolymers, the intensity of the mullite peak in the raw material is weakened, and the dispersion peak in fly ash shifted to a high angle at the position of 27–29°, which is a characteristic peak of geopolymer gel. The diffraction spectra of the geopolymers activated by spent caustic and pure NaOH solution showed the similar characteristic peak, indicating that spent caustic can partially replace NaOH as the alkali activator under the same degree of alkalinity, and the impurities such as organic in the spent caustic have little effect on the structure of the geopolymer. In addition, with the increase in the alkali activator concentration, the characteristic peak of zeolite appeared in the sample and the intensity gradually increased.

It is consistent with previous research results that zeolites formation is as a result of the reaction parallel to geopolymerization [22].
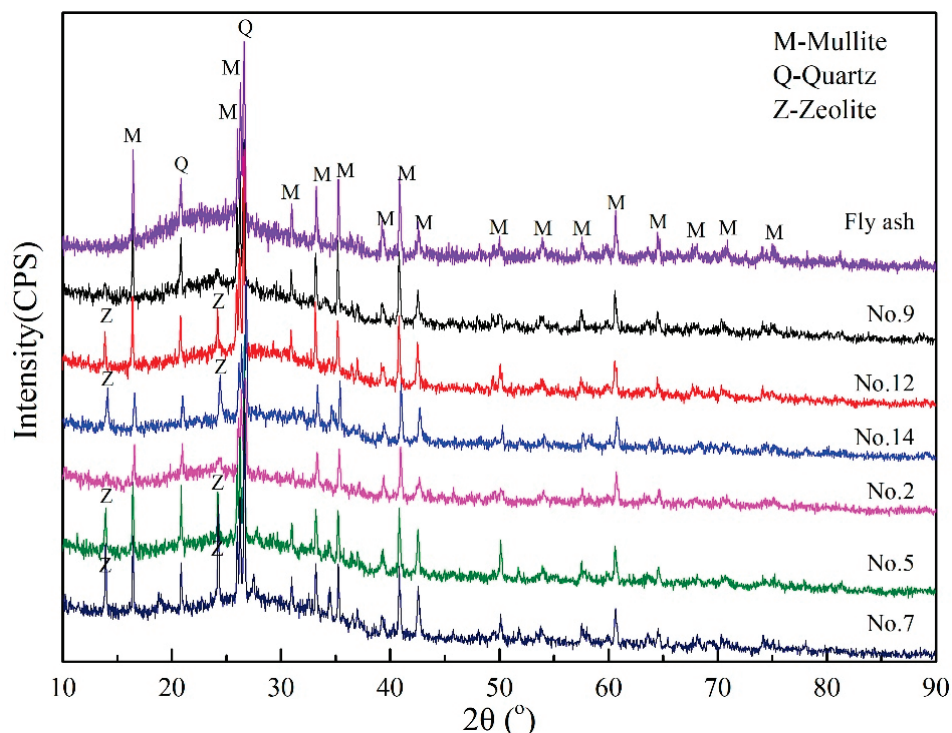
Figure 4. The X-ray diffractograms of fly ash and geopolymers synthesized with different alkali activators.

3.3. Nuclear Magnetic Resolution (NMR) Spectra

Figure 5 showed the ^{29}Si NMR spectra of geopolymers synthesized with different alkali activator after 28 days. The Gaussian peak deconvolution of this spectrum can be used to separate and quantify $Q^4(mAl)$ species of silicon ($0 \leq m \leq n \leq 4$, m) [23]. The resonance of a $Q^4(mAl)$ center with the replacement of each aluminum by silicon is an approximate -5 ppm difference in δ, with $Q^4(4Al)$, $Q^4(3Al)$, $Q^4(2Al)$, $Q^4(1Al)$ and $Q^4(0Al)$ resonating at approximately -84, -89, -93, -99 and -108 ppm, respectively [24]. It was also observed that the peak of -86.8 ppm was related to the Q^2 structure in C-S-H gel [25]. The peaks beyond -110 ppm represent the different crystalline silica phases in fly ash [26]. Table 3 presents ^{29}Si NMR date for the samples after deconvolution. For the samples No. 3 and No. 10, a broad peak ranged from -70 to -120 ppm was shown, which is similar to the spectrum of fly ash. It indicated that a large number of fly ash was not activated to form geopolymer gel. Compared with sample No. 10, the content of $Q^4(4Al)$ and $Q^4(3Al)$ in sample No. 3 is higher, while that of $Q^4(0Al)$ and Crystalline silica is opposite. Considering that the Al-rich gel is the primary reaction product of the alkali activation of fly ash [27], it suggested that the addition of spent caustic promotes the decomposition of fly ash and the formation of geopolymers at a low degree of alkalinity, which is consistent with the results of compressive strength. For the samples No. 8 and No. 13, the structure of the geopolymer gel was similar, and it indicated that the effect of the alkali activator with spent caustic is the same as that with pure NaOH solution, and the organic in spent caustic has no influence on the long-term development of geopolymers.

Table 3. Deconvolution results of ^{29}Si MAS NMR spectra of different geopolymers.

Sample	No. 3	No. 8	No. 10	No. 13
$Q^4(0Al)$	26.96%	1.42%	30.07%	10.44%
$Q^4(1Al)$	28.18%	2.59%	27.01%	19.02%

Table 3. *Cont.*

Sample	No. 3	No. 8	No. 10	No. 13
$Q^4(2Al)$	3.14%	26.96%	0.45%	19.81%
$Q^4(3Al)$	30.73%	31.20%	33.13%	22.93%
$Q^4(4Al)$	5.66%	24.47	1.35%	17.98%
$Q^2(0Al)$	1.03%	13.36%	1.14%	9.82%
Crystalline silica	4.30%	/	6.85%	/
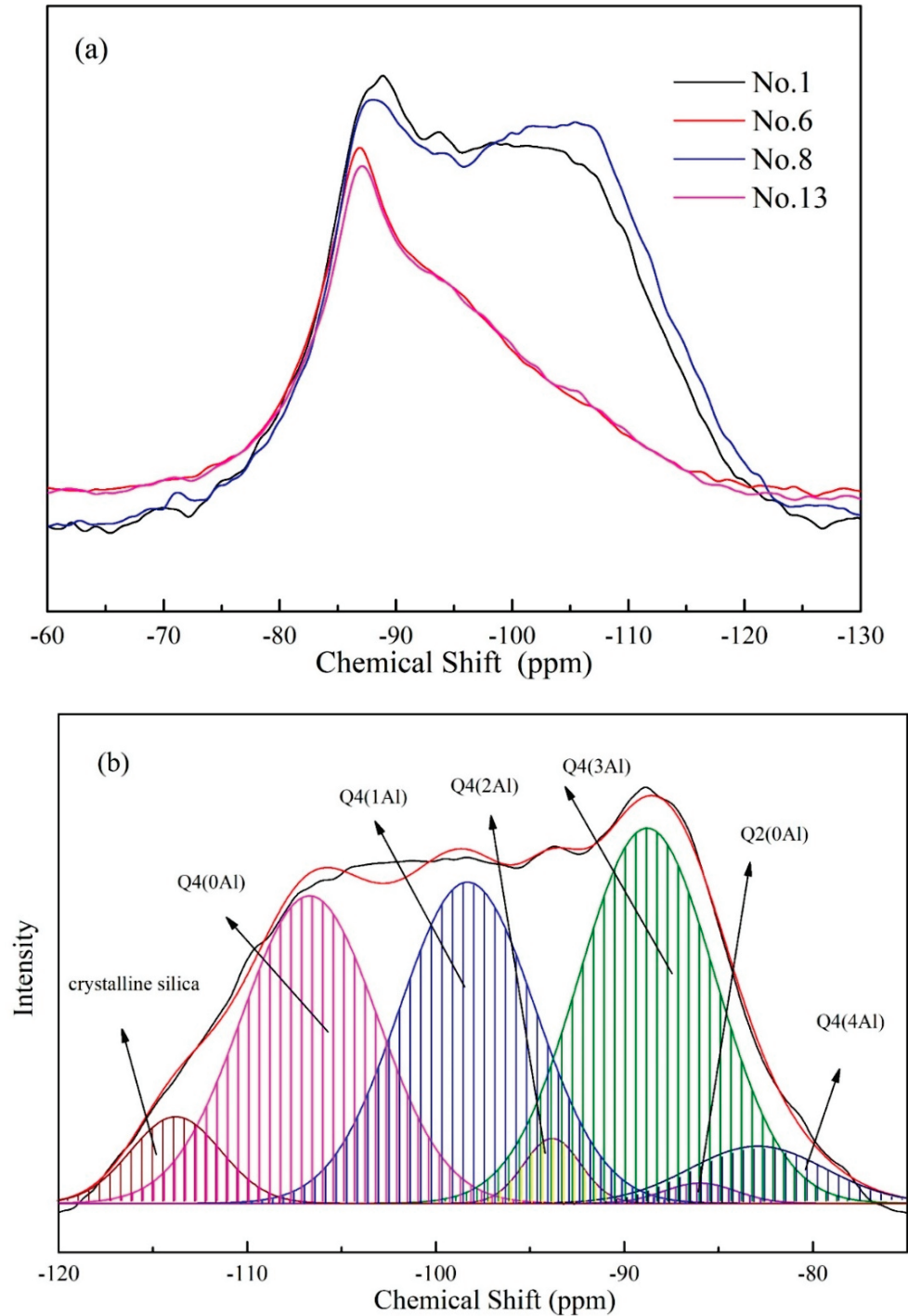
Figure 5. *Cont.*
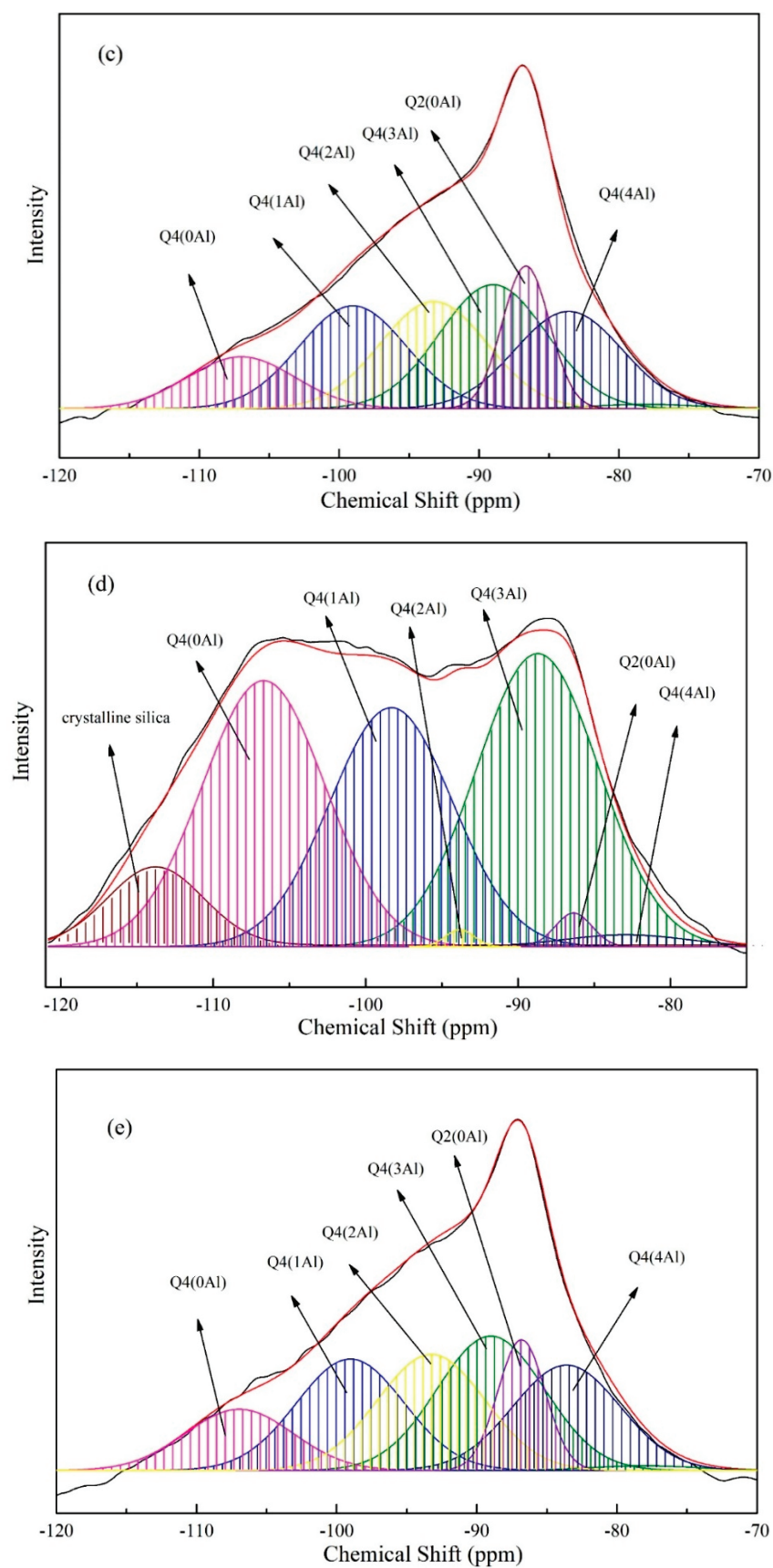
Figure 5. ^{29}Si NMR spectra (**a**) and their deconvolution of geopolymers with synthesized with different alkali activators, No. 1 (**b**), No. 6 (**c**), No. 8 (**d**) and No. 13 (**e**).

3.4. Pore Structure

The porosity and pore distribution of geopolymers with different alkali activators is shown in Figure 6. Under the same alkalinity condition, the porosity and pore size distribution of different geopolymers are similar, indicating that the alkali in the spent caustic has the same activation effect to NaOH. This resulted in a similar structure of the formed geopolymers, which is consistent with the results of XRD and NMR. However, the pore with a size between 100–500 nm decreased, while the number of pores with a size above 1 um increased. It leads to a slight increase in the porosity from 30.01% to 32.86%, but this has no noticeable effect on compressive strength.
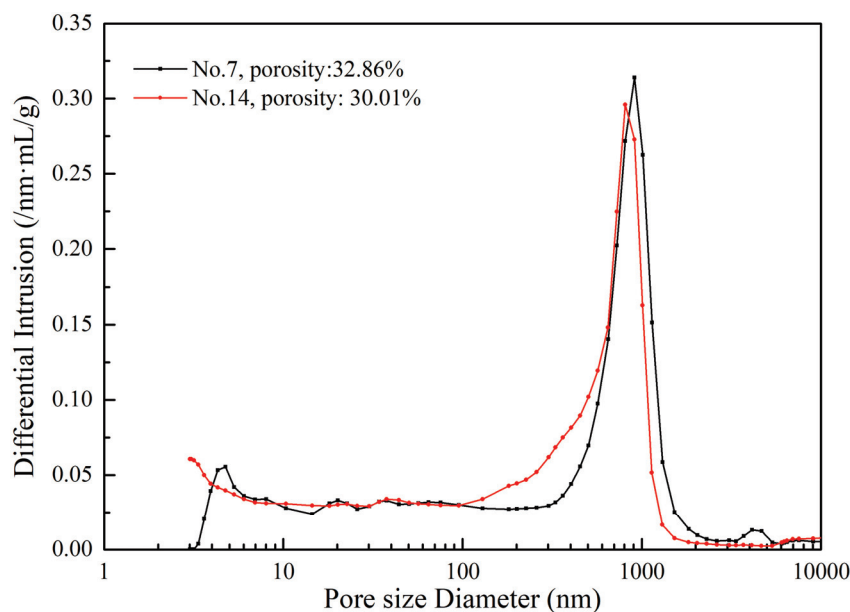
Figure 6. The porosity and pore size distribution of geopolymers synthesized with different alkali activator.

3.5. Organics Immobilization

The measurement of total organic carbon (TOC) was used to quantify the leaching of organics from geopolymers [28]. The organics immobilization efficiency of geopolymers was given in Figure 7. As the content of NaOH increased from 2 mol to 14 mol, the concentration of organics in the leachate decreased from 43.24 to 6.72 mg/L, and the immobilization efficiency increased from 0.4% to 84.5%. It suggests that the geopolymers can effectively immobilize the organics in the spent caustic, and the immobilization efficiency shows positive correlation with degree of alkalinity. This may be due to the formation of more zeolite structures in the process of activating fly ash with high concentration of alkali activator, and the adsorption of zeolite is the main way for geopolymers to immobilize organics [29]. In a previous study, Al-Mashaqbeh et al. [13] reported that geopolymers can be used to immobilized organic dyes, and the immobilization efficiency is 94%, which is higher than found in this work. Considering that the concentration of organic dye is 3000 mg/L, which is much lower than the 4341 mg/L level in this study, this result is acceptable. In addition, the Si/Al ratio has a significant impact on the immobilization of organics, and in further study, we will investigate its effect on the immobilization of organics in spent caustic.
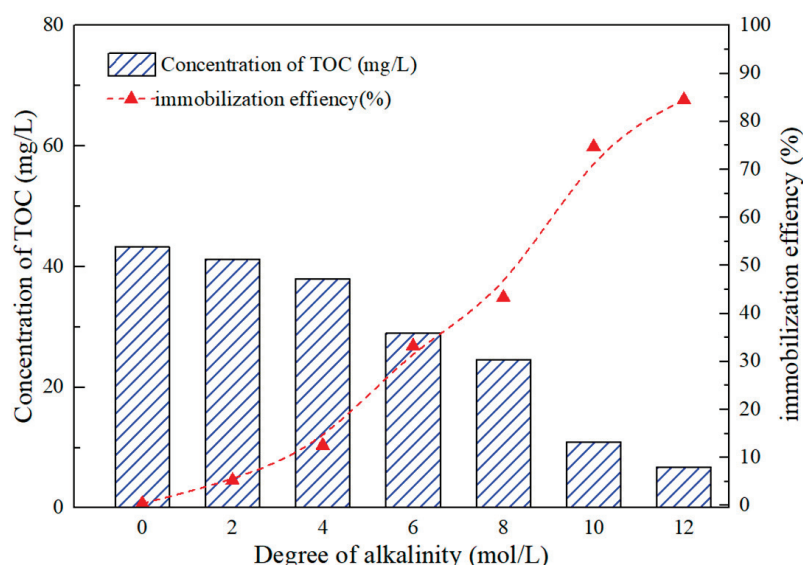
Figure 7. The concentration of TOC in the leachate and the organics immobilization efficiency of geopolymers synthesized with different alkali activator.

4. Conclusions

In this study, fly ash-based geopolymers were prepared by using spent caustic as alkali activator and the influence of spent caustic on the formation of geopolymers was studied. The result is as follows:

(1) The spent caustic can partially replace the NaOH to synthesize geopolymers, and the organics in spent caustic can be immobilized in geopolymers. The method can not only make the spent caustic harmless, but also utilize the strong alkalinity of the spent caustic to reduce the cost of preparing the geopolymer.

(2) When the degree of alkalinity is higher than 4 mol/L, the geopolymers prepared by the mixed activator of spent caustic and sodium hydroxide have better 28 days compressive strength than that synthesized with pure NaOH solution, and the highest strength can reach 21.86 Mpa.

(3) With the degree of alkalinity increasing, the immobilization efficiency of organics in geopolymers is improved, and the maximum can reach 84.5%. The organics in the spent caustic will hinder geopolymerization at the initial stage but has little effect on the chemical structure and phase of the final product.

References

1. Rahi, M.N.; Jaeel, A.J.; Abbas, A.J. Treatment of petroleum refinery effluents and wastewater in Iraq: A mini review. *Proc. IOP Conf. Ser. Mater. Sci. Eng.* **2021**, *1058*, 012072. [CrossRef]
2. Ntagia, E.; Fiset, E.; Hong, L.T.C.; Vaiopoulou, E.; Rabaey, K. Electrochemical treatment of industrial sulfidic spent caustic streams for sulfide removal and caustic recovery. *J. Hazard Mater.* **2020**, *388*, 121770. [CrossRef] [PubMed]
3. Vaiopoulou, E.; Provijn, T.; Prévoteau, A.; Pikaar, I.; Rabaey, K. Electrochemical sulfide removal and caustic recovery from spent caustic streams. *Water Res.* **2016**, *92*, 38–43. [CrossRef]
4. Alipour, Z.; Azari, A. COD removal from industrial spent caustic wastewater: A review. *J. Environ. Chem. Eng.* **2020**, *8*, 103678. [CrossRef]
5. Su, P.; Zhang, J.; Yang, B. The Current Status of Hazardous Waste Management in China: Identification, Distribution, and Treatment. *Environ. Eng. Sci.* **2022**, *39*, 81–97. [CrossRef]
6. Nunez, P.; Hansen, H.K.; Rodriguez, N.; Guzman, J.; Gutierrez, C. Electrochemical generation of Fenton's reagent to treat spent caustic wastewater. *Sep. Sci. Technol.* **2009**, *44*, 2223–2233. [CrossRef]
7. Elmi, R.; Nejaei, A.; Farshi, A.; Ramazani, M.E.; Alaie, E. Comparison of two methods of neutralization and wet air oxidation for treating wastewater spent caustic produced by oil refineries. *Environ. Monit. Assess.* **2021**, *193*, 854. [CrossRef]
8. Duxson, P.; Provis, J.L.; Lukey, G.C.; Van Deventer, J.S. The role of inorganic polymer technology in the development of 'green concrete'. *Cem. Concr. Res.* **2007**, *37*, 1590–1597. [CrossRef]
9. Wan, Q.; Rao, F.; Song, S.; Morales-Estrella, R.; Xie, X.; Tong, X. Chemical forms of lead immobilization in alkali-activated binders based on mine tailings. *Cem. Concr. Compos.* **2018**, *92*, 198–204. [CrossRef]
10. Shi, C.; Fernández-Jiménez, A. Stabilization/solidification of hazardous and radioactive wastes with alkali-activated cements. *J. Hazard Mater.* **2006**, *137*, 1656–1663. [CrossRef] [PubMed]
11. Reeb, C.; Pierlot, C.; Davy, C.; Lambertin, D. Incorporation of organic liquids into geopolymer materials-A review of processing, properties and applications. *Ceram. Int.* **2021**, *47*, 7369–7385. [CrossRef]
12. Cantarel, V.; Nouaille, F.; Rooses, A.; Lambertin, D.; Poulesquen, A.; Frizon, F. Solidification/stabilisation of liquid oil waste in metakaolin-based geopolymer. *J. Nucl. Mater.* **2015**, *464*, 16–19. [CrossRef]
13. Al-Mashaqbeh, A.; El-Eswed, B.; Banat, R.; Khalili, F.I. Immobilization of organic dyes in geopolymeric cementing material. *Environ. Nanotechnol. Monit. Manag.* **2018**, *10*, 351–359. [CrossRef]
14. Duxson, P.; Fernández-Jiménez, A.; Provis, J.L.; Lukey, G.C.; Palomo, A.; van Deventer, J.S. Geopolymer technology: The current state of the art. *J. Mater. Sci.* **2007**, *42*, 2917–2933. [CrossRef]
15. Turner, L.K.; Collins, F.G. Carbon dioxide equivalent (CO2-e) emissions: A comparison between geopolymer and OPC cement concrete. *Constr. Build. Mater.* **2013**, *43*, 125–130. [CrossRef]
16. McLellan, B.C.; Williams, R.P.; Lay, J.; Van Riessen, A.; Corder, G.D. Costs and carbon emissions for geopolymer pastes in comparison to ordinary portland cement. *J. Clean. Prod.* **2011**, *19*, 1080–1090. [CrossRef]
17. Salas, D.A.; Ramirez, A.D.; Ulloa, N.; Baykara, H.; Boero, A.J. Life cycle assessment of geopolymer concrete. *Constr. Build Mater.* **2018**, *190*, 170–177. [CrossRef]
18. Yuan, W.; Zhang, L.; Liu, Y.; Fu, P.; Huang, Y.; Wang, L.; Ma, H.; Wang, H. Sulfide removal and water recovery from ethylene plant spent caustic by suspension crystallization and its optimization via response surface methodology. *J. Clean. Prod.* **2020**, *242*, 118439. [CrossRef]
19. Ellis, C.E. Wet air oxidation of refinery spent caustic. *Environ. Prog.* **1998**, *17*, 28–30. [CrossRef]
20. Karamalidis, A.; Voudrias, E. Leaching of VOCs from cement-based stabilized/solidified refinery oily sludge using solid phase microextraction. *Environ. Technol.* **2007**, *28*, 1173–1185. [CrossRef]
21. Zhang, Q.; Ji, T.; Yang, Z.; Wang, C.; Wu, H.-C. Influence of different activators on microstructure and strength of alkali-activated nickel slag cementitious materials. *Constr. Build. Mater.* **2020**, *235*, 117449. [CrossRef]
22. Rożek, P.; Król, M.; Mozgawa, W. Geopolymer-zeolite composites: A review. *J. Clean. Prod.* **2019**, *230*, 557–579. [CrossRef]
23. Lee, S.K.; Stebbins, J.F. The degree of aluminum avoidance in aluminosilicate glasses. *Am. Mineral.* **1999**, *84*, 937–945. [CrossRef]
24. Engelhardt, G.; Michel, D. *High-Resolution Solid-State NMR of Silicates and Zeolites*; John Wiley & Sons: Hoboken, NJ, USA, 1987.
25. Richardson, I.G. The nature of CSH in hardened cements. *Cem. Concr. Res.* **1999**, *29*, 1131–1147. [CrossRef]
26. Peng, Z.; Vance, K.; Dakhane, A.; Marzke, R.; Neithalath, N. Microstructural and 29Si MAS NMR spectroscopic evaluations of alkali cationic effects on fly ash activation. *Cem. Concr. Compos.* **2015**, *57*, 34–43. [CrossRef]
27. Criado, M.; Fernández-Jiménez, A.; Palomo, A.; Sobrados, I.; Sanz, J. Effect of the SiO2/Na2O ratio on the alkali activation of fly ash. Part II: 29Si MAS-NMR Survey. *Microporous Mesoporous Mater.* **2008**, *109*, 525–534. [CrossRef]
28. Luo, H.; Cheng, Y.; He, D.; Yang, E.-H. Review of leaching behavior of municipal solid waste incineration (MSWI) ash. *Sci. Total Environ.* **2019**, *668*, 90–103. [CrossRef]
29. Gokhale, C.; Lorenzen, L.; Van Deventer, T. The Immobilisation of Organic Waste by Geopolymerisation. Master's Thesis, University of Stellenbosch, Stellenbosch, South Africa, 2001.

Article

Hydrogel Beads of Amidoximated Starch and Chitosan as Efficient Sorbents for Inorganic and Organic Compounds

Diana Felicia Loghin, Melinda Maria Bazarghideanu, Silvia Vasiliu [ID], Stefania Racovita [ID], Marius-Mihai Zaharia [ID], Tudor Vasiliu and Marcela Mihai *

Petru Poni Institute of Macromolecular Chemistry, Aleea Grigore Ghica Voda 41A, 700487 Iasi, Romania
* Correspondence: marcela.mihai@icmpp.ro

Abstract: The synthesis of hydrogel beads involving natural polymers is, nowadays, a leading research area. Among natural polymers, starch and chitosan represent two biomolecules with proof of efficiency and low economic impact in various utilization fields. Therefore, herein, the features of hydrogel beads obtained from chitosan and three sorts of starch (potato, wheat and rise starches), grafted with acrylonitrile and then amidoximated, were deeply investigated for their use as sorbents for heavy metal ions and dyes. The hydrogel beads were prepared by ionotropic gelation/covalent cross-linking of chitosan and functionalized starches. The chemical structure of the hydrogel beads was analyzed by FT-IR spectroscopy; their morphology was revealed by optical and scanning electron microscopies, while the influence of the starch functionalization strategies on the crystallinity changes was evaluated by X-ray diffraction. Molecular dynamics simulations were used to reveal the influence of the grafting reactions and grafted structure on the starch conformation in solution and their interactions with chitosan. The sorption capacity of the hydrogel beads was tested in batch experiments, as a function of the beads' features (synthesis protocol, starch sort) and simulated polluted water, which included heavy metal ions (Cu^{2+}, Co^{2+}, Ni^{2+} and Zn^{2+}) and small organic molecules (Direct Blue 15 and Congo red).

Keywords: grafted starch; ionotropic gelation; covalent cross-linking; molecular dynamics simulation; sorption capacity

1. Introduction

In the last few years, extensive research has been undertaken to obtain specialized and selective sorbents containing natural polymers as a cheap and environmentally friendly solution for water cleaning. In this respect, polysaccharide-based hydrogels were studied, taking advantage of their low cost, availability, non-toxicity and biodegradability [1,2]. Among the polysaccharides, starch [3–8] and chitosan (CS) [9–15] have attracted the attention of the scientific community due to their physico-chemical characteristics, chemical stability, and excellent selectivity resulting from the presence of chemical reactive groups (hydroxyl, acetamido or amino functions) in polymeric chains. Moreover, these products are abundant, renewable, and biodegradable, and are able to physically and chemically bind to a wide range of molecules [16–22].

A number of studies have shown that polymers containing amidoxime groups have high complex-forming capabilities with metal ions and can be successfully used in metal ion removal from aqueous solutions [23–30]. Amidoxime hydrogel beads of modified alginate and amidoximated synthetic polymers have been successfully synthesized and used as sorbents for dyes, showing selective adsorption towards cationic dyes in the presence of anionic/cationic mixed dyes [31]. Usually, the synthesis of a sorbent with amidoxime groups involves the incorporation of a nitrile group into a polymer matrix, followed by the conversion of the nitrile group into an amidoxime group by treatment with an alkaline solution of hydroxylamine. For instance, sorbents containing amidoxime

groups have been obtained by reacting acrylonitrile-divinyl benzene copolymer beads with hydroxylamine [32]. The introduction of amidoxime groups into acrylonitrile-grafted cellulose by interaction with hydroxylamine has also been investigated [33].

Starch is an interesting bio-material, due to its abundance and low cost, but has poor mechanical properties and the fact that it is highly hydrophilic. To overcome these drawbacks, chemical modification of starch is usually applied, mainly by grafting reactions. A large range of polymers can be grafted on starch by ring-opening and radical polymerizations of various monomers in order to modulate the properties of the final products [34]. For example, poly(amidoxime) ion exchange resins were synthesized from polacrylonitrile grafted sago starch, with their batch binding capacity for different metal ions being pH dependent [27,35]. In our previous studies, potato starch (PS) was grafted with acrylonitrile (AN) by the redox initiation by Ce^{4+} ions [36] and then the amidoximated (Ax) derivative was obtained [37]. Ionic composites based on crosslinked CS and amidoximated potato starch were also obtained and used as super-sorbents for copper ions, with reusability up to five sorption/desorption cycles, with no significant decrease in their sorption capacity [36]. Furthermore, the acrylonitryle grafted reaction, with the same Ce^{4+} ions as the initiator, was tested on three sorts of starch, namely PS, wheat (WS) and rice (RS) starches, followed by obtaining soluble derivatives by hydrolysis [5] The studies showed that the amylose/amylopectin content in starch and the grain size influenced the grafting performance, which reached 13.81%, 9.71% and 8.22% for PS, WS and RS, respectively [5].

Therefore, herein, the features of three sorts of starch (PS, WS and RS) grafted with acrylonitrile (PSgAN, WSgAN and RSgAN) and then amidoximated (PSgAx, WSgAx and RSgAx) were deeply investigated, following the formation of composite hydrogel beads with CS. The current study starts with the premise that the use of starch from different botanical sources in grafting reactions can influence the properties of the obtained materials, and consequently their properties. Thus, we aimed to prepare hydrogel beads by ionotropic gelation and covalent cross-linking of CS and functionalized starches as SgAN or SgAx. The chemical structure of functionalized starches and the obtained hydrogel beads was followed by FT-IR spectroscopy; their morphology was revealed by optical and scanning electron microscopy, while the samples' crystallinity changes in relation to the functionalization strategies was evaluated by X-ray diffraction. Molecular dynamics simulations were used to determine the influence of the grafting reactions and grafted structure on the starch conformation in solution and their interactions with chitosan. The sorption capacity of the beads for Cu^{2+}, Co^{2+}, Ni^{2+} and Zn^{2+} ions and for Direct Blue 15 and Congo red dyes was followed in batch experiments, as a function of the beads' features (synthesis protocol, starch sort), and contact time.

2. Results and Discussion

2.1. Starch Functionalization

Previous studies showed that the grafting reaction, in the current applied conditions, took place on the amylose part of starch [36] and the amylose contents of the used starch were as follows: 20–21% in PS, 23–30% in WS and 17–30% in RS [5]. Herein, the three types of starch were functionalized by grafting acrylonitrile to the amylose component of starch (SgAN samples), followed by amidoxime transformation (SgAx samples) (see details in Section 4.2). SEM images (Figure 1(aA)) revealed that starch granules have different morphologies. PS has a spherical, elliptical or irregular shape, whereas WS is predominantly spherical shaped, both with a smooth surface; RS particles show polyhedron-type shapes with sharp edges. Figure 1(bA,cA) show that PS and WS granules after AN grafting (SgAN), and also after amidoximation (SgAx), had irregular shapes and sizes, most of them being smaller than the initial granules, whereas RS-based samples show small changes in morphology, mainly with the loss of sharp edges.
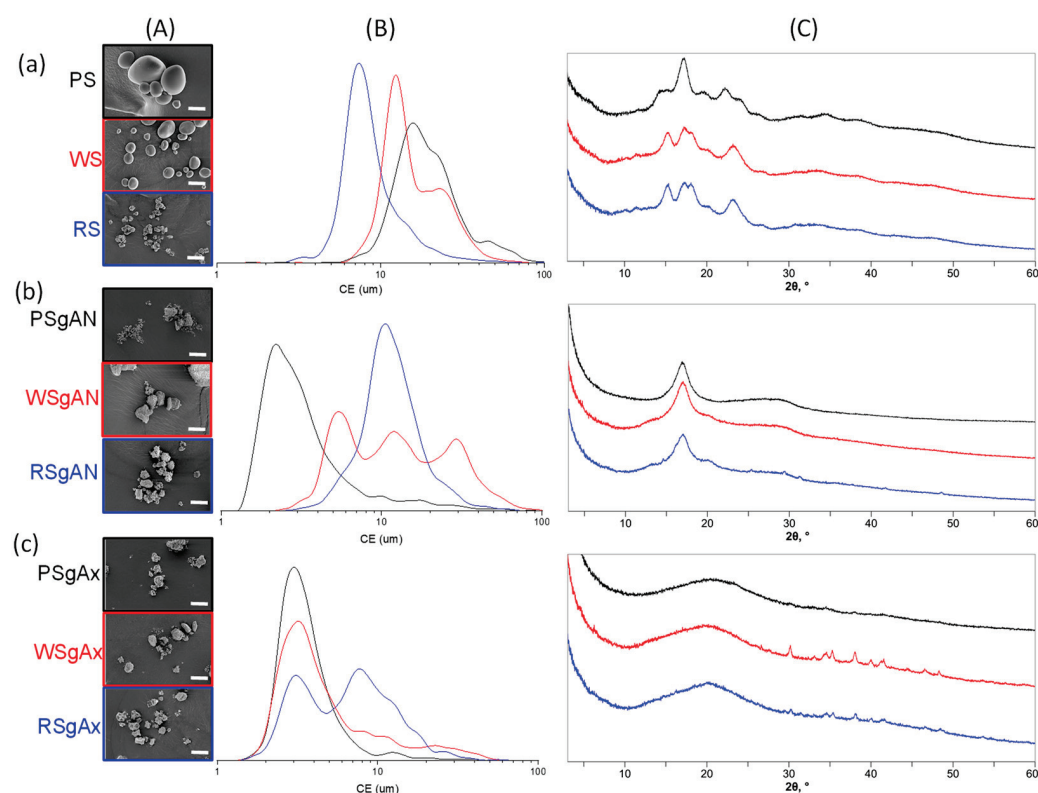
Figure 1. SEM images (scale bar 20 μm) (**A**), circular equivalent (CE) diameter (**B**) and X-ray diffractograms (**C**) of initial (**a**) and grafted AN (**b**) and Ax (**c**) starches.

The particle size analysis of native starches (Figure 1(aB)) shows that PS has the largest granule size (mean diameter, Dm = 15.58 μm), with WS and RS being characterized by lower particle sizes (Dm = 10.1 μm and 8.7 μm) and similar particle size distribution (with a shoulder for larger sizes suggesting particle aggregation), which was almost unimodal for each starch type. After AN grafting, the size distribution (Figure 1(bB)) undergoes SEM observation (Figure 1(bA)), and shows that the highest grain fragmentation is observed for the PSgAN and WSgAN, with smaller particle aggregation being found for RSgAN. After amidoximation, the samples show a population of particles with a mean diameter of about 3 μm (Figure 1(cB)) and the aggregation is characteristic also for the RS grains. Moreover, the size and morphology modifications observed in Figure 1A,B can be explained by the selectivity of the grafting and amidoximation reactions to the amylose part of the starch grains and the amylopectin part was partially removed during the starch grain functionalization process [36]. Thus, during the gelatinization process, which took place in the first reaction step, the amorphous amylose part of the grains becomes available to the Ce^{4+} ions, which interacts with the -OH groups located at the C2 and C3 carbon atoms.

The powder XRD diffraction analyses of PS, WS and RS and grafted starch are presented in Figure 1C. Generally, the X-ray diffraction results of starch beads are classified as A, B or C type, and depend upon the double-helical amylopectin chain arrangement. The A type pattern is a result of close-packed arrangements with a water molecule connection between the double helix, the B type is open hexagonal packing with water in the central cavity and type C is quite similar to the A pattern, except for the appearance of the peak around 5° [38]. The X-ray diffractogram of PS revealed a typical B-type pattern [39], with a strong reflection peak (100) at around 17°, relatively low intensity peaks at around 5° and 22° and shoulders around 15° and 24° (2θ). The diffractograms of WS and RS were practically identical, with the strongest peaks at approximatively 15°, 17° and 23° (2θ). The A-type pattern of WS and RS can be proved by the appearance of the shoulder at around 18° (2θ), a signal that is characteristic to this starch type. After being grafted with

AN (Figure 1(bC)), the characteristic diffraction peaks of native starch disappeared in the XRD patterns with the appearance of a new intense peak around 17° (2θ), which can be ascribed to the structure modification following the AN grafting. As compared to native and AN-grafted starch, the XRD spectra of SgAx displayed a typical V-type crystalline structure [40] with a wide peak at around 20° (2θ). This wide peak can be attributed to the hydroxylamine functionalization reactions, which lead to the partially destroyed crystallinity of starch. The XRD results also confirmed our previous studies [36], where it was shown by ^{1}H-NMR studies that the grafting reaction takes place mainly at the amylose component of starch, the amorphous component of starch molecules.

Molecular dynamics (MD) simulations were performed in order to visualize the conformation modifications of the starch (amylose) backbone after AN grafting reaction and its further amidoxime functionalization. The different types of patterns observed in starch crystallization are determined mainly by the interaction between two starch molecules. This is why the three simulated systems contained two identical starch molecules (amylose, SgAN and SgAx) solvated in water (see details in Section 4.5). Figure 2 depicts the initial conformation of the system and the final structure obtained after 200 ns of simulation.
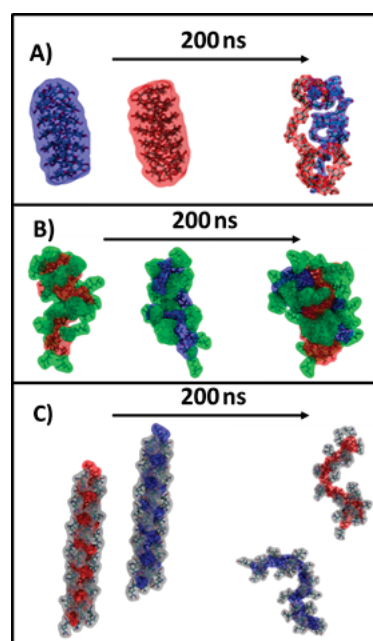
Figure 2. Snapshots depicting the starting and final structure of the 3 simulated systems: (**A**) amylose from starch, (**B**) SgAN and (**C**) SgAx. The starch molecules are colored in red and blue, the AN side chains are colored in green and the Ax side chains are colored in silver. Water has been omitted for clarity.

The amylose starch molecules start with separated conformation, with a distance between the two molecules of >20 Å, to eliminate any bias in the interaction that could take place. After 200 ns, it can be observed in Figure 2A,B that the unfunctionalized and the SgAN molecules are interacting with each other, while the SgAx molecules remain separate. The unfunctionalized starch molecules are wrapped around each other in a way that is similar to a double-helical structure (Figure 2A). Similar observations were found in the literature [41], which also showed that this association could have two main crystal forms, A and B, as already observed for our starch samples in Figure 1C. The AN grafted starch behaves in a similar manner to the previous system, with the main starch chains wrapped around each other and the side chains exposed to the exterior (Figure 2B). The Ax functionalized starch behaves differently to the other investigated starch, in that the molecules remain isolated for the entire simulation (Figure 2C). The structures obtained in the MD simulation corroborate well with the XRD result (Figure 1C). In detail, in the

case of the unfunctionalized starch molecules, the amylopectin crystalline part of the starch, and also the amylose part, can interact with each other and assemble in structures that are precursors to the A or B type patterns. In the case of the SgAN, although the amylose main chains interact with each other in a similar way to the previous system, the side chains located at the exterior and the absence of amylopectin leads to a decrease in crystallinity. Thus, the reflection peak (100) at around 17° observed in all SgAN samples (Figure 1(bC)) can be ascribed to the remaining organization of the starch main chains while the AN side chains determine a loose structure. In the case of SgAx, the MD simulation clearly depicts the V-type pattern of single starch molecules in an extended conformation.

2.2. Hydrogel Beads of Functionalized Starch and Chitosan

The composite hydrogel beads formation follows two routes, which include using SgAN or SgAx as precursors and obtaining three types of composite beads, CS/SgAN, Cs/SgAN-Ax and Cs/SgAx (see details in Section 4.3). The beads are sphere shaped, as observed in the optical images of wet beads, and are porous, as shown by the SEM images of the surface of lyophilized beads (Figure 3).
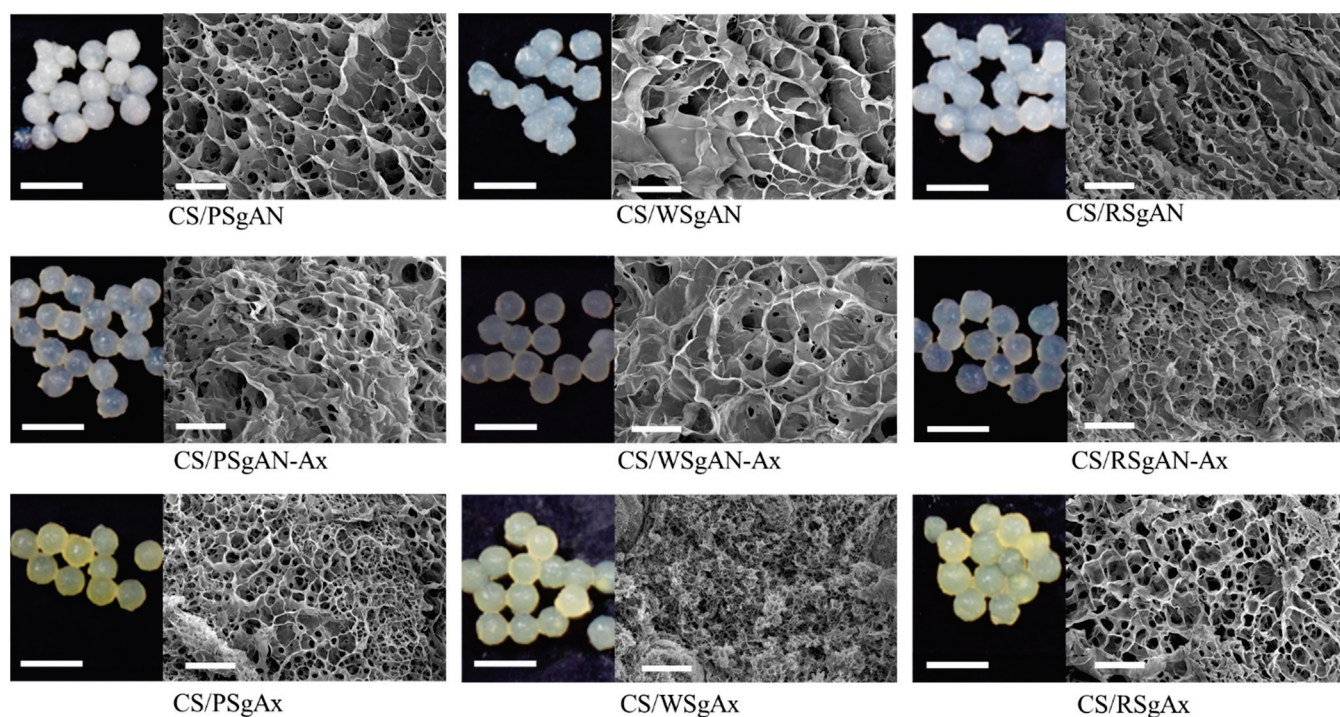
Figure 3. Optical (scale bar 5 mm) and SEM (scale bar 20 μm) images of composite beads.

The optical images in Figure 3 show some color changes as a function of the composite bead synthesis pathway: the beads obtained with SgAx keep the yellow color of amidoximated starches, whereas after post-amidoximation translucid beads were observed, with a slight yellow tinge. In addition, the beads' size in swelled form is not influenced by the synthesis pathway, as is the surface morphology observed in the SEM images. Thus, CS/SgAN beads have uniform pore distribution at the beads' surface, with thin walls. After bead amidoximation (CS/SgAN-Ax samples), the porosity slowly decreased and the pore walls becomes thicker. A different morphology of the composite beads was obtained when SgAx was employed in the bead formation process, i.e., a smaller size of the pores was obtained for all the investigated samples, most probably since the -NH$_2$ groups in SgAx could also be crosslinked by epichlorohydrin (ECH), as is the case for the similar groups in CS; thus, a double crosslinked network is formed.

The samples' porosity in the swollen state was estimated by measuring 50 pores in each SEM image from Figure 3; the resulted mean values of area, perimeter, aspect ratio (ratio of major/minor axis of pores) and Feret diameter (the longest distance between any two points along the selection boundary) are included in Table 1.

Table 1. Pore size analysis as area, perimeter, Feret diameter and aspect ratio (mean values ± standard deviation).

Sample	Area, μm^2	Perimeter, μm	Feret Diameter, μm	Aspect Ratio
CS/PSgAN	25.26 ± 29.71	15.69 ± 8.87	5.59 ± 3.21	1.35 ± 1.67
CS/WSgAN	29.50 ± 26.47	18.83 ± 11.00	6.18 ± 3.98	1.80 ± 1.25
CS/RSgAN	14.03 ± 9.16	12.74 ± 4.07	4.46 ± 1.48	1.15 ± 1.46
CS/PSgAN-Ax	27.74 ± 34.35	16.89 ± 8.69	6.17 ± 3.31	1.42 ± 1.53
CS/WSgAN-Ax	34.35 ± 32.53	19.27 ± 12.53	6.85 ± 4.32	1.95 ± 1.62
CS/RSgAN-Ax	16.89 ± 9.67	14.14 ± 4.02	5.00 ± 1.43	1.26 ± 1.56
CS/PSgAx	16.28 ± 13.63	11.93 ± 5.03	4.32 ± 1.70	1.29 ± 1.18
CS/WSgAx	14.37 ± 7.13	11.40 ± 3.04	3.97 ± 1.31	1.31 ± 1.12
CS/RSgAx	15.52 ± 10.99	11.24 ± 4.48	4.03 ± 1.62	1.58 ± 1.46

Thus, the obtained values of the aspect ratio are higher than 1.00 (circles), meaning that the pores have elongated shapes. In addition, the Feret diameter values showed that the larger (the higher diameter) and the more irregular shaped (with higher aspect ratio values) pores were obtained when WS was used in hydrogel bead synthesis and were smaller with RS. The same trend was observed after bead amidoximation (SgAN-Ax samples). Larger amylose contents in RS (up to 30%) favor better grafting reactions and resulted in its better embedment into the hydrogel beads, leading to smaller pore sizes. PS and WS, with almost the same amylose content (up to 20 and 23–30%, respectively) formed hydrogel beads with larger pores. The amidoximated starch directly used in bead formation led to smaller size pores, as the starch had a very small influence on their porosity. In this synthesis route, the SgAx participation to crosslinking along with CS, and also the elongated form of SgAx both contributed to obtaining homogeneous beads with very close pore sizes, irrespective of the starch source. This observation is also supported by the MD simulations of the Ax-grafted starch that showed the side chains extended in the solvent, which were completely free to interact with ECH (Figure 2). To further support this observation, MD simulations of two systems containing two starch molecules of SgAN or SgAx and one CS molecule were performed (Figure 4).

The MD simulations showed that CS is able to interact with the SgAN molecules, coming into contact with both the AN side chains and the amylose backbone (detail of Figure 4A), while in the case of SgAx molecules, no contact between the CS an SgAx can be observed for the entire simulation (Figure 4B). This is due to the fact that both molecule types have a positive charge and repel each other.

The hydrogel beads' elemental composition was followed by EDAX analysis and Table 2 shows the obtained results both at their surface and in the sections. The values were compared with the values calculated taking into account the ratio between the grafted starch in the synthesis process and CS (1:4) and ECH (1:0.37), considering, for functionalized starches, the mean grafting of three units to each monomer unit.
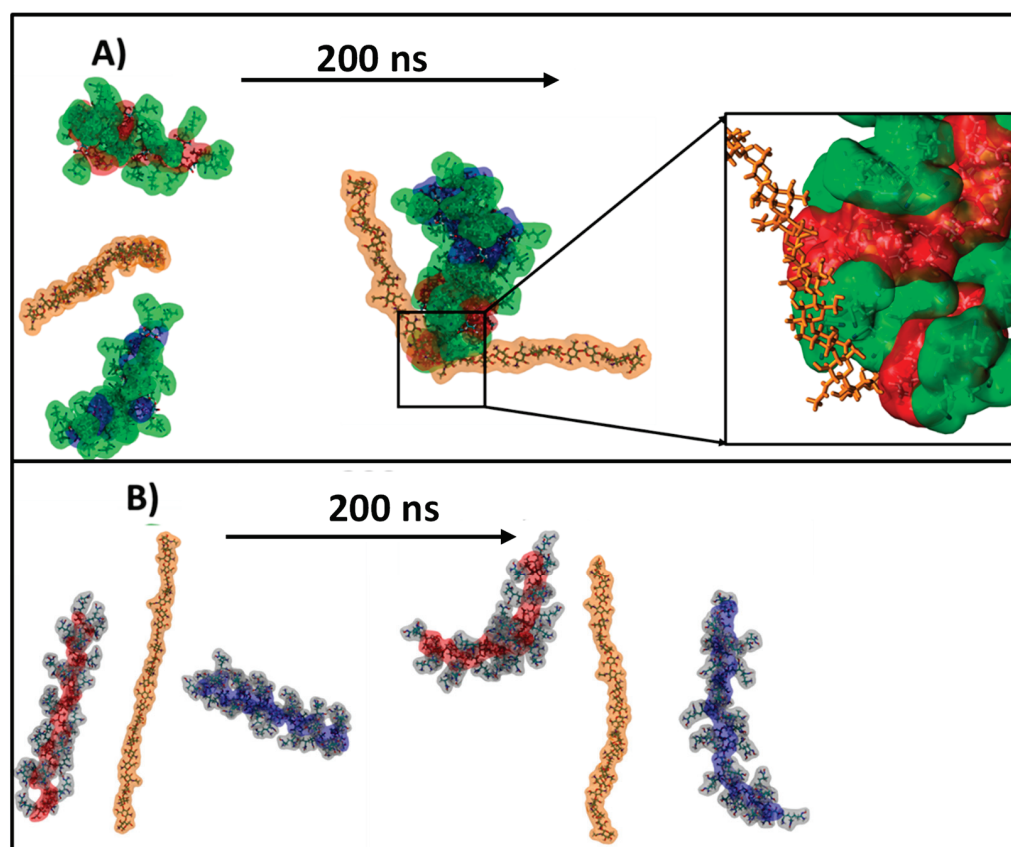
Figure 4. Snapshots depicting the starting and final structure of the simulated systems containing CS and (**A**) SgAN and (**B**) SgAx. The starch molecules are colored in red and blue, the AN side chains are colored in green, the Ax side chains are colored in silver and the chitosan is colored in orange. Water has been omitted for clarity.

Table 2. The C/N and C/O atomic ratios calculated and determined by EDAX for composite beads.

Sample	C/N			C/O		
	PS	**WS**	**RS**	**PS**	**WS**	**RS**
			Calculated			
CS/SgAN		5.06			1.41	
CS/SgAN-Ax		3.54			1.24	
			At surface/In section			
CS/SgAN	7.44/5.46	6.56/6.27	6.28/6.35	2.03/1.95	1.89/1.80	2.16/1.93
CS/SgAN-Ax	6.40/4.74	6.31/5.35	5.80/5.31	2.17/2.05	1.85/1.70	1.85/1.79
CS/SgAx	6.43/4.91	6.21/5.46	5.45/5.65	1.89/1.81	1.87/1.89	1.84/1.67

Thus, the C/N atomic ratios are higher than the calculated values both at the surface and inside the beads. The lower N content in the beads can be ascribed to a synergy of factors, mainly because of the lower contribution of the AN-grafted side chains in starch and/or a higher contribution of the CS chains inside the beads. By considering the small length of the grafting chains, we may assume that the grafted chains can be hindered by the macromolecule conformation and, as observed in the MD simulation, with the SgAx behaving as elongated macromolecules, with easily accessible functional groups. This is also related to the contribution of CS to the formation of the beads, with the partial crosslinking of SgAx decreasing the amount of ECH available to crosslink the CS chains and the free chains being most probably partially removed during the final washing steps.

The above-mentioned observations are sustained by the C/O atomic ratios, which are higher than the calculated ones. The comparison of the C/N and C/O atomic ratios at the surface and inside the beads revealed that there are some differences in the elemental composition and that inside the beads, the atomic ratio values are smaller than outside but are the closest to the calculated values.

Further proof of the samples' chemical structure was obtained by FTIR and is shown in Figures S1–S3 (supplementary information), where the characteristic peak of AN is observed just in the CS/SgAN samples and the characteristic peaks for starch and CS are found in all the spectra. Nevertheless, as shown in previous studies [36], the formation of amidoxime can be demonstrated in FTIR at about 1650 cm^{-1} or 933 cm^{-1}, assigned to the C=N and N-O bonds in oximes, respectively. Therefore, the 1800–1500 cm^{-1} area was selected and the peak deconvolution was performed for both types of amidoximated beads, CS/SgAN-Ax and CS/SgAX (Figure 5, Table S1).
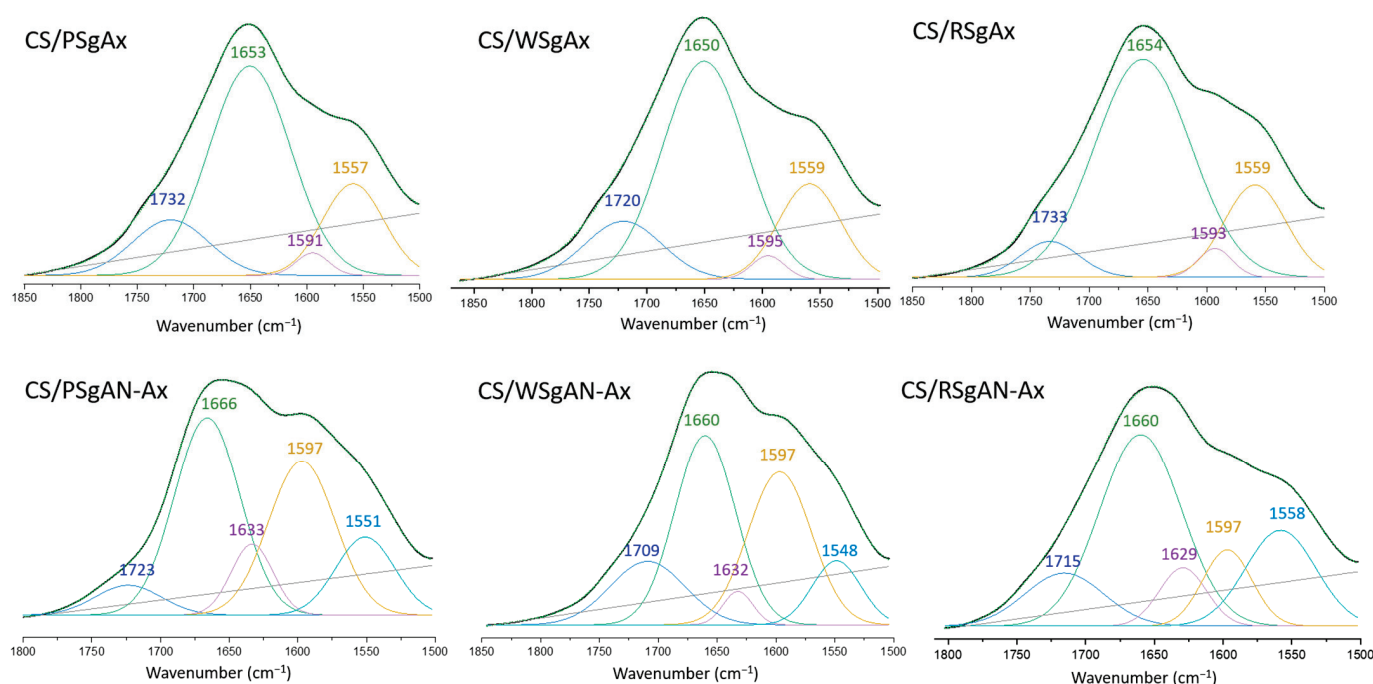
Figure 5. Deconvolution of 1800–1500 cm^{-1} region of FTIR spectra of CS/amidoximated starch beads obtained by the two procedures.

Thus, the region 1800–1500 cm^{-1} of the three spectra of the CS/SgAx samples is deconvoluted in four individual peaks, irrespective of starch nature, which can be ascribed as follows: 1733–1720 cm^{-1} to carbonyl groups C=O, resulting from the grafting reaction and anhydro glucose ring opening, 1654–1650 cm^{-1} to C=N in the oxime groups (the highest contribution), 1591–1595 cm^{-1} to -NH$_2$ groups on both CS and modified starch (with the smaller contribution) and 1557–1559 cm^{-1} to vibrations of the protonated amine group. The same region in the FTIR spectra of the composite beads obtained by the amidoximation of the already formed CS/SgAN beads (namely CS/SgAN-Ax samples) demonstrated five individual peaks, with the peak ascribed to C=N in the oxime groups being shifted to about 1660 cm^{-1} and the new peak at about 1630 cm^{-1} being ascribed to the -OH groups bending. Furthermore, for these samples, the contribution of the peak at 1660 cm^{-1} diminished and the contribution of that at about 1597 cm^{-1} increased, suggesting a higher amount of free amino groups obtained by the post bead formation amidoximation reaction groups, which are evidently not involved in the crosslinking reactions with ECH.

The modifications in the starch/CS crystallinity after hydrogel bead synthesis was followed by X-ray diffraction (Figure 6).
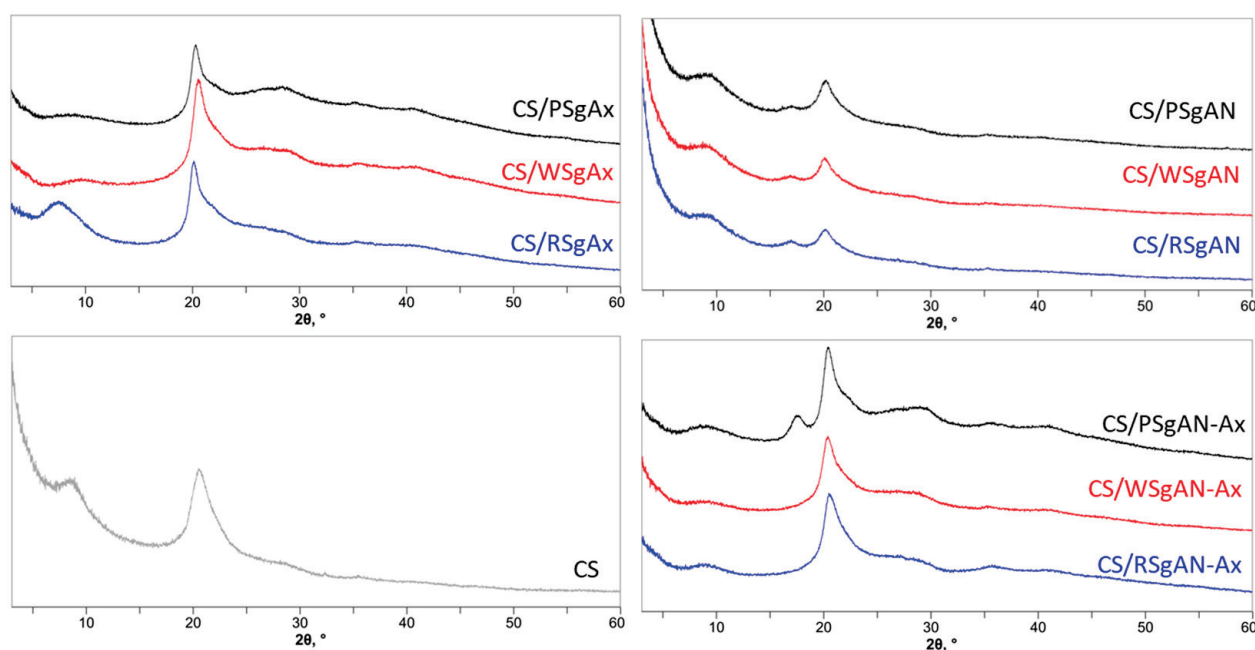
Figure 6. X-ray diffractograms of CS/SgAx, SgAN and SgAN-AX composite beads as compared to bare CS.

The chitosan sample shows diffraction peaks at about 9° and 20° (2θ), which could be found in all the samples after hydrogel bead formation, as shown in Figure 6. In addition, the diffraction peak at 17° (2θ), characteristic for grafted starch (Figure 1(bC,cC)), was observed in the CS/SgAN samples and was also found after their amidoximation for beads obtained with PSgAN. For the samples obtained with the other AN-grafted starch (RS and WS) and that with SgAx, the peak at 17° (2θ) was not observed, with the peak at about 9° being evident mainly in CS/RSgAx beads. To conclude, the X-ray diffraction analysis showed that the samples prepared by the two methods, either using SgAN and beads post amidoximation or by using SgAx, still contain the functionalized starch structures, suggesting good incorporation of functionalized starch dispersion into the beads.

2.3. Swelling Behavior of Hydrogel Beads

The swelling behavior represents an important characteristic of a sorbent in its capacity to retain different ions or small molecules. Therefore, the swelling degree was evaluated as a function of time and pH (Figure 7). As shown in Figure 7a, in distilled water with a pH of about 6, the swelling equilibrium was reached in almost five hours for all the beads, irrespective of the sort of starch or the method applied in bead synthesis. Furthermore, there were almost no differences between the swelling degree values for the beads prepared with SgAx compared to those obtained with SgAN and those amidoximated. There are small differences between the swelling of the samples prepared with different sorts of starch, which can be ascribed to the differences in the starch grain sizes (Figure 1), with the largest PS grains resulting in a larger swelling capacity, as compared to the other starch sorts. Nevertheless, the swelling is also connected to the amylose/amylopectin ratio, which is almost 20/80 in PS, 23/77 in WS and 30/70 in RS [5]. Thus, for the lower grain size of WS and RS, the larger amylose content in RS results in a larger swelling capacity compared to that of the WS-based hydrogel beads.
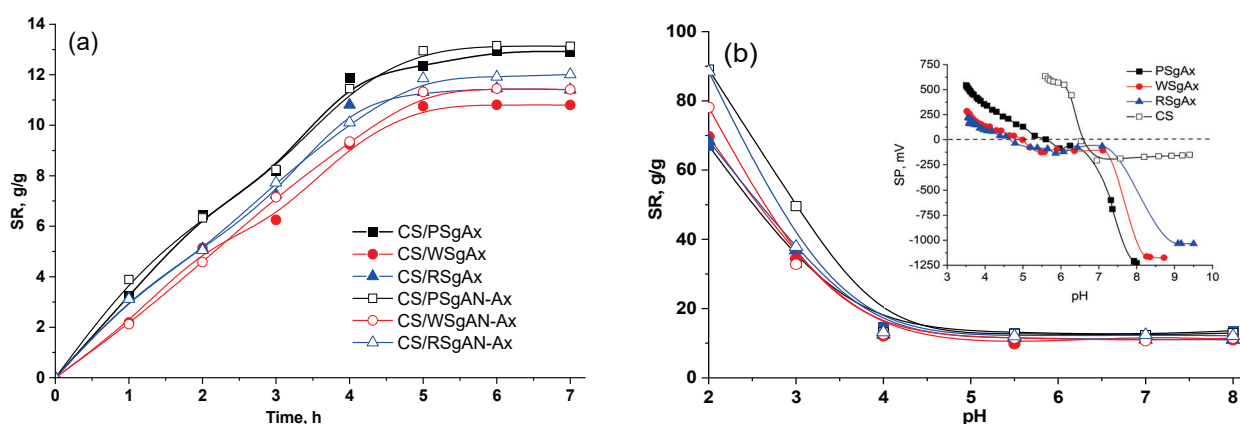
Figure 7. Swelling of the composite hydrogel beads as a function of time at pH = 6 (**a**) and different pH values (**b**); inset in (**b**) potentiometric titration curves of SgAx and CS.

Almost similar and constant values were obtained when the pH of the swelling media varied between 4 and 8 (Figure 7b), irrespective of the sort of the starch and the bead preparation procedure. As shown in the inset in Figure 7b, the point of zero charges of CS is located at a pH of about 6.5; below this pH value, in the presence of hydronium ions, the primary amino groups ($-NH_2$) of chitosan can be protonated ($-NH_3^+$). The amidoximated starches show different points of zero charges, for example, at 4.6, 5 and 5.7 for RSgAx, WSgAx and PSgAx, respectively. Before these values, the primary amino groups of amidoximated starch and CS are protonated; therefore, below pH 4, the interpolymeric electrostatic repulsions in the composite beads and also the intramolecular repulsions between the ionized groups lead to an increase in the bead size; consequently, the equilibrium swelling ratio values increase with the pH decrease (swell between 70 and 90% at pH 2). On the contrary, at pH values up to the CS isoelectric point (6.5), ionization of the -OH groups in the amidoxime functional groups occurs, which could be associated with the protonated amino groups, decreasing the beads' swelling capacity. Furthermore, the swelled beads are stable across the whole range of the tested pHs, suggesting that the crosslinking process was effective.

2.4. Sorption of Metal Ions by Hydrogel Beads

Composite hydrogel beads with amidoximated groups (CS/SgAN-Ax and CS/SgAx) were tested as supports for the uptake of Cu^{2+}, Co^{2+}, Ni^{2+} and Zn^{2+} ions from aqueous solutions, in batch experiments. The influence of contact time on the hydrogel beads' sorption capacity for metal ions is represented graphically in Figure 8, and shows that the time required to reach the equilibrium was about four hours for all the studied metal ions. For each metal ion, the hydrogel beads' sorption capacity was influenced by the nature of the starch used to obtain the beads and the manner in which the beads were obtained. Nevertheless, the best sorption capacity for the investigated ions was obtained when CS/PSgAx hydrogel beads were used, with the highest affinity to Cu^{2+}. Furthermore, with some exceptions, the beads obtained with SgAx show better sorption capacities for the investigated ions, as compared to the beads post-amidoximation, following the same trend as that found for the beads' swelling vs. time (Figure 7a). For each sorbent, the beads' affinity for the tested metal ions follows the same order, which is as follows: $Cu^{2+} > Ni^{2+} > Zn^{2+} \approx Co^{2+}$.
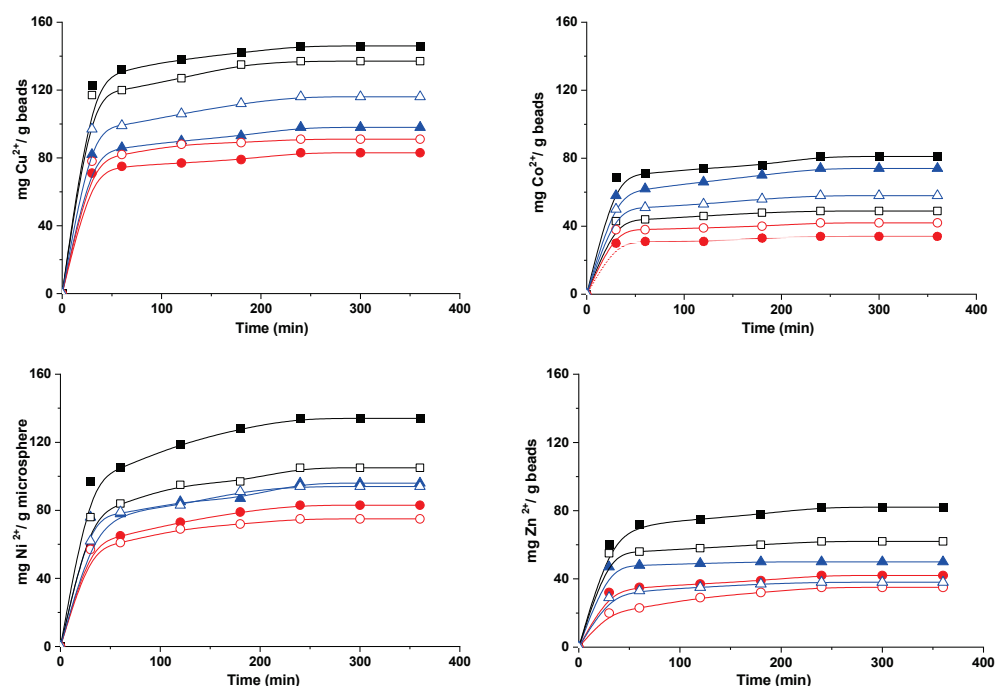
Figure 8. Sorption of Cu^{2+}, Co^{2+}, Ni^{2+} and Zn^{2+} onto composite beads based on PS (square), WS (circle) and RS (triangle) and using hydrogel beads CS/SgAx (close symbols) or CS/SgAN-Ax (open symbols).

The sorption capacity is usually influenced by the ions' properties, such as ionic radii, hydrated radius, atomic weight, electronegativity, and others, as already observed in other studies [42–45]. In this study, the ionic radius (Pauling) (Co 0.745 Å, Zn 0.74 Å, Cu 0.73 Å, and Ni 0.69 Å) and hydrated ionic radius (Zn 4.30 Å, Co 4.23 Å, Cu 4.19 Å, and Ni 4.04 Å) [46] represent the influence parameters. Furthermore, as shown in a previous study [47], the ions' coordination with nitrogen ligands is usually arranged in preferential structures, with the octahedral structure being preferred by Co^{2+} and Ni^{2+}, tetrahedral by Zn^{2+} and square planar by Cu^{2+}. Nevertheless, the found affinity for ion sorption in noncompetitive conditions towards the amidoximated starch-based beads of $Cu^{2+} > Ni^{2+} > Zn^{2+} \approx Co^{2+}$ suggests that most probably, sorption is favored by the lower ionic radius and by the structural arrangements that allow for the smallest energy consumption, with copper ions best fulfilling these conditions.

Another important parameter is the initial concentration, which herein was set to 300 mg/L and corresponds to different molar concentrations, i.e., Zn 4.587 mmol/L, Co 5.093 mmol/L, Cu 4.724 mmol/L, and Ni 5.11 mmol/L. Thus, the molar sorption capacity of the gel beads was calculated as the moles of metal ions sorbed after 360 min per moles of active sites in the hydrogel (Figure 9). Each amylose unit is grafted with a mean of three amidoxime groups and each group has three active sites (Figure 9a) and each chitosan deacetylated unit has one active site (primary amino group) to interact with the metal ions. Thus, taking into account the amount of each component used in hydrogel bead preparation (see Section 4.3) and the number of active sites of each component, the calculated amount of active sites to interact with metal ions per gram of gels was found to be 3.55 mmol/g. As shown in Figure 9b, PSgAx-based hydrogel beads have the highest sorption capacity for all the investigated ions and their higher swelling degree most probably allowed the ions to easily reach the active sites. The similar beads obtained with RS and WS followed the same trend as the swelling degree, assuming a sorption process controlled by diffusion. Nevertheless, even if CS/PSgAN-Ax beads have similar swelling capacity to that of the CS/PSgAx beads (Figure 7), their sorption capacity is lower, irrespective of the sorbed metal ion, suggesting lower active sites are available for the coordination of the metal ions. The hydrogel beads prepared with the other two sorts of starch (RS and WS) show different

behavior for each tested ion and as a function of the bead preparation procedure (using SgAx or post-amidoximated beads). Therefore, the complex sorption process as a function of the beads' features, as well as the metal ions' characteristics, should be carefully and deeper investigated.
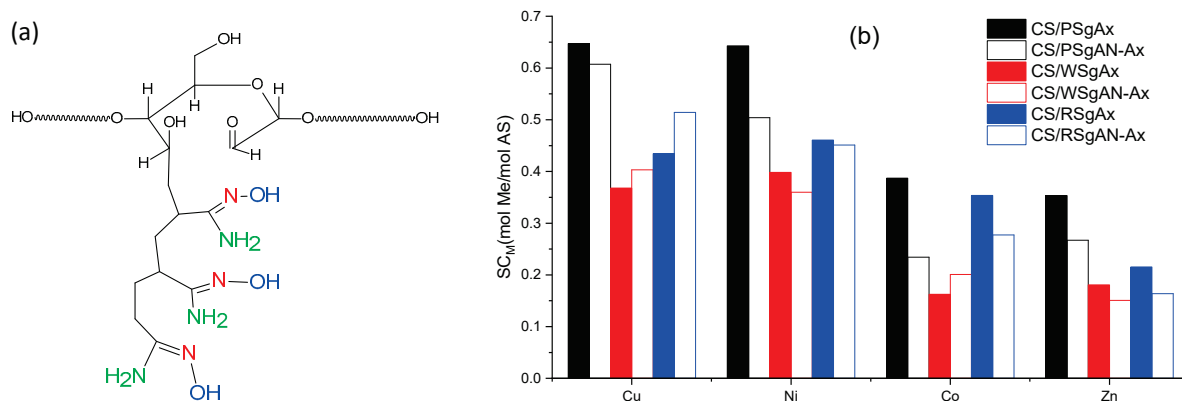
Figure 9. (**a**) Schematical representation of the three active sites (colored) of amidoxime functional group and (**b**) sorption capacity of hydrogel beads CS/SgAN-Ax or CS/SgAx expressed as moles of metal (Me)/moles of active sites (AS) in hydrogel beads.

2.5. Sorption of Dyes

Organic dyes are among the major concerns of water pollutants. Congo red (CR) and Direct Blue-15 (DB15) are organic dyes that can be easily dissolved in water, causing difficulties in their removal from contaminated water. Furthermore, they are toxic and carcinogenic, causing various diseases. Both dyes are secondary diazo dyes, with complex aromatic structures that make them non-biodegradable and quite stable. Moreover, they contain anionic sulphonic groups that can electrostatically interact with the protonated amino groups in the composite hydrogel beads. The sorption capacity of the hydrogel beads with amidoxime groups for both CR and DB15 is represented in Figure 10. The time required for dye adsorption was about six hours, as can be observed in the Figure 10, with higher values being obtained when CR was sorbed as compared to DB15. These differences are influenced by several factors, such as the origin of the starch, the bead synthesis method and the dyes' characteristics.
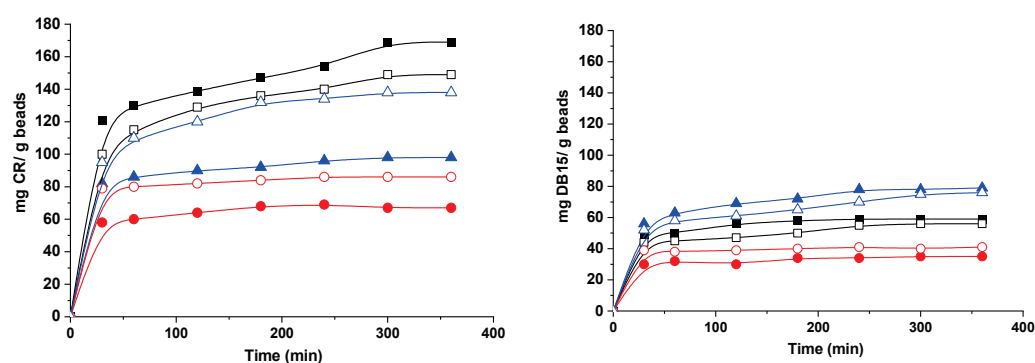
Figure 10. Sorption of dyes onto composite beads based on PS (square), WS (circle) and RS (triangle) and using CS/SgAx (close symbols) or CS/SgAN-Ax (open symbols) hydrogel beads.

Thus, PS-based hydrogel beads show the best affinity to CR, whereas for DB1, better results were obtained with RS-based hydrogel beads and lower values were found when hydrogel beads with WS functionalized starch were used, irrespective of the dye sorbed. Furthermore, better results were obtained with CS/SgAx than with CS/SgAN-Ax. This correlates with the chemical structure of the hydrogel beads and the amino groups of both CS and amidoximated starch could interact, in specific conditions, with the negatively

charged dye molecules. The influence of the presence of ionic groups on the hydrogel matrix and their interaction with ionizable groups of dyes was also observed in other studies [48] The size of the dye molecules could also influence the hydrogels' sorption capacities, with CR having the molar mass of 696.665 g/mol and DB15 of 992.80 g/mol, and is in direct relation to the hydrogel beads' porosity (Figure 3). Thus, CS/PSgAx and CS/RSgAx show higher pore sizes as compared to CS/WSgAx; therefore, the smaller CR molecules could be sorbed inside them, whereas the sorption of DB15 with larger molecules was hindered.

3. Conclusions

In this study, the features of three sorts of starch (PS, WS and RS) grafted with acrylonitrile and then amidoximated were deeply investigated, following the formation of composite hydrogel beads with CS, and tested as sorbents for four heavy metal ions (Cu^{2+}, Co^{2+}, Ni^{2+} and Zn^{2+}) and two dyes (DB15 and CR). The MD simulations show that the AN-functionalized starch behaves in a similar manner to the native one, as the main starch chains wrapped around each other and the side chains were exposed to the exterior, whereas the Ax-functionalized starch molecules remained isolated for the entire simulation. The structures obtained in the MD simulation corroborate well with the XRD result; in the case of the SgAN, the side chains located at the exterior of the wrapped arrangement and the absence of amylopectin leads to a decrease in crystallinity, whereas for SgAx, the V-type pattern of single starch molecules in a coiled conformation is found. The comparison of the C/N and C/O atomic ratios at the surface and inside the beads revealed that there are some differences in the elemental composition and that inside the beads, the atomic ratios values are smaller than outside, but are the closest to the calculated values. FTIR spectra of the CS/SgAx samples were deconvoluted in four individual peaks, irrespective of starch nature, which can be ascribed to both components' functional groups, since the CS/SgAN beads post-amidoximation shows five individual peaks. The new peak and also the variation in the others' intensity suggested a high amount of free amino groups obtained by the post bead formation amidoximation reaction, groups which are obviously not involved in any crosslinked reactions with ECH. The hydrogel beads show good sorption capacities for Cu^{2+}, Co^{2+}, Ni^{2+} and Zn^{2+} ions and for Direct Blue 15 and Congo red dyes, with their performances being influenced by the synthesis protocol and starch sort. Future studies must continue with other sorption-related experiments as a function of different parameters (pH, concentration, temperature) to elucidate the sorption mechanism for both inorganic and organic molecules.

4. Materials and Methods

4.1. Materials

CS powder, from Sigma-Aldrich, was used as received. The degree of acetylation of 15% and the average molar mass of 385 kDa were determined by the methods previously reported [49]. PS (humidity content < 10%, ash < 0.5%) and WS (humidity content < 15%, ash < 0.5%) were purchased from Fluka and were used as received. RS, epichlorohydrin (ECH), sodium hydroxide, methanol p.a., hydroxylamine chlorohydrate, metal ion salts ($CoSO_4 \cdot 7H_2O$; $NiSO_4 \cdot 6H_2O$; $ZnSO_4 \cdot 7H_2O$ and $CuSO_4 \cdot 5H_2O$), Direct Blue 15 (DB15) and Congo red (CR) were purchased from Sigma-Aldrich and were used as received. Acrylonitrile was distilled at about 77 °C and kept at a low temperature.

4.2. Starch Functionalization

The starches grafted with acrylonitrile (SgAN), obtained using potato (PSgAN), wheat (WSgAN), or rise (WSgAN) starch, were synthesized and characterized as described in [5], using $Ce(SO_4)_2$ as the initiator in H_2SO_4 0.4 M, at 27 °C, under stirring for 1 h, and then separated in methanol. The polyamidoxime-grafted starch (SgAx) samples were obtained by analogous reactions of nitrile groups of SgAN, using hydroxylamine in an alkaline medium [36]. SgAN was introduced in a two-necked flask, which was equipped with a

stirrer and condenser placed in a thermostatic water bath. Then, the hydroxylamine solution was added to the flask, and the reaction was carried out under stirring for 5 h at 70 °C, and then for 24 h at room temperature without stirring. After completion of the reaction, the SgAx was separated from the solution by filtration and washed intensively with methanol:water (80:20, *v/v*) solution. The same procedure was applied for all the types of starch. The AN average grafted length of three AN/starch structural units was determined from the ^{1}H-NMR spectra of SgAN [5] as the ratio of the integral AN characteristic peak at 3.1 ppm (ascribed to protons from CH groups) and starch characteristic peak located at 3.65 ppm (attributed to hydrogen at C2, C3 and C5 atoms).

4.3. Hydrogel Bead Synthesis

The composite beads were obtained by two similar methods that have already been published [36], using CS and amidoxime or acrylonitrile-grafted potato, wheat and rise starches, obtaining CS/SgAN and CS/SgAx beads. Shortly after, 0.5 g of SgAx or SgAN were first dispersed in 100 mL solution of CS 2% (*w/v*), and then 2 mL ECH was added as the crosslinker. The obtained mixture was dripped (through a syringe pump, ISPLab02) into an aqueous solution of sodium tripolyphosphate of 0.05 M, at room temperature, under gentle stirring (100 rpm). After 4 h, the formed beads were separated and transferred to an aqueous solution of 400 mL 0.1 M NaOH for 2 h, under slow stirring.

The beads prepared using SgAN were subjected to amidoximation by analogous reactions, obtaining CS/SgAN-Ax beads; the CS/SgAN beads and 70 mL hydroxylamine solution were introduced into a two-necked flask equipped with stirrer and condenser, and the reaction was carried out under mild stirring for 5 h at 70 °C. Finally, the prepared microspheres (obtained by both methods) were washed with distilled water at a neutral pH, and dried at 104 °C (Moisture Analyzers Precisa XM 60-HR, Precisa Gravimetrics AG, Dietikon, Switzerland).

4.4. Characterization Methods

Information on the surface morphology was evaluated using the Various G4 UC scanning electron microscope (Thermo Scientific, Brno-Černovice, Czech Republic), whereas the elemental composition with an energy dispersive X-ray spectroscopy analyzer (Octane Elect Super SDD detector, Ametek, Mahwah, NJ, USA) were analyzed by SEM. The investigations were carried out on samples sputtered with 10 nm platinum (Leica EM ACE200 Sputter, Leica, Wetzlar, Germany) in a high vacuum mode, using secondary electrons (Everhart-Thornley detector, FEI Company, Brno, Czech Republic) and concentric backscattered detectors. The samples' porosity in the swollen state was estimated by selecting 50 pores in each SEM image using ImageJ 1.48v analyzing software (LOCI, University of Wisconsin-Madison, Madison, WI, USA) [50], measuring the area, perimeter, aspect ratio and Feret diameter of each one.

Optical images were obtained with a Nikon D3300 HDSLR camera, with an AF-P DX NIKKOR 18–55 mm f/3.5–5.6 G VR lens.

FTIR analysis of the grafted samples was performed using a Bruker FT-IR spectrometer. Each spectrum was scanned in the range 400–4000 cm^{-1}, using 45 scans with a resolution of 4 cm^{-1} by the KBr pellet technique, using 2 mg of each sample. The spectra deconvolution was carried out using the Opus 4.7v software (Universität Stuttgart, Stuttgart, Germany).

The native starch, grafted starched (with AN and Ax) and CS-based composite beads were examined by X-ray diffraction by a Rigaku Miniflex 600 diffractometer (Rigaku, Tokyo, Japan), using CuKα-emissions in the angular range 3–60° (2θ), with a scanning step of 0.01° and a recording rate of 2°/min.

The diameter (circular equivalent) of native and AN and Ax-grafted starched was determined by a Morphologi G3SE particle characterization system (Malvern Instruments, Malvern, UK). The samples were carefully spread out over a glass plate. To evaluate the hydrogel beads' diameter, only full shaped particles, which were non-aggregated, were measured.

Potentiometric titrations were carried out with a particle charge detector (PCD 03, Mütek, Germany). The pH variation between 3 and 10 was achieved using 0.1 and 0.01 M solutions of NaOH and HCl, respectively. The potential measurements were carried out using 1 mg beads in 10 mL Millipore water, at room temperature.

4.5. Molecular Dynamics Simulation

Three systems containing two starch molecules solvated in water and two systems containing two starch molecules and one chitosan molecule were built using the Amber-Tools 18 software (University of California, San Francisco, CA, USA) [51]. Each starch molecule contained 26 repetitive units of linear starch (amylose), and the grafted starch had three units of acrylonitrile or amidoxime grafted to each starch monomer. The chitosan molecule had 26 chitosan monomer units with 15% acetylation. The partial atomic charges were obtained by RESP using the R.E.D.-III.5 tools software [52]. The MD simulations were performed using the GAFF2 forcefield [53] for the starch molecules, the GLYCAM forcefield for the chitosan and the TIP3P water model [54] for the solvent and ions. GROMACS 2020 [55] was used to run the simulation with a temperature set at 300 K, by using V-rescale temperature coupling with a time constant of 0.5 ps. The pressure was controlled by the Parrinello–Rahman barostat and isotropic pressure coupling, with a constant time of 2.0 ps and compressibility of 4.5×10^{-5}. Each simulation had a length of 200 ns, the composition of simulated systems being introduced in Table 3.

Table 3. Molecular dynamic composition of the simulated systems.

System	Number of Water Molecules TIP3P	Number of Starch/CS Molecules	Length of the Grafted Chain	Box Size	Simulation Time (ns)
Sg	10,914	2/-	-	$70 \times 70 \times 70$	200
SgAN	16,988	2/-	3	$85 \times 85 \times 85$	200
SgAx	16,852	2/-	3	$81 \times 81 \times 81$	200
SgAN + CS	72,345	2/1	3	$130 \times 130 \times 130$	200
SgAx + CS	72,389	2/1	3	$130 \times 130 \times 130$	200

4.6. Composite Beads' Swelling Behavior

The swelling behavior of the composite beads was studied using the conventional gravimetric procedure, by immersing the dry samples for different time intervals in Millipore water with different pHs, at 25 °C. Swollen composite hydrogel beads were weighed at predetermined intervals, after wiping the excess surface liquid using filter paper. To calculate the swelling ratio, SR, the three measurements made for each sample and the mean data were used in Equation (1).

$$SR = (W_t - W_0)/W_0, \text{g/g}, \tag{1}$$

where W_0 and W_t are the weights of the samples in the dried state and in the swollen state at time t, respectively.

4.7. Sorption Experiments

Sorption experiments were conducted using glass bottles containing 0.1 g of the sorbents and 20 mL solution of metal ions or dyes, with an initial pH of about 6, initial concentration of metal ions of 300 mg/L and initial concentration of the dye solutions of 3×10^{-5} M. The glass bottles were placed on a slow-moving platform shaker (LCD Digital Linear Shaker, SK-L330-Pro, DLAB Scientific Inc., Los Angeles, CA, USA) for 5–6 h. The concentrations of metal ions in the solution, before and after sorption, were analyzed using an atomic adsorption spectrometer (AAS) (ContrAA 800 Spectrometer Analytik Jena, Jena, Germany). The concentration of dyes, before and after sorption, was determined using a UV–Vis spectrophotometer (UV–Vis SPEKOL 1300, Analytik Jena, Jena, Germany), based on the calibration curves determined at the specific wavelength of 497 nm for CR and

597 nm for DR15. The sorption capacity (SC) of the hydrogel beads was calculated with Equations (2) and (3).

$$SC = (Cs\ V)/m, \text{mg}/\text{g} \qquad (2)$$

where Cs = sorbed concentration of ions or dyes [g/L], V = volume of the sorption solution and m = weight of used sample [g].

$$SC_M = C_{sM}/M_{AS} \qquad (3)$$

where Cs = sorbed concentration of ions after 360 min (mol Me/g hydrogel beads), and M = active sites (AS) of hydrogel beads (mol AS/g hydrogel beads).

Supplementary Materials: The following supporting information can be downloaded at: https://www.mdpi.com/article/10.3390/gels8090549/s1, Figure S1: FTIR spectra of CS/SgAN; Figure S2: FTIR spectra of CS/SgAN-Ax; Figure S3: FTIR spectra of CS/SgAx; Table S1: FTIR spectra deconvolution detailed in the region 1800–1500 cm^{-1}.

Author Contributions: Conceptualization, D.F.L. and M.M.; methodology, D.F.L., S.V. and S.R.; software, T.V.; validation, D.F.L., T.V. and M.-M.Z.; formal analysis, D.F.L. and M.M.; investigation, D.F.L., M.M.B. and M.-M.Z.; resources, D.F.L. and M.M.; data curation, D.F.L. and M.-M.Z.; writing—original draft preparation, D.F.L., M.M.B, T.V. and M.M.; writing—review and editing, M.M.; visualization, M.M.; supervision, M.M.; project administration, D.F.L. and M.M.; funding acquisition, D.F.L. and M.M. All authors have read and agreed to the published version of the manuscript.

Conflicts of Interest: The authors declare no conflict of interest.

References

1. O'Connell, D.W.; Birkinshaw, C.; O'Dwyer, T.F. Heavy metal adsorbents prepared from the modification of cellulose: A review. *Bioresour. Technol.* **2008**, *99*, 6709–6724. [CrossRef] [PubMed]
2. Wojnárovits, L.; Földváry, C.M.; Takács, E. Radiation-induced grafting of cellulose for adsoption of hazardous water pollutans: A review. *Radiat. Phys. Chem.* **2010**, *79*, 848–862. [CrossRef]
3. Abdel-Aal, S.E.; Gad, Y.H.; Dessouki, A.M. Use of rice straw and radiation-modified maize starch/acrylonitrile in the treatment of wastewater. *J. Hazard. Mater.* **2006**, *129*, 204–215. [CrossRef] [PubMed]
4. Chen, Q.; Yu, H.; Wang, L.; ul Abdin, Z.; Chen, Y.; Wang, J.; Zhou, W.; Yang, X.; Khan, R.U.; Zhang, H.; et al. Recent progress in chemical modification of starch and its applications. *RSC Adv.* **2015**, *5*, 67459–67474. [CrossRef]
5. Loghin, D.F.; Dragan, E.S.; Mihai, M. Comparative chemical modification of starches as a function of their origin: Synthesis and analysis. *Rev. Roum. Chim.* **2019**, *64*, 915–921. [CrossRef]
6. Ojogbo, E.; Ogunsona, E.O.; Mekonnen, T.H. Chemical and physical modifications of starch for renewable polymeric materials. *Mater. Today Sustain.* **2020**, *7*, 100028. [CrossRef]
7. Wang, X.; Huang, L.; Zhang, C.; Deng, Y.; Xie, P.; Liu, L.; Cheng, J. Research advances in chemical modifications of starch for hydrophobicity and its applications: A review. *Carbohydr. Polym.* **2020**, *240*, 116292. [CrossRef]
8. Ma, X.; Liu, X.; Anderson, D.P.; Chang, P.R. Modification of porous starch for the adsorption of heavy metal ions from aqueous solution. *Food Chem.* **2015**, *181*, 133–139. [CrossRef]
9. Mourya, V.K.; Inamdar, N.N. Chitosan-modifications and applications: Opportunities galore. *React. Funct. Polym.* **2008**, *68*, 1013–1051. [CrossRef]
10. Boddu, V.M.; Abburi, K.; Talbott, J.L.; Smith, E.D.; Haasch, R. Removal of arsenic (III) and arsenic (V) from aqueous medium using chitosan-coated biosorbent. *Water Res.* **2008**, *42*, 633–642. [CrossRef]
11. Cocarta, A.I.; Gutanu, V.; Dragan, E.S. Comparative sorption of Co^{2+}, Ni^{2+} and Cr^{3+} onto chitosan/poly(vinyl amine) composite beads. *Cellul. Chem. Technol.* **2019**, *49*, 775–782.
12. Brion-Roby, R.; Gagnon, J.; Nosrati, S.; Deschênes, J.-S.; Chabot, B. Adsorption and desorption of molybdenum(VI) in contaminated water using a chitosan sorbent. *J. Water Process. Eng.* **2018**, *23*, 13–19. [CrossRef]

13. Wei, S.; Ching, Y.C.; Chuah, C.H. Synthesis of chitosan aerogels as promising carriers for drug delivery: A review. *Carbohydr. Polym.* **2020**, *231*, 115744. [CrossRef]

14. Negm, N.A.; Hefni, H.H.H.; Abd-Elaal, A.A.A.; Badra, E.A.; Abou Kana, M.T.H. Advancement on modification of chitosan biopolymer and its potential applications. *Int. J. Biol. Macromol.* **2020**, *152*, 681–702. [CrossRef]

15. Ali, N.; Khan, A.; Malik, S.; Badshah, S.; Bilal, M.; Iqbal, H.M.N. Chitosan-based green sorbent material for cations removal from an aqueous environment. *J. Environ. Chem. Eng.* **2020**, *8*, 104064. [CrossRef]

16. Apopei, D.F.; Dinu, M.V.; Trochimczuk, A.W.; Dragan, E.S. Sorption isotherms of heavy metal ions onto semi-interpenetrating polymer network cryogels based on polyacrylamide and anionically modified potato starch. *Ind. Eng. Chem. Res.* **2012**, *51*, 10462–10471. [CrossRef]

17. Musarurwa, H.; Tavengwa, N.T. Application of carboxymethyl polysaccharides as bio-sorbents for the sequestration of heavy metals in aquatic environments. *Carbohydr. Polym.* **2020**, *237*, 116142. [CrossRef] [PubMed]

18. Xiang, B.; Fan, W.; Yi, X.; Wang, Z.; Gao, F.; Li, Y.; Gu, H. Dithiocarbamate-modified starch derivatives with high heavy metal adsorption performance. *Carbohydr. Polym.* **2016**, *136*, 30–37. [CrossRef] [PubMed]

19. Qi, X.; Liu, R.; Chen, M.; Li, Z.; Qin, T.; Qian, Y.; Zhao, S.; Liu, M.; Zeng, Q.; Shen, J. Removal of copper ions from water using polysaccharide-constructed hydrogels. *Carbohydr. Polym.* **2019**, *209*, 101–110. [CrossRef]

20. Kumar, R.; Sharma, R.K.; Singh, A.P. Cellulose based grafted biosorbents—Journey from lignocellulose biomass to toxic metal ions sorption applications—A review. *J. Mol. Liq.* **2017**, *232*, 62–93. [CrossRef]

21. Wang, S.; Vincent, T.; Faur, C.; Guibal, E. Modeling competitive sorption of lead and copper ions onto alginate and greenly prepared algal-based beads. *Bioresour. Technol.* **2017**, *231*, 26–35. [CrossRef] [PubMed]

22. Joly, N.; Ghemati, D.; Aliouche, D.; Martin, P. Interaction of metal ions with mono- and polysaccharides for wastewater treatment: A review. *Nat. Prod. Chem. Res.* **2020**, *8*, 373.

23. Chauhan, G.S.; Jaswal, S.C.; Verma, M. Post functionalization of carboxymethylated starch and acrylonitrile based networks through amidoximation for use as ion sorbents. *Carbohydr. Polym.* **2006**, *66*, 435–443. [CrossRef]

24. Zohuriaan-Mehr, M.J.; Pourjavadi, A.; Salehi-Rad, M. Modified CMC. 2. Novel carboxymethylcellulose-based poly(amidoxime) chelating resin with high metal sorption capacity. *React. Funct. Polym.* **2004**, *61*, 23–31. [CrossRef]

25. Anirudhan, T.S.; Divya, L.; Bringle, C.D.; Suchithra, P.S. Removal of Copper(II) and Zinc(II) from aqueous solutions using a lignocellulosic-based polymeric adsorbent containing amidoxime chelating functional groups. *Sep. Sci. Technol.* **2010**, *45*, 2383–2393. [CrossRef]

26. Liu, X.; Chen, H.; Wang, C.; Qu, R.; Ji, C.; Sun, C.; Zhang, Y. Synthesis of porous acrylonitrile/methyl acrylate copolymer beads by suspended emulsion polymerization and their adsorption properties after amidoximation. *J. Hazard. Mater.* **2010**, *175*, 1014–1021. [CrossRef]

27. Lutfor, M.R.; Silong, S.; Zin, W.M.; Ab Rahman, M.Z.; Ahmad, M.; Haron, J. Preparation and characterization of poly(amidoxime) chelating resin from polyacrylonitrile grafted sago starch. *Eur. Polym. J.* **2000**, *36*, 2105–2113. [CrossRef]

28. Masoumi, A.; Ghaemy, M. Removal of metal ions from water using nanohydrogel tragacanthgum-g-polyamidoxime: Isotherm and kinetic study. *Carbohydr. Polym.* **2014**, *108*, 206–215. [CrossRef]

29. Xu, C.; Wang, J.; Yang, T.; Chen, X.; Liu, X.; Ding, X. Adsorption of uranium by amidoximated chitosan-grafted polyacrylonitrile, using response surface methodology. *Carbohydr. Polym.* **2015**, *121*, 79–85. [CrossRef]

30. Elwakeel, K.Z.; El-Bindary, A.A.; Kouta, E.Y.; Guibal, E. Functionalization of polyacrylonitrile/Na-Y-zeolite composite with amidoxime groups for the sorption of Cu(II), Cd(II) and Pb(II) metal ions. *Chem. Eng. J.* **2018**, *332*, 727–736. [CrossRef]

31. Xu, S.; Jin, Y.; Li, R.; Shan, M.; Zhang, Y. Amidoxime modified polymers of intrinsic microporosity/alginate composite hydrogel beads for efficient adsorption of cationic dyes from aqueous solution. *J. Colloid Interface Sci.* **2022**, *607*, 890–899. [CrossRef] [PubMed]

32. Egawa, H.; Kabay, N.; Shuto, T.; Jyo, A. Recovery of uranium from seawater. XII. Preparation and characterization of lightly crosslinked highly porous chelating resins containing amidoxime groups. *J. Appl. Polym. Sci.* **1992**, *46*, 129–142. [CrossRef]

33. Kubota, H.; Shigehisa, Y. Introduction of amidoxime groups into cellulose and its ability to adsorb metal ions. *J. Appl. Polym. Sci.* **1995**, *56*, 147–151. [CrossRef]

34. Meimoun, J.; Wiatz, V.; Saint-Loup, R.; Parcq, J.; Favrelle, A.; Bonnet, F.; Zinck, P. Modification of starch by graft copolymerization. *Starch/Stärke* **2017**, *69*, 1600351. [CrossRef]

35. Rahman, M.L.; Sarjadi, M.S.; Guerin, S.; Sarkar, S.M. Poly (amidoxime) resins for efficient and eco-friendly metal extraction. *ACS Appl. Polym. Mater.* **2022**, *4*, 2216–2232. [CrossRef]

36. Dragan, E.S.; Apopei, D.F. Synthesis and swelling behavior of pH-sensitive semi-interpenetrating polymer network composite hydrogels based on native and modified potatoes starch as potential sorbent for cationic dyes. *Chem. Eng. J.* **2011**, *178*, 252–263. [CrossRef]

37. Dragan, E.S.; Loghin Apopei, D.F.; Cocarta, A.I. Efficient sorption of Cu^{2+} by composite chelating sorbents based on potato starch-graft-polyamidoxime embedded in chitosan beads. *ACS Appl. Mater. Interfaces* **2014**, *6*, 16577–16592. [CrossRef]

38. Imberty, A.; Chanzy, H.; Pérez, S.; Bulèon, A.; Tran, V. The double-helical nature of the crystalline part of A-starch. *J. Mol. Biol.* **1988**, *201*, 365–378. [CrossRef]

39. Manek, R.V.; Builders, P.F.; Kolling, W.M.; Emeje, M.; Kunle, O.O. Physicochemical and binder properties of starch obtained from Cyperus esculentus. *AAPS PharmSciTech* **2012**, *13*, 379–388. [CrossRef]

40. Kim, J.-Y.; Lim, S.-T. Preparation of nano-sized starch particles by complex formation with n-butanol. *Carbohydr. Polym.* **2009**, *76*, 110–116. [CrossRef]

41. Khatami, M.H.; Barbera, W.; De Haan, H.W. Using geometric criteria to study helix-like structures produced in molecular dynamics simulations of single amylose chains in water. *RSC Adv.* **2021**, *11*, 11992–12002. [CrossRef] [PubMed]

42. Zaharia, M.-M.; Bucatariu, F.; Doroftei, F.; Loghin, D.-F.; Vasiliu, A.-L.; Mihai, M. Multifunctional CaCO$_3$/polyelectrolyte sorbents for heavy metal ions decontamination of synthetic waters. *Colloids Surf. A Physicochem. Eng. Asp.* **2021**, *613*, 126084. [CrossRef]

43. Bucatariu, F.; Ghiorghita, C.A.; Zaharia, M.M.; Schwarz, S.; Simon, F.; Mihai, M. Removal and separation of heavy metal ions from multicomponent simulated waters using silica/polyethyleneimine composite microparticles. *ACS Appl. Mater. Interfaces* **2020**, *12*, 37585–37596. [CrossRef] [PubMed]

44. Wang, Y.; Wu, F.; Mu, Y.; Zeng, E.Y.; Meng, Y.; Zhao, X.; Giesy, J.P.; Feng, C.; Wang, P.; Liao, H.; et al. Directly Predicting water quality criteria from physicochemical properties of transition metals. *Sci. Rep.* **2016**, *6*, 22515. [CrossRef]

45. Feizi, M.; Jalali, M. Removal of heavy metals from aqueous solutions using sunflower, potato, canola and walnut shell residues. *J. Taiwan Inst. Chem. Eng.* **2015**, *54*, 125–136. [CrossRef]

46. Arshadi, M.; Amiri, M.J.; Mousavi, S. Kinetic, equilibrium and thermodynamic investigations of Ni(II), Cd(II), Cu(II) and Co(II) adsorption on barley straw ash. *Water Resour. Ind.* **2014**, *6*, 1–17. [CrossRef]

47. Rulíšek, L.; Vondrášek, J. Coordination geometries of selected transition metal ions (Co^{2+}, Ni^{2+}, Cu^{2+}, Zn^{2+}, Cd^{2+}, and Hg^{2+}) in metalloproteins. *J. Inorg. Biochem.* **1998**, *71*, 115–127. [CrossRef]

48. Chen, Z.; Song, X.; Soh, W.W.M.; Wen, Y.; Zhu, J.; Zhang, M.; Li, J. In situ synthesis of magnetic poly(DMAEAB-co-NIPAm)@Fe3O4 composite hydrogel for removal of dye from water. *Gels* **2021**, *7*, 201. [CrossRef]

49. Santos, C.; Seabra, P.; Veleirinho, B.; Delgadillo, I.; Lopes da Silva, J.A. Acetylation and molecular mass effects on barrier and mechanical properties of shortfin squid chitosan membranes. *Eur. Polym. J.* **2006**, *42*, 3277–3285. [CrossRef]

50. Rueden, C.T.; Schindelin, J.; Hiner, M.C.; DeZonia, B.E.; Walter, A.E.; Arena, E.T.; Eliceiri, K.W. ImageJ2: ImageJ for the next generation of scientific image data. *BMC Bioinform.* **2017**, *18*, 529. [CrossRef]

51. Case, D.A.; Ben-Shalom, I.Y.; Brozell, S.R.; Cerutti, D.S.; Cheatham, T.E.I.; Cruzeiro, V.W.D.; Darden, T.A.; Duke, R.E.; Ghoreishi, D.; Gilson, M.K.; et al. *AMBER 2018*; University of California: San Francisco, CA, USA, 2018.

52. Dupradeau, F.Y.; Pigache, A.; Zaffran, T.; Savineau, C.; Lelong, R.; Grivel, N.; Lelong, D.; Rosanski, W.; Cieplak, P. The R.E.D. tools: Advances in RESP and ESP charge derivation and force field library building. *Phys. Chem. Chem. Phys.* **2010**, *12*, 7821–7839. [CrossRef] [PubMed]

53. Wang, J.; Wolf, R.M.; Caldwell, J.W.; Kollman, P.A.; Case, D.A. Development and testing of a general Amber Force Field. *J. Comput. Chem.* **2004**, *25*, 1157–1174. [CrossRef] [PubMed]

54. Jorgensen, W.L.; Chandrasekhar, J.; Madura, J.D.; Impey, R.W.; Klein, M.L. Comparison of simple potential functions for simulating liquid water. *J. Chem. Phys.* **1983**, *79*, 926–935. [CrossRef]

55. Abraham, M.J.; Murtola, T.; Schulz, R.; Páll, S.; Smith, J.C.; Hess, B.; Lindahlad, E. GROMACS: High performance molecular simulations through multi-level parallelism from laptops to supercomputers. *SoftwareX* **2015**, *1*, 19–25. [CrossRef]

Photopolymerizable Ionogel with Healable Properties Based on Dioxaborolane Vitrimer Chemistry

Fengdi Li, Giao T. M. Nguyen, Cédric Vancaeyzeele [ID] **, Frédéric Vidal and Cédric Plesse** *

Laboratory of Physicochemistry of Polymers and Interfaces, CY Cergy Paris Université, 5 Mail Gay Lussac, 95000 Neuville sur Oise, France; fengdi.li@cyu.fr (F.L.); tran-minh-giao.nguyen@cyu.fr (G.T.M.N.); cedric.vancaeyzeele@cyu.fr (C.V.); frederic.vidal@cyu.fr (F.V.)
* Correspondence: cedric.plesse@cyu.fr

Abstract: Ionogels are solid polymer gel networks loaded with ionic liquid (IL) percolating throughout each other, giving rise to ionically conducting solid electrolytes. They combine the mechanical properties of polymer networks with the ionic conductivity, non-volatility, and non-flammability of ILs. In the frame of their applications in electrochemical-based flexible electronics, ionogels are usually subjected to repeated deformation, making them susceptible to damage. It appears critical to devise a simple and effective strategy to improve their durability and lifespan by imparting them with healing ability through vitrimer chemistry. In this work, we report the original in situ synthesis of polythioether (PTE)-based vitrimer ionogels using fast photopolymerization through thiol-acrylate Michael addition. PTE-based vitrimer was prepared with a constant amount of the trithiol crosslinker and varied proportions of static dithiol spacers and dynamic chain extender BDB containing dynamic exchangeable boronic ester groups. The dynamic ionogels were prepared using 50 wt% of either 1-Ethyl-3-methylimidazolium bis(trifluoromethylsulfonyl) imide or 1-Ethyl-3-methylimidazolium trifluoromethanesulfonate, both of which were selected for their high ionic conductivity. They are completely amorphous (T_g below $-30\ ^\circ C$), suggesting they can be used at low temperatures. They are stretchable with an elongation at break around 60%, soft with Young's modulus between 0.4 and 0.6 MPa, and they have high ionic conductivities for solid state electrolytes in the order of $10^{-4}\ S \cdot cm^{-1}$ at room temperature. They display dynamic properties typical of the vitrimer network, such as stress relaxation and healing, retained despite the large quantity of IL. The design concept illustrated in this work further enlarges the library of vitrimer ionogels and could potentially open a new path for the development of more sustainable, flexible electrochemical-based electronics with extended service life through repair or reprocessing.

Keywords: ionogel; vitrimer; polythioether; solid electrolyte; self-healing

1. Introduction

Ionogels belong to the general class of polymer gels, which may be regarded as solid and liquid phases that percolate throughout each other. They are termed ionically conducting membranes when the ionic liquid (IL) is loaded within a polymer gel network. Such materials are more precisely achieved by in situ polymerization of the gel network in the presence of ILs or by swelling a polymer network with ILs [1]. Ionogels combine the mechanical properties of crosslinked polymer networks with the ionic conductivity, non-volatility, and non-flammability of ILs [1–6]. The remarkable physicochemical properties of ionogels make them promising candidates for applications in flexible electronics. Our group has previously reported the synthesis of such ionogels based on polythioether (PTE) networks and ILs for use as solid electrolytes in electrochemical devices [1,4]. More precisely, these ionogels were obtained from the reaction of multifunctional thiols on diacrylate using thiol-ene Michael addition chemistry in the presence of ILs. The thiol-ene Michael addition is a reaction that involves a base- or nucleophile-catalyzed addition of a thiolate

anion to electron-deficient alkenes such as maleimides, vinyl sulfones, acrylates, and methacrylates [7]. The sole difference between base- and nucleophile-catalyzed reactions lies in the way the thiolate anion is generated. Classified as a 'click' chemistry, the thiol-ene Michael addition is rapid, highly efficient, generates no by-product, and exhibits a nearly ideal 1: 1 stoichiometric reactivity [8,9]. Owing to the stoichiometric reactivity of the thiol-ene Michael addition, a fine-tuning of the surface functionality and mechanical properties of ionogels was possible [1].

In the frame of their applications in electrochemical-based flexible electronics, ionogels are usually subjected to repeated deformation, making them susceptible to damage. Thus, it is critical to devise a simple and effective strategy to improve their durability and lifespan. Imparting ionogels with healing ability seems to be a promising approach because of their capability to repair mechanically induced damage. Hydrogen bonds, ionic bonds, and metal–ligand coordination have all been explored to develop healable ionogels [10–13]. Even though ionic and hydrogen bonds have been shown to demonstrate effective self-healing properties, these physical networks are generally vulnerable to heat, water, and other polar solvents. Another strategy to endow materials with self-healing capability is to introduce reversible covalent bonds within a chemically crosslinked network. The fabrication of dynamic reversible polymer networks has become a popular strategy, notably by introducing exchangeable chemical bonds into polymer networks, which are known as covalent adaptable networks (CANs). CANs are further divided into dissociative and associative mechanisms based on the intrinsic mechanism of the bond-exchange reaction [14]. In dissociative CANs, bonds are first broken and then reformed in response to external stimuli, such as heat or light [14–16]. Healable ionogels have been reported using dissociative bond-exchange reactions [17,18]. However, dissociative CANs allow topological rearrangements due to a sudden viscosity drop and uncrosslinking, which is a drawback in applications requiring stability toward solvents, easy shaping, and a welding process. CANs that rely on an associative bond exchange reaction are characterized by a constant crosslink density [19]. As the bond cleavage is accompanied by the simultaneous formation of a new crosslink, such systems can change their topology with no loss of connectivity, making such networks permanent and insoluble. More specifically, in 2011, the term 'vitrimers' was introduced by Leibler et al. for thermally activated associative CANs [20]. A few groups have reported vitrimer ionogels. Healable and reprocessable gelatine ionogels based on the reversible exchange of imine bonds have been designed for flexible supercapacitors [21]. Xu et al. reported polyurethane (PU) ionogels that can be readily healed at room temperature and restore their original performance owing to the dynamic boronic ester crosslinker used in the polymer network [22]. The exchange reactions between boronic ester linkages do not generally need a catalyst, initiator, or elevated temperature, and the activation energy of this exchange is relatively low. Another team also showcased healable and recyclable boronic ester-based ionogels using 1-butyl-3-methylimidazolium tetrafluoro-borate [23].

The goal of this work was to synthesize an original ionically conducting polythioether-based vitrimer based on ionogels using fast photopolymerization (Figure 1). The ionogels' mechanical properties can be fine-tuned thanks to the 1:1 stoichiometric reactivity of thiol-acrylate Michael addition. Either 1-Ethyl-3-methylimidazolium bis(trifluoromethylsulfonyl) imide (EMIM TFSI) or 1-Ethyl-3-methylimidazolium trifluoromethanesulfonate (EMIM Triflate) was chosen as ionic liquid in these ionogels due to their high ionic conductivity. While keeping the 1:1 stoichiometric ratio between thiol and acrylate groups, and the amount of the crosslinker constant, the choice of the thiol spacers is varied between dynamic dithiol-containing boronic ester spacer and non-dynamic dithiol spacer to wisely control the dynamic properties. The thermal properties, mechanical properties, and ionic conducting behavior of these ionogels were studied to highlight their wide working temperature range, good mechanical properties, and polymer electrolyte propensity. The dynamic properties of these solid-state electrolytes were examined with healing and stress relaxation experiments.

This work further enlarges the library of vitrimer ionogels and provides one simple and effective method to develop healable ionogels with satisfying ionic conductivity.
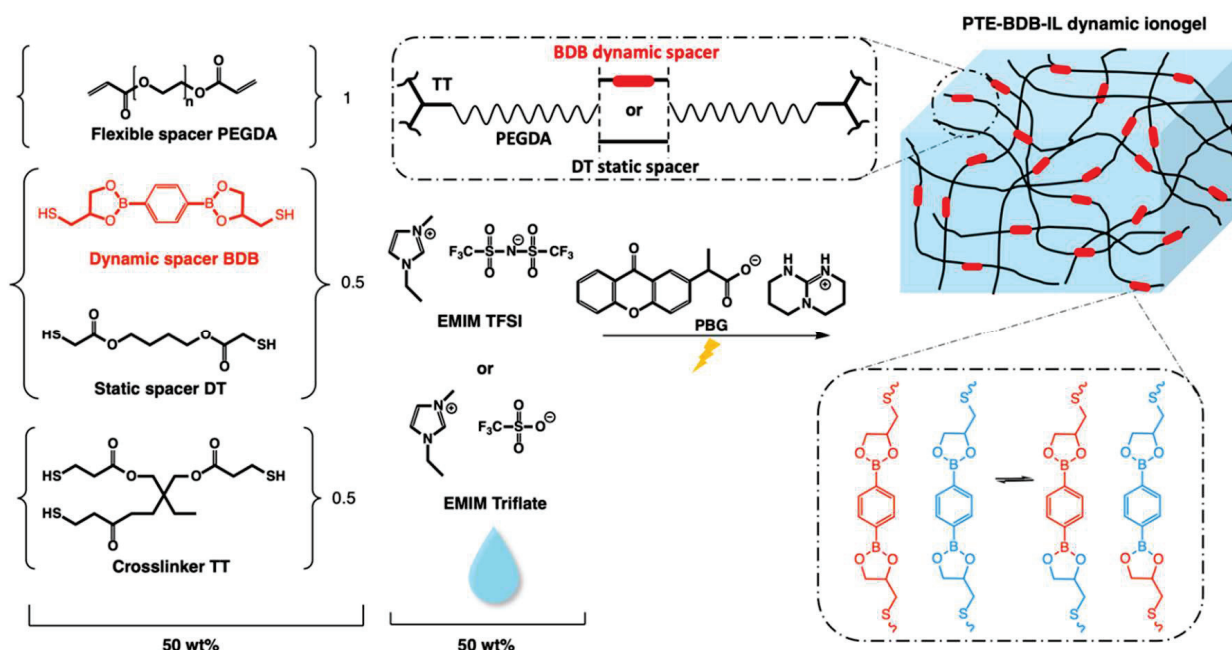
Figure 1. Chemical composition and illustration of the PTE-BDB-IL dynamic ionogels based on boronic ester exchange reaction. We used a 1:1 stoichiometric ratio of acrylate and thiols (1.0 diacrylate:0.5 dithiol:0.5 trithiol). Samples were prepared in different proportions between the flexible spacer DT and the boronic ester dynamic spacer BDB, which is capable of a fast bond exchange reaction. Fifty wt% of either EMIM TFSI or EMIM Triflate compared to the total weight is used to prepare PTE-BDB-IL dynamic ionogels.

2. Results and Discussion

We have previously reported the preparation and characterization of PTE-based ionogels using thiol-ene Michael addition between a mixture of different thiol and acrylate functional groups [1]. The resulting soft and stretchable ionogels can withstand repeated use and considerably large deformation without failure, making them potential candidates for use in the development of wearable and stretchable electronic devices. Therefore, in this study, similar compositions of ionogel were used as a starting point for the preparation of PTE-based dynamic ionogels. That is, using poly(ethylene glycol) diacrylate (PEGDA) as an electron-deficient partner, 1,4-Butanediol Bis(thioglycolate) (dithiol, DT), trimethylolpropane tris(3-mercoptopropianate) (trithiol, TT) as a thiol partner with their a functional group molar ratio of 100:50:50 in the presence of 50 wt% ionic liquid relative to the total mixture weight.

2.1. Synthesis and Characterization of PTE-BDB Dynamic Networks

In this study, we use a novel dithiol bearing boronic ester groups (2,2′-(1,4-Phenylene)-bis[4-mercaptan-1,3,2-dioxaborolane], BDB, Figure 1) to introduce exchangeable bonds into our PTE-based ionogel. This dithiol has recently been reported to be used as a dynamic crosslinker with pendant vinyl groups of styrene-butadiene rubber chains via a thermally initiated thiol-ene "click" reaction [24]. In this frame, BDB was synthesized following the protocol reported by Chen et al. [24]. Dynamic PTE-BDB networks were prepared by photopolymerization with the presence of 1 wt% of photobase generator (PBG vs the total weight of precursor mixture). While keeping the 1:1 stoichiometric ratio between thiol and acrylate groups, and the amount of trithiol crosslinker (0.5 molar ratio of thiol groups of TT), the choice of the thiol spacers (0.5 molar ratio, by reactive bonds) is varied between dynamic BDB and static DT to control the dynamic properties. Three systems

were prepared: (i) non-vitrimer system PTE-BDB0 with 50 mol% of thiols from the DT static spacer (i.e., 100% of dithiol spacers being static DT); (ii) partial vitrimer system (PTE-BDB25) with 0.25 molar ratio of BDB and 0.25 molar ratio of DT static spacer; (iii) full vitrimer system PTE-BDB50 with 50 mol% of thiols from BDB dynamic spacer (i.e., 100% of dithiol spacer being the dynamic BDB). The chemical structures of all chemicals are illustrated in Figure 1. The composition and properties of all samples are reported in Table 1.

Table 1. Compositions and characterizations of PTE-BDB networks.

Sample	Functional Groups Molar Ratio (%)				Extractable Content (wt%)	T_g (DSC) (°C)	Young's Modulus (MPa)	Elongation at Break (%)
	BDB	DT	TT	PEGDA				
PTE-BDB0	0	50	50	100	3.9	−45.8	1.2 ± 0.1	79 ± 20
PTE-BDB25	25	25	50	100	8.0	−41.0	1.5 ± 0.1	76 ± 42
PTE-BDB50	50	0	50	100	12.5	−33.3	1.3 ± 0.1	68 ± 5

Rheological studies were carried out on PTE-BDB samples (containing 0 mol%, 25 mol% or 50 mol% of dynamic spacers) by pouring the precursor mixtures into the rheometer followed by an in-situ photopolymerization at 30 °C. The storage modulus (G′) and loss modulus (G″) were recorded as a function of time (Figure 2a). The gel points, where G′ and G″ curves intersected, were reached within 30 s for the PTE-BDB25 and PTE-BDB50 samples and within 20 s for the PTE-BDB0 sample, thanks to the fast thiol-ene Michael addition. PTE-BDB25 and PTE-BDB50 samples reached a G′ plateau of about 400 kPa within 5 min, while PTE-BDB0 reached a G′ plateau of 800 kPa within 3 min. The slower polymerization kinetics indicate that the thiol functional groups of the BDB dynamic spacer are less reactive than the thiol groups of the DT static spacer. This observation is in agreement with the increased steric hindrance of the BDB chain extender, which would slow the chain transfer step of thiol-ene Michael addition [25]. The lower storage modulus could imply less efficient incorporation of the more rigid BDB crosslinker.

The soluble fractions of all samples were extracted in DCM at 60 °C under 100 bar to verify the successful formation of polymer networks. Those of the PTE-BDB25 and PTE-BDB50 samples were 8 wt% and 12.5 wt%, respectively, which were higher than that of the PTE-BDB0 sample without a dynamic spacer (3.9 wt%). BDB accounted for 8 wt% of the total weight of precursors for preparing the PTE-BDB25 sample and 15.7 wt% for the PTE-BDB50 sample. To verify that BDB was successfully incorporated into the polymer networks, extractable contents were examined by ¹H NMR. The NMR spectrum of the soluble fractions of the PTE-BDB25 and PIL-BDB50 samples can be found in Figures S2 and S3, respectively. Integrations of peaks originating from precursors were examined, and the ratios between PEGDA, BDB, DT, and TT were calculated. PTE-BDB25 and PTE-BDB50 samples were prepared using PEGDA, BDB, DT, and TT precursors with functional group ratios of 100:25:25:50 and 100:50:0:50, respectively. Therefore, in the case of stoichiometric reactivity, the theoretical ratios of PEGDA/BDB/DT/TT extracted should be 6/1.5/1.5/2 for the PTE-BDB25 sample and 6/3/0/2 for the PTE-BDB50 sample. Based on the calculation, residues of all samples after extraction were found to demonstrate ratios close to the theoretical values, even if the proportion of BDB tended to be progressively overrepresented in the extractable fraction with increasing dynamic crosslinker content (6/1.9/1.1/1.7 for PTE-BDB25 and 6/4.9/0/3 for PTE-BDB50). These results indicate that all thiol and acrylate precursors participated in the polymerization successfully but also confirm the less reactive nature of BDB.
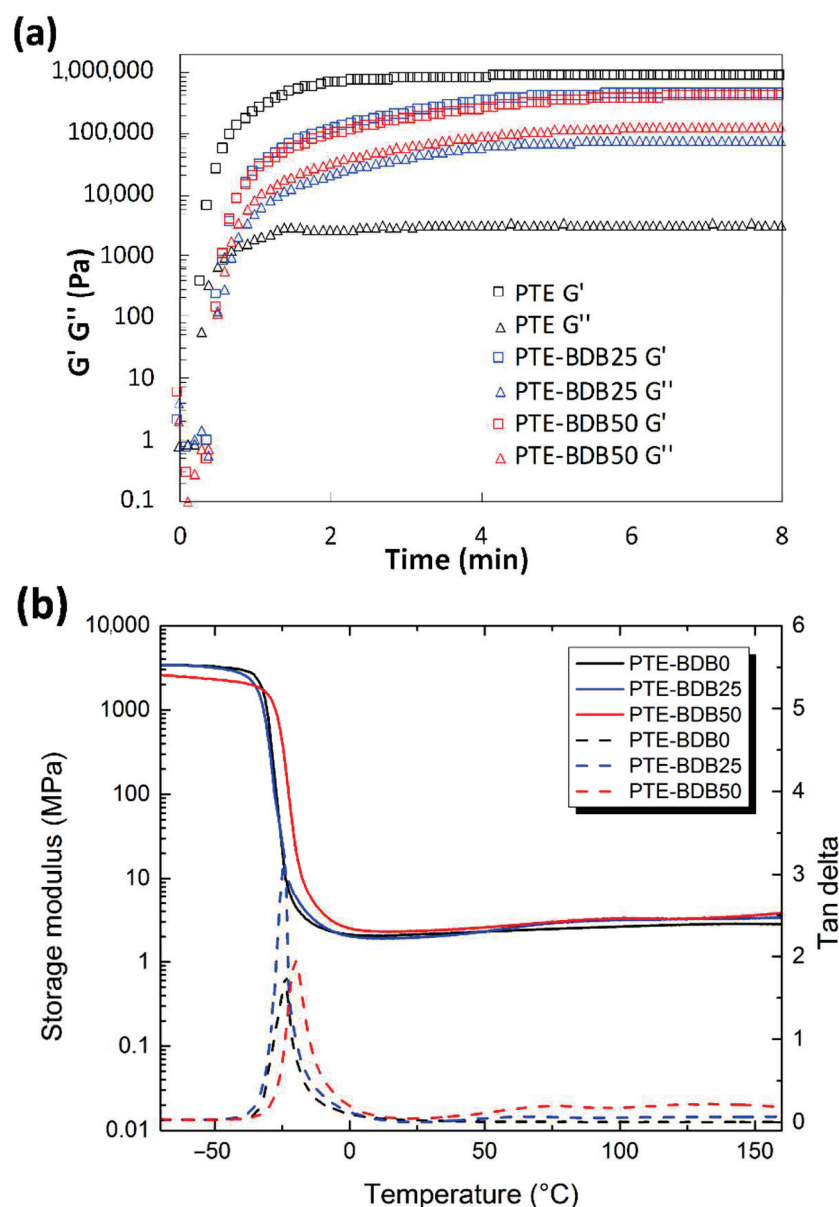
Figure 2. (**a**) Rheological studies of PTE-BDB0, PTE-BDB25, and PTE-BDB50 precursor mixtures during in-situ photopolymerization; (**b**) DMA curves of PTE-BDB series samples.

Thermal and mechanical properties: Differential scanning calorimetry (DSC), dynamic mechanical analysis (DMA), and tensile strength tests were conducted to study the thermomechanical properties of these materials and to evaluate how dynamic spacer content impacts these properties. All samples were completely amorphous, and no crystallization or melting was observed (Figure S4). Moreover, these materials demonstrate only one glass transition. The onset T_g values are listed in Table 1. There is an evident shift to higher T_g values when the aromatic BDB chain extenders replace the more flexible DT spacers, as previously reported [26,27]. The more rigid BDB moieties restrict the segmental chain mobility of the polymer networks, leading to a stronger glass propensity. Figure 2b shows the storage modulus and tan d versus temperature of all samples with different contents of BDB chain extenders. At low temperatures, the storage modulus of the glassy states of all samples was about 2 GPa, and then decreased remarkably when the samples went through an evident and narrow α relaxation. All curves exhibited only one transition, which is in line with the results obtained by DSC. The values of the relaxation temperature T_α values, which correspond to the peak of tan δ versus the temperature curve, are around -23 °C. In

addition, the storage moduli of all samples in rubbery states were similar. The influence of BDB spacer loading on the mechanical properties of polymer networks was examined using tensile strength tests (Table 1). By replacing 25 mol% of the DT spacer with the BDB spacer, Young's modulus increased from 1.2 MPa for the PTE-BDB0 sample to 1.5 MPa for the PTE-BDB25 sample. The Young's modulus then slightly decreases to 1.3 MPa for the PTE-BDB50 sample, probably due to the higher soluble fraction, which suggests that crosslinking is less advanced compared to PTE-BDB25. The resulting PTE-BDB50 network, in this case, contains more dangling chains and is therefore softer. The elongation at break values of all systems remained similar at around 70%.

Stress relaxation behavior: Owing to bond exchange reactions of vitrimers at elevated temperatures, these materials demonstrate macroscopic flow and stress relaxation enabled by reversible rearrangement of the crosslinked network, without risking permanent loss of material properties [28]. In contrast, conventional thermosets are resistant at elevated temperatures (but below the degradation temperature) to relaxation under an applied strain due to their stable crosslinked networks [29]. To study the exchange dynamics of boronic ester groups, PTE-BDB samples were subjected to stress relaxation experiments at various temperatures by monitoring the decrease in stress over time at a constant strain of 3%.

Figure 3a compares the relaxation curves of samples containing 0, 25, and 50 mol% of BDB spacers at 80 °C, where the relaxation percentage was plotted as a function of time. PTE-BDB0 sample containing no BDB dynamic spacer relaxed very few percentages of the stress before reaching a plateau, demonstrating the typical elastic response of a thermoset. Upon increasing the BDB content and decreasing the fraction of the permanent network, samples demonstrated stress relaxation behavior, with PTE-BDB25 and PTE-BDB50 relaxed about 50% and 65% of the stress, respectively, within 500 s. These results provide convincing evidence of the exchange reaction between boronic ester groups, allowing network rearrangement in the PTE-BDB samples. Figure 3b,c compare the stress relaxation behavior of the PTE-BDB25 and PTE-BDB50 samples at different temperatures, respectively. At 30 °C, PTE-BDB25 and PTE-BDB50 rapidly relaxed 5% and 30% of the stress, followed by a stress plateau. By increasing the temperature from 30 °C to 140 °C, both the relaxation rate and the eventual relaxation extent of the PTE-BDB25 and PTE-BDB50 samples increased. These results indicate that at low temperatures, the boronic ester exchange is limited and the network rearrangement is almost 'frozen'. At elevated temperatures, the exchange reaction is activated and demonstrates its temperature-dependent nature as the relaxation rate increases with temperature. At 140 °C, the stress relaxation percentages of PTE-BDB25 and PTE-BDB50 stabilized at 83% and 92%, respectively. Full stress relaxation could not be reached even after 1 h, indicating the probable presence of random non-dynamic TT-PEGDA-TT segments within the polymer networks, leading to materials demonstrating vitrimer-like behaviors [30].

Relaxation time is defined as the time required to relax to 37% (1/e) of initial stress [31]. The relaxation time of the PTE-BDB25 and PTE-BDB50 samples can be found in Table S1. PTE-BDB50 sample with a higher BDB fraction exhibits shorter relation times than the PTE-BDB25 sample at the same temperature. A faster network rearrangement is expected with an increasing number of exchangeable boronic ester linkages. Moreover, the relaxation times exhibited an Arrhenius-like temperature dependence (Figure 3d), indicating the associative exchange mechanism of the boronic ester exchange reaction [24]. Accordingly, the activation energies (E_a) were calculated to be 75.6 kJ·mol^{-1} and 49.9 kJ·mol^{-1} from the slope of the Arrhenius linear fit of PTE-BDB25 and PTE-BDB50, respectively. These values are within the range of 50–90 kJ·mol^{-1} reported in the literature, where the same dioxaborolane groups are used as dynamic chain extenders [27,32]. The more available boronic ester groups existing in the PTE-BDB50 network resulted in faster exchange kinetics and consequently lower activation energy of the viscous flow. As another characteristic key for vitrimer materials, the hypothetical topology freezing temperature (T_v) is conventionally chosen as the temperature at which the viscosity equals 10^{12} Pa.s that describes the liquid-

to-solid transition of a glass-forming liquid [14,20]. The hypothetical T_v values can be calculated from the relaxation times using the method described in the experimental section. T_v of PTE-BDB25 and PTE-BDB50 were calculated to be 11.7 °C and −31 °C, respectively (Table S1). Despite the low T_g and T_v values, as indicated by the relaxation experiments, a relaxation stress plateau was observed at 30 °C for both materials, confirming their stable topological behavior at room temperature.
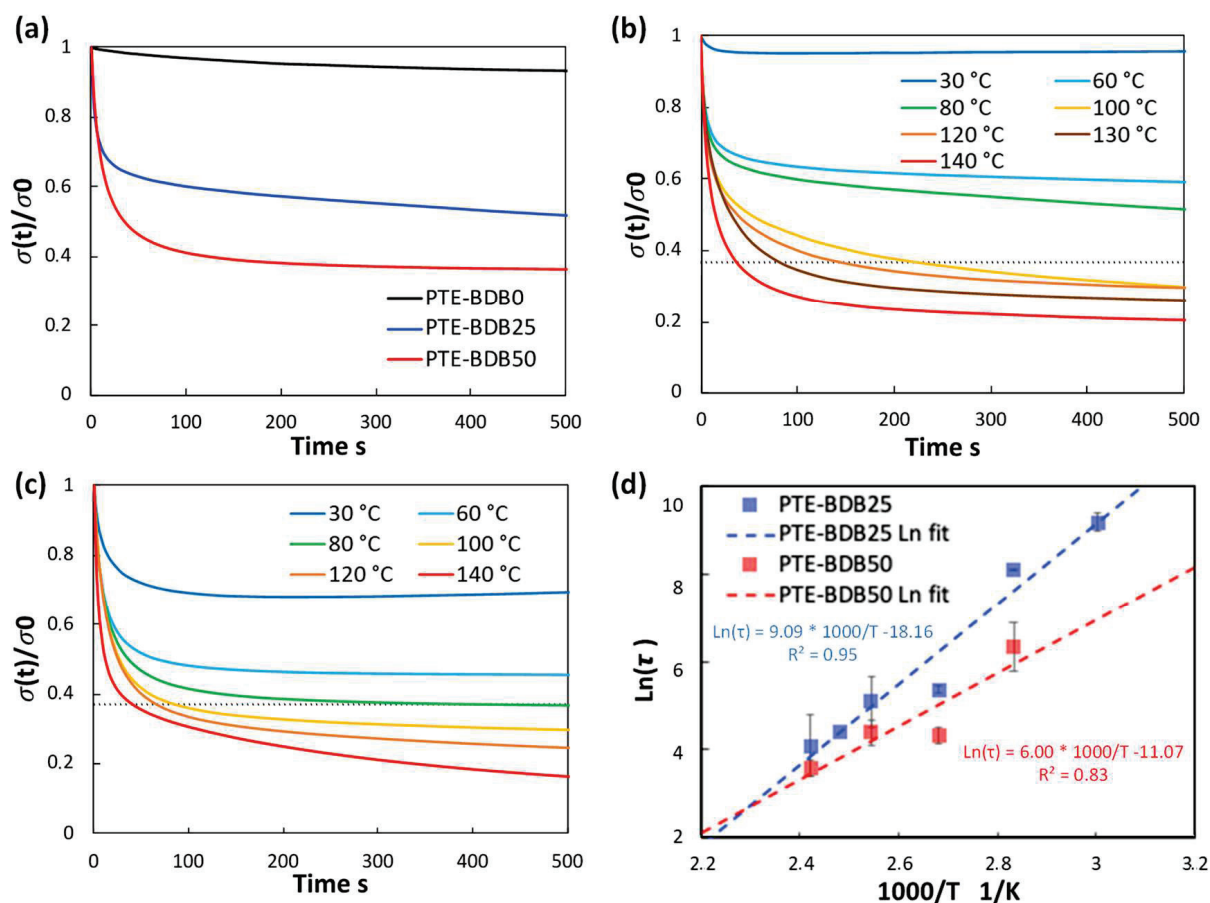
Figure 3. (**a**) Stress relaxation behaviors of PTE-BDB samples with 0, 25, and 50 mol% of BDB dynamic chain extender at 80 °C; (**b**) Stress relaxation curves of PTE-BDB25 sample at different temperatures; (**c**) Stress relaxation curves of PTE-BDB50 sample at different temperatures; (**d**) Arrhenius linear fit of relaxation times of PTE-BDB25 and PTE-BDB50 samples plotted as a function of 1000/T.

Healing behavior: Vitrimers are polymers that can change their topology through dynamic exchange reactions without degenerating the network, maintaining a constant crosslink density [14,20,33–36]. To examine the dynamic exchange of boronic ester groups, the healing abilities of PTE-BDB series samples were studied by cutting film samples into two pieces and stacking them face-to-face. The films were clipped between two glass plates at 120 °C for 2 h. Pictures of all samples before and after the healing test are shown in Figure 4. After 2 h, the two pieces of PTE-BDB0 could be easily separated, and no healing effect could be observed. In contrast, the two pieces of the PTE-BDB25 and PTE-BDB50 samples could not be separated without breaking them. However, the two film pieces were not fully fused, indicating incomplete healing, which is consistent with the incomplete stress relaxation described earlier. These results proved that boronic ester exchange is directly responsible for the healing behavior of our materials.
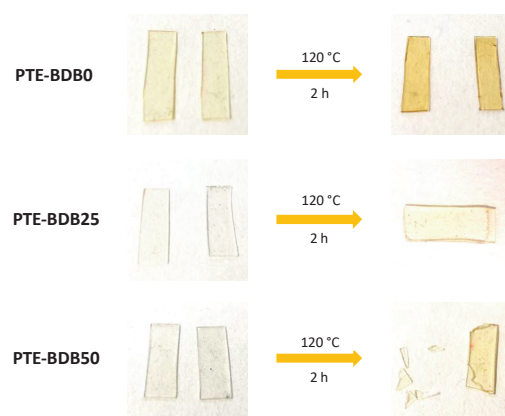
Figure 4. Healing behavior of PTE-BDB samples at 120 °C for 2 h.

2.2. Synthesis and Characterization of PTE-BDB-IL Dynamic Ionogels

PTE-BDB25 and PTE-BDB50 samples demonstrated dynamic properties such as stress relaxation and healing thanks to the network reorganization enabled by the exchange reaction of boronic ester bonds. To combine these interesting properties with ionically conducting behavior, ionic liquids were incorporated into these networks. A content of 25 mol% of BDB dynamic spacer was selected because of the higher dimensional stability of the PTE-BDB25 sample. Fifty wt% of either EMIM TFSI or EMIM Triflate was incorporated into the reagent mixture in order to achieve in situ ionogel formation. The chemical formula of the precursors and illustration of the PTE-BDB-IL dynamic ionogels based on the boronic ester exchange reaction are shown in Figure 1. Table 2 compares the compositions and properties of the PTE-BDB-IL ionogels with the PTE-BDB25 sample.

Table 2. Compositions and details of the PTE-BDB-IL samples.

Sample	IL Type	IL Content (wt%)	Extractable Content (wt%)	T_g (DSC) (°C)	T_α (DMA) (°C)	Young's Modulus (MPa)	Elongation at Break (%)
PTE-BDB25			8	−41.0	−24.2	1.2 ± 0.1	79 ± 20
PTE-BDB25-TFSI50	EMIM TFSI	50	53.8	−49.4	−28.0	0.4 ± 0.1	61 ± 4
PTE-BDB25-TfO50	EMIM Triflate	50	56.3	−51.8	−29.8	0.6 ± 0.1	52 ± 4

Soluble fractions of PTE-BDB25-TFSI50 and PTE-BDB25-TfO50 TfO50 (i.e., PTE sample containing 25 mol% of BDB and 50 wt% of EMIM Triflate) in DCM were 53.8% and 56.3% respectively. Considering that 50 wt% of ILs were used to prepare the ionogels, these results demonstrated that the polymer networks are well formed. The rheological properties of the PTE-BDB25-TFSI50 (i.e., PTE sample containing 25 mol% of BDB and 50 wt% of EMIM TFSI) and PTE-BDB25 precursor mixtures were monitored during photopolymerization and compared to the PTE-BDB25 sample (Figure 5a). As the liquid precursor solution turned into solid crosslinked ionogel when exposed under UV, the liquid-to-solid transition indicated by the cross-over of the G″ and G′ curves was attributed to the gel point [37–39]. The gel points of both samples were reached within 30 s, as in the case of the corresponding single network, demonstrating the fast polymerization kinetics of the thiol-ene Michael addition. G′ plateaus of 200 kPa for the PTE-BDB25-TFSI50 sample and 120 kPa for the PTE-BDB25-TfO50 sample were reached within 5 min. They are lower than the G′ plateau of PTE-BDB25 (400 kPa) prepared in bulk, which indicates material softening in the presence of ILs.
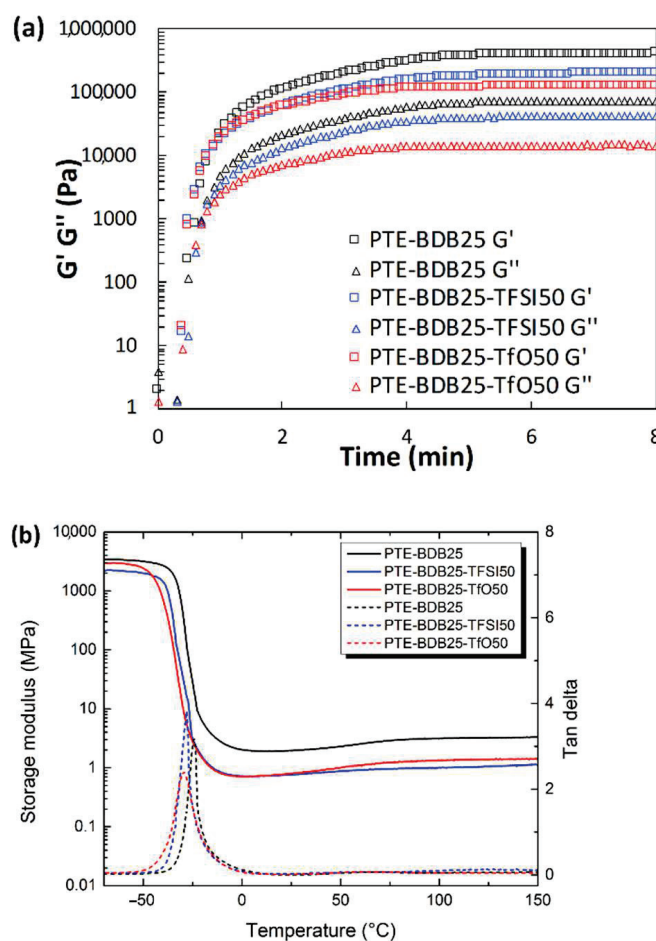
Figure 5. (**a**) Rheological studies of the PTE-BDB25-TFSI50 and PTE-BDB25-TfO50 precursor mixtures during in situ photopolymerization compared with PTE-BDB25 samples; (**b**) DMA tests of PTE-BDB-IL ionogels and PTE-BDB25 sample.

Thermal and mechanical properties of the ionogels: The thermal properties of ionogel samples were studied and compared with the PTE-BDB25 sample (Figure 5b). All samples are completely amorphous materials; no crystallization or melting could be seen in the thermograms, even at temperatures lower than the melting point of the pure ionic liquids (Figure S5). These materials displayed only one glass transition, suggesting that these ionogels can be potentially utilized at temperatures as low as −20 °C. T_g values of −49.4 °C and −51.8 °C were found for PTE-BDB25-TFSI50 and PTE-BDB25-TfO50, respectively, which were lower than that of PTE-BDB25 (−41 °C). Indeed, the plasticizing effect of ILs is responsible for the lower T_g values of ionogels. The storage modulus and tan d versus temperature of all samples are compared in Figure 5b. The addition of ILs resulted in a slightly lower storage modulus at both glassy and rubber states and lower T_{α} values. Tensile tests were conducted on the PTE-BDB25-TFSI50 and PTE-BDB25-TfO50 samples. The values of Young's modulus and elongation at break are listed in Table 2. Compared to the PTE-BDB25 sample, these ionogels demonstrated lower tensile strengths and similar stretchability to the presence of ILs.

Dynamic behavior of the ionogels: PTE-BDB-IL ionogels were also subjected to stress relaxation experiments carried out between 60 and 140 °C to study whether the addition of ILs would modify the dynamic properties enabled by the boronic ester groups of the PTE-BDB25 network. Table S2 compares the stress relaxation behaviors of the PTE-BDB25, PTE-BDB25-TFSI50, and PTE-BDB25-TfO50 samples. Stress relaxation curves of the PTE-BDB25-TFSI50 and PTE-BDB25-TfO50 at different temperatures can be found in Figure 6a,b, respectively. In both cases, the relaxation rate increases with temperature, as the relax-

ation process is essentially controlled by the thermally activated boronic ester exchange reaction, the rate of which increases with temperature. The relaxation behavior of ionogel is represented as Arrhenius-like temperature dependence in Figure 6c. As for the single networks, E_a and T_v were calculated to be 78.7 kJ·mol^{-1} and 0.3 °C for PTE-BDB25-TFSI50, 72.0 kJ·mol^{-1} and 2.0 °C for PTE-BDB25-TfO50, which were comparable to those values of PTE-BDB25 sample (75.6 kJ·mol^{-1} and 11.7 °C). The similar E_a values indicate that the ILs are spectator compounds in regard to the exchange reaction. However, the behavior of PTE-BDB25-TFSI50 seems to deviate from the expected linear behavior. This can be due to experimental error but also to the presence of TFSI$^-$ counterion susceptible to form boron-TFSI adduct responsible for a significant decrease of relaxation times, as previously reported in the presence of LiTFSI salt [40]. The T_v displayed the same 10 °C decrease as observed for the T_g. We can assume that this comes from the already mentioned IL plasticizing effect, which promotes the mobility and rearrangement of the polymer chain at low temperature.
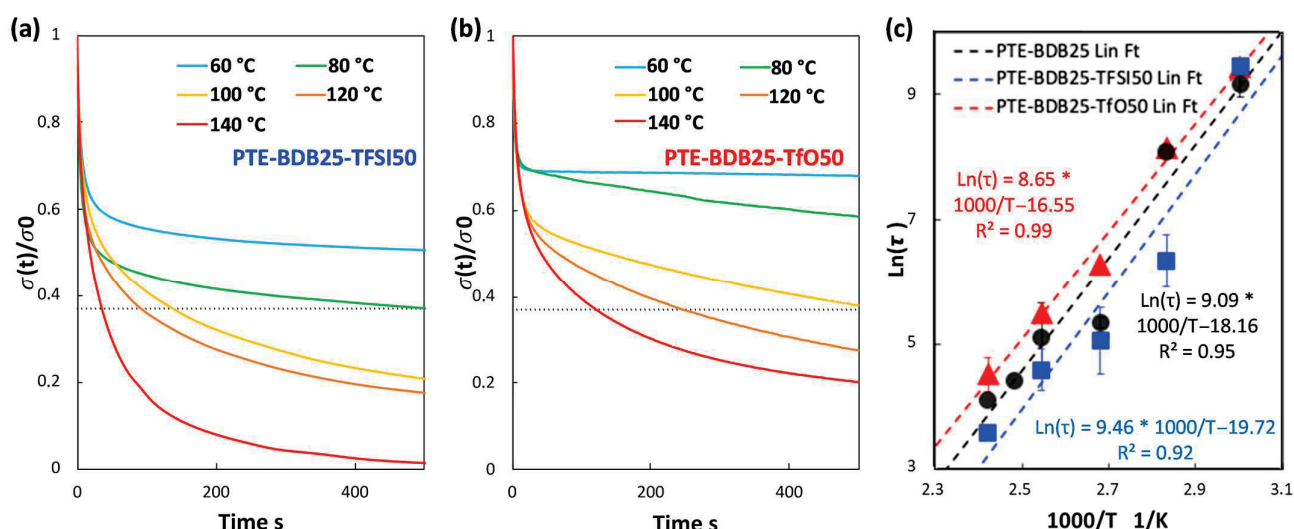
Figure 6. (**a**) Stress relaxation tests of PTE-BDB25-TFSI50 sample at various temperatures; (**b**) The stress relaxation tests of the PTE-BDB25-TfO50 sample at various temperatures; (**c**) Arrhenius linear plot extracted from relaxation times of the (■) PTE-BDB25-TFSI50, (▲) PTE-BDB25-TFSI50, and (●) PTE-BDB25 samples at different temperatures.

Ionic conducting and healing profiles of the ionogels: After demonstrating that the presence of ILs does not inhibit the boronic ester dynamic exchange. The ionic conductivity behaviors of PTE-BDB-IL ionogels at different temperatures were studied using electrochemical impedance spectroscopy (Figure 7a). At 25 °C, PTE-BDB25-TFSI50 and PTE-BDB25-TfO50 demonstrated ionic conductivities of 1.3×10^{-4} S·cm^{-1} and 1.1×10^{-4} S·cm^{-1}, respectively. Such conductivity has been proven to be satisfying for a wide range of flexible electronic applications, such as sensors and solid electrolytes [13]. By increasing the temperature, the ionic conductivities increased as the ion mobility rose, eventually reaching 1.3×10^{-3} S·cm^{-1} and 1.4×10^{-3} S·cm^{-1} at 80 °C respectively. The temperature dependence of these ionogels can be described by the Vogel–Tamman–Fulcher (VTF) equation [41–43]:

$$\sigma = AT^{-\frac{1}{2}} e^{-\frac{E_a}{R(T-T_0)}} \tag{1}$$

where A is a temperature-independent constant associated with the number of charge carriers, E_a is the pseudo-activation energy related to polymer segmental motion, and R stands for the gas constant. T_0 is a reference temperature usually correlated with the ideal glass transition temperature at which free volume disappears or at which the configurational entropy of the polymer chain reaches zero. In either scenario, T_0 is usually 35 to 50 K below T_g [44–46]. The VTF behaviors of all PTE-BDB-IL samples were investigated

with T_0 set to T_g—50 K. The values of R^2 of the VTF linear fit are above 0.99, showing that the VTF model is suitable for describing the ionic behavior of these materials and that polymer chain segmental mobility plays a role in facilitating ion conduction. The VTF of the two samples are very similar, with the parameter A found to be 5.6 S·K$^{1/2}$·cm^{-1} for the PTE-BDB25-TFSI50 sample and 5.7 S·K$^{1/2}$·cm^{-1} for the PTE-BDB25-TfO50 sample, and the E_a of ionic conduction of 8.1 kJ·mol^{-1} and 8.5 kJ·mol^{-1} respectively.
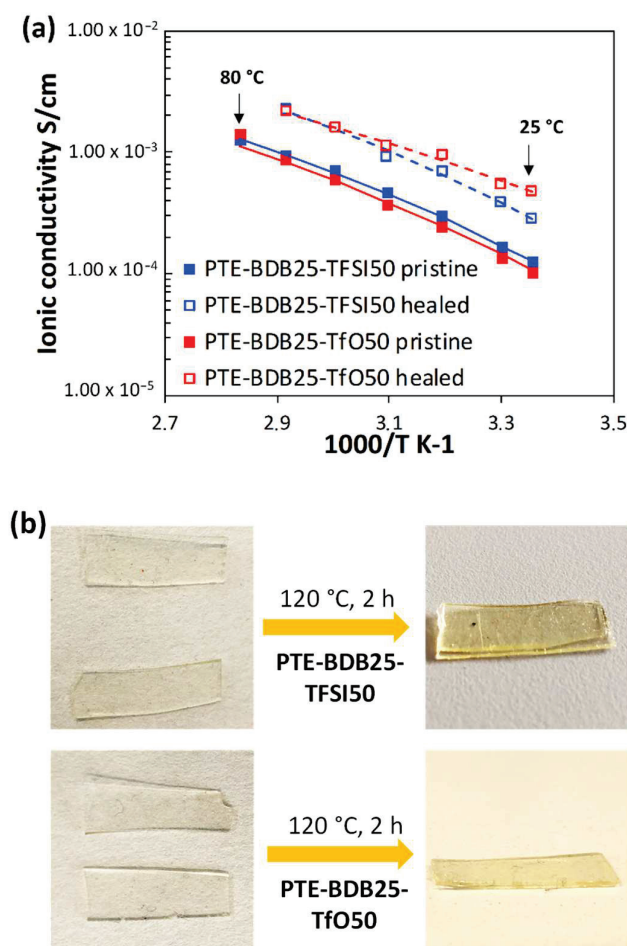
Figure 7. (**a**) Ionic conducting behaviors of PTE-BDB25-TFSI50 and PTE-BDB25-TfO50 samples at different temperatures before and after the healing test at 120 °C for 2 h; (**b**) Pictures of PTE-BDB25-TFSI50 and PTE-BDB25-TfO50 samples before and after healing.

PTE-BDB-IL ionogels are also expected to display healing properties because of the dynamic exchange of boronic ester bonds. The two IL-loaded PTE-BDB25 sample films were stacked face-to-face and subjected to a healing experiment at 120 °C for 2 h. For both samples, the two films could not be separated after 2 h, demonstrating healing behavior similar to that of the PTE-BDB25 sample (Figure 7b). To evaluate the healing efficiency of these ionogels, the cross-sections of the stacked samples were examined by scanning electron microscopy (SEM) after healing. A scar of 263 nm between the two stacked films was observed for the PTE-BDB25-TFSI50 sample (Figure 8a), while a slightly larger scar of 2.6 mm was found in the PTE-BDB25-TfO50 sample (Figure 8b). These results demonstrate the healing abilities of these ionogels thanks to the bond exchange reaction, while the remaining scars are consistent with the incomplete relaxation observed at 120 °C. Moreover, the fast relaxation rate in the presence of TFSI⁻ anions may induce a better healing efficiency than triflate anions within the same healing duration. For healable ionogels, the materials must retrieve their ionically conducting behavior after failure. Thus, ionic conductivity measurements were carried out on the samples after the healing experiment. It was found

that the healed samples demonstrated similar behaviors as pristine samples, and the ionic conductivity remained in the order of magnitude (Figure 7a). These results indicate that the topology rearrangement of the polymer electrolytes enabled by boronic ester groups allows the materials to heal and recover their original ionically conducting profile.

(a)

PTE-BDB25-TFSI50

= 263.2 nm

263 nm

4 μm

(b)

PTE-BDB25-TfO50

= 2.581 μm

2.6 μm

4 μm
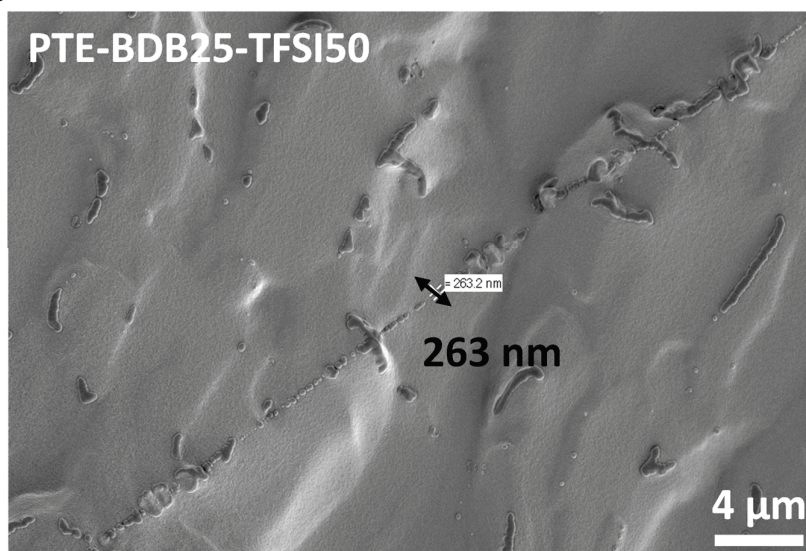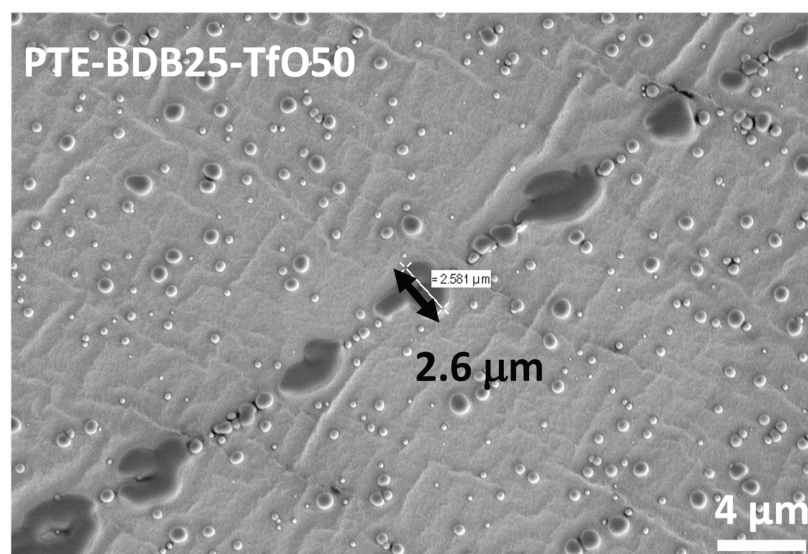
Figure 8. (**a**) SEM image of PTE-BDB25-TFSI50 healed sample cut transection; (**b**) SEM image of PTE-BDB25-TfO50 healed sample cut transection.

3. Conclusions

In this work, we demonstrated the in-situ preparation of polythioether-based vitrimer ionogels, taking advantage of the thiol-acrylate Michael addition. In the first step, to select the best polymer network of dynamic ionogels, dynamic PTE-based polymer networks were prepared by keeping the amount of trithiol crosslinker constant. The choice of the dithiol spacers varies between a dynamic chain extender BDB containing boronic ester groups (from 0 to 50 mol% of total thiol functions) and static dithiol to control the dynamic properties of these materials, with relaxation times varying with the composition of the samples from 160 min at 60 °C to 36 s at 140 °C. These PTE-BDB networks exhibited vitrimer properties, such as healing and stress relaxation, at elevated temperatures, thanks to the

boronic ester exchange reaction. In the second part, dynamic ionogels were prepared using 50 wt% of either EMIM TFSI or EMIM Triflate compared to the total weight. The resulting materials are completely amorphous (T_g around $-50\,^{\circ}$C), suggesting that these ionogels can be potentially utilized at low temperatures. These ionogels are stretchable with an elongation at break around 60%, soft with Young's modulus between 0.4 to 0.6 MPa, and demonstrated ionic conductivities in the order of 10^{-4} S·cm^{-1} at room temperature. It has been found that the dynamic properties of these materials, such as stress relaxation (with relaxation time in the same range) and healing, are retained and not significantly modified in the presence of a large quantity of IL. This work further enlarges the library of vitrimer ionogels, and we can envision an easy surface functionalization with either thiol or acrylate groups of these ionogels, thanks to the stoichiometric reactivity of thiol-acrylate Michael addition. The design concept illustrated in this work could potentially open a new path for the development of flexible electrochemical-based electronics with extended service life through repair or reprocessing.

4. Materials and Methods

4.1. Materials

The photobase generator (PBG) 2-(9-Oxoxanthen-2-yl)propionic acid 1,5,7-triazabicyclo [4.4.0]dec-5-ene salt, 1,4-Butanediol Bis(thioglycolate) (dithiol, DT), and heptane were purchased from TCI Chemicals (Zwijndrecht, Belgium). Poly(ethylene glycol) diacrylate (PEGDA, Mn = 700 g·mol^{-1}), trimethylolpropane tris(3-mercoptopropianate) (trithiol, TT), triethylamine, 1-Ethyl-3-methylimidazolium trifluoromethanesulfonate (EMIM Triflate), and 1-thioglycerol were purchased from Sigma-Aldrich (De Schnelldorf, Germany). Magnesium sulfate heptahydrate (MgSO$_4$.7H$_2$O) was obtained from Acros Organics (Geel, Belgium). Dichloromethane (DCM) was obtained from VMR Chemicals (Fontenay sous Bois, France). 1-Ethyl-3-methylimidazolium bis(trifluoromethylsulfonyl)imide (EMIM TFSI) was purchased from Solvionic (Toulouse, France). Finally, benzene-1,4-diboronic acid was purchased from Apollo Scientific (Stockport, UK).

4.2. Synthesis of 2,2′-(1,4-Phenylene)-bis[4-mercaptan-1,3,2-dioxaborolane] (BDB)

The synthesis of dithiol-containing boronic ester 2,2′-(1,4-Phenylene)-bis[4-mercaptan-1,3,2-dioxaborolane] (BDB) was reported by Chen et al. [24]. Benzene-1,4-diboronic acid (3.0 g, 18.1 mmol) and 1-thioglycerol (4.01 g, 37.1 mmol) were dissolved in tetrahydrofuran (80 mL) and water (0.1 mL). Five grams of magnesium sulfate was added to the mixture. After stirring at room temperature for 24 h, the mixture was filtered and concentrated. The resulting solid is purified by repeatedly filtering and washing with abundant heptane, and concentrated to obtain the target compound as white solids (yield 80%). The successful synthesis of BDB was explicitly confirmed by ^{1}H NMR (Figure S1). ^{1}H NMR (400 MHz, CDCl$_3$) δ 7.83 (s, 4H), 4.74 (m, 2H), 4.49 (dd, 2H), 4.18 (dd, 2H), 2.81 (dd, 4H), 1.48 (t, 2H).

4.3. Preparation of PTE-BDB Dynamic Networks

In a vial, the dithiol-containing boronic ester (BDB) is solubilized with acetone ($m_{solvent} = 0.5' m_{PEGDA}$) before introducing thiol precursors (TT and/or DT) and the acrylate precursor PEGDA. In parallel, the photobase generator PBG (1 wt% of the total weight of thiol and acrylate precursors) is dissolved in EtOH (50 mg·mL^{-1}) and then added into the vial under a light-protected condition. The mixture was poured into a mold consisting of two glass plates separated by a 0.5 mm thick Teflon spacer. Free-standing PTE-BDB films are obtained by curing the precursor solution with a UV curing conveyor system (Primarc UV Technology, Slough, UK, Minicure, Mercury vapor Lamp, UV intensity 100 W·cm^{-2}, duration of each scan 4 s). Fifty UV passages were applied for each sample. The acetone was evaporated under vacuum after synthesis at 50 $^{\circ}$C for 1 day.

4.4. Preparation of PTE-BDB-IL Dynamic Ionogels

In a vial, the dithiol-containing boronic ester (BDB) is solubilized with acetone ($m_{solvent} = 0.5'm_{PEGDA}$) before introducing thiol precursors (TT and/or DT), acrylate precursor PEGDA), and either EMIM TFSI or EMIM Triflate (50 wt% vs total weight). In parallel, the photobase generator PBG (1 wt% of the total weight of thiol and acrylate precursors) is dissolved in EtOH (50 mg·mL^{-1}) and then added into the vial under a light-protected condition. The mixture was cast into a mold consisting of two glass plates separated by a 0.5 mm thick Teflon spacer. Free-standing PTE-BDB-IL films are obtained by curing the precursor solution with a UV curing conveyor system after 50 scanning passages (Primarc UV Technology, Minicure, Mercury vapor Lamp, UV intensity 100 W·cm^{-2}, duration of each scan 4 s). The acetone was evaporated under vacuum after synthesis at 50 °C for 1 day. The resulting network was named PTE-BDBX-TFSIY or PTE-BDBX-TfOY for a PTE network containing X mol% of BDB and Y wt% of EMIM TFSI or EMIM Triflate.

4.5. Methods and Techniques

Nuclear Magnetic Resonance Spectroscopy (NMR): ^{1}H NMR spectra were recorded at 297 K on a AVANCE 400 spectrometer (Bruker, Karlsruhe, Germany) at 400 MHz and referenced to the residual solvent peaks (^{1}H, δ 7.26 ppm for CDCl$_3$).

Infrared spectroscopy (IR): Attenuated total reflection (ATR)-FT-IR spectroscopy was performed using a Tensor 27 (Bruker, Champs-sur-Marne, France) FT-IR instrument equipped with an ATR accessory unit.

Extractable content: Soxhlet experiments were performed with a BUCHI SpeedExtractor E-914 (Villebon sur Yvette, France). The extractable content was determined by 3 cycles of extraction in DCM at 60 °C under 100 bar. Each cycle lasted about 15 min.

Rheology: Rheological measurements were performed with an Anton Paar Physica MCR 301 rheometer (Graz, Austria) equipped with a CTD 450 temperature control device and a plate-plate geometry (Gap 500 μm, diameter 25 mm, plate; polymerization system made from a lower glass plate coupled with a UV lamp 142 mW·cm^{-2}). A 1% deformation was imposed at 1 Hz. The storage modulus (G′) and loss modulus (G″) were recorded as a function of time. The solution of precursors of materials was put in the rheometer geometry, and measurements began immediately with UV exposure at 30 °C.

Thermogravimetric analysis (TGA): TGA experiments were performed in air on a Q50 model (TA Instruments, New Castle, DE, USA) applying a heating rate of 10 °C·min^{-1} to 600 °C.

Differential Scanning Calorimetry (DSC): Glass transitions of the materials were determined by DSC. Sequences of temperature ramps (heating, cooling jump, heating, cooling, heating) in the −80 to 180 °C range were performed at 20 °C·min^{-1} ramping up and 5 °C·min^{-1} cooling down using a TA Instruments Q100 model (New Castle, USA) equipped with a liquid cooling accessory and calibrated using sapphire and high purity indium metal. All samples were prepared in hermetically sealed pans (5−10 mg/sample) and were referenced to an empty pan. The reported T_g values were obtained from the second heating cycle.

Tensile testing: Traction experiments were performed on a Dynamic Mechanical Analyzer instrument (TA Instruments, Q800 model, New Castle, USA) in tensile mode at room temperature. A strain rate of 20%·min^{-1} to 500% was applied with an initial strain of 0.05% and a preload force of 0.01 N to obtain stress-strain curves.

Dynamic mechanical analysis (DMA): DMA experiments were conducted on Q800 (TA Instruments, New Castle, USA) in tension mode. Heating ramps were performed from −70 °C to 200 °C at a constant rate of 3 °C·min^{-1} with a maximum strain amplitude of 0.05% at a fixed frequency of 1 Hz, and a preload force of 0.01 N.

Stress relaxation measurement: Stress relaxation measurements were carried out on the Q800 at different temperatures. A preload force of 0.01 N and a constant strain of 3% were applied, and stress decay was monitored over time.

Ionic conductivity: Ionic conductivity was measured by electrochemical impedance spectroscopy using a VSP 150 potentiostat (Biologic SA, Grenoble, France). Samples were placed between two gold electrodes and placed in a thermostated cell under an argon atmosphere. Experiments were carried out in a temperature range from 25 to 100 °C, in the frequency range from 2 MHz to 1 Hz with a rate of 6 points per decade, and for an oscillation potential of 10 mV. The ionic conductivity σ *(S·cm^{-1})* is calculated using Equation (2):

$$\sigma = \frac{1}{Z}\frac{d}{S} \tag{2}$$

where Z is the real part of the complex impedance (ohms), d the thickness of the sample (cm), and S is the sample area (cm^2).

Healing test: Sample films were first cut into two pieces and stacked together. The films were protected by Teflon films, pressured by 2 glass plates with clips, and then heated at 120 °C for 2 h in the oven.

Scanning electronic microscopy (SEM): The samples were mounted directly on SEM stubs, sputtered with 4 nm of platinum (ACE600, Leica, Wetzlar, Germany), and imaged using a Field Emission Gun Scanning Electron Microscope (GeminiSEM300, Carl Zeiss, Oberkochen, Germany) with an acceleration voltage of 2 keV under a high vacuum. Secondary electrons were collected. Scan speed and line averaging were adjusted during the observation.

Calculation of topology freezing temperature T_v and activation energy of the viscous flow E_a: Based on Maxwell's model for viscoelastic fluids, the stress relaxation behavior of the vitrimer can be described with Equation (3), where the relaxation time t is determined as the time required to relax to 37% (1/e) of the initial stress [31]:

$$\frac{\sigma_{(t)}}{\sigma_0} = e^{-\frac{t}{\tau}} \tag{3}$$

For vitrimers, relaxation times reflect associative exchange reactions, and their temperature dependence can be fitted to the Arrhenius equation (Equation (4)) [33,47] :

$$\tau(T) = \tau_0 e^{\frac{E_a}{RT}} \tag{4}$$

The values of t were then plotted as a function of temperature to determine the activation energy E_a of the associative exchange reaction. The topology freezing temperature T_v is another key characteristic of vitrimer materials. Conventionally, the hypothetical T_v is chosen as the temperature at which the viscosity equals 10^{12} Pa·s as this value describes the liquid-to-solid transition of a glass-forming liquid [14,20]. The relation between viscosity η and the characteristic relaxation time τ can be expressed with the Maxwell relation (Equation (5)) [48]:

$$\eta = G\cdot\tau = \frac{E'}{2(1+v)}\cdot\tau \tag{5}$$

where G stands for the shear modulus, v for the Poisson's ratio, and E' for the storage modulus at the rubbery plateau. Using the Poisson's ratio = 0.5 usually used for rubbers, [33,48] T_v is determined by combining Equations (4) and (5).

Supplementary Materials: The following supporting information can be downloaded at: https://www.mdpi.com/article/10.3390/gels8060381/s1. Figure S1: ^{1}H NMR of 2,2′-(1,4-Phenylene)-bis[4-mercaptan-1,3,2-dioxaborolane] (BDB) in CDCl$_3$; Figure S2: ^{1}H NMR of the extractable content of PTE-BDB25 sample in CDCl$_3$; Figure S3: ^{1}H NMR of the extractable content of PTE-BDB50 sample in CDCl$_3$.; Figure S4: DSC curves of thermal cured PTE-BDB series samples.; Figure S5: DSC curves of thermal cured PTE-BDB-IL dynamic ionogels and PTE-BDB25 sample. Table S1: Relaxation times extracted from stress relaxation tests of PTE-BDB samples and their corresponding theoretical T_v and E_a associated with the boronic ester exchange reaction.; Table S2: Relaxation times extracted

from stress relaxation tests of PTE-BDB-IL samples and their corresponding theoretical T_v and E_a associated with the boronic ester exchange reaction.

References

1. Zhong, Y.; Nguyen, G.T.M.; Plesse, C.; Vidal, F.; Jager, E.W.H. Tailorable, 3D Structured and Micro-Patternable Ionogels for Flexible and Stretchable Electrochemical Devices. *J. Mater. Chem. C* **2019**, *7*, 256–266. [CrossRef]
2. Le Bideau, J.; Viau, L.; Vioux, A. Ionogels, Ionic Liquid Based Hybrid Materials. *Chem. Soc. Rev.* **2011**, *40*, 907–925. [CrossRef] [PubMed]
3. Andrzejewska, E.; Marcinkowska, A.; Zgrzeba, A. Ionogels—Materials Containing Immobilized Ionic Liquids. *Polimery/Polymers* **2017**, *62*, 344–352. [CrossRef]
4. Zhong, Y.; Nguyen, G.T.M.; Plesse, C.; Vidal, F.; Jager, E.W.H. Highly Conductive, Photolithographically Patternable Ionogels for Flexible and Stretchable Electrochemical Devices. *ACS Appl. Mater. Interfaces* **2018**, *10*, 21601–21611. [CrossRef] [PubMed]
5. Ren, Y.; Guo, J.; Liu, Z.; Sun, Z.; Wu, Y.; Liu, L.; Yan, F. Ionic Liquid–Based Click-Ionogels. *Sci. Adv.* **2019**, *5*, eaax0648. [CrossRef]
6. Wang, S.; Zhang, D.; He, X.; Yuan, J.; Que, W.; Yang, Y.; Protsak, I.; Huang, X.; Zhang, C.; Lu, T.; et al. Polyzwitterionic Double-Network Ionogel Electrolytes for Supercapacitors with Cryogenic-Effective Stability. *Chem. Eng. J.* **2022**, *438*, 135607. [CrossRef]
7. Long, K.F.; Wang, H.; Dimos, T.T.; Bowman, C.N. Effects of Thiol Substitution on the Kinetics and Efficiency of Thiol-Michael Reactions and Polymerizations. *Macromolecules* **2021**, *54*, 3093–3100. [CrossRef]
8. Hoyle, C.E.; Bowman, C.N. Thiol-Ene Click Chemistry. *Angew. Chem. Int. Ed.* **2010**, *49*, 1540–1573. [CrossRef]
9. Moon, N.G.; Mondschein, R.J.; Long, T.E. Poly(β-Thioesters) Containing Monodisperse Oxamide Hard Segments Using a Chemoselective Thiol-Michael Addition Reaction. *Polym. Chem.* **2017**, *8*, 2598–2608. [CrossRef]
10. Xiang, S.; Zheng, F.; Chen, S.; Lu, Q. Self-Healable, Recyclable, and Ultrastrong Adhesive Ionogel for Multifunctional Strain Sensor. *ACS Appl. Mater. Interfaces* **2021**, *13*, 20653–20661. [CrossRef]
11. Weng, D.; Xu, F.; Li, X.; Li, S.; Li, Y.; Sun, J. Polymeric Complex-Based Transparent and Healable Ionogels with High Mechanical Strength and Ionic Conductivity as Reliable Strain Sensors. *ACS Appl. Mater. Interfaces* **2020**, *12*, 57477–57485. [CrossRef] [PubMed]
12. Shi, Y.; Wang, Y.; Gu, Y.; Zheng, L.; Ma, S.; Xu, X. Self-Healable and Stretchable Ionogels Serve as Electrolytes and Substrates for Integrated All-in-One Micro-Supercapacitors. *Chem. Eng. J.* **2020**, *392*, 123645. [CrossRef]
13. Qu, X.; Niu, W.; Wang, R.; Li, Z.; Guo, Y.; Liu, X.; Sun, J. Solid-State and Liquid-Free Elastomeric Ionic Conductors with Autonomous Self-Healing Ability. *Mater. Horiz.* **2020**, *7*, 2994–3004. [CrossRef]
14. Denissen, W.; Winne, J.M.; Du Prez, F.E. Vitrimers: Permanent Organic Networks with Glass-like Fluidity. *Chem. Sci.* **2016**, *7*, 30–38. [CrossRef]
15. Wemyss, A.M.; Bowen, C.; Plesse, C.; Vancaeyzeele, C.; Nguyen, G.T.M.; Vidal, F.; Wan, C. Dynamic Crosslinked Rubbers for a Green Future: A Material Perspective. *Mater. Sci. Eng. R Rep.* **2020**, *141*, 100561. [CrossRef]
16. Van Zee, N.J.; Nicolaÿ, R. Vitrimers: Permanently Crosslinked Polymers with Dynamic Network Topology. *Prog. Polym. Sci.* **2020**, *104*, 101233. [CrossRef]
17. Tang, Z.; Lyu, X.; Xiao, A.; Shen, Z.; Fan, X. High-Performance Double-Network Ion Gels with Fast Thermal Healing Capability via Dynamic Covalent Bonds. *Chem. Mater.* **2018**, *30*, 7752–7759. [CrossRef]
18. Li, T.; Wang, Y.; Li, S.; Liu, X.; Sun, J. Mechanically Robust, Elastic, and Healable Ionogels for Highly Sensitive Ultra-Durable Ionic Skins. *Adv. Mater.* **2020**, *32*, 2002706. [CrossRef]
19. Winne, J.M.; Leibler, L.; Du Prez, F.E. Dynamic Covalent Chemistry in Polymer Networks: A Mechanistic Perspective. *Polym. Chem.* **2019**, *10*, 6091–6108. [CrossRef]
20. Montarnal, D.; Capelot, M.; Tournilhac, F.; Leibler, L. Silica-Like Malleable Materials from Permanent Organic Networks. *Science* **2011**, *334*, 965–968. [CrossRef]

21. Liu, J.; Song, H.; Wang, Z.; Zhang, J.; Zhang, J.; Ba, X. Stretchable, Self-Healable, and Reprocessable Chemical Cross-Linked Ionogels Electrolytes Based on Gelatin for Flexible Supercapacitors. *J. Mater. Sci.* **2020**, *55*, 3991–4004. [CrossRef]

22. Xu, J.; Wang, H.; Du, X.; Cheng, X.; Du, Z.; Wang, H. Self-Healing, Anti-Freezing and Highly Stretchable Polyurethane Ionogel as Ionic Skin for Wireless Strain Sensing. *Chem. Eng. J.* **2021**, *426*, 130724. [CrossRef]

23. Tang, J.; Yang, J.; Yang, H.; Miao, R.; Wen, R.; Liu, K.; Peng, J.; Fang, Y. Boronic Ester-Based Dynamic Covalent Ionic Liquid Gels for Self-Healable, Recyclable and Malleable Optical Devices. *J. Mater. Chem. C* **2018**, *6*, 12493–12497. [CrossRef]

24. Chen, Y.; Tang, Z.; Zhang, X.; Liu, Y.; Wu, S.; Guo, B. Covalently Cross-Linked Elastomers with Self-Healing and Malleable Abilities Enabled by Boronic Ester Bonds. *ACS Appl. Mater. Interfaces* **2018**, *10*, 24224–24231. [CrossRef] [PubMed]

25. Huang, S.; Kim, K.; Musgrave, G.M.; Sharp, M.; Sinha, J.; Stansbury, J.W.; Musgrave, C.B.; Bowman, C.N. Determining Michael Acceptor Reactivity from Kinetic, Mechanistic, and Computational Analysis for the Base-Catalyzed Thiol-Michael Reaction. *Polym. Chem.* **2021**, *12*, 3619–3628. [CrossRef]

26. Meng, F.; Saed, M.O.; Terentjev, E.M. Elasticity and Relaxation in Full and Partial Vitrimer Networks. *Macromolecules* **2019**, *52*, 7423–7429. [CrossRef]

27. Wang, S.; Xue, L.L.; Zhou, X.Z.; Cui, J.X. "Solid-Liquid" Vitrimers Based on Dynamic Boronic Ester Networks. *Chin. J. Polym. Sci.* **2021**, *39*, 1292–1298. [CrossRef]

28. Chen, M.; Zhou, L.; Wu, Y.; Zhao, X.; Zhang, Y. Rapid Stress Relaxation and Moderate Temperature of Malleability Enabled by the Synergy of Disulfide Metathesis and Carboxylate Transesterification in Epoxy Vitrimers. *ACS Macro Lett.* **2019**, *8*, 255–260. [CrossRef]

29. Han, J.; Liu, T.; Hao, C.; Zhang, S.; Guo, B.; Zhang, J. A Catalyst-Free Epoxy Vitrimer System Based on Multifunctional Hyperbranched Polymer. *Macromolecules* **2018**, *51*, 6789–6799. [CrossRef]

30. Kaiser, S.; Jandl, J.; Novak, P.; Schlögl, S. Design and Characterisation of Vitrimer-like Elastomeric Composites from HXNBR Rubber. *Soft Matter* **2020**, *16*, 8577–8590. [CrossRef]

31. Wright, T.; Tomkovic, T.; Hatzikiriakos, S.G.; Wolf, M.O. Photoactivated Healable Vitrimeric Copolymers. *Macromolecules* **2019**, *52*, 36–42. [CrossRef]

32. Lei, Y.; Zhang, A.; Lin, Y. Reprocessability of Dynamic Polydioxaborolane Networks Activated by Heat, Moisture and Mechanical Force. *Polymer* **2020**, *209*, 123037. [CrossRef]

33. Denissen, W.; Rivero, G.; Nicolaÿ, R.; Leibler, L.; Winne, J.M.; Du Prez, F.E. Vinylogous Urethane Vitrimers. *Adv. Funct. Mater.* **2015**, *25*, 2451–2457. [CrossRef]

34. Röttger, M.; Domenech, T.; Van Der Weegen, R.; Breuillac, A.; Nicolaÿ, R.; Leibler, L. High-Performance Vitrimers from Commodity Thermoplastics through Dioxaborolane Metathesis. *Science* **2017**, *356*, 62–65. [CrossRef]

35. Breuillac, A.; Kassalias, A.; Nicolaÿ, R. Polybutadiene Vitrimers Based on Dioxaborolane Chemistry and Dual Networks with Static and Dynamic Cross-Links. *Macromolecules* **2019**, *52*, 7102–7113. [CrossRef]

36. Fortman, D.J.; Brutman, J.P.; De Hoe, G.X.; Snyder, R.L.; Dichtel, W.R.; Hillmyer, M.A. Approaches to Sustainable and Continually Recyclable Cross-Linked Polymers. *ACS Sustain. Chem. Eng.* **2018**, *6*, 11145–11159. [CrossRef]

37. Ishida, H.; Allen, D.J. Gelation Behavior of Near-Zero Shrinkage Polybenzoxazines. *J. Appl. Polym. Sci.* **2001**, *79*, 406–417. [CrossRef]

38. Puchot, L.; Verge, P.; Fouquet, T.; Vancaeyzeele, C.; Vidal, F.; Habibi, Y. Breaking the Symmetry of Dibenzoxazines: A Paradigm to Tailor the Design of Bio-Based Thermosets. *Green Chem.* **2016**, *18*, 3346–3353. [CrossRef]

39. Bidault, L.; Deneufchatel, M.; Vancaeyzeele, C.; Fichet, O.; Larreta-Garde, V. Self-Supported Fibrin-Polyvinyl Alcohol Interpenetrating Polymer Networks: An Easily Handled and Rehydratable Biomaterial. *Biomacromolecules* **2013**, *14*, 3870–3879. [CrossRef]

40. Jing, B.B.; Evans, C.M. Catalyst-Free Dynamic Networks for Recyclable, Self-Healing Solid Polymer Electrolytes. *J. Am. Chem. Soc.* **2019**, *141*, 18932–18937. [CrossRef]

41. Vogel, D.H. Das Temperaturabhaengigkeitsgesetz Der Viskositaet von Fluessigkeiten. *Phys. Zeitschrift* **1921**, *22*, 645.

42. Fulcher, G.S. Analysis of Recent Measurements of the Viscosity of Glasses—Ii1. *J. Am. Ceram. Soc.* **1925**, *8*, 789–794. [CrossRef]

43. Tammann, G.; Hesse, W. Die Abhängigkeit Der Viscosistat von Der Temperatur Bei Unterkühlten Flüssigkeiten'. *Allg. Chem.* **1926**, *156*, 245–257. [CrossRef]

44. Adam, G.; Gibbs, J.H. On the Temperature Dependence of Cooperative Relaxation Properties in Glass-Forming Liquids. *J. Chem. Phys.* **1965**, *43*, 139–146. [CrossRef]

45. Angell, C.A. Fast Ion Motion in Glassy and Amorphous Materials. *Solid State Ion.* **1983**, *10*, 3–16. [CrossRef]

46. Wintersgill, M.C.; Fontanella, J.J. *Polymer Electrolyte Reviews*; MacCallum, J.R., Vincent, C.A., Eds.; Elsevier: London, UK; New York, NY, USA, 1989; Volume 2, ISBN 9780333227794.

47. Yang, Y.; Zhang, S.; Zhang, X.; Gao, L.; Wei, Y.; Ji, Y. Detecting Topology Freezing Transition Temperature of Vitrimers by AIE Luminogens. *Nat. Commun.* **2019**, *10*, 1–8. [CrossRef] [PubMed]

48. He, C.; Shi, S.; Wang, D.; Helms, B.A.; Russell, T.P. Poly(Oxime-Ester) Vitrimers with Catalyst-Free Bond Exchange. *J. Am. Chem. Soc.* **2019**, *141*, 13753–13757. [CrossRef]

Hybrid Epoxy-Alkyl Sol–Gel Coatings Reinforced with SiO$_2$ Nanoparticles for Corrosion Protection of Anodized AZ31B Mg Alloy

Emilia Merino [1,*], Alicia Durán [1], Silvia Ceré [2] and Yolanda Castro [1,*]

[1] Instituto de Cerámica y Vidrio (CSIC), Campus de Cantoblanco, 28049 Madrid, Spain; aduran@icv.csic.es
[2] Institute of Materials Science and Technology (INTEMA), University of Mar del Plata and National Research Council (CONICET), Av. Colón 10850, Mar del Plata 7600, Argentina; smcere@fi.mdp.edu.ar
* Correspondence: ecmerino@icv.csic.es (E.M.); castro@icv.csic.es (Y.C.)

Abstract: AZ31B Mg alloys were anodized at different potentials using an alkaline electrolyte. Then, an epoxy-alkyl silane sol reinforced with SiO$_2$ nanoparticles was prepared by sol–gel and deposited on top of the optimized anodic layers. 1-Methyl imidazole was added to the sol to promote a partial epoxy ring aperture and improve the condensation degree of the inorganic network. The results showed the curing temperature affects the inorganic polycondensation of the organic-inorganic network; this effect was analyzed by ^{29}Si and ^{13}C solid-state NMR spectroscopy. Electrochemical impedance spectroscopy in 3.5 wt% NaCl solution revealed that the corrosion resistance is enhanced by the anodized process obtained for Mg alloy anodized at 100 V/2 min. However, a quick deterioration of the oxide film with immersion time was evident, showing a reduction of the protection efficiency (ηE%) of 76.5% after 16 h/immersion. The deposition of an epoxy-alkyl coating improved the ηE% up to 98.6% after 72 h/immersion. The proposed hybrid coating used for post-sealing the porous anodized Mg alloy looks like a good alternative protective barrier to control the corrosion process of Mg alloys. A suitable compromise between cross-linking network and curing temperature is necessary to obtain a good barrier coating.

Keywords: magnesium alloy; anodizing process; sol–gel; corrosion performance; hybrid inorganic-organic sol–gel coating

1. Introduction

Magnesium and its alloys have become a hot research topic due to their excellent mechanical and physical properties such as low density, easy recyclability, and lightweight properties making them attractive for different industries (aerospace sectors, automotive and biomedical) [1]; especially for those industries where using lightweight metals on their products is indispensable to decrease their overall energy consumption [2]. Nevertheless, the wider applicability of Mg alloys has been limited by their high corrosion susceptibility [3].

Currently, various surface modification techniques are under study to improve the corrosion resistance property of light alloys [4,5]. Among these surface techniques, the electrochemical anodization process and sol–gel technique are considered and accepted as the most popular industrial processes, since they can provide relatively thick, hard, adherent, and corrosion abrasion-resistant oxide films [6]. A variety of commercial anodized coatings (Anomag, Keronite, Tagnite, HAE, Magoxid, Dow 17) have been considered to protect magnesium alloys against corrosion [7–9]. Dow 17 and HAE are reported as the most successful ones, but both employ electrolytes composed of toxic chromate and/or harmful fluorides [10].

To reduce the environmental impact and the health hazards concerned in handling fluoride/chromate-based baths, researchers have focused on seeking environmentally

friendly solutions. Mizutani et al. [11] studied the anodization of pure Mg, AZ91, and AZ31 at various voltages (3, 10, and 80 V) in 1 mol L^{-1} NaOH and tested their corrosion resistance in the 0.1 wt% NaCl solution. They concluded that the films anodized at the lowest potential, mainly composed of magnesium hydroxide, showed the most effective anti-corrosion properties. This finding differs from Salman et al. [12], who reported that the film anodized at high voltage (100 V), mainly composed of Mg oxide, exhibited the most effective corrosion resistance properties. Since the results appearing in the literature show such contradictions, it was necessary to better understand the different phenomena acting in the anodizing processes at different working voltages as well as the corrosion mechanisms acting in the anodized coatings to establish the suitable conditions.

Although this approach is convenient to improve the corrosion resistance, current works show that a coating alone does not completely prevent the corrosion of Mg alloys [13,14]. In this sense, the combination of different deposition techniques could be the most effective method to mitigate corrosion damage. In our work, the use of the sol–gel technique as a post-treatment process was considered and studied to obtain a combined coating system. The most remarkable advantage of this technique is the opportunity to obtain organic–inorganic hybrid sol–gel coatings with desirable cross-linking structures and corrosion protection properties [15]. The properties of hybrid films are associated with their composition and density, which can be modified through the inclusion of a variety of organo-functional groups in the silane network [16]. Some authors have proposed the use of silanes precursors such as tetraethyl orthosilicate (TEOS), 3-glycidoxypropyltrimethoxysilane (GPTMS), and methyltriethoxysilane (MTES) to achieve good passive corrosion protection, avoiding the penetration of corrosive agents. For example, Guo et al. [17] used a TEOS, GPTMS, and triethylenetetramine (TETA) based sol–gel coating to improve the protection properties of the anodized layer on Mg AZ31B. Although the electrochemical response showed a rise in the corrosion resistance, the tests were performed in a non-aggressive environment (0.005 M of NaCl). On the other hand, Malayoglu et al. [18] observed an improvement in the corrosion performance for anodized AM60 and AM50 B Mg alloys post-sealing with a silica sol–gel film by using TEOS and MTES. In this case, MTES was added to provide a hydrophobic effect, associated with the -CH_3 functionality group.

Our recent work has proposed an alternative pathway to achieve an interconnected structure film using GPTMS, colloidal SiO_2 nanoparticles, TEOS, and 1-methyl imidazole [19]. The 1-methyl imidazole acts on the epoxy group, opening the ring and generating a highly crosslinking hybrid network, that can block the intrusion of the corrosive electrolyte and enhance the corrosion resistance performance of AZ31B Mg alloy. This dense 3D-cross-linked film with SiO_2 nanoparticles free of a methyl group (as a network modifier) reduced the permeability of the film against the corrosive electrolyte and therefore increased the corrosion resistance of the material. However, the hybrid sol–gel film was not able to protect the anodized Mg alloy and rapid degradation of the system occurred after 8 h of immersion in NaCl.

So, the corrosion performance of silica sol–gel coating depends on the synthesis parameter such as the type of precursor and the curing process, including temperature and time. A suitable compromise between all of the parameters is necessary to obtain a good barrier.

In this paper, an epoxy-alkyl silane coating reinforced with SiO_2 nanoparticles and catalyzed with 1-methyl imidazole (MI) was synthesized and deposited on an anodized Mg alloy. The effect of MI in the hydrolysis and condensation of metal alkoxides, which results in the formation of a hybrid network, was analyzed. The electrochemical impedance spectroscopy (EIS) technique was used to provide not only information about the instantaneous corrosion rate but also about the kinetic of the films in highly concentrated aqueous solution (3.5 wt% NaCl); in an attempt to mimic the most abundant and common corrosive agent on the earth (seawater).

2. Results and Discussion

After the pre-cleaned process, the Mg alloys were anodized by varying the potential from 3 to 100 V using a 1 mol L^{-1} NaOH aqueous electrolyte. Three different behaviors were observed depending on the anodizing potential. For 3 V, the dissolution of magnesium (reaction 1) and the alkalization of the media (reaction 2) take place and the film starts to grow since the Mg^{2+} ions react with OH$^-$ ions to yield Mg (OH)$_2$. (reaction 3).

$$Mg \rightarrow Mg^{2+} + 2e^- \tag{1}$$

$$2H_2O + 2e^- \rightarrow H_2 + 2OH^- \tag{2}$$

$$Mg^{2+} + 2OH^- \rightarrow Mg(OH)_2 \tag{3}$$
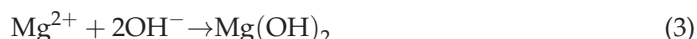
At 10 V, a new direct electrochemical oxidation of Mg to MgO (reaction 4) also takes place.

$$Mg + 2OH^- \rightarrow MgO + H_2O + 2e^- \tag{4}$$

For working voltages of 30 V and 70 V, a slight evolution of hydrogen was observed during the anodization process. However, when the working voltage changes to 100 V, a new phenomenon (called uniform sparking) appears. The sparking arc occurs by the action of a strong electric field (break down event) which vanishes with time. After 2 min of anodizing time, a deterioration of the coating is clear, indicating that anodizing times longer than 2 min are not adequate for an anodizing voltage of 100 V.

Yahalom et al. [20] reported that the temperature of the sparking arc during the anodization procedure could reach temperatures above 1000 °C, provoking the increase in temperature of the alloy surface. This high temperature could induce a dehydration process (reaction 5) as reported by Feitknecht and Braun [21], increasing the amount of MgO in the surface film.

$$Mg(OH)_2 \rightarrow MgO + H_2O \tag{5}$$
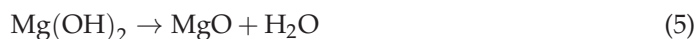
X-ray diffraction patterns of anodized magnesium alloy obtained at different voltages are depicted in Figure 1.
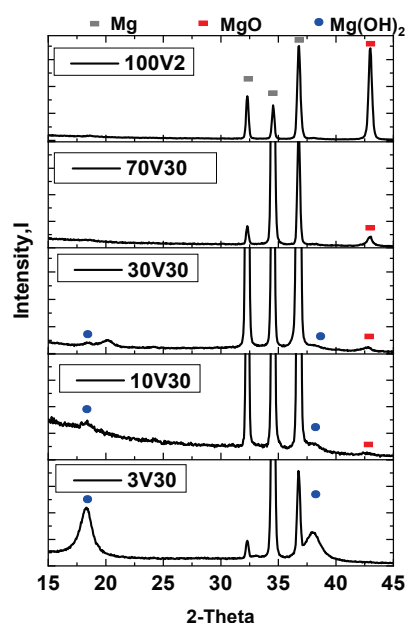
Figure 1. XRD patterns of anodized AZ31B alloy coatings obtained at different working voltages.

X-ray diffraction patterns show that as the anodizing potential increases, the intensity of Mg(OH)$_2$ diffractions peaks (●) decreases, and MgO peaks (■) increase. Therefore, anodic films obtained at low voltage (3 V) are enriched in Mg(OH)$_2$, while coatings obtained at

100 V contain more MgO. According to Lei et al. [22], a high proportion of MgO in the oxide coating could protect more of the Mg substrate from corrosion attack than Mg(OH)$_2$. These results are congruent with previously proposed mechanisms and with the literature reports [12]. In conclusion, the applied voltage governs the relative concentrations of magnesium oxide and hydroxide in the anodic film.

Figure 2 shows the surface and cross-section morphology of anodized films obtained at different potentials. For the anodizing process at 3 V (3V30), a homogeneous and cracked film appears (Figure 2a). The cross-section shows an anodized layer with a coating thickness of around 7 μm (Figure 2b). This morphology is associated with a dark greyish coating (Figure 2c).
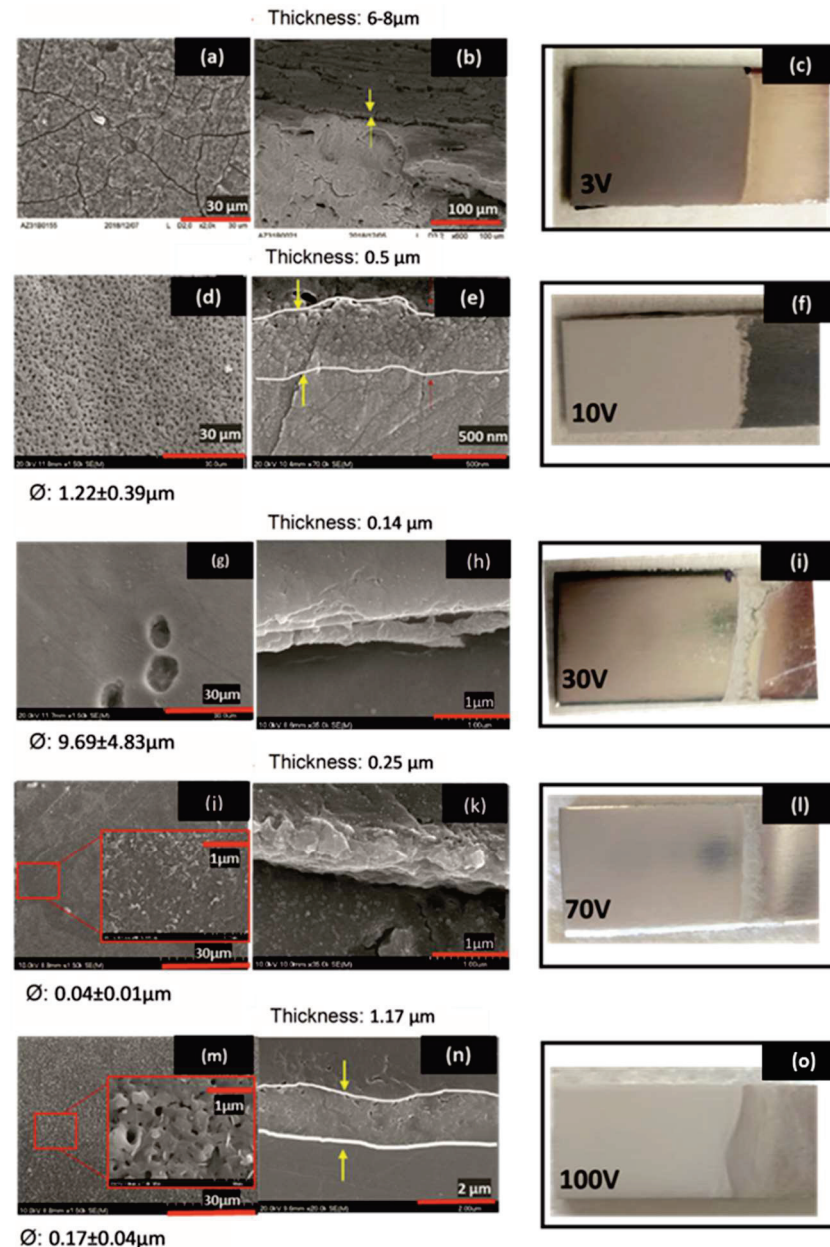
Figure 2. FESEM images of the morphology, cross-section, and aspect of the anodized AZ31B alloys samples (**a**–**c**) 3V30, (**d**–**f**) 10V30min, (**g**–**i**) 30V30, (**j**–**l**) 70V30, and (**m**–**o**) 100V2 in 1 mol L^{-1} NaOH electrolyte; ∅: Average of the diameter pores size.

A homogeneous and crack-free anodized porous film is obtained by increasing the anodization potential up to 10 V (10V30). FESEM images reveal a uniform porous coating

structure with a pore size of 1.2 ± 0.4 μm in diameter (Figure 2d) and a coating thickness of ~0.5 μm (Figure 2e). The surface morphology corresponds to the light greyish aspect shown in Figure 2f.

At higher anodizing potentials, 30 V (30V30) and 70 V (70V30), crack-free surfaces with non-uniform morphology are obtained as shown in FESEM images (Figure 2g,j). However, for the anodizing process at 100 V for 2 min (100V2), a homogenous flower-shaped appearance is observed (Figure 2m), corresponding to the vigorous sparking conditions.

At 30 V, 70 V, and 100 V, the average pore size was around 9.7 ± 4.8 μm, 40 ± 10 nm, and 170 ± 40 nm, and the thickness of the anodized film was 0.14 μm, 0.25 μm, and 1.17 μm (Figure 2h,k,n)), respectively. The surface films anodized at 30 V and 70 V exhibited a bright reflective finishing (Figure 2i,l), while 100 V sample presents a dense white color (Figure 2o).

The contact angle for anodized AZ31B substrates was measured. The highest contact angle was obtained for the as-received substrate (93.5 ± 4.5°) and the lowest contact angle for the 3V30 (immediately adsorption) and 100V2 (35.7 ± 1.2°) samples. The low wettability of as-received substrates is associated with the higher roughness surface of 2.2 μm, susceptible to trapped air in the micro-nanostructure, increasing the water contact angle [3]. On the other hand, the higher wettability of the 3V30 and 100V2min samples is associated with the cracked $Mg(OH)_2$ enriched coating and with the porous-smoother surface, respectively.

Figure 3a,b shows the Bode plots of the anodized films obtained at 3V30, 10V30, 30V30, 70V30, and 100V2, along with the as-received and pre-cleaned substrates. EIS data were fitted using the equivalent circuits proposed in Figure 3c,d.

In general, the equivalent circuits include the electrolyte resistance (Rs), the charge transfer resistance (Rdl), the electrical double-layer capacitance (CPE1), the electrolyte resistance into the coating pores (Rox), the constant phase element of the anodized film (CPE2), a finite length Warburg short-circuit (Ws), and the resistance (RL) of an inductance (L1) process. The CPE behavior is generally attributed to a distribution of time constant and is calculated using the following formula (Equation (1)):

$$CPE = 1/Q(j\omega)^{\alpha} \tag{6}$$

where Q is a parameter independent of frequency having units of $\Omega^{-1}cm^{-2}s^{\alpha}$ for $\alpha \neq 1$, and $F\,cm^{-2}$ when $\alpha = 1$, and α may vary from -1 to 1, with 1 as the ideal capacitor [23].

The Bode plot shows that the impedance spectrum of anodized film at 3V30min has a similar trend as the as-received and pretreated AZ31B specimens. These spectra show a decreasing trend in the impedance magnitude lZl and phase angles values closed to 40° at the low frequencies domain (f < 1). This behavior relates to the presence of an inductive loop (RL, L1) at low frequencies, included in the representation of the equivalent circuit in Figure 3c. The inductive behavior can be associated with the breakdown of the protective coating [24] or with the relaxation processes of adsorbed species such as $Mg(OH)_{ads}^{+}$ or $Mg(OH)_2$ onto the electrode surface as a consequence of the pitting corrosion process [25,26]. The presence of cracks in the anodized coating at 3V30 facilitates the fast diffusion of (Cl^-) ions through the coating, easily reaching the inner Mg matrix. Further, the main composition of the anodized coating, $Mg(OH)_2$, provides relatively low corrosion resistance to the AZ31B alloy since the chloride ions can transform the $Mg(OH)_2$ to $MgCl_2$, a more soluble species [2], promoting the dissolution of the Mg alloy [22]. (reaction 6)

$$Mg(OH)_2 + 2Cl^- \rightarrow MgCl_2 + 2OH^- \tag{7}$$
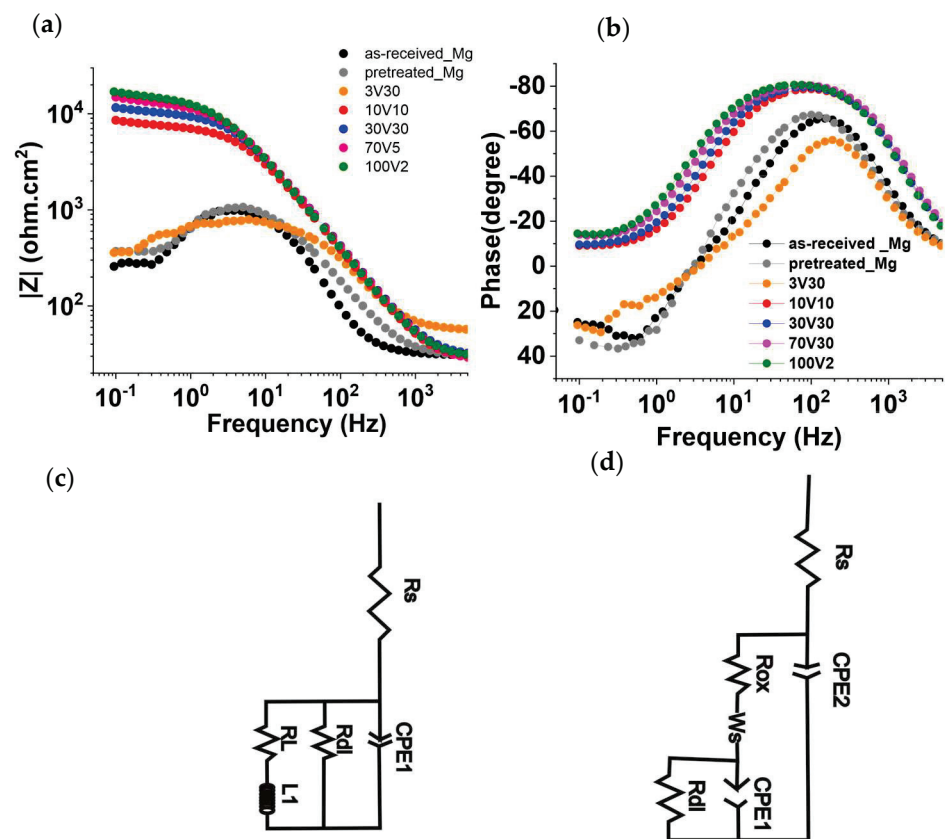
Figure 3. (**a**,**b**) Bode plot for anodized coatings at different working voltages. Equivalent circuit for (**c**) as-received, pretreated, and anodized film at 3V30 and (**d**) anodized films at 10V10, 30V30, 70V30, and 100V2 after 2 h of immersion in 3.5% wt NaCl solution.

In this case, neither the etching process nor the Mg(OH)$_2$ coating obtained after the anodizing process is enough to obtain a good corrosion barrier.

For 10V30min, 30V30min, 70V30min, and 100V2min samples, a different trend is observed in the low frequencies domain (f < 1), with a significant increase in the impedance modulus lZl. In this case, the equivalent circuit (Figure 3d) included a finite length Warburg short-circuit (Ws) and two-time constants (Rox, CPE2, Rdl, and CPE1).

The time constant at high frequency is related to the porous anodized layer (Rox, CPE2), and the time constant at low frequency is attributed to the internal layer structure of the anodized coating, which corresponds with a charge transfer metal–film interface resistance (Rdl), and a capacitive element CPE1. The Warburg element in the equivalent circuit corresponds to the diffusive process occurring through the anodized films in the absence of corrosion products. The change from adsorption to mass transport processes likely suggests that the anodized coating blocks the easy diffusion of the electrolyte to the substrate, due to the crack-free coating morphology [27]. Considering the proposed equivalent circuit Figure 3c,d, the total corrosion resistance for each system and Rp (polarization resistance) values were calculated as the sum of all the faradaic resistance (Table 1). Additionally, to compare the pseudo-CPE capacitance with the classic capacitance, the effective capacitance (C$_{eff}$) was also calculated using the Hirschorn et al. [28] model based on the Brug's equation (Equation (2)) and considering a parallel surface distribution [29].

$$C_{eff} = CPEcoat^{\left(\frac{1}{\alpha coat}\right)} \left(\frac{Rs * Rp}{Rs + Rp}\right)^{\frac{1-\alpha coat}{\alpha\, \alpha coat}} \tag{8}$$

Table 1. Impedance parameters of anodized coated specimens obtained via the EIS data fitted with the equivalent circuit.

Sample	R_SG (Ωcm^2)	Rox (Ωcm^2)	RdL (Ωcm^2)	RL (Ωcm^2)	CPE1 (CPE1)	CPE1 (α1)	CPE2 (CPE2)	CPE2 (α2)	CPE3 (CPE3)	CPE3 (α3)	Rp (Ωcm^2)	C_{eff} (Fcm^{-2})	ηE (%)
100V2	-	11,873 (±65)	1284 (±62.19)	-	2.5×10^{-5} (±2.×10⁻⁶)	1	5.2×10^{-6} (±1.0×10⁻⁸)	0.95 (±2.4×10⁻⁴)	-	-	13,557	3.32×10^{-6}	98.5
100V2_(16h)	-	-	2190 (±47.77)	1483 (±107.36)	1.3×10^{-5} (±6.46×10⁻⁷)	0.91 (±7.25×10⁻³)	-	-	-	-	884.2	6.21×10^{-6}	76.6
70V30	-	10,127 (±299)	1340 (±275)	-	2.2×10^{-5} (±9.9×10⁻⁶)	1	4.9×10^{-6} (±5.5×10⁻⁸)	0.95 (±0.01)	-	-	11,467	3.11×10^{-6}	98.2
30V30	-	8025 (±89)	777.4 (±82.27)	-	2.2×10^{-5} (±5.9×10⁻⁶)	1	4.8×10^{-6} (±1.8×10⁻⁸)	0.96 (±5.0×10⁻⁴)	-	-	8802	3.34×10^{-6}	97.6
10V10	-	6019 (±56)	561.3 (±45.25)	-	2.4×10^{-5} (±4.8×10⁻⁶)	1	5.3×10^{-6} (±1.7×10⁻⁸)	0.96 (±4.23×10⁻⁴)	-	-	6580	3.69×10^{-6}	96.8
3V30	-	-	684.2 (±7.4)	345.1 (±20.43)	7.4×10^{-6} (±3.8×10⁻⁷)	0.94 (±7.22×10⁻³)	-	-	-	-	229.3	4.43×10^{-6}	9.6
SG_110	14,365 (±1202.5)	152,350 (±2074)	34618 (±2001)	-	4.4×10^{-7} (±5.3×10⁻⁸)	1	1.5×10^{-9} (±1.0×10⁻¹⁰)	1	3.7×10^{-8} (±1.0×10⁻⁹)	0.83 (±2.4×10⁻³)	201,333	2.21×10^{-9}	99.9
SG_110_(72h)	-	72.58 (±10.38)	14831 (±198.6)	-	2.5×10^{-6} (±1.4×10⁻⁷)	0.78 (±6.2×10⁻³)	1.4×10^{-7} (±1.1×10⁻⁸)	1	-	-	14903.6	1.42×10^{-7}	98.6
SG_160	10,629 (±1297.4)	203,740 (±2421.2)	18,773 (±2065.1)	-	9.6×10^{-7} (±2.2×10⁻⁷)	1	8.5×10^{-9} (±1.7×10⁻⁹)	0.9	1.1×10^{-8} (±1.8×10⁻⁹)	0.89 (±1.2×10⁻²)	233142	1.74×10^{-9}	99.9
SG_160_(72h)	-	-	1973 (±56.87)	7145 (±849.4)	5.4×10^{-6} (±5.8×10⁻⁷)	0.86 (±1.31×10⁻²)	-	-	-	-	1546.07	1.29×10^{-6}	86.6
Pretreated_Mg	-	-	1041 (±24.36)	305.4 (±18.8)	1.4×10^{-5} (±8.9×10⁻⁷)	1	-	-	-	-	236.1	1.46×10^{-5}	-
Asreceived_Mg	-	-	690.1 (±4.7)	296.4 (±8.2)	2.3×10^{-5} (±4.7×10⁻⁷)	1	-	-	-	-	207.3	2.34×10^{-5}	-

Both the Rp and C_{eff} values for each condition are also included in Table 1. The polarization resistance for the as-received, pre-cleaned, and the anodized film obtained at 3V30 min showed the lowest values, around 200 Ω cm^2. However, an increment of Rp values appears when increasing anodizing potential, following the order: 100V2 > 70V30 > 30V30 > 10V30. Coated specimens with high polarization resistance values present better corrosion resistance [30]. Therefore, the best corrosion resistance performance was obtained for 100V2 coating.

Although the 100V2 sample showed the highest Rp values (13,557 $\Omega \cdot$cm^2), non-significant differences can be observed along with the C_{eff} values since all coated samples showed values in the order of 10^6 F cm^{-2}. This means that in general the oxide coatings obtained at different anodizing potentials and times show similar electrolyte uptake phenomena (electrolyte penetration/adsorption) and therefore, the corrosion process slows down by a double effect of a decrease in charge transfer area associated with the small pore size obtained at a higher anodizing voltage (between 40 nm–0.17 μm for 70 and 100 V, respectively), and/or the low anodic dissolution of the coating due to the presence of MgO in the coating composition, more stable than Mg(OH)$_2$, regardless of the differences in oxide thickness. These results differ from Mizutani et al. [11] but are similar to those of Salman et al. [12], where the presence of MgO is decisive to control the corrosion processes much better than oxide film composed of Mg(OH)$_2$.

Although the anodized coating obtained at 100V2 increases the corrosion resistance of the naked substrate, its corrosion protective performance is still not comparable to other anodized systems obtained using more complex electrolytes. For example, Ying Long et al. [31] reported a corrosion resistance of 32,205 $\Omega \cdot$cm^2 for an anodized coating obtained using an alkaline electrolyte that contains Na(OH) and/or Na$_2$SiO$_4$ and alumina nanoparticles as additives. Therefore, to improve the corrosion resistance of the AZ31B alloy, in this work, the anodized specimens were sealed using an epoxy-alkyl hybrid silica sol–gel (SGMI) prepared following the process described in the experimental section. A homogeneous and transparent SiO$_2$ sol, with an adequate viscosity of around 3.6 mPa.s and a neutral pH was obtained.

FTIR measurements were performed to study the effect of adding MI in the organic-inorganic polymerization of the hybrid sol. Figure 4a) shows the FTIR spectra of hybrid silica sols prepared with and without the addition of MI, and Figure 4b,c show the corresponding FTIR spectrum and its deconvoluted peaks in the region between 1350 and 850 cm^{-1}. For both spectra, the characteristic peak of the Si–O–Si bond at 1027 cm^{-1} was identified, confirming that the inorganic polymerization reaction took place [32]. A band at 1260 cm^{-1} is ascribed to Si–C of the CH$_3$ group of MTES precursor, and a peak at 910 cm^{-1} is associated with the stretching vibration of the epoxy ring [32]. The broad peak around 1250–850 cm^{-1} was deconvoluted; the band at 1270 cm^{-1} assigned to Si-CH$_3$ was chosen to normalize the integrated area (Table 2). It is possible to identify two bands at 1100 cm^{-1} and 1010 cm^{-1} associated with the longitudinal optic (LO) and the transversal optic (TO) modes of Si-O-Si vibrations, respectively. The ratio of the LO and TO modes is associated with the porosity of the silica network [33,34]. As observed, the ratio LO/TO decreases from 0.88 to 0.60 with the addition of MI indicating the increment of inorganic condensation and a less porous structure. Furthermore, the ratio between the epoxy (910 cm^{-1}) and Si-CH$_3$ bands also decreases (approximately 50%) with the addition of MI, indicating a partial opening of the epoxy ring groups to form a more cross-linked network.

In order to evaluate the effect of the sintering temperature on the structural features of the hybrid network, the silica sol was cured at 110 °C and 160 °C and characterized by solid-state ^{29}Si and ^{13}C NMR. Two intense peaks at −70 and −60 ppm are observed (Figure 5) and assigned to T^3 (RSi(OSi)$_3$), and T^2 (RSi(OSi)$_2$OH) units (R: –CH$_3$, propyl chain of GPTMS). In the range between −100 and −130 ppm a broad band, which corresponds to Q^n (Si(OSi)$_4$) of the Ludox nanoparticles, was also observed. The absence of T^0 and T^1 units indicates a high polycondensation of the silica network. It is noteworthy to observe that the relative intensity of the T^2 peak decreases from 110 °C to 160 °C, meaning that

the degree of condensation of the inorganic phase increases. Therefore, the formation of a cross-linked inorganic network is evident when the film is treated at 160 °C. On the other hand, polymerization of epoxy groups was also monitored by ^{13}C solid-state CPMAS-NMR (not shown) and there is no evidence of an increase in the organic polymerization with temperature.

(**a**)

(**b**)   (**c**)
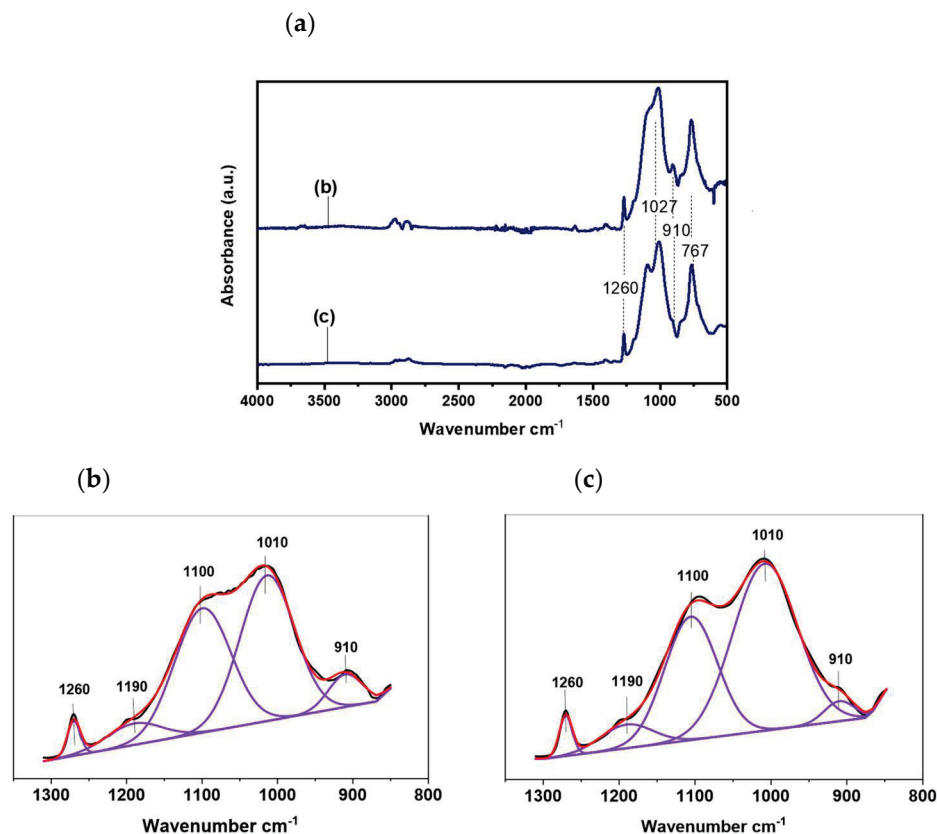
Figure 4. FTIR spectra of the silica sol–gel without MI and with MI (**a**) and the corresponding integral of the deconvoluted peaks in the region 1350–1850 cm^{-1} (**b**,**c**).

Table 2. Normalized bands intensity of the sol–gel without MI (SG) and with MI (SGMI) observed in the region 850–1350 cm^{-1} of the FTIR spectra.

	Normalized Integrated Area					LO/TO	Epoxy/-CH$_3$
Peak/cm^{-1}	910	1010	1100	1190	1270	-	-
SG	2.54	18.3	16.13	2.69	1	0.88	2.54
SGMI	1.17	21.03	12.68	2.39	1	0.60	1.17

Thus, Mg alloy anodized at 100V2 was sealed using the SiO$_2$ sol and heat-treated at the two different temperatures, 110 °C and 160 °C for one hour. Figure 6 shows the FESEM images of surface morphology and cross-section of the sealed system sintered at 110 °C/1h. Homogeneous, smooth, and crack-free coated surfaces are obtained with a total thickness of ~3.2 μm (anodized and silica coatings) at 110 °C and 160 °C, respectively. The contact angle measured for the sealed system was 78.8 ± 4.2°, higher compared to 35.7 ± 1.2° for 100V2 oxide coating.
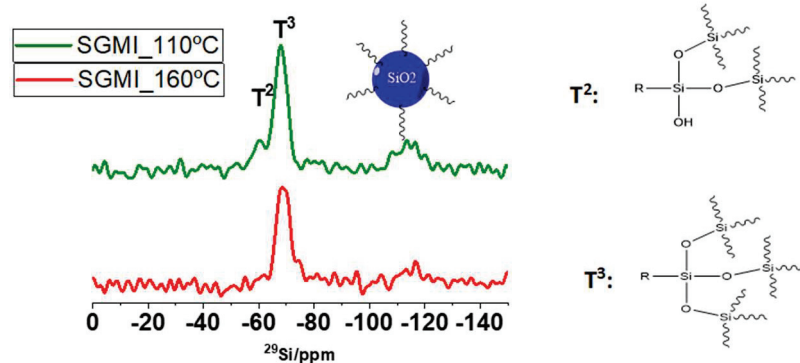
Figure 5. ^{29}Si NMR spectra taken from cured SGMI sol at 110 °C and 160 °C in the region of 0 and -150 ppm.

(**a**)   (**b**)
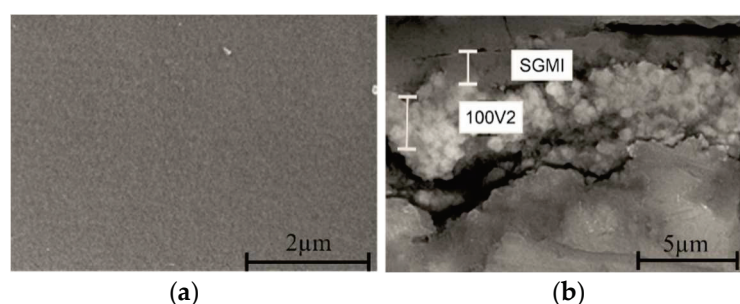
Figure 6. FESEM surface morphology (**a**) and cross-sectional (**b**) images of sealed system heat treatment at 110 °C/h.

The corrosion resistance properties of SGMI_160 and SGMI_110 systems were evaluated by electrochemical impedance spectroscopy (EIS), Figure 7. Rp and effective capacitance (C_{eff}) values were also calculated considering the equivalent circuits presented in Figure 7c, which include the electrolyte resistance (Rs) and tree-time constants (Table 1). R_SG and CPE3 represent the resistance and the capacitance related to the hybrid organic–inorganic coating. Rox and CPE2 are the resistance and the capacitance of the anodized film, and Rdl and CPEdl are attributed to the charge transfer process in the film/substrate interface region. Warburg element impedance disappears from the equivalent circuits unlike the proposed anodized circuit (Figure 3d), indicating that silica sol–gel coating seals the pathways for diffusion of corrosive species through the anodized coating. The coating protection efficiency (ηE) obtained by the EIS test was calculated (Table 1) by the following relationship (Equation (3)):

$$\eta E\% = \frac{Rp(coat) - Rp}{Rp(coat)} \times 100 \tag{9}$$

where $Rp(coat)$ and Rp are the values of polarization resistance of the anodic film/hybrid silica sol–gel system and the bare Mg alloy, respectively.

Better corrosion resistance properties are obtained for both SGMI_160 and SGMI_110 systems compared with 100V2 anodized sample and bare Mg alloy since the polarization resistance (Rp) values are one order of magnitude higher than the 100V2 anodized sample and three orders of magnitude higher than bare Mg alloy. These results indicate that the proposed sealed system is more effective against corrosion than the use of a single-anodized layer system.
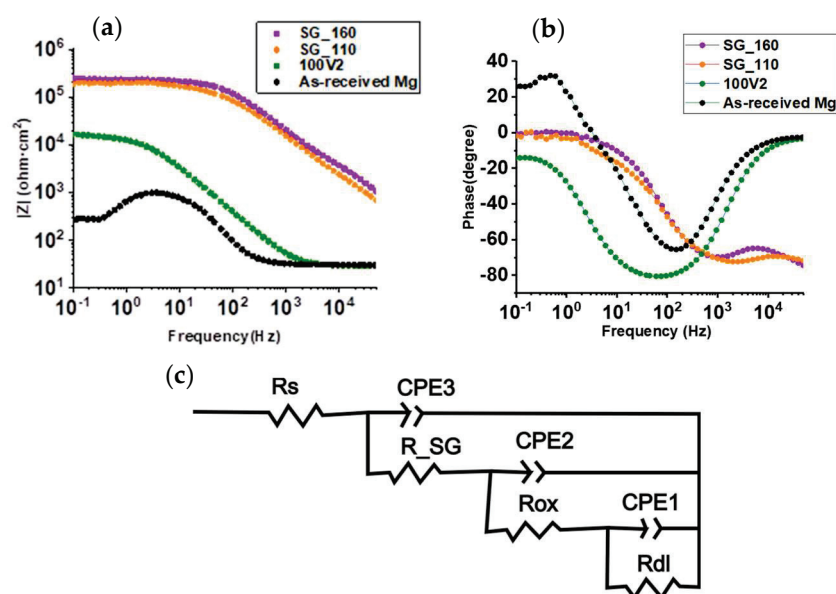
Figure 7. (**a**,**b**) Bode plots for the anodized coating (100V2min), SG_160, SG_110 and as-received Mg alloy after 2 h of immersion in 3.5% wt NaCl solution. (**c**) equivalent circuit for SG_110 and SG_160.

The highly cross-linking silica coating reduces the penetration of the electrolyte through the anodized coating (water uptake), which is in good agreement with the lower C_{eff} value of the sealed system, three orders of magnitude lower (10^{-9} F·cm^{-2}) than the anodized Mg alloy (10^{-6} F·cm^{-2}).

Further, the corrosion behavior of SGMI_110 and SGMI_160 samples were analyzed as a function of immersion time in 3.5% NaCl and compared to 100V2 oxide film. Bode and Phase Angle plots (Figure 8a,b) show that the impedance magnitude lZl value at the low-frequency domain (f < 1 Hz) decreases with the immersion time, indicating a diminution of the corrosion resistance properties of the coating systems. For the 100V2 sample, the Rp value drops significantly from 13,557 Ω cm^2 to 884.2 Ω cm^2 after 16 h of immersion showing a loss of the protection efficiency from 98.4% to 75.5%. Short-term corrosion protection is observed for the anodized coating associated with the fast electrolyte uptake through the hydrophilic porous oxide film. On the other hand, the polarization resistances for SGMI_160 and SGMI_110 systems were 1546 Ω cm^2 and 14,903 Ω cm^2 after 72 h; one or two orders of magnitude higher than in the case of the anodized coatings (884.2 Ω cm^2) after 16 h of immersion. As can be seen, longer-term corrosion protection was obtained for the less cross-linking structural network (SGMI-110), with a protection efficiency of 98.6 % after 72 h of immersion compared to SGMI-160. The quicker decay of the corrosion resistance performance of SGMI-160 can be associated with the internal stresses and higher rigid film structure that led to the formation of micro-cracks (not observed by FESEM) at high heat-treatment temperature.

These results suggest that MgO enriched coating can be considered a good first approach to block the corrosion process of Mg alloys. However, higher corrosion activity and consequently low polarization resistance are observed after the beginning of the immersion tests, indicating that the anodized coating does not provide long-term corrosion protection. Sealing of the anodized coating with a silica sol–gel improves the corrosion resistance properties of Mg alloys. The control of the sol–gel synthesis and the right choice of the treatment temperature allow for improving the corrosion resistance and the stability of the protective system with time.
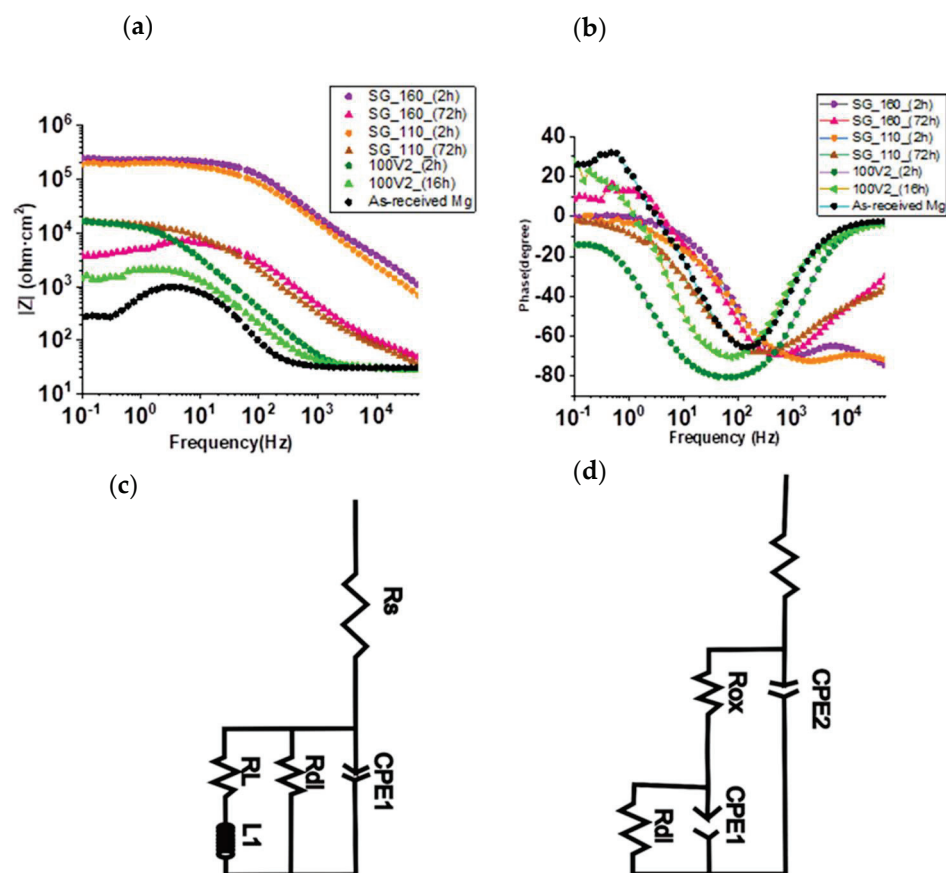
Figure 8. (**a**,**b**) Bode plots for the anodized coating (100V2min), SG_160, SG_110, and as-received Mg alloy at different immersion times in 3.5% wt. NaCl solution. (**c**) equivalent circuit for 100V2min and SG_160 after 16 h and 72 h immersion time, respectively, and (**d**) equivalent circuit for SG_110 after 72 h of immersion.

3. Conclusions

In this study, the anodizing process of AZ31B Mg alloy was studied as a function of potential and time, evaluating the effect of these conditions on the corrosion performance of the anodized samples. Relevant differences were identified related to the morphology and composition of the anodized films. The anodized film obtained at 3 V for 30 min exhibited a cracked morphology, mainly composed of Mg $(OH)_2$, showing the worst corrosion resistance performance. As the anodized potential increases, cracked-free and MgO enriched coating appear. The most MgO-enriched and dense anodized coating (small pore size) was obtained when the AZ31B Mg alloy was anodized at 100 V for 2 min; this coating showed a higher value of Rp and a non-significant difference in the C_{eff} values with respect to the other anodized coatings indicating that the improvement in the corrosion resistance can be likely attributed to the small pore size and the existence of MgO-enriched coatings. However, the coating barrier properties degrade fast with the immersion time. The sealing of the anodized sample using the epoxy-alkyl sol–gel coating reinforced with SiO_2 nanoparticles decreases the effective capacitance (C_{eff}) value and slows down the corrosion rate of the Mg alloys in concentrated NaCl solution. The MI addition promotes the aperture of the epoxy ring and a more cross-linked network with a less porous structure, thus increasing the anodized Mg alloy corrosion resistance. The use of different curing temperatures in terms of corrosion performance did not show a remarkably different electrochemical contribution during the first two hours of immersion.

The curing temperature plays an important role in the corrosion protection performance with immersion time. Although better corrosion performance is expected with higher condensed Si–O–Si structure film, internal stresses and the degree of network rigid-

ity could lead to a faster decay of the corrosion resistance performance of the silane coating with time.

4. Materials and Methods

Commercially available AZ31B Mg alloy with composition: 10.1% Al, 0.3% Mn, 1.0% Zn, <0.5% Fe, and Mg balance (Dugopa S.A, Madrid, Spain) was cut to a size of 5×2 cm^2. To remove oil and surface imperfections, the AZ31B Mg samples were dipped in 2 vol% H$_3$PO$_4$ (85%, Aldrich, Madrid, Spain) and 10 vol% HNO$_3$ (65%, VWR, Barcelona, Spain) acid solution for 20 s, then rinsed with water and finally neutralized with 5 wt% NaOH (99%, Scharlab, Barcelona, Spain) solution.

4.1. Preparation of the Anodizing Coating

Anodization experiments were performed in an aqueous electrolyte of 1 mol L^{-1} NaOH (99.9%, Scharlab, Barcelona, Spain) at room temperature using a DC power supply (Magna Power, 12 A, 500 V, Flemington, NJ, USA). A platinum foil was fixed as the cathode and the pre-cleaned AZ31B substrate as the anode.

Different anodizing tests were performed by varying the potentials from 3 to 100 V. All the samples were anodized for 30 min except the ones at 100 V that were treated for 2 min. The samples were labeled as XVY, where XV corresponds to the anodizing potential (3, 10, 30, 70, and 100 V) and Y to the anodization time (2 and 30 min).

4.2. Preparation and Deposition of the Epoxy-Alkyl-Silane Coating

A modified silane sol was synthesized at room temperature by mixing 0.17 mol of 3-(glycidyloxypropyl) trimethoxysilane (GPTMS, ABCR, 98%, Karlsruhe, Germany), 0.5 mol of methyltriethoxysilane (MTES, Aldrich, 99%, Madrid, Spain), 0.33 mol of colloidal SiO$_2$ nanoparticles suspension (Ludox-4S, Aldrich, aqueous suspension 40 wt%, particle size 20 nm, pH9, Madrid, Spain), and 0.014 mol of nitric acid HNO$_3$ (VWR, 65%, Barcelona, Spain). After the reaction, 0.014 mol of 1-Methylimidazole (MI, Aldrich, 99%, Madrid, Spain) diluted in ethanol (EtOH, Panreac, 99.8%, Madrid, Spain) was incorporated to obtain a transparent sol.

The viscosity of the sol was controlled with an A&D Vibro Viscosimeter SV-10 equipment (Malvern Panalytical, Madrid, Spain), and pH was measured by a pH paper indicator (VWR, Barcelona, Spain).

The structural changes in the silica sol preparation were analyzed by Fourier Transformed Spectroscopy (FTIR) (Perkin Elmer Spectrum 100 spectrometer, PerkinElmer, INC, Madrid, Spain), a spectrometer with an attenuated total reflectance accessory. FTIR spectra were measured with a resolution of 4 cm^{-1} and 8 scans for each measurement.

The anodized samples were coated with the sol using a withdrawal rate of 30 cm/min. After the deposition, the samples were cured at two temperatures between 160 °C and 110 °C for 1 h. The samples were labeled as SGMI_160 and SGMI_110 for the system composed of the oxide coating plus the silica sol–gel coating heat-treated at 160 °C and 110 °C, respectively.

Solid-state ^{29}Si MAS and ^{13}C CPMAS-NMR spectra were recorded using a Bruker Avance-400 pulse spectrometer equipped with a fast Fourier transform unit. Samples were spun at 10 kHz around an axis inclined 54 ° 44′ with respect to the external magnetic field. The resonance frequencies used were 79.5 and 100.63 MHz (9.4 T magnetic field). ^{29}Si MAS spectra were recorded after irradiation of samples with a $\pi/2$ (5-μs) pulse. In order to avoid saturation effects, the recycle delay time used was 10 s. A contact time of 2 ms and a recycle delay of 5 s were used in ^{13}C CPMAS-NMR experiments. All measurements were taken at room temperature with TMS (tetramethylsilane) as an external standard. The error in chemical shift values was estimated to be lower than 0.5 ppm.

4.3. Characterization of the Coatings

The surfaces morphology of samples was characterized using Field Emission Scanning Electron Microscopy (FESEM, Hitachi S4700, Japan, Tokyo). The images obtained by FESEM were evaluated using ImageJ software (U. S. National Institutes of Health, Bethesda, Rockville, MD, USA). The surface roughness (Ra-parameter) was determined using a Zeta 20 optical profiling microscope (KLA Corporation, Milpitas, CA, USA) set at 20× magnification and a resolution of 0.1 nm. A 'Drop Shape Analysis System' Kruss DSA 100 system (Kruss, Hamburg, Germany) was used to measure the water contact angle. An analytical X'Pert PRO theta/theta diffractometer (Malvern Panalytical, Madrid, Spain) was used to analyze the crystallographic structure of anodized films. A grazing angle of $0.5°$ and 2θ range of $10–50°$ with a step size of $0.05°$ and accumulation time of 20 s per step and Cu-Kα radiation ($\lambda = 0.15418$ nm) as the excitation source was used to perform the experiment.

The electrochemical characterization was developed in a Gamry FAS2 electrochemical unit (Gamry, United Kingdom, Warminster) with DC and AC signals. Electrochemical Impedance Spectroscopy (EIS) was measured using a saturated calomel electrode (SCE, Radiometer, Hach Lange GmbH, Germany, Düsseldorf) as the reference electrode, the metal samples as the working electrode, and the platinum wire as the counter electrode. The testing was carried out in 3.5 wt% NaCl electrolyte solution considering an area of 0.78 cm^2. EIS results were conducted in a frequency range of 10^5 Hz to 0.1 Hz with an application of an AC voltage at the open circuit potential with a sinusoidal amplitude of 10 mV rms. After each sample was measured three times, the most representative measurement was plotted. The impedance plots were fitted in the Zview 2.0 software using a compatible equivalent circuit that simulates the corrosion behavior of the anodized and non-anodized samples.

Author Contributions: Conceptualization, E.M., A.D. and Y.C.; methodology, E.M. and Y.C.; vali E.M. and Y.C.; formal analysis, E.M., S.C. and Y.C.; investigation, E.M. and Y.C.; writing—original draft preparation, E.M.; writing—review and editing, S.C., Y.C. and A.D.; supervision, Y.C.; project administration, A.D.; funding acquisition, A.D. All authors have read and agreed to the published version of the manuscript.

Institutional Review Board Statement: Not applicable.

Informed Consent Statement: Not applicable.

Conflicts of Interest: The authors declare no conflict of interest.

References

1. Abbasi, S.; Aliofkhazraei, M.; Mojiri, H.; Amini, M.; Ahmadzadeh, M.; Shourgeshty, M. Corrosion behavior of pure Mg and AZ31 magnesium alloy. *Prot. Met. Phys. Chem. Surf.* **2017**, *53*, 573–578. [CrossRef]
2. Esmaily, M.; Svensson, J.E.; Fajardo, S.; Birbilis, N.; Frankel, G.S.; Virtanen, S.; Arrabal, R.; Thomas, S. Fundamentals and advances in magnesium alloy corrosion. *Prog. Mater. Sci.* **2017**, *89*, 92–193. [CrossRef]
3. Yeganeh, M.; Mohammadi, N. Superhydrophobic surface of Mg alloys: A review. *J. Magnes. Alloy.* **2018**, *6*, 59–70. [CrossRef]
4. Wan, H.; Hu, X. One-step solve-thermal process for the construction of anticorrosion bionic superhydrophobic surfaces on magnesium alloy. *Mater. Lett.* **2016**, *174*, 209–212. [CrossRef]
5. Sreekanth, D.; Rameshbabu, N.; Venkateswarlu, K. Effect of various additives on morphology and corrosion behavior of ceramic coatings developed on AZ31 magnesium alloy by plasma electrolytic oxidation. *Ceram. Int.* **2012**, *38*, 4607–4615. [CrossRef]
6. Salman, S.A.; Okido, M. Anodization of magnesium (Mg) alloys to improve corrosion resistance. In *Handbook of Corrosion Prevention of Magnesium Alloys*; Song, G.-L., Ed.; Woodhead Publishing: Cambridge, UK, 2013; pp. 197–231. [CrossRef]

7. Blawert, C.; Dietzel, W.; Ghali, E.; Song, G. Anodizing treatments for magnesium alloys and their effect on corrosion resistance in various environments. *Adv. Eng. Mater.* **2006**, *8*, 511–533. [CrossRef]

8. Shi, Z.; Song, G.; Atrens, A. Influence of anodising current on the corrosion resistance of anodised AZ91D magnesium alloy. *Corros. Sci.* **2006**, *48*, 1939–1959. [CrossRef]

9. Gray, J.E.; Luan, B. Protective coatings on magnesium and its alloys—A critical review. *J. Alloys Compd.* **2002**, *336*, 88–113. [CrossRef]

10. Salman, S.A.; Okido, M. Anodization and corrosion of magnesium (Mg) alloys. In *Handbook of Corrosion Prevention of Magnesium Alloys*; Song, G.-L., Ed.; Woodhead Publishing: Cambridge, UK, 2013; pp. 232–281. [CrossRef]

11. Mizutani, Y.; Kim, S.J.; Ichino, R.; Okido, M. Anodizing of Mg alloys in alkaline solutions. *Surf. Coat. Technol.* **2003**, *169–170*, 143–146. [CrossRef]

12. Salman, S.A.; Mori, R.; Ichino, R.; Okido, M. Effect of Anodizing Potential on the Surface Morphology and Corrosion Property of AZ31 Magnesium Alloy. *Mater. Trans.* **2010**, *51*, 1109–1113. [CrossRef]

13. Merino, E.; Durán, A.; Castro, Y. The Role of Silane Sol-Gel Coatings on the Corrosion Protection of Magnesium Alloys. In *Magnesium Chemistry—Current Trends and Future Perspectives*; Sunkari, S.S.S., Ed.; IntechOpen: London, UK, 2022; Available online: https://www.intechopen.com/online-first/80226 (accessed on 5 March 2022). [CrossRef]

14. Toorani, M.; Aliofkhazraei, M. Review of electrochemical properties of hybrid coating systems on Mg with plasma electrolytic oxidation process as pretreatment. *Surf. Interfaces* **2019**, *14*, 262–295. [CrossRef]

15. Zhang, D.; Peng, F.; Liu, X. Protection of magnesium alloys: From physical barrier coating to smart self-healing coating. *J. Alloys Compd.* **2021**, *853*, 157010. [CrossRef]

16. Li, Q. Sol-gel coatings to improve the corrosion resistance of magnesium (Mg) alloys. In *Handbook of Corrosion Prevention of Magnesium Alloys*; Song, G.-L., Ed.; Woodhead Publishing: Cambridge, UK, 2013; pp. 469–485. [CrossRef]

17. Guo, X.; An, M. Experimental study of electrochemical corrosion behaviour of bilayer on AZ31B Mg alloy. *Corros. Sci.* **2010**, *52*, 4017–4027. [CrossRef]

18. Malayoglu, U.; Tekin, K.C.; Shrestha, S. Influence of post-treatment on the corrosion resistance of PEO coated AM50B and AM60B Mg alloys. *Surf. Coat. Technol.* **2010**, *205*, 1793–1798. [CrossRef]

19. Merino, E.; Durán, A.; Castro, Y. Integrated corrosion-resistant system for AZ31B Mg alloy via plasma electrolytic oxidation (PEO) and sol-gel processes. *Int. J. Appl. Glass Sci.* **2021**, *12*, 519–530. [CrossRef]

20. Yahalom, J.; Zahavi, J. Experimental evaluation of some electrolytic breakdown hypotheses. *Electrochim. Acta* **1971**, *16*, 603–607. [CrossRef]

21. Feitknecht, W.; Braun, H. Der Hydratation von Magnesiumoxid mit Wasserdampf. *Helv. Chim. Acta* **1967**, *50*, 2040–2053. [CrossRef]

22. Lei, T.; Ouyang, C.; Tang, W.; Li, L.F.; Zhou, L.S. Preparation of MgO coatings on magnesium alloys for corrosion protection. *Surf. Coat. Technol.* **2010**, *204*, 3798–3803. [CrossRef]

23. Jorcin, J.B.; Orazem, M.E.; Pébère, N.; Tribollet, B. CPE analysis by local electrochemical impedance spectroscopy. *Electrochim. Acta* **2006**, *51*, 1473–1479. [CrossRef]

24. Zomorodian, A.; Brusciotti, F.; Fernandes, A.; Carmezim, M.J.; e Silva, T.M.; Fernandes, J.C.S.; Montemor, M.F. Anti-corrosion performance of a new silane coating for corrosion protection of AZ31 magnesium alloy in Hank's solution. *Surf. Coat. Technol.* **2012**, *206*, 4368–4375. [CrossRef]

25. King, A.D.; Birbilis, N.; Scully, J.R. Accurate electrochemical measurement of magnesium corrosion rates; A combined impedance, mass-loss and hydrogen collection study. *Electrochim. Acta* **2014**, *121*, 394–406. [CrossRef]

26. Baril, G.; Galicia, G.; Deslouis, C.; Pébère, N.; Tribollet, B.; Vivier, V. An Impedance Investigation of the Mechanism of Pure Magnesium Corrosion in Sodium Sulfate Solutions. *J. Electrochem. Soc.* **2006**, *154*, C108. [CrossRef]

27. Liang, J.; Srinivasan, P.B.; Blawert, C.; Dietzel, W. Influence of chloride ion concentration on the electrochemical corrosion behaviour of plasma electrolytic oxidation coated AM50 magnesium alloy. *Electrochim. Acta* **2010**, *55*, 6802–6811. [CrossRef]

28. Hirschorn, B.; Orazem, M.E.; Tribollet, B.; Vivier, V.; Frateur, I.; Musiani, M. Constant-Phase-Element Behavior Caused by Resistivity Distributions in Films: I. Theory. *J. Electrochem. Soc.* **2010**, *157*, C452. [CrossRef]

29. Hirschorn, B.; Orazem, M.E.; Tribollet, B.; Vivier, V.; Frateur, I.; Musiani, M. Determination of effective capacitance and film thickness from constant-phase-element parameters. *Electrochim. Acta* **2010**, *55*, 6218–6227. [CrossRef]

30. Xue, Y.; Pang, X.; Jiang, B.; Jahed, H. Corrosion and corrosion fatigue performances of micro-arc oxidation coating on AZ31B cast magnesium alloy. *Mater. Corros.* **2018**, *70*, 268–280. [CrossRef]

31. Long, Y.; Wu, L.; Zhang, Z.; Atrens, A.; Pan, F.; Tang, A.; Zhang, G. Enhanced Corrosion Resistance of Anodic Films Containing Alumina Nanoparticles on as-rolled AZ31 alloy. *Int. J. Electrochem. Sci.* **2018**, *13*, 7157–7174. [CrossRef]

32. Milo, I.; Durán, A.; Castro, Y. Hybrid sol–gel coatings based on GPTMS/TEOS containing colloidal SiO$_2$ and cerium nitrate for increasing corrosion protection of aluminium alloy 7075-T6. *Int. J. Electrochem. Sci.* **2018**, *85*, 546–557. [CrossRef]

33. Fidalgo, A.; Ilharco, L.M. The defect structure of sol-gel-derived silica/polytetrahydrofuran hybrid films by FTIR. *J. Non-Cryst. Solids* **2001**, *283*, 144–154. [CrossRef]

34. Sassi, Z.; Bureau, J.C.; Bakkali, A. Spectroscopic study of TMOS–TMSM–MMA gels: Previously identification of the networks inside the hybrid material. *Vib. Spectrosc.* **2002**, *28*, 299–318. [CrossRef]

Biocompatible Chitosan-Based Hydrogels for Bioabsorbable Wound Dressings

Ramona Lungu [1], Maria-Alexandra Paun [2,3], Dragos Peptanariu [1], Daniela Ailincai [1], Luminita Marin [1], Mihai-Virgil Nichita [4], Vladimir-Alexandru Paun [5] and Viorel-Puiu Paun [6,7,*]

1   "Petru Poni" Institute of Macromolecular Chemistry, Gr. Ghica Voda Alley, 41A, 700487 Iasi, Romania; lungu.ramona@icmpp.ro (R.L.); peptanariu.dragos@icmpp.ro (D.P.); ailincai.daniela@icmpp.ro (D.A.); lmarin@icmpp.ro (L.M.)

2   School of Engineering, Swiss Federal Institute of Technology (EPFL), 1015 Lausanne, Switzerland; maria-alexandra.paun@epfl.ch or maria_paun2003@yahoo.com

3   Division Radio Monitoring and Equipment, Section Market Access and Conformity, Federal Office of Communications (OFCOM), 2501 Bienne, Switzerland

4   Doctoral School, Faculty of Applied Sciences, University Politehnica of Bucharest, 060042 Bucharest, Romania; mihai_nichita9@yahoo.com

5   Five Rescue Research Laboratory, 75004 Paris, France; vladimir.alexandru.paun@ieee.org

6   Physics Department, Faculty of Applied Sciences, University Politehnica of Bucharest, 060042 Bucharest, Romania

7   Academy of Romanian Scientists, 50085 Bucharest, Romania

*   Correspondence: viorel.paun@physics.pub.ro or viorel_paun2006@yahoo.com

Abstract: Supramolecular hydrogels based on chitosan and monoaldehydes are biomaterials with high potential for a multitude of bioapplications. This is due to the proper choice of the monoaldehyde that can tune the hydrogel properties for specific practices. In this conceptual framework, the present paper deals with the investigation of a hydrogel as bioabsorbable wound dressing. To this aim, chitosan was cross-linked with 2-formylphenylboronic acid to yield a hydrogel with antimicrobial activity. FTIR, NMR, and POM procedures have characterized the hydrogel from a structural and supramolecular point of view. At the same time, its biocompatibility and antimicrobial properties were also determined in vitro. Furthermore, in order to assess the bioabsorbable character, its biodegradation was investigated in vitro in the presence of lysosome in media of different pH, mimicking the wound exudate at different stages of healing. The biodegradation was monitored by gravimetrical measurements, SEM microscopy and fractal analyses of the images. The fractal dimension values and the lacunarity of SEM pictures were accurately calculated. All these successful investigations led to the conclusion that the tested materials are at the expected high standards.

Keywords: hydrogel; biocompatibility; antimicrobial activity; biodegradation; SEM image; fractal analysis

1. Introduction

Wounds are a major health concern when they occur on large skin portions as a result of injury or illness, such as burns, chronic skin ulcers, venous stasis, or diabetes mellitus [1–3]. Long wound healing periods increase the risk of side effects such as infections, which lead to disfigurements and permanent physical disabilities, affecting the mental and socioeconomic status of patients [4]. Thus, many researchers have focused their attention to find solutions for rapid wound closure and developing an aesthetically satisfactory scar. To this aim, strategies including antibacterial ointments, synthetic growth factors, polyurethanes, polymeric hydrogels, and fiber dressings have been developed over the years [5–8]. Polymeric hydrogels showed the advantage of supporting a hydrated environment, adsorbing excess fluids [9–11]. Among them, those based on polysaccharides demonstrated non-toxic, biodegradable, and biocompatible properties, providing a good

ability to improve the re-epithelization and acceleration of wound closure [12]. Chitosan biopolymer is a preferred polysaccharide to this aim, which demonstrated an acceleration of wound re-epithelialization due to its hemostasis potential and the stimulation of fibroblast proliferation, angiogenesis, regular collagen deposition, and the ability to favor the synthesis of natural hyaluronic acid (HA) at the wound site [13,14]. It was also reported that the healing ability is improved by the loading of antibacterial agents which prevent the bacterial invasion of wounds [15].

One major disadvantage of wound dressings is their adhesion to lesions, requiring mechanical debridement, which is damaging for the newly formed tissue and traumatic for the patient. To overcome this issue, the use of biodegradable chitosan for wound dressings is advantageous because it can be adsorbed into the skin during the re-epithelization process. Data in the literature show that during the healing period, the pH of wound exudate is a dynamic parameter, increasing from 8.5 to 10 in the first four days after the wound occurrence and decreasing slowly to 5.5 (the pH of the normal dermis) up to the total closure of wound [16]. However, even though a plethora of studies have been carried on chitosan-based materials, less attention has been directed to the influence of pH on their degradation.

In this light, the goal of this study was to investigate the biodegradation rate of a chitosan-based hydrogel as a function of the pH exudate over the wound healing period. To fulfill this objective, a chitosan-based hydrogel suitable for wound healing, exerting strong antimicrobial activity and excellent biocompatibility, was synthetized, and its enzymatic biodegradation rate as a pH function was monitored by gravimetrical measurements and SEM. A fractal theoretical application has been specially developed to support the quantitative investigation of SEM images and develop a better understanding of the biodegradation mechanism.

2. Experimental Investigation

2.1. Materials

Low-molecular-weight chitosan (178 kDa calculated by viscosimetry and a degree of deacetylation of 85% calculated from ^{1}H-NMR [17]), 2-formyl-phenyl-boronic acid (**2FPBA**) (95%), glacial acetic acid, sodium hydroxide and lysozyme 40,000 U/mL were purchased from Sigma-Aldrich and used without further purification. Phosphate-buffered solution (PBS), pH 7.4, was prepared in our laboratory, and the pH was further varied using small amounts of sodium hydroxide or glacial acetic acid.

2.2. Synthesis of the Hydrogel

The studied hydrogel has been synthetized reacting the chitosan with 2-formyl-phenyl-boronic acid in homogeneous medium by an acid condensation reaction, as follows: 60 mg of chitosan was added to 2 mL of 0.7% acetic acid aqueous solution, and stirred for 30 min at room temperature, up to chitosan's complete dissolution. Furthermore, the chitosan solution was heated up to 55 °C, and then a 1 mL solution of 2-formylphenyl boronic acid in water (2.3%, *w/v*) was slowly dropwise under vigorous magnetic stirring (1500 rot/min). In less than 10 min, the reaction mixture transformed into a soft material, which passed the inverted tube test, indicating the formation of hydrogel. The hydrogel was kept at 55 °C, without stirring, for 3 h, in order to facilitate the shifting of the imination equilibrium to the products.

2.3. Equipment and Methods

The *freeze-drying* was performed with a LABCONCO FreeZone Freeze Dry System, at −50 °C, 1.510 mbar, for 24 h, after previously freezing in liquid nitrogen.

ATR-FTIR spectra were registered with a Bruker Vertex 70 Ettlingen FTIR spectrometer (Billerica, MA, USA), on pieces of lyophilized hydrogel. The spectrum was recorded in the 600–4000 cm^{-1} spectral range, with 32 scans at 4 cm^{-1} resolution, and processed with OPUS 6.5 software and OriginProBit9.

¹H-NMR spectra were recorded on a Bruker Avance DRX 400 MHz Spectrometer (Billerica, MA, USA), at room temperature. To this aim, the hydrogel was prepared directly into the NMR tube, replacing the bi-distilled water with deuterated water. The spectrum was recorded at different moments, starting with the initial moment (t0) when the hydrogelation occurred up, to 72 h. The chemical shifts are reported as δ values (ppm) relative to the residual peak of deuterated water.

Polarized optical microscopy images were acquired with a Zeiss Axio Imager M2 microscope (Zeiss, Wetzlar, Germany) on hydrogels and xerogels. The changes in the hydrogel morphology were monitored with a field-emission scanning electron microscope, SEM EDAX-Quanta 200 (Waltham, MA, USA), operating at an acceleration voltage of 20 keV.

Cytotoxicity of the hydrogel was assessed on normal human dermal fibroblasts (NHDF, PromoCell, Heidelberg, Germany) by MTS assay using the CellTiter 96® AQueous One Solution Cell Proliferation Assay (Promega, Madison, WI, USA), according to the manufacturer's instructions, and a direct contact procedure, according to ISO 10993-5:2009(E), for the biologic evaluation of medical devices [17]. First, the cells were grown in alpha-MEM (Lonza, Basel, Switzerland) supplemented with 10% fetal bovine serum (FBS, Gibco, Thermo Fisher Scientific, Waltham, MA, USA) and 1% penicillin–streptomycin–amphotericin B mixture (10 K/10 K/25 μg, Lonza, Basel, Switzerland) in a humidified atmosphere with 5% CO_2 at 37 °C. Furthermore, the cells were seeded at a density of 0.5×10^5 cells/mL into 96-well tissue-culture-treated plates in 100 μL culture medium/well and allowed to adhere for 24 h. Cells were then incubated for another 24 h with 100 μL culture medium and 10 (±0.01) mg of hydrogel sample was obtained by serial dilution to reach concentrations of 2FPBA from 0.284% to 0.004438%. Before incubating, the hydrogel samples were exposed to UV light (253.7 nm) for 30 min. Control cells were incubated only with culture medium. The next day, the medium in the wells containing the tested materials was replaced with 100 μL fresh medium and MTS reagent (20 μL) was added 3 h prior to absorbance readings at 490 nm on a microplate reader (EnSight, PerkinElmer, Rodgau, Germany). Experiments were performed in triplicate and the viability of the cells when in contact with hydrogel samples was expressed as a percentage of the control cells' viability. Graphical data are expressed as the means ± standard error of the mean.

Antimicrobial tests were performed on pieces of hydrogels against three reference strains: *Escherichia coli* ATCC 25922, *Staphylococcus aureus* ATCC 6583 and *Candida albicans* ATCC 10231 [18]. Shortly, the hydrogel films were put into contact with the pathogen and their growth inhibition was measured using a caliper.

2.4. Enzymatic Biodegradation Tests

Pieces of hydrogels weighting from 147 mg to 258 mg (corresponding to 4–7 mg xerogel) were incubated in lysozyme solution (376 U/mL) in saline PBS of different pH values (5.5, 7.4, 8.5, 9 and 10) or lysozyme solution (4830 U/mL) in saline PBS of pH = 8.5, at a xerogel/media ratio of 1 mg/1 mL. In order to monitor the hydrolytic degradability, one sample was immersed in a PBS solution of pH 8.5, without adding lysozyme. At different moments relevant for wound healing—1 h and 1, 3, 7 and 14 days—the hydrogel pieces were taken from the media, washed with distilled water in order to remove the salts from PBS, lyophilized, and weighted with an analytical balance in order to establish the mass loss, applying the equation: $mass\ loss = \frac{mi-mf}{mf} \times 100$, where m_i is the weight of the initial xerogel and m_f is the weight of the lyophilized hydrogel at different moments of investigation. The experiments were performed in triplicate, and the results are expressed in terms of the mass loss ± S.D. obtained from the three independent measurements. All the samples resulted from the experiment were subjected to SEM in order to analyze the changes impacted by biodegradation.

3. Results and Discussion

3.1. Structural and Supramolecular Characterization

An antimicrobial hydrogel was synthetized by the acid condensation reaction of chitosan with 2-formyl-phenyl-boronic acid in water (Figure 1), in view of investigating its biodegradability depending on pH, following the evolution of the pH exudate over the wound healing period. This hydrogel has been designed in view of applications for wound healing; thus, compared with the reported data [19], the synthetic procedure has been modified, i.e., the reaction was realized in a water biodispersant, avoiding the use of other organic solvents. The hydrogel state was confirmed by the inverted tube test (Figure 1).
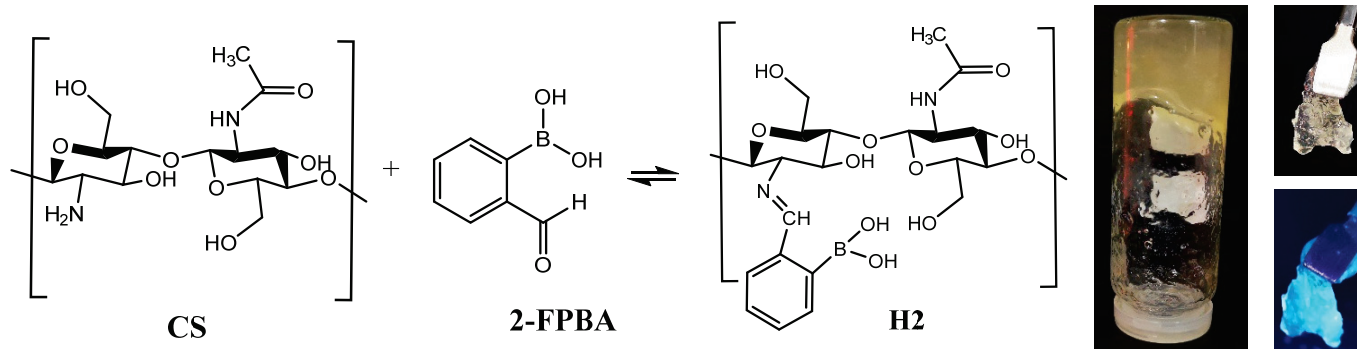
Figure 1. Imination reaction of chitosan with 2-formyl-phenyl-boronic acid and images of the obtained hydrogel, in normal light and when illuminated with a UV lamp.

The structure and supramolecular architecture of the hydrogel were investigated by ^{1}H-NMR, FTIR, and polarized light microscopy. As can be seen in Figure 2, ^{1}H-NMR of the hydrogel showed both chemical shifts of imine and aldehyde protons, indicating that an imination equilibrium was established during the hydrogelation. Their ratio evolved over the hydrogelation period, according to an imination degree of 18.9% in the first few minutes, to 26.1% after one hour.
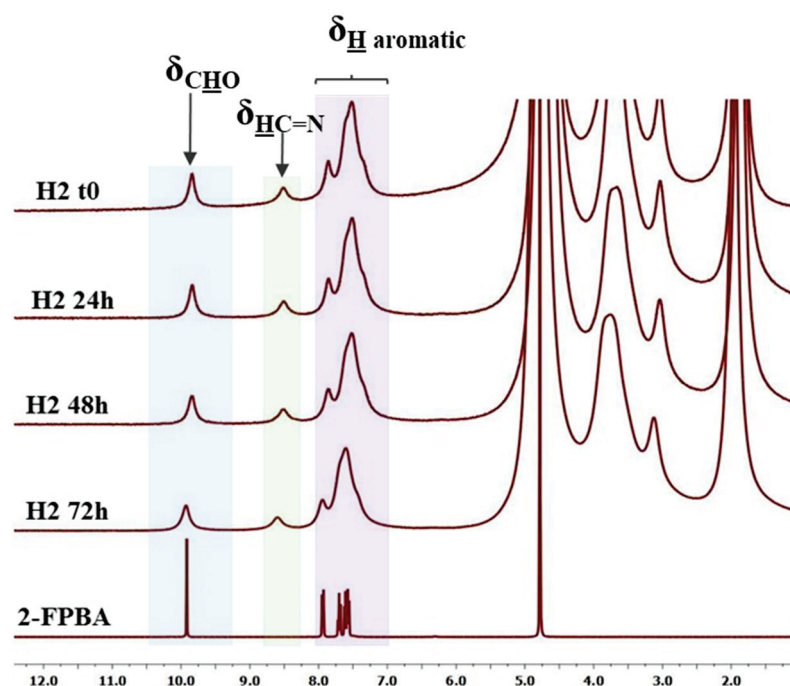
Figure 2. ^{1}H-NMR spectra of the hydrogel during hydrogelation, from hydrogel occurrence (t0) to 72 h, compared with the **2-FPBA** reference.

On the other hand, the FTIR spectrum on the corresponding lyophilized hydrogel showed the occurrence of the absorption band characteristic for the imine linkage at 1628 cm^{-1} [18–22] and no band specific for the aldehyde group [22–24], proving that the imination equilibrium was shifted to the products during the water removal process (Figure 3). This confirmed that the imination was a reversible process, which could be modified under the influence of external stimuli. In addition, the broad band characteristic for the vibration of hydroxyl and amine units in chitosan and the H-bonds prompted by them with the maxima at 3357 and 3300 cm^{-1}, and that characteristic to hydroxyl units in aldehyde and the H-bonds prompted by them with the maximum at 3353 cm^{-1}, shifted at higher wavenumbers in the hydrogel product (3403 cm^{-1}), indicating the formation of a new H-bond environment [18,19]. Considering the structure of the chitosan and **2-FPBA** reagents and the imine product which resulted between them, it was estimated that the new H-bonds derived from the intermolecular interactions among the hydroxyl units of **2-FPBA** and the amine and hydroxyl units of chitosan on one hand, derived and from the intra- and intermolecular interactions between the hydroxyl groups and the nitrogen atom of the new imine units on the other hand. The stabilization of imine units by imino-boronate bonds [25] by "imine-clip" stabilization [26–28] is possible too.
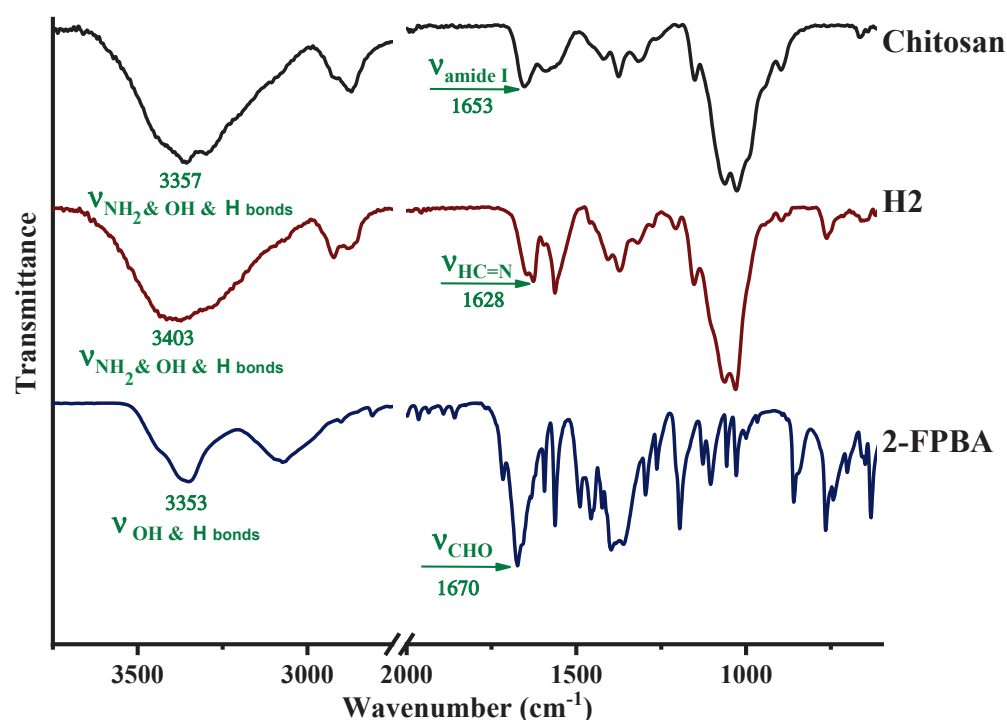
Figure 3. FTIR spectra of the lyophilized hydrogel compared with chitosan and **2-FPBA** references.

POM images of the hydrogel showed bright birefringence with a banded texture identified for layered supramolecular architectures, proving that the new formed imine units self-ordered during the hydrogelation into a layered architecture pattern, similar to lyotropic liquid crystals (Figure 4) [29,30]. Furthermore, the hydrogel showed an emission of blue light when illuminated with a UV lamp (Figure 1), in line with the formation of supramolecular fluorophores [26]. This is in agreement with our previous studies, which proved that the hydrogelation of chitosan with monoaldehydes is possible due to an imination reaction followed by the self-assembly of the newly formed imine units into layered clusters playing the role of crosslinking nodes [26,30].

(**a**)   (**b**)
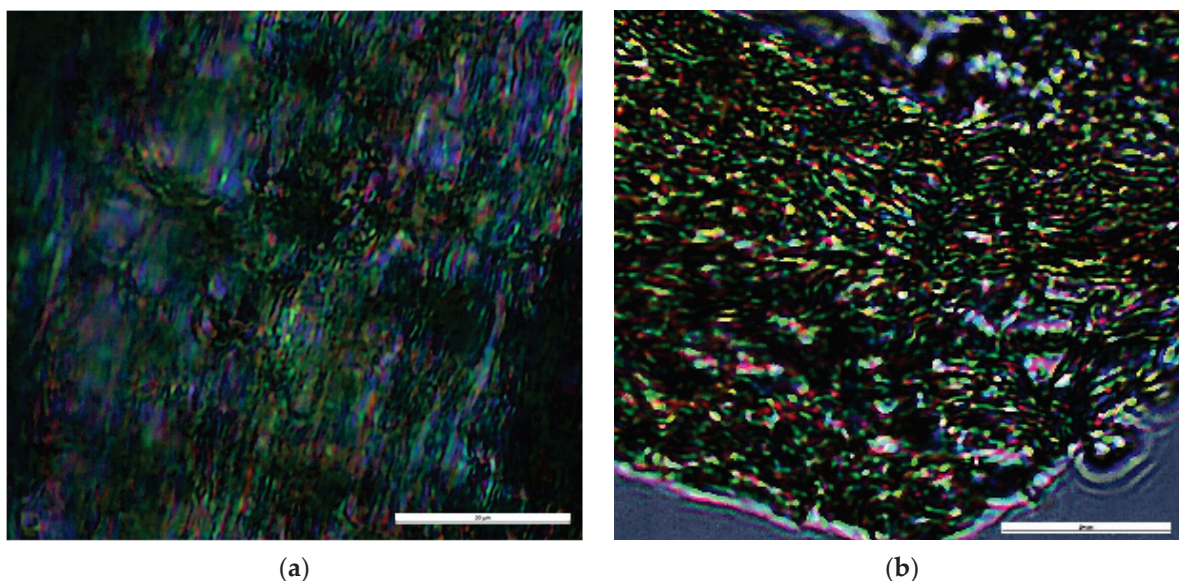
Figure 4. Images of the hydrogel under polarized light (scale bar: 20 μm), acquired on (**a**) thick and (**b**) thin sample of hydrogel.

3.2. In Vitro Biologic Properties

This hydrogel was designed for wound healing; therefore, its cytotoxicity against normal human dermal fibroblasts (NHDF) was investigated in order to establish the **2-FPBA** level for which the hydrogels can be safely used in contact with tissues (Figure 5). To do this, the hydrogel was diluted to rich concentrations of **2-FPBA** in hydrogel from 0.284 up to 0.004438%. As can be seen, except for the concentration of 0.284%, the hydrogels showed cell viability higher than 70% which, according to ISO 10993-5:2009(E) for the biologic evaluation of medical devices, indicates that they can be safely used in bioapplications [17].
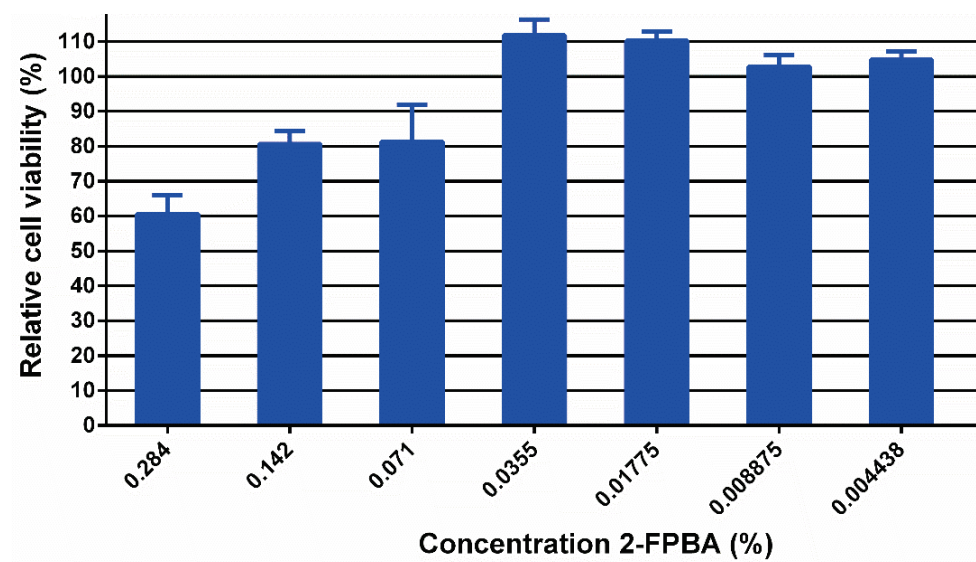
Figure 5. Cytotoxicity tests of hydrogels on normal human dermal fibroblasts.

It should be stressed that the hydrogel showed strong antimicrobial activity against relevant pathogens, reaching inhibition zones of 9 mm (*S. aureus*), 15 mm (*E. coli*) and 17 mm (*C. albicans*) [18]. Moreover, for the 2FPBA concentration of 0.142% in hydrogel, the antifungal effect recorded a microbial burden reduction of 99.999% against the Candida species in 24 h, proving that, for this concentration, the hydrogels can successfully be applied on wounds to assure complete protection against infections [19]. The antimicrobial

activity has been correlated with the reversibility of the imination, which favored the equilibrium shifting to the reagents once they were consumed in the pathogen killing process [18,19].

3.3. Biodegradation Investigation

In this line of thought, the rational question arising is to what extent the hydrogels can be applied on wounds without the need for traumatic debridement, while they are an active barrier against microbial infections. In this view, a biodegradation experiment was performed in media of different pH values, corresponding to that of pH exudate over the wound healing period. The results are presented in Figure 6. First, the clear influence of lysozyme on biodegradation can be seen, a mass loss up to 45% being reached compared with 17% in its absence. Furthermore, it is observed that the pH of the lysozyme medium clearly influenced the biodegradation rate. Thus, whereas in the medium of pH = 7.4 characteristic to the physiological environment the mass loss was 32%, in that of pH = 8.5 and 9, characteristic to the exudate of wounds in the first 4 days of healing, the mass loss increased to 42% and 45%, respectively. This is particularly important because this pH is favorable for the proliferation of infection [31] and faster biodegradation of the hydrogel indicates the faster release of the antimicrobial aldehyde assuring a self-defense environment. Interestingly, at pH 10, (characteristic for day 4 of the healing period), the biodegradation rate slowed down, reaching a mass loss of 30%. The increase in lysosome concentration, representative of infected tissues, inflicted a slightly increase in degradation, leading to a mass loss 43%. On the other hand, at pH = 5.5, which is characteristic for the normal dermis [32], the biodegradation abruptly amplified, leading to a mass loss of 75% in the first day, and totally vanishing by day 2. This suggests that the hydrogel will be rapidly adsorbed into the newly formed tissue, with no need for a traumatic debridement, favoring smooth tissue regeneration without trauma. This suggests wound healing without scars.
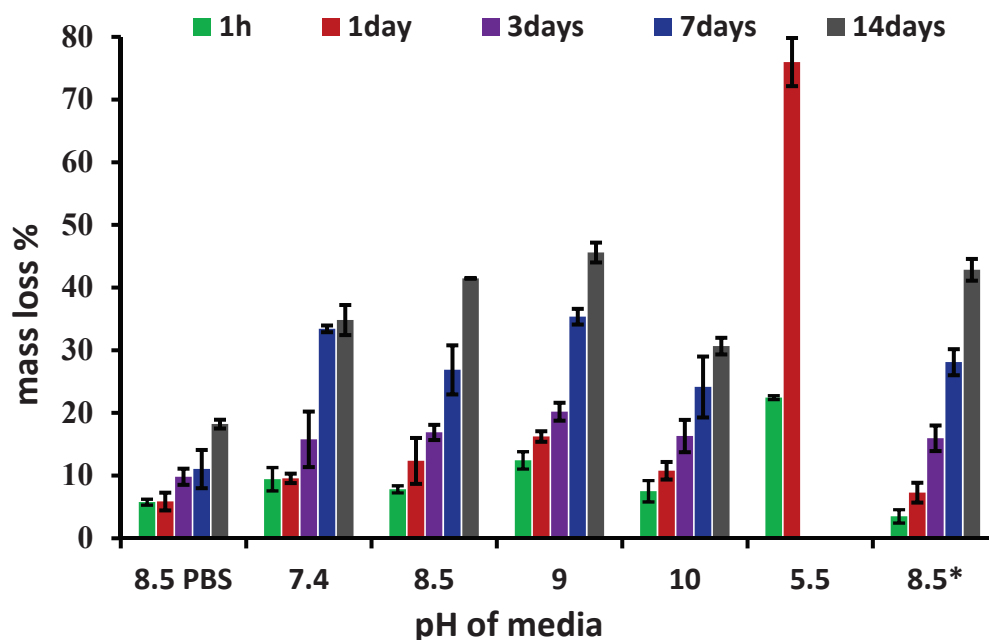
Figure 6. The mass loss of hydrogel over 14 days, in lysozyme media (376 U/mL) of different pH (* indicates a lysozyme concentration of 4830 U/mL; 8.5PBS indicates the absence of lysozyme).

The evolution of the hydrogel morphology during the degradation was investigated by SEM (Figure 7).
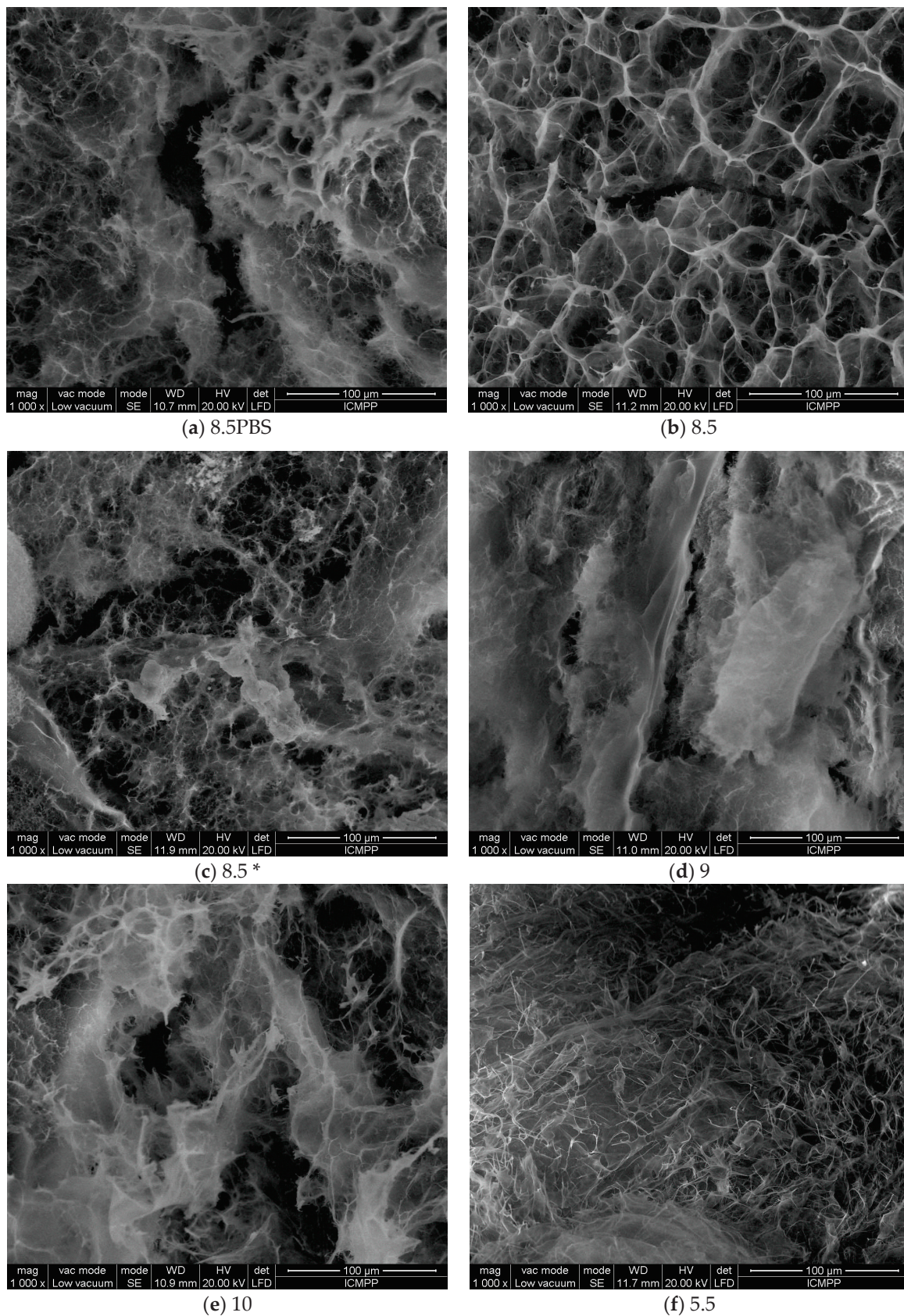
Figure 7. The morphology of the hydrogel after the enzymatic biodegradation over 14 days at different pH (**a**–**e**) and after the first day of biodegradation in medium of pH = 5.5 (**f**). (* indicates a lysozyme concentration of 4830 U/mL; 8.5PBS indicates the absence of lysozyme).

In PBS, without enzyme, the pores of hydrogel appeared collapsed, and ruptures occurred, in line with the release of the aldehyde and partial dissolution of the chitosan. Interestingly, no such effect was observed at pH = 8.5 in the presence of a lysozyme concentration characteristic to the non-infected wounds in the first minutes after wound occurrence; the morphology appeared less affected. On the other hand, at pH = 9.5 and 10, characteristic to a wound exudate over the healing period of the first four days, which is determinant for the evolution of wound to a complete recovery of tissue, the hydrogel showed a loose morphology, in agreement with the massive mass loss. Furthermore, at pH = 5.5, characteristic for the normal dermis, massive biodegradation was evident, with the hydrogel morphology transforming into a fibrous one, suitable for tissue regeneration.

3.4. Application Results of Fractal and Lacunar Analysis Algorithms

Fractal geometry is the mathematical completion that Euclidean geometry and crystalline (or quasi-crystalline) symmetry were lacking. Fractal analysis, which is the main vein/lode exploited with this new way of thinking, works with two basic notions, namely, fractal size and lacunarity.

The fractal dimension alone does not characterize the object studied from a fractal point of view. There are many sets (mathematical objects) that have the same fractal dimension but a completely different spatial structure. Thus, two sets of Cantor type have the same fractal dimension, but differ in their lacunarity, another characteristic which is required, not only intuited, but also clearly defined.

Fractal analysis uses this term, respective lacunarity, to describe the uniformity of texture in images. It can also characterize the size of a space, the homogeneity of objects, and the rotational and translational invariance of an image.

A low gap coefficient refers to a homogeneity, defined as low (or reduced) lacunarity, which implies gaps of similar size and low rotation variance. On the other hand, a high coefficient of gaps refers to heterogeneity, defined as a large (or high) lacunarity, which implies a larger number of gaps.

The SEM images of Figure 7, indicated by the abbreviation 8.5PBS (image A), 8.5 (image B) and 8.5 × (image C) were investigated by fractal analysis [33–36] in Figures 8–10. The abbreviation 8.5PBS indicates the absence of lysozyme. In our images, we used a magnitude of 1000×.

The pictures were preprocessed in order to optimize the binary process (the luminance was removed from the original image). Binarization involved setting a threshold according to which the pixels (gray levels in the image) were set to 0 or 1 (55 for the first image, 60 for the second, and 57 for the third).

For image A, we determined the following values obtained by applying the fractal analysis procedure: the fractal dimension d = 1.9131 with a standard deviation of ± 0.10211 and lacunarity $\lambda = 0.5995$.

For image B, we determined the following values obtained by applying the fractal analysis procedure: the fractal dimension d = 1.9171 with a standard deviation of ± 0.10422 and lacunarity $\lambda = 0.6581$.

For image C, we determined the following values obtained by applying the fractal analysis procedure: the fractal dimension d = 1.9213 with a standard deviation of ± 0.10675 and lacunarity $\lambda = 0.6069$.

(**a**)

(**b**)

(**c**)

(**d**)

(**e**)

(**f**)

Figure 8. Fractal investigation of image A: (**a**) Black and white version of image A, (**b**) Grayscale version extracted from the background, (**c**) Grayscale version with luminance, (**d**) Binary version, (**e**) Box-count representation, (**f**) Voxel representation.

(**a**)

(**b**)

(**c**)

(**d**)

(**e**)

(**f**)

Figure 9. Fractal investigation of image B: (**a**) Black and white version of image B, (**b**) Grayscale version extracted from the background, (**c**) Grayscale version with luminance, (**d**) Binary version, (**e**) Box-count representation, (**f**) Voxel representation.

(**a**)

(**b**)

(**c**)

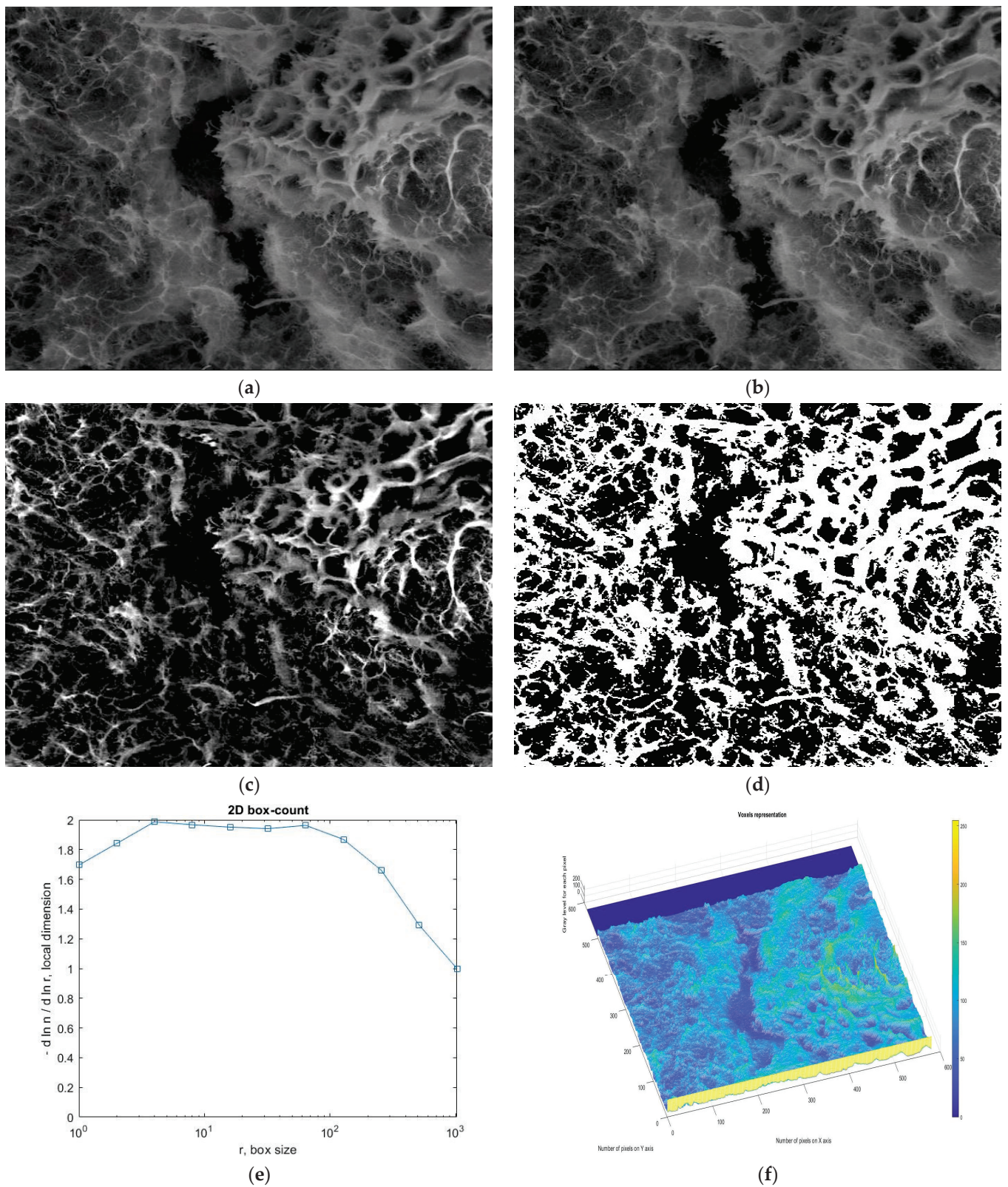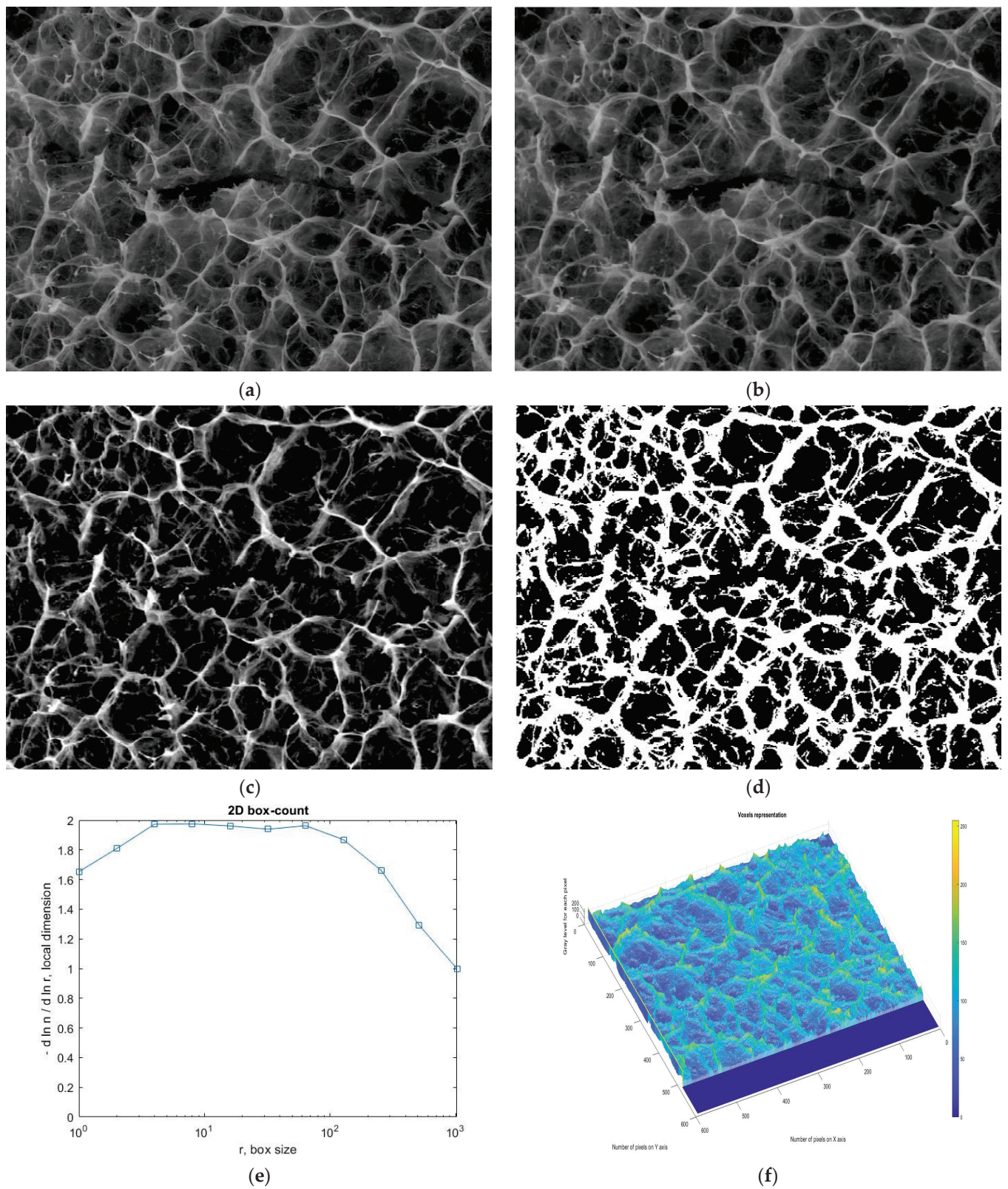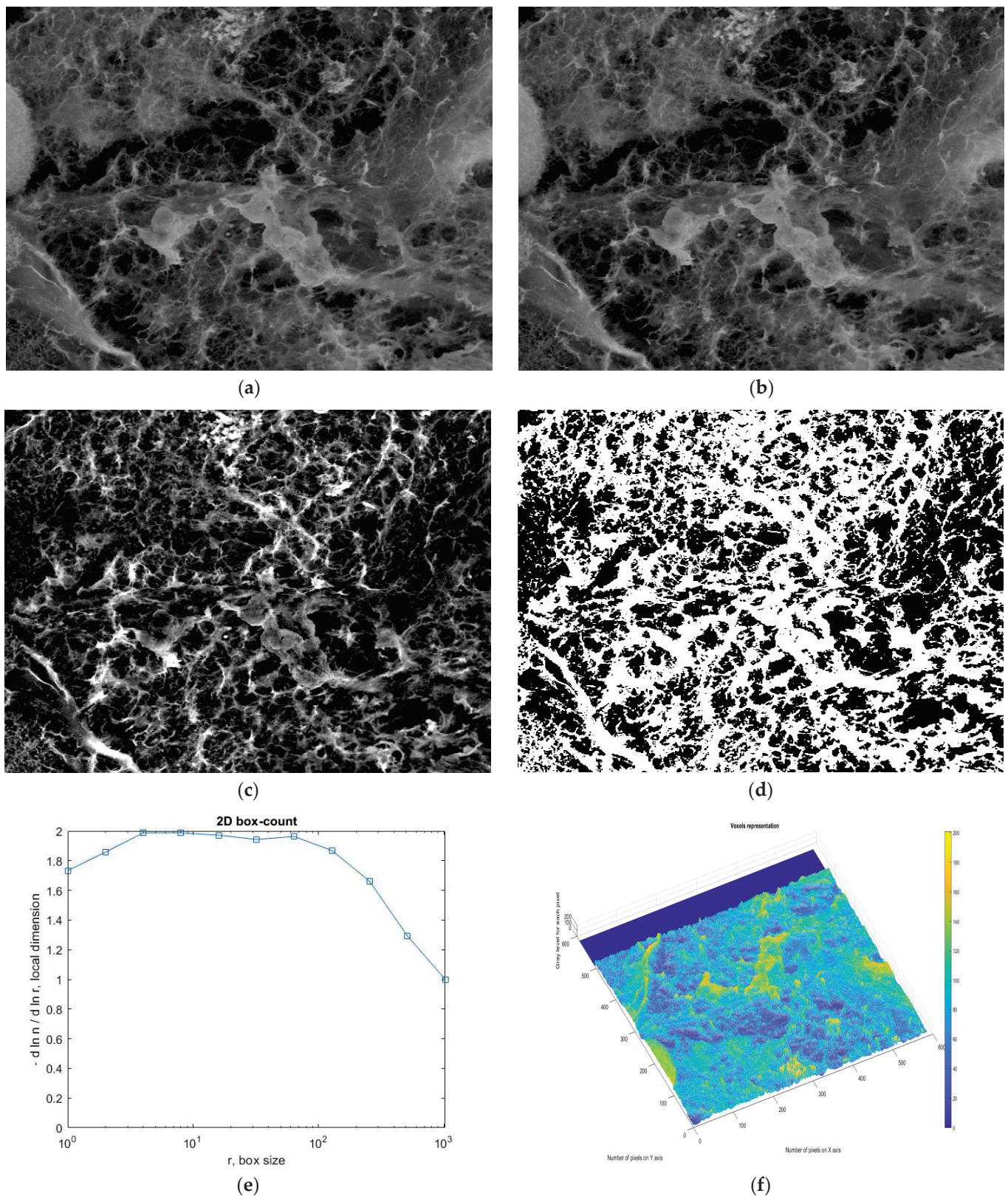(**d**)

(**e**)

(**f**)

Figure 10. Fractal investigation of image C: (**a**) Black and white version of image C, (**b**) Grayscale version extracted from the background, (**c**) Grayscale version with luminance, (**d**) Binary version, (**e**) Box-count representation, (**f**) Voxel representation.

4. Conclusions

A chitosan-based hydrogel with biocompatibility and antimicrobial properties suitable for wound healing has been synthetized by an acid condensation reaction with 2-forml-phenyl-boronic acid to yield imine units and their supramolecular ordering into ordered clusters with the role of crosslinking nodes.

The hydrogel proved to have a lack of toxicity against normal dermal human fibroblasts and antimicrobial activity against relevant pathogens, such as *E. coli*, *S. aureus* and *C. albicans*. The investigation of the hydrogel biodegradation as a function of the pH of the wound exudate over the healing period demonstrated that the biodegradation rate is modulated by pH over the healing period, and is favorable to re-epithelization and avoiding traumatic debridement.

The topographic assessments of SEM images of the hydrogels degraded in lysozyme media of different pH, based on the evaluation by fractal analysis, showed that the evolution of the values of fractal dimension and lacunarity ($d = 1.9131 \pm 0.10211$ and lacunarity $\lambda = 0.5995$ for image A, fractal dimension $d = 1.9171 \pm 0.10422$ and lacunarity $\lambda = 0.6581$ for image B and fractal dimension $d = 1.9213 \pm 0.10675$ and lacunarity $\lambda = 0.6069$ for image C) fitted well on the values of mass loss, confirming once more that the biodegradation rate is modulated by pH.

Author Contributions: Conceptualization, L.M. and V.-P.P.; methodology, L.M., M.-A.P. and D.P.; software, D.A., M.-V.N. and V.-A.P.; validation, L.M., V.-P.P. and D.A.; formal analysis, L.M. and D.A.; investigation, R.L., D.P., D.A. and M.-A.P.; resources, L.M.; data curation, D.A., L.M. and M.-A.P.; writing—original draft preparation, R.L., L.M. and V.-P.P.; writing—review and editing, L.M. and V.-P.P.; visualization, V.-A.P. and M.-V.N.; supervision, L.M. and V.-P.P.; project administration, L.M.; funding acquisition, L.M. All authors have read and agreed to the published version of the manuscript.

Institutional Review Board Statement: Not applicable.

Informed Consent Statement: Not applicable.

Data Availability Statement: The data used to support the findings of this study cannot be accessed due to commercial confidentiality.

Conflicts of Interest: The authors declare no conflict of interest.

References

1. Gurtner, G.C.; Werner, S.; Barrandon, Y.; Longaker, M.T. Wound repair and regeneration. *Nature* **2008**, *453*, 314–321. [CrossRef] [PubMed]
2. Shpichka, A.; Butnaru, D.; Bezrukov, E.A.; Sukhanov, R.B.; Atala, A.; Burdukovskii, V.; Zhang, Y.; Timashev, P. Skin tissue regeneration for burn injury. *Stem Cell Res. Ther.* **2019**, *10*, 94. [CrossRef] [PubMed]
3. Hall, A.H.; Mathieu, L.; Maibach, H.I. Acute chemical skin injuries in the United States: A review. *Crit. Rev. Toxicol.* **2018**, *48*, 540–554. [CrossRef] [PubMed]
4. Sani, H.; Lenghoven, D. Permanent physical disfigurement and disability due to burns injury: Case series. *Int. J. Hum. Health Sci.* **2020**, *4*, 319–321. [CrossRef]
5. Yazarlu, O.; Iranshahi, M.; Kashani, H.R.K.; Reshadat, S.; Habtemariam, S.; Iranshahy, M.; Hasanpour, M. Perspective on the application of medicinal plants and natural products in wound healing: A mechanistic review. *Pharmacol. Res.* **2021**, *174*, 105841. [CrossRef] [PubMed]
6. Ghandforoushan, P.; Golafshan, N.; Kadumudi, F.B.; Castilho, M.; Dolatshahi-Pirouz, A.; Orive, G. Injectable and adhesive hydrogels for dealing with wounds. *Expert Opin. Biol. Ther.* 2022; *accepted/in press*. [CrossRef] [PubMed]
7. Anisiei, A.; Oancea, F.; Marin, L. Electrospinning of chitosan-based nanofibers: From design to prospective applications. *Rev. Chem. Eng.* **2020**, *3*, 325–336. [CrossRef]
8. Kamińska, M.; Cybulska, A.; Skonieczna-Żydecka, K.; Augustyniuk, K.; Grochans, E.; Karakiewicz, B. Effectiveness of Hydrocolloid Dressings for Treating Pressure Ulcers in Adult Patients: A Systematic Review and Meta-Analysis. *Int. J. Environ. Res. Public Health* **2020**, *17*, 7881. [CrossRef]
9. Fan, F.; Saha, S.; Hanjaya-Putra, D. Biomimetic Hydrogels to Promote Wound Healing. *Front. Bioeng. Biotechnol.* **2021**, *9*. [CrossRef]

10. Savencu, I.; Iurian, S.; Porfire, A.; Bogdan, C.; Tomuță, I. Review of advances in polymeric wound dressing films. *React. Funct. Polym.* **2021**, *168*, 105059. [CrossRef]

11. Duceac, I.A.; Verestiuc, L.; Dimitriu, C.D.; Maier, V.; Coseri, S. Design and Preparation of New Multifunctional Hydrogels Based on Chitosan/Acrylic Polymers for Drug Delivery and Wound Dressing Applications. *Polymers* **2020**, *12*, 1473. [CrossRef] [PubMed]

12. Albuquerque, P.B.S.; de Oliveira, W.F.; Silva, P.M.D.S.; Correia, M.T.D.S.; Kennedy, J.F.; Coelho, L.C.B.B. Skincare application of medicinal plant polysaccharides—A review. *Carbohydr. Polym.* **2021**, *277*, 118824. [CrossRef] [PubMed]

13. Liu, H.; Wang, C.; Li, C.; Qin, Y.; Wang, Z.; Yang, F.; Li, Z.; Wang, J. A functional chitosan-based hydrogel as a wound dressing and drug delivery system in the treatment of wound healing. *RSC Adv.* **2018**, *8*, 7533–7549. [CrossRef]

14. Alven, S.; Aderibigbe, B.A. Chitosan and Cellulose-Based Hydrogels for Wound Management. *Int. J. Mol. Sci.* **2020**, *21*, 9656. [CrossRef] [PubMed]

15. Golmohammadi, R.; Najar-Peerayeh, S.; Moghadam, T.T.; Hosseini, S.M.J. Synergistic Antibacterial Activity and Wound Healing Properties of Selenium-Chitosan-Mupirocin Nanohybrid System: An in Vivo Study on Rat Diabetic Staphylococcus aureus Wound Infection Model. *Sci. Rep.* **2020**, *10*, 2854. [CrossRef]

16. Ono, S.; Imai, R.; Ida, Y.; Shibata, D.; Komiya, T.; Matsumura, H. Increased wound pH as an indicator of local wound infection in second degree burns. *Burns* **2015**, *41*, 820–824. [CrossRef]

17. Andreica, B.-I.; Ailincai, D.; Sandu, A.-I.; Marin, L. Amphiphilic chitosan-g-poly(trimethylene carbonate)—A new approach for biomaterials design. *Int. J. Biol. Macromol.* **2021**, *193*, 414–424. [CrossRef]

18. Marin, L.; Ailincai, D.; Mares, M.; Paslaru, E.; Cristea, M.; Nica, V.; Simionescu, B.C. Imino-chitosan biopolymeric films. Obtaining, self-assembling, surface and antimicrobial properties. *Carbohydr. Polym.* **2015**, *117*, 762–770. [CrossRef]

19. Ailincai, D.; Marin, L.; Morariu, S.; Mares, M.; Bostanaru, A.-C.; Pinteala, M.; Simionescu, B.C.; Barboiu, M. Dual crosslinked iminoboronate-chitosan hydrogels with strong antifungal activity against Candida planktonic yeasts and biofilms. *Carbohydr. Polym.* **2016**, *152*, 306–316. [CrossRef]

20. Lungu, R.; Anisiei, A.; Rosca, I.; Sandu, A.-I.; Ailincai, D.; Marin, L. Double functionalization of chitosan based nanofibers towards biomaterials for wound healing. *React. Funct. Polym.* **2021**, *167*, 105028. [CrossRef]

21. Anisiei, A.; Bostanaru, A.-C.; Mares, M.; Marin, L. Imination of chitosan nanofibers in a heterogeneous system. Synthesis optimization and impact on fiber morphology. *Cellul. Chem. Technol.* **2021**, *55*, 785–793. [CrossRef]

22. Anisiei, A.; Rosca, I.; Sandu, A.-I.; Bele, A.; Cheng, X.; Marin, L. Imination of Microporous Chitosan Fibers—A Route to Biomaterials with "On Demand" Antimicrobial Activity and Biodegradation for Wound Dressings. *Pharmaceutics* **2022**, *14*, 117. [CrossRef] [PubMed]

23. Satapathy, S.; Prabakaran, P.; Prasad, E.; Satapathy, S. Augmenting Photoinduced Charge Transport in a Single-Component Gel System: Controlled In Situ Gel-Crystal Transformation at Room Temperature. *Chem.—A Eur. J.* **2018**, *24*, 6217–6230. [CrossRef] [PubMed]

24. Satapathy, S.; Prasad, E. Charge Transfer Modulated Self-Assembly in Poly(aryl ether) Dendron Derivatives with Improved Stability and Transport Characteristics. *ACS Appl. Mater. Interfaces* **2016**, *8*, 26176–26189. [CrossRef] [PubMed]

25. Adamczyk-Woźniak, A.; Cyrański, M.K.; Frączak, B.T.; Lewandowska, A.; Madura, I.D.; Sporzyński, A. Imino- and aminomethylphenylboronic acids: Stabilizing effect of hydrogen bonds. *Tetrahedron* **2012**, *68*, 3761–3767. [CrossRef]

26. Iftime, M.-M.; Morariu, S.; Marin, L. Salicyl-imine-chitosan hydrogels: Supramolecular architecturing as a cross-linking method toward multifunctional hydrogels. *Carbohydr. Polym.* **2017**, *165*, 39–50. [CrossRef]

27. Bratskaya, S.; Privar, Y.; Skatova, A.; Slobodyuk, A.; Kantemirova, E.; Pestov, A. Carboxyalkylchitosan-based hy-drogels with "imine clip": Enhanced stability and amino acids-induced disassembly under physiological condi-tions. *Carbohydr. Polym.* **2021**, *274*, 118618. [CrossRef]

28. Bratskaya, S.; Skatova, A.; Privar, Y.; Boroda, A.; Kantemirova, E.; Maiorova, M.; Pestov, A. Stimuli-Responsive Dual Cross-Linked *N*-Carboxyethylchitosan Hydrogels with Tunable Dissolution Rate. *Gels* **2021**, *7*, 188. [CrossRef]

29. Dierking, I.; Al-Zangana, S. Lyotropic Liquid Crystal Phases from Anisotropic Nanomaterials. *Nanomaterials* **2017**, *7*, 305. [CrossRef]

30. Marin, L.; Popa, M.; Anisiei, A.; Irimiciuc, S.-A.; Agop, M.; Petrescu, T.-C.; Vasincu, D.; Himiniuc, L. A Theoretical Model for Release Dynamics of an Antifungal Agent Covalently Bonded to the Chitosan. *Molecules* **2021**, *26*, 2089. [CrossRef]

31. Rippke, F.; Berardesca, E.; Weber, T.M. pH and Microbial Infections. *Immunodefic. Skin* **2018**, *54*, 87–94.

32. Kuo, S.-H.; Shen, C.-F.; Cheng, C.-M. Role of pH Value in Clinically Relevant Diagnosis. *Diagnosis* **2020**, *10*, 107. [CrossRef] [PubMed]

33. Karperien, A.L.; Jelinek, H.F. Box-Counting Fractal Analysis: A Primer for the Clinician. In *Springer Series in Computational Neuroscience*; Springer Science & Business Media: Berlin/Heidelberg, Germany, 2016; pp. 13–43.

34. Karperien, A.; Jelinek, H.F.; Milošević, N.T. Reviewing Lacunarity Analysis and Classification of Microglia in Neuroscience. In Proceedings of the 8th European Conference on Mathematical and Theoretical Biology, Kraków, Poland, 28 June–2 July 2011.

35. Nichita, M.V.; Paun, M.A.; Paun, V.A.; Paun, V.P. Fractal analysis of brain glial cells. Fractals dimension and lacunarity. *Univ. Politeh. Buchar. Sci. Bull. Ser. A Appl. Math. Phys.* **2019**, *81*, 273–284.

36. Bordescu, D.; Paun, M.A.; Paun, V.A.; Paun, V.P. Fractal analysis of Neuroimagistic. Lacunarity degree, a precious indicator in the detection of Alzheimer's disease. *Univ. Politeh. Buchar. Sci. Bull. Ser. A Appl. Math. Phys.* **2018**, *80*, 309–320.

Article

Analysis of Three-Dimensional Cell Migration in Dopamine-Modified Poly(aspartic acid)-Based Hydrogels

David Juriga [1,*], Eszter Eva Kalman [2,3], Krisztina Toth [1,3], Dora Barczikai [1], David Szöllősi [1], Anna Földes [3], Gabor Varga [3], Miklos Zrinyi [1], Angela Jedlovszky-Hajdu [1,†] and Krisztina S. Nagy [1,3,*,†]

[1]   Department of Biophysics and Radiation Biology, Semmelweis University, H-1089 Budapest, Hungary; toth.krisztina.105@gmail.com (K.T.); barczikai.dora@med.semmelweis-univ.hu (D.B.); szollosi.sote@gmail.com (D.S.); mikloszrinyi@gmail.com (M.Z.); hajdu.angela@med.semmelweis-univ.hu (A.J.-H.)

[2]   Department of Molecular Biology, Semmelweis University, H-1083 Budapest, Hungary; kalman.eszter@med.sememlweis-univ.hu

[3]   Department of Oral Biology, Semmelweis University, H-1089 Budapest, Hungary; foldes.anna@dent.semmelweis-univ.hu (A.F.); varga.gabor@dent.semmelweis-univ.hu (G.V.)

*   Correspondence: juriga.david@med.semmelweis-univ.hu (D.J.); nagy.krisztina@dent.semmelweis-univ.hu (K.S.N.)

†   These authors contributed equally to this work.

Abstract: Several types of promising cell-based therapies for tissue regeneration have been developing worldwide. However, for successful therapeutical application of cells in this field, appropriate scaffolds are also required. Recently, the research for suitable scaffolds has been focusing on polymer hydrogels due to their similarity to the extracellular matrix. The main limitation regarding amino acid-based hydrogels is their difficult and expensive preparation, which can be avoided by using poly(aspartamide) (PASP)-based hydrogels. PASP-based materials can be chemically modified with various bioactive molecules for the final application purpose. In this study, dopamine containing PASP-based scaffolds is investigated, since dopamine influences several cell biological processes, such as adhesion, migration, proliferation, and differentiation, according to the literature. Periodontal ligament cells (PDLCs) of neuroectodermal origin and SH-SY5Y neuroblastoma cell line were used for the in vitro experiments. The chemical structure of the polymers and hydrogels was proved by ^{1}H-NMR and FTIR spectroscopy. Scanning electron microscopical (SEM) images confirmed the suitable pore size range of the hydrogels for cell migration. Cell viability assay was carried out according to a standardized protocol using the WST-1 reagent. To visualize three-dimensional cell distribution in the hydrogel matrix, two-photon microscopy was used. According to our results, dopamine containing PASP gels can facilitate vertical cell penetration from the top of the hydrogel in the depth of around 4 cell layers (~150 μm). To quantify these observations, a detailed image analysis process was developed and firstly introduced in this paper.

Keywords: poly(aspartic acid) hydrogel; dopamine; three-dimensional cell migration; hydrogel scaffold; SH-SY5Y

1. Introduction

Tissue engineering is a rapidly developing and promising field that applies living cells growing on complex biocompatible matrices called scaffolds, to create tissue-like structures [1–3]. These scaffolds can be used for medical therapies repairing the injured or diseased area of tissues [1–3], but they are also suitable for testing the efficacy and toxicity of various drugs [2,4]. A high number of research projects related to tissue engineering are focusing on hydrogels, due to their structural similarity to the natural environment of the living cells, i.e., the extracellular matrix (ECM). Additionally, hydrogels have favorable mechanical properties that can be customized according to the targeted tissue type [5]. The

adequate behavior of the cells can be achieved by incorporating growth or differentiation factors [6], as well as other bioactive agents like proteins, peptides, or small molecules into the hydrogel matrix [1,3,7,8].

Since several components of the ECM are amino acid-based macromolecules, i.e., proteins such as collagen or elastin, amino acid-based hydrogels can mimic the ECM, especially from the chemical point of view. However, the application of amino acid-based hydrogels as scaffolds is presently limited due to their difficult and expensive preparation [9]. Currently, there are only a few types of synthetic poly(amino acids) available, such as polylysine or poly(aspartic acid) (PASP) that can be suitable for this purpose [10,11]. In our previous studies, the chemical constitution and the physical properties of PASP-based hydrogels have been comprehensively investigated [12–14] and successfully tailored for applications as a scaffold [8,15]. We have demonstrated that thiol groups in the PASP hydrogels facilitate cell adhesion and proliferation [15]. Since the anhydrous form of PASP, namely poly(succinimide) (PSI) is very reactive, it can be covalently modified with various biologically active molecules (such as RGD tripeptide, taurine, doxorubicin, or dopamine) [16,17]. This feature gives us several opportunities to further improve its properties for tissue engineering and other biomedical applications [11,18].

Dopamine (DA) is one of the major neurotransmitters in the central nervous system, participating in the modulation of various functions [19] as well as the acquisition of new memories [20]. In addition, recent intense research efforts inspired by the investigation of adhesive proteins of marine mussels led to the recognition that DA also plays an important role in cell adhesion [21,22] and enhances the bioadhesive properties of different coatings and hydrogels [23–25]. Besides these important functions, the release of DA plays a key role in stem-cell-based tooth repair during dental pulp injury [26]. According to the literature, DA show an interesting biphasic effect on neurons. Although it is cytotoxic at high concentrations, it has been proved to have trophic or cell protective effect at low concentrations [27–29]. The main aim of this study is to investigate of the concentration dependent effect of the covalently bound DA in the hydrogel on the cell viability, morphology, and distribution. In accordance with this aim, SHSY-5Y and PDLC were used in the in vitro experiments, since both cell types show neurogenic activity, and the presence of dopamine receptors has been published [26].

Human wisdom teeth are novel and promising sources of postnatal stem and progenitor cells, such as PDLCs for tissue engineering purposes [30,31]. PDLCs can be isolated from the root surface of wisdom teeth by a minimally invasive intervention [32] and they have differentiation capacity into multiple cell lineages, such as fibroblasts, cementoblasts, adipocytes, osteoblasts, and chondrocytes [6,30,33], as well as neuron-like cells [31]. Furthermore, PDLCs proved to exhibit potential for regeneration of cementum, bone, periodontal fibers [32], and tendon [34], and even nerves in vivo due to their neuroectodermal origin [35]. Up to now, mostly natural polymers like collagen [36], chitosan [4], alginate/hyaluronic acid [35], or synthetic, biocompatible polymers, such as poly(glycolic acid), poly(lactic acid) [37], or poly(ethylene glycol) [38] have been suggested to prepare scaffolds for PDLCs.

As the terminally differentiated mature neurons cannot be propagated in cell culture, tumor cell lines consisting of neuroblasts (i.e., primitive nerve cells representing a previous stage of the neural differentiation process) are often used in neurobiological research. The advantages of the SH-SY5Y neuroblastoma cell line are the human origin, ease of maintenance, and well-established protocols for generating a more mature neuron-like phenotype [39,40]. Previously, this cell line was cultured mainly in scaffolds composed of natural polymers like collagen [41], bacterial nanocellulose [42], gelatin [43], or alginate/gelatin scaffolds [43].

Consequently, our study aimed to fabricate PASP-based hydrogels grafted with dopamine to combine the prosperous properties of amino acid-based polymers and dopamine in tissue regeneration. Our aims involved the characterization of these hydrogels, and in vitro studies using two relevant cell types, namely PDLCs and the SH-SY5Y neurob-

lastoma cell line. Thus, in the present study, DA-modified thiolated PASP hydrogels are introduced as novel scaffolds for three-dimensional cell cultivation. The hydrogel scaffolds were characterized both physically and chemically, moreover the effect of dopamine concentration on the morphology, proliferation as well as two- and three-dimensional distribution of PDLCs and SH-SY5Y cells in the hydrogels have been studied in vitro. In addition, a novel method was developed and firstly introduced in this paper to quantify the vertical penetration and migration ability of the cells.

2. Results and Discussion

2.1. Characterization of PSI, PASP Based Polymers, and PASP-Based Hydrogels

Since the preparation of the hydrogels consists of several steps (modification of the PSI with DA, crosslinking of the PSI-DA, hydrolysis of the PSI-based gels, and cleavage of the disulfide bonds to thiol groups) (Section 4.1), we aimed to determine the chemical structures of the intermediate and the final products of the preparation. To characterize the chemical structure of the PSI and PASP-based polymers after DA modification and the final PASP form of the hydrogels following the formation of the thiol groups, FTIR spectrometry was used (Figure 1a,b). Since DA can be released from the main polymer during the cleavage of the peptide bond between DA [18] and the main polymer, the DA content of the hydrogel can change during hydrolysis. As the DA content of the polymer was very low (every 10th, 20th, and 40th monomer was modified, respectively), the changes in DA concentration during hydrolysis were monitored by 1H-NMR spectroscopy (Figure 1a). Since NMR measurement cannot be used easily to determine the chemical structure of the polymer matrix, PSI-DA polymers were hydrolyzed into PASP polymers (with the same method that we applied during the preparation of the hydrogels) and the chemical structure of the PASP-based polymers were determined.
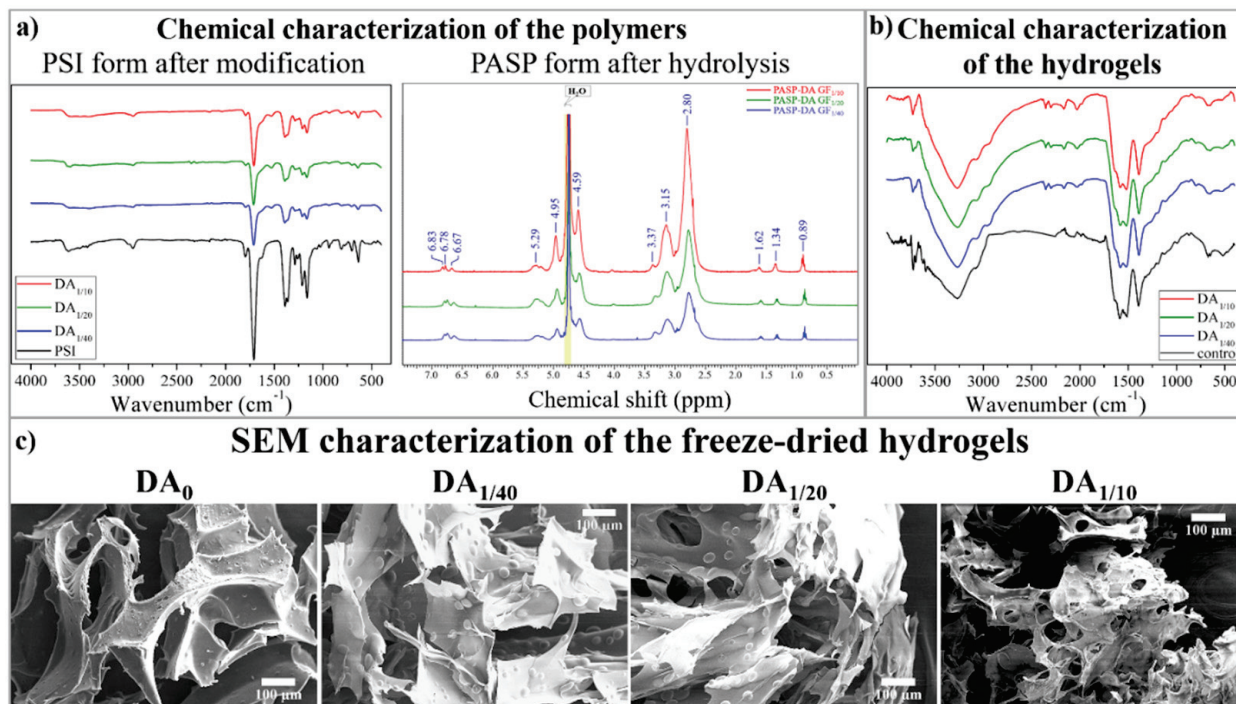
Figure 1. FTIR and NMR spectra of PSI and PASP-based polymers (**a**) and FTIR spectra of PASP-based hydrogels (**b**). SEM images of the freeze-dried dopamine-containing and dopamine-free control (DA$_0$) gel (**c**).

On the FTIR spectra of the PSI-DA polymers (Figure 1a, left spectra), only minor differences can be recognized between the samples. The main difference is that a new peak appeared at wavenumber 1510 cm^{-1} on the spectra of the dopamine-modified polymers.

This peak is related to the stretching motion of the C–N bonds in the amide group, which proves the successful modification of the PSI main polymer. The list of the other peaks can be found in the Supplementary Materials (Section S5) and in our previous publication [18].

The ^{1}H-NMR spectra of the different PASP-DA polymers can be seen in Figure 1a (right spectra). The peaks at 4.59 ppm and 2.81 ppm can be assigned to methine and methylene hydrogen of aspartic acid monomer units [44,45]. The peaks at 3.36 ppm are related to the –CH$_2$ unit in the dopamine, while the peaks at 6.67, 6.78, and 6.83 ppm belong to the hydrogens in the catechol group of dopamine. The peaks at 0.89, 1.34, and 1.62 ppm can be assigned to the protons in N,N-dibutyl-amine. The presence of these peaks shows that secondary amines can react with the succinimide ring, as was published in our previous articles [8,18]. The peaks at 3.15 and 5.29 ppm are connected to the methylene and methine groups in the succinimide rings, which proves that the polymers contain unreacted succinimide rings despite the hydrolysis. The residual amount of succinimide rings indicates that the applied time period for hydrolysis is not enough to produce PASP completely. Therefore, longer reaction time (several days) was applied for hydrolysis during hydrogel preparation. Due to the very small amount of modification, the exact ratios between the DA and unmodified succinimide rings cannot be determined.

The FTIR spectra of the thiolated hydrogels can be seen in Figure 1b. No significant differences can be recognized between FTIR spectra of the hydrogels due to the small amount of modification. The wide peak between wavenumbers 2800 and 4200 cm^{-1} and the disappearance of the peak at 1720 cm^{-1} prove the successful hydrolysis and the poly(aspartic acid) structure of the hydrogels. The only difference between the dopamine-containing and the DA$_0$ hydrogel can be seen at wavenumber 2966 cm^{-1}. This peak is related to the C–H stretching in the aromatic ring of dopamine, which proves the presence of dopamine in the polymer matrices after hydrolysis. Our spectra are similar to the spectra that can be found in the literature [14,44].

The microscopic structure of the different hydrogels was investigated by SEM (Figure 1c) and the average pore size of the freeze-dried hydrogels was determined (Table 1).

Table 1. Average pore size of the hydrogels with different dopamine content.

	DA$_0$	DA$_{1/40}$	DA$_{1/20}$	DA$_{1/10}$
Average pore size	120 ± 13 μm	121 ± 25 μm	110 ± 35 μm	87 ± 27 μm

The pore size of the gels was found to be between 80 and 120 μm, which is significantly higher than the diameter of PDLCs (around 30–40 μm) [32]. This pore size range can support the vertical migration of PDLCs into the polymer matrices, as was proved by Kim and co-workers [46]. According to our results, both the average pore size (Table 1) and the mass swelling degree (Table 2) depend on the dopamine content of the hydrogel. An inverse correlation can be observed between these two properties and the dopamine content (Tables 1 and 2). The higher dopamine content in the hydrogel resulted in weaker polymer–solvent interaction, leading to smaller mass swelling [47,48]. The smaller mass swelling degree indicates a denser polymer matrix that results in a smaller average pore size after freeze-drying the hydrogels.

Table 2. The released amount of DA and DA concentration of the hydrogels at the time point of cell seeding, and the mass swelling degree of the hydrogels.

Sample	Released Amount of DA (%)	DA Concentration in the Hydrogels after Hydrolysis (mmol/L)	Mass Swelling Degree
PASP-DA$_{1/40}$	48.7 ± 4.81	4.73 ± 0.31	29.3 ± 0.6
PASP-DA$_{1/20}$	58.3 ± 3.43	9.43 ± 0.78	21.8 ± 0.4
PASP-DA$_{1/10}$	54.2 ± 3.44	23.96 ± 2.8	18.3 ± 0.3

2.2. Dopamine Release during the Hydrolysis of the Gels

According to the abovementioned physical and chemical characterization of the hydrogels by NMR and FTIR, there is remaining DA on the polymer and in the hydrogel after hydrolysis. Since we already know that DA can be released from the PASP in alkaline circumstances [18], the DA release was also investigated during the gel hydrolysis in parallel with the characterization. The effect of dopamine on different cell types is significantly concentration-dependent [49,50]; therefore, it is crucial to know the exact DA concentration to understand the results of the cell experiments. The released amount of dopamine and the dopamine concentration of the hydrogels applied in the cell experiments can be found in Table 2.

According to Table 2, approximately 50% of the dopamine was released from the hydrogel samples, which is in good correlation with our previous results regarding PSI-DA polymer conjugates [18]. Due to the DA release, the concentration of the DA in the different hydrogels was significantly changed after hydrolysis. Although the applied amount of the dopamine at the gel synthesis was 2 and 4 times higher in $DA_{1/10}$ compared to $DA_{1/20}$ and $DA_{1/40}$, respectively, the DA concentration ratio of $DA_{1/10}$ to $DA_{1/20}$ and $DA_{1/40}$ after the hydrolysis became 2.5 and 5, respectively. This discrepancy is a result of the different swelling degrees of the hydrogels, which can be calculated as the ratio of the swelled and dried hydrogels. The lower mass swelling degree indicates higher polymer, and therefore higher DA, content in the same amount of swelled hydrogels. Although these DA concentrations are higher than the lethal concentration for different cell types including the SH-SY5Y cells, in our case the covalent bonds between DA and the polymer matrices prolonged the release of the DA. Consequently, the free dopamine concentration in the cell culture medium was significantly lower than the calculated DA content in the hydrogels.

2.3. Cell Viability and Morphology on Different PASP-DA Hydrogels

Dopamine has a variety of effects on various organs: it has an essential role in normal brain function (involved in modulation of learning, memory, and coordination of movement) [19,20], and it is also an important regulator of blood pressure [51]. Dopamine exerts its effect on the cells through its cell surface receptors, which have five types: D1R, D2R, D3R, D4R, and D5R [51]. DA can enhance the adhesion of different cell types [23–25,52] onto various surfaces, but the effect of dopamine in vitro is highly concentration-dependent [27,53]. Low concentrations of dopamine have a cell-protective, namely anti-apoptotic effect, but at higher concentrations, it can be toxic due to the induction of apoptosis [28,49,50].

Since the main aim of this study was to investigate the concentration-dependent effect of dopamine on cell viability, morphology, and distribution, we chose two relevant cell types: primary cultures of PDLCs and the SH-SY5Y neuroblastoma cells line. Due to the neuroectodermal origin of the tooth, dental stem, and progenitor cells like PDLCs can differentiate into neuronal phenotype in vitro [31,54]. As SH-SY5Y cells can be differentiated into functionally mature neurons with dopaminergic characteristics, this cell line is a suitable model for dopaminergic neurons [37,39,55]. In addition, the presence of different types of dopamine receptors was detected on both dental stem cells [26], and SH-SY5Y cells [55]; therefore, dopamine can exert a direct effect on both PDLCs and SH-SY5Y cells.

Figure 2 shows the changes in viability of PDLCs (Figure 2a) and SH-SY5Y cells (Figure 2b) on the four different hydrogel types during the 2-week-long experiment. The data measured on day 1 depend mainly on cell adhesion while those of later time points refer to cell proliferation. Therefore, the viability data on day 1 on the hydrogel without dopamine were chosen as reference values.
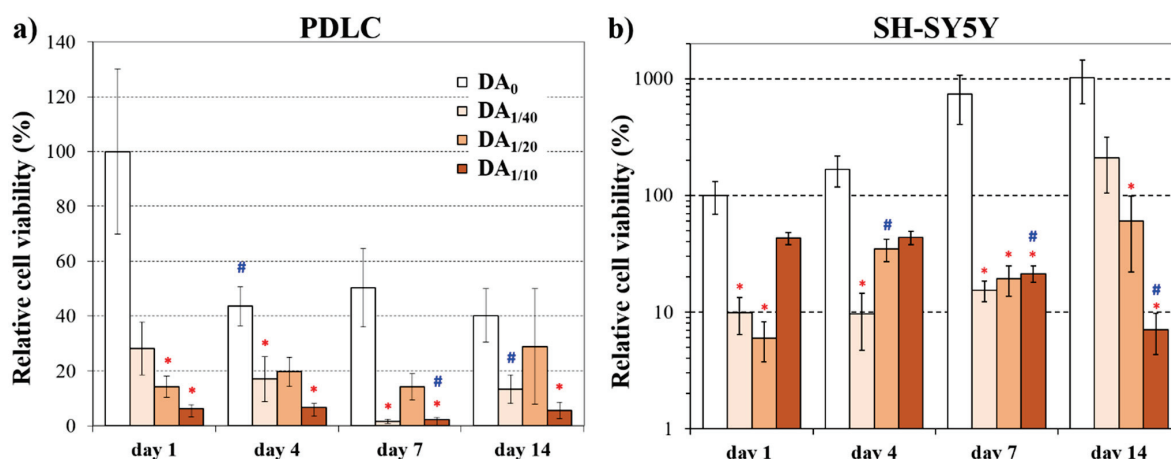
Figure 2. Relative cell viability of PDLCs (**a**) and SH-SY5Y cells (**b**) on the hydrogels 1, 4, 7, and 14 days after cell seeding. The viability was normalized to the value measured on the dopamine-free (DA$_0$) gel on day 1. In case of the SH-SY5Y cells, a logarithmic scale was applied, as this cell line originates from a tumor and it grows much faster than the PDLC cells. * significant difference ($p < 0.05$) compared to the DA$_0$ gel at the same time point. # significant difference ($p < 0.05$) compared to the same gel type at the previous time point.

We found that the highest dopamine concentration (DA$_{1/10}$) in the hydrogel resulted in the lowest cell viability values of PDLCs (Figure 2a) compared to the other gels at each time point of the experiments. Although the viability was the highest on the DA-free gel (DA$_0$) at day 1, remarkably lower viability data was measured on this gel type from day 4. This observation suggests that a great amount of PDLCs could adhere to the DA-free gels, but on this gel type, they were not able to proliferate. Previous studies on PASP hydrogels are also in line with our observations, and it has been described that these gels provide a suitable surface for cell adhesion and proliferation of PDLCs [15] and MG-63 osteosarcoma cells [8]. However, the viability of PDLCs did not change notably on DA-containing gels during the 14-day-long experiment. Therefore, the cells that adhered to these gels by day 1 remained viable for two weeks. Nevertheless, no significant difference was detected between the DA$_0$ gel and DA$_{1/40}$ or DA$_{1/20}$ gel on day 14 while the viability on DA$_{1/10}$ gel was significantly lower than those on DA$_0$ gel at this time point. The lower cell viability on DA$_{1/10}$ was probably caused by the high local DA concentration, which can exceed the lethal concentration of DA. For example, more than 100 μM concentration of dopamine induced cell death in the PC12 cell line, which consisted of a mixture of rat neuroblasts and eosinophilic cells [49]. Concentration-dependent cytotoxicity of dopamine on a rat mesencephalic/neuroblastoma hybrid cell line was also observed at concentrations between 5 and 50 μM [50]. The high DA concentration released from PASP-DA$_{1/10}$ during cell experiments can explain the lower cell viability. Therefore, our results confirm the concentration-dependent, biphasic behavior of dopamine, as also described in the literature [29,49].

To date, several natural macromolecules like collagen [36], chitosan [4], and hyaluronic acid/alginate [35], as well as synthetic polymers like poly(glycolic acid), poly(lactic acid) [37], or poly(ethylene glycol) [38], have been tested as to whether they are suitable for cultivation of PDL cells. According to these results, PDLCs show good affinity to different natural and synthetic polymers and can adhere, proliferate, and even differentiate into neurogenic and osteogenic lineages on the previously mentioned matrices. In our previous publication, the proliferation and osteogenic differentiation of PDLCs on several types of PASP hydrogels without dopamine was also demonstrated. The viability of PDLCs shows a slight decrease on hyaluronic acid/alginate hydrogels scaffolds [35], which is in alignment with our viability results. The neurogenic differentiation ability of the PDLCs can also explain the vertical migration of the cells into the hydrogel which will be demonstrated later (in

Section 2.4). Although several publications underline the role of dopamine in controlling cell behavior [21–25], as far as we know, this is the first study applying a dopamine-functionalized scaffold to affect PDLCs adhesion, migration, and proliferation.

In the case of the SH-SY5Y cells (Figure 2b), the viability on the DA-free gel was the highest compared to the other gel types during the whole experimental period. Besides, an enormous elevation was observed on this DA_0 gel until day 14, suggesting a very intense proliferation. The viability data measured on the three DA-containing gel types were in a similar range at each time point until day 7. However, a remarkable difference was observed between them on day 14, when the highest value of $DA_{1/40}$ gel reached the level of the DA_0 gel. According to the literature, the SH-SY5Y neuroblastoma cell line can adhere and proliferate on various scaffolds consisting of natural polymers like alginate/gelatin [56], hyaluronic acid/poly(caprolactone) [57], collagen [41], gelatin [43], or nanocellulose [42]. In these studies, it was also demonstrated that the viability of the SH-SY5Y cells is highly dependent on the constitution of the scaffold material and also on the concentration of different molecules. To the best of our knowledge, dopamine-modified polymer-based materials have never been used for the cultivation of SH-SY5Y cells previously.

Comparing the viability values of the two cell types, we can conclude that for PDLCs, the $DA_{1/20}$, while for the SH-SY5Y cell line, the $DA_{1/40}$ gel proved to be the most suitable for long-term survival and proliferation. Although the 1/10 dopamine concentration seems to have a slightly promoting effect for adhesion of SH-SY5Y cells, this concentration is toxic for both cell types in the long term. At high concentrations, DA usually leads to a significant decrease in the number of viable cells regardless of cell type, while at low concentrations it can support cell attachment, proliferation, and differentiation, similarly to our results [22,58–60]. Since the same number of cells were seeded on the gel disk from both cell types, the explanation for the difference in the range of relative viability may be due to the tumor origin of the SH-SY5Y cell line. We observed that the tumor cell line proliferated at a higher rate than PDLCs even under standard culture conditions in Petri dishes before seeding them for these experiments. SH-SY5Y cells usually form clusters on three-dimensional hydrogel matrices [42,56,61], which can also be seen in Figure 3; this behavior can explain the discrepancy between the viability and microscopic results. Clusters can cause insufficient nutrition supply and hampered diffusion, therefore the WST-1 reagent cannot be converted to formazane by the mitochondria since it cannot reach the inner region of the clusters [42]. Consequently, the real number of viable cells can be better demonstrated by microscopic methods.
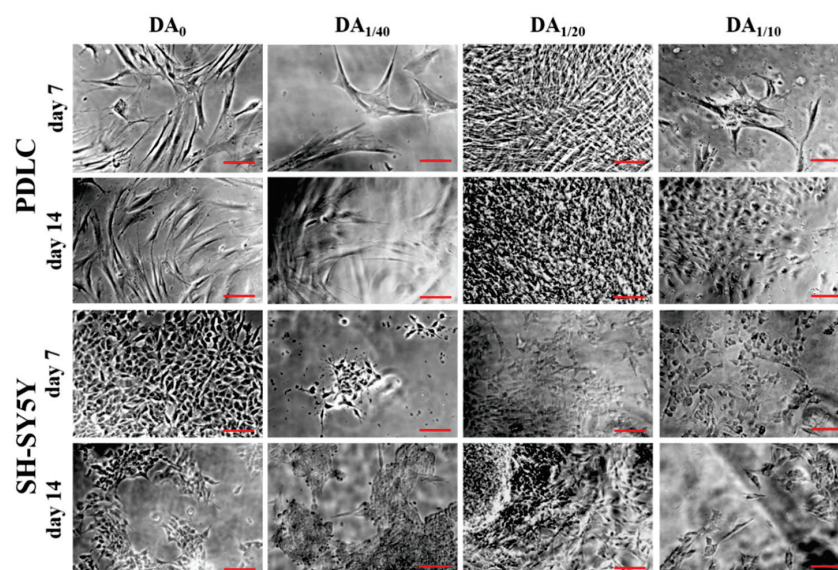

Figure 3. Phase-contrast microscopic images of PDLCs and SH-SY5Y cells growing on the 4 different gel types for 1 or 2 weeks. The scale bars indicate 100 μm.

Using a phase-contrast microscope, cell growth on the surface of the gels can be visualized (Figure 3). A relatively higher number of PDLCs with healthy, fibroblast-like morphology was observed on the DA-free gel at days 7 and 14. This spindle-shaped cell form with a small number of long processes is typical for this cell type [30–32]. Regarding the DA-containing gels, only a few adhered cells could be seen on $DA_{1/10}$ and $DA_{1/40}$ gels during the whole experiment. However, the highest amount of fibroblast-like PDLCs was found on $DA_{1/20}$ gels at each time point. The smaller cell size and the star cell shape or, at higher cell density, polygonal cell shape of the SH-SY5Y neuroblastoma cells are striking on the photomicrographs (Figure 3), which is in line with the description of the manufacturer (ECACC cell line). The highest amount of SH-SY5Y cells was found on DA_0 gel at each time point. However, a large number of these cells could be detected under the phase-contrast microscope on day 14 on all DA-containing gel types as well with the lowest cell number on $DA_{1/10}$ gels.

The aforementioned microscopic observations regarding cell morphology and proliferation on different gel types are in line with our viability results suggesting that while $DA_{1/20}$ gels provide optimal DA concentration for adhesion and proliferation of both PDLCs and SH-SY5Y cells (Figure 2), higher DA-content can be toxic for both cell types.

These findings confirm the concentration-dependent effect of dopamine on cell viability, which is typical not only for dopamine treatment of cells cultured on the plastic surface, but also for cells grown on dopamine-containing hydrogel scaffolds. Biocompatibility studies with other sorts of dopamine-functionalized hydrogels are in accordance with our results, as none of these scaffolds have proved to be toxic. Extracts of dopamine-modified poly(ethylene glycol) hydrogels were demonstrated to have no toxic effect on mouse fibroblasts [60]. However, in that study, the DA content of the gels used for cell experiments was fixed and only the influence of the sterilization method on cell viability was investigated. In line with our results, the viability of human primary fibroblasts and embryonic fibroblast cell lines was slightly reduced after treatment with dopamine-modified alginate [25]. During development of a novel bioadhesive, gelatin-dopamine conjugates did not prove to be cytotoxic for human dermal fibroblasts [62]. Similarly to us, they observed that the adhesive property could be improved by increasing DA content only until a maximum point, with higher DA content leading to a decrease in adhesiveness. Finally, solutions with different concentrations of dopamine-modified poly(α,β-aspartic acid) derivatives did not influence the viability of mouse embryonal fibroblast cells [63]. In this work, in contrast to our study, only the cytotoxicity of the DA-modified polymer solutions with different concentrations was investigated and not of the prepared hydrogels.

The difference in the amount of covalently bound DA results in different free DA concentration and also different DA release kinetics. Both bound and free DA affect the microenvironment of the cells and induces different cell behavior by different concentration gradient of DA in the hydrogels. Nanoscale forces play a key role in tissue engineering [64], as can be seen in the cell morphology and viability, but also in the cell migration results.

2.4. Three-Dimensional Distribution of PDLCs and SH-SY5Y Cells on PASP-DA Hydrogels

The effect of the polymer solutions on cell viability, proliferation, and morphology is different than the effect of the hydrogels since the cells can uptake the polymers in solutions. However, several results show that the cells growing on three-dimensional polymer matrices can digest the bonds in the polymer matrix which may lead to the uptake of polymers or small molecules and induce vertical cell migration [65–67]. Since phase-contrast microscopy shows mainly the cell morphology on the hydrogel surfaces, but cannot provide information about the three-dimensional distribution of the cells and three-dimensional structure of the hydrogels, two-photon microscopy was applied. To visualize the cells in the inner parts of the hydrogels, they were labeled with the Vybrant DiD vital dye before seeding (Figure 4).
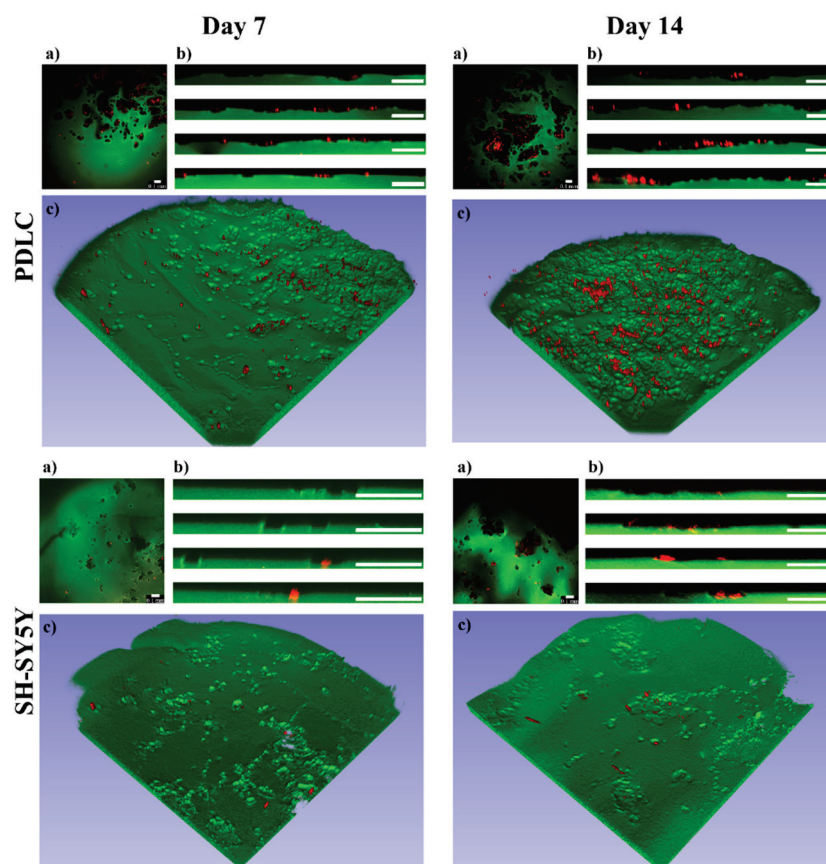
Figure 4. PDLC and SH-SY5Y cell (red) distribution on the PASP-DA$_{1/20}$ hydrogels (green) on days 7 and 14. The upper view (**a**), cross-sectional view (**b**), and three-dimensional images (**c**) were constructed from Z-stack measurements of the hydrogels. Scale bars indicate 0.1 mm.

As can be seen on the three-dimensional images (Figure 4c), the topography of the PASP-DA$_{1/20}$ hydrogels significantly changed due to the cells (hydrogel structure before cell seeding can be seen in Supplementary Section S6—Figure S3) and several cavities were formed in every sample. These cavities are clearly observable both on the upper view (Figure 4a) and the cross-sectional view images (Figure 4b). The lack of the green signal indicates the presence of the cavities in the hydrogel matrices, while the red color shows that the cells can be found at another height than the hydrogel upper surface. This indicates that both PDLCs and SH-SY5Y cells were able to degrade and digest the hydrogel matrixes facilitating their vertical migration into the hydrogel matrices. According to the two-photon microscopic analysis, no similar cavity formation was discovered on the PASP-DA$_0$, PASP-DA$_{1/10}$, and PASP-DA$_{1/40}$ hydrogels at any measurement time (Supplementary Section S6—Figures S3–S5). Therefore, not only are the aforementioned cellular viability, proliferation activity, and differentiation [49,50] DA concentration-dependent, but this phenomenon is also related to the migration properties of the cells toward the inner parts of the hydrogel matrix, observation of which has never been published before.

Although there are several examples for culturing SH-SY5Y [41,43,68–70] and PDLCs [15,36,71,72] on various hydrogels, the migration mechanisms of these cells have barely been described. In general, cells are able to migrate in 3D matrixes by different mechanisms, such as mesenchymal, amoeboid, and lobopodial movements [66]. The sort of migration mechanism is supposedly influenced by not just the cell type, but also by the environmental properties (topography of ECM, the molecular composition and concentration, stiffness, substrates, elasticity, rigidity, density, pore size, cellular interactions). The amoeboid cells do not align to ECM fibers by contractile forces while mesenchymal cells

create special contacts with the ECM through their receptors. In addition, mesenchymal cells can proteolytically digest the ECM, and thereby create pathways for themselves during migration. A highly crosslinked matrix can induce lobopodial migration, which is a hybrid mechanism of the amoeboid and the mesenchymal migration [65,66]. According to these theories and our results, the vertical migratory mechanism of the PDLCs and SH-SY5Y cells into PASP-DA$_{1/20}$ hydrogels could be mesenchymal or lobopodial. The observed cavities in the hydrogels indicate that cells may proteolytically digest the PASP polymers or the crosslinks in the matrix that can be induced by dopamine. In the case of the other hydrogel types without DA (Supplementary Section S6—Figures S4 and S5), no vertical migration was observed that shows the crucial role of the dopamine concentration in the vertical migration of the cells.

Nevertheless, migration facilitated by our DA-containing hydrogels could be in connection with the oxidative stress generated during metabolism of dopamine. It is well known that degradation of dopamine produces reactive oxygen species (ROS) [73], which can promote cell migration by redox regulation of key signaling pathways [74], or enhances migration of tumor cells, and thereby the invasion and metastasis of cancer [75]. Moreover, the important role of ROS signaling was demonstrated during neurodevelopment as a modulator of proliferation and migration as well [76]. It was described that the hexokinase enzyme located in mitochondrial membrane is not only a potent regulator of ROS signaling but also a novel target of dopamine signaling in neural progenitor cells [77]. Even in the case of SH-SY5Y human neuroblastoma cells, it was found that exposure to dopamine inhibited mitochondrial respiration [78]. Based on the abovementioned results, we suppose that PDLCs (with ectodermal origin and neuronal differentiation potential) and SH-SY5Y cells (consisting of immature neurons) may apply the same sort of mechanism for migration in the DA-containing PASP-hydrogels due to the release of DA and generation of ROS as the invading tumor cells. To quantify the vertical migration of the cells topographical analysis was carried out on the two-photon microscopic images. The extent of vertical cellular migration was calculated at each (x, y) point on the horizontal plane as the vertical distance between the hydrogel surface digested by the cells and an estimated original surface. The surface estimation was based on fitting a 3rd degree bivariate polynomial on the hydrogel surface and shifting its zero value to be equal to the mode of the hydrogel surface. This method is based on the assumption that cells (due to their relatively low number) affect only the shape of the surface locally and the large-scale features of the original hydrogel can be found by fitting a slowly varying function on the surface. The distance between the estimated original surface and the surface digested by the cells was further analyzed: negative peaks representing local maxima of cellular migration distance (locally deepest points of the surface) were found and the peaks' topographic prominences were also calculated. Topographic prominence represents how much a peak's depth stands out compared to its surroundings: it is the difference in distance between a peak and (in the case of negative peaks) its highest contour. Intuitively, a gel surface with deep peaks but low prominences might correspond to a large group of cells migrating together creating a large cavity, while the same depth values with high prominences would represent cells that at some point migrate in smaller groups or individually. The prominence and depth data are illustrated in Figure 5.

According to these results, most of the cavities are in connection with each other and only a few of them are separated. This may confirm that the cells, especially the SH-SY5Y cells, are organizing themselves into clusters at first with high cell density [61]. These clusters are clearly observable on the phase-contrast microscopic images (Figure 3, SH-SY5Y day 14). This cluster formation inhibits intracellular communication and vertical migration of the SH-SY5Y cells, which was also described by Q. Chen and co-workers [56]. The three-dimensional images (Figure 4c) also prove this statement, where the cavities made by the cells are also connected to each other, and they form extended valleys in the hydrogel matrices. The distribution of the absolute depth of the pixels follows a Gaussian

distribution (Figure 5b) in the case of every sample. To compare the different cell types and measurement days with each other, the average depth of the peaks was calculated (Table 3).
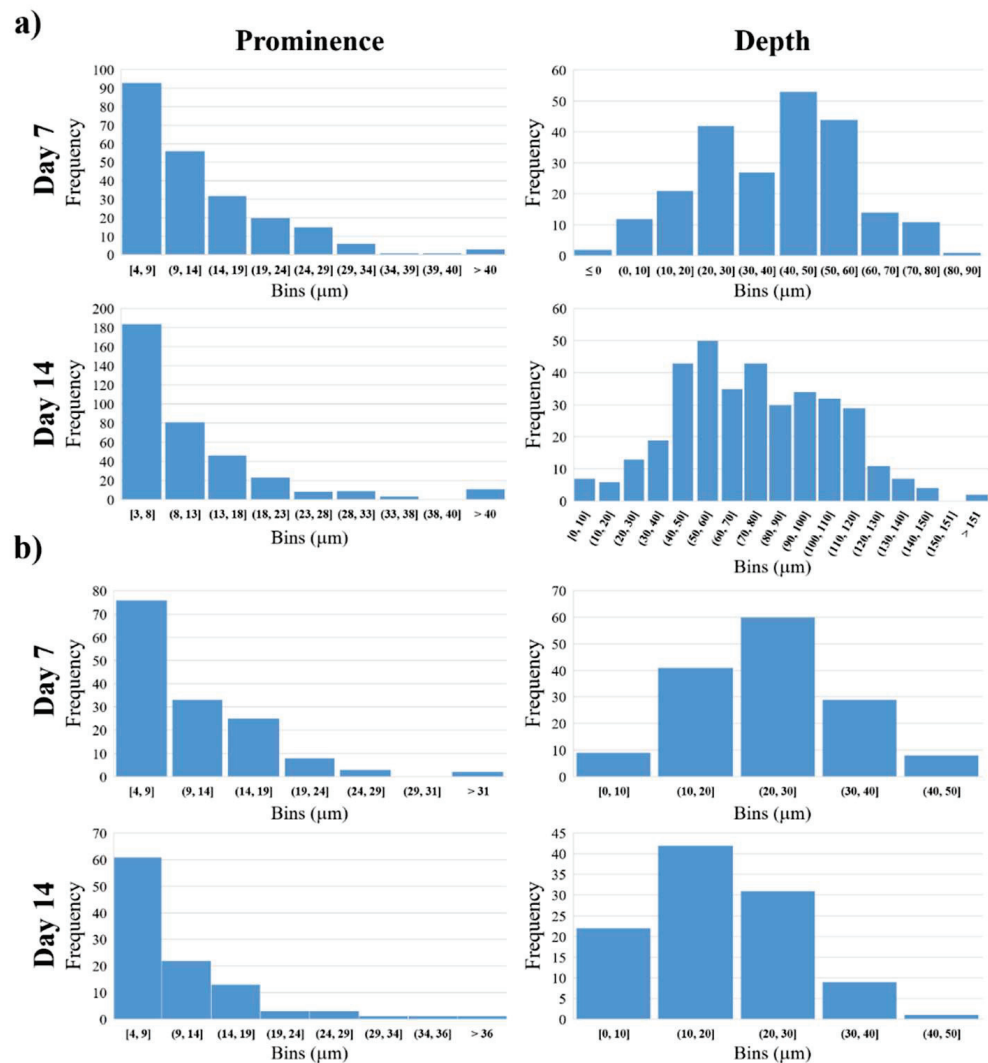

Figure 5. Distribution of the prominence and depth of the migration distance from the fitted surface in the PASP-DA$_{1/20}$ in the case of PDLC (**a**) and SH-SY5Y (**b**).

Table 3. Average depth of the migration distance from the fitted surface in μm on PASP-DA$_{1/20}$ in the case of different cell lines.

	Average Depth (μm)	
	PDLC	**SH-SY5Y**
Day 7	39 ± 18	24 ± 9
Day 14	75 ± 30	18 ± 8

According to our results (Table 3 and Figure 5b), the PDLCs were able to migrate deeper into the polymer gel matrix than the SH-SY5Y cells. The vertical migration ability of the PDLCs is time-dependent, since the cells were able to reach almost double deepness after 14 days of seeding than after 7 days. The average size of a PDLC is around 30 μm [32]; therefore, the deepest cavities in the hydrogel after 7 days correspond to approximately 2–3 cell layers, while after 14 days they reached a depth of around 4–5 cell layers. The different migration data of PDLCs and SH-SY5Y cells can be explained by the significant

size difference between the two cell types (the average size of the SH-SY5Y is around 12 μm) [40].

Although the mechanism behind the migration of the SH-SY5Y cells has not been clarified yet, similar behavior has been described in several studies. G. Akcay and co-workers investigated the vertical migration of SH-SY5Y cells into photopolymerized poly(ethylene glycol)-diacrylate hydrogels [61]. According to their results, the migration of the cells was induced by the stiff-to-soft material transition, and the cells were able to migrate into the hydrogels up to 60 μm. They concluded that SH-SY5Y cells in the 3D hydrogels exhibit a spherical morphology—unlike in 2D, where they have a flat shuttle-like shape with long pseudopods—due to the mechanical support and the limited space to spread [56,61]. Similar behavior of PDLCs has never been described in any type of hydrogel matrix.

The vertical migration of the cells is a crucial behavior for tissue replacement, and makes these hydrogels a very promising candidate for this application. The novel method we developed for the representation, quantification and analysis of the vertical migration can be used to describe this kind of changes in other sorts of matrices in the future. Currently, there is no similar method available in the literature.

Our future plan is to further optimize the composition of the DA-containing PASP gels in order to make them more suitable for proliferation and migration of cells. As the use of antioxidants could prevent dopamine-induced cell death in many cases [79], one of the promising ways would be the incorporation of antioxidants into these gels.

3. Conclusions

In this work, poly(aspartic acid) hydrogels with different dopamine content (PASP-$DA_{1/40}$, PASP-$DA_{1/20}$, PASP-$DA_{1/10}$) were synthesized for cell cultivation. The chemical constitution of the hydrogels was confirmed and the exact dopamine content after hydrogel preparation was determined. To test the hydrogels as scaffolds, PDLCs and SH-SY5Y cell lines were used. Both cell types showed a concentration-dependent reaction to the presence of dopamine in the scaffold: dopamine at low concentration (PASP-$DA_{1/40}$ or PASP-$DA_{1/20}$) did not affect cell viability but at higher concentration (PASP-$DA_{1/10}$) it induced apoptosis and lowered the number of viable cells. We observed for the first time in the literature the unique migration phenomena of the cells into the hydrogels induced by a specific dopamine concentration (PASP-$DA_{1/20}$) in the case of both cell types. Either PDLCs or SH-SY5Y cells were able to degrade the hydrogel matrices, making the way free for themselves to migrate into the hydrogels.

To quantify the depth of the cell migration, a new method was developed based on the two-photon microscopic measurements of the hydrogel matrices. According to these results, PDLCs were able to penetrate into the hydrogel matrix even to a depth of 150 μm, which is equal to the size of 4–5 cell layers, while SH-SY5Y showed lower migration capacity that can be explained by the neurogenic origin of the cells.

Consequently, based on our results and due to the wide differentiation capacity of PDLSCs and other types of progenitor cells, several sorts of artificial tissues can be constructed in the future. Our new image analysis method can be used widely to quantify the three-dimensional migration of the cells in various matrices.

4. Materials and Methods

4.1. Preparation of Dopamine Modified Poly(succinimide)s

At first, poly(succinimide) (PSI) was synthesized as described in our previous publications [8,12–15,80]. In the second step, dopamine (DA) modified poly(succinimide) (PSI-DA) was synthesized with different dopamine (Sigma Aldrich; 99.9%) content (Figure 6, Step 1). The detailed method of synthesis was published previously [8,13,15,18] and can also be found in the Supplementary Materials, together with the exact constitution of the reaction mixtures (Supplementary Information Section S1).
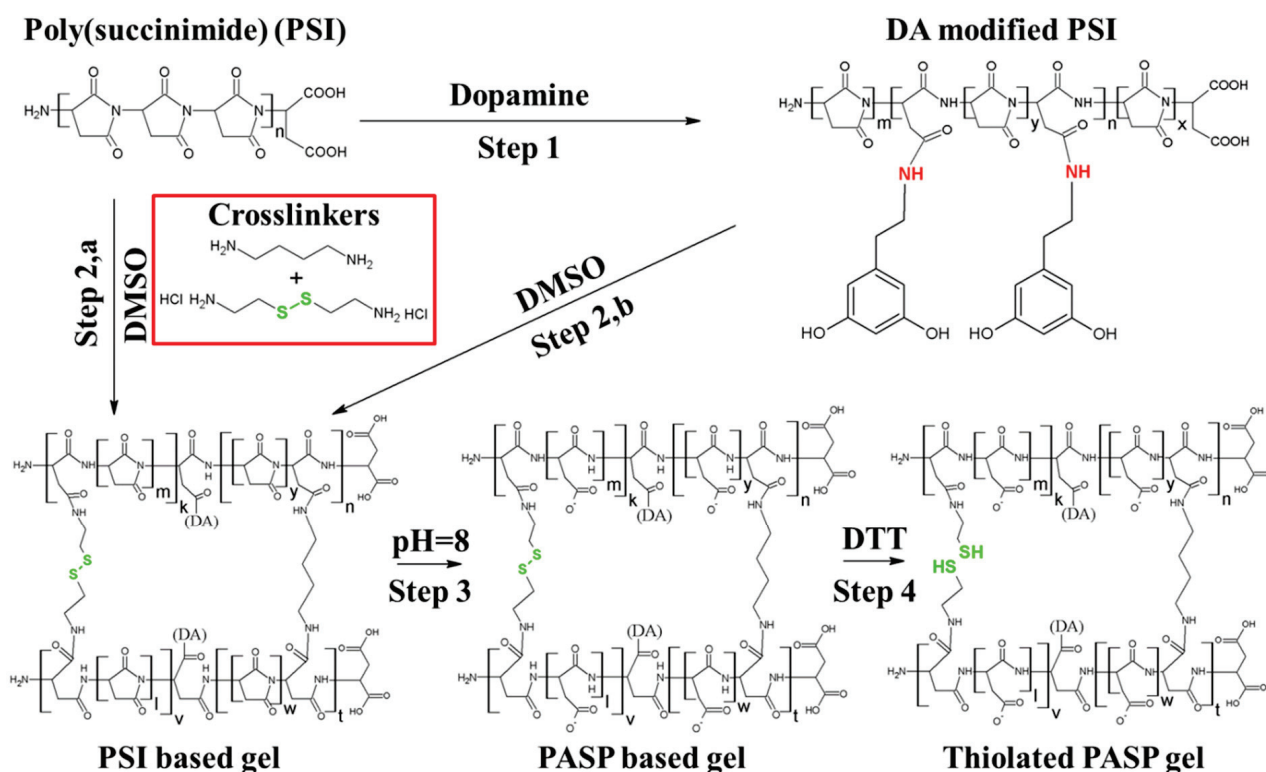
Figure 6. Chemical synthesis of dopamine-containing gels.

4.2. Chemical Characterization by Nuclear Magnetic Resonance (NMR) Spectroscopy

For ^{1}H-NMR characterization, the PSI-DA polymers were treated with the same materials, i.e., pH = 8 imidazole buffer (imidazole: ACS reagent, ≥99%, Sigma-Aldrich, Budapest, Hungary), citric-acid*H_2O (ACS reagent, ≥99.9%, VWR), sodium chloride (99–100%, Sigma-Aldrich) that were used for hydrolyzation of PSI-based gels into PASP gels. All ^{1}H NMR spectra were obtained using a JEOL SC400 spectrometer (JEOL Ltd., Riken, Tokyo, Japan) operating at 400 MHz. Then, 25 mg of polymer powders were dissolved in 0.6 mL of D_2O in 5 mm NMR tubes. All spectra were recorded at 23.5 °C ± 0.5 °C and tetramethylsilane was used as an internal standard. The pulse angle was 45°, and a 2 s delay was applied with 8 kHz spectral width, while 16 K data points and 16 scans were done at each measurement. To evaluate spectra, the ACD/Labs NMR software was used.

4.3. Preparation and Characterization of DA Containing PASP-Based Hydrogels

To prepare DA-containing hydrogels, PSI-DA polymers were crosslinked with 1,4-diaminobutane (DAB) and cystamine (CYS) according to our previously published method [8,12,15], where pure PSI was used instead of PSI-DA polymers. The reaction steps can be seen in Figure 6. To form thiolated PASP hydrogels, PSI-DA gels were treated with pH = 8 imidazole buffer, and afterwards with pH = 8 0.1M dithiothreitol (DTT) solution (≥99%, Sigma). For the cell experiments, the gel samples were treated with phosphate-buffered saline (PBS) (pH = 7.5, c = 150 mM) (Sigma Aldrich). Since the PSI was modified with different amounts of DA (statistically every 10th, 20th, and 40th monomer was modified with dopamine), the dopamine content of the hydrogels was indicated in their abbreviation PASP-DA$_X$, where X shows the molar ratio of the modified monomer units compared to the whole number of monomers. The control hydrogels (DA$_0$) were not modified with DA, but they contained the same amount of crosslinkers and thiol side-chains as the DA-modified hydrogels. The details can be seen in the Supplementary Information (Supplementary Information Sections S2 and S3 and Figure S1).

To determine the pore size of the hydrogels, the samples were freeze-dried and investigated by scanning electron microscopy (SEM, ZEISS, Budaörs, Hungary). Microscopic

images were taken using a ZEISS EVO 40 XVP scanning electron microscope equipped with an Oxford INCA X-ray spectrometer (EDS, Oxford Instruments, Abingdon, UK). The applied accelerating voltage was 20 kV. The samples were fixed on a special conductive sticker. Before the examination, the samples were sputter-coated with palladium in a thickness of 20–30 nm with a 2SPI Sputter Coating System. The average pore size of the samples was determined by the Fiji (ImageJ v1.53) image analysis program from 20 parallel measurements.

The chemical structure of the hydrogels was investigated by Fourier transform infrared spectroscopy (FTIR, JASCO, Budapest, Hungary) according to the method described in our previous paper [14].

4.4. Determination of the DA Content of the PASP Hydrogels

To determine the released amount of dopamine, rectangular gel films were immersed into pH = 8 imidazole-based buffer and after 1 day the UV absorbance was measured by an Agilent 8453 spectrophotometer (Agilent, Budapest, Hungary) at 280 nm. Following the measurement, the buffer was changed, and 24 h later the absorbance was measured again. The amount of the released dopamine was determined by using a calibration curve (Supplementary Section S4—Figure S2).

4.5. Culturing of PDLCs and SH-SY5Y Cells

PDLCs were obtained from impacted human wisdom teeth removed at the Department of Dentoalevolar Surgery of the Semmelweis University (Budapest, Hungary) under ethical guidelines approved by the Ethical Committee of the Hungarian Medical Research Council. This study was approved by the Semmelweis University Regional and Institutional Committee of Science and Research Ethics, the number of the ethical permissions are 17458/2012/EKU and 25459/2019/EKU. Isolation of PDLCs was performed according to our previously published protocol [15,81].

The PDLCs were cultured in Minimal Essential Medium Alpha (αMEM, Gibco, Thermo Fisher, Waltham, USA) supplemented with 10% fetal bovine serum (FBS, Gibco), 2 mM L-glutamine (Gibco), 100 units/mL penicillin and 100 mg/mL streptomycin (Gibco).

The SH-SY5Y human neuroblastoma cell line was purchased from Sigma-Aldrich (Budapest, Hungary) and maintained according to the manufacturer's protocol. The growth medium of these cells consisted of a 1:1 mixture of Eagle's MEM and Ham's F12 medium supplemented with 15% FBS (Gibco), 2 mM L-glutamine (Gibco), 100 units/mL penicillin, and 100 mg/mL streptomycin (Gibco), as well as 1% non-essential amino acids (NEAA, Gibco).

4.6. Cell Viability Assay

Before the cell seeding, hydrogel discs were incubated in the cell culture medium for 2 h with a medium change after 1 h. Subsequently, the gel discs were placed into the appropriate cell culture plates and sterilized by UV irradiation for 1 h.

For measuring cell viability, gel discs with a diameter of 6 mm were placed into Nunclon Sphera 96-well microplates with surface treatment allowing very low cell attachment (Nunc, Roskilde, Denmark). Then, 20,000 PDLCs in 200 μL culture medium were seeded on each gel disc. In case of the SH-SY5Y cell line, 10,000 cells were seeded in 200 μL culture medium on each gel disc since we observed that this cell type does not tolerate high cell density. With each gel type, 5 parallel experiments were carried out and the whole experiment was repeated 3 times with new cell cultures of both cell types. Cell viability was assessed after 1-, 4-, 7-, and 14-day-long cultivation on the gel discs using the cell proliferation reagent WST-1 (Roche, Basel, Switzerland) as we described recently [8].

4.7. Cell Morphological Studies

For the investigation of cellular morphology, 40,000 PDLCs or 20,000 SH-SY5Y cells in 800 μL culture medium were seeded on gel discs with a diameter of 10 mm placed into

24-well plates (Sigma-Aldrich, St. Louis, MO, USA). After 1, 4, 7, and 14 days, the cell cultures were observed under a phase-contrast microscope (Nikon Eclipse TS100, Nikon, Tokyo Japan) with a $10\times$ objective. Photomicrographs were taken with a high-performance CCD camera (COHU, USA) applying the Scion image software.

To visualize the 3-dimensional distribution of the cells in the hydrogels, Vybrant DiD (Molecular Probes, Thermo Fisher, Waltham, MA, USA) labeling and 2 photon microscopy were applied according to our previous paper [8].

4.8. Analysis of the Two-Photon Microscopic Images

To determine the penetration depth of the cells in the hydrogel matrices, image analysis was carried out using the Python (version 3.7.6) Programming Language. First, color deconvolution was used on the microscopic image stacks to reduce the effects of fluorescence crosstalk and create an image stack containing only the hydrogel without the cells. Small bright imaging artifacts were removed using the outlier removal algorithm of NIH ImageJ implemented in python. The surface of the gel was estimated by finding the depth value (z distance) corresponding to the half-maximum intensity point for all pixels in the (x, y) plane. A third-degree polynomial was fitted to the resulting surface depth map to estimate the shape of the original hydrogel surface before the cells were applied. The difference between the depth map and this estimated original surface corresponds to the effect of the cellular penetration on the shape of the hydrogel surface. This penetration image was calculated and after Gaussian smoothing and subtracting its mode (which acts as an estimate for zero depth) was used for further processing and analysis as follows. Negative peaks with a depth of at least 5 μm were found using the h_minima function in the scikit-image python package [82]. Depth values and peak prominences were also calculated for each peak. Areas near the edges of the images with very low signal-to-noise ratios were excluded using a binary mask. Histograms of peak depths, prominences, and penetration image values were constructed. 3D Slicer 4.10.2 [83] was used to create 3D rendered images from the image stacks to further visualize the hydrogel surface along with the cells.

4.9. Statistical Analysis

Statistical evaluation of the viability data was carried out applying the STATISTICA 10 software using Kruskal-Wallis non-parametric ANOVA followed by median test. In the case of $p < 0.05$, a difference was considered as statistically significant.

Supplementary Materials: The following supporting information can be downloaded at: https://www.mdpi.com/article/10.3390/gels8020065/s1, Table S1. Applied amount of the chemicals in PSI-DA synthesis; Figure S1. PSI-based gel films with different dopamine content; Figure S2. UV-VIS calibration curve of DA release measurement in ph8 buffer solution; Figure S3. Upper view, cross-sectional view, and three-dimensional images were constructed from Z-stack measurements of a poly(aspartic acid)-based hydrogel. The hydrogel was treated with the same experimental method used in cell experiments. Scale bars indicate 0.1 mm; Figure S4. PDLC distribution (red) on the different hydrogel surfaces (green) on day 7 and 14. Upper view, cross-sectional view, and three-dimensional images were constructed from Z-stack measurements of the hydrogels. Scale bars indicate 0.1 mm; Figure S5. SH-SY5Y cell distribution (red) on the different hydrogel surfaces (green) on day 7 and 14. Upper view, cross-sectional view, and three-dimensional images were constructed from Z-stack measurements of the hydrogels. Scale bars indicate 0.1 mm.

Author Contributions: Conceptualization, D.J.; methodology, D.J., E.E.K., K.T. and D.B.; software, D.S.; investigation, D.J.; resources, G.V., M.Z. and A.J.-H.; data curation, D.J.; writing—original draft preparation, D.J., K.T., A.J.-H. and K.S.N.; writing—review and editing, D.J., A.J.-H. and K.S.N.; visualization, D.J.; supervision, A.F., G.V., M.Z., A.J.-H. and K.S.N. All authors have read and agreed to the published version of the manuscript.

Institutional Review Board Statement: Not applicable.

Informed Consent Statement: Not applicable.

Conflicts of Interest: The authors declare no conflict of interest.

References

1. Berthiaume, F.; Maguire, T.J.; Yarmush, M.L. Tissue Engineering and Regenerative Medicine: History, Progress, and Challenges. *Annu. Rev. Chem. Biomol. Eng.* **2011**, *2*, 403–430. [CrossRef] [PubMed]
2. Wobma, H.; Vunjak-Novakovic, G. Tissue Engineering and Regenerative Medicine 2015: A Year in Review. *Tissue Eng. Part B Rev.* **2016**, *22*, 101–113. [CrossRef] [PubMed]
3. Bajaj, P.; Schweller, R.M.; Khademhosseini, A.; West, J.L.; Bashir, R. 3D Biofabrication Strategies for Tissue Engineering and Regenerative Medicine. *Annu. Rev. Biomed. Eng.* **2014**, *16*, 247–276. [CrossRef]
4. Abdelfattah, M.I.; Nasry, S.A.; Mostafa, A.A. Characterization and Cytotoxicity Analysis of a Ciprofloxacin Loaded Chitosan/Bioglass Scaffold on Cultured Human Periodontal Ligament Stem Cells: A Preliminary Report. *Maced. J. Med. Sci.* **2016**, *4*, 461–467. [CrossRef] [PubMed]
5. Drury, J.L.; Mooney, D.J. Hydrogels for Tissue Engineering: Scaffold Design Variables and Applications. *Biomaterials* **2003**, *24*, 4337–4351. [CrossRef]
6. Ling-Ling, E.; Xu, W.H.; Feng, L.; Liu, Y.; Cai, D.Q.; Wen, N.; Zheng, W.J. Estrogen Enhances the Bone Regeneration Potential of Periodontal Ligament Stem Cells Derived from Osteoporotic Rats and Seeded on Nano-Hydroxyapatite/Collagen/Poly(L-Lactide). *Int. J. Mol. Med.* **2016**, *37*, 1475–1486. [CrossRef]
7. Jo, B.S.; Lee, Y.; Suh, J.S.; Park, Y.S.; Lee, H.J.; Cho, J.; Lee, G.; Chung, C.P.; Park, K.D.; Jeong, Y. A Novel Calcium-Accumulating Peptide/Gelatin in Situ Forming Hydrogel for Enhanced Bone Regeneration. *J. Biomed. Mater. Res.* **2018**, *106*, 1–30. [CrossRef] [PubMed]
8. Juriga, D.; Nagy, K.; Jedlovszky-Hajdú, A.; Perczel-Kovách, K.; Chen, Y.M.; Varga, G.; Zrínyi, M. Biodegradation and Osteosarcoma Cell Cultivation on Poly(Aspartic Acid) Based Hydrogels. *ACS Appl. Mater. Interfaces* **2016**, *8*, 23463–23476. [CrossRef]
9. Discher, D.E.; Mooney, D.J.; Zandstra, P.W. Growth Factors, Matrices, and Forces Combine and Control Stem Cells. *Science* **2009**, *324*, 1673–1677. [CrossRef]
10. Svobodová, J.; Proks, V.; Karabiyik, Ö.; Koyuncu, A.C.C.; Köse, G.T.; Rypáček, F.; Studenovská, H. Poly(Amino Acid)-Based Fibrous Scaffolds Modified with Surface-Pendant Peptides for Cartilage Tissue Engineering. *J. Tissue Eng. Regen. Med.* **2017**, *11*, 831–842. [CrossRef]
11. Adelnia, H.; Tran, H.D.N.; Little, P.J.; Blakey, I.; Ta, H.T. Poly(Aspartic Acid) in Biomedical Applications: From Polymerization, Modification, Properties, Degradation, and Biocompatibility to Applications. *ACS Biomater. Sci. Eng.* **2021**, *7*, 2083–2105. [CrossRef]
12. Zrinyi, M.; Gyenes, T.; Juriga, D.; Kim, J. Acta Biomaterialia Volume Change of Double Cross-Linked Poly(Aspartic Acid) Hydrogels Induced by Cleavage of One of the Crosslinks Thermal Treatment. *Acta Biomater.* **2013**, *9*, 5122–5131. [CrossRef]
13. Molnar, K.; Juriga, D.; Nagy, P.M.; Sinko, K.; Jedlovszky-Hajdu, A.; Zrinyi, M. Electrospun Poly(Aspartic Acid) Gel Scaffolds for Artificial Extracellular Matrix. *Polym. Int.* **2014**, *63*, 1608–1615. [CrossRef]
14. Juriga, D.; Sipos, E.; Heged, O.; Varga, G.; Zrínyi, M.; Nagy, K.S.; Jedlovszky-hajdú, A. Fully Amino Acid-Based Hydrogel as Potential Scaffold for Cell Culturing and Drug Delivery. *Beilstein J. Nanotechnol.* **2019**, *10*, 2579–2593. [CrossRef] [PubMed]
15. Hegedus, O.; Juriga, D.; Sipos, E.; Voniatis, C.; Juhász, Á.; Idrissi, A.; Zrínyi, M.; Varga, G.; Jedlovszky-Hajdú, A.; Nagy, K.S. Free Thiol Groups on Poly(Aspartamide) Based Hydrogels Facilitate Tooth-Derived Progenitor Cell Proliferation and Differentiation. *PLoS ONE* **2019**, *14*, e0226363. [CrossRef] [PubMed]
16. Németh, C.; Gyarmati, B.; Abdullin, T.; László, K.; Szilágyi, A. Poly(Aspartic Acid) with Adjustable PH-Dependent Solubility. *Acta Biomater.* **2017**, *49*, 486–494. [CrossRef] [PubMed]
17. Németh, C.; Szabó, D.; Gyarmati, B.; Gerasimov, A.; Varfolomeev, M.; Abdullin, T.; László, K.; Szilágyi, A. Effect of Side Groups on the Properties of Cationic Polyaspartamides. *Eur. Polym. J.* **2017**, *93*, 805–814. [CrossRef]

18. Juriga, D.; Laszlo, I.; Ludanyi, K.; Klebovich, I.; Chae, C.H.; Zrinyi, M. Kinetics of Dopamine Release from Poly(Aspartamide)-Based Prodrugs. *Acta Biomater.* **2018**, *76*, 225–238. [CrossRef] [PubMed]
19. Foley, P.B. Dopamine in Psychiatry: A Historical Perspective. *J. Neural Transm.* **2019**, *126*, 473–479. [CrossRef] [PubMed]
20. Papalini, S.; Beckers, T.; Vervliet, B. Dopamine: From Prediction Error to Psychotherapy. *Transl. Psychiatry* **2020**, *10*, 164. [CrossRef]
21. Lee, J.S.; Yi, J.K.; An, S.Y.; Heo, J.S. Increased Osteogenic Differentiation of Periodontal Ligament Stem Cells on Polydopamine Film Occurs via Activation of Integrin and PI3K Signaling Pathways. *Cell. Physiol. Biochem.* **2014**, *34*, 1824–1834. [CrossRef] [PubMed]
22. Han, L.; Lu, X.; Liu, K.; Wang, K.; Fang, L.; Weng, L.T.; Zhang, H.; Tang, Y.; Ren, F.; Zhao, C.; et al. Mussel-Inspired Adhesive and Tough Hydrogel Based on Nanoclay Confined Dopamine Polymerization. *ACS Nano* **2017**, *11*, 2561–2574. [CrossRef]
23. Cencer, M.; Liu, Y.; Winter, A.; Murley, M.; Meng, H.; Lee, B.P. Effect of PH on the Rate of Curing and Bioadhesive Properties of Dopamine Functionalized Poly(Ethylene Glycol) Hydrogels. *Biomacromolecules* **2014**, *15*, 2861–2869. [CrossRef] [PubMed]
24. Cui, J.; Iturri, J.; Paez, J.; Shafiq, Z.; Serrano, C.; d'Ischia, M.; del Campo, A.; Shafi, Z.; Serrano, C.; Ischia, M.; et al. Dopamine-Based Coatings and Hydrogels: Toward Substitution-Related Structure–Property Relationships. *Macromol. Chem. Phys.* **2014**, *215*, 2403–2413. [CrossRef]
25. Scognamiglio, F.; Travan, A.; Borgogna, M.; Donati, I.; Marsich, E.; Bosmans, J.W.A.M.; Perge, L.; Foulc, M.P.; Bouvy, N.D.; Paoletti, S. Enhanced Bioadhesivity of Dopamine-Functionalized Polysaccharidic Membranes for General Surgery Applications. *Acta Biomater.* **2016**, *44*, 232–242. [CrossRef] [PubMed]
26. Baudry, A.; Alleaume-Butaux, A.; Dimitrova-Nakov, S.; Goldberg, M.; Schneider, B.; Launay, J.M.; Kellermann, O. Essential Roles of Dopamine and Serotonin in Tooth Repair: Functional Interplay between Odontogenic Stem Cells and Platelets. *Stem Cells* **2015**, *33*, 2586–2595. [CrossRef]
27. Wang, W.; Zhao, L.; Bai, F.; Zhang, T.; Dong, H.; Liu, L. The Protective Effect of Dopamine against OGD/R Injury-Induced Cell Death in HT22 Mouse Hippocampal Cells. *Environ. Toxicol. Pharmacol.* **2016**, *42*, 176–182. [CrossRef]
28. Varella, M.H.; De Mello, F.G.; Linden, R. Evidence for an Antiapoptotic Role of Dopamine in Developing Retinal Tissue. *J. Neurochem.* **1999**, *73*, 485–492. [CrossRef]
29. Bozzi, Y.; Borrelli, E. Dopamine in Neurotoxicity and Neuroprotection: What Do D2 Receptors Have to Do with It? *Trends Neurosci.* **2006**, *29*, 167–174. [CrossRef]
30. Seo, B.; Miura, M.; Gronthos, S.; Bartold, P.M.; Batouli, S.; Brahim, J.; Young, M.; Robey, P.G.; Wang, C.; Shi, S. Investigation of Multipotent Postnatal Stem Cells from Human Periodontal Ligament. *Natl. Libr. Med.* **2004**, *369*, 149–155. [CrossRef]
31. Ivanovski, S.; Gronthos, S.; Shi, S.; Bartold, P.M. Stem Cells in the Periodontal Ligament. *Oral Dis.* **2006**, *12*, 358–363. [CrossRef] [PubMed]
32. Gay, I.C.; Chen, S.; MacDougall, M. Isolation and Characterization of Multipotent Human Periodontal Ligament Stem Cells. *Orthod. Craniofac. Res.* **2007**, *10*, 149–160. [CrossRef] [PubMed]
33. Gronthos, S.; Mankani, M.; Brahim, J.; Robey, P.G.; Shi, S. Postnatal Human Dental Pulp Stem Cells (DPSCs) in Vitro and in Vivo. *Proc. Natl. Acad. Sci. USA* **2000**, *97*, 13625–13630. [CrossRef]
34. Zhen, L.; Liu, H. Differentiation of Human Periodontal Ligament Stem Cells into Neuron-like Cells in Vitro. *West China J. Stomatol.* **2009**, *27*, 71–74.
35. Menicanin, D.; Mrozik, K.M.; Wada, N.; Marino, V.; Shi, S.; Bartold, P.M.; Gronthos, S. Periodontal-Ligament-Derived Stem Cells Exhibit the Capacity for Long-Term Survival, Self-Renewal, and Regeneration of Multiple Tissue Types in Vivo. *Stem Cells Dev.* **2014**, *23*, 1001–1011. [CrossRef]
36. Ansari, S.; Diniz, I.M.; Chen, C.; Sarrion, P.; Tamayol, A.; Wu, B.M.; Moshaverinia, A. Human Periodontal Ligament- and Gingiva-Derived Mesenchymal Stem Cells Promote Nerve Regeneration When Encapsulated in Alginate/Hyaluronic Acid 3D Scaffold. *Adv. Healthc. Mater.* **2017**, *6*, 1–10. [CrossRef]
37. Moshaverinia, A.; Xu, X.; Chen, C.; Ansari, S.; Zadeh, H.H.; Snead, M.L.; Shi, S. Application of Stem Cells Derived from the Periodontal Ligament Orgingival Tissue Sources for Tendon Tissue Regeneration. *Biomaterials* **2014**, *35*, 2642–2650. [CrossRef]
38. Fraser, D.; Nguyen, T.; Benoit, D.S.W. Matrix Control of Periodontal Ligament Cell Activity Via Synthetic Hydrogel Scaffolds. *Tissue Eng. Part A* **2021**, *27*, 733–747. [CrossRef] [PubMed]
39. Kovalevich, J.; Langford, D. Considerations for the Use of SH-SY5Y Neuroblastoma Cells in Neurobiology. *Methods Mol. Biol.* **2013**, *1078*, 9–21. [CrossRef]
40. Xicoy, H.; Wieringa, B.; Martens, G.J.M. The SH-SY5Y Cell Line in Parkinson's Disease Research: A Systematic Review. *Mol. Neurodegener.* **2017**, *12*, 10. [CrossRef]
41. Desai, A.; Kisaalita, W.S.; Keith, C.; Wu, Z.Z. Human Neuroblastoma (SH-SY5Y) Cell Culture and Differentiation in 3-D Collagen Hydrogels for Cell-Based Biosensing. *Biosens. Bioelectron.* **2006**, *21*, 1483–1492. [CrossRef] [PubMed]
42. Innala, M.; Riebe, I.; Kuzmenko, V.; Sundberg, J.; Gatenholm, P.; Hanse, E.; Johannesson, S. 3D Culturing and Differentiation of SH-SY5Y Neuroblastoma Cells on Bacterial Nanocellulose Scaffolds. *Artif. Cells Nanomed. Biotechnol.* **2014**, *42*, 302–308. [CrossRef]
43. Lin, C.H.; Nicol, C.J.B.; Cheng, Y.C.; Yen, C.; Wang, Y.S.; Chiang, M.C. Neuroprotective Effects of Resveratrol against Oxygen Glucose Deprivation Induced Mitochondrial Dysfunction by Activation of AMPK in SH-SY5Y Cells with 3D Gelatin Scaffold. *Brain Res.* **2020**, *1726*, 146492. [CrossRef]
44. Gyarmati, B.; Krisch, E.; Szilágyi, A. In Situ Oxidation-Induced Gelation of Poly(Aspartic Acid) Thiomers. *React. Funct. Polym.* **2014**, *84*, 29–36. [CrossRef]

45. Szilágyi, B.Á.; Gyarmati, B.; Horvát, G.; Laki, Á.; Budai-Szűcs, M.; Csányi, E.; Sandri, G.; Bonferoni, M.C.; Szilágyi, A. The Effect of Thiol Content on the Gelation and Mucoadhesion of Thiolated Poly(Aspartic Acid). *Polym. Int.* **2017**, *66*, 1538–1545. [CrossRef]

46. Kim, H.Y.; Kim, N.H.; Lee, S.J.; Song, J.E.; Kwon, S.Y.; Wha, C.J.; Dongwon, L.; Khang, G. Effect of Pore Sizes of PLGA Scaffolds on Mechanical Properties and Cell Behaviour for Nucleus Pulposus Regeneration in Vivo. *Pediatr. Endocrinol. Rev.* **2015**, *13*, 512–520. [CrossRef]

47. Flory, P.J. *Principles of Polymer Chemistry*, 1st ed.; Flory, P.J., Ed.; Cornell University Press: Ithaca, NY, USA, 1953.

48. Horkay, F.; Hecht, A.-M.; Geissler, E. Thermodynamic Interaction Parameters in Polymer Solutions and Gels. *J. Polym. Sci. Part B Polym. Phys.* **1995**, *33*, 1641–1646. [CrossRef]

49. Koshimura, K.; Tanaka, J.; Murakami, Y.; Kato, Y. Effects of Dopamine and L-DOPA on Survival of PC12 Cells. *J. Neurosci. Res.* **2000**, *62*, 112–119. [CrossRef]

50. Zhang, J.; Kravtsov, V.; Amarnath, V.; Picklo, M.J.; Graham, D.G.; Montine, T.J. Enhancement of Dopaminergic Neurotoxicity by the Mercapturate of Dopamine: Relevance to Parkinson's Disease. *J. Neurochem.* **2000**, *74*, 970–978. [CrossRef] [PubMed]

51. Armando, I.; Villar, V.A.M.; Jose, P.A. Dopamine and Renal Function and Blood Pressure Regulation. *Compr. Physiol.* **2011**, *1*, 1075–1117. [CrossRef]

52. Ko, C.-C.; Wang, Z.; Chen, S.; Bai, B.; Lee, D.J.; Diachina, S.; Li, Y.; Wong, S.W.; Tseng, H.C. Dopaminergic Enhancement of Cellular Adhesion in Bone Marrow Derived Mesenchymal Stem Cells (MSCs). *J. Stem Cell Res. Ther.* **2017**, *7*, 395. [CrossRef]

53. Wang, S.; Mou, Z.; Ma, Y.; Li, J.; Li, J.; Ji, X.; Wu, K.; Li, L.; Lu, W.; Zhou, T. Dopamine Enhances the Response of Sunitinib in the Treatment of Drug-Resistant Breast Cancer: Involvement of Eradicating Cancer Stem-like Cells. *Biochem. Pharmacol.* **2015**, *95*, 98–109. [CrossRef] [PubMed]

54. Kadar, K.; Kiraly, M.; Porcsalmy, B.; Molnar, B.; Racz, G.Z.; Blazsek, J.; Kallo, K.; Szabo, E.L.; Gera, I.; Gerber, G.; et al. Differentiation Potential of Stem Cells from Human Dental Origin-Promise for Tissue Engineering. *J. Physiol. Pharmacol.* **2009**, *60* (Suppl. 7), 167–175.

55. Xie, H.R.; Hu, L.S.; Li, G.Y. SH-SY5Y Human Neuroblastoma Cell Line: In Vitro Cell Model of Dopaminergic Neurons in Parkinson's Disease. *Chin. Med. J. Engl.* **2010**, *123*, 1086–1092. [CrossRef] [PubMed]

56. Chen, Q.; Tian, X.; Fan, J.; Tong, H.; Ao, Q. An Interpenetrating Alginate/Gelatin Network for Three-Dimensional (3D) Cell Cultures and Organ Bioprinting. *Molecules* **2020**, *25*, 756. [CrossRef] [PubMed]

57. Entekhabi, E.; Nazarpak, M.H.; Moztarzadeh, F.; Sadeghi, A. Design and Manufacture of Neural Tissue Engineering Scaffolds Using Hyaluronic Acid and Polycaprolactone Nanofibers with Controlled Porosity. *Mater. Sci. Eng. C* **2016**, *69*, 380–387. [CrossRef]

58. Wang, X.; Gu, Z.; Jiang, B.; Li, L.; Yu, X. Surface Modification of Strontium-Doped Porous Bioactive Ceramic Scaffolds via Poly(DOPA) Coating and Immobilizing Silk Fibroin for Excellent Angiogenic and Osteogenic Properties. *Biomater. Sci.* **2016**, *4*, 678–688. [CrossRef]

59. Liu, Y.; Meng, H.; Qian, Z.; Fan, N.; Choi, W.; Zhao, F.; Lee, B.P. A Moldable Nanocomposite Hydrogel Composed of a Mussel-Inspired Polymer and a Nanosilicate as a Fit-to-Shape Tissue Sealant. *Angew. Chem.-Int. Ed.* **2017**, *56*, 4224–4228. [CrossRef]

60. Liu, Y.; Meng, H.; Konst, S.; Sarmiento, R.; Rajachar, R.; Lee, B.P. Injectable Dopamine-Modified Poly(Ethylene Glycol) Nanocomposite Hydrogel with Enhanced Adhesive Property and Bioactivity. *ACS Appl. Mater. Interfaces* **2014**, *6*, 16982–16992. [CrossRef]

61. Akcay, G.; Luttge, R. Stiff-to-Soft Transition from Glass to 3d Hydrogel Substrates in Neuronal Cell Culture. *Micromachines* **2021**, *12*, 165. [CrossRef]

62. Gowda, A.H.J.; Bu, Y.; Kudina, O.; Krishna, K.V.; Bohara, R.A.; Eglin, D.; Pandit, A. Design of Tunable Gelatin-Dopamine Based Bioadhesives. *Int. J. Biol. Macromol.* **2020**, *164*, 1384–1391. [CrossRef]

63. Gong, C.; Lu, C.; Li, B.; Shan, M.; Wu, G. Injectable Dopamine-Modified Poly(α,β-Aspartic Acid) Nanocomposite Hydrogel as Bioadhesive Drug Delivery System Chu. *J. Biomed. Mater. Res. Part A* **2017**, *105*, 1000–1008. [CrossRef] [PubMed]

64. Ellis-Behnke, R.; Jonas, J.B. Redefining Tissue Engineering for Nanomedicine in Ophthalmology. *Acta Ophthalmol.* **2011**, *89*, 108–114. [CrossRef]

65. Hadden, W.J.; Young, J.L.; Holle, A.W.; McFetridge, M.L.; Kim, D.Y.; Wijesinghe, P.; Taylor-Weiner, H.; Wen, J.H.; Lee, A.R.; Bieback, K.; et al. Stem Cell Migration and Mechanotransduction on Linear Stiffness Gradient Hydrogels. *Proc. Natl. Acad. Sci. USA* **2017**, *114*, 5647–5652. [CrossRef]

66. Yamada, K.M.; Sixt, M. Mechanisms of 3D Cell Migration. *Nat. Rev. Mol. Cell Biol.* **2019**, *20*, 738–752. [CrossRef] [PubMed]

67. Dravid, A.; Raos, B.; Aqrawe, Z.; Parittotokkaporn, S.; O'Carroll, S.J.; Svirskis, D. A Macroscopic Diffusion-Based Gradient Generator to Establish Concentration Gradients of Soluble Molecules Within Hydrogel Scaffolds for Cell Culture. *Front. Chem.* **2019**, *7*, 638. [CrossRef]

68. Stocco, E.; Barbon, S.; Lora, L.; Grandi, F.; Sartore, L.; Tiengo, C.; Petrelli, L.; Dalzoppo, D.; Parnigotto, P.P.; Macchi, V.; et al. Partially Oxidized Polyvinyl Alcohol Conduitfor Peripheral Nerve Regeneration. *Sci. Rep.* **2018**, *8*, 604. [CrossRef] [PubMed]

69. Kondaveeti, S.; Semeano, A.T.S.; Cornejo, D.R.; Ulrich, H.; Petri, D.F.S. Magnetic Hydrogels for Levodopa Release and Cell Stimulation Triggered by External Magnetic Field. *Colloids Surf. B Biointerfaces* **2018**, *167*, 415–424. [CrossRef]

70. Santhosh, M.; Choi, J.H.; Choi, J.W. Magnetic-Assisted Cell Alignment within a Magnetic Nanoparticle-Decorated Reduced Graphene Oxide/Collagen 3D Nanocomposite Hydrogel. *Nanomaterials* **2019**, *9*, 1293. [CrossRef]

71. Ashworth, J.C.; Mehr, M.; Buxton, P.G.; Best, S.M.; Cameron, R.E. Optimising Collagen Scaffold Architecture for Enhanced Periodontal Ligament Fibroblast Migration. *J. Mater. Sci. Mater. Med.* **2018**, *29*, 166. [CrossRef]

72. Matsugami, D.; Murakami, T.; Yoshida, W.; Imamura, K.; Bizenjima, T.; Seshima, F.; Saito, A. Treatment with Functionalized Designer Self-Assembling Peptide Hydrogels Promotes Healing of Experimental Periodontal Defects. *J. Periodontal Res.* **2021**, *56*, 162–172. [CrossRef] [PubMed]

73. Meiser, J.; Weindl, D.; Hiller, K. Complexity of Dopamine Metabolism. *Cell Commun. Signal.* **2013**, *11*, 1–18. [CrossRef]

74. Hurd, T.R.; DeGennaro, M.; Lehmann, R. Redox Regulation of Cell Migration and Adhesion. *Trends Cell Biol.* **2012**, *22*, 107–115. [CrossRef] [PubMed]

75. Reczek, C.R.; Chandel, N.S. The Two Faces of Reactive Oxygen Species in Cancer. *Annu. Rev. Cancer Biol.* **2017**, *1*, 79–98. [CrossRef]

76. Bórquez, D.A.; Urrutia, P.J.; Wilson, C.; Van Zundert, B.; Núñez, M.T.; González-Billault, C. Dissecting the Role of Redox Signaling in Neuronal Development. *J. Neurochem.* **2016**, *137*, 506–517. [CrossRef]

77. Assis-de-Lemos, G.; Monteiro, J.; Oliveira-Valença, V.M.; Melo, G.A.; Reis, R.A.d.M.; Rehen, S.K.; Silveira, M.S.; Galina, A. Dopamine Signaling Impairs ROS Modulation by Mitochondrial Hexokinase in Human Neural Progenitor Cells. *Biosci. Rep.* **2021**, *41*, 1–15. [CrossRef] [PubMed]

78. Brenner-Lavie, H.; Klein, E.; Ben-Shachar, D. Mitochondrial Complex I as a Novel Target for Intraneuronal DA: Modulation of Respiration in Intact Cells. *Biochem. Pharmacol.* **2009**, *78*, 85–95. [CrossRef]

79. Rana, D.; Colombani, T.; Mohammed, H.S.; Eggermont, L.J.; Johnson, S.; Annabi, N.; Bencherif, S.A. Strategies to Prevent Dopamine Oxidation and Related Cytotoxicity Using Various Antioxidants and Nitrogenation. *Emergent Mater.* **2019**, *2*, 209–217. [CrossRef]

80. Jedlovszky-Hajdu, A.; Molnar, K.; Nagy, P.M.; Sinko, K.; Zrinyi, M. Preparation and Properties of a Magnetic Field Responsive Three-Dimensional Electrospun Polymer Scaffold. *Colloids Surf. A Physicochem. Eng. Asp.* **2016**, *503*, 79–87. [CrossRef]

81. Nagy, K.; Láng, O.; Láng, J.; Perczel-Kovách, K.; Gyulai-Gaál, S.; Kádár, K.; Kőhidai, L.; Varga, G. A Novel Hydrogel Scaffold for Periodontal Ligament Stem Cells. *Interv. Med. Appl. Sci.* **2018**, *10*, 1–9. [CrossRef]

82. Available online: http://citebay.com/how-to-cite/scikit-image/ (accessed on 1 December 2021).

83. CitingSlicer. Available online: https://www.slicer.org/wiki/CitingSlicer (accessed on 1 December 2021).

MDPI